Technische Universität Darmstadt
Fachbereich Elektro- und Informationstechnik
Institut für Elektrische Energiewandlung

TECHNISCHE UNIVERSITÄT DARMSTADT

Design of a Bearingless Permanent Magnet Synchronous Machine with a Star Point-Connected Axial Active Magnetic Bearing

Zur Erlangung des akademischen Grades Doktor-Ingenieur (Dr.-Ing.)
genehmigte Dissertation

von

Daniel Dietz, M.Sc.
geboren am 27.12.1990
in Limburg an der Lahn

Referent:	Prof. Dr.-Ing. habil. Dr. h.c. Andreas Binder
Korreferent:	o.Univ.-Prof. DI Dr. sc. techn. Wolfgang Amrhein
Tag der Einreichung:	14.09.2021
Tag der mündlichen Prüfung:	14.01.2022

D17
Darmstadt 2022

Dietz, Daniel: Design of a Bearingless Permanent Magnet Synchronous Machine with a Star Point-Connected Axial Active Magnetic Bearing
Darmstadt, Technische Universität Darmstadt
Jahr der Veröffentlichung der Dissertation auf TUprints: 2022
URN: urn:nbn:de:tuda-tuprints-20975
URI: https://tuprints.ulb.tu-darmstadt.de/id/eprint/20975
Tag der mündlichen Prüfung: 14.01.2022

Erklärungen laut Promotionsordnung

§ 8 Abs. 1 lit. c PromO

Ich versichere hiermit, dass die elektronische Version meiner Dissertation mit der schriftlichen Version übereinstimmt.

§ 8 Abs. 1 lit. d PromO

Ich versichere hiermit, dass zu einem vorherigen Zeitpunkt noch keine Promotion versucht wurde.

§ 9 Abs. 1

Ich versichere hiermit, dass die vorliegende Dissertation selbstständig und nur unter Verwendung der angegebenen Quellen verfasst wurde.

§ 9 Abs. 2

Die Arbeit hat bisher noch nicht zu Prüfungszwecken gedient.

Daniel Dietz Darmstadt, den 14.09.2021

Vorwort - Die vorliegende Arbeit habe ich während meiner Zeit am *Institut für Elektrische Energiewandlung* der *TU Darmstadt* in den Jahren 2016 bis 2021 angefertigt.
Sie wurde ermöglicht durch meinen Doktorvater, *Prof. Dr.-Ing. habil. Dr. h.c. Andreas Binder*, der mir frühzeitig sein Vertrauen schenkte und meine Finanzierung von Beginn an sicherstellte. Dafür bedanke ich mich herzlich. Auch bekräftigte er mich von Beginn an darin, im Rahmen der Promotion eine lagerlose Prototypmaschine zu bauen. Der Bau und die Inbetriebnahme dieses Prototyps haben für mich, insbesondere vor dem Hintergrund der zunehmend simulativen Ingenieursarbeit, eine besondere Bedeutung. Auch dafür möchte ich mich bei ihm bedanken.
Meinem Doktorvater bin ich auch zum Dank verpflichtet, da ich unter seiner Anleitung gelernt habe, sinnvoll zwischen wissenschaftlicher Tiefe und ingenieursmäßiger Breite abzuwägen. Darüber hinaus bedanke ich mich für die Unterstützung beim Abfassen der wissenschaftlichen Veröffentlichungen.
Herzlich bedanken möchte ich mich bei Herrn *o.Univ.-Prof. DI Dr. sc. techn. Wolfgang Amrhein*, der sich bereit erklärt hat, das Korreferat für diese Arbeit zu übernehmen.
Inhaltlich knüpft die Arbeit an die meiner Vorgänger, *Tobias Schneider*, *Dr. Gabriel Bergmann* und *Dr. Gael Messager* an. Mein Dank gilt vor allem *Dr. Gael Messager*, der mir – oftmals in seiner Freizeit – eine Einführung in die Thematik der lagerlosen Maschinen gegeben und mich auch in technischen Fragestellungen beraten hat. Ich möchte betonen, dass die Idee des nullstromgespeisten Axiallagers initial auf ihn zurückging. Er hat damit meine Begeisterung für das Thema geweckt.
Der Bau des Prototyps wurde seitens der *KEBA Industrial Automation Germany GmbH* unterstützt. Dafür bedanke ich mich bei Herrn *Dr. Christian Redemann* und bei Herrn *Timo Michel*. Die Realisierung des Prototyps gelang nicht zuletzt mit Hilfe der Arbeit unserer technischen Mitarbeiter *Klaus Gütlich* und *Andreas Fehringer*. Nur durch deren immerwährende Hilfsbereitschaft konnte der Prototyp erfolgreich fertiggestellt werden. Vielen Dank dafür. Ich danke der *Deutschen Forschungsgemeinschaft DFG* für die finanzielle Unterstützung unter der Projektnummer BI 701/22/1.
Der aus meiner Sicht wichtigste Faktor zur Steigerung der Qualität einer wissenschaftlichen Arbeit ist der persönliche Austausch unter fachlich nahestehenden Kollegen. Deshalb bin ich dankbar für die außerordentliche Kollegialität, die ich mit den wissenschaftlichen Mitarbeitern am *Institut für Elektrische Energiewandlung* teilen konnte. Im Einzelnen möchte ich mich bedanken bei Herrn *Dr. Marcel Lehr* und Herrn

Dr. Kersten Reis, die mich durch die Betreuung der Abschlussarbeiten im Studium für die elektrischen Maschinen begeistert haben, und bei Herrn *Dr. Björn Deusinger*, der mich sowohl hinsichtlich der IT als auch in der Messtechnik stark unterstützt hat. Einen nicht messbaren, aber sehr wichtigen Beitrag zur Arbeit hat der Austausch mit meinen Kollegen *Robin Köster*, *Nicolas Erd*, *Sascha Neusüs*, *Alexander Möller*, *Dr. Martin Weicker*, *Maximilian Clauer*, *Dr. Jeongki An*, *Dr. Xing Li*, *Omid Safdarzadeh* und *Dr. Yves Gemeinder* geleistet. Neben den interessanten fachlichen Diskussionen denke ich gerne an unsere privaten Aktivitäten zurück. Sie alle sind Kollegen und Freunde gleichermaßen und dafür bin ich sehr dankbar.

Allen Studierenden, die ihre Abschlussarbeit unter meiner Betreuung verfasst haben, danke ich, weil sie zur Reflektierung des Dissertationsinhaltes beigetragen haben. Im Einzelnen sind dies: *Nils Rickertsen*, *Lukas Moser*, *Sebastian Pilatus*, *Stefan Tölle*, *Hendrik Hoffmann*, *Emre Akkus*, *Alexander Möller*, *Alexander Bäumle*, *Linus Groß*, *Marcel Bock* und *Felix Hilgert*.

Nicht unerwähnt lassen möchte, dass ich mir im Rahmen meiner Werksstudententätigkeit bei der *Continental Teves AG & Co. oHG* in den Jahren 2007 bis 2015 unter der Leitung von *Dr. Martin Semsch* und Anleitung von *Rainer Fröhlich* viele praktische Fertigkeiten aneignen konnte, die mir bei der Umsetzung der Promotion hilfreich waren. Danke dafür.

Auch bei meinen Eltern, *Cornelia* und *Udo Dietz* möchte ich mich bedanken. Sie gaben mir jederzeit den nötigen Rückhalt und den Ausgleich, der für mein Studium und die Promotion ebenso wichtig war.

Von Herzen danke ich mich meiner Frau *Friederike*, die mich auf diesem gemeinsamen Weg durch Höhen und Tiefen uneingeschränkt unterstützte, mir den Rücken freihielt und ihn stärkte. Erst dadurch ermöglichte sie mir überhaupt erst die intensive Beschäftigung mit dieser Arbeit.

Daniel Dietz — Bad Mergentheim im März 2021

Aufgabenstellung und Resultat - Lagerlose Maschinen können überall dort eingesetzt werden, wo bislang herkömmlich magnetgelagerte Systeme zum Einsatz kommen. Aufgrund der Komponentenreduzierung, der axialen Verkürzung des Antriebs und des Einsatzes von 3-phasigen Umrichtermodulen stellen sie eine attraktive Lösung dar.
Bislang ist der flächendeckende industrielle Einsatz lagerloser Maschinen jedoch ausgeblieben. Zwei wesentliche Gründe dafür sind: Die Kosten eines magnetgelagerten Antriebs konnten durch den Einsatz eines lagerlosen Motors nicht wesentlich gesenkt werden und die Baugröße lagerloser Motoren ist aufgrund von parasitären Rotor-Störkräften auf niedrige elektromagnetische Ausnutzungen bzw. bislang auf die Leistungsklasse < 60 kW beschränkt.
Diese Arbeit soll die beiden Aspekte aufgreifen und einen Beitrag dazu leisten, die Attraktivität lagerloser Maschinen zu steigern. Daraus ergeben sich explizit zwei Untersuchungsfelder, die im Rahmen dieser Arbeit behandelt werden sollen.

Reduktion der Systemkosten durch Reduktion der Anzahl an leistungselektronischen Stellelementen
Das für diesen Maschinentypus notwendige axiale aktive Magnetlager soll mit einem Nullstrom aus den Sternpunkten der Wicklung der lagerlosen Maschine gespeist werden, sodass der ansonsten notwendige 4-Quadrantensteller entfallen kann. Folgende Fragen sollen beantwortet werden:

- Ist eine Nullstromspeisung für magnetgelagerte Antriebe als Ersatz für den 4-Quadrantensteller geeignet? Die Eignung soll an einer permanentmagneterregten, lagerlosen Maschine mit 1 kW Nennleistung bei 60000 min^{-1} validiert werden.
- Inwiefern beeinflussen sich innerhalb der lagerlosen Maschine die 3-phasigen Ströme zur Drehmoment- und Tragkrafterzeugung und der Nullstrom zur Speisung des axialen Magnetlagers?
- Inwiefern beeinflussen sich umrichterseitig die 3-phasigen Wechselspannungen zur Drehmoment- und Tragkrafterzeugung und die Spannung zur Speisung des axialen Magnetlagers bei gegebener Zwischenkreisspannung?

Reduktion der Störkräfte auf den Rotor
Störkräfte auf den Rotor entstehen vor allem aufgrund der Rückwirkung der Rotorwirbelströme auf das von der Tragwicklung erregte Luftspaltfeld (Wirbelstromeffekt) und durch die Interaktion des drehmomentbildenden Stator-Luftspaltfelds mit dem tragkraftbildenden Stator-Luftspaltfeld (Überlagerungseffekt). Folgende Fragen sollen beantwortet wer-

den, wobei der Fokus auf der wirbelstromverursachten Störkraft liegt:

- Wie können der Wirbelstrom- und der Überlagerungseffekt rechnerisch und messtechnisch am Prototypen quantifiziert werden?
- Welche geometrischen bzw. elektromagnetischen Größen beeinflussen den Wirbelstrom- bzw. Überlagerungseffekt?
- Welchen Einfluss hat die Wahl des Permanentmagnetmaterials auf den Wirbelstromeffekt? Ein messtechnischer Vergleich soll anhand der Prototypmaschine mit einem Sm_2Co_{17}- und einem NdFeB-Läufer im selben Stator erfolgen.
- Welche Auswirkungen haben der Wirbelstrom- und der Überlagerungseffekt auf die Rotor-Positionsregelung der lagerlosen Maschine?
- Durch welche konstruktiven Maßnahmen können die beiden Effekte reduziert werden, sodass die elektromagnetische Ausnutzung und die Maschinengröße erhöht werden können?

Erkenntnisse aus der Untersuchung der Nullstromspeisung des Axial-Magnetlagers:

- Messungen an der Prototyp-Maschine und Simulationen in der *Simulink*-Umgebung zeigen: Eine Nullstromspeisung weist eine vergleichbare Dynamik in der Rotorpositionsregelung – im Vergleich zur herkömmlichen Vollbrückenspeisung – auf, solange der Umrichter nicht nahe seiner Spannungsgrenze betrieben wird.
- Finite-Elemente-Simulationen zeigen: Die Nullstromspeisung ruft innerhalb des Aktivteils der lagerlosen Maschine keine nennenswerten Effekte hervor. Das durch die Nullstromspeisung erregte, stehende Luftspaltfeld ist von vernachlässigbar kleiner Amplitude. Deshalb ändert sich auch der magnetische Sättigungszustand der Maschine nicht. Auch die Erhöhung der Stromwärmeverluste ist vernachlässigbar. In der Prototypmaschine geht durch die gewählte Wicklungstopologie kein magnetisches Luftspaltfeld von der Nullstromspeisung aus.
- Simulativ wurden zwei Modulationsverfahren verglichen: Eine Raumzeiger- und eine trägersignalbasierte Pulsweitenmodulation. Die Wahl eines geeigneten Modulationsverfahrens ermöglicht, entweder die Erzeugung eines 3-phasigen Spannungssystems oder die der Nullspannung zu priorisieren. Wird eine Priorisierung – etwa die Erzeugung des 3-phasigen Spannungssystems – gewählt, ergeben sich keine modulationsbedingten Einkopplungen in Form von zusätzlichen Spannungsoberschwingungen vom Nullspannungs- auf das 3-phasige Spannungssystem. Bei Betrieb an der Umrichterspannungsgrenze kann jedoch

keine Spannung mehr für das Nullstromsystem gestellt werden.
Wird wie beim gebauten Prototypmotor keine Priorisierung vorgenommen, besteht für beide Spannungssysteme ein lineares Verhalten zwischen Referenz- und Ausgangsspannung unterhalb der Spannungsgrenze. Oberhalb der Spannungsgrenze besteht ein nicht-lineares Verhalten. In diesem nicht-linearen Bereich kommt es zu $3 \cdot f_s$-frequenten Spannungsoberschwingungen in der Axiallagerspannung und zu $2 \cdot f_s$-frequenten Schwingungen in der Strangspannung des 3-phasigen Systems. Messungen und Simulationen zeigen, dass beide Schwingungen das Schweben des Rotors aufgrund seiner mechanischen Trägheit nicht gefährden.

Erkenntnisse aus der Untersuchung des Wirbelstrom- bzw. Überlagerungseffekts:

- Zur Berechnung der Störkräfte auf den Rotor liefert eine zweidimensionale, lineare analytische Feldberechnung aufgrund der zu vernachlässigenden magnetischen Sättigung belastbare Ergebnisse, wenn der axiale Endeffekt der Wirbelstromschleifen mit Hilfe einer effektiven elektrischen Leitfähigkeit berücksichtigt wird. Ohne diese Anpassung ist eine Worst-Case-Abschätzung möglich. Messtechnisch können die Störkräfte bei zentrischer Rotorposition aus dem der Tragkraft proportionalen Tragstrom bestimmt werden.
- Messungen, Finite-Elemente-Simulationen und analytische Berechnungen zeigen: Der wirbelstrombedingte Fehlwinkel der Rotor-Tragkraft ist nahezu linear von der Rotordrehzahl (= Schlupffrequenz der Tragfeldwelle) und der effektiven elektrischen Leitfähigkeit der Permanentmagnete abhängig, da die Wirbelströme im Permanentmagneten resistiv begrenzt sind. Folgende Faktoren erhöhen die wirbelstrombedingten Störkräfte: Ein großes Verhältnis aus Bohrungsdurchmesser zu Tragfeldpolteilung (tieferes Eindringen des Tragfelds in die Rotorbereiche), eine hohe elektrische Leitfähigkeit der Permanentmagnete und ein hohe Rotordrehzahl. Folgende Faktoren erhöhen die Störkräfte aufgrund des Überlagerungseffekts: Ein hoher Strombelag der Antriebswicklung (abhängig vom gewählten Kühlsystem und der gewählten Permanentmagneterregung bzw. -höhe) und eine niedrige Polpaarzahl (erhöhte Ankerrückwirkung).
- Durch Simulationen und Berechnungen weitgehend bestätigte Messungen an einem Sm_2Co_{17}- und an einem NdFeB-Läufer zeigen: Der Wirbelstrom- und Überlagerungseffekt ist für die gebaute Prototypmaschine aufgrund der geringen Abmessungen vernachlässigbar. Der wirbelstrombedingte Tragkraft-Fehlwinkel ist pro-

portional zur elektrischen Leitfähigkeit des Permanentmagnetmaterials.

- Anhand von analytischen Berechnungen und Zeitbereichssimulationen in *Simulink* wird gezeigt: Der Wirbelstromeffekt führt aufgrund seiner Drehzahlabhängigkeit zu einer drehzahlabhängigen Veränderung der Eigenwerte der Starrkörpereigenbewegungen des Rotors. Der Überlagerungseffekt führt zu einer antriebsstromproportionalen Verschiebung der Eigenwerte. Im motorischen Betrieb wirken die Störkräfte einander entgegen. Im generatorischen Betrieb, d.h. bei negativem Antriebsstrom, addieren sich die Störkräfte konstruktiv. Die Verschiebung der Eigenwerte kann zur Instabilität der Positionsregelung führen. Die Frage der maximal zulässigen Störkraft kann nur unter Berücksichtigung der rotordynamischen Eigenschaften beantwortet werden.
- Die Störkräfte treten verstärkt bei großen Bohrungsdurchmessern und niedriger Polzahl auf. Folgende Maßnahmen können zur Reduktion der Störkräfte getroffen werden: Eine Erhöhung der Tragfeldpolpaarzahl (geringeres Eindringen des Tragfelds in den Rotor), eine Vergrößerung der Permanentmagnethöhe (Reduktion des Statorstrombelags bei gleicher Ausnutzung) und eine Segmentierung der Permanentmagnete (Reduktion der effektiven elektrischen Leitfähigkeit)). Zur Erhöhung der Abgabeleistung kann die Aktivlänge erhöht werden, falls die Biegeeigenfrequenzen des Rotors ausreichend hoch sind.

Unter Berücksichtigung dieser Auslegungsrichtlinien kann das Prinzip der lagerlosen Maschine auf hochausgenutzte Maschinen im 100 kW-Bereich angewendet werden. Durch die Anwendung einer Nullstromspeisung für eine axiale Magnetlagerung kann die Anzahl der leistungselektronischen Komponenten reduziert werden.

Task and Outline - Bearingless machines can be used in all those applications, which up to now have been well suited for common active magnetic bearings. Due to the reduction of system components, due to the axial shortening of the machine and due the use of standard 3-phase inverter modules bearingless concepts are an attractive solution.
However, an extensive industrial use of bearingless motors has not been established, yet. Two of the main reasons for that are: The costs of a magnetically levitated drive could not considerably be reduced by the use of bearingless motors, and the size of bearingless machines is constrained nowadays to lower electromagnetic utilization values and power classes < 60 kW due to parasitic rotor forces.
This work addresses both aspects and aims at enhancing the attractiveness of bearingless drives. From that, two fields of research arise, which are to be treated in this work.

Reduction of the system costs by the reduction of the number of power electronic switches
The required axial active magnetic bearing is to be fed by a zero-sequence current from the star points of the bearingless machine windings, so that the otherwise needed 4-quadrant chopper may be omitted. The following questions shall be answered:

- Is a zero-sequence current feeding feasible for magnetically levitated drives as substitution of the 4-quadrant chopper feeding? The feasibility shall be validated with a permanent magnet bearingless PM synchronous machine of 1 kW rated power at 60000 min^{-1}.
- On the machine side, to what extent do the 3-phase AC currents for torque and suspension force generation influence the zero-sequence current and vice versa?
- On the inverter side at a given DC-link voltage, to what extent do the 3-phase AC voltages for torque and suspension force generation influence the zero-sequence voltage and vice versa?

Reduction of the parasitic radial forces, acting on the rotor
Parasitic forces on the rotor occur predominantly from the reaction of the rotor eddy currents to the suspension winding air gap field (eddy current effect). Also they occur from the interaction between torque-generating stator air gap field with the suspension force-generating stator air gap field (superposition effect). The following questions shall be answered, where the focus is on the eddy current effect:

- How can the eddy current effect and the superposition effect be quantified by measurements and calculations?

- Which geometrical and electromagnetic quantities influence the eddy current and the superposition effect?
- Which influence has the choice of the permanent magnet material on the eddy current effect? A comparison shall be given by measurements at a prototype machine with a Sm_2Co_{17}- and a NdFeB-rotor in the same stator.
- Which consequences do the eddy current effect and the superposition effect have for the rotor position control of the bearingless machine?
- By which constructive measures both effects may be mitigated, so that the electromagnetic utilization and the machine dimensions can be enlarged?

Conclusions from the investigation of the zero-sequence current feeding in an axial magnetic bearing:

- Measurements at the prototype machine and simulations in the *Simulink* environment show: A zero-sequence current feeding exhibits similar dynamics of the position control – compared to a 4-quadrant chopper feeding – unless the inverter is not operated close to its voltage limit.
- Finite element simulations show: The zero-sequence current does not lead to significant effects in the active part of the bearingless machine. The standstill air gap field, excited by the zero-sequence current is of negligible amplitude. Therefore, the magnetic saturation in the machine is not much influenced by the zero-sequence current. Also the increase of the copper losses is negligible. In the prototype machine, no air gap field is excited by the zero-sequence current due to the selected special winding topology.
- By simulation, two voltage modulation techniques are compared: A space vector and carrier-based pulse width modulation. The choice of a feasible modulation technique allows a prioritization of either the 3-phase AC voltage system or of the zero-sequence voltage. If a prioritization is selected, e.g. the generation of a 3-phase AC voltage system, no modulation-based coupling in the form of additional voltage harmonics in the 3-phase AC voltage spectrum occurs from the zero-sequence current feeding. When operated at the inverter voltage limit, however, no voltage for the axial active magnetic bearing is available anymore.

  If no prioritization is applied – as in the prototype machine – for both, the 3-phase AC voltage and the axial bearing voltage, a linear relation between reference and actual voltage exists below the inverter voltage limit. A non-linear relation exists

above the voltage limit. In this non-linear region, $3 \cdot f_S$-frequent voltage harmonics may occur in the axial bearing voltage. $2 \cdot f_S$-frequent oscillations may occur in the phase voltage of the 3-phase system. Measurements and simulations show, that both voltage oscillations do not endanger the rotor levitation due to the mechanical inertia of the rotor.

Conclusions from the investigation of the eddy current and superposition effect:

- For the calculation of the parasitic rotor forces, a 2-dimensional, linear analytical field calculation yields accurate results due to the negligible impact of magnetic saturation. The axial end effect of the eddy currents is considered with an effective electric conductivity. Without this effective conductivity, only a worst-case estimation is possible. By measurements, the parasitic forces can be identified from the suspension currents, proportional to the suspension forces, at centric rotor position.
- Measurements, finite element simulations and analytical calculations show: The eddy current force error angle depends approximately linear on the rotor speed (= slip frequency of the suspension fundamental field) and on the effective electrical conductivity, since the eddy currents in the permanent magnets are resistance-limited. The following factors increase the eddy current-related parasitic forces: A large ratio of bore diameter to suspension winding pole pitch (deeper intruding of the suspension field into the rotor parts), a high electric conductivity of the permanent magnets and a high rotor speed. The following factors increase the superposition effect: A high current loading of the drive winding (depending on the cooling system and the selected permanent magnet excitation and height, respectively) and a low pole count (increased armature reaction).
- By simulation and calculation largely confirmed measurements at a Sm_2Co_{17}- and at a NdFeB-rotor show: The eddy current and superposition effects are negligibly small for the built prototype machine due to the small machine dimensions. The eddy current-related error angle of the suspension force is proportional to the electric conductivity of the permanent magnet material.
- Analytical calculations and simulations in time domain in the *Simulink* environment show: The eddy current effect leads, as it is depending on speed, to a speed-depending shift of the eigenvalues of the rigid body eigenmodes. The superposition effect leads to a shift which is proportional to the torque-generating drive current. In motor operation, both parasitic forces counteract each other. In generator mode,

i.e. at a negative q-component of the drive current, both parasitic forces add up. The shift of the eigenvalues may lead to position control instability. The question regarding the maximum admissible force error angle can only be answered under consideration of the rotor dynamic properties.

- The parasitic forces occur especially in machines with large bore diameters and low pole counts. The following measures can be taken to mitigate these disturbing forces: An increase of the suspension winding pole count (less intruding of the suspension field into the rotor parts), an increase of the permanent magnet height (reduction of the stator current loading at equal machine utilization) and a segmentation of the permanent magnets (decrease of the effective electric conductivity). To increase the output power, the active length may be enlarged, unless the rotor bending eigenfrequencies are sufficiently high.

With consideration of these design guidelines, the bearingless motor principle can be applied to highly-utilized machines in the 100 kW-range. By the usage of the zero-sequence current feeding for the axial active magnetic bearing supply the number of power electronic switches may be reduced.

Kurzfassung - In dieser Dissertation wird die lagerlose Synchronmaschine mit genutetem Stator, zylindrischem Rotor mit bandagierten Oberflächenmagneten und sechs aktiv geregelten Freiheitsgraden als Hochdrehzahl-Antrieb untersucht. Die Arbeit besitzt zwei inhaltliche Schwerpunkte: Die Maschinenauslegung unter Berücksichtigung von baugrößenabhängigen Skalierungseffekten und eine neuartige Variante, das axiale Magnetlager zu speisen.

Da die betrachteten lagerlosen Maschinen in der Regel eine geringe magnetische Sättigung aufweisen und mit verteilten Wicklungen ausgestattet sind, wird zunächst die zweidimensionale analytische Feldberechnung herangezogen, um die Rotortragkraft und parasitäre Rotorkräfte zu berechnen. Diese Berechnungen bilden die Grundlage für die folgende elektromagnetische Grobauslegung der lagerlosen Maschine.

Zu Beginn der Auslegung werden die Randbedingungen erläutert, die sich geometrisch für die kombinierte Antriebs- und Tragwicklung, strukturmechanisch für die Bandagenhöhe und thermisch für die Verlust- und Abgabeleistungsdichte ergeben. Anhand von zwei unterschiedlichen Baugrößen, nämlich Außendurchmesser: 75 mm, Aktivlänge: 40 mm, Nennleistung: $\approx$ 1.5 kW und Außendurchmesser: 130 mm, Aktivlänge: 125 mm, Nennleistung: $\approx$ 60 kW, wird gezeigt, wie sich die Wahl der Polpaarzahl, des Bohrungsdurchmessers und der Magnethöhe auf die regelungstechnischen Eigenschaften der Maschine auswirken. Dabei wird deutlich, dass eine Vergrößerung der Magnethöhe, eine Erhöhung der Polpaarzahl und die Verringerung des Bohrungsdurchmessers die lateralen Störkräfte auf den Rotor durch Rotorwirbelströme und Ankerrückwirkung verringern. Um Skalierungseffekte abzuleiten, kommt die analytische Berechnung zur Anwendung, wobei der Fokus auf der zweidimensionalen elektrodynamischen Feldberechnung liegt. Anhand einer 1 kW / 60000 min^{-1}-Prototypmaschine, bestehend aus einem lagerlosen Motor und einem kombinierten aktiven Radial-Axial-Magnetlager, wird die Genauigkeit der analytisch und simulativ gewonnen Ergebnisse validiert.

Um die Anzahl der nötigen leistungselektronischen Halbbrücken zu verringern, wird außerdem ein Konzept untersucht, bei dem das axiale Magnetlager durch einen Strom zwischen den beiden Sternpunkten der kombinierten Wicklung des lagerlosen Motors gespeist wird. Dazu wird die herkömmliche Raumzeiger-Pulsweitenmodulation für dreiphasige Systeme auf ein doppelt-dreiphasiges System erweitert, in dem der Axial-lagerstrom dem Summenstrom eines dreiphasigen Wicklungssystems im Sternpunkt entspricht. Dieser Strom kann durch die Beeinflussung des elektrischen Potentials der beiden Sternpunkte geregelt werden. Allerdings können bei diesem Konzept

die Ströme des Axialmagnetlagers und der Drehstromwicklungen unerwünschte Schwingungen aufweisen, wenn der Umrichter nahe der Spannungsgrenze betrieben wird oder verhältnismäßig hohe Axiallagerströme hochdynamisch bereitgestellt werden müssen. Das vorgestellte Konzept des Axiallagers mit Nullstromspeisung wird dennoch als vielversprechend eingestuft, da in der hier betrachteten Anwendung als Turboladerantrieb diese Störeffekte nicht auftreten.

Abstract - The bearingless synchronous machine is considered with slotted stator, cylindrical rotor with sleeve-protected surface-mounted permanent magnets and six actively controlled degrees of freedom as high-speed drive. The focus is set on two key aspects: The machine design under consideration of size-dependent scaling effects and a novel kind of feeding the excitation winding of the axial active magnetic bearing.
Since the considered bearingless PM machines typically exhibit a low degree of magnetic saturation and are equipped with distributed windings, the two-dimensional analytical calculation is used to calculate the rotor suspension force and disturbing rotor forces. These calculations are used in the subsequent electromagnetic design process.
At the beginning of the design process, boundary conditions are discussed, that are derived geometrically for the combined drive and suspension winding, structural mechanically for the sleeve height and thermally for the loss and output power density. On the basis of two different machine sizes, on the one hand $\approx$ 1.5 kW and on the other hand $\approx$ 60 kW at 75 mm and 130 mm outer diameter, respectively, at corresponding active axial length of 40 mm and 125 mm, this work shows, how the choice of pole count, bore diameter and magnet height influences the properties relevant for the rotor position control. It is concluded that an increase in pole count, a reduction in bore diameter and an increase in magnet height reduce the undesired parasitic lateral rotor forces, caused by rotor eddy currents and armature reaction. In order to investigate scaling effects, an analytical calculation is used, where the focus is set on the two-dimensional electrodynamic field calculation. By means of a 1 kW / 60000 min^{-1}-prototype drive, consisting of a bearingless machine and a combined active radial-axial magnetic bearing, the accuracy of the results from calculation and simulation is verified.
In order to reduce the number of required power electronic half-bridges, a concept is investigated, in which the axial magnetic bearing is supplied by a current between the star points of the combined winding sections in the bearingless machine. To do so the concept of the widely used space vector pulse-width modulation for 3-phase systems is extended to a double 3-phase system in a way that the axial magnetic bearing current corresponds to the sum current in the star point of one 3-phase system. This current can be controlled by the variation of the two star point electric potentials. However, additional current oscillations in the axial bearing current and in the 3-phase current can occur if the inverter is operated close to its voltage limit or if relatively high axial bearing currents must be provided at high dynamics. Anyway, the concept is considered a promising approach, since in this application as turbo-charger drive the disturbing effects do not occur.

Contents

Applied Notation and Symbols

Abbreviations

1D	1-dimensional
2D	2-dimensional
3D	3-dimensional
4Q-CB-PWM	4-quadrant chopper feeding with carrier-based pulse width modulation
AMB	Active magnetic bearing
BM	Bearingless motor
CB-PWM	Zero-sequence current feeding with carrier-based pulse width modulation
COG	Center of gravity
DOF	Degree of freedom
EDB	Electrodynamic bearing
EMF	Electro-motive force
FE(M)	Finite element (method)
IGBT	Insulated gate bipolar transistor
IM	Induction machine
MMF	Magneto-motive force
MOSFET	Metal-oxide field effect transistor
(N)DE	(Non-)drive end
PCB	Printed circuit board
PM	Permanent magnet
PMB	Passive magnetic bearing
PMSM	Permanent magnet synchronous machine
PWM	Pulse width modulation
RMS	Root mean square
SRM	Switched reluctance machine
SV-PWM	Zero-sequence current feeding with space-vector pulse width modulation
SynRM	Synchronous reluctance machine

Notations

$\parallel$	Parallel
$\perp$	Perpendicular
$(\ldots)^*$	Complex conjugated
$x, X, \hat{X}$	Actual value, RMS value, peak value
$\underline{x}$	Complex number, complex space vector
$\vec{x}$	Vector
$\boldsymbol{X}$	Matrix
$\boldsymbol{I}$	Unity matrix
$\boldsymbol{O}$	Zero matrix
Δx	Difference related to quantity x

Greek Letters

α	Arbitrary angle, heat transfer coefficient, α_{eq}: pole coverage
$\underline{\alpha}$	Complex scaling coefficient of *Bessel* functions
γ	Circumferential coordinate, circumferential angle
δ	Air gap width
ε	Arbitrary bearing force error angle, mechanical elongation
η	Efficiency
ϑ	Absolute temperature
Θ	Magneto-motive force MMF, moment of inertia
κ	Electric conductivity
λ	Air gap permeance function
μ	Permeability, rotor field space harmonic order
ν	Stator field space harmonic order, *Poisson* ratio
ξ	Radius-dependent component of magnetic vector potential
ρ	Mass density
σ	Mechanical stress

τ	Circumferential dimension (e.g. τ_p: pole pitch)
Φ	Magnetic flux
φ	Phase shift angle of a sinusoidal quantity, electric potential
φ_x, φ_y, φ_z,	Rotation angle around the *y*-, *x*-, *z*-axis
ψ	Magnetic flux linkage
Ω	Mechanical angular velocity
ω	Angular frequency

Latin Letters

A	Area, magnetic vector potential
$\boldsymbol{A}$	State space system matrix
a	Number of parallel winding branches
B	Magnetic flux density
$\boldsymbol{B}$	State space input matrix
b	Breadth
$\boldsymbol{C}$	State space output matrix
c	Permanent magnet magnetization coefficient, material compliance
$\boldsymbol{D}$	State space feed-through matrix
d	Depth, duty cycle
E	Electric field strength, *Young*'s modulus
F	Force
f	Frequency, force density
G	Transfer function, frequency response
g	Gravitational acceleration
h	Height
H	Magnetic field strength
I	Electric current, modified *Bessel* function of first kind
J	Electric current density
K	Electric current loading, modified *Bessel* function of second kind
$\boldsymbol{K}$	Arbitrary coefficient matrix
k	Time harmonic order
L	Inductance
l	Length

M	Torque, magnetization
m	Phase count, mass, modulation
N	Winding turn count
n	Rotational speed, denominator, arbitrary natural number
P	Active power
p	Number of pole pairs
Q	Slot count, reactive power
q	Number of slots per pole and phase
$\vec{q}$	Position signal vector
R	Electric resistance
r	radial component, radius
S	Apparent power
s	Variable in *Laplace* space, slip
T	Period
t	Time, number of base winding schemes
THD	Total harmonic distortion
U	Electric voltage
u	Displacement, arbitrary natural number
$\vec{u}$	State space input vector
V	Volume
v	Translational speed, arbitrary natural number
$WTHD0$	Weighted total harmonic distortion with respect to $U_{\mathrm{DC}}/2$
W	Energy
$\underline{X}$,$\underline{Y}$	General (complex) field coefficients to be solved
x	x-coordinate
$\vec{x}$	State vector
y	y-coordinate, coil pitch
$\vec{y}$	State space output vector
z	z-coordinate, numerator

Subscripts

0	Static value, no-load related, zero-sequence

1	Fundamental, load related
$+$	Mathematically positive rotation sense
$-$	Mathematically negative rotation sense
α, β	Perpendicular stator fixed space vector quantities
γ	Tangential
δ	Air gap quantity
σ	Stray-
a	Amplitude
A	3-phase system A
act	Active
add	Additional
air	Air
an	Analytical
att	Attenuation
av	Average value
ax	Axial
B	3-phase system B
Bin	Associated to the author in [1]
b	Winding overhang
be	Bearing coordinates
bend	Bending
C	*Carter*
c	Coil
cal	Calculated
CE	Collector-emitter
COG	Center of gravity
comag	Related to the magnetic co-energy
comp	Comparison
con	conical
cor	Corrected
crit	Critical
Cu	Copper, generally conductor
cur	Curvature
D	Drive winding, derivative controller gain, damping

d	Direct axis, dissipation, tooth, distribution
DC	DC quantity
DE	Drive end
def	Deformation
dis	Disturbance
DS	Drain-source
E	Penetration (German:“Eindring-“)
e	Electrical
ecc	Eccentricity
eff	Effective
eq	Equivalent
err	Error
even	Even
exp	expansion
F	Force
f	Frequency
Fe	Iron, generally highly-permeable magnetic material
FEM	Finite element method
flex	Flexible
filt	Filtered
Fr	Friction
Ft	*Foucault*: eddy current related
G	Gravity
h	Main
hori	horizontal
i	Inner
I	Integral controller gain
I+	Topology with higher current rating
in	Input
inv+AMB	Inverter and active magnetic bearing
L	Suspension (=levitation) winding, generally levitation
lim	Limitation
Lo	*Lorentz*
m	Mechanical, ultimate strength

M	Torque
mag	Magnetic
max	Maximum
min	Minimum
mot	Motor
MW	*Maxwell* (reluctance related)
N	Rated, related to the winding star point N
n	Natural
N+	Topology with higher winding turn count
NDE	Non-drive end
Nd	Related to the NdFeR-rotor
o	Outer, open-loop, summation of higher harmonic orders
odd	Odd
off	Off
offs	Offset
on	On
P	Proportional controller gain, pulsation
p	Perpendicular, magnetic pole
par	Parallel
pas	Passive
PM	Permanent magnet
Po	*Poisson*
pol	Polar
q	Quadrature axis, number of poles per slot and phase
Q	Slot
R	Rotor
r	Radial, relative
r+	Topology with increased bore diameter
ref	Reference value
rem	Remanence
RL	*Ohm*ic-inductive
Ruo	Associated to the authors in [2]
Rus	Associated to the authors in [3]
S	Stator

s	Phase, magnetic stiffness
samp	Sampling
sat	Saturation
scal	Scaling
se	Sensor coordinates
seg	Segmented
sep	Separated windings
share	Percentage of slot cross section
simp	Simplified
sl	Bandage (sleeve)
Sm	Related to the Sm_2Co_{17}-rotor
st	Step
sup	Superposition
sw	Switching
syn	Synchronous
th	Thermal
thrust	Thrust
tot	Total
tri	Triangular
U	Voltage
us	Undersize
vert	vertical
vM	*von Mises*
w	Winding, closed-loop
x	*x*-coordinate
y	*y*-coordinate, yoke
z	*z*-coordinate

1. Introduction

Active magnetic self-bearing motors are usually referred to as bearingless motors (BM). They combine two functions into a single device: the torque generation by an electric machine and the rotor suspension force generation by an active magnetic bearing [4, 5]. Since BM enable axially short rotors and exhibit an increased power density compared to common magnetically levitated motor systems, they are technically attractive for high-speed applications. Achievements in the fields of sensors, power electronics and micro controllers contributed to the breakthrough of bearingless motors in past decades [6]. The diversity in the field of BM – especially for small power ratings – is huge. However, for power classes > 1 kW a slotted poly-phase stator with six actively controlled rotor degrees of freedom is the topology of choice in order to compensate for the rotor forces efficiently. The rotor field of these machines is typically generated by surface-mounted permanent magnets (PM). Recently, speed values up to 100000 min^{-1} [7] and power ratings up to 60 kW have been reached with this topology [8]. However, efficiency and machine utilization are limited and do not compete with classical permanent magnet synchronous machines for power classes > 20 kW. For example, one of the largest built prototype machines (40 kW/40000 min^{-1}) exhibits $\eta = 0.924$ efficiency and $\sigma_{\mathrm{thrust}} = 16\ \mathrm{kN \cdot m^{-2}}$ thrust force density [9]. Rising attention should be paid to developing bearingless high speed drives which are competitive to classical electrical machines also in the high power range.

This work focuses on the design and the control of these bearingless PM synchronous machines. To verify the theory a 1 kW/60000 min^{-1}-prototype machine was built (Fig. 1.1), which is called *LLM4*. A schematic overview of this prototype is given in Fig. 6.1. It was successfully operated at rated speed, as Fig. 1.2 shows.

Chapter 1 discusses current trends in magnetically levitated motor systems and classifies this work in the context of bearingless machine technology.

Chapter 2 focuses on the analytical magnetic field calculation of high-speed permanent magnet machines, taking rotor eddy currents in the solid rotor parts into account. A

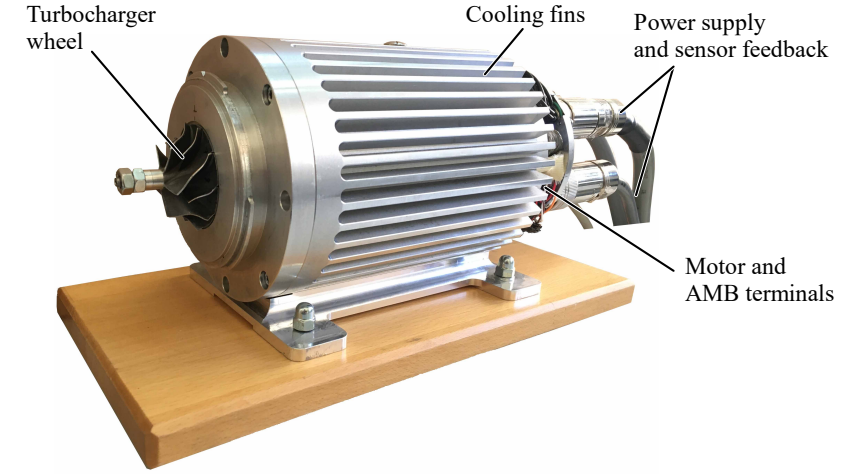

(a) Assembled machine

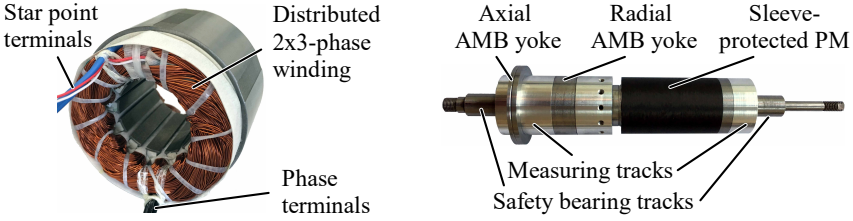

(b) Stator

(c) Rotor

Fig. 1.1.: Built bearingless PM synchronous machine with 1 kW/60000 min^{-1}

comparison with finite element simulations is drawn.

In **Chapter 3**, aspects which are particularly important for the design of bearingless high-speed machines are discussed by the example of a 1 kW and a 40 kW machine. Design guidelines and scaling laws are derived.

In **Chapter 4**, the machine parameters of the built prototype machine *LLM4* are determined by measurement, simulation and analytical calculation, and a comparison is drawn.

The position control of the rigid rotor is addressed in **Chapter 5**, emphasizing the parasitic coupling between the rotor degrees of freedom due to the gyroscopic effect, rotor eddy currents and the superposition of the drive and suspension air gap field.

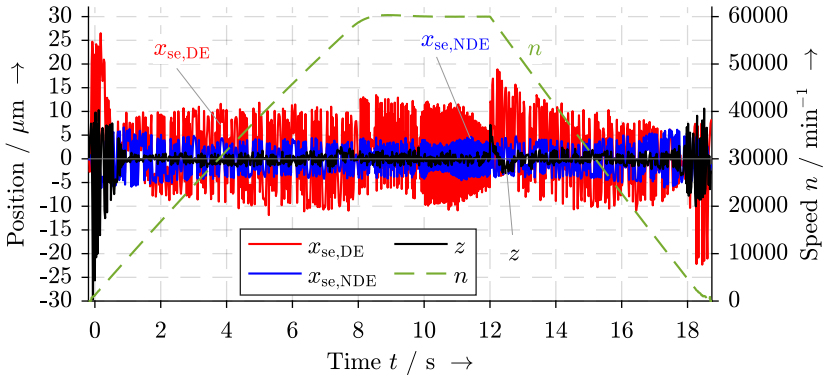

Fig. 1.2.: Measured position signals $x_{\mathrm{se,DE}}$ at the drive end, $x_{\mathrm{se,NDE}}$ at the non-drive end and axial position z during run-up to rated speed $n_{\mathrm{N}} = 60000\ \mathrm{min}^{-1}$ and deceleration (aliasing effect visible due to sampling frequency: $f_{\mathrm{samp}} = 51$ Hz), controller sampling frequency $f_{\mathrm{sw}}/2 = 16.5$ kHz

Chapter 6 gives an introduction into the zero-sequence current feeding of an axial active magnetic bearing in the context of voltage source inverter modulation techniques.
Chapter 7 shows the operational behavior of the zero-sequence current-fed axial magnetic bearing and outlines the constraints on the inverter and motor side.

1.1. Motivation for Bearingless Motor Applications

The use of actively controlled magnetic levitation is motivated by a number of merits that are accompanied by the rotor levitation. According to [4, 5, 10] the most important of these are:

- **Absence of lubrification and wear**
  The contact free rotor rotation leads to the absence of contaminating wear. Additionally, lubrification as in ball or journal bearings is not needed. Thus, magnetically suspended drives are suited for the use in vacuum pumps, pharmaceutical applications and clean environments. The most important applications are the use as blood pump or artificial heart pump [11]. However, if not driven within a fluent medium, a safety bearing is needed which must be prepared in a way that it complies with

the aforementioned benefits.

- **Absence of bearing friction**
  In high-speed machines (rotor circumference speed $v_R > 100\ \mathrm{m \cdot s^{-1}}$) the maximum speed of conventionally supported rotors is often limited by the friction losses in the bearings. Magnetically suspended rotors can push the speed limit towards other limits such as the material yield strength or the air friction losses and possibly increase the drive efficiency.

- **Online adaption of rotor dynamics**
  The stiffness and the damping of the levitated rotor system, equivalently described as spring-mass-damper system, can be adjusted by the position controller during operation. Thus, it is possible to pass critical speeds with small vibration amplitudes. Further, this enables the "compensation" of the rotor unbalance, e.g. by shifting the rotational axis to the principal axis of inertia and allowing for "force-free" rotation [12].

- **Low maintenance costs and long lifetime**
  Once the magnetic bearing system is working properly, the maintenance costs are lower and the lifetime is longer compared to conventional bearings.

- **Compactness of bearingless motors**
  Due to the integration of the AMB into the electric machine, the bearingless motor technology reduces the axial machine length l. This increases the machine's power density compared to classical magnetically levitated drives. Also, shorter rotors exhibit higher 1^{st} order bending frequencies $f_{\mathrm{bend},1} \propto 1/l^2$, which eases the rotor position control [12] (Appendix A.16).

In contrast, some drawbacks prevent the technology from the breakthrough in industry applications:

- **Low force density of magnetic bearings**
  The low force density of magnetic bearings reduces the power density of the overall drive system, which is a key factor for high speed drives. Due to the large magnetically effective air gap, the force density of bearingless machines is even lower. Further, they occupy a considerable portion of the axial motor length, which is limited to keep flexible rotor modes at high frequencies (first bending mode eigen-

frequency: $f_{\text{bend},1} \propto 1/l^2$) [12].

- **Need for qualified staff**
  In order to operate a magnetic bearing system, mechatronically qualified engineers must be available even after system launch in the case of a failure or system adjustment.

- **Electromagnetic compatibility**
  As high precision mechatronic system, sensor signals are prone to electromagnetic coupling of the surrounding actuators, so that costly shielding is required.

1.2. Classification of (Electro-) Magnetic Levitation Systems

There are manifold levitation systems that rely on magnetic or electromagnetic forces. The system in this work is based on only two of these principles which are marked shaded in Fig. 1.3. The goal of this subsection is to give an overview of the common magnetic bearing principles in order to classify this work in the context of magnetic levitation. The overview is inspired by [13].
Generally, two different kinds of forces are distinguished if electric charges are only considered in a macroscopic perspective as current i and magnetic material properties in a macroscopic perspective by means of the magnetic permeability μ: the *Lorentz*-force $\vec{F}_{\text{Lo}}$ (1.1) and the *Maxwell*-force $\vec{F}_{\text{MW}}$ (also called reluctance force) (1.2). The first one describes the force on a straight, current (I) carrying conductor with orientation $\vec{l}$ and length $\left|\vec{l}\right|$, exposed to a magnetic field of flux density $\vec{B}$. The force is oriented perpendicular to the current flow in the conductor and to the field direction, which is in the context of rotor-stator arrangements tangential to the rotor surface. For a certain $\vec{B}$ and for absence of magnetic saturation, the suspension force $\vec{F}_{\text{Lo}}$ depends linearly on the current $\vec{I}$.

$$\vec{F}_{\text{Lo}} = I \cdot \left(\vec{l} \times \vec{B}\right) \tag{1.1}$$

The current I in (1.1) can be actively controlled as in the case of a bearingless machine. Alternatively, it is induced as in the case of the so called AC bearings (electrodynamic levitation). These AC bearings require alternating flux (stator) and highly conductive material (rotor) so that the opposed currents in stator and rotor generate repulsive forces but suffer from high losses in the rotor and low damping coefficients. Alternatively, the

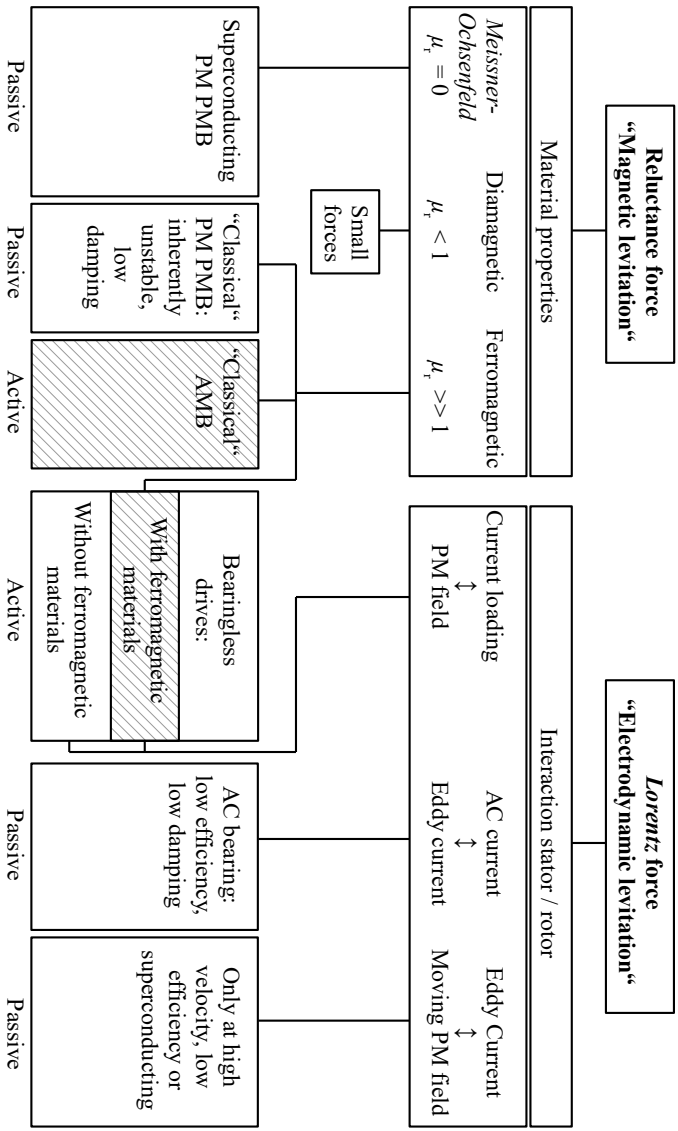

Fig. 1.3.: Classification of magnetic levitation systems, similar to [13], shaded: relevant principles for this work (μ_r: relative permeability)

alternating flux can be replaced by a fast movement of a PM close to a conducting surface in order to use the same principle.

The *Maxwell* force $\vec{F}_{\mathrm{MW}}$ is meant to be the force on magnetized material in an external magnetic field. The different magnetization properties yield different magnetic reluctances along the air gap circumference, allowing radial and tangential magnetic force components. This reluctance force can be derived via the *Maxwell* stress tensor or the principle of virtual displacement (1.2) for a magnetic body with sections of different magnetic permeability values μ. It is calculated according (1.2) via the change in magnetic field energy $\partial W_{\mathrm{mag}}$ at the virtual change in position ∂x of the considered body. The movement ∂x by the force $\vec{F}_{\mathrm{MW}}$ leads a reduction of the magnetic field energy by $\partial W_{\mathrm{mag}}$ and to an increase of the magnetic co-energy by $\partial W_{\mathrm{comag}}$. In magnetically saturated materials, the latter approach via the magnetic co-energy is usually preferred. The *Maxwell* force is aligned with the direction $\vec{e}_{\mathrm{x}}$ of the virtual displacement and depends via $W_{\mathrm{mag}} \propto B^2$ on the flux density B. Therefore, it is inverse to the square of a distance between two highly permeable magnetic surfaces.

$$\vec{F}_{\mathrm{MW}} = -\frac{\partial W_{\mathrm{mag}}}{\partial x} \cdot \vec{e}_{\mathrm{x}} = \frac{\partial W_{\mathrm{comag}}}{\partial x} \cdot \vec{e}_{\mathrm{x}} \tag{1.2}$$

The most popular representative of the magnetic levitation system, which uses reluctance forces as magnetic pull, is the active magnetic bearing (AMB). By means of position signals the force-generating magnetic field of the electromagnet is controlled by a current amplifier. Therefore, stable levitation is possible in all degrees of freedom (DOF). In contrast, passive magnetic bearings (PMB), equipped with PM, cannot suspend a ferromagnetic rotor stable in all six DOFs [14, 15]. In many applications [16, 17, 18], however, these bearings are used in combination with AMBs in order to reduce the number of actively controlled DOFs.

Another exotic group of PMB is based on the diamagnetic effect ($\mu_{\mathrm{r}} < 1$). However, only the resistance-free development of eddy currents in superconductors [19, 20] leads to a diamagnetic effect which results in technical relevant forces. Others, like graphite, show also this effect, but at very low forces.

Often – and also in bearingless PM machines with a slotted stator – the resulting force on a body is composed of both force components. A general approach to calculate forces on current-carrying bodies in a magnetic field, which are also magnetized, is the integral of *Maxwell* stress components on the surface around the considered body. The *Maxwell*

stress tensor (Section 2.1) is used to calculate the forces with the knowledge of the orthogonal flux density components at the body surface.

1.3. Working Principle of Bearingless Motors

The term *bearingless motor* comprises each type of electric machine which takes over the active position control in at least one lateral DOF. Therefore, there are many different types. In the following their working principle is described shortly. Bearingless drives which control either passively any DOF (e.g. [21]) or only one DOF (e.g. [22]) besides the rotation around the axial z-axis are not considered here, since they have not shown to be suitable for high power applications [10].

1.3.1. Bearingless Motors using a Rotating Magnetic Suspension Field

This kind of machine can produce a radial bearing force and torque within one motor unit. Hence, it controls three DOFs: x, y, φ_z. Therefore, either a second (half-) motor unit or a radial AMB on the opposite shaft end is required in order to control five DOFs (torque and radial forces in two planes). The remaining DOF, the axial rotor movement, must be controlled by either a separate axial AMB [23, 24], by using two conical bearingless motor units [25, 9] or by using two axial flux machines [26, 27]. The bearingless prototype machine *LLM4* uses a rotating magnetic suspension field on the rotor drive end (DE), whereas a commercially available combined radial/axial AMB with PM bias flux is used at the non-drive end (NDE).

Such machines usually are designed to use predominantly either *Lorentz*- or reluctance forces. The considered bearingless PMSM (surface-mounted PM ring and slotted stator) produces torque solely from *Lorentz*-force. It generates a lateral bearing force by approximately 60% reluctance and 40% *Lorentz*-force. In any case this type of machine with $2p$ PM rotor poles imposes the conditions of Table 1.1 for constant torque and lateral bearing force in steady state [4]. The subscript L refers to the stator air gap field, which generates the levitation force, and the subscript D refers to the stator air gap field, which generates torque. v_{syn} and f_{syn} are the synchronous velocity and the electric frequency of the rotor field. The principle is not limited to PM machines but is also applied to induction machines [28, 29, 30, 31], switched reluctance machines [32, 33, 34], synchronous reluctance machines [35, 36], flux switching machines [37, 38] or hysteresis machines

[39, 40]. Often the principle is applied to slice motors [41, 42, 43, 44], which passively stabilize three DOFs (axial and two tilting movements) and do not require a separate axial and radial AMB as highly compact solution.
The biggest disadvantage of this principle is that the torque-generating magnetic stator drive field of pole count $2p_D = 2p$ produces a disturbing force component in interaction with the suspension field wave. This force is aligned perpendicular to the reference force because the drive field is oriented perpendicular to the rotor field for torque generation (superposition effect, Section 2.5). Another shortcoming is that the cascaded current control of the rotor position control is based on field-oriented control, so that the rotor angle information is needed. This is in contrast to the common active magnetic bearings.

Table 1.1.: Conditions of bearingless motors with $p \pm 1$-winding topologies for constant torque and radial suspension force (D: drive, L: levitation/suspension)

Torque	Lateral bearing force
$p_D = p$	$p_L = p \pm 1$
$v_{syn,D} = v_{syn}\ \left(f_{s,D} = f_{syn}\right)$	$v_{syn,L} = (p/p_L) \cdot v_{syn}\ \left(f_{s,L} = f_{syn}\right)$

***Lorentz*-Force Generation**

The *Lorentz*-force generation is independent of the surrounding material properties. Therefore, "thick" PMs in combination with air gap windings [43] can be used, which has the positive side effect of low iron losses and an increased current loading.
The generation of torque as circumferential *Lorentz*-force $\vec{F}_{Lo}$ is depicted in Fig. 1.4. The mainly radial rotor field $\vec{B}_R$ (2.5) encounters perpendicularly the stator current loading $\vec{K}_D$, which points in z-direction and is assumed to be sinusoidally distributed in circumferential direction with periodicity $p_D = p$ (see (2.15), (2.16)). That means, only the tangential stator field interacts with the rotor field. For constant torque, both the stator and the rotor field need to move synchronously ($v_{syn,D} = v_{syn}$) as to see from Fig. 1.4a and 1.4b. The generation of lateral bearing force as circumferential *Lorentz*-force $\vec{F}_{Lo}$ is depicted in Fig. 1.5. The principle is equivalent to the aforementioned torque generation. In contrast, the stator suspension current loading $\vec{K}_L$ is of periodicity $p_L = p + 1$ and moves with half synchronous frequency ($v_{syn,L} = v_{syn} \cdot p/p_L$), which results in a rotor

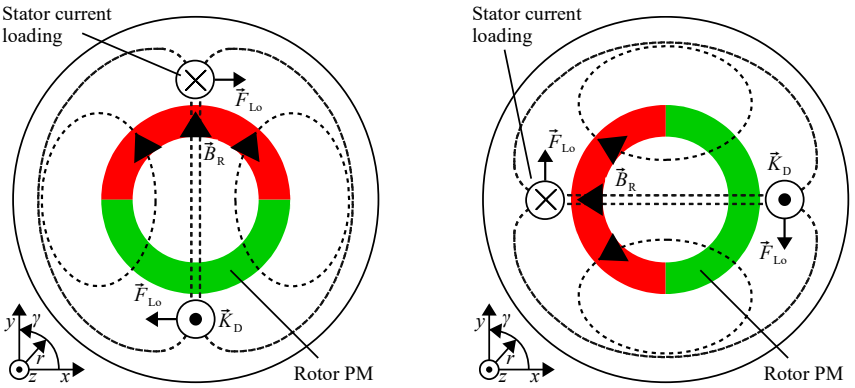

(a) At rotor position $\gamma_S = 0$

(b) At rotor position $\gamma_S = \pi/2$ (after a quarter rotor rotation)

Fig. 1.4.: Constant torque generation in a 2-pole PM synchronous machine via *Lorentz*-force in circumferential direction

slip frequency of $f_R = -n$ (see Section 2.1). For configurations of $p_L = p - 1$ this follows similarly. However, for inner rotor topologies the *Lorentz*-force counteracts the reluctance force.

Reluctance Force Generation

The generation of a lateral bearing force as radial reluctance force $\vec{F}_{MW}$ is depicted in Fig. 1.6. In this case, stator and rotor core must be of high permeability ($\mu_r \gg 1$) to ensure that the magnetic field enters the magnetized stator and rotor perpendicularly to the surfaces. The force acts as a magnetic pull perpendicularly to these stator and rotor surfaces. Here, slotted stator topologies are often used [42]. The PM should be thin for a small effective air gap which results in a predominantly radial and along the air gap constant magnetic air gap field. The air gap flux density results in attractive forces on the rotor, independent of its direction positive or negative ($F_{MW} \propto B_r^2$). These attractive forces are balanced in circumferential direction if a magnetic field wave of either even or odd periodicity is in effect. However, if a p-pole field is superimposed by a $p \pm 1$-pole field, the radial air gap flux density is not balanced in circumferential direction. The resulting reluctance force vector $\vec{F}_{MW}$ points in the direction of radial flux concentration so that it is aligned with the *Lorentz*-force vector on the rotor (Fig. 1.5). In contrast to the

Lorentz-force generation, here the radial suspension winding field $\vec{B}_{\mathrm{L,r}}$ interacts with the biasing radial rotor field $\vec{B}_{\mathrm{R,r}}$. For the considered machine, the suspension field wave is of periodicity $p_{\mathrm{L}} = p+1$ and moves with half synchronous frequency ($v_{\mathrm{syn,L}} = v_{\mathrm{syn}} \cdot p/p_{\mathrm{L}}$). Besides the $p \pm 1$-principle there are also machines that produce axial force by means of rotating magnetic fields, moving synchronously with the rotor field. These machines consist of two either conical motor units [9, 25] or axial flux machine motor units [26, 45, 22], often referred to as *single-drive bearingless motor*. If the field-weakening current component of both machine units is opposite, the net attractive reluctance force on the rotor in axial direction is different from zero. On both shaft ends the machine units produce torque via the *Lorentz*-force. The radial bearing forces can be generated either by PMBs [26] or by the $p \pm 1$-principle [9, 25] on both shaft ends, stabilizing the radial and tilting motions of the remaining four DOFs.

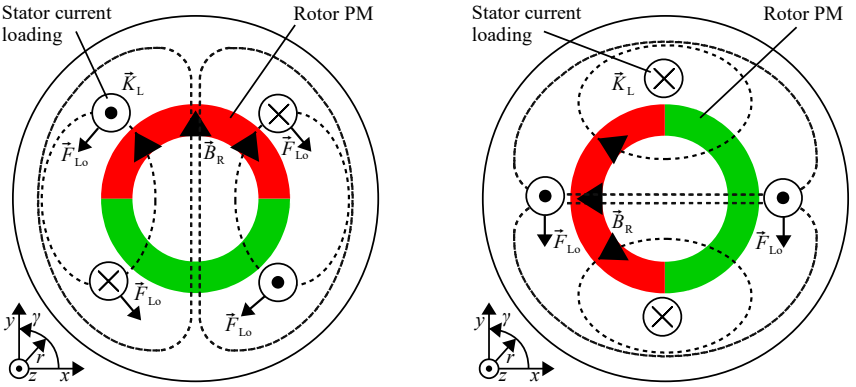

(a) At rotor position $\gamma_{\mathrm{S}} = 0$

(b) At rotor position $\gamma_{\mathrm{S}} = \frac{\pi}{2}$ (after a quarter rotor rotation)

Fig. 1.5.: Constant lateral rotor force generation in positive y-direction in a 2-pole bearingless PM synchronous machine via *Lorentz*-force in circumferential direction ($p_{\mathrm{L}} = p+1$)

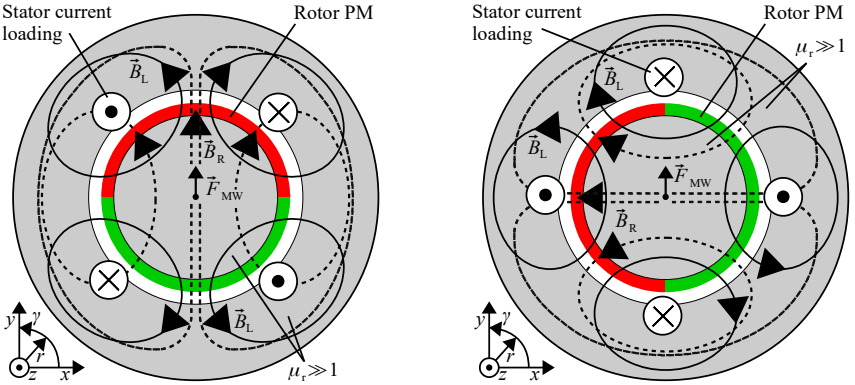

(a) At rotor position $\gamma_S = 0$

(b) At rotor position $\gamma_S = \frac{\pi}{2}$ (after a quarter rotor rotation)

Fig. 1.6.: Constant lateral rotor force generation in positive y-direction in a 2-pole bearingless PM synchronous machine via reluctance force in radial direction ($p_L = p + 1$)

1.3.2. Bearingless Motors using a Constant Magnetic Suspension Field

In contrast to a bearingless motors with a rotating magnetic suspension field, here the magnetic flux for the suspension force is a magnetic DC flux, so that the condition $p_L = p \pm 1$ is not required. The great advantage of these machines is that the position control does not require the rotor angular position, which enables higher control dynamics. There is no coupling between the torque and radial bearing force generation apart from saturation influences. The following topologies make use of this principle.

Axial Force / Torque Bearingless Motor

The *Axial force / torque motor* by *Bauer* [18] uses the interaction of an injected common-mode current component in the winding overhang of a 3-phase winding with a surrounding radially magnetized homopolar PM. The current is oriented in circumferential direction and generates an axial *Lorentz*-force with the radial PM field. The polarity of the two homopolar PM rings is different on both winding overhangs so that the net axial force is proportional to the common mode current. The torque of this machine, however, is classically generated according to Fig. 1.4. That means, two DOFs are actively controlled

whereas the remaining radial and tilting movements are controlled via PMBs on both shaft ends. The most recent prototype of this machine type is equipped with printed-circuit-board (PCB) windings [46].

Consequent Pole Bearingless Machines

Consequent pole bearingless machines [47, 48] are radial flux machines which can produce torque and radial bearing force within one motor unit. The axial movement and the radial movement on the second shaft end can be controlled by a separate magnetic bearing. The rotor active part of these machines is equipped with radially magnetized PMs, embedded on the rotor surface with no alternating magnetization. Therefore, the effective pole pair number is doubled. Torque is generated classically with field oriented control. The magnetic DC flux for the suspension force control is generated by a single winding for each DOF, equivalently to common AMBs. The bias magnetic field is given by the rotor PM. The radial force as a pure reluctance force occurs if the flux is weakened or enhanced on one rotor side. In order to decrease the force ripple, pole pair numbers $p > 3$ are recommended [48].

Homopolar Bearingless Machines

The axial stabilization of the rotor movement for *Homopolar bearingless machines* (similar to the *Arco*-type machine [49]), sometimes referred to as *Hybrid-type bearingless machines* can be done by a separate axial AMB [50], by using a disk-like rotor shape [51] or by passive stabilization via PMBs. The torque is generated in one or two motor units at the shaft ends via AC magnetic flux. Often reluctance rotors are used. The remaining four DOFs are controlled by a magnetic DC flux in axial and radial direction. Usually an axially magnetized PM between the motor units is used for biasing the radial magnetic air gap fields in the air gaps of the two motor units. Also a superconducting coil can be used for the excitation. The suspension force principle in the two motor units is equivalent to the classical AMB function. That means, the radial reluctance force is different from zero if the radial homopolar flux is weakened or enhanced on one rotor side by the DC flux of the suspension coils arranged at the stator circumference.

1.4. Trends of Bearingless Motors

The increased manufacturing effort and the necessary complex position control have limited bearingless motor solutions for industrial use up to now [10]. Especially the motor

topologies with special, e.g. conical rotor shapes [9, 52, 53], suffer from this drawback. Due to the technical attractiveness, research is done on the reduction of the bearingless drive system costs, where the focus is mainly on four measures:

- **The use of passive magnetic bearings**
  The most prominent approach is using *Earnshaw*'s theorem [14] together with *Braunbek*'s extension [15] and replace actively controlled degrees of freedom by means of PMB. Nevertheless, due to their inherently given low stiffness these systems are only suited for fractional horse power applications [22, 54, 26]. The most promising approach in this context is the bearingless slice motor [54]: Due to its disk-shaped rotor the radial tilting and axial lateral motions are stabilized by attractive reluctance forces. This type is successfully applied to blood pumps which use the conveyed medium in order to increase system damping [4]. For higher power classes, disk-shaped rotors are usually limited to low-speed applications due to their high centrifugal force, acting on the rotor. Therefore, cylindrical rotors must be used which usually prevent the usage of passive magnetic stabilization.

- **The use of electrodynamic force generation**
  Another way to omit the costly and sophisticated control of AMBs is the use of electrodynamic bearings (EDB), which can be considered passive (rightmost group in Fig. 1.3). They generate lateral *Lorentz*-force usually due to eddy currents in stator-fixed coils in interaction with a rotating rotor-fixed magnetic field. However, they exhibit limited load capacity, high losses and braking forces and produce only a lateral force when off-centered. Thus, in [27] active magnetic levitation is provided at low speed, whereas the electrodynamic levitation is used at sufficiently high speed values. Further, they do not produce any stiffness at standstill, and additional damping has to be added for stable dynamical behavior. Nevertheless, in [55] a short-circuited winding as a suspension winding is put into the stator of a 300 W/15000 min^{-1} PM machine, producing a non-controlled lateral rotor force, if the rotor is off-centered and rotating.

- **The use of combined windings, often referred to as integrated windings**
  In the last decade researchers have found that the use of a single winding, that produces both torque for motor operation and either radial [16, 56, 57, 58, 59, 60, 61] or axial force for rotor levitation [54, 45], has advantages compared to the use of two separate winding sets. The advantage results from the superposition of the torque-

and force-related currents in the same coil conductor. Since at certain time instants phase currents are opposed, I^2R-losses decrease, compared to two separate conductors. Furthermore, the entire slot cross section is shared by both currents, saving the required conductor cross section. This allows for a flexible current allocation, depending on the operating point. In the end, the electromagnetic utilization can be increased for the same thermal utilization (Section 3.3.1). Apart from the thermal merits of the combined winding, it is important to note that even the manufacturing is simplified compared to the insertion of two separated single-layer windings. For instance, as explained in [61], the combined winding is electromagnetically equal to a three-zone two-layer winding with $2p = 4$ poles except for the splitting of the winding at the serial connectors between two adjacent pole pairs. Therefore, it can be assembled in one part and does not require two winding patterns of different windings as in the case of the machine with separated windings.
The use of combined windings is limited to certain pole pair combinations which is explained in Section 3.2 and 3.3.

- **The control of one DOF by a zero-sequence current**
  In order to reduce the number of power switches and to apply the conventional inverter technology, the use of standard 3-phase inverter modules for magnetic bearing applications is promising [26, 16, 62, 63, 64, 65]. There are two research departments which have focused on this.
  One is the *Institute for Electric Drives and Power Electronics*, *Johannes Kepler University Linz, Austria*, in corporation with the *Linz Center of Mechatronics* GmbH. In [62] they present a PM-biased combined radial-axial magnetic bearing, one for each shaft side, in which a radial force is generated by a 3-phase winding system. The axial force is generated if a zero-sequence current is injected in the two bearings, weakening or enhancing the PM bias flux in the axial air-gaps on each shaft end. Further, in [54, 18] a so called axial force / torque motor is described, which generates an axial force by the interaction of a zero-sequence current in the winding overhangs with a radially magnetized homopolar PM.
  The second research group from *Shizuoka University* and *Tokyo Institute of Technology, Japan*, present a technique in [66], where they feed a PM synchronous machine with a 3-phase current system, applying field-oriented control. In addition they inject a zero-sequence current i_0 and put an arbitrary AMB between the star point of the motor winding system and the neutral clamp of the pulse-width-

modulated voltage source inverter (compare Fig. 6.2a). Hence, i_0 is used to control the force in the additional AMB by superimposing i_0 with the AC phase currents of the machine. In [67, 68] they extend this principle to an outer-rotor 6-pole/6-slot bearingless slice motor with three actively controlled degrees of freedom (x, y, φ_z): A 3-phase 4-pole winding yields the air gap magnetic field for radial rotor force generation. A single-phase 6-pole winding yields the torque-generating stator field. This single-phase winding is fed by the star-point current of the suspension winding system, consisting of the zero-sequence currents. In [59] a combined winding is used instead of two separated windings, applying the same principle by means of current superposition. The axial and remaining tilting motions (z, φ_x, φ_y) are controlled passively.
In this work, the zero-sequence current feeding technique is used for the supply of the axial AMB. Details regarding the realization are presented in Chapter 6, whereas operational constraints are discussed in Chapter 7.

1.5. Classification of this Manuscript in the Context of Bearingless High-Speed Drives

One of the first persons who came up with the idea of a BM was *Hermann* in 1975 [69, 70, 71] who bases his explanations on *Sequenz* [72] from 1950 [73]. The idea was extended by *Meinke* in 1976 [74]. The reason for the discovery of bearingless drives in this decade is that they rely on vector control theory, power electronics and digital signal processing, which all started to be devoloped in these times. Starting at the end of the 1980s at the *ETH Zurich*, namely with dissertations by *Bichsel* [75], *Schöb* [28], *Barletta* [76] and *Bikle* [29], a considerable number of researches have been focusing on bearingless drives. When looking for launched prototype BMs, the following research groups (A ... I, referring to Table A.1 and Fig. 1.7) can be listed:

- *Institute for Electric Drives and Power Electronics*, *Johannes Kepler University*; *Linz Center of Mechatronics* (*LCM*), Austria, currently headed by Prof. *Amrhein* ($\rightarrow$ research group A)

- *Department of Information Technology and Electrical Engineering*, *ETH Zurich*, Switzerland, currently headed by Prof. *Kolar* ($\rightarrow$ research group B)

- *College of Engineering*, *University of Wisconsin Madison*, USA, currently headed by Prof. *Severson* ($\rightarrow$ research group C)
- *Department of Electrical & Electronic Engineering*, *Tokyo Institute of Technology*, Japan, currently headed by Prof. *Chiba* ($\rightarrow$ research group D)
- *Center for Research in Mechatronics*, *Université Catholique de Louvain*, Belgium, currently headed by Prof. *Kluyskens* ($\rightarrow$ research group E)
- *Chair of Electrical Machines*, *University of Nottingham*, United Kingdom, currently headed by Prof. *Gerada* ($\rightarrow$ research group F)
- *Chair of Electrical Energy Conversion Systems and Drives*, *Chemnitz University of Technology*, Germany, currently headed by Prof. *Werner* ($\rightarrow$ research group G)
- *Institute for Electrical Energy Conversion*, *Technical University of Darmstadt*, Germany, currently headed by Prof. *Binder* ($\rightarrow$ research group H)
- *Graduate School of Information Science and Technology*, *Hokkaido University*, Japan ($\rightarrow$ research group I)

Apart from that, many other research groups focus on magnetic bearing technology, e.g. the *Chair of Electrical Machines and Drives*, *Technical University of Dresden*, Germany, mostly not dealing with bearingless drives. For further details about the history of bearingless drives please refer to [4, 5, 73].

In order to relate this work to other bearingless drives, Fig. 1.7 gives an overview of built prototypes from the past two decades. Magnetically suspended drives, which do not incorporate bearingless motor units, are not shown. Only built prototype machines are listed. The data is further described in Table A.1 in Appendix A.1, sorted by descending maximum speed. Among the listed motors, the following contributions are named explicitly due to outstanding prototype performances: The authors in [77] (no. 27) present a 3000 min^{-1}/1.5 kW machine with the to date highest efficiency of 95%. In [8] (no. 7) a 37000 min^{-1}/60 kW machine is presented which is the to date highest rated power value. A maximum speed of 1000000 min^{-1} is achieved in [78] with air bearings. The highest speed a bearingless machine has ever achieved was 500000 min^{-1} in [79] (no. 1).

The achievable speed is preliminary limited by the achievable maximum mechanical stress in the rotor parts. For sleeve-protected PM machines, it was empirically found that the maximum speed is limited by the value $n_\text{N} \cdot \sqrt{P_\text{N}} = 800000\ \text{min}^{-1} \cdot \sqrt{\text{kW}}$ [80, 81].

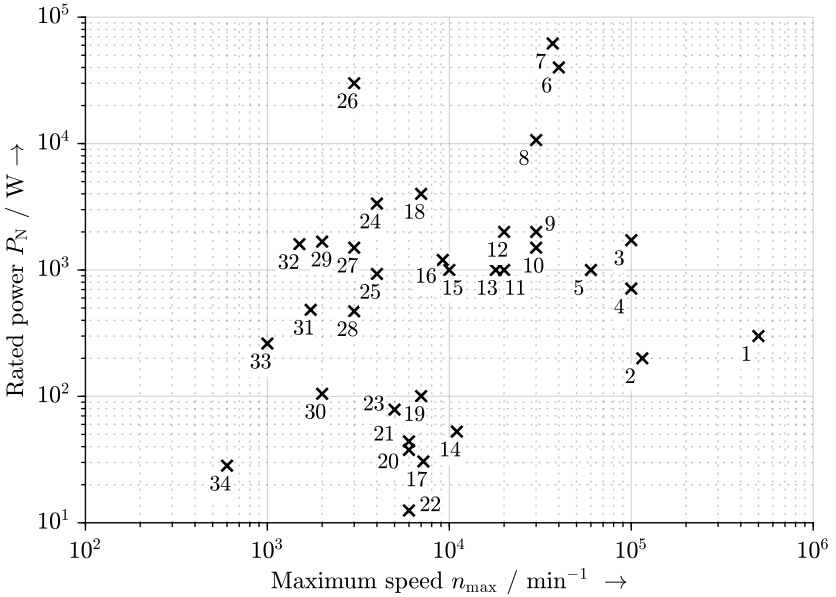

Fig. 1.7.: Rated data ($P_N(n_{max})$) for a selection of bearingless motor prototypes: no. 1 ... 34 refer to Appendix A.1, Table A.1

For solid-rotor induction machines it is given by $n_N \cdot \sqrt{P_N} = 1000000\,\text{min}^{-1} \cdot \sqrt{\text{kW}}$. Most practical applications require lower speeds ($< 100000\,\text{min}^{-1}$), but are not restricted to small power ratings. Thus, research about bearingless machines should be done for high-power drives (> 50 kW). The most important contributions to this are a 3000 min^{-1}/30 kW [82] induction machine, a 40000 min^{-1}/40 kW PMSM [9] and the 37000 min^{-1}/60 kW PMSM [8].

2. Field and Force Calculation in Bearingless High-Speed Machines

Throughout this chapter 2-dimensional (2D) magnetic field calculation is used, neglecting end effects. Note that the eddy current inducing suspension field typically has a rather high ratio of pole pitch $\tau_{\mathrm{p,L}}$ to active length l_{Fe}. In case of the built prototype machine *LLM4*, it is $\tau_{\mathrm{p,L}}/l_{\mathrm{Fe}} = 0.7$. Thus, axial end effects may have a major influence which is discussed in Section 2.4.1.

2.1. Bearing Force and Air Gap Torque Calculation

In order to calculate forces acting on the rotor, generated within the active part of the bearingless machine, the 2D *Maxwell* stress tensor in cylindrical coordinates (2.2) is integrated over a closed surface around the rotor in the air gap at the radius r_{cal} (2.1). Note that in numerical simulations the closed surface is typically chosen to be in the middle of the mechanical air gap for higher numeric accuracy. The forces are expressed in stator-fixed coordinates with the mechanical circumference angle γ_{m}. The field calculation in Section 2.2 is done in rotor-fixed coordinates with the circumference angle $\gamma_{\mathrm{R}} = \gamma_{\mathrm{m}} - 2\pi \cdot n \cdot t$.

$$\begin{pmatrix} F_{\mathrm{x}}(t) \\ F_{\mathrm{y}}(t) \\ M_{\delta}(t) \end{pmatrix} = \int_0^{l_{\mathrm{Fe}}} \int_0^{2\pi} \begin{pmatrix} f_{\mathrm{r}}(\gamma_{\mathrm{m}},t) \cdot \cos(\gamma_{\mathrm{m}}) - f_{\gamma}(\gamma_{\mathrm{m}},t) \cdot \sin(\gamma_{\mathrm{m}}) \\ f_{\mathrm{r}}(\gamma_{\mathrm{m}},t) \cdot \sin(\gamma_{\mathrm{m}}) + f_{\gamma}(\gamma_{\mathrm{m}},t) \cdot \cos(\gamma_{\mathrm{m}}) \\ r_{\mathrm{cal}} \cdot f_{\gamma}(\gamma_{\mathrm{m}},t) \end{pmatrix} \cdot r_{\mathrm{cal}} \cdot \mathrm{d}\gamma_{\mathrm{m}} \mathrm{d}z \tag{2.1}$$

$$\left. \begin{pmatrix} f_{\mathrm{r}}(\gamma_{\mathrm{m}},t) \\ f_{\gamma}(\gamma_{\mathrm{m}},t) \end{pmatrix} \right|_{r=r_{\mathrm{cal}}} = \frac{1}{2 \cdot \mu_0} \cdot \begin{pmatrix} B_{\mathrm{r}}^2(r_{\mathrm{cal}},\gamma_{\mathrm{m}},t) - B_{\gamma}^2(r_{\mathrm{cal}},\gamma_{\mathrm{m}},t) \\ 2 \cdot B_{\mathrm{r}}(r_{\mathrm{cal}},\gamma_{\mathrm{m}},t) \cdot B_{\gamma}(r_{\mathrm{cal}},\gamma_{\mathrm{m}},t) \end{pmatrix} \tag{2.2}$$

Due to the assumed material linearity for the analytical calculation, the overall radial and tangential field components B_{r} and B_{γ} are given by the superposition of the stator and rotor field waves.

In the expressions $\hat{B}\cdot\cos(\nu'\cdot\gamma_\mathrm{R}-2\pi\cdot k_\mathrm{D}\cdot t-\varphi_\mathrm{D})$ and $\hat{B}\cdot\cos\big(\nu'_\mathrm{L}\cdot\gamma_\mathrm{R}-2\pi\cdot k_\mathrm{L}\cdot t-\varphi_\mathrm{L}\big)$, the subscript D (L) is used for the stator drive (suspension) field waves of absolute space order $\nu'=\nu\cdot p$ ($\nu'_\mathrm{L}=\nu_\mathrm{L}\cdot p_\mathrm{L}$) and of time order k_D (k_L). Rotor field waves (subscript: R) are described in stator-fixed coordinates with $\mu'=\mu\cdot p$ being the space and time harmonic order ($k_\mathrm{R}=\mu'$). γ_m is the mechanical circumference angle (Fig. 2.1). Generally, the time harmonic order in stator-fixed coordinates is defined with respect to the rotational frequency, i.e. $k=1$ means $1\cdot f_\mathrm{m}=f_\mathrm{m}=n$. The formulation is necessary to explain the occurrence of force harmonics due to magnetic saturation (Section 2.6) and eccentricity (Section 2.7). For the calculation of the average air gap torque and the suspension force, the consideration of the fundamental field waves, i.e. $\nu=1$, $\nu_\mathrm{L}=1$ and $\mu=1$, all being at $k_\mathrm{D}=k_\mathrm{L}=\mu'=p$, is sufficient. In this case the angular frequency is the synchronous frequency $k\cdot 2\pi\cdot n=p\cdot 2\pi\cdot n=\omega_\mathrm{syn}$. The radial field wave components are shown in (2.3)–(2.5), the tangential field wave components are shown in (2.6)–(2.8).
The rotor field waves move synchronously with the rotor ($k=\mu'$), thus, no eddy currents in the conductive rotor parts occur. The stator field waves of order ν, ν_L, apart from the fundamental drive winding field wave, move asynchronously to the rotor ($k=p=\text{const.}$). Also the fundamental suspension winding field wave ($\nu_\mathrm{L}=1$) of absolute order $p_\mathrm{L}=\pm1$ and time order $k=p\neq p_\mathrm{L}$ has a wave velocity different from the synchronous velocity. The damping of the asynchronous field wave amplitudes is included in the absolute value $|\underline{B}|$ of the complex phasor $\underline{B}=|\underline{B}|\cdot e^{j\cdot\Delta\gamma_\mathrm{Ft}}$. The phase shifting of the asynchronous field waves is considered by the angle $\Delta\gamma_\mathrm{Ft}$ of the complex phasor.

$$\begin{aligned}
B_{\mathrm{D},\nu',k_\mathrm{D},\mathrm{r}}(r,\gamma_\mathrm{m},t)&=\mathrm{Re}\big\{\underline{B}_{\mathrm{D},\nu',k_\mathrm{D},\mathrm{r}}(r)\cdot e^{j\cdot\nu'\gamma_\mathrm{m}}\cdot e^{-j\cdot(k_\mathrm{D}\cdot2\pi\cdot n\cdot t+\varphi_\mathrm{D})}\big\} &(2.3)\\
&=\big|\underline{B}_{\mathrm{D},\nu',k_\mathrm{D},\mathrm{r}}(r)\big|\cdot\cos\big(\nu'\gamma_\mathrm{m}-k_\mathrm{D}\cdot2\pi\cdot n\cdot t-\varphi_\mathrm{D}-\Delta\gamma_{\mathrm{Ft},\nu',\mathrm{r}}\big)\\
B_{\mathrm{L},\nu'_\mathrm{L},k_\mathrm{L},\mathrm{r}}(r,\gamma_\mathrm{m},t)&=\mathrm{Re}\big\{\underline{B}_{\mathrm{L},\nu'_\mathrm{L},k_\mathrm{L},\mathrm{r}}(r)\cdot e^{j\cdot\nu'_\mathrm{L}\gamma_\mathrm{m}}\cdot e^{-j\cdot(k_\mathrm{L}\cdot2\pi\cdot n\cdot t+\varphi_\mathrm{L})}\big\} &(2.4)\\
&=\Big|\underline{B}_{\mathrm{L},\nu'_\mathrm{L},k_\mathrm{L},\mathrm{r}}(r)\Big|\cdot\cos\Big(\nu'_\mathrm{L}\gamma_\mathrm{m}-k_\mathrm{L}\cdot2\pi\cdot n\cdot t-\varphi_\mathrm{L}-\Delta\gamma_{\mathrm{Ft},\nu'_\mathrm{L},\mathrm{r}}\Big)\\
B_{\mathrm{R},\mu',\mu',\mathrm{r}}(r,\gamma_\mathrm{m},t)&=\mathrm{Re}\big\{\underline{B}_{\mathrm{R},\mu',\mu',\mathrm{r}}(r)\cdot e^{j\cdot\mu'\gamma_\mathrm{m}}\cdot e^{-j\cdot(\mu'\cdot2\pi\cdot n\cdot t+\varphi_\mathrm{R})}\big\} &(2.5)\\
&=\hat{B}_{\mathrm{R},\mu',\mu',\mathrm{r}}(r)\cdot\cos\big(\mu'\gamma_\mathrm{m}-\mu'\cdot2\pi\cdot n\cdot t-\varphi_\mathrm{R}\big)\\
B_{\mathrm{D},\nu',k_\mathrm{D},\gamma}(r,\gamma_\mathrm{m},t)&=\mathrm{Re}\big\{\underline{B}_{\mathrm{D},\nu',k_\mathrm{D},\gamma}(r)\cdot e^{j\cdot\nu'\gamma_\mathrm{m}}\cdot e^{-j\cdot\left(k_\mathrm{D}\cdot2\pi\cdot n\cdot t+\varphi_\mathrm{D}+\frac{\pi}{2}\right)}\big\} &(2.6)\\
&=\big|\underline{B}_{\mathrm{D},\nu',k_\mathrm{D},\gamma}(r)\big|\cdot\sin\big(\nu'\gamma_\mathrm{m}-k_\mathrm{D}\cdot2\pi\cdot n\cdot t-\varphi_\mathrm{D}-\Delta\gamma_{\mathrm{Ft},\nu',\gamma}\big)\\
B_{\mathrm{L},\nu'_\mathrm{L},k_\mathrm{L},\gamma}(r,\gamma_\mathrm{m},t)&=\mathrm{Re}\big\{\underline{B}_{\mathrm{L},\nu'_\mathrm{L},k_\mathrm{L},\gamma}(r)\cdot e^{j\cdot\nu'_\mathrm{L}\gamma_\mathrm{m}}\cdot e^{-j\cdot\left(k_\mathrm{L}\cdot2\pi\cdot n\cdot t+\varphi_\mathrm{L}+\frac{\pi}{2}\right)}\big\} &(2.7)\\
&=\Big|\underline{B}_{\mathrm{L},\nu'_\mathrm{L},k_\mathrm{L},\gamma}(r)\Big|\cdot\sin\Big(\nu'_\mathrm{L}\gamma_\mathrm{m}-k_\mathrm{L}\cdot2\pi\cdot n\cdot t-\varphi_\mathrm{L}-\Delta\gamma_{\mathrm{Ft},\nu'_\mathrm{L},\gamma}\Big)
\end{aligned}$$

$$B_{\mathrm{R},\mu',\mu',\gamma}(r,\gamma_\mathrm{m},t) = \mathrm{Re}\left\{\underline{B}_{\mathrm{R},\mu',\mu',\gamma}(r)\cdot e^{j\cdot\mu'\gamma_\mathrm{m}}\cdot e^{-j\cdot\left(\mu'\cdot 2\pi\cdot n\cdot t+\varphi_\mathrm{R}+\frac{\pi}{2}\right)}\right\} \\ = \hat{B}_{\mathrm{R},\mu',\mu',\gamma}(r)\cdot\sin\left(\mu'\gamma_\mathrm{m}-\mu'\cdot 2\pi\cdot n\cdot t-\varphi_\mathrm{R}\right) \tag{2.8}$$

Inserting the radial and tangential components of the rotor and the suspension winding air gap field waves, satisfying $\nu'_\mathrm{L}=\mu'+1$, from (2.7),(2.8) and (2.4),(2.5) into (2.1),(2.2) yields the general expression for the radial force vector $\vec{F}_\mathrm{L}(t)=F_\mathrm{x}(t)\cdot\vec{e}_\mathrm{x}+F_\mathrm{y}(t)\cdot\vec{e}_\mathrm{y}$ (2.9), (2.10). The tangential component of the rotor air gap field is here neglected for clarity, since its contribution to the suspension force is $<1\%$. These equations are needed for the description of the eddy current effect in Section 2.4.

$$F_\mathrm{x}(t)=\frac{\pi\cdot r_\mathrm{cal}\cdot l_\mathrm{Fe}}{2\cdot\mu_0}\cdot\hat{B}_{\mathrm{R},\mu',\mu',\mathrm{r}}(r_\mathrm{cal})\cdot \\ \left[\left|\underline{B}_{\mathrm{L},\nu'_\mathrm{L},k_\mathrm{L},\mathrm{r}}(r_\mathrm{cal})\right|\cdot\sin\left(\left(\mu'-k_\mathrm{L}\right)\cdot n\cdot t\cdot 2\pi+\varphi_\mathrm{R}-\varphi_\mathrm{L}-\Delta\varphi_{\mathrm{Ft},\nu'_\mathrm{L},\mathrm{r}}\right)+\right. \\ \left.\left|\underline{B}_{\mathrm{L},\nu'_\mathrm{L},k_\mathrm{L},\gamma}(r_\mathrm{cal})\right|\cdot\sin\left(\left(\mu'-k_\mathrm{L}\right)\cdot n\cdot t\cdot 2\pi+\varphi_\mathrm{R}-\varphi_\mathrm{L}-\Delta\varphi_{\mathrm{Ft},\nu'_\mathrm{L},\gamma}\right)\right] \tag{2.9}$$

$$F_\mathrm{y}(t)=\frac{\pi\cdot r_\mathrm{cal}\cdot l_\mathrm{Fe}}{2\cdot\mu_0}\cdot\hat{B}_{\mathrm{R},\mu',\mu',\mathrm{r}}(r_\mathrm{cal})\cdot \\ \left[\left|\underline{B}_{\mathrm{L},\nu'_\mathrm{L},k_\mathrm{L},\mathrm{r}}(r_\mathrm{cal})\right|\cdot\cos\left(\left(\mu'-k_\mathrm{L}\right)\cdot n\cdot t\cdot 2\pi+\varphi_\mathrm{R}-\varphi_\mathrm{L}-\Delta\varphi_{\mathrm{Ft},\nu'_\mathrm{L},\mathrm{r}}\right)+\right. \\ \left.\left|\underline{B}_{\mathrm{L},\nu'_\mathrm{L},k_\mathrm{L},\gamma}(r_\mathrm{cal})\right|\cdot\cos\left(\left(\mu'-k_\mathrm{L}\right)\cdot n\cdot t\cdot 2\pi+\varphi_\mathrm{R}-\varphi_\mathrm{L}-\Delta\varphi_{\mathrm{Ft},\nu'_\mathrm{L},\gamma}\right)\right] \tag{2.10}$$

If no rotor eddy currents are present, the phase shift is $\Delta\gamma_\mathrm{Ft}=0$. So the tangential and radial field amplitudes can be added as real values and (2.9), (2.10) can be simplified to (2.11), here only shown for the x-direction. In (2.11), $f_\mathrm{L}=(k_\mathrm{L}-\mu')\cdot n$ is the suspension force frequency, e.g. needed to counteract a f_L-frequent disturbance force. $\varphi_{\mathrm{F,ref}}$ is the angle, which determines the direction of the suspension force, e.g. $\varphi_{\mathrm{F,ref}}=0$ for $F_\mathrm{L}=F_\mathrm{y}$. For the standstill bearing force vector, the time harmonic orders are $\mu'=k_\mathrm{L}=p$ and the space harmonic orders are $\mu'=p$, $\nu'_\mathrm{L}=p_\mathrm{L}=p\pm 1$. Hence, for steady state levitation at a given speed n, the suspension winding is fed with a f_syn-frequent current system I_L like the drive winding current system I_D. For a pulsating or rotating bearing force vector of frequency $f_\mathrm{L}=(k_\mathrm{L}-p)\cdot n$, the space harmonic orders are equal but the suspension winding time harmonic order gets $k_\mathrm{L}=p+f_\mathrm{L}/n$. The frequency of the suspension winding current system is then $n\cdot(p+f_\mathrm{L}/n)=n\cdot p+f_\mathrm{L}=f_\mathrm{syn}+f_\mathrm{L}$. Note that f_L is associated with a counter-clockwise rotating force vector. The counter-clockwise direction of rotation is

mathematically the positive direction of rotation.

$$F_{\mathrm{x}}(t) = \frac{\pi \cdot r_{\mathrm{cal}} \cdot l_{\mathrm{Fe}}}{2 \cdot \mu_0} \cdot \hat{B}_{\mathrm{R},\mu',\mu',\mathrm{r}}(r_{\mathrm{cal}}) \cdot \left[\hat{B}_{\mathrm{L},\nu'_{\mathrm{L}},k_{\mathrm{L}},\mathrm{r}}(r_{\mathrm{cal}}) + \hat{B}_{\mathrm{L},\nu'_{\mathrm{L}},k_{\mathrm{L}},\gamma}(r_{\mathrm{cal}}) \right] \cdot \sin\left(-\underbrace{\left(k_{\mathrm{L}} - \mu'\right) \cdot n}_{f_{\mathrm{L}}} \cdot t \cdot 2\pi + \underbrace{\varphi_{\mathrm{R}} - \varphi_{\mathrm{L}}}_{\varphi_{\mathrm{F,ref}}} \right) \tag{2.11}$$

All considerations were so far made in stator-fixed coordinates. For the analytical magnetic field calculation, including rotor eddy currents, the formulation in rotor-fixed coordinates is needed. The circumference angle in rotor-fixed coordinates is $\gamma_{\mathrm{R}} = \gamma_{\mathrm{m}} - 2\pi \cdot n \cdot t$. The levitation air gap field wave components in rotor-fixed coordinates are given in (2.12), (2.13).

$$B_{\mathrm{L},\nu'_{\mathrm{L}},k_{\mathrm{L}},\mathrm{r}}(r,\gamma_{\mathrm{R}},t) = \mathrm{Re}\left\{ \underline{B}_{\mathrm{L},\nu'_{\mathrm{L}},k_{\mathrm{L}},\mathrm{r}}(r) \cdot e^{j \cdot \nu'_{\mathrm{L}} \gamma_{\mathrm{R}}} \cdot e^{-j \cdot [(k_{\mathrm{L}} - \nu'_{\mathrm{L}}) \cdot 2\pi \cdot n \cdot t + \varphi_{\mathrm{L}}]} \right\} \tag{2.12}$$

$$B_{\mathrm{L},\nu'_{\mathrm{L}},k_{\mathrm{L}},\gamma}(r,\gamma_{\mathrm{R}},t) = \mathrm{Re}\left\{ \underline{B}_{\mathrm{L},\nu'_{\mathrm{L}},k_{\mathrm{L}},\gamma}(r) \cdot e^{j \cdot \nu'_{\mathrm{L}} \gamma_{\mathrm{R}}} \cdot e^{-j \cdot \left[(k_{\mathrm{L}} - \nu'_{\mathrm{L}}) \cdot 2\pi \cdot n \cdot t + \varphi_{\mathrm{L}} + \frac{\pi}{2}\right]} \right\} \tag{2.13}$$

(2.12), (2.13) contain the rotor frequency f_{R} (= slip frequency). For the fundamental suspension winding air gap field wave, the rotor frequency is given in (2.14). It shows that f_{R} only depends on the suspension force oscillation frequency f_{L} and on the rotor speed n. Even for a standstill bearing force vector, eddy currents are induced due to $f_{\mathrm{R}} = |-n|$ for topologies with $p_{\mathrm{L}} = p+1$. Also the slip s is given in (2.14). It decreases for higher pole count p, which is compensated by a higher synchronous frequency f_{syn} for constant speed n.

$$\begin{aligned} f_{\mathrm{R}}|_{\nu'_{\mathrm{L}}=p_{\mathrm{L}}} &= (k_{\mathrm{L}} - p_{\mathrm{L}}) \cdot n = \left[\left(\frac{f_{\mathrm{L}}}{n} + p \right) - p_{\mathrm{L}} \right] \cdot n = f_{\mathrm{L}} + f_{\mathrm{syn}} - n \cdot (p \pm 1) \\ &= \begin{cases} f_{\mathrm{L}} - n & \Rightarrow s|_{\nu'_{\mathrm{L}}=p_{\mathrm{L}}} = \frac{f_{\mathrm{L}}}{f_{\mathrm{syn}}} - \frac{1}{p} \quad \text{for } p_{\mathrm{L}} = p+1 \\ f_{\mathrm{L}} + n & \Rightarrow s|_{\nu'_{\mathrm{L}}=p_{\mathrm{L}}} = \frac{f_{\mathrm{L}}}{f_{\mathrm{syn}}} + \frac{1}{p} \quad \text{for } p_{\mathrm{L}} = p-1 \end{cases} \end{aligned} \tag{2.14}$$

For the stator winding field calculation, a current loading model [83] is used in Section 2.2. The current loading field waves are $\underline{K}_{\mathrm{D},\nu',k_{\mathrm{D}}}(\gamma_{\mathrm{m}},t)$ (2.15) for the drive winding and $\underline{K}_{\mathrm{L},\nu'_{\mathrm{L}},k_{\mathrm{L}}}(\gamma_{\mathrm{m}},t)$ (2.16) for the suspension winding.

$$\underline{K}_{\mathrm{D},\nu',k_{\mathrm{D}}}(\gamma_{\mathrm{m}},t) = \frac{m \cdot k_{\mathrm{w},\nu'} \cdot N_{\mathrm{s}} \cdot \hat{I}_{\mathrm{D},k_{\mathrm{D}}}}{\pi \cdot r_{\mathrm{S,i}}} \cdot e^{-j \cdot (k_{\mathrm{D}} \cdot 2\pi \cdot n \cdot t - \varphi_{\mathrm{D}})} \tag{2.15}$$

$$\underline{K}_{\mathrm{L},\nu'_{\mathrm{L}},k_{\mathrm{L}}}(\gamma_{\mathrm{m}},t)=\frac{m\cdot k_{\mathrm{w},\nu'_{\mathrm{L}}}\cdot N_{\mathrm{s}}\cdot\hat{I}_{\mathrm{D,L}}}{\pi\cdot r_{\mathrm{S,i}}}\cdot e^{-j\cdot(k_{\mathrm{L}}\cdot 2\pi\cdot n\cdot t-\varphi_{\mathrm{L}})} \tag{2.16}$$

A rotating or standstill force vector is generated by a single current loading wave (2.16). The time order is $k_{\mathrm{L}}=p$ for the standstill and $k_{\mathrm{L}}=p+f_{\mathrm{L}}/n$ for a rotating force vector with rotation frequency f_{L}. That means, the rotating radial bearing force vector is composed of a f_{L}-pulsating force in x- and y-direction according to (2.9), (2.10). If the bearing force vector moves synchronously with the rotor ($f_{\mathrm{L}}=n$), e.g. to counteract rotor unbalance forces, the slip frequency (2.14) is zero and no eddy currents are induced.
To include the bearing force generation in the rotor position control (Chapter 5), a pulsating bearing force vector of variable frequency f_{L}, e.g. in x- or y-direction, must be considered. Results for a pulsating suspension force vector are given in Section 2.4.2. Within the framework of harmonic contributions, a pulsating force vector is composed of two rotating force vectors of half amplitude and opposite rotation sense. Therefore, the necessary forward $B_{\mathrm{L},p_{\mathrm{L}},k_{\mathrm{f}}}$ and backward $B_{\mathrm{L},p_{\mathrm{L}},k_{\mathrm{b}}}$ rotating fundamental suspension field waves are superimposed to $B_{\mathrm{L},p_{\mathrm{L}},k_{\mathrm{L}},\mathrm{r,p}}(r,\gamma_{\mathrm{R}},t)$ and $B_{\mathrm{L},p_{\mathrm{L}},k_{\mathrm{L}},\gamma,\mathrm{p}}(r,\gamma_{\mathrm{R}},t)$ (2.17) – (2.18), where $k_{\mathrm{f}}=p+f_{\mathrm{L}}/n$ and $k_{\mathrm{b}}=p-f_{\mathrm{L}}/n$ are the associated time harmonic orders. Thus, the field calculation is separately done for each field wave $B_{\mathrm{L},p_{\mathrm{L}},k_{\mathrm{f}}}$ and $B_{\mathrm{L},p_{\mathrm{L}},k_{\mathrm{b}}}$ and its superposition yields the pulsating suspension force according to (2.9) – (2.10).

$$B_{\mathrm{L},\nu'_{\mathrm{L}},k_{\mathrm{L}},\mathrm{r,p}}(r,\gamma_{\mathrm{R}},t)=\mathrm{Re}\Big\{\underline{B}_{\mathrm{L},\nu'_{\mathrm{L}},k_{\mathrm{f}},\mathrm{r}}(r)\cdot e^{j\cdot\nu'_{\mathrm{L}}\gamma_{\mathrm{R}}}\cdot e^{-j\cdot[(k_{\mathrm{f}}-\nu'_{\mathrm{L}})\cdot 2\pi\cdot n\cdot t+\varphi_{\mathrm{L}}]}+ \tag{2.17}$$
$$\underline{B}_{\mathrm{L},\nu'_{\mathrm{L}},k_{\mathrm{b}},\mathrm{r}}(r)\cdot e^{j\cdot\nu'_{\mathrm{L}}\gamma_{\mathrm{R}}}\cdot e^{-j\cdot[(k_{\mathrm{b}}-\nu'_{\mathrm{L}})\cdot 2\pi\cdot n\cdot t+\varphi_{\mathrm{L}}]}\Big\}$$

$$B_{\mathrm{L},\nu'_{\mathrm{L}},k_{\mathrm{L}},\gamma,\mathrm{p}}(r,\gamma_{\mathrm{R}},t)=\mathrm{Re}\Big\{\underline{B}_{\mathrm{L},\nu'_{\mathrm{L}},k_{\mathrm{f}},\gamma}(r)\cdot e^{j\cdot\nu'_{\mathrm{L}}\gamma_{\mathrm{R}}}\cdot e^{-j\cdot\left[(k_{\mathrm{f}}-\nu'_{\mathrm{L}})\cdot 2\pi\cdot n\cdot t+\varphi_{\mathrm{L}}-\frac{\pi}{2}\right]}+ \tag{2.18}$$
$$\underline{B}_{\mathrm{L},\nu'_{\mathrm{L}},k_{\mathrm{b}},\gamma}(r)\cdot e^{j\cdot\nu'_{\mathrm{L}}\gamma_{\mathrm{R}}}\cdot e^{-j\cdot\left[(k_{\mathrm{b}}-\nu'_{\mathrm{L}})\cdot 2\pi\cdot n\cdot t+\varphi_{\mathrm{L}}-\frac{\pi}{2}\right]}\Big\}$$

Inserting the radial and tangential components of the rotor and the drive winding air gap field waves, satisfying $\nu'=\mu'$, from (2.7), (2.8) and (2.3), (2.4) into (2.1), (2.2) yields the general expression for the air gap torque (2.19), with which – apart from the average

torque – the torque ripple can be calculated.

$$M_\delta(t) = \frac{\pi \cdot r_{\mathrm{cal}}^2 \cdot l_{\mathrm{Fe}}}{2 \cdot \mu_0} \cdot \tag{2.19}$$
$$\Big[\hat{B}_{\mathrm{R},\mu',\mu',\mathrm{r}}(r_{\mathrm{cal}}) \cdot \Big|\underline{B}_{\mathrm{D},\nu'_{\mathrm{D}},k_{\mathrm{D}},\gamma}(r_{\mathrm{cal}})\Big| \cdot \sin\Big((\mu' - k_{\mathrm{D}}) \cdot n \cdot t \cdot 2\pi + \varphi_{\mathrm{D}} - \varphi_{\mathrm{R}} + \Delta\varphi_{\mathrm{Ft},\nu'_{\mathrm{D}},\gamma}\Big) +$$
$$\hat{B}_{\mathrm{R},\mu',\mu',\gamma}(r_{\mathrm{cal}}) \cdot \Big|\underline{B}_{\mathrm{D},\nu'_{\mathrm{D}},k_{\mathrm{D}},\mathrm{r}}(r_{\mathrm{cal}})\Big| \cdot \sin\Big((\mu' - k_{\mathrm{D}}) \cdot n \cdot t \cdot 2\pi + \varphi_{\mathrm{D}} - \varphi_{\mathrm{R}} + \Delta\varphi_{\mathrm{Ft},\nu'_{\mathrm{D}},\mathrm{r}}\Big)\Big]$$

For the calculation of the average torque, the fundamental rotor and drive winding air gap field waves are inserted into (2.19), yielding (2.20).

$$M_\delta = \frac{\pi \cdot r_{\mathrm{cal}}^2 \cdot l_{\mathrm{Fe}}}{2 \cdot \mu_0} \cdot \big[\hat{B}_{\mathrm{R},p,p,\mathrm{r}}(r_{\mathrm{cal}}) \cdot \hat{B}_{\mathrm{D},p,p,\gamma}(r_{\mathrm{cal}}) \cdot \sin(\varphi_{\mathrm{D}} - \varphi_{\mathrm{R}}) + \tag{2.20}$$
$$\hat{B}_{\mathrm{R},p,p,\gamma}(r_{\mathrm{cal}}) \cdot \hat{B}_{\mathrm{D},p,p,\mathrm{r}}(r_{\mathrm{cal}}) \cdot \sin(\varphi_{\mathrm{D}} - \varphi_{\mathrm{R}})\big]$$

The rotor and stator air gap magnetic field waves can be determined in different ways (Table 4.2). In the following, the 2D analytical calculation is presented and compared to 2D simulation results based on the FEM technique.

2.2. Magnetoquasistatic Field Calculation Allowing for Eddy Currents at Centric Rotor Position

The 2D magnetic field calculation for bearingless PM machines has the following benefits when compared to a FEM simulation:

- High-speed machines exhibit low flux densities for low iron losses (*LLM4*: $\hat{B}_{\mathrm{r}} < 0.5$ T). Thus, the material permeability μ can be considered constant with good accuracy (constraints shown in Section 2.6).
- The PM of such machines is oftentimes a solid ring. Therefore, the model of the inner rotor is rotationally symmetric.
- Within this investigation, the calculation time of the analytical model in *Matlab* on a PC according to Table 4.1 is about 5 s per parameter set. Due to the transient settling process of the rotor eddy currents an accurate 2D FEM simulation with the software *JMAG Designer 19.1* on the same PC takes about 30 min for the 1 kW machine (outer diameter 75 mm) and about 1 h for the 40 kW machine (outer diameter

135 mm). A comparable 3D FEM simulation with the software *JMAG Designer 19.1* on the same PC for the 1 kW machine takes about 2 d.

- Analytical calculations yield due to the formulas insight into the results and the inter-dependence of parameters and thereby re-traceability of certain effects.

2.2.1. Model Assumptions

The dimensions r_{sh}, r_{PM}, $r_{S,i}$, $r_{S,o}$ and material parameters permeability μ_r and conductivity κ of the machine are depicted in Fig. 2.1 and Table 2.1. The materials are considered to be homogeneous ($\mu_r = \text{const.}$, $\kappa = \text{const.}$) and isotropic. Table 2.1 shows typical material properties that comply with the used materials (Sections 3.7.1, 3.7.3). The five considered areas are: rotor shaft (sh) $i = 1$, PM ring (PM) $i = 2$, air gap (δ) $i = 3$, stator (S) $i = 4$ and the exterior (ex) $i = 5$.

No slotting is considered, so the field distortion due to the stator slot opening effect is neglected, since it does not influence the disturbing forces by rotor eddy currents and since it only decreases the fundamental field waves by $< 5\%$ (Section 2.3) due to the bigger magnetically effective air gap, caused by the PM ring with $\mu_{PM} \approx \mu_0$. For clarity, only the space fundamental of the rotor field ($\mu' = p$, $\mu = 1$) and of the suspension field are considered ($\nu'_L = p_L$, $\nu_L = 1$). The time harmonic order k_L of the suspension field wave depends on the bearing force frequency f_L (Section 2.1). The fundamental of the drive winding field moves synchronously with the rotor, thus, not causing any rotor eddy currents. Its calculation runs completely magnetostatically but similar to the suspension winding field wave calculation. The calculation process is only shown for the suspension winding field.

Table 2.1.: Model dimensions and material properties for the 2D analytical field calculation of the *LLM4*

	radius / mm	κ / MS $\cdot$ m^{-1}	μ_r	$B_{rem}\,(70^\circ\text{C})$ / T
Shaft	$r_{sh} = 12.25$	1.25	400	-
PM	$r_{PM} = 15$	$0.8^{1)}$; $1.25^{2)}$; $1.8^{3)}$	$1.07^{1)}$; $1.06^{2)}$; $1.06^{3)}$	$1.096^{1)}$; $0.947^{2)}$; $0.947^{3)}$
Air gap	$r_{S,i} = 17.5$	-	1	-
Stator	$r_{S,o} = 37.5$	-	1000	-

[1]) NdFeB; [2]) Sm_2Co_{17}; [3]) $SmCo_5$

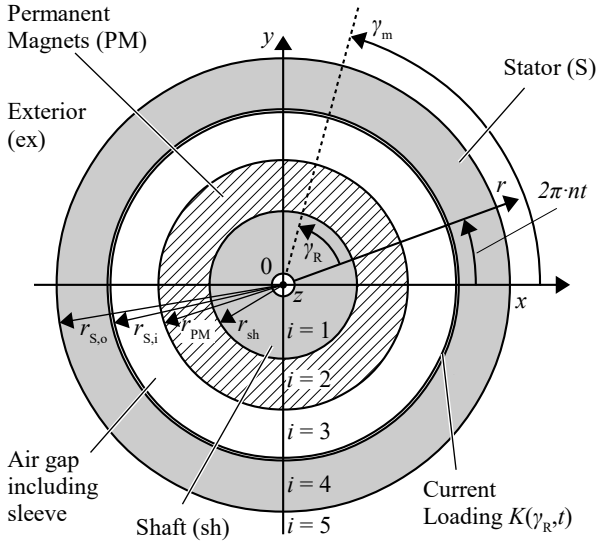

Fig. 2.1.: Model region definitions for the 2D analytical field calculation

For the drive winding field, only the results are given.

2.2.2. Calculation Approach

The r-γ_R-plane (Fig. 2.1) is considered, employing the approach via the magnetic vector potential $\vec{A} = \vec{e}_z \cdot \underline{A}_z$, which is assumed to have no variation in z-direction ($\frac{\partial \underline{A}_z}{\partial z} = 0; \forall\, z$). A calculation via the magnetic scalar potential approach as in [23] is not possible for the stator field, since it does not allow for eddy currents in the model regions. The procedure comprises the stator field calculation allowing for rotor eddy currents, employing the current loading ($\underline{K}$) approach on the stator inner surface (Section 2.2.3) and the magnetostatic calculation of the parallel-magnetized PM ring (Section 2.2.4). For any force calculation, the magnetic fields of both calculations are superimposed and included into the calculation of Section 2.1. Used references for the stator field calculations are [83, 84, 85, 86]. The rotor field calculation is well treated in [87, 88].

The governing differential equations, resulting from the *Maxwell* equations and the approach via the magnetic vector potential $\vec{A}$ are given by (2.21–2.23). (2.21) holds for any non-conductive and non-magnetic material. (2.22) is valid for the PM region in the ro-

tor field calculation and (2.23) for the conductive shaft and PM region in the stator field calculation.

$$\Delta \vec{A} = 0 \tag{2.21}$$

$$\Delta \vec{A} = -\mu_0 \cdot \mathrm{rot}\, \vec{M} \tag{2.22}$$

$$\Delta \vec{A} = \mu \cdot \kappa \cdot \frac{\partial}{\partial t} \vec{A} \tag{2.23}$$

2.2.3. Stator Field Calculation Including Eddy Currents

The magnetic vector potential $\vec{A}$ is assumed to vary sinusoidally in circumferential direction γ (rotor-fixed circumference angle γ_R) and time t: $\vec{A}_{\mathrm{L},p_\mathrm{L},k_\mathrm{L}} = \vec{e}_\mathrm{z} \cdot \underline{A}_{\mathrm{L},p_\mathrm{L},k_\mathrm{L},\mathrm{z}}$. Therefore, the complex calculus (2.24) is chosen, where $\underline{\xi}_{\mathrm{L},p_\mathrm{L},k_\mathrm{L},\mathrm{z}}$ is the radius-, frequency- and material-dependent complex z-component of $\underline{A}_{\mathrm{L},p_\mathrm{L},k_\mathrm{L},\mathrm{z}}$ of $\vec{A}$, incorporating the spatial phase lag due to the eddy current reaction field. The space harmonic order is given by $\nu'_\mathrm{L} = \nu_\mathrm{L} \cdot p_\mathrm{L} = p_\mathrm{L}$. The time harmonic order is k_L, which is related to the rotor angular frequency $\omega_\mathrm{R} = 2\pi \cdot f_\mathrm{R}$ via (2.14).

Inserting (2.24) into (2.23) in steady state in polar coordinates r, γ, yields the *Bessel*-type differential equation (2.25) for the radius-dependent z-component $\underline{\xi}_i$ of region i. The general solutions are given by (2.26) in the non-conductive ($\kappa_i = 0$) and in the conductive ($\kappa_i > 0$) regions, where $\underline{\alpha}_{k_\mathrm{L},i} = \sqrt{j \cdot \omega_\mathrm{R} \mu_i \kappa_i}$. In (2.26), I_{p_L} and K_{p_L} are the modified *Bessel* functions of 1st and 2nd kind of order p_L [89]. The complex radius-dependent components $\underline{B}_{\mathrm{r},i}$, $\underline{B}_{\gamma,i}$ of the magnetic flux density of the region i are determined by (2.27), (2.28). In order to calculate the tangential field component $\underline{B}_{\gamma,i}$ the derivative with regards to r according to (2.29) is needed. This, in case of conductive regions, is constituted from (2.30) by means of the so called recursion equations [89]. The modified *Bessel*, needed in regions with $\kappa_i > 0$, are given in the Appendix A.7. From this, one can identify the ascending and decaying behavior similar to the magnetostatic functions r^{p_L} and r^{-p_L} at $\kappa_i = 0$.

$$\underline{A}_{\mathrm{L},p_\mathrm{L},k_\mathrm{L},\mathrm{z},i}(r,\gamma_\mathrm{R},t) = \underline{\xi}_{\mathrm{L},p_\mathrm{L},k_\mathrm{L},\mathrm{z},i}(r,\kappa_i,\mu_i,\omega_\mathrm{R}) \cdot e^{j \cdot p_\mathrm{L} \gamma_\mathrm{R}} \cdot e^{-j \cdot (\omega_\mathrm{R} t + \varphi_\mathrm{L})} \tag{2.24}$$

$$0 = r^2 \cdot \frac{\mathrm{d}^2 \underline{\xi}_i}{\mathrm{d}r^2} + r \cdot \frac{\mathrm{d}\underline{\xi}_i}{\mathrm{d}r} - \left(j \cdot \omega_\mathrm{R} \mu_i \kappa_i \cdot r^2 + p_\mathrm{L}^2 \right) \cdot \underline{\xi}_i \tag{2.25}$$

$$\underline{\xi}_i = \begin{cases} \underline{C}_i \cdot I_{p_\mathrm{L}}\left(\underline{\alpha}_{k_\mathrm{L},i} \cdot r\right) + \underline{D}_i \cdot K_{p_\mathrm{L}}\left(\underline{\alpha}_{k_\mathrm{L},i} \cdot r\right) \; ; & \text{for } \kappa_i > 0 \\ C_i \cdot r^{p_\mathrm{L}} + D_i \cdot r^{-p_\mathrm{L}} \; ; & \text{for } \kappa_i = 0 \end{cases} \tag{2.26}$$

$$\underline{B}_{\mathrm{L},p_\mathrm{L},k_\mathrm{L},\mathrm{r},i}(r) = \frac{e^{-j\cdot p_\mathrm{L}\cdot\gamma_\mathrm{R}}}{r} \cdot \frac{\partial \underline{A}_{\mathrm{L},p_\mathrm{L},k_\mathrm{L},\mathrm{z},i}(r,\gamma_\mathrm{R})}{\partial \gamma_\mathrm{R}} = j \cdot \frac{p_\mathrm{L}}{r} \cdot \underline{\xi}_i \tag{2.27}$$

$$\underline{B}_{\mathrm{L},p_\mathrm{L},k_\mathrm{L},\gamma,i}(r) = -\frac{\partial \underline{A}_{\mathrm{L},p_\mathrm{L},k_\mathrm{L},\mathrm{z},i}(r,\gamma_\mathrm{R})}{\partial r} \cdot e^{-j\cdot p_\mathrm{L}\cdot\gamma_\mathrm{R}} = -\frac{\partial \underline{\xi}_i}{\partial r} \tag{2.28}$$

$$\frac{\partial \underline{\xi}_i}{\partial r} = \begin{cases} \underline{C}_i \cdot \frac{\partial I_{p_\mathrm{L}}}{\partial r}\left(\underline{\alpha}_{k_\mathrm{L},i} \cdot r\right) + \underline{D}_i \cdot \frac{\partial K_{p_\mathrm{L}}}{\partial r}\left(\underline{\alpha}_{k_\mathrm{L},i} \cdot r\right) \; ; & \text{for } \kappa_i > 0 \\ \frac{p_\mathrm{L}}{r} \cdot \left(C_i \cdot r^{p_\mathrm{L}} - D_i \cdot r^{-p_\mathrm{L}}\right) \; ; & \text{for } \kappa_i = 0 \end{cases} \tag{2.29}$$

$$\begin{cases} I'_{p_\mathrm{L},i} = \frac{\partial I_{p_\mathrm{L}}\left(\underline{\alpha}_{k_\mathrm{L},i} \cdot r\right)}{\partial r} = \underline{\alpha}_{k_\mathrm{L},i} \cdot \left[I_{p_\mathrm{L}-1,i} - \frac{p_\mathrm{L}}{\underline{\alpha}_{k_\mathrm{L},i} \cdot r} \cdot I_{p_\mathrm{L},i}\right] \\ K'_{p_\mathrm{L},i} = \frac{\partial K_{p_\mathrm{L}}\left(\underline{\alpha}_{k_\mathrm{L},i} \cdot r\right)}{\partial r} = \underline{\alpha}_{k_\mathrm{L},i} \cdot \left[-K_{p_\mathrm{L}-1,i} - \frac{p_\mathrm{L}}{\underline{\alpha}_{k_\mathrm{L},i} \cdot r} \cdot K_{p_\mathrm{L},i}\right] \end{cases} \tag{2.30}$$

The coefficients $\underline{C}_i$ and $\underline{D}_i$ (2.26) are calculated via the boundary conditions at the transitions from one region (i) to the adjacent region ($i+1$), where the radial component of magnetic flux density and the tangential component of the magnetic field intensity is continuous. That is, $\underline{B}_{\mathrm{L},p_\mathrm{L},k_\mathrm{L},\mathrm{r},i} = \underline{B}_{\mathrm{L},p_\mathrm{L},k_\mathrm{L},\mathrm{r},i+1}$ and $\underline{H}_{\mathrm{L},p_\mathrm{L},k_\mathrm{L},\gamma,i} = \underline{H}_{\mathrm{L},p_\mathrm{L},k_\mathrm{L},\gamma,i+1}$. Additionally, the transition from air gap (δ) to stator (S) is considered via *Ampere*'s law by $\underline{H}_{\mathrm{L},p_\mathrm{L},k_\mathrm{L},\gamma,\delta} - \underline{H}_{\mathrm{L},p_\mathrm{L},k_\mathrm{L},\gamma,\mathrm{S}} = \underline{K}_{\mathrm{L},p_\mathrm{L},k_\mathrm{L},\mathrm{z},i}(\gamma_\mathrm{R},t)$, incorporating the current loading $\underline{K}(\gamma_\mathrm{R},t)$. In the origin $r = 0$ the field is finite, hence, $\underline{D}_1 = \underline{D}_\mathrm{sh} = 0$. The magnetic field for $r \to \infty$ is zero, hence $\underline{B}_{\mathrm{r,ex}} = 0$ and $\underline{C}_1 = \underline{C}_\mathrm{ex} = 0$. In [84] the calculation via "transfer functions" is chosen which directly gives the complex solution of $\underline{\xi}$ at a certain radius r. This approach is restricted to one current loading layer $\underline{K}$ in the model and only yields the field quantities at the region transitions. Therefore, the classical approach via matrix calculus is chosen (2.31). The argument of the modified *Bessel* function is the outer radius $r'_{k_\mathrm{L},i}$ for the region of subscript i, scaled by the coefficient $\underline{\alpha}_{k_\mathrm{L},i}$: $r'_{k_\mathrm{L},i} = r_i \cdot \underline{\alpha}_{k_\mathrm{L},i}$. This approach leads for each harmonic order ν' respectively here p_L to the solution of the 8×8-matrix equation system for the five area problem ($i = 1,2,3,4,5$) to determine the 8 coefficients $\underline{C}_i$ and $\underline{D}_i$, here: $\underline{C}_1 = \underline{C}_\mathrm{sh}$, $\underline{C}_2 = \underline{C}_\mathrm{PM}$, $\underline{D}_2 = \underline{D}_\mathrm{PM}$, $\underline{C}_3 = \underline{C}_\delta$, $\underline{D}_3 = \underline{D}_\delta$, $\underline{C}_4 = \underline{C}_\mathrm{S}$, $\underline{D}_4 = \underline{D}_\mathrm{S}$ and $\underline{D}_5 = \underline{D}_\mathrm{ex}$. Note that for clarity the subscript ν' respectively here p_L for each of the coefficients is omitted for clarity, i.e. $\underline{C}_{i,\nu'} = \underline{C}_i$ and $\underline{D}_{i,\nu'} = \underline{D}_i$. The equation is solved by applying *Cramer*'s rule [90]. For faster computation in *Matlab*, the linear equation system is solved symbolically (Appendix A.8). The substitution follows afterwards. The solutions of the coefficients $\underline{C}_i$ and $\underline{D}_i$ are not given here, since the

solution ends in bulky expressions. To complete the field wave expressions in rotor-fixed coordinates, the complex radius-dependent components $\underline{B}_{\mathrm{L},p_\mathrm{L},k_\mathrm{L},\mathrm{r}}$, $\underline{B}_{\mathrm{L},p_\mathrm{L},k_\mathrm{L},\gamma}$ are inserted into (2.12), (2.13). To transform them into stator-fixed coordinates for the suspension force calculation, they are transformed into stator-fixed coordinates by multiplication with $e^{-j\cdot(2\pi\cdot n\cdot t)}$.

$$
\begin{bmatrix}
\frac{j\cdot p_\mathrm{L}}{r_\mathrm{sh}}\cdot I_{p_\mathrm{L}}\left(r'_{k_\mathrm{L},\mathrm{sh}}\right) & -\frac{j\cdot p_\mathrm{L}}{r_\mathrm{sh}}\cdot I_{p_\mathrm{L}}\left(r'_{k_\mathrm{L},\mathrm{sh}}\right) & -\frac{j\cdot p_\mathrm{L}}{r_\mathrm{sh}}\cdot K_{p_\mathrm{L}}\left(r'_{k_\mathrm{L},\mathrm{sh}}\right) & 0 \\
-\underline{\alpha}_{k_\mathrm{L},\mathrm{sh}}\cdot\frac{I'_{p_\mathrm{L}}\left(r'_{k_\mathrm{L},\mathrm{sh}}\right)}{\mu_\mathrm{sh}} & \underline{\alpha}_{\mathrm{PM},k_\mathrm{L}}\cdot\frac{I'_{p_\mathrm{L}}\left(r'_{k_\mathrm{L},\mathrm{sh}}\right)}{\mu_\mathrm{PM}} & \underline{\alpha}_{\mathrm{PM},k_\mathrm{L}}\cdot\frac{K'_{p_\mathrm{L}}\left(r'_{k_\mathrm{L},\mathrm{sh}}\right)}{\mu_\mathrm{PM}} & 0 \\
0 & \frac{j\cdot p_\mathrm{L}}{r_\mathrm{PM}}\cdot I_{p_\mathrm{L}}\left(r'_{k_\mathrm{L},\mathrm{PM}}\right) & \frac{j\cdot p_\mathrm{L}}{r_\mathrm{PM}}\cdot K_{p_\mathrm{L}}\left(r'_{k_\mathrm{L},\mathrm{PM}}\right) & -j\cdot p_\mathrm{L}\cdot r_\mathrm{PM}^{p_\mathrm{L}-1} \\
0 & -\underline{\alpha}_{\mathrm{PM},k_\mathrm{L}}\cdot\frac{I'_{p_\mathrm{L}}\left(r'_{k_\mathrm{L},\mathrm{PM}}\right)}{\mu_\mathrm{PM}} & -\underline{\alpha}_{\mathrm{PM},k_\mathrm{L}}\cdot\frac{K'_{p_\mathrm{L}}\left(r'_{k_\mathrm{L},\mathrm{PM}}\right)}{\mu_\mathrm{PM}} & p_\mathrm{L}\cdot\frac{r_\mathrm{PM}^{p_\mathrm{L}-1}}{\mu_0} \\
0 & 0 & 0 & j\cdot p_\mathrm{L}\cdot r_\mathrm{S,i}^{p_\mathrm{L}-1} \\
0 & 0 & 0 & -p_\mathrm{L}\cdot\frac{r_\mathrm{S,i}^{p_\mathrm{L}-1}}{\mu_0} \\
0 & 0 & 0 & 0 \\
0 & 0 & 0 & 0
\end{bmatrix}
\cdot
\begin{pmatrix}
\underline{C}_\mathrm{sh} \\ \underline{C}_\mathrm{PM} \\ \underline{D}_\mathrm{PM} \\ \underline{C}_\delta \\ \underline{D}_\delta \\ \underline{C}_\mathrm{S} \\ \underline{D}_\mathrm{S} \\ \underline{D}_\mathrm{ex}
\end{pmatrix}
$$

$$
\begin{bmatrix}
0 & 0 & 0 & 0 \\
0 & 0 & 0 & 0 \\
-j\cdot p_\mathrm{L}\cdot r_\mathrm{PM}^{-p_\mathrm{L}-1} & 0 & 0 & 0 \\
-p_\mathrm{L}\cdot\frac{r_\mathrm{PM}^{-p_\mathrm{L}-1}}{\mu_0} & 0 & 0 & 0 \\
j\cdot p_\mathrm{L}\cdot r_\mathrm{S,i}^{-p_\mathrm{L}-1} & -j\cdot p_\mathrm{L}\cdot r_\mathrm{S,i}^{p_\mathrm{L}-1} & -j\cdot p_\mathrm{L}\cdot r_\mathrm{S,i}^{-p_\mathrm{L}-1} & 0 \\
p_\mathrm{L}\cdot\frac{r_\mathrm{S,i}^{-p_\mathrm{L}-1}}{\mu_0} & p_\mathrm{L}\cdot\frac{r_\mathrm{S,i}^{p_\mathrm{L}-1}}{\mu_\mathrm{S}} & -p_\mathrm{L}\cdot\frac{r_\mathrm{S,i}^{-p_\mathrm{L}-1}}{\mu_\mathrm{S}} & 0 \\
0 & j\cdot p_\mathrm{L}\cdot r_\mathrm{S,o}^{p_\mathrm{L}-1} & j\cdot p_\mathrm{L}\cdot r_\mathrm{S,o}^{-p_\mathrm{L}-1} & -j\cdot p_\mathrm{L}\cdot r_\mathrm{S,o}^{-p_\mathrm{L}-1} \\
0 & -p_\mathrm{L}\cdot\frac{r_\mathrm{S,o}^{p_\mathrm{L}-1}}{\mu_\mathrm{S}} & p_\mathrm{L}\cdot\frac{r_\mathrm{S,o}^{-p_\mathrm{L}-1}}{\mu_\mathrm{S}} & p_\mathrm{L}\cdot\frac{r_\mathrm{S,o}^{-p_\mathrm{L}-1}}{\mu_0}
\end{bmatrix}
\cdot
\begin{pmatrix}
\underline{C}_\mathrm{sh} \\ \underline{C}_\mathrm{PM} \\ \underline{D}_\mathrm{PM} \\ \underline{C}_\delta \\ \underline{D}_\delta \\ \underline{C}_\mathrm{S} \\ \underline{D}_\mathrm{S} \\ \underline{D}_\mathrm{ex}
\end{pmatrix}
$$

$$
= \begin{pmatrix}
0 \\ 0 \\ 0 \\ 0 \\ 0 \\ -\frac{m\cdot k_{\mathrm{w},p_\mathrm{L}}\cdot N_\mathrm{s}\cdot\hat{I}_{\mathrm{L},k_\mathrm{L}}}{\pi\cdot r_\mathrm{S,i}} \\ 0 \\ 0
\end{pmatrix}
\quad ; \qquad \text{where } k_{w,p_\mathrm{L}} = k_{\mathrm{w,L}} \tag{2.31}
$$

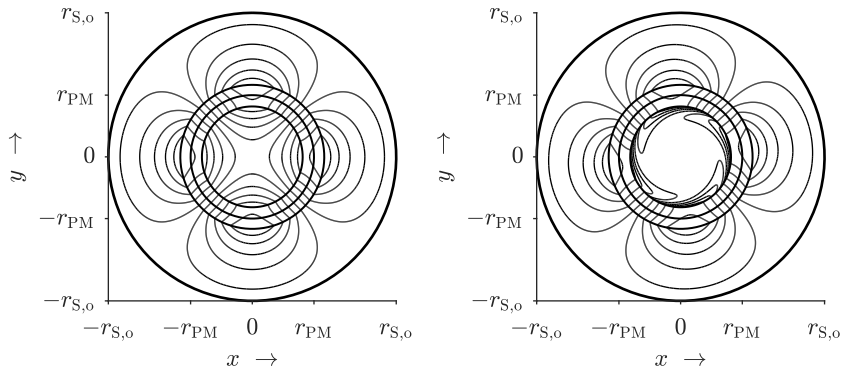

(a) Without eddy currents

(b) With eddy currents in the region $i = 1$ and $i = 2$ (PM material: Sm_2Co_{17})

Fig. 2.2.: Analytically calculated magnetic field lines as lines $|\underline{A}_z| = \text{const.}$ of the suspension field for the *LLM4* at the time instant $t = 0$ (model data from Table 2.1, $n = 60000\ \text{min}^{-1}$, $i_{\mathrm{q,L}} = 5.78$ A, counter-clockwise rotor rotation)

Exemplary, the suspension winding magnetic field is given in Fig. 2.2. Fig. 2.2a shows the magnetic field lines if no eddy currents are present. Fig. 2.2b gives the field distribution in the presence of eddy currents in the regions $i = 1$ and $i = 2$. One can clearly see that the eddy currents squeeze the magnetic field to the rim of the rotor shaft.

Closed-Form Expressions for the Stator Field Magnetic Flux Density Components

Most machine output quantities (Section 4.1) or equivalent circuit components (Section 4.2) are based on the magnetic air gap field. For the formulation of machine constants such as the torque-current coefficient k_{M}, closed-form expressions for the field components are necessary. However, manageable terms are only available for the magnetostatic calculation. They can be derived if the aforementioned calculations are carried out without any material conductivity ($\kappa = 0$), hence, without eddy currents. The solution coefficients are real numbers then and the approach functions have the form $C \cdot r^{\nu'} + D \cdot r^{-\nu'}$ instead of modified *Bessel* functions (2.26), (2.29). The term for the radial and tangential stator flux density components $B_{\mathrm{S},\nu',k,\mathrm{r}}$, $B_{\mathrm{S},\nu',k,\gamma}$ of the arbitrary space order $\nu' = \nu \cdot p$ and $\nu'_{\mathrm{L}} = \nu_{\mathrm{L}} \cdot p_{\mathrm{L}}$ respectively are given in (2.32), (2.34). The time harmonic order is defined here as $k = k_{\mathrm{L}} = p$, so that the angular synchronous frequency is $\omega_{\mathrm{syn}} = 2\pi \cdot n \cdot p$. The general subscript "S" for stator is used, since the equations are valid for both the drive

"D" and the suspension winding field wave "L" without eddy currents. The following simplifications are made, complying with "2D$_{\mathrm{simp}}$ " in Table 4.1: $\mu_{\mathrm{r,S,Fe}}, \mu_{\mathrm{r,R,Fe}} \to \infty$; $r_{\mathrm{S,o}} \to \infty$. The short form for $\mu_{\mathrm{r,PM}} = 1$ is given by (2.33, 2.35).

$$B_{\mathrm{S},\nu',p,\mathrm{r}}(r,\gamma_{\mathrm{m}},t) = \mu_0 \cdot \frac{m \cdot N_{\mathrm{s}} \cdot k_{\mathrm{w},\nu'} \cdot \hat{I}_{\mathrm{s}}}{\pi \cdot r_{\mathrm{S,i}}} \cdot \cos\left(\nu' \cdot \gamma_{\mathrm{m}} - \omega_{\mathrm{syn}} t - \varphi_{\mathrm{S}}\right) \cdot \frac{r_{\mathrm{S,i}}^{\nu'+1}}{r_{\mathrm{PM}}^{2\cdot\nu'}} \cdot \left\{ \frac{r^{\nu'-1} \cdot \left[\left(\frac{r_{\mathrm{sh}}}{r_{\mathrm{PM}}}\right)^{2\cdot\nu'} \cdot \left(\mu_{\mathrm{r,PM}} - 1\right) + \mu_{\mathrm{r,PM}} + 1\right]}{\left(\mu_{\mathrm{r,PM}} - 1\right) \cdot \left(\frac{r_{\mathrm{sh}}^{2\cdot\nu'} \cdot r_{\mathrm{S,i}}^{2\cdot\nu'}}{r_{\mathrm{PM}}^{4\cdot\nu'}} - 1\right) + \left(\mu_{\mathrm{r,PM}} + 1\right) \cdot \left(\frac{r_{\mathrm{S,i}}^{2\cdot\nu'} - r_{\mathrm{sh}}^{2\cdot\nu'}}{r_{\mathrm{PM}}^{2\cdot\nu'}}\right)} + \frac{r^{-\nu'-1} \cdot r_{\mathrm{PM}}^{2\cdot\nu'} \cdot \left[\left(\frac{r_{\mathrm{sh}}}{r_{\mathrm{PM}}}\right)^{2\cdot\nu'} \cdot \left(\mu_{\mathrm{r,PM}} + 1\right) + \mu_{\mathrm{r,PM}} - 1\right]}{\left(\mu_{\mathrm{r,PM}} - 1\right) \cdot \left(\frac{r_{\mathrm{sh}}^{2\cdot\nu'} \cdot r_{\mathrm{S,i}}^{2\cdot\nu'}}{r_{\mathrm{PM}}^{4\cdot\nu'}} - 1\right) + \left(\mu_{\mathrm{r,PM}} + 1\right) \cdot \left(\frac{r_{\mathrm{S,i}}^{2\cdot\nu'} - r_{\mathrm{sh}}^{2\cdot\nu'}}{r_{\mathrm{PM}}^{2\cdot\nu'}}\right)} \right\} \tag{2.32}$$

$$B_{\mathrm{S},\nu',p,\mathrm{r}}(r,\gamma_{\mathrm{m}},t) = \mu_0 \cdot \frac{m \cdot N_{\mathrm{s}} \cdot k_{\mathrm{w},\nu'} \cdot \hat{I}_{\mathrm{s}}}{\pi \cdot r_{\mathrm{S,i}}} \cdot \cos\left(\nu' \cdot \gamma_{\mathrm{m}} - \omega_{\mathrm{syn}} t - \varphi_{\mathrm{S}}\right) \cdot r_{\mathrm{S,i}}^{\nu'+1} \cdot \frac{r^{\nu'-1} + r_{\mathrm{sh}}^{2\cdot\nu'} \cdot r^{-\nu'-1}}{r_{\mathrm{S,i}}^{2\cdot\nu'} - r_{\mathrm{sh}}^{2\cdot\nu'}} \quad \text{for } \mu_{\mathrm{r,PM}} = 1 \tag{2.33}$$

$$B_{\mathrm{S},\nu',p,\gamma}(r,\gamma_{\mathrm{m}},t) = -\mu_0 \cdot \frac{m \cdot N_{\mathrm{s}} \cdot k_{\mathrm{w},\nu'} \cdot \hat{I}_{\mathrm{s}}}{\pi \cdot r_{\mathrm{S,i}}} \cdot \sin\left(\nu' \cdot \gamma_{\mathrm{m}} - \omega_{\mathrm{syn}} t - \varphi_{\mathrm{S}}\right) \cdot \frac{r_{\mathrm{S,i}}^{\nu'+1}}{r_{\mathrm{PM}}^{2\cdot\nu'}} \cdot \left\{ \frac{r^{-\nu'-1} \cdot r_{\mathrm{PM}}^{2\cdot\nu'} \cdot \left[\left(\frac{r_{\mathrm{sh}}}{r_{\mathrm{PM}}}\right)^{2\cdot\nu'} \cdot \left(\mu_{\mathrm{r,PM}} + 1\right) + \mu_{\mathrm{r,PM}} - 1\right]}{\left(\mu_{\mathrm{r,PM}} - 1\right) \cdot \left(\frac{r_{\mathrm{sh}}^{2\cdot\nu'} \cdot r_{\mathrm{S,i}}^{2\cdot\nu'}}{r_{\mathrm{PM}}^{4\cdot\nu'}} - 1\right) + \left(\mu_{\mathrm{r,PM}} + 1\right) \cdot \left(\frac{r_{\mathrm{S,i}}^{2\cdot\nu'} - r_{\mathrm{sh}}^{2\cdot\nu'}}{r_{\mathrm{PM}}^{2\cdot\nu'}}\right)} - \frac{r^{\nu'-1} \cdot \left[\left(\frac{r_{\mathrm{sh}}}{r_{\mathrm{PM}}}\right)^{2\cdot\nu'} \cdot \left(\mu_{\mathrm{r,PM}} - 1\right) + \mu_{\mathrm{r,PM}} + 1\right]}{\left(\mu_{\mathrm{r,PM}} - 1\right) \cdot \left(\frac{r_{\mathrm{sh}}^{2\cdot\nu'} \cdot r_{\mathrm{S,i}}^{2\cdot\nu'}}{r_{\mathrm{PM}}^{4\cdot\nu'}} - 1\right) + \left(\mu_{\mathrm{r,PM}} + 1\right) \cdot \left(\frac{r_{\mathrm{S,i}}^{2\cdot\nu'} - r_{\mathrm{sh}}^{2\cdot\nu'}}{r_{\mathrm{PM}}^{2\cdot\nu'}}\right)} \right\} \tag{2.34}$$

$$B_{\mathrm{S},\nu',p,\gamma}(r,\gamma_{\mathrm{m}},t) = -\mu_0 \cdot \frac{m \cdot N_{\mathrm{s}} \cdot k_{\mathrm{w},\nu'} \cdot \hat{I}_{\mathrm{s}}}{\pi \cdot r_{\mathrm{S,i}}} \cdot \sin\left(\nu' \cdot \gamma_{\mathrm{m}} - \omega_{\mathrm{syn}} t - \varphi_{\mathrm{S}}\right) \cdot r_{\mathrm{S,i}}^{\nu'+1} \cdot \frac{r^{\nu'-1} - r_{\mathrm{sh}}^{2\cdot\nu'} \cdot r^{-\nu'-1}}{r_{\mathrm{S,i}}^{2\cdot\nu'} - r_{\mathrm{sh}}^{2\cdot\nu'}} \quad \text{for } \mu_{\mathrm{r,PM}} = 1 \tag{2.35}$$

Eddy Current Density Plot in Conductive Rotor Regions

In order to get insight into the eddy current density distribution in the regions $i = 1$ and

$i = 2$ a contour plot of the eddy current density J_z is a useful tool (Fig. 2.3). The eddy current density $\vec{J} = J_z \cdot \vec{e}_z$ is calculated via the first *Maxwell* equation (2.36) which is given here by (2.37) for the suspension winding field fundamental for the region i. In addition to (2.30) the second derivatives of the modified *Bessel* functions with regard to r are needed. They are given by (2.38). Alternatively, in rotor-fixed coordinates the eddy current distribution can be retrieved by (2.39) [91].

$$\vec{J} = \operatorname{rot} \vec{H} \tag{2.36}$$

$$\begin{aligned} J_{\mathrm{L},p_\mathrm{L},k_\mathrm{L},\mathrm{z},i}(r,\gamma,t) &= \frac{1}{r} \cdot \left[\frac{\partial \left[r \cdot H_{\mathrm{L},p_\mathrm{L},k_\mathrm{L},\gamma,i}(r,\gamma_\mathrm{R},t) \right]}{\partial r} - \frac{\partial H_{\mathrm{L},p_\mathrm{L},k_\mathrm{L},\mathrm{r},i}(r,\gamma_\mathrm{R},t)}{\partial \gamma_\mathrm{R}} \right] \\ &= \frac{1}{\mu_i \cdot r} \cdot \left[B_{\mathrm{L},p_\mathrm{L},k_\mathrm{L},\gamma,i}(r,\gamma_\mathrm{R},t) + r \cdot \frac{\partial B_{\mathrm{L},p_\mathrm{L},k_\mathrm{L},\gamma,i}(r,\gamma_\mathrm{R},t)}{\partial r} - \right. \\ &\qquad \left. \frac{\partial B_{\mathrm{L},p_\mathrm{L},k_\mathrm{L},\mathrm{r},i}(r,\gamma_\mathrm{R},t)}{\partial \gamma_\mathrm{R}} \right] \end{aligned}$$

$$\begin{aligned} J_{\mathrm{L},p_\mathrm{L},k_\mathrm{L},\mathrm{z},i}(r,\gamma_\mathrm{R},t=0) = \mathrm{Re}\Bigg\{ & \frac{-1}{\mu_i \cdot r} \cdot \left[\left[\underline{C}_i \cdot I'_{p_\mathrm{L}} \left(\underline{\alpha}_{k_\mathrm{L},i} \cdot r \right) + \underline{D}_i \cdot K'_{p_\mathrm{L}} \left(\underline{\alpha}_{k_\mathrm{L},i} \cdot r \right) \right] \right. \\ & + r \cdot \left[\underline{C}_i \cdot I''_{p_\mathrm{L}} \left(\underline{\alpha}_{k_\mathrm{L},i} \cdot r \right) + \underline{D}_i \cdot K''_{p_\mathrm{L}} \left(\underline{\alpha}_{k_\mathrm{L},i} \cdot r \right) \right] \\ & \left. - \frac{p_\mathrm{L}^2}{r} \cdot \left[\underline{C}_i \cdot I_{p_\mathrm{L}} \left(\underline{\alpha}_{k_\mathrm{L},i} \cdot r \right) + \underline{D}_i \cdot K_{p_\mathrm{L}} \left(\underline{\alpha}_{k_\mathrm{L},i} \cdot r \right) \right] \right] \cdot e^{j \cdot p_\mathrm{L} \gamma_\mathrm{R}} \Bigg\} \end{aligned} \tag{2.37}$$

$$\left\{ \begin{aligned} I''_{p_\mathrm{L},i} &= \tfrac{\partial^2 I_{p_\mathrm{L},i}}{\partial r^2} = \underline{\alpha}^2_{k_\mathrm{L},i} \cdot \left\{ I_{p_\mathrm{L}-2,i} - \tfrac{p_\mathrm{L}-1}{\underline{\alpha}_{k_\mathrm{L},i} \cdot r} \cdot I_{p_\mathrm{L}-1,i} \right. \\ &\quad \left. - \tfrac{p_\mathrm{L}}{\underline{\alpha}_{k_\mathrm{L},i}} \cdot \left[- \tfrac{1}{r^2 \cdot \underline{\alpha}_{k_\mathrm{L},i}} \cdot I_{p_\mathrm{L},i} + \tfrac{1}{r} \cdot \left(I_{p_\mathrm{L}-1,i} - \tfrac{p_\mathrm{L}}{\underline{\alpha}_{k_\mathrm{L},i} \cdot r} \cdot I_{p_\mathrm{L},i} \right) \right] \right\} \\ K''_{p_\mathrm{L},i} &= \tfrac{\partial^2 K_{p_\mathrm{L},i}}{\partial r^2} = \underline{\alpha}^2_{k_\mathrm{L},i} \cdot \left\{ K_{p_\mathrm{L}-2,i} + \tfrac{p_\mathrm{L}-1}{\underline{\alpha}_{k_\mathrm{L},i} \cdot r} \cdot K_{p_\mathrm{L}-1,i} \right. \\ &\quad \left. - \tfrac{p_\mathrm{L}}{\underline{\alpha}_{k_\mathrm{L},i}} \cdot \left[- \tfrac{1}{r^2 \cdot \underline{\alpha}_{k_\mathrm{L},i}} \cdot K_{p_\mathrm{L},i} - \tfrac{1}{r} \cdot \left(K_{p_\mathrm{L}-1,i} + \tfrac{p_\mathrm{L}}{\underline{\alpha}_{k_\mathrm{L},i} \cdot r} \cdot K_{p_\mathrm{L},i} \right) \right] \right\} \end{aligned} \right. \tag{2.38}$$

$$\underline{E}_{z,i} = -\frac{\partial \underline{A}_{z,i}}{\partial t} \quad \rightarrow \quad \underline{\vec{J}}_{z,i} = -\underline{\kappa}_i \cdot \frac{\partial \underline{A}_{z,i}}{\partial t} \tag{2.39}$$

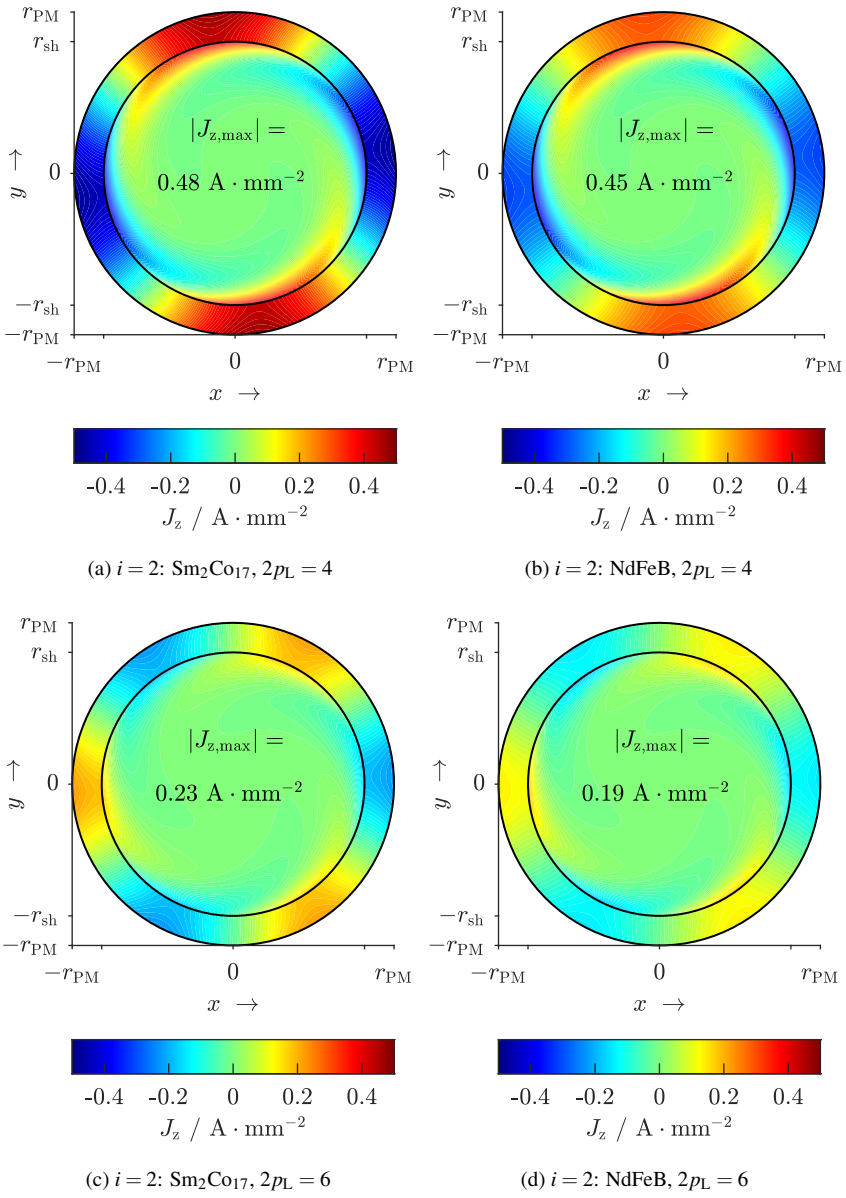

(a) $i = 2$: Sm_2Co_{17}, $2p_L = 4$

(b) $i = 2$: NdFeB, $2p_L = 4$

(c) $i = 2$: Sm_2Co_{17}, $2p_L = 6$

(d) $i = 2$: NdFeB, $2p_L = 6$

Fig. 2.3.: Analytically calculated current density J_z in the rotor parts $i = 1$ and $i = 2$ (Sm_2Co_{17} vs. NdFeB) of the *LLM4* due to the suspension field fundamental at $2p_L = 4$ and $2p_L = 6$ at the time instant $t = 0$ (model from Table 2.1, $n = 60000\ \text{min}^{-1}$, with identical current loading at $i_{q,L} = 5.78$ A)

In [92] the traveling field multi-layer problem in the context of eddy currents is extensively discussed in *Cartesian* coordinates. From this, mainly five parameters can be identified which influence the eddy current reaction field (Table 2.2).
The parameters 1 and 2 incorporate geometrical properties, i.e. the ratio between the size of the current source and the distance between current source and eddy currents. The parameters 3 and 4 introduce the frequency dependence of the eddy current reaction field and help deciding, whether the eddy currents are resistance- or inductance-limited. The parameters 5 and 6 depend on the penetration depth $d_{\mathrm{E,PM}}$ of the eddy current flow in the conducting region (Fig. 2.4a).
The influence of the parameters 3, 4 and 5, including the PM material conductivity κ_{PM},

Table 2.2.: Parameters influencing the eddy current reaction field in bearingless PM synchronous machines

1	$\frac{\tau_{\mathrm{p,L}}}{\delta_{\mathrm{eff}}-h_{\mathrm{PM}}}$	The bigger the pole pitch of the exciting field wave relative to the distance between the PM and stator bore, the bigger are the field on the PM surface and the field reaction in the PM.
2	$\frac{\tau_{\mathrm{p,L}}}{h_{\mathrm{PM}}}$	The bigger the pole pitch of the exciting field wave relative to the PM height, the more the intruding suspension field is dominated by its radial field component. I.e. very thin PMs ($h_{\mathrm{PM}} \to 0$) are mainly penetrated by a suspension field orthogonal to the PM surface. Compared to the use of thicker PMs, this increases the eddy current reaction field, since the reaction field is determined by the orthogonally intruding field component.
3	$\frac{h_{\mathrm{PM}}}{d_{\mathrm{E,PM}}}$	The bigger the PM height relative to the penetration depth, the larger is the eddy current reaction field in the PM. The more the eddy currents are inductance-limited in the PM.
4	$\frac{\tau_{\mathrm{p,L}}}{d_{\mathrm{E,PM}}}$	The bigger the pole pitch of the inducing field wave relative to the penetration depth, the bigger is the eddy current reaction field. The more the eddy currents are resistance-limited.
5	$\kappa_{i=2} = \kappa_{\mathrm{PM}}$	The bigger the electric conductivity of the PM material, the smaller gets the penetration depth $d_{\mathrm{E,PM}}$, shielding the field from the shaft.
6	f_{R}	The bigger the frequency of the inducing field, the smaller gets the penetration depth d_{E} with the side effect of inductance-limited eddy currents.

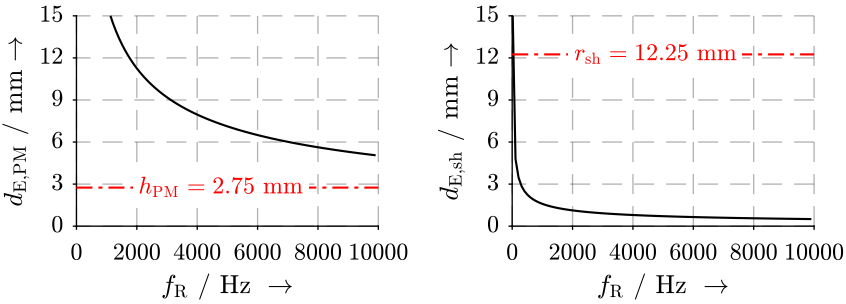

(a) PM (b) Shaft

Fig. 2.4.: Analytically calculated penetration depths d_{E} of PM ($i = 2$) and shaft ($i = 1$) for $\kappa_2 = \kappa_{\mathrm{PM}} = 1\ \mathrm{MS \cdot m^{-1}}$, $\mu_{\mathrm{r},2} = \mu_{\mathrm{r,PM}} = 1$, $\kappa_1 = \kappa_{\mathrm{sh}} = 1.25\ \mathrm{MS \cdot m^{-1}}$ and $\mu_{\mathrm{r},1} = \mu_{\mathrm{r,sh}} = 400$

are visible in Fig. 2.3: The eddy current density J_{z} is higher in the Sm_2Co_{17}-PM (Fig. 2.3a, Fig. 2.3c) than in the NdFeB-PM due to its higher conductivity (Table 2.1, Fig. 2.3b, Fig. 2.3d), leading to a better shielding against the rotor shaft. The influence of the parameters 1, 2 and 4, including the suspension winding pole pitch $\tau_{\mathrm{p,L}}$, are also visible in Fig. 2.3: In case of the 4-pole suspension field (Fig. 2.3a, 2.3b), the eddy currents intrude deeper into the rotor parts than in case of the 6-pole suspension field (Fig. 2.3c, 2.3d), having only 2/3 of the 4-pole pole pitch. Thus, the air gap field damping by the rotor eddy currents is much higher for low pole counts $2p_{\mathrm{L}}$ and for large bore diameters $2 \cdot r_{\mathrm{S,i}}$. This finding mainly determines the scalability of the eddy current effect (Section 3.6).

Note that the penetration depth $d_{\mathrm{E,PM}}$ of the eddy currents in the PM considerably depends on the speed $n = f_{\mathrm{R}}$, i.e. on the slip frequency (Fig. 2.4a), whereas the penetration depth $d_{\mathrm{E,sh}}$ in the shaft is very small due to the high permeability $\mu_{\mathrm{r,sh}} \gg 1$ and does not vary much with speed (Fig. 2.4b) for $f_{\mathrm{R}} > 500$ Hz. In relation to feasible shaft diameters (*LLM4*: $r_{\mathrm{sh}} = 12.25$ mm) the penetration depth $d_{\mathrm{E,sh}}$ is a lot smaller than the shaft radius. The eddy currents in the shaft are inductance-limited and only present at the surface for typical frequencies due to $\mu_{\mathrm{r,sh}} \gg 1$. The penetration depth $d_{\mathrm{E,PM}}$ of eddy currents in the PM, however, is bigger than the PM height $d_{\mathrm{E,PM}} \gg h_{\mathrm{PM}}$. Therefore, the eddy currents in the PM change from resistance- to inductance-limitation at very high speed because the condition $d_{\mathrm{E,PM}} \gg h_{\mathrm{PM}}$ is not fulfilled for thin PM rings and high speed (Fig. 2.4a).

2.2.4. Rotor PM Field Calculation

The no-load flux density distribution ($\underline{K} = 0$) is calculated, following the procedure of Section 2.2.3. The governing differential equations for the region i (Fig. 2.1) are given in (2.40). (2.41) denotes the approach function for the z-component A_z of the magnetic vector potential $\vec{A}$ and (2.42) the approach function of the radius-dependent component ξ. μ_i is the permeability of the i^{th} region and $\mu' = \mu \cdot p$ the absolute space harmonic order. No eddy currents may occur in the rotor due to the rotor PM field. Stator eddy currents are neglected here due to the laminated stator iron core. The radial and tangential flux density components of the rotor field $B_{\mathrm{R},\mu',\mu',\mathrm{r}}(r,\gamma_\mathrm{m},t)$ and $B_{\mathrm{R},\mu',\mu',\gamma}(r,\gamma_\mathrm{m},t)$ are given in (2.5) and (2.8) in the stator-fixed coordinate system for the bearing force calculation. They are composed of a product of r-, γ_m- and t-dependent functions. The time harmonic order k_R in the stator reference frame, where $k_\mathrm{R} = 1$ yields the rotational frequency n, is always $k_\mathrm{R} = \mu'$, whereas it is $k_\mathrm{R} = 0$ in the rotor reference frame. Thus, the subscript of the time harmonic order is omitted in the following for clarity. The resulting flux density components $B_{\mathrm{R},\mu',\mathrm{r}}(r,\gamma_\mathrm{R})$ and $B_{\mathrm{R},\mu',\gamma}(r,\gamma_\mathrm{R})$ are transformed into stator-fixed coordinates afterwards by multiplication with $e^{-j\cdot\mu'\cdot 2\pi\cdot n\cdot t}$.

$$\begin{aligned}\Delta\,\vec{A}_{\mathrm{R},\mu',\mathrm{z},i} &= r^2\cdot\frac{\mathrm{d}^2\xi_{\mathrm{R},\mu',i}}{\mathrm{d}r^2} + r\cdot\frac{\mathrm{d}\xi_{\mathrm{R},\mu',i}}{\mathrm{d}r} - \mu'^2\cdot\xi_{\mathrm{R},\mu',i} \qquad (2.40)\\ &= \begin{cases} -\mu_0\cdot\frac{1}{r}\cdot\left[\frac{\partial r\cdot M_\gamma(\gamma_\mathrm{R})}{\partial r} - \frac{\partial M_\mathrm{r}(\gamma_\mathrm{R})}{\partial\gamma}\right]; & \text{for } \vec{M} = \left(M_\mathrm{r}, M_\gamma, M_\mathrm{z}\right)^\mathrm{T} \neq \vec{0} \\ 0; & \text{for } \vec{M} = \left(M_\mathrm{r}, M_\gamma, M_\mathrm{z}\right)^\mathrm{T} = \vec{0} \end{cases}\end{aligned}$$

$$\underline{A}_{\mathrm{R},\mu',\mathrm{z},i}(r,\gamma_\mathrm{R}) = \xi_{\mathrm{R},\mu',i}\left(r,\mu_i,\vec{M}\right)\cdot e^{j\cdot\mu'\gamma_\mathrm{R}} \qquad (2.41)$$

$$\xi_{\mathrm{R},\mu',i} = \begin{cases} X_\mathrm{PM}\cdot r^{\mu'} + Y_\mathrm{PM}\cdot r^{-\mu'} + r\cdot c_{\mu'}(r); & \text{for } \vec{M} = \left(M_\mathrm{r}, M_\gamma, M_\mathrm{z}\right)^\mathrm{T} \neq \vec{0} \\ X_i\cdot r^{\mu'} + Y_i\cdot r^{-\mu'}; & \text{for } \vec{M} = \left(M_\mathrm{r}, M_\gamma, M_\mathrm{z}\right)^\mathrm{T} = \vec{0} \end{cases} \qquad (2.42)$$

The solution coefficients X_i and Y_i in (2.42) are described in the context of equation (2.50). The coefficient $c_{\mu'}$ (2.44) comprises the influence of the PM magnetization vector $\vec{M}(\gamma_\mathrm{R}) = M_\mathrm{r}(\gamma_\mathrm{R})\cdot\vec{e}_\mathrm{r} + M_\gamma(\gamma_\mathrm{R})\cdot\vec{e}_\gamma + M_\mathrm{z}(\gamma_\mathrm{R})\cdot\vec{e}_\mathrm{z}$ (2.43) as a disturbing component, where $\hat{M}_{\mu',\mathrm{r}}$ and $\hat{M}_{\mu',\gamma}$ are the *Fourier* coefficients of the magnetization pattern. Here, a parallel magnetization pattern (Fig. 2.5) is considered, as usual for bearingless high speed machines. The calculation for a radial magnetization pattern is given in Appendix A.9.

For $\mu' > 1$, the coefficient $c_{\mu'}(r)$ (2.44) can be obtained by assuming the radius-dependent component $\xi_{\mathrm{R},\mu',\mathrm{PM,res}}$ of the residual vector potential $A_{\mathrm{R},\mu',\mathrm{z,PM,res}}$ to be

$\xi_{\mathrm{R},\mu',\mathrm{PM,res}} = r \cdot c_{\mu'}(r)$. Inserting the approach function $\xi_{\mathrm{R},\mu',i}\left(r,\mu_i,\vec{M}\right)\cdot e^{j\cdot\mu'\gamma_\mathrm{R}}$ into (2.40), together with (2.43) yields (2.44) [87]. It is important to note that $\vec{M}(\gamma_\mathrm{R})$ is invariant in radial direction for $\mu' > 1$. For $\mu' = 1$ the derivation of $c_1(r)$ is given in [88].

$$\vec{M}(\gamma_\mathrm{R}) = \begin{pmatrix} M_\mathrm{r}(\gamma_\mathrm{R}) \\ M_\gamma(\gamma_\mathrm{R}) \\ M_\mathrm{z}(\gamma_\mathrm{R}) \end{pmatrix} = \sum_{\mu=1,3,5\ldots}^{\infty} \begin{pmatrix} \hat{M}_{\mu',\mathrm{r}} \cdot \cos(\mu' \cdot \gamma_\mathrm{R}) \\ \hat{M}_{\mu',\gamma} \cdot \sin(\mu' \cdot \gamma_\mathrm{R}) \\ 0 \end{pmatrix} \tag{2.43}$$

$$c_{\mu'}(r) = \begin{cases} \mu_0 \cdot \frac{\mu' \cdot \hat{M}_{\mu',\mathrm{r}} + \hat{M}_{\mu',\gamma}}{\mu'^2 - 1}; & \text{for } \mu' > 1 \\ -\mu_0 \cdot \frac{\hat{M}_{\mu',\mathrm{r}} + \hat{M}_{\mu',\gamma}}{2} \cdot \ln(r); & \text{for } \mu' = 1 \end{cases} \tag{2.44}$$

By adding the component $r \cdot c_{\mu'}(r)$ in the approach function for $\xi_{\mathrm{R},\mu',\mathrm{PM}}$ (2.42), the solution of the *Poisson* equation for the PM region is treated in the same way as the solution of the *Laplace* equation, which finally leads to the linear equation system (2.52). To solve this, the *Fourier* coefficients $\hat{M}_{\mu',\mathrm{r}}$ and $\hat{M}_{\mu',\gamma}$ are calculated first. For the here considered parallel magnetization pattern, the magnetization vector $\vec{M}$ exhibits a radial and a tangential component. These components are illustrated in Fig. 2.6. The *Fourier* coefficients $\hat{M}_{\mu',\mathrm{r}}$ and $\hat{M}_{\mu',\gamma}$ from (2.43), (2.44) are given in (2.45) and (2.46), with $M_\mathrm{r}(\gamma_\mathrm{R})$ and $M_\gamma(\gamma_\mathrm{R})$ illustrated in Fig. 2.6.

$$\hat{M}_{\mu',\mathrm{r}} = \frac{p}{\pi} \cdot \int_{-\frac{\pi}{p}}^{\frac{\pi}{p}} M_\mathrm{r}(\gamma_\mathrm{R}) \cdot \cos\left(\mu' \cdot \gamma_\mathrm{R}\right) \cdot \mathrm{d}\gamma_\mathrm{R} \tag{2.45}$$

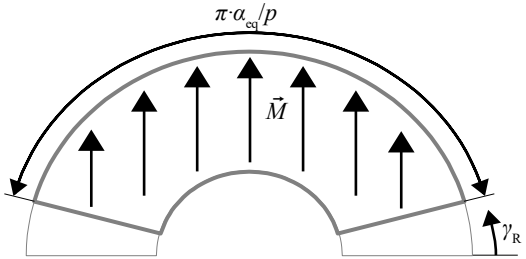

Fig. 2.5.: Pole pitch of a parallel magnetized PM of a 2-pole magnet with the magnetization vector $\vec{M}$

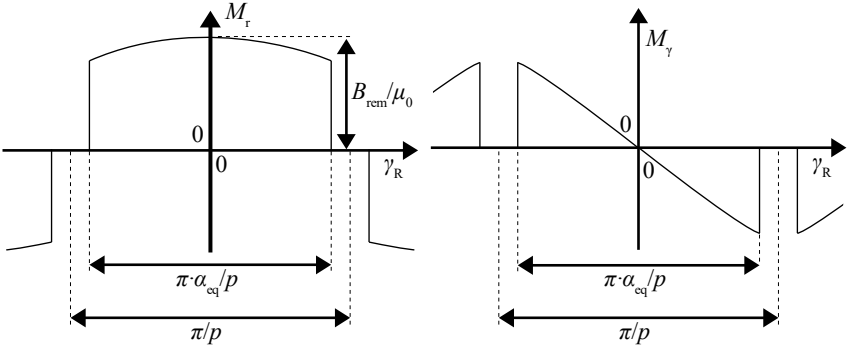

(a) Radial component M_r (b) Tangential component M_γ

Fig. 2.6.: Radial and tangential magnetization component for a parallel magnetization pattern, similar to [86]

$$\hat{M}_{\mu',\gamma} = \frac{p}{\pi} \cdot \int_{-\frac{\pi}{p}}^{\frac{\pi}{p}} M_\gamma(\gamma_R) \cdot \sin\left(\mu' \cdot \gamma_R\right) \cdot \mathrm{d}\gamma_R \tag{2.46}$$

The obtained solution according to [86] is given by (2.47) and (2.48), where sinc is the non-normalized *sinus cardinalis* function [89], which is defined as $\mathrm{sinc}\,(x) = \frac{\sin(x)}{x}$.

$$\hat{M}_{\mu',r} = \begin{cases} \frac{B_{rem}}{\mu_0} \cdot \alpha_{eq} \cdot \left[\mathrm{sinc}\left(\frac{(\mu'+1)\cdot\pi\cdot\alpha_{eq}}{2\cdot p}\right) + \mathrm{sinc}\left(\frac{(\mu'-1)\cdot\pi\cdot\alpha_{eq}}{2\cdot p}\right)\right] ; & \text{for } \mu' > 1 \\ \frac{B_{rem}}{\mu_0} \cdot \alpha_{eq} \cdot \left[\mathrm{sinc}\left(\frac{(\mu'+1)\cdot\pi\cdot\alpha_{eq}}{2\cdot p}\right) + 1\right] ; & \text{for } \mu' = 1 \end{cases} \tag{2.47}$$

$$\hat{M}_{\mu',\gamma} = \begin{cases} \frac{B_{rem}}{\mu_0} \cdot \alpha_{eq} \cdot \left[\mathrm{sinc}\left(\frac{(\mu'+1)\cdot\pi\cdot\alpha_{eq}}{2\cdot p}\right) - \mathrm{sinc}\left(\frac{(\mu'-1)\cdot\pi\cdot\alpha_{eq}}{2\cdot p}\right)\right] ; & \text{for } \mu' > 1 \\ \frac{B_{rem}}{\mu_0} \cdot \alpha_{eq} \cdot \left[\mathrm{sinc}\left(\frac{(\mu'+1)\cdot\pi\cdot\alpha_{eq}}{2\cdot p}\right) - 1\right] ; & \text{for } \mu' = 1 \end{cases} \tag{2.48}$$

The radius-dependent flux density components $B_{R,\mu',r,i}(r)$ and $B_{R,\mu',\gamma,i}(r)$ for region i are obtained via $\vec{B} = \mathrm{rot}\,\vec{A}$ as in (2.49) and (2.50). The coefficients X_i and Y_i (2.49), (2.50) are calculated via the boundary conditions at the transitions from one region (i) to the adjacent region ($i+1$), where the radial component of magnetic flux density and the tangential component of the magnetic field intensity is continuous. That is, $B_{R,\mu',r,i} = B_{R,\mu',r,i+1}$ and $H_{R,\mu',\gamma,i} = H_{R,\mu',\gamma,i}$. In the origin $r = 0$ the field is finite, hence $Y_1 = Y_{sh} = 0$. The magnetic field for $r \to \infty$ is zero, hence $\underline{B}_{r,ex} = 0$ and $X_5 = X_{ex} = 0$. This approach leads for each harmonic order μ' to the solution of the 8×8-matrix equation system (2.52) for

the five area problem ($i = 1,2,3,4,5$) to determine the 8 coefficients $X_1 = X_{\mathrm{sh}}$, $X_2 = X_{\mathrm{PM}}$, $Y_2 = Y_{\mathrm{PM}}$, $X_3 = X_\delta$, $Y_3 = Y_\delta$, $X_4 = X_{\mathrm{S}}$, $Y_4 = Y_{\mathrm{S}}$ and $X_5 = X_{\mathrm{ex}}$. Note that for clarity the subscript μ' for each of the coefficients is omitted for clarity, i.e. $X_{i,\mu'} = X_i$ and $Y_{i,\mu'} = Y_i$. The solutions of the coefficients for the air gap region are given in Appendix A.8. Note that the flux density expression for the PM region consists of the field solution (2.52) and the magnetization (2.43), as given in (2.51).

$$B_{\mathrm{R},\mu',\mathrm{r},i}(r) = \frac{e^{-j\cdot\mu'\gamma_{\mathrm{R}}}}{r}\cdot\frac{\partial A_{\mathrm{R},\mu',\mathrm{z},i}(r,\gamma_{\mathrm{R}})}{\partial\gamma_{\mathrm{R}}} = j\cdot\frac{\mu'}{r}\cdot\xi_{\mathrm{R},\mu',i} \tag{2.49}$$

$$B_{\mathrm{R},\mu',\gamma,i}(r) = -e^{-j\cdot\mu'\gamma_{\mathrm{R}}}\cdot\frac{\partial A_{\mathrm{R},\mu',\mathrm{z},i}(r,\gamma_{\mathrm{R}})}{\partial r} = -\frac{\partial\xi_{\mathrm{R},\mu',i}}{\partial r} \tag{2.50}$$

$$= \begin{cases} -\mu'\cdot\left(X_{\mathrm{PM}}\cdot r^{\mu'-1} + Y_{\mathrm{PM}}\cdot r^{-\mu'-1}\right) - c_{\mu'}(r) - r\cdot\frac{\partial c_{\mu'}(r)}{\partial r}; & \text{for } \vec{M} = \begin{pmatrix} M_{\mathrm{r}} \\ M_\gamma \\ M_{\mathrm{z}} \end{pmatrix} \neq \vec{0} \\ -\mu'\cdot\left(X_i\cdot r^{\mu'-1} + Y_i\cdot r^{-\mu'-1}\right); & \text{for } \vec{M} = \begin{pmatrix} M_{\mathrm{r}} \\ M_\gamma \\ M_{\mathrm{z}} \end{pmatrix} = \vec{0} \end{cases}$$

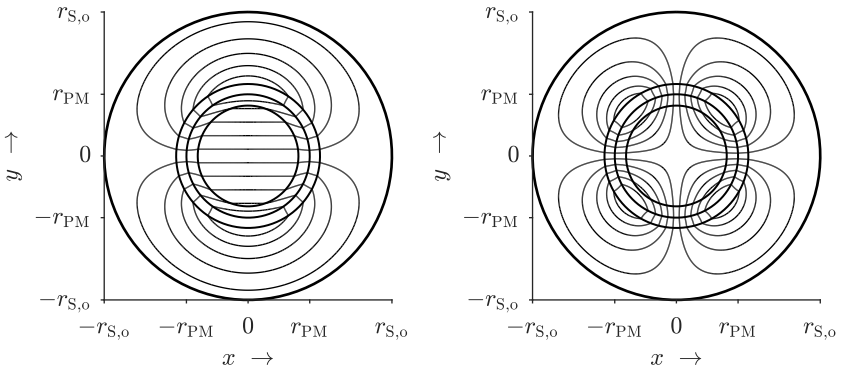

(a) $2p = 2$ (b) $2p = 4$ (not applied in *LLM4*)

Fig. 2.7.: Analytically calculated magnetic field lines as lines $|\underline{A}_{\mathrm{z}}| = \text{const.}$ of the rotor field for the *LLM4* at the time instant $t = 0$ ($B_{\mathrm{rem}} = 1$ T, parallel magnetization, $\alpha_{\mathrm{eq}} = 1$, harmonics $\mu < 14$ considered)

$$\vec{B}_{\mathrm{R},\mu',\mathrm{PM}}(r,\gamma_\mathrm{R}) = \mu_0 \cdot \mu_\mathrm{r} \cdot \vec{H}_\mathrm{PM}(r,\gamma_\mathrm{R}) + \mu_0 \cdot \vec{M}(\gamma_\mathrm{R}) \tag{2.51}$$

To complete the field wave expressions in stator-fixed coordinates, the radius-dependent components $B_{\mathrm{R},\mu',\mathrm{r},i}(r)$, $B_{\mathrm{R},\mu',\gamma,i}(r)$ are inserted into (2.5), (2.8). As an example, the analytically calculated field line plot ($|\underline{A}_\mathrm{z}| = \text{const.}$) for a 2-pole parallel magnetization as in the *LLM4* and for a 4-pole parallel magnetization are shown in Fig. 2.7. The field plots of a radial magnetization pattern and for $\alpha_\mathrm{eq} < 1$ can be found in Appendix A.9.

$$\begin{bmatrix}
r_\mathrm{sh}^{\mu'-1} & -r_\mathrm{sh}^{\mu'-1} & -r_\mathrm{sh}^{-\mu'-1} & 0 & 0 & 0 & 0 \\
-\frac{r_\mathrm{sh}^{\mu'-1}}{\mu_\mathrm{sh}} & \frac{r_\mathrm{sh}^{\mu'-1}}{\mu_\mathrm{PM}} & -\frac{r_\mathrm{sh}^{-\mu'-1}}{\mu_\mathrm{PM}} & 0 & 0 & 0 & 0 \\
0 & r_\mathrm{PM}^{\mu'-1} & r_\mathrm{PM}^{-\mu'-1} & -r_\mathrm{PM}^{\mu'-1} & -r_\mathrm{PM}^{-\mu'-1} & 0 & 0 \\
0 & -\frac{r_\mathrm{PM}^{\mu'-1}}{\mu_\mathrm{PM}} & \frac{r_\mathrm{PM}^{-\mu p-1}}{\mu_\mathrm{PM}} & \frac{r_\mathrm{PM}^{\mu'-1}}{\mu_0} & -\frac{r_\mathrm{PM}^{-\mu'-1}}{\mu_0} & 0 & 0 \\
0 & 0 & 0 & r_\mathrm{S,i}^{\mu'-1} & r_\mathrm{S,i}^{-\mu'-1} & -r_\mathrm{S,i}^{\mu'-1} & -r_\mathrm{S,i}^{-\mu'-1} \\
0 & 0 & 0 & -\frac{r_\mathrm{S,i}^{\mu'-1}}{\mu_0} & \frac{r_\mathrm{S,i}^{-\mu'-1}}{\mu_0} & \frac{r_\mathrm{S,i}^{\mu'-1}}{\mu_\mathrm{S}} & -\frac{r_\mathrm{S,i}^{-\mu'-1}}{\mu_\mathrm{S}} \\
0 & 0 & 0 & 0 & 0 & r_\mathrm{S,o}^{\mu'-1} & r_\mathrm{S,o}^{-\mu'-1} \\
0 & 0 & 0 & 0 & 0 & -\frac{r_\mathrm{S,o}^{\mu'-1}}{\mu_\mathrm{S}} & \frac{r_\mathrm{S,o}^{-\mu'-1}}{\mu_\mathrm{S}}
\end{bmatrix}$$

$$\cdot \begin{pmatrix} X_\mathrm{sh} \\ X_\mathrm{PM} \\ Y_\mathrm{PM} \\ X_\delta \\ Y_\delta \\ X_\mathrm{S} \\ Y_\mathrm{S} \\ Y_\mathrm{ex} \end{pmatrix} = \begin{pmatrix} c_{\mu'}(r_\mathrm{sh}) \\ -\frac{1}{\mu_\mathrm{PM}} \cdot \frac{1}{\mu'} \cdot \left[c_{\mu'} + r_\mathrm{sh} \cdot \frac{\partial c_{\mu'}(r)}{\partial r} + \mu_0 \cdot \hat{M}_{\mu',\gamma} \right] \Big|_{r=r_\mathrm{sh}} \\ -c_{\mu'}(r_\mathrm{PM}) \\ \frac{1}{\mu_\mathrm{PM}} \cdot \frac{1}{\mu'} \cdot \left[c_{\mu'} + r_\mathrm{PM} \cdot \frac{\partial c_{\mu'}(r)}{\partial r} + \mu_0 \cdot \hat{M}_{\mu',\gamma} \right] \Big|_{r=r_\mathrm{PM}} \\ 0 \\ 0 \\ 0 \\ 0 \end{pmatrix} \tag{2.52}$$

Closed-Form Expressions for the Rotor Field Magnetic Flux Density Components

For the formulation of machine constants such as the torque current coefficient k_M (see Section 4.1), closed-form expressions are not only necessary for the stator, but also for the rotor field components. The rotor field components are based on the aforementioned magnetostatic calculations (2.40), (2.41), (2.42), (2.49) and (2.50). Therefore, manageable

terms can be derived. The procedure is equivalent to the derivation of the closed-form expressions of the stator field components. Since bearingless machines of different pole counts are considered in Section 3.5, 3.6, the terms for the tangential and radial stator flux density components of order $p = 1$ are given in (2.53), (2.55) and of order $\mu' > 1$ are given in (2.57), (2.59). They are valid for a parallelly magnetized PM of full pole coverage ($\alpha_{\mathrm{eq}} = 1$). The following simplifications are made, complying with "$\mathrm{2D_{simp}}$ " in Table 4.1: $\mu_{\mathrm{r,Fe}} \to \infty$, $r_{\mathrm{S,o}} \to \infty$. The short form for $\mu_{\mathrm{r,PM}} = 1$ is given by (2.54), (2.56) for $p = 1$ and by (2.58), (2.60) for $\mu' > 1$. The coefficient $c_{\mu'}$ and the tangential magnetization amplitude $\hat{M}_{\mu',\gamma}$ result from (2.44) and (2.46).
For $\mu' = p = 1$:

$$B_{\mathrm{R},1,1,\mathrm{r}}(r,\gamma_{\mathrm{m}},t) = B_{\mathrm{rem}} \cdot \cos\left(\gamma_{\mathrm{m}} - \omega_{\mathrm{syn}} t - \varphi_{\mathrm{R}}\right) \cdot \frac{\left[\left(1+\frac{r_{\mathrm{S,i}}}{r}\right)^2\right] \cdot \left[1-\left(\frac{r_{\mathrm{sh}}}{r_{\mathrm{PM}}}\right)^2\right]}{\left(\mu_{\mathrm{r}}^{\mathrm{PM}}-1\right) \cdot \left(\frac{r_{\mathrm{sh}}^2 \cdot r_{\mathrm{S,i}}^2}{r_{\mathrm{PM}}^4}-1\right) + \left(\mu_{\mathrm{r}}^{\mathrm{PM}}+1\right) \cdot \frac{r_{\mathrm{S,i}}^2 - r_{\mathrm{sh}}^2}{r_{\mathrm{PM}}^2}} \tag{2.53}$$

$$B_{\mathrm{R},1,1,\mathrm{r}}(r,\gamma_{\mathrm{m}},t) = \frac{B_{\mathrm{rem}}}{2} \cdot \cos\left(\gamma_{\mathrm{m}} - \omega_{\mathrm{syn}} t - \varphi_{\mathrm{R}}\right) \cdot \frac{\left[\left(1+\frac{r_{\mathrm{S,i}}}{r}\right)^2\right] \cdot \left[1-\left(\frac{r_{\mathrm{sh}}}{r_{\mathrm{PM}}}\right)^2\right]}{\left(\frac{r_{\mathrm{S,i}}}{r_{\mathrm{PM}}}\right)^2 - \left(\frac{r_{\mathrm{sh}}}{r_{\mathrm{PM}}}\right)^2} \quad \text{for } \mu_{\mathrm{r,PM}} = 1 \tag{2.54}$$

$$B_{\mathrm{R},1,1,\gamma}(r,\gamma_{\mathrm{m}},t) = B_{\mathrm{rem}} \cdot \sin\left(\gamma_{\mathrm{m}} - \omega_{\mathrm{syn}} t - \varphi_{\mathrm{R}}\right) \cdot \frac{\left[\left(\frac{r_{\mathrm{S,i}}}{r}\right)^2 - 1\right] \cdot \left[1-\left(\frac{r_{\mathrm{sh}}}{r_{\mathrm{PM}}}\right)^2\right]}{\left(\mu_{\mathrm{r}}^{\mathrm{PM}}-1\right) \cdot \left(\frac{r_{\mathrm{sh}}^2 \cdot r_{\mathrm{S,i}}^2}{r_{\mathrm{PM}}^4}-1\right) + \left(\mu_{\mathrm{r}}^{\mathrm{PM}}+1\right) \cdot \frac{r_{\mathrm{S,i}}^2 - r_{\mathrm{sh}}^2}{r_{\mathrm{PM}}^2}} \tag{2.55}$$

$$B_{\mathrm{R},1,1,\gamma}(r,\gamma_{\mathrm{m}},t) = \frac{B_{\mathrm{rem}}}{2} \cdot \sin\left(\gamma_{\mathrm{m}} - \omega_{\mathrm{syn}} t - \varphi_{\mathrm{R}}\right) \cdot \frac{\left[\left(\frac{r_{\mathrm{S,i}}}{r}\right)^2 - 1\right] \cdot \left[1-\left(\frac{r_{\mathrm{sh}}}{r_{\mathrm{PM}}}\right)^2\right]}{\left(\frac{r_{\mathrm{S,i}}}{r_{\mathrm{PM}}}\right)^2 - \left(\frac{r_{\mathrm{sh}}}{r_{\mathrm{PM}}}\right)^2} \quad \text{for } \mu_{\mathrm{r,PM}} = 1 \tag{2.56}$$

For $\mu' > 1$:

$$B_{\mathrm{R},\mu',\mu',\mathrm{r}}(r,\gamma_\mathrm{m},t) = \cos\left(\mu'\cdot\gamma_\mathrm{m} - \mu'\cdot 2\pi\cdot n\cdot t - \varphi_\mathrm{R}\right)\cdot \frac{r_{\mathrm{S,i}}^{2\cdot\mu'} + r^{2\cdot\mu'}}{r_{\mathrm{PM}}^{3\cdot\mu'}\cdot r^{2\cdot\mu'+1}}\cdot \tag{2.57}$$

$$\left\{\frac{c_{\mu'}\cdot\left[2\cdot r_{\mathrm{PM}}^{\mu'}\cdot r_{\mathrm{sh}}^{\mu'+1} - (1-\mu')\cdot r_{\mathrm{PM}}^{2\cdot\mu'+1} - (1+p)\cdot r_{\mathrm{sh}}^{2\cdot\mu'}\cdot r_{\mathrm{PM}}\right]}{\left(\mu_{\mathrm{r,PM}}-1\right)\cdot\left(\frac{r_{\mathrm{sh}}^{2\cdot\mu'}\cdot r_{\mathrm{S,i}}^{2\cdot\mu'}}{r_{\mathrm{PM}}^{4\cdot\mu'}} - 1\right) + \left(\mu_{\mathrm{r,PM}}+1\right)\cdot\left(\frac{r_{\mathrm{S,i}}^{2\cdot\mu'} - r_{\mathrm{sh}}^{2\cdot\mu'}}{r_{\mathrm{PM}}^{2\cdot\mu'}}\right)} + \right.$$

$$\left.\frac{\hat{M}_{\mu',\gamma}\cdot\left[2\cdot r_{\mathrm{PM}}^{2\cdot\mu'}\cdot r_{\mathrm{sh}}^{\mu'+1} - r_{\mathrm{PM}}^{2\cdot\mu'+1} - r_{\mathrm{PM}}\cdot r_{\mathrm{sh}}^{2\cdot\mu'}\right]}{\left(\mu_{\mathrm{r,PM}}-1\right)\cdot\left(\frac{r_{\mathrm{sh}}^{2\cdot\mu'}\cdot r_{\mathrm{S,i}}^{2\cdot\mu'}}{r_{\mathrm{PM}}^{4\cdot\mu'}} - 1\right) + \left(\mu_{\mathrm{r,PM}}+1\right)\cdot\left(\frac{r_{\mathrm{S,i}}^{2\cdot\mu'} - r_{\mathrm{sh}}^{2\cdot\mu'}}{r_{\mathrm{PM}}^{2\cdot\mu'}}\right)}\right\}$$

$$B_{\mathrm{R},\mu',\mu',\mathrm{r}}(r,\gamma_\mathrm{m},t) = \cos\left(\mu'\cdot\gamma_\mathrm{m} - \mu'\cdot 2\pi\cdot n\cdot t - \varphi_\mathrm{R}\right)\cdot \tag{2.58}$$

$$\frac{r_{\mathrm{S,i}}^{2\cdot\mu'} + r^{2\cdot\mu'}}{2\cdot r^{\mu'+1}\cdot r_{\mathrm{PM}}^{\mu'}\cdot\left(r_{\mathrm{S,i}}^{2\cdot\mu'} - r_{\mathrm{sh}}^{2\cdot\mu'}\right)}\cdot$$

$$\left\{c_{\mu'}\cdot\left[2\cdot r_{\mathrm{PM}}^{\mu'}\cdot r_{\mathrm{sh}}^{\mu'+1} - \left(1-\mu'\right)\cdot r_{\mathrm{PM}}^{2\cdot\mu'+1} - (1+p)\cdot r_{\mathrm{sh}}^{2\cdot\mu'}\cdot r_{\mathrm{PM}}\right] + \right.$$

$$\left.\hat{M}_{\mu',\gamma}\cdot\left[2\cdot r_{\mathrm{PM}}^{2\cdot\mu'}\cdot r_{\mathrm{sh}}^{\mu'+1} - r_{\mathrm{PM}}^{2\cdot\mu'+1} - r_{\mathrm{PM}}\cdot r_{\mathrm{sh}}^{2\cdot\mu'}\right]\right\} \quad \text{for } \mu_{\mathrm{r,PM}} = 1$$

$$B_{\mathrm{R},\mu',\mu',\gamma}(r,\gamma_\mathrm{m},t) = \cos\left(\mu'\cdot\gamma_\mathrm{m} - \mu'\cdot 2\pi\cdot n\cdot t - \varphi_\mathrm{R}\right)\cdot \frac{r_{\mathrm{S,i}}^{2\cdot\mu'} - r^{2\cdot\mu'}}{r_{\mathrm{PM}}^{3\cdot\mu'}\cdot r^{2\cdot\mu'+1}}\cdot \tag{2.59}$$

$$\left\{\frac{c_{\mu'}\cdot\left[2\cdot r_{\mathrm{PM}}^{\mu'}\cdot r_{\mathrm{sh}}^{\mu'+1} - (1-\mu')\cdot r_{\mathrm{PM}}^{2\cdot\mu'+1} - (1+p)\cdot r_{\mathrm{sh}}^{2\cdot\mu'}\cdot r_{\mathrm{PM}}\right]}{\left(\mu_{\mathrm{r,PM}}-1\right)\cdot\left(\frac{r_{\mathrm{sh}}^{2\cdot\mu'}\cdot r_{\mathrm{S,i}}^{2\cdot\mu'}}{r_{\mathrm{PM}}^{4\cdot\mu'}} - 1\right) + \left(\mu_{\mathrm{r,PM}}+1\right)\cdot\left(\frac{r_{\mathrm{S,i}}^{2\cdot\mu'} - r_{\mathrm{sh}}^{2\cdot\mu'}}{r_{\mathrm{PM}}^{2\cdot\mu'}}\right)} + \right.$$

$$\left.\frac{\hat{M}_{\mu',\gamma}\cdot\left[2\cdot r_{\mathrm{PM}}^{2\cdot\mu'}\cdot r_{\mathrm{sh}}^{\mu'+1} - r_{\mathrm{PM}}^{2\cdot\mu'+1} - r_{\mathrm{PM}}\cdot r_{\mathrm{sh}}^{2\cdot\mu'}\right]}{\left(\mu_{\mathrm{r,PM}}-1\right)\cdot\left(\frac{r_{\mathrm{sh}}^{2\cdot\mu'}\cdot r_{\mathrm{S,i}}^{2\cdot\mu'}}{r_{\mathrm{PM}}^{4\cdot\mu'}} - 1\right) + \left(\mu_{\mathrm{r,PM}}+1\right)\cdot\left(\frac{r_{\mathrm{S,i}}^{2\cdot\mu'} - r_{\mathrm{sh}}^{2\cdot\mu'}}{r_{\mathrm{PM}}^{2\cdot\mu'}}\right)}\right\}$$

$$B_{\mathrm{R},\mu',\mu',\gamma}(r,\gamma_\mathrm{m},t) = \cos\left(\mu'\cdot\gamma_\mathrm{m} - \mu'\cdot 2\pi\cdot n\cdot t - \varphi_\mathrm{R}\right)\cdot \tag{2.60}$$

$$\frac{r_{\mathrm{S,i}}^{2\cdot\mu'} - r^{2\cdot\mu'}}{2\cdot r^{\mu'+1}\cdot r_{\mathrm{PM}}^{\mu'}\cdot\left(r_{\mathrm{S,i}}^{2\cdot\mu'} - r_{\mathrm{sh}}^{2\cdot\mu'}\right)}\cdot$$

$$\left\{c_{\mu'}\cdot\left[2\cdot r_{\mathrm{PM}}^{\mu'}\cdot r_{\mathrm{sh}}^{\mu'+1} - \left(1-\mu'\right)\cdot r_{\mathrm{PM}}^{2\cdot\mu'+1} - (1+p)\cdot r_{\mathrm{sh}}^{2\cdot\mu'}\cdot r_{\mathrm{PM}}\right] + \right.$$

$$\left.\hat{M}_{\mu',\gamma}\cdot\left[2\cdot r_{\mathrm{PM}}^{2\cdot\mu'}\cdot r_{\mathrm{sh}}^{\mu'+1} - r_{\mathrm{PM}}^{2\cdot\mu'+1} - r_{\mathrm{PM}}\cdot r_{\mathrm{sh}}^{2\cdot\mu'}\right]\right\} \quad \text{for } \mu_{\mathrm{r,PM}} = 1$$

2.3. Comparison Between 2D Analytical Calculation and FEM Simulation of Magnetic Fields in the *LLM4*

Table 2.3 gives a comparison of the fundamental air gap flux density components for the *LLM4* (data see Appendix A.2), which are determined by 2D FEM simulation (*JMAG Designer 19.1*) and by the analytical calculation of Section 2.2.3, 2.2.4. The stator iron lamination (M270-35A) is modeled in the FEM simulation by a $B(H)$-curve according to Appendix A.14 [93]. Since the iron parts of the *LLM4* are not magnetically saturated, only the slot opening effect leads to deviations between analytical calculation and simulation, because it is not considered in the analytical calculation. The radial field components by analytical calculation are bigger than the simulation-based solution.

The simplest option to account for the slot opening effect is the multiplication of the air gap width $\delta_{\mathrm{eff}} = \delta + h_{\mathrm{sl}} + h_{\mathrm{PM}}$ (Appendix A.2) with the *Carter* coefficient k_{C} [94, 95], which is here $k_{\mathrm{C}} = 1.025$. However, the assumptions made for the derivation of the *Carter* factor are: Air gap curvature is neglected, the pole pitch is much bigger than the slot pitch, the air gap tangential component is zero and two adjacent slots are far from each other. The *LLM4* exhibits a large effective air gap $\delta_{\mathrm{eff}} = 5.25$ mm. The bore diameter is rather small, so that air gap curvature may not be neglected. A more elaborate alternative to

Table 2.3.: Comparison between analytically calculated and numerically simulated air gap fundamental field wave amplitudes in the middle of the mechanical air gap (2D) for the motor *LLM4* (percentage values denote the difference to the simulation results)

	Without eddy currents		With eddy currents	
	Simulation	Analytical	Simulation	Analytical
$\hat{B}_{\mathrm{R},1,1,\mathrm{r}}$ / mT	440.28	443.86 (+0.81%)	440.28	443.86 (+0.81%)
$\hat{B}_{\mathrm{R},1,1,\gamma}$ / mT	12.26	11.73 (−4.31 %)	12.26	11.73 (−4.31 %)
$\hat{B}_{\mathrm{D},1,1,\mathrm{r}}$ / mT	30.62	32.13 (+4.93%)	30.62	32.13 (+4.93%)
$\hat{B}_{\mathrm{D},1,1,\gamma}$ / mT	10.20	10.26 (+0.62%)	10.20	10.26 (+0.62%)
$\hat{B}_{\mathrm{L},2,1,\mathrm{r}}$ / mT	8.48	8.80 (+4.53 %)	7.92	8.10 (+2.22 %)
$\hat{B}_{\mathrm{L},2,1,\gamma}$ / mT	4.98	5.03 (+0.95%)	5.02	5.08 (+1.12%)
$\Delta\gamma_{\mathrm{Ft,r}}$	0	0	12.21°	12.88° (+5.54 %)
$\Delta\gamma_{\mathrm{Ft},\gamma}$	0	0	−1.08°	−1.06° (+1.85 %)

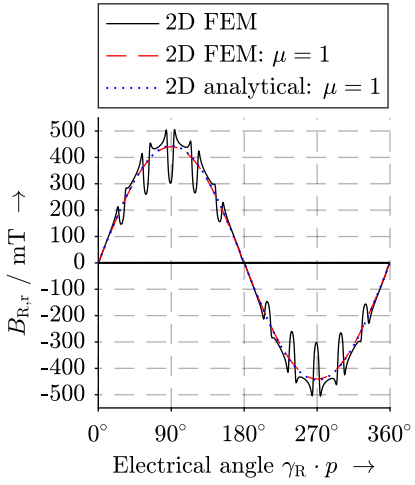

(a) Rotor field: Sm_2Co_{17}

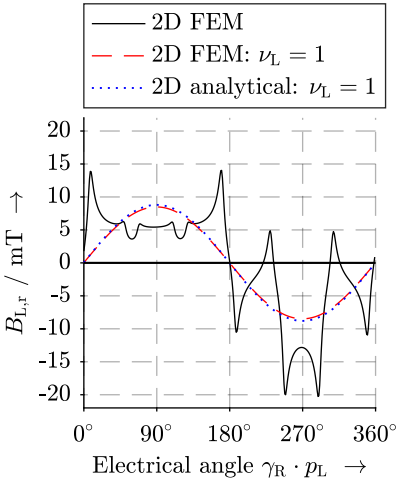

(b) Suspension winding field: $i_{\mathrm{q,L}} = 5.8$ A

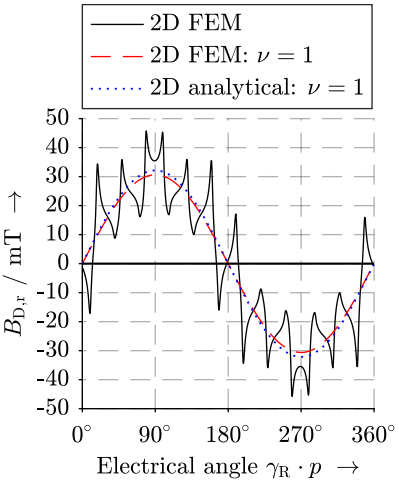

(c) Drive winding field: $i_{\mathrm{q,D}} = 10.5$ A

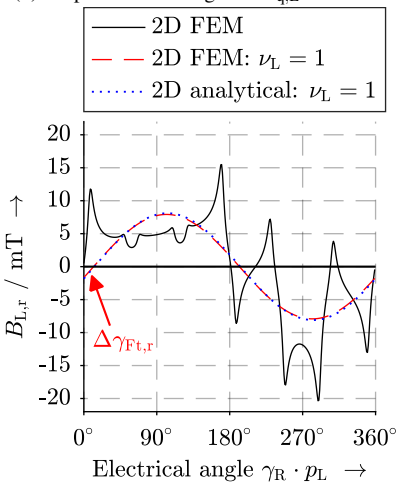

(d) Suspension winding field with eddy currents: $i_{\mathrm{q,L}} = 5.8$ A ($\Delta\gamma_{\mathrm{Ft,r}} \approx 12.5°$, Sm_2Co_{17})

Fig. 2.8.: Comparison between analytically calculated and numerically simulated air gap flux density radial component for the *LLM4* at $n = 60000$ min^{-1} in the middle of the mechanical air gap

analytically address the modulation of the air gap field by the stator slot openings with air gap curvature in PM machines is shown in [96]. It is based on a conformal mapping method via the *Schwarz-Christoffel*-transformation, as developed by [97, 98, 99]. As for the derivation of the *Carter* coefficient, the air gap field wave is modulated with a periodical permeance function.

The deviation between the analytical calculation and the simulation results is $< 6\%$ (Table 2.3). Also the reduction of the radial air gap field component by rotor eddy currents is well represented by the analytical calculation, so that the slot opening effect may be generally neglected for the analytical calculations. Fig. 2.8 compares the spatial distribution of the radial component of the air gap field waves to the determined field fundamentals from Table 2.3.

2.4. Rotor Eddy Current Effect and Suspension Force Vector Deflection

In bearingless machines, having a suspension winding pole count of $2p_\mathrm{L} = 2p \pm 2$, the fundamental suspension winding air gap field wave $B_{\mathrm{L},\nu'_\mathrm{L}=p_\mathrm{L},k_\mathrm{L}=p}$ is of time order $k_\mathrm{L} = p$ in stator-fixed coordinates for a standstill radial suspension force F_L. Thus, the suspension winding is fed with the same frequency $k_\mathrm{L} \cdot n = p \cdot n = f_\mathrm{syn}$ as the drive winding for the torque generation. Consequently, even for a standstill force vector the suspension wind-

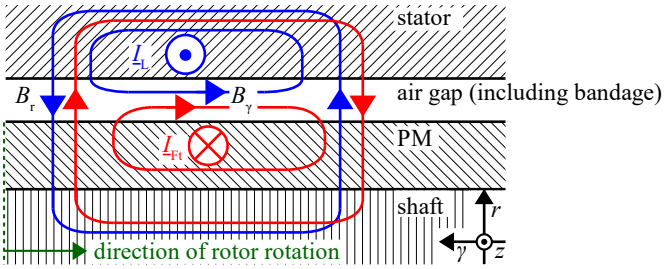

Fig. 2.9.: Schematic representation of the interaction between suspension field (blue) and eddy current reaction field (red) in steady state, air gap curvature neglected, $\underline{I}_\mathrm{L}$: stator current in suspension winding, $\underline{I}_\mathrm{Ft}$: Rotor eddy currents, mainly opposing $\underline{I}_\mathrm{L}$: Radial field component B_r is reduced and tangential field component B_γ is increased by the "red" reaction field of eddy currents

ing field fundamental moves asynchronously to the rotor and induces eddy currents with the frequency f_R (2.14). Since high-speed machines, such as the *LLM4*, are typically equipped with a solid steel rotor shaft and a non-segmented PM ring, the conductive rotor is prone to these eddy currents.

The rotor eddy currents state an additional heat source in the rotor and lead, therefore, to higher rotor temperatures. However, the rotor eddy currents in such high-speed machines are not dominated by the suspension winding field due to their very low stator field amplitude (Section 2.3). They are mainly determined by the rotor PM air gap field modulation with the stator-slot frequent permeance function, since the rotor field amplitude is much higher than the suspension winding field amplitude (Section 2.3).

The much more critical consequence of the rotor eddy currents is the reduction of the suspension winding radial field component $\mathrm{Re}\left\{\underline{B}_{\mathrm{L},p_\mathrm{L},p,\mathrm{r}}\right\} < \hat{B}_{\mathrm{L},p_\mathrm{L},p,\mathrm{r}}$ and the shift of the location of the field amplitude, called deflection, $\Delta\gamma_{\mathrm{Ft},p_\mathrm{L},\mathrm{r}} > 0$ (Fig. 2.8d). The tangential field component is increased by $\mathrm{Re}\left\{\underline{B}_{\mathrm{L},p_\mathrm{L},p,\gamma}\right\} > \hat{B}_{\mathrm{L},p_\mathrm{L},p,\gamma}$ and shifted by $\Delta\gamma_{\mathrm{Ft},p_\mathrm{L},\gamma} < 0$. This field deformation is visualized in Fig. 2.9 and in Fig. 2.8d. The eddy current distribution lags the exciting stator field wave by $\Delta\gamma_{\mathrm{Ft},p_\mathrm{L},\mathrm{r}} > 0$. This lag depends on the nature of the eddy currents: Resistance-limited eddy currents cause a high lag in phase ($\Delta\gamma_{\mathrm{Ft},p_\mathrm{L},\mathrm{r}} \to 90°$), whereas inductance-limited eddy currents excite a reaction field which is approximately in phase opposition to the inducing field ($\Delta\gamma_{\mathrm{Ft},p_\mathrm{L},\mathrm{r}} \to 180°$), like in Fig. 2.9. The tangential suspension air gap field wave is only slightly increased by field of the rotor eddy currents, so that the eddy current effect is dominated by the reduction and shift of the radial air gap field wave. Whether the eddy currents are either resistance- or inductance-limited, depends on the geometry and material properties (Table 2.2). The eddy currents in the PM of the *LLM4* at high-speed operation are still resistance-limited, due to $d_{\mathrm{E,PM}} \gg h_{\mathrm{PM}}$ (Section 3.7.1), whereas they are inductance-limited in the shaft $d_{\mathrm{E,sh}} \ll r_{\mathrm{sh}}$ (Fig. 2.4). All considerations include the eddy currents in the PM and in the shaft at same time, however, the disturbing forces are dominated by the PM eddy currents. The following investigations are partially presented in [O13].

2.4.1. Standstill Suspension Force Vector

According to (2.9), (2.10), the bearing force amplitude $\left|\vec{F}_\mathrm{L}\right|$ is decreased ($\left|\vec{F}_\mathrm{L}\right| < \left|\vec{F}_{\mathrm{L,ref}}\right|$) by eddy currents due to $\left|\underline{B}_{\mathrm{L},p_\mathrm{L},p,\mathrm{r}}\right| < \hat{B}_{\mathrm{L},p_\mathrm{L},p,\mathrm{r}}$. The spatial alignment φ_F of the bearing force vector is different from the set-point bearing force vector ($\varphi_{\mathrm{F,ref}} \neq \varphi_\mathrm{F}$), due

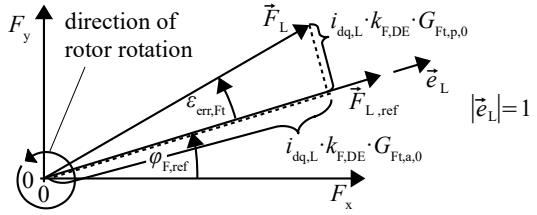

Fig. 2.10.: Suspension force vector ($\vec{F}_L$) deflection by $G_{Ft,a,0}$ and $G_{Ft,p,0}$ due to the eddy current effect ($i_{dq,L}$: suspension current, $k_{F,DE}$: force-current coefficient without eddy currents)

to $\Delta\gamma_{Ft,p_L,r} > 0$, $\Delta\gamma_{Ft,p_L,\gamma} < 0$. The occurring spatial error angle $\varepsilon_{err,Ft}$ (Fig. 2.10) of a standstill reference suspension force vector $\vec{F}_{L,ref} = F_{L,ref} \cdot \vec{e}_L$ is given in (2.61) for $F_{L,ref} \cdot \vec{e}_L = F_{y,ref} \cdot \vec{e}_y$, whereas (2.62) shows the decrease of the bearing force vector by the ratio $G_{Ft,a,0} = F_y / F_{y,ref}$. The orthogonal disturbance force F_x as ratio $G_{Ft,p,0} = F_x / F_{y,ref}$ is given in (2.63). $G_{Ft,a}$ and $G_{Ft,p}$ are included in the state space model of the rotor position control in Section 5.3.1. With the 2D analytical calculation ($2D_{an}$) from Section 2.2, with a 2D FEM simulation ($2D_{FEM}$) or with a 3D FEM simulation ($3D_{FEM}$), the resulting forces F_x and F_y are inserted into (2.61), (2.62), (2.63) for the evaluation of the eddy current effect.

$$\varepsilon_{err,Ft} = \operatorname{atan}\left(\frac{F_x}{F_y}\right) \tag{2.61}$$

$$= \operatorname{atan}\left(\frac{\left|\underline{B}_{L,p_L,p,r}(r_{cal})\right| \cdot \sin\left(\Delta\gamma_{Ft,p_L,r}\right) + \left|\underline{B}_{L,p_L,p,\gamma}(r_{cal})\right| \cdot \sin\left(\Delta\gamma_{Ft,p_L,\gamma}\right)}{\left|\underline{B}_{L,p_L,p,r}(r_{cal})\right| \cdot \cos\left(\Delta\gamma_{Ft,p_L,r}\right) + \left|\underline{B}_{L,p_L,p,\gamma}(r_{cal})\right| \cdot \cos\left(\Delta\gamma_{Ft,p_L,\gamma}\right)}\right)$$

$$G_{Ft,a,0} = \frac{F_y}{F_{y,ref}} = \frac{\operatorname{Re}\left\{\underline{B}_{L,p_L,p,r}(r_{cal}) + \underline{B}_{L,p_L,p,\gamma}(r_{cal})\right\}}{\hat{B}_{L,p_L,p,r}(r_{cal}) + \hat{B}_{L,p_L,p,\gamma}(r_{cal})} \tag{2.62}$$

$$G_{Ft,p,0} = \frac{F_x}{F_{y,ref}} = \frac{F_x}{F_y} \cdot \frac{F_y}{F_{y,ref}} = \tan\left(\varepsilon_{err,Ft}\right) \cdot G_{Ft,a,0} \tag{2.63}$$

The force amplitude attenuation $G_{Ft,a,0}$ and especially the error angle $\varepsilon_{err,Ft}$ are dominated by the eddy current reaction in the PM, which account for more than 90% of $\varepsilon_{err,Ft}$ and $G_{Ft,a,0}$ (Table 2.4).

Identification of the Eddy Current Effect by Measurement

In order to identify the eddy current effect by measurement, an accurate determination of the rotor angle $\gamma_S = p \cdot 2\pi \cdot n \cdot$ is important. Thus, the time span t_{cal} between current cur-

rent evaluation and rotor angle ($\gamma_{S,act}$) evaluation and PWM output must be compensated in the inverter by a feed-forward of the rotor angle ($\gamma_{S,cor}$) (2.64). The compensated rotor angle is $\tilde{\gamma}_S$.

$$\tilde{\gamma}_S = \left(\gamma_{S,act} \pm \gamma_{S,cor}\right), \mathrm{mod}(2\pi) = \left(\gamma_{S,act} \pm t_{cal} \cdot \omega_{syn}\right), \mathrm{mod}(2\pi) \tag{2.64}$$

For the used inverter (Appendix, Table A.3) with a 150 MHz processor the calculation takes about 2500 cycles, leading to $t_{cal} = 2500/150\ \mathrm{MHz} = 16.7\ \mu\mathrm{s}$. At $n = 60000\ \mathrm{min}^{-1}$ this equals 1.7% of the electrical period, leading to an angle deviation of 6°. The feed-forward is positive for the drive current system ($+\gamma_{S,cor}$) and negative for the suspension current system ($-\gamma_{S,cor}$), since the rotation of the corresponding current space vectors in the $\alpha\beta$-plane is opposite. For the correct adjustment of t_{cal}, the equivalent circuit of the drive winding field in the rotor-fixed coordinate frame is used: The rotor is accelerated to half rated speed by speed control. Then the speed control is switched off, so that the rotor slows down by braking no-load losses ($i_{q,D} = 0$). In this situation the voltage drop in the d_D-axis is zero and not speed-dependent, if the rotor angle is determined correctly. If this is not the case, t_{cal} has to be adapted in (2.64). The feed-forward for the suspension current system is realized by $-t_{cal}$.

Additionally the rotor angle determination for high-speed machines is prone to a non-linear sensor delay over the wide speed range of $n = 0$ ... $60000\ \mathrm{min}^{-1}$. So, despite of the angle correction (2.64), the rotor angle $\tilde{\gamma}_S$ can differ from the real value γ_S. To analyze this additional error angle $\varepsilon_{err,inv}$, a speed-down test by no-load losses ($i_{q,D} = 0$) is conducted. The error angle $\varepsilon_{err,inv}$ is calculated by (2.65). Fig. 2.11 shows the measured result for the *LLM4*. For the accurate determination of $\varepsilon_{err,Ft}$, the angle $\varepsilon_{err,inv}$ must be considered as an offset (2.66).

$$\varepsilon_{err,inv} = \mathrm{atan}\left(\frac{u_{d,D}\big|_{i_{q,D}=i_{d,D}=0}}{u_{q,D}\big|_{i_{q,D}=i_{d,D}=0}}\right) \tag{2.65}$$

Table 2.4.: Analytically calculated force error angle $\varepsilon_{err,Ft}$ and amplitude attenuation $G_{Ft,a,0}$ if only single rotor parts are considered electrically conductive

	Eddy currents only in shaft: $\kappa_{PM} = 0$, $\kappa_{sh} = 1.25\ \mathrm{MS \cdot m^{-1}}$	Eddy currents only in PM: $\kappa_{sh} = 0$, $\kappa_{PM} = 1.25\ \mathrm{MS \cdot m^{-1}}$	Eddy currents in shaft and PM: $\kappa_{sh} = \kappa_{PM}$, $\kappa_{PM} = 1.25\ \mathrm{MS \cdot m^{-1}}$
$\varepsilon_{err,Ft}$	0.63°	6.93°	7.09°
$G_{Ft,a,0}$	0.990	0.967	0.951

$$\gamma_S = \tilde{\gamma}_S - \varepsilon_{err,inv} \tag{2.66}$$

The suspension currents $i_{d,L}$ and $i_{q,L}$ give information about the radial bearing force vector $\vec{F}_L = F_y \cdot \vec{e}_y$, which points opposite to the gravitational force at standstill. As speed increases, the disturbing orthogonal force $F_x \propto G_{Ft,p,0}$ (Fig. 2.10) increases due to the eddy current effect. So the orthogonal suspension current $i_{d,L}$ increases. In order to exclude the superposition effect (Section 2.5) of the drive and suspension field, the rotor is accelerated to rated speed by speed control and, then, slows down by braking no-load losses with $i_{q,D} = i_{d,D} = 0$.

The suspension currents ($i_{d,L}$ associated to a force in x-direction, $i_{q,L}$ associated to a force in y-direction) give access to the radial forces on the rotor at rotation. Rotational-frequent oscillations are filtered, so that most of the geometrical inaccuracies in the machine do not influence the position controller output. Only DC effects, such as the eddy current effect on a standstill bearing force vector, are visible. The tuning of the rotor initial angle is carefully done in a way, that for an oscillation of the reference position signal in y-direction no variation of the position in x-direction occurs. Together with the aforementioned speed-dependent correction of the rotor angle γ_S, the error angle $\varepsilon_{err,Ft}$ is determined via (2.67). The force amplitude reduction $G_{Ft,a,0}$ is determined via (2.68).

$$\varepsilon_{err,Ft} \approx \tan\left(\frac{i_{d,L,act}}{i_{q,L,act}}\right) - \varepsilon_{err,inv} \tag{2.67}$$

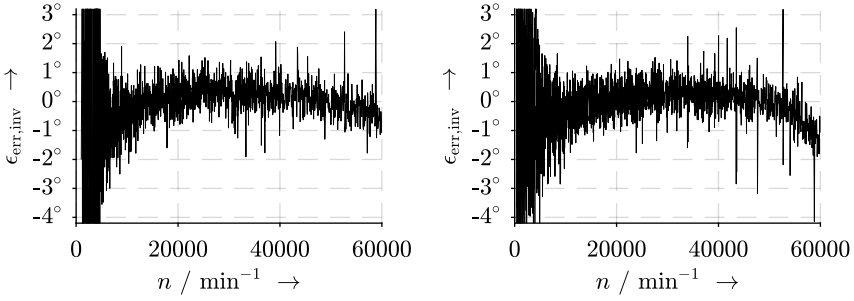

(a) Sm_2Co_{17}-rotor (b) NdFeB-rotor

Fig. 2.11.: Measured error angle $\varepsilon_{err,inv}$ (2.65) due to rotor angle sensor delay at varying speed n for two different rotors

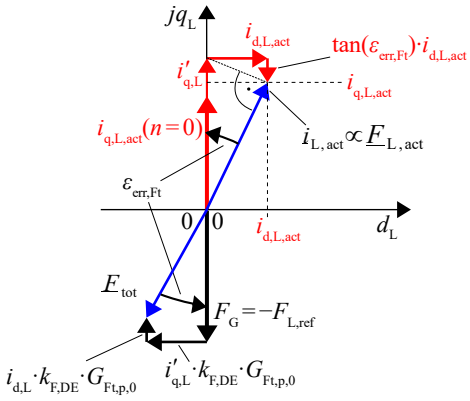

Fig. 2.12.: Schematic suspension current space vector and rotor force vector in the complex d_L-q_L-plane at force equilibrium (correct rotor angle determination provided)

$$G_{Ft,a,0} \approx \frac{i_{q,L,act}\,(n=0)}{i'_{q,L}} = \frac{\frac{i_{q,L,act}(n=0)}{\cos(\varepsilon_{err,inv})}}{\frac{i_{q,L,act}}{\cos(\varepsilon_{err,inv})} + \tan\left(\varepsilon_{err,Ft}\right)\cdot i_{d,L,act}} \tag{2.68}$$

For the calculation of $\varepsilon_{err,Ft}$ (2.67), the measured currents $i_{d,L,act}$ and $i_{q,L,act}$ are directly used. The calculation of $G_{Ft,a,0}$, requires the measured current $i_{q,L,act}\,(n=0)$ at zero speed and the current $i'_{q,L}$ (Fig. 2.12). Fig. 2.12 shows schematically, how the suspension current space vectors and the rotor force vectors are composed in the stator-fixed d_L-q_L-reference frame of the suspension winding. Due to the oscillation of the measured suspension currents as a switching ripple, caused by the PWM-voltage feeding, a linear fitting function is also shown in Fig. 2.13, enabling a better comparison to the calculated results.

The measured and calculated results for the *LLM4* are shown in Fig. 2.13. Table 2.5 summarizes the eddy current related disturbing force angle $\varepsilon_{err,Ft}$ and bearing force attenuation $G_{Ft,a,0}$ in the *LLM4* at rated speed $n_N = 60000\ \text{min}^{-1}$ for both analyzed rotor PM materials Sm_2Co_{17} and NdFeB.

Generally, the NdFeB-rotor exhibits a 34% smaller force error angle (measured value) due to the lower electric conductivity κ_{PM}, which is 35% smaller than for Sm_2Co_{17} (Table 2.1, Section 3.7.1). The proportionality $\kappa_{PM} \propto \varepsilon_{err,Ft}$ holds for resistance-limited eddy currents and is confirmed by the scaling factor $k_{scal,Ft}$ in Section 3.5, equation (3.39). The 2D cal-

culation and simulation results agree well, but overestimate the error angle by 72% due to the neglected axial end effect. Even for slim rotors ($l_{\mathrm{Fe}} / \left(2 \cdot r_{\mathrm{S,i}}\right) > 1$), the end effects are considerable, since the suspension winding pole pitch $\tau_{\mathrm{p,L}}$ (here: $\tau_{\mathrm{p,L}} = 27.5$ mm) may be in the range of the axial length l_{Fe} (here: $l_{\mathrm{Fe}} = 40$ mm). More details about this are addressed in Section 3.7.2. But even the 3-dimensional (3D) FEM simulation overesti-

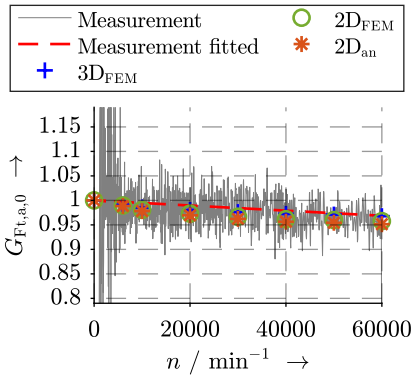

(a) Force amplitude attenuation $G_{\mathrm{Ft,a,0}}$: Sm_2Co_{17}-rotor

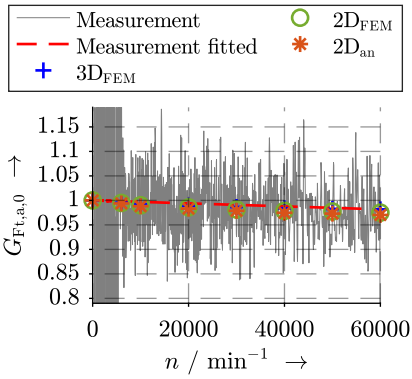

(b) Force amplitude attenuation $G_{\mathrm{Ft,a,0}}$: NdFeB-rotor

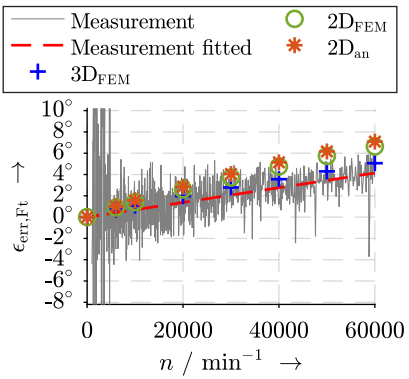

(c) Force error angle $\varepsilon_{\mathrm{err,Ft}}$: Sm_2Co_{17}-rotor

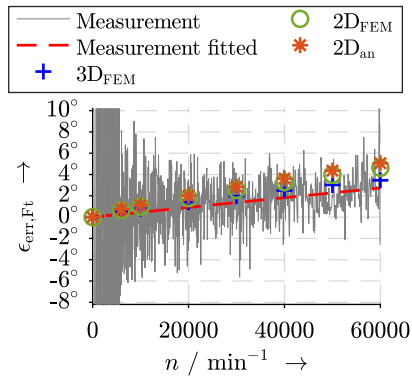

(d) Force error angle $\varepsilon_{\mathrm{err,Ft}}$: NdFeB-rotor

Fig. 2.13.: Comparison of different determination techniques for the force amplitude attenuation $G_{\mathrm{Ft,a,0}}$ and the force error angle $\varepsilon_{\mathrm{err,Ft}}$ according to Fig. 2.10 (linear fitting function for measurements)

Table 2.5.: Comparison of different determination techniques for the eddy current disturbing forces in the *LLM4* at $n_N = 60000\ \text{min}^{-1}$ (Details about determination techniques: Table 4.1)

Rotor PM material	Sm_2Co_{17}		NdFeB	
	$G_{Ft,a,0}$	$\varepsilon_{err,Ft}$	$G_{Ft,a,0}$	$\varepsilon_{err,Ft}$
$2D_{an}$	0.951	7.09°	0.970	5.06°
$2D_{FEM}$	0.958	6.63°	0.975	4.63°
$3D_{FEM}$	0.968	5.06°	0.987	3.47°
Measurement	0.969	4.13°	0.982	2.73°

mates the error angle by 22% in comparison to the measurement. This deviation may be due to material degradation at the PM surface during the mounting of the bandage or by slightly orthotropic conductivity properties of the PM ring, which could not be identified in the simple conductivity measurement from Section 3.7.1. The simulated amplitude attenuation $G_{Ft,a,0}$ of the 3D simulations agree well with the measured results. Following the results from Fig. 2.13, the speed dependency of $G_{Ft,a,0}$ and $G_{Ft,p,0} \propto \varepsilon_{err,Ft}$ can be considered linear (2.69) (2.70). Since the speed n is equal to the slip frequency $f_R = n$ (2.14), this holds as long as the eddy currents are resistance-limited. The linear relationship is also found in the eddy current effect scaling factor $k_{scal,Ft}$ (Section 3.5, equation (3.39)). This way, it can be easily included into the rotor position control model.

$$G_{Ft,a,0}(n) \approx 1 - \frac{n}{n_N} \cdot \left[1 - G_{Ft,a,0}(n = n_N)\right] \tag{2.69}$$

$$G_{Ft,p,0}(n) \approx -\frac{n}{n_N} \cdot G_{Ft,p,0}(n = n_N) = -\frac{n}{n_N} \cdot \tan\left(\varepsilon_{err,Ft}(n = n_N)\right) \cdot G_{Ft,a,0}(n = n_N) \tag{2.70}$$

2.4.2. Pulsating Suspension Force Vector

For the representation of the eddy current effect in the model of the rotor position control (Section 5.3.1), one does not know in advance, if the pure representation of the eddy current effect by the real values $G_{Ft,a,0}(n)$ and $G_{Ft,p,0}(n)$ is sufficiently precise, since the slip frequency $f_R = n + f_L$ (2.14) also depends on the suspension force frequency f_L. f_L may be different from zero, if the position controller counteracts rotor unbalance

forces or any external disturbance force. Thus, the decrease in force amplitude depends on speed n and f_L. To describe this, a pulsating reference suspension force vector $\vec{F}_\mathrm{L,ref}(t)$ is considered in y-direction at a fixed speed n (2.71).

$$\vec{F}_\mathrm{L,ref}(t) = F_\mathrm{L,ref}(t)\cdot\vec{e}_\mathrm{y}\ ;\ \text{where } F_\mathrm{L,ref}(t) = \hat{F}_\mathrm{L,ref}\cdot\cos(-\omega_\mathrm{L}\cdot t) = \mathrm{Re}\left\{\hat{F}_\mathrm{L,ref}\cdot e^{-j\omega_\mathrm{L}\cdot t}\right\} = \mathrm{Re}\left\{\underline{F}_\mathrm{L,ref}\right\} \tag{2.71}$$

Due to the eddy current effect, the actual force $\vec{F}_\mathrm{L}$ exhibits a smaller amplitude $\left|\vec{F}_\mathrm{L}\right|$ and lags in time. This is represented by the complex suspension force amplitude response $\underline{G}_\mathrm{Ft,a}(j\omega_\mathrm{L}) = \underline{F}_\mathrm{L}/\underline{F}_\mathrm{L,ref}$. Also it exhibits a perpendicular suspension force ($\varepsilon_\mathrm{err,Ft} \neq 0 \Rightarrow F_\mathrm{x} \neq 0$), which is represented by the perpendicular force response $\underline{G}_\mathrm{Ft,p}(j\omega_\mathrm{L}) = \underline{F}_\mathrm{x}/\underline{F}_\mathrm{L,ref}$ for a fixed speed n. For $\omega_\mathrm{L} = 0$ (= standstill suspension force vector), these functions are $\underline{G}_\mathrm{Ft,a}(0) = G_\mathrm{Ft,a,0}$ and $\underline{G}_\mathrm{Ft,p}(0) = G_\mathrm{Ft,p,0}$. For the representation in the *Laplace* domain – which is necessary for the inclusion into the position control model – the frequency response data is approximated by linear time-invariant transfer function in Section 5.3.1: $\underline{G}_\mathrm{Ft,a}(j\omega_\mathrm{L}) \Rightarrow \tilde{G}_\mathrm{Ft,a}(s)$ and $\underline{G}_\mathrm{Ft,p}(j\omega_\mathrm{L}) \Rightarrow \tilde{G}_\mathrm{Ft,p}(s)$.
It was not possible to "measure" $\underline{G}_\mathrm{Ft,a}(j\omega_\mathrm{L})$ and $\underline{G}_\mathrm{Ft,p}(j\omega_\mathrm{L})$ at the *LLM4*, since only the actual rotor position signals and actual suspension currents are accessible, but not the actual rotor force. Instead $\underline{G}_\mathrm{Ft,a}(j\omega_\mathrm{L})$ and $\underline{G}_\mathrm{Ft,p}(j\omega_\mathrm{L})$ are determined by the analytical calculation (Section 2.2) and by a 2D transient FEM simulation. The required pulsating suspension force vector is composed of two rotating force vectors of half amplitude and opposite rotation sense. Therefore, the necessary forward (subscript: f) $B_{\mathrm{L},p_\mathrm{L},k_\mathrm{f}}$ and backward (subscript: b) $B_{\mathrm{L},p_\mathrm{L},k_\mathrm{b}}$ rotating fundamental suspension field waves are superimposed to $B_{\mathrm{L},p_\mathrm{L},k_\mathrm{L},\mathrm{r,p}}(r,\gamma_\mathrm{R},t)$ and $B_{\mathrm{L},p_\mathrm{L},k_\mathrm{L},\gamma,\mathrm{p}}(r,\gamma_\mathrm{R},t)$ as shown in (2.17), (2.18). Analytically the field calculation is separately done for each forward and backward field wave $B_{\mathrm{L},p_\mathrm{L},k_\mathrm{f}}$ and $B_{\mathrm{L},p_\mathrm{L},k_\mathrm{b}}$. The superposition yields the pulsating suspension force. In the 2D FEM the two rotating 3-phase current systems of half-amplitude and opposite rotation sense in stator-fixed coordinates are fed simultaneously. In a first step, this is done, without allowing for rotor eddy currents to determine the pulsating reference force $\underline{F}_\mathrm{L,ref}$. Afterwards, the suspension force is determined for varying pulsation frequencies f_L. The actual forces $\underline{F}_\mathrm{y}$ (aligned) and $\underline{F}_\mathrm{x}$ (perpendicular) are determined with rotor eddy currents. With the 2D FEM simulation, a full electrical period with occurring eddy currents in steady-state must be simulated. The settling process to reach steady-state may take up to one electrical period, whereas the much faster analytical calculation inherently considers the steady state.

Table 2.6.: Two different model properties for PM Sm_2Co_{17} for the determination of the suspension force frequency response

BM	*LLM4*	*LLM4*$_{r+}$
P_N / kW; n_N / min^{-1}	1; 60000	40; 40000
p; p_L	1; 2	
$I_{L,N}$; $I_{D,N}$ / A	5.8; 12	10.5; 105
$r_{S,i}$; $r_{S,o}$; l_{Fe} / mm	17.5; 37.5; 40	30; 67.5; 125
r_{sh}; r_{PM}; h_{sl} / mm	12.25; 15; 1.5	18; 26; 3
κ_{PM}; κ_{sh} / MS $\cdot$ m^{-1}	1.25 (Sm_2Co_{17}); 1.25 (X39CrMo17-1)	
$\mu_{r,PM}$; $\mu_{r,sh}$	1.05 (Sm_2Co_{17}); 400 (X39CrMo17-1)	

As stated in Section 2.4.1, the prototype machine *LLM4* exhibits only a small eddy current effect. Its measured error angle even for the higher conductive Sm_2Co_{17} PM material is $\varepsilon_{err,Ft} < 4.2^\circ$ for speed values up to $n = 60000$ min^{-1}. Thus, in the following the results of two different bearingless motor topologies, the *LLM4* and the *LLM4*$_{r+}$ (Table 2.6), are given. The latter exhibits a bigger error angle $\varepsilon_{err,Ft} < 11^\circ$ for speed values up to $n_N = 40000$ min^{-1}. The bigger eddy current effect results from the bigger machine bore diameter (Table 2.6), resulting in a bigger suspension winding pole pitch $\tau_{p,L}$, so that the suspension field fundamental intrudes deeper into the rotor parts (compare Table 2.2).

Fig. 2.14a and Fig. 2.14b visualize the calculated amplitude and phase frequency response data of the aligned suspension force component $\underline{G}_{Ft,a}$ for the motors *LLM4* and *LLM4*$_{r+}$. For the perpendicular force frequency response $\underline{G}_{Ft,p}$, the calculated results are given in Fig. 2.14c and 2.14d. Both results are valid for rated speed n_N (Table 2.6). A constant suspension force response is given for frequencies $f_L < 500$ ... 1000 Hz. Since the controller bandwidth is typically in the range of < 500 Hz for the position control, it can be expected that the eddy current-originated disturbance forces can be well approximated by their "static" values $\underline{G}_{Ft,a} \approx G_{Ft,a,0}$, $\underline{G}_{Ft,p} \approx G_{Ft,p,0}$. This simplification can only be verified, however, by examining the influence of the simplification $\underline{G}_{Ft,a} \approx G_{Ft,a,0}$, $\underline{G}_{Ft,p} \approx G_{Ft,p,0}$ on the system eigenvalues (Section 5.3.1).

Fig. 2.14 verifies the good coincidence of the analytical calculation with the 2D FEM results. For the inclusion into the plant model of the rotor position control, the frequency response data is required not only for rated speed, but also for varying speed values, which is time consuming. Due to the good coincidence of the analytical and the numerical cal-

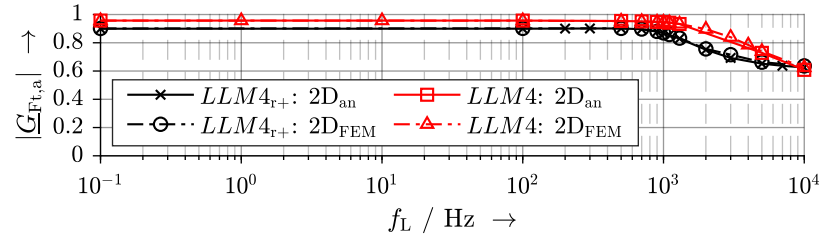

(a) Amplitude response of the aligned suspension force

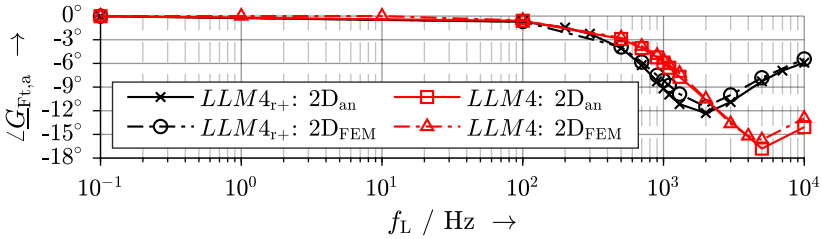

(b) Phase response of the aligned suspension force

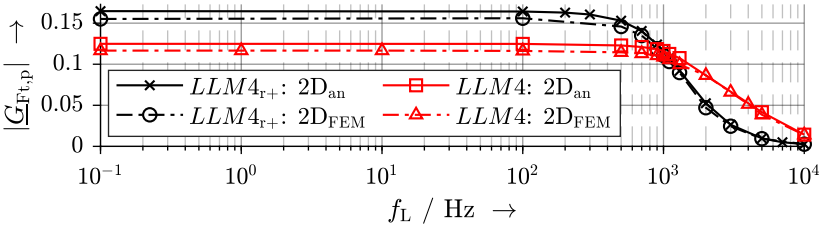

(c) Amplitude response of the perpendicular suspension force

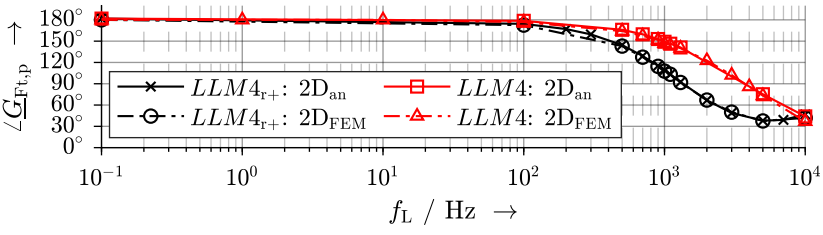

(d) Phase response of the perpendicular suspension force

Fig. 2.14.: Analytical and numerical calculation for the aligned ($\underline{G}_{\mathrm{Ft,a}}$) and perpendicular ($\underline{G}_{\mathrm{Ft,p}}$) f_{L}-pulsating suspension force frequency response

culation results, the much faster analytical calculation is used to calculate $\underline{G}_{\mathrm{Ft,a}}$ and $\underline{G}_{\mathrm{Ft,p}}$ for varying speed n.

For frequencies $f_{\mathrm{L}} > 500$ ... 1000 Hz the eddy currents become increasingly inductance-limited, i.e. $d_{\mathrm{E,PM}} \approx h_{\mathrm{PM}}$ (Fig. 2.4a), so that their lagging is shifted towards 180°. Thus, the perpendicular force diminishes as $\left|\underline{G}_{\mathrm{Ft,p}}\right| \to 0$. The amplitude of the force, aligned with the reference force, reduces with the frequency f_{L} to the fixed value $\left|\underline{G}_{\mathrm{Ft,a}}\right| \to \approx 0.6$. For very high frequencies $f_{\mathrm{L}} > 2000$ ... 5000 Hz the phase angle of the aligned suspension force also reduces. This is a well-known phenomenon [91] for inductance-limited eddy currents. Bearingless induction motors, for example, employ this principle for the suspension force generation, however, with highly-conductive rotor material instead of high frequencies. A more detailed analysis for $f_{\mathrm{L}} > 10000$ Hz was not conducted, since this certainly is beyond the controller's band width.

2.5. Superposition of Drive and Suspension Winding Field and Force-Current Disturbance Coefficient

The drive winding field exhibits the same pole count as the rotor field. In q-current operation this stator field lags the rotor field spatially by 90° electrically, shifting the overall $2p$-pole field wave and changing its amplitude called "armature reaction". Therefore, the suspension force vector $\vec{F}_{\mathrm{L}}$ can be divided into one component, which is aligned with the reference force, assumed as $F_{\mathrm{y}} \cdot \vec{e}_{\mathrm{y}} = -F_{\mathrm{G}} \cdot \vec{e}_{\mathrm{y}}$, and into one, which is aligned perpendicular to the reference force ($F_{\mathrm{x}} \cdot \vec{e}_{\mathrm{x}} = F_{\mathrm{err,sup}} \cdot \vec{e}_{\mathrm{x}}$). The disturbing force component results in the error angle $\varepsilon_{\mathrm{err,sup}} = \mathrm{atan}\left(F_{\mathrm{x}}/F_{\mathrm{y}}\right)$, which states a limit for the machine's electromagnetic utilization (see Section 3.6).

The force $F_{\mathrm{err,sup}}$ is present even without magnetic iron saturation and without rotor eddy currents. It occurs, since the integration of the *Maxwell* stress tensor (2.1) is non-zero for the superposition of two field waves, meeting the requirement $\nu'_{\mathrm{L}} = \nu \pm 1$. This holds for the suspension winding air gap fundamental ($\nu'_{\mathrm{L}} = p_{\mathrm{L}}$) and for the drive winding air gap fundamental ($\nu' = p$). Since no eddy currents contribute to this effect, and the time harmonic orders of the two field waves are identical ($k_{\mathrm{L}} = p$), equation (2.11) can be adopted for the force calculation, so that a non-zero constant disturbing force $F_{\mathrm{err,sup}} = F_{\mathrm{x}}$ (2.72)

occurs. No force aligned with the reference force occurs ($F_y = 0$), equation (2.73).

$$F_x = \frac{\pi \cdot r_{cal} \cdot l_{Fe}}{2 \cdot \mu_0} \cdot \hat{B}_{D,p,p,r}(r_{cal}) \cdot \left[\hat{B}_{L,p_L,p,r}(r_{cal}) + \hat{B}_{L,p_L,p,\gamma}(r_{cal})\right] \cdot \sin\left(\underbrace{\varphi_D - \varphi_L}_{\frac{\pi}{2}}\right) = F_{err,sup} \text{ ; for } \varphi_D = \varphi_R + \frac{\pi}{2} \ (q-\text{current operation}) \tag{2.72}$$

$$F_y = \frac{\pi \cdot r_{cal} \cdot l_{Fe}}{2 \cdot \mu_0} \cdot \hat{B}_{D,p,p,r}(r_{cal}) \cdot \left[\hat{B}_{L,p_L,p,r}(r_{cal}) + \hat{B}_{L,p_L,p,\gamma}(r_{cal})\right] \cdot \cos\left(\underbrace{\varphi_D - \varphi_L}_{\frac{\pi}{2}}\right) = 0 \text{ ; for } \varphi_D = \varphi_R + \frac{\pi}{2} \ (q-\text{current operation}) \tag{2.73}$$

If the magnetic iron saturation is negligible, as for the *LLM4*, the suspension currents $i_{q,L}$, $i_{d,L}$ and the drive currents $i_{q,D}$, $i_{d,D}$ are in a linear relationship to $F_{err,sup}$ via the factor $k_{err,sup}$ (2.74). The determination of $k_{err,sup}$ is preferably done for pure q-current operation of the drive winding ($i_{d,D} = 0$) and for pure y-force generation of the suspension winding ($i_{d,L} = 0$).

$$\begin{aligned} F_{err,sup} = k_{err,sup} \cdot \hat{i}_L \cdot \hat{i}_D \Rightarrow k_{err,sup} = \frac{F_{err,sup}}{\hat{i}_L \cdot \hat{i}_D} \\ \Rightarrow F_x = k_{err,sup} \cdot i_{q,L} \cdot i_{q,D};\ F_x = k_{err,sup} \cdot i_{d,L} \cdot i_{d,D}; \\ F_y = k_{err,sup} \cdot i_{q,L} \cdot i_{d,D};\ F_y = k_{err,sup} \cdot i_{d,L} \cdot i_{q,D} \end{aligned} \tag{2.74}$$

In [23] $k_{err,sup}$ is given for a 2-pole rotor, whereas here the term is valid for $2p$-poles. In the following $k_{err,sup}$ is determined via an 1-dimensional analytical field calculation ($1D_{an}$), a 2D analytical field calculation ($2D_{an}$), 2- and 3-dimensional FEM simulations ($2D_{FEM}$, $3D_{FEM}$) and via measurements. The different determination methods are characterized in Table 4.1.

$1D_{an}$: 1D analytical calculation

The calculation is done at $r = r_{cal} = r_{S,i}$, and only $p_L = p + 1$ is considered.

$$F_{err,sup} = \frac{\mu_0 \cdot l_{Fe} \cdot m^2 \cdot k_{w,D} \cdot k_{w,L} \cdot N_s^2 \cdot \hat{I}_{s,D} \cdot \hat{I}_{s,L}}{2 \cdot \pi \cdot r_{S,i} \cdot \delta_{eff}^2 \cdot p \cdot p_L} \cdot \left(r_{S,i}^2 + r_{S,i} \cdot \delta_{eff} + p \cdot p_L \cdot \delta_{eff}^2\right) \tag{2.75}$$

$$k_{\mathrm{err,sup}} = \frac{\mu_0 \cdot l_{\mathrm{Fe}} \cdot m^2 \cdot k_{\mathrm{w,D}} \cdot k_{\mathrm{w,L}} \cdot N_{\mathrm{s}}^2}{2 \cdot \pi \cdot r_{\mathrm{S,i}} \cdot \delta_{\mathrm{eff}}^2 \cdot p \cdot p_{\mathrm{L}}} \cdot \left(r_{\mathrm{S,i}}^2 + r_{\mathrm{S,i}} \cdot \delta_{\mathrm{eff}} + p \cdot p_{\mathrm{L}} \cdot \delta_{\mathrm{eff}}^2 \right) \tag{2.76}$$

2D$_{\mathrm{an}}$: 2D analytical calculation

The stator field calculation from Section 2.2.3 is used without rotor eddy currents. Only the fundamentals ($\nu' = p$, $\nu'_{\mathrm{L}} = p_{\mathrm{L}}$) are included. The evaluation of the *Maxwell* stress tensor is done at $r = r_{\mathrm{cal}} = r_{\mathrm{S,i}} - \delta/2$.

2D$_{\mathrm{an,simp}}$: 2D analytical calculation

In contrast to 2D$_{\mathrm{an}}$, the stator yoke and rotor shaft relative permeabilities $\mu_{\mathrm{r,S}}$, $\mu_{\mathrm{r,sh}}$ are set to infinity to get a "shorter" term (2.77). In order to keep the term manageable only $p_{\mathrm{L}} = p + 1$ is considered.

$$\begin{aligned} k_{\mathrm{err,sup}} = {} & l_{\mathrm{Fe}} \cdot m^2 \cdot k_{\mathrm{w,L}} \cdot k_{\mathrm{w,D}} \cdot N_{\mathrm{s,L}} \cdot N_{\mathrm{s,D}} \cdot \mu_0 \cdot \frac{r \cdot {r_{\mathrm{si}}}^{2p+1}}{\pi} \cdot \\ & \left(\frac{\begin{array}{r} \left[{r_{\mathrm{PM}}}^{2p+2} \cdot \left(\mu_{r,\mathrm{PM}} + 1 \right) + {r_{\mathrm{sh}}}^{2p+2} \cdot \left(\mu_{r,\mathrm{PM}} - 1 \right) \right] \cdot \\ \left[\left({r_{\mathrm{PM}}}^{4p} + r^{2p} \cdot {r_{\mathrm{sh}}}^{2p} \right) \cdot \left(\mu_{r,\mathrm{PM}} - 1 \right) + \right. \\ \left. \left(r^{2p} \cdot {r_{\mathrm{PM}}}^{2p} + {r_{\mathrm{PM}}}^{2p} \cdot {r_{\mathrm{sh}}}^{2p} \right) \cdot \left(\mu_{r,\mathrm{PM}} + 1 \right) \right] \end{array}}{\begin{array}{r} r \cdot \left[\left({r_{\mathrm{PM}}}^{2p+2} \cdot {r_{\mathrm{sh}}}^{2p+2} - {r_{\mathrm{PM}}}^{2p+2} \cdot {r_{\mathrm{si}}}^{2p+2} \right) \cdot \left(\mu_{r,\mathrm{PM}} + 1 \right) + \right. \\ \left. \left({r_{\mathrm{PM}}}^{4p+4} - {r_{\mathrm{sh}}}^{2p+2} \cdot {r_{\mathrm{si}}}^{2p+2} \right) \cdot \left(\mu_{r,\mathrm{PM}} - 1 \right) \right] \cdot \left[\left({r_{\mathrm{PM}}}^{4p} - {r_{\mathrm{sh}}}^{2p} \cdot {r_{\mathrm{si}}}^{2p} \right) \cdot \right. \\ \left. \left(\mu_{r,\mathrm{PM}} - 1 \right) + \left({r_{\mathrm{PM}}}^{2p} \cdot {r_{\mathrm{sh}}}^{2p} - {r_{\mathrm{PM}}}^{2p} \cdot {r_{\mathrm{si}}}^{2p} \right) \cdot \left(\mu_{r,\mathrm{PM}} + 1 \right) \right] \end{array}} + \right. \\ & \left. \frac{\begin{array}{r} {r_{\mathrm{PM}}}^{2p+2} \cdot \left[{r_{\mathrm{PM}}}^{2p+2} \cdot \left(\mu_{r,\mathrm{PM}} - 1 \right) + {r_{\mathrm{sh}}}^{2p+2} \cdot \left(\mu_{r,\mathrm{PM}} + 1 \right) \right] \cdot \\ \left[\left({r_{\mathrm{PM}}}^{4p} - r^{2p} \cdot {r_{\mathrm{sh}}}^{2p} \right) \cdot \left(\mu_{r,\mathrm{PM}} - 1 \right) - \right. \\ \left. \left(r^{2p} \cdot {r_{\mathrm{PM}}}^{2p} - {r_{\mathrm{PM}}}^{2p} \cdot {r_{\mathrm{sh}}}^{2p} \right) \cdot \left(\mu_{r,\mathrm{PM}} + 1 \right) \right] \end{array}}{\begin{array}{r} r^{2p+3} \cdot \left[\left({r_{\mathrm{PM}}}^{2p+2} \cdot {r_{\mathrm{sh}}}^{2p+2} - {r_{\mathrm{PM}}}^{2p+2} \cdot {r_{\mathrm{si}}}^{2p+2} \right) \cdot \left(\mu_{r,\mathrm{PM}} + 1 \right) + \right. \\ \left. \left({r_{\mathrm{PM}}}^{4p+4} - {r_{\mathrm{sh}}}^{2p+2} \cdot {r_{\mathrm{si}}}^{2p+2} \right) \cdot \left(\mu_{r,\mathrm{PM}} - 1 \right) \right] \cdot \left[\left({r_{\mathrm{PM}}}^{4p} - {r_{\mathrm{sh}}}^{2p} \cdot {r_{\mathrm{si}}}^{2p} \right) \cdot \right. \\ \left. \left(\mu_{r,\mathrm{PM}} - 1 \right) + \left({r_{\mathrm{PM}}}^{2p} \cdot {r_{\mathrm{sh}}}^{2p} - {r_{\mathrm{PM}}}^{2p} \cdot {r_{\mathrm{si}}}^{2p} \right) \cdot \left(\mu_{r,\mathrm{PM}} + 1 \right) \right] \end{array}} \right) \end{aligned} \tag{2.77}$$

Identification of the Superposition Effect by Measurement

The disturbing force $F_{\mathrm{err,sup}}$ becomes visible by measurements, if the *LLM4* is operated with a horizontally centered rotor, so that the rotor force in y-direction is $F_{\mathrm{y}} = k_{\mathrm{F,DE}} \cdot i_{\mathrm{q,L}} = -F_{\mathrm{G}}$ and in x-direction it is $F_{\mathrm{x}} = k_{\mathrm{F,DE}} \cdot i_{\mathrm{d,L}} = 0$. A change in load-torque M leads to a change in $i_{\mathrm{q,D}}$ and, thus, leads to a perpendicular force $F_{\mathrm{err,sup}} = -k_{\mathrm{F,DE}} \cdot i_{\mathrm{d,L}} \neq 0$.

Fig. 2.15 shows the measured currents $i_{\mathrm{d,L}}$ and $i_{\mathrm{q,L}}$, referring to the bearing force in x- and y-direction. A low speed of 12000 min^{-1} is considered, leading to a very small eddy current effect (Section 2.4.1). At $t = 100$ ms a change in load from $i_{\mathrm{q,D}} = 0.5$ A to $i_{\mathrm{q,D}} = -10$ A occurs to decelerate the rotor. The motor is in operation with horizontal shaft axis position so that only $i_{\mathrm{q,L}}$ is required for levitation, compensating for the gravitational force. It shows that the current, referring to a force in x-direction, also changes by the difference $\Delta i_{\mathrm{d,L}} = 1.1$ A. In Fig. 2.15, the current $i_{\mathrm{d,L}}$ shows a small damped oscillation, after the disturbance has happened, and it is not stationary constant. This is, because Fig. 2.15 shows the transient response to the superposition effect. In order to quantify the superposition disturbance force $F_{\mathrm{err,sup}}$ and the force error angle $\varepsilon_{\mathrm{err,sup}}$, measurements in stationary conditions are required. Three different loads are applied to the *LLM4* with the Sm_2Co_{17}- and the NdFeB-rotor: *Load A*, *Load B* and *Load C* . Details and power measurements for these loads are shown in Section 4.3.3. The *Load A*, *Load B* and *Load C*

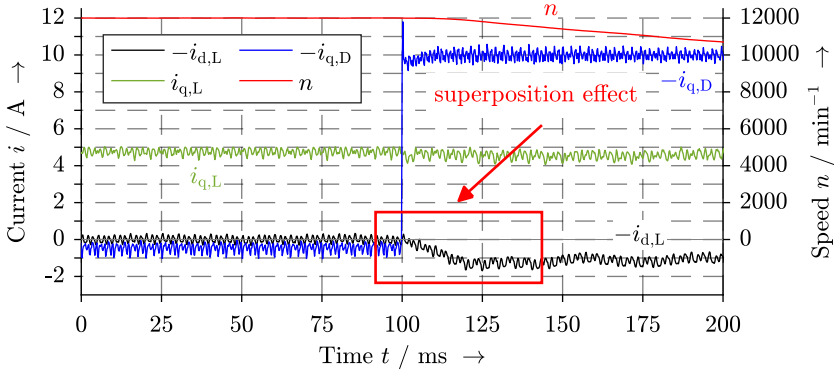

Fig. 2.15.: Measured drive ($-i_{\mathrm{q,D}}$, inverted) and suspension currents ($-i_{\mathrm{d,L}}$, inverted), ($i_{\mathrm{q,L}}$) of the *LLM4* at $n = 12000$ min^{-1} during a change in machine torque ($\Delta i_{\mathrm{q,D}} = -10.5$ A)

consist of loading the *LLM4* with turbo-charger propellers of different sizes in open air without any propeller housing, so that accordingly a different load torque for the different air flow rates is present at the shaft.

For the determination of $F_{\mathrm{err,sup}}$, the *LLM4* is driven with horizontal rotor shaft position, so that $i_{\mathrm{q,L}}$ compensates the gravitational force F_{G} and $i_{\mathrm{d,L}}$ compensates the disturbance by the superposition effect. Comparing the suspension current $i_{\mathrm{d,L}}$ at motor load (subscript: 1) and at motor no-load (subscript: 0), enables the determination of $F_{\mathrm{err,sup}}$ via the knowledge of the force-current coefficient $k_{\mathrm{F,DE}}$ (Section 4.1.2). Since the measurements at load and no-load are done at the same speed n, no angle correction as for the eddy current effect in Section 2.4.1 is required.

The factor $k_{\mathrm{scal,G}}$ (2.78) represents the ratio of the suspension force in y-direction with and without a propeller mounted. Thus, it is proportional to the propeller weight. It is needed in (2.79), to transform the no-load suspension current $i_{\mathrm{d,L,0}}$ for a subtraction from $i_{\mathrm{d,L,1}}$.

$$k_{\mathrm{scal,G}} = \frac{i_{\mathrm{q,L,1}}}{i_{\mathrm{q,L,0}}} \tag{2.78}$$

For the difference $\Delta i_{\mathrm{d,L}}$ (2.79) between no-load and load current for the force in x-direction, the offset current $i_{\mathrm{d,0,offs}}$ must be considered. $i_{\mathrm{d,L,0,offs}}$ is the measured current $i_{\mathrm{d,L}}$ at generator no-load ($i_{\mathrm{q,D}} = 0$). It is taken from the measurements of the eddy current effect (Section 2.4.1). $i_{\mathrm{d,L,0,offs}}$ compensates the non-zero rotor force in x-direction due to the eddy current effect and due to other external DC forces, resulting e.g. from sensor eccentricity.

$$\Delta i_{\mathrm{d,L}} = i_{\mathrm{d,L,1}} - i_{\mathrm{d,L,0,offs}} - \left(i_{\mathrm{d,L,0}} - i_{\mathrm{d,L,0,offs}}\right) \cdot k_{\mathrm{scal,G}} \tag{2.79}$$

With the knowledge of the force-current coefficient $k_{\mathrm{F,DE}}$ (Section 4.1.2), the disturbance force $\Delta F_{\mathrm{err,sup}}$, which results from the difference in the drive current $i_{\mathrm{q,D,1}} - i_{\mathrm{q,D,0}}$ at load and no-load, is calculated (2.80).

$$\Delta F_{\mathrm{err,sup}} = k_{\mathrm{F,DE}} \cdot \Delta i_{\mathrm{d,L}} \tag{2.80}$$

Relating $\Delta F_{\mathrm{err,sup}}$ to the difference in drive current $i_{\mathrm{q,D,1}} - i_{\mathrm{q,D,0}}$ and to the suspension current $i_{\mathrm{q,L,1}}$ leads to the disturbance force-current factor $k_{\mathrm{err,sup}}$ (2.81).

$$k_{\mathrm{err,sup}} = \frac{\Delta F_{\mathrm{err,sup}}}{\left(i_{\mathrm{q,D,1}} - i_{\mathrm{q,D,0}}\right) \cdot i_{\mathrm{q,L,1}}} \tag{2.81}$$

Table 2.7.: Measured superposition effect quantities of the *LLM4* for different machine loads according to Section 4.3.3, values for both rotors: Sm_2Co_{17}/NdFeB, $k_{\mathrm{err,sup}}$ referenced to current peak values

	Load A	*Load B*	*Load C*
Mechanical output power P_{m} / W	841.3 / 831.4	977.1 / 976.6	1061.4 / 1053.8
Air gap torque M_{δ} / mNm	151.3 / 150.7	187.1 / 187.3	252.4 / 251.3
Propeller weight scaling $k_{\mathrm{scal,G}}$	1.21	1.28	1.41
Offset current[1)] $i_{\mathrm{d,L,offs}}$ / A	1.11 / 1.42	1.09 / 1.41	1.06 / 1.38
Superposition force $F_{\mathrm{err,sup}}$ / N	0.23 / 0.19	0.31 / 0.24	0.41 / 0.35
Superposition error angle $\varepsilon_{\mathrm{err,sup}}$	2.28° / 1.91°	2.89° / 2.30°	3.34° / 3.07°
Superposition factor $k_{\mathrm{err,sup}}$ / $\mathrm{N \cdot A^{-2}}$	3.80 / 3.88	3.97 / 3.87	3.73 / 3.99

[1)] Measured at $i_{\mathrm{q,D}} = 0$

For the non-saturated *LLM4*, a multiplication of $k_{\mathrm{err,sup}}$ with the applied suspension current $i_{\mathrm{q,L,1}}$ and drive current $i_{\mathrm{q,D,1}}$ finally yields the disturbance force $F_{\mathrm{err,sup}}$ and the force error angle $\varepsilon_{\mathrm{err,sup}}$ (2.82), which are purely based on the superposition effect.

$$F_{\mathrm{err,sup}} = k_{\mathrm{err,sup}} \cdot i_{\mathrm{q,D,1}} \cdot i_{\mathrm{q,L,1}}; \qquad \varepsilon_{\mathrm{err,sup}} = \operatorname{atan}\left(\frac{F_{\mathrm{err,sup}}}{k_{\mathrm{F,DE}} \cdot i_{\mathrm{q,L,1}}}\right) \tag{2.82}$$

Table 2.7 summarizes the results for *Load A*, *Load B* and *Load C*. It shows that $k_{\mathrm{err,sup}}$

Table 2.8.: Comparison of different determination techniques for the superposition effect quantities of the *LLM4* at *Load A* (Section 4.3.3), values for both rotors: Sm_2Co_{17}/NdFeB, $k_{\mathrm{err,sup}}$ referenced to current peak values

	$k_{\mathrm{err,sup}}$ / $\mathrm{N \cdot A^{-2}}$	$\varepsilon_{\mathrm{err,sup}}$	$F_{\mathrm{err,sup}}$ / N
$1D_{\mathrm{an}}$	5.00 / 5.00	2.92° / 2.32°	0.30 / 0.24
$2D_{\mathrm{an,simp}}$	4.31 / 4.31	2.88° / 2.30°	0.26 / 0.21
$2D_{\mathrm{an}}$	4.03 / 4.03	2.81° / 2.23°	0.24 / 0.20
$2D_{\mathrm{FEM}}$	3.78 / 3.78	2.61° / 2.00°	0.23 / 0.18
$3D_{\mathrm{FEM}}$	3.79 / 3.79	2.63° / 2.01°	0.23 / 0.18
Measurement	3.80 / 3.88	2.28° / 1.91°	0.20 / 0.16

is constant, independent of the motor load and independent of the rotor field amplitude, since $k_{\mathrm{err,sup}} \approx 3.85\ \mathrm{N \cdot A^{-2}}$ is similar for all measurements. The disturbance force $F_{\mathrm{err,sup}}$ and the force error angle $\varepsilon_{\mathrm{err,sup}}$ increase with the machine's load and with a smaller rotor field. The force $\varepsilon_{\mathrm{err,sup}}$ is nearly proportional to the current product $i_{\mathrm{q,D}} \cdot i_{\mathrm{qL}}$ (Fig. 2.16). Since the remanence flux density of the Sm_2Co_{17}-PM is roughly by 10% smaller than for the NdFeB-PM, the Sm_2Co_{17}-rotor exhibits an approximately 10% bigger force error angle $\varepsilon_{\mathrm{err,sup}}$ than the NdFeB-rotor.

For *Load A*, Table 2.8 compares the measurement results to the analytical calculation and numerical simulation results. The 2D and 3D FEM simulation results both match the measurement results quite well, since the superposition effect is not much influenced by axial end effects: It is independent of rotor eddy currents and it is independent of the PM field, which is much bigger in 3D than in 2D due to the axially longer PM ($1.2 \cdot l_{\mathrm{Fe}}$). The 1D and 2D analytical calculations overestimate the superposition disturbance force due to the neglected slot opening effect. Moreover, the 1D calculation neglects the air gap curvature and the radius-dependency of the air gap flux density. Note that the calculated rotor force values via the *Maxwell* stress tensor integration (2.1) are independent of the closed integration surface around the rotor.

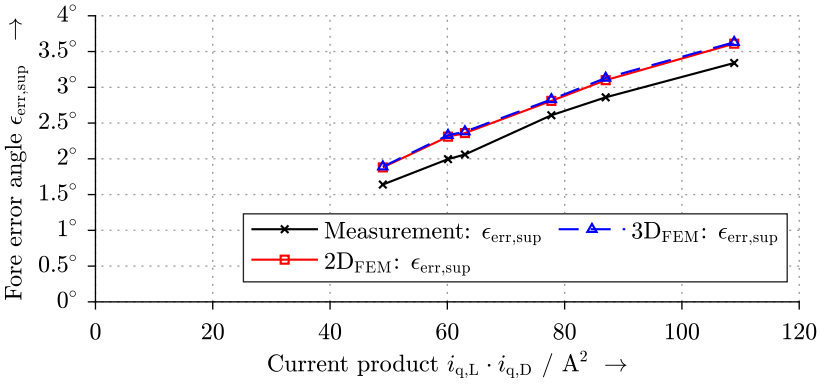

Fig. 2.16.: Measured and simulated force error angle $\varepsilon_{\mathrm{err,sup}}$ for varying machine load *Load A*, *Load B*, *Load C* with the Sm_2Co_{17}- and the NdFeB-rotor at the prototype machine *LLM4*

2.6. Saturation-based Force-Ripple and Constraints of the Linear Calculation

The built prototype machine *LLM4* exhibits a stator tooth flux density of $B_{\mathrm{d,S}} = 0.82$ T. For bearingless machines with such low magnetic flux density values in the iron parts, there is no iron saturation, so the linear analytical calculation shows – apart from slot opening effects – good accordance with non-linear 2D FEM simulated results. Since high-speed machines typically employ air gap flux densities $B < 0.7$ T, the linear analytical calculation often yields accurate results.

If bearingless machines are highly-utilized or employ an iron sheet material with a low loss coefficient, the air gap flux density can reach values up to $B = 1$ T, so that the magnetic circuit iron parts may saturate. Then, the linear analytical calculation is not precise anymore, and a non-linear 2D FEM simulation is required. Magnetic saturation leads to a modulation of the stator and rotor field waves with a 2^{nd} harmonic saturation wave, so that additional field harmonics occur – especially a 3^{rd} harmonic. These harmonics may cause additional torque and suspension force ripple. The occurrence of these ripples is discussed in this section by example of the non-saturated *LLM4* (Fig. 2.17a) and the magnetically saturated $LLM4_{\mathrm{I+}}$ (Fig. 2.17b, overview of investigated topologies given in Table A.4), whose slot cross section is bigger by the factor 2.3, allowing for a 2.3-times higher drive current $i_{\mathrm{q,D}}$ at a 2.3-times lower winding resistance R_{s} per phase.

Table 2.9 shows the loss composition, the fed currents and the calculated efficiency of the *LLM4* and the $LLM4_{\mathrm{I+}}$. A significant increase of efficiency from $\eta_{\mathrm{mot,1}} = 0.846$ (*LLM4*) to $\eta_{\mathrm{mot,1}} = 0.905$ ($\mathrm{LLM4_{I+}}$) is found. The increase is due to the very small utilization of the *LLM4* with $P_{\mathrm{d}} = 145.3$ W total losses and its surface cooling by natural air convection, whereas the $LLM4_{\mathrm{I+}}$ with $P_{\mathrm{d}} = 216.1$ W requires forced air cooling. The comparison shows that a higher machine utilization can be advantageous for bearingless machines.

For each of the two designs from Fig. 2.17, the rotor force is calculated over one electric period $1/f_{\mathrm{syn}} = 1$ ms, comparing the linear analytical calculation (Section 2.2.3, 2.2.4) with the non-linear 2D FEM-simulated results based on the $B(H)$-curve of the used iron lamination (Appendix A.14) [93]. To make the saturation effect visible, the simulations are done with magnetically linear material ("no sat"), i.e. $\mu_{\mathrm{r,Fe}} = 1000$, and with magnetically non-linear material ("sat"). The characteristics marked with "ec" ("no ec") show results with (without) rotor eddy currents. The characteristics with "D" ("no D") show results with (without) drive current feeding $i_{\mathrm{q,D}}$.

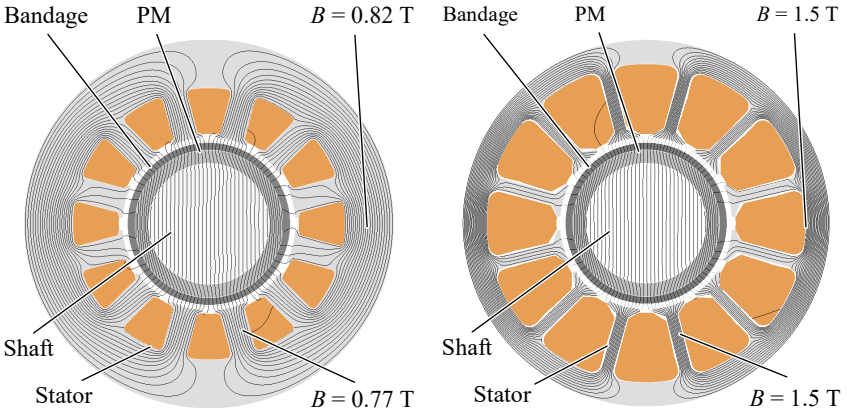

(a) *LLM4*: $i_{q,D} = 10.5$ A, $i_{q,L} = 5.89$ A (b) $LLM4_{I+}$: $i_{q,D} = 24.15$ A, $i_{q,L} = 5.89$ A

Fig. 2.17.: Field line plot for the *LLM4* and the $LLM4_{I+}$ from 2D FEM simulation at full load conditions

Fig. 2.18 compares the different values of the air gap torque M_δ with respect to the analytically calculated air gap torque ($= M_{\delta,\mathrm{ref}}$). The *LLM4* (Fig. 2.18a, 2.18c) does not exhibit

Table 2.9.: Calculated losses and output power of the *LLM4* and the $LLM4_{I+}$ in comparison ($LLM4_{I+}$ with 2.3-times bigger slot and conductor cross section)

	LLM4	$LLM4_{I+}$
Suspension current $\hat{I}_{q,L}$ / A	5.78	5.78
Drive current $\hat{I}_{q,D}$ / A	10.5	26.15
Motor fundamental input power $P_{e,1,in,1}$ / W	941.3	2273.7
Copper losses $P_{Cu,1}$ / W	8.5	17.6
Iron losses $P_{Fe,s,1}$ / W	65.0	126.1
Air friction losses P_{Fr} / W	69.2[1)]	69.2[1)]
Rotor eddy current losses $P_{Ft,R,1}$ / W	2.6	3.2
Total losses P_d / W	145.3	216.1
Air gap torque M_δ / mNm	138.7	339.0
Mechanical output power P_m / W	796.0	2057.6
Motor efficiency (fundamental) $\eta_{mot,1}$	0.846	0.905

[1)] From measurement (Section 4.3.3)

any significant torque oscillations and due to the absence of magnetic saturation, the analytical calculation fits the simulated results. Despite magnetic saturation, the *LLM4*$_{\mathrm{I}+}$ (Fig. 2.18b, 2.18d) does not exhibit any significant torque oscillations. The air gap torque M_δ mean value in the non-linear simulation is 2.1% smaller than in the linear analytical calculation. The low harmonic content of the air gap torque is due to the use of a distributed winding, the parallelly magnetized rotor PM and the big effective air gap δ_{eff}.
From this, one would not expect the suspension force to have significant saturation-originated ripple. However, the comparison of the non-linear simulated suspension force F_{L}, related to the linear analytically calculated suspension force without eddy currents ($= F_{\mathrm{L,ref}}$) in Fig. 2.19, shows that suspension force oscillations are clearly visible in the *LLM4*$_{\mathrm{I}+}$ due to magnetic saturation in contrast to the *LLM4*. Fig. 2.19 shows the calculated rotor force F_{L}, aligned with the reference force $F_{\mathrm{L,ref}}$. Fig. 2.19d shows that the force

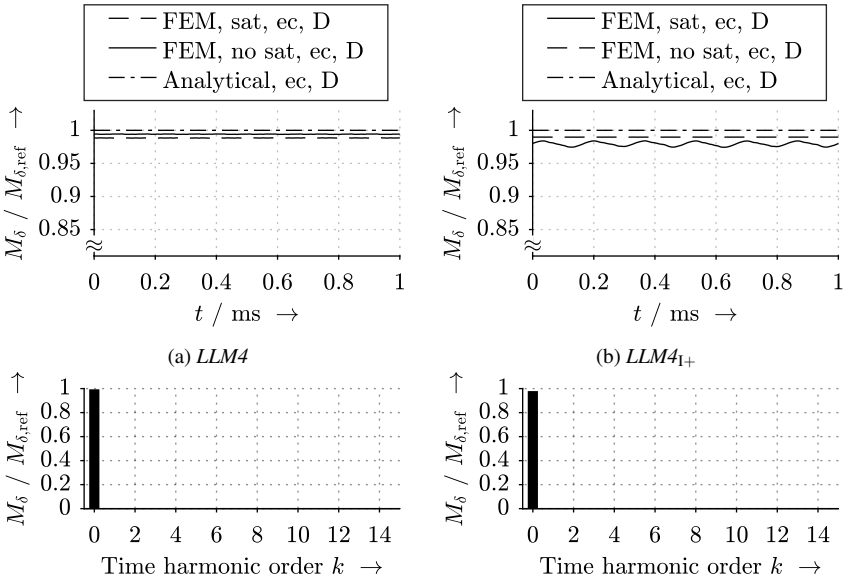

Fig. 2.18.: Comparison of analytically calculated and simulated air gap torque M_δ with magnetically linear and non-linear stator iron material for the motors *LLM4* and *LLM4*$_{\mathrm{I}+}$: (a),(b) in time domain; (c),(d) in frequency domain (stator-fixed coordinate system, $M_{\delta,\mathrm{ref}}$: analytical calculation without rotor eddy currents)

ripple harmonics are of time order $k = 2$ and $k = 4$. Also the suspension force mean value is reduced to 0.9 with respect to the reference force, which is mainly caused by the saturation and partly by the rotor eddy currents (Section 2.4). The *LLM4* (Fig. 2.19a, 2.19c) does not exhibit any significant force oscillations. The mean value of the suspension force is only reduced to $G_{\mathrm{Ft,a,0}} = 0.96$ by the eddy current effect.

Fig. 2.20 shows the force error angle $\varepsilon_{\mathrm{err,sup}}$, resulting solely from the field superposition effect. For the non-saturated *LLM4* (Fig. 2.20a, 2.20c), a calculation with magnetically linear material assumption ($\mu_{\mathrm{r,Fe}} = 1000$) yields results similar to the non-linear FEM simulation. The force error angle is small ($\varepsilon_{\mathrm{err,sup}} = 2.5^\circ$) and not oscillating. The $LLM4_{\mathrm{I+}}$ (Fig. 2.20b, 2.20d) exhibits a 2.2 times bigger error angle mean value ($\varepsilon_{\mathrm{err,sup}} = 6.1^\circ$) due to the 2.3 times higher drive current $i_{\mathrm{q,D}}$. Also oscillations with time harmonic order $k = 2$

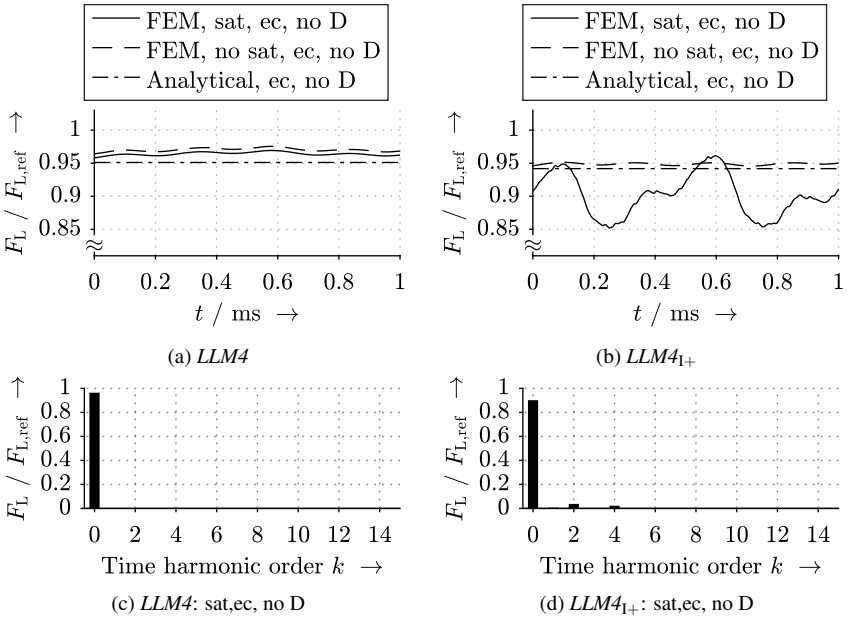

(a) *LLM4*

(b) $LLM4_{\mathrm{I+}}$

(c) *LLM4*: sat,ec, no D

(d) $LLM4_{\mathrm{I+}}$: sat,ec, no D

Fig. 2.19.: Comparison of analytically calculated and simulated aligned suspension force F_{L} with magnetically linear and non-linear stator iron material for the motors *LLM4* and $LLM4_{\mathrm{I+}}$: (a),(b) in time domain; (c),(d) in frequency domain (stator-fixed coordinate system, $F_{\mathrm{L,ref}}$: analytical calculation without rotor eddy currents)

and $k = 4$ are visible.

Fig. 2.21 shows the force error angle $\varepsilon_{\mathrm{err,Ft}}$, resulting solely from the eddy current effect. For the non-saturated *LLM4* (Fig. 2.21a, 2.21c), a calculation with magnetically linear material assumption yields results similar to the non-linear FEM simulation. The force error angle is small ($\varepsilon_{\mathrm{err,Ft}} = 7°$) and not oscillating. The *LLM4*$_{\mathrm{I+}}$ (Fig. 2.21b, 2.21d) exhibits the same error angle mean value as the *LLM4* due the identical rotor structure. Oscillations with harmonic order $k = 2$ and $k = 4$ are visible.

The analysis has shown that in a machine with noticeable magnetic saturation in the stator, like the *LLM4*$_{\mathrm{I+}}$ (Fig. 2.17b), the electromagnetic rotor force can exhibit a considerable force ripple. Still, the magnetically linear analytical calculation can be used for determining the mean value of the error angles $\varepsilon_{\mathrm{err,sup}}$ and $\varepsilon_{\mathrm{err,Ft}}$. The proneness to a force ripple but not to an air gap torque ripple is due to the fact that for lateral rotor forces the condition

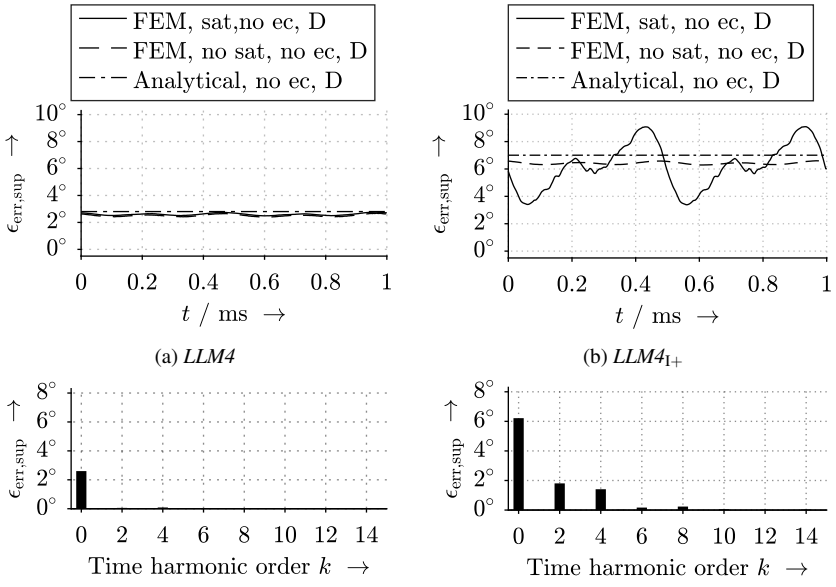

(a) *LLM4*

(b) *LLM4*$_{\mathrm{I+}}$

(c) *LLM4*: sat, no ec, D

(d) *LLM4*$_{\mathrm{I+}}$: sat, no ec, D

Fig. 2.20.: Comparison of analytically calculated and simulated force error angle $\varepsilon_{\mathrm{err,sup}}$ due to the superposition effect with magnetically linear and non-linear stator iron material for the motors *LLM4* and *LLM4*$_{\mathrm{I+}}$: (a),(b) in time domain; (c),(d) in frequency domain (stator-fixed coordinate system)

for two field waves of space order ν'_1 and ν'_2 is $\nu'_1 = \nu'_2 \pm 1$. For a non-zero air gap torque it is $\nu'_1 = \nu'_2$. In bearingless machines the condition $\nu'_1 = \nu'_2 \pm 1$ is more often fulfilled than $\nu'_1 = \nu'_2$ due to the use of distributed windings.

The occurrence of additional magnetic field waves due to iron saturation is explained via a saturation-dependent permeance function $\lambda_{\mathrm{sat},\tilde{\nu}',\tilde{k}}$ (2.83), where $\tilde{k}$ is the time harmonic order and $\tilde{\nu}'$ is the permeance absolute space harmonic order of the considered field wave of space order $\nu' = \nu \cdot p$. This second harmonic permeance function describes the permeance of the saturated, magnetically non-linear stator iron material.

$$\lambda_{\mathrm{sat},\tilde{\nu}',\tilde{k}}(\gamma,t) = \lambda_0 - \hat{\lambda}_{\mathrm{sat},\tilde{\nu}',\tilde{k}} \cdot \cos\left(\tilde{\nu}' \cdot \gamma - \tilde{k} \cdot n \cdot t\right) \text{ , where } \tilde{k} = 2 \cdot k \text{ ; } \tilde{\nu}' = 2 \cdot \nu p \qquad (2.83)$$

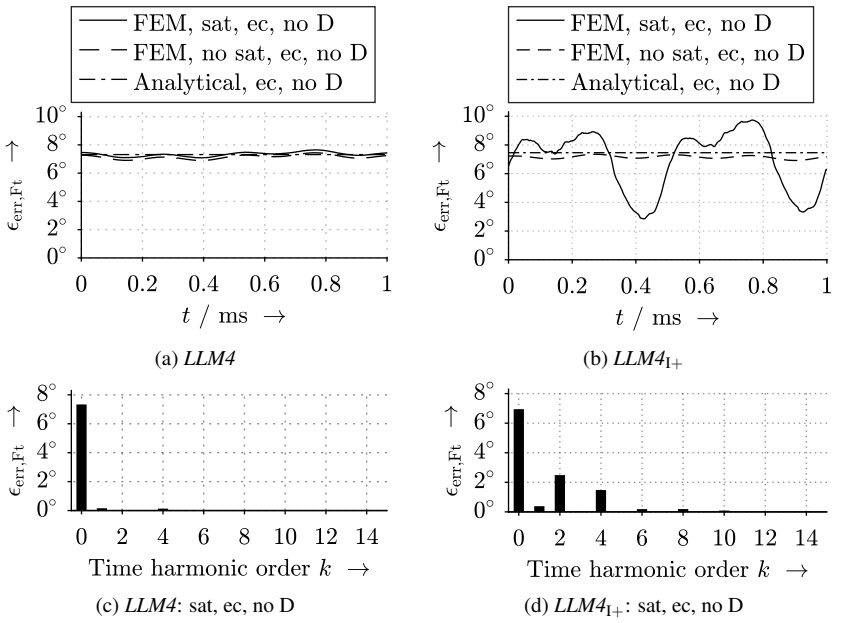

(a) *LLM4*

(b) $LLM4_{\mathrm{I+}}$

(c) *LLM4*: sat, ec, no D

(d) $LLM4_{\mathrm{I+}}$: sat, ec, no D

Fig. 2.21.: Comparison of analytically calculated and simulated force error angle $\varepsilon_{\mathrm{err,Ft}}$ due to the eddy current effect with magnetically linear and non-linear stator iron material for the motors *LLM4* and $LLM4_{\mathrm{I+}}$: (a),(b) in time domain; (c),(d) in frequency domain (stator-fixed coordinate system)

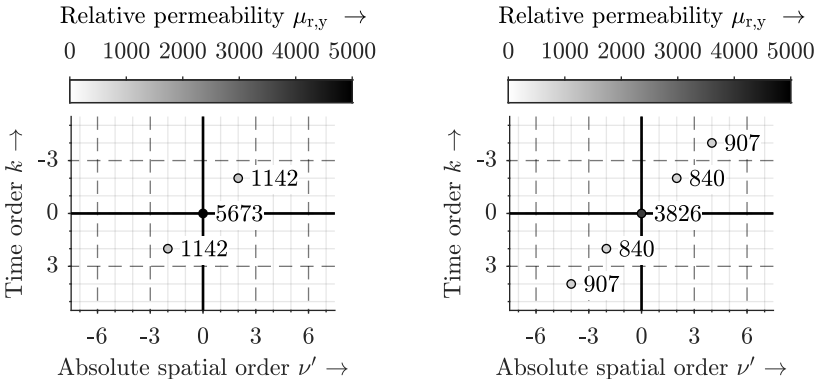

(a) *LLM4* (b) $LLM4_{I+}$

Fig. 2.22.: 2D *Fourier* spectrum of the relative permeability $\mu_{r,y}$ in the stator yoke of the *LLM4* and the $LLM4_{I+}$ (retrieved from a 2D FEM simulation), based on [100]

For a magnetic field wave of space order $\nu' = \nu \cdot p$ and time order k, the permeance function is of space order $\tilde{\nu}' = 2 \cdot \nu \cdot p$, as N- and S-pole saturate in the same way, and since for the saturation effect the absolute value of the flux density is relevant. It is of time order $\tilde{k} = 2 \cdot k$, since the permeance function moves synchronously with the considered field wave, which causes the saturation [101]. The term λ_0 is proportional to the average relative permeability $\mu_{r,Fe}$ in the stator iron. The term $\hat{\lambda}_{sat,\tilde{\nu}',\tilde{k}}$ represents the reduction of the relative permeability at the north and the south poles of a field wave with $2\nu \cdot p$ poles. In Fig. 2.22 the calculated absolute values of the *Fourier* coefficients of the relative permeability $\mu_{r,Fe,y}$ in the stator yoke are given, applying a 2D discrete *Fourier* transformation [100]. Motor operation at *Load A* is considered (Section 4.3.3). In the $LLM4_{I+}$ the mean value λ_0 decreases by 32%, compared to the *LLM4*, and additional harmonics of time and space order $\nu' = k = 2p$, $4p$, $6p$, ... occur for the $LLM4_{I+}$. The lower value λ_0 for the $LLM4_{I+}$ promotes the effect of the permeance harmonics $\hat{\lambda}_{sat,\tilde{\nu}',\tilde{k}}$. Relevant permeance function harmonics only occur from the dominating 2-pole rotor field wave of order $\nu' = 1$. A modulation with these permeance functions leads to a $\nu \cdot p$-pole field wave of reduced amplitude and to an additional $3 \cdot \nu \cdot p$-pole field wave. The $2\nu \cdot p$-pole field wave of reduced amplitude leads to a reduction of the air gap torque (Fig. 2.18d), and to a reduction of the suspension force F_L (Fig. 2.19d). Note that this saturation effect leads to a cross-coupling of the torque-generating current $i_{q,D}$ and the levitation currents

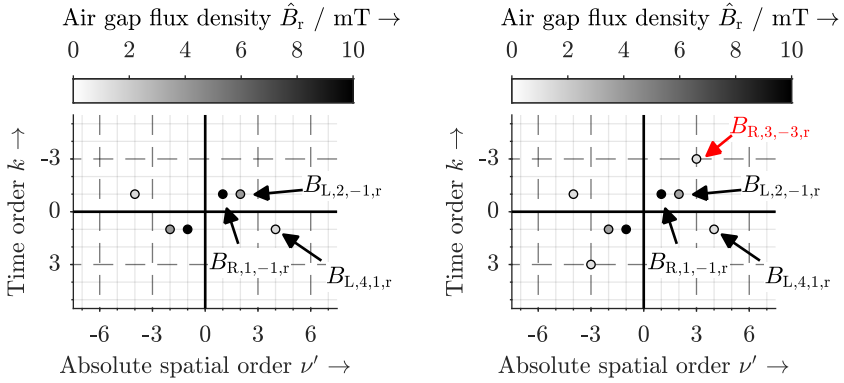

(a) *LLM4* (b) *LLM4*$_{\mathrm{I}+}$

Fig. 2.23.: 2D *Fourier* spectrum of the air gap flux density radial component B_r in the middle of the mechanical air gap for the *LLM4* and the *LLM4*$_{\mathrm{I}+}$ (retrieved from a 2D FEM simulation), based on [100]

$i_{\mathrm{d,L}}$, $i_{\mathrm{q,L}}$, which can be harmful for the rotor position control.

All field waves in the machine are modulated by the permeance function (2.83). However, only the modulation of the dominant $2p$-pole rotor field $B_{\mathrm{R},3,-3,\mathrm{r}}$ leads to a noticeable $3 \cdot 2p$-pole field wave for the *LLM4*$_{\mathrm{I}+}$ (Fig. 2.23b). This is shown in Fig. 2.23, where the 2D *Fourier* amplitude spectrum of the radial component of the air gap field is compared between *LLM4* and *LLM4*$_{\mathrm{I}+}$.

According to (2.11), the radial rotor force oscillates with the frequency $f_{\mathrm{P,F}}$ (2.84).

$$f_{\mathrm{P,F}} = \left| n \cdot \left(k - \mu' \right) \right| = \left| f_{\mathrm{syn}} \cdot \left(\frac{k}{p} - \mu \right) \right| \tag{2.84}$$

Considering the *Fourier* spectrum for the *LLM4*$_{\mathrm{I}+}$ in Fig. 2.23b, the occurrence of the suspension force ripple ($k = 2$, $k = 4$) is explained by:

- The additional saturation-originated rotor field wave $B_{\mathrm{R},3,3,\mathrm{r}}$ ($k = 3$, $\mu' = 3$) and the suspension winding field fundamental $B_{\mathrm{L},2,1,\mathrm{r}}$ ($k = 1$, $\nu' = 2$) lead to an additional suspension force, oscillating with the frequency $|(1-3) \cdot n| = 2 \cdot n$.

- The additional saturation-originated rotor field wave $B_{\mathrm{R},3,3,\mathrm{r}}$ ($k = 3$, $\mu' = 3$) and the suspension winding field harmonic of order $\nu' = 4$, i.e. $B_{\mathrm{L},4,-1,\mathrm{r}}$ ($k = -1$,

$\nu' = 4$), lead to a second additional suspension force, oscillating with the frequency $|(-1-3)\cdot n| = 4\cdot n$.

2.7. Rotor Forces by Magnetic Eccentricity

For the considered high-speed bearingless PM synchronous machines, the mounting of the bandage onto the rotor magnet ring, applying a shrink-fitting (Section 3.4), is by far the most crucial part of the rotor assembly. Thus, little attention is usually paid to the mounting of the permanent magnet onto the steel shaft. However, this mounting is also problematic, since the PM only exhibits a very low tensile ultimate strength R_m (Table A.6). Therefore, the PM must be mounted onto the shaft without any undersize, so that a small single-sided air gap δ_ecc (Fig. 2.24) between PM and shaft can occur, which is rotor-fixed. After the mounting, the surface of the PM is grinded, so that an apparently rotational symmetric rotor results on which the bandage fits. By the grinding process, the PM height at the maximum eccentricity air gap is reduced to $h_\mathrm{PM} - \delta_\mathrm{ecc}$. The single-sided air gap together with the single-sided reduced PM height leads to a flux concentration at the opposite side of the maximum eccentricity air gap width δ_ecc (Fig. 2.24b), resulting in a modulation of the fundamental air gap field (Fig. 2.24c). For the *LLM4*, the Sm_2Co_{17}- and the NdFeB-rotors exhibit an eccentricity air gap of $\delta_\mathrm{ecc} = 50\ \mu$m and $\delta_\mathrm{ecc} = 180\ \mu$m. It was measured manually at two remaining unused PM rings. The following results are also presented in [O12].

Usually in high-speed bearingless machines the radial component of the rotor air gap field fundamental amplitude $\hat{B}_{\mathrm{R},p,p,\mathrm{r}}$ is much bigger than the stator field amplitude. In the considered bearingless machine prototype the rotor air gap field is about 15-times higher than the stator field. Therefore, the stator field is neglected in this analysis. Eccentricity problems can be analytically calculated by using the so-called bi-linear conformal mapping method [102]. Alternatively, the perturbation method according to [103, 23] can be used. Here, a magnetostatic 2D FEM simulation with magnetically linear ($\mu_\mathrm{r,Fe} = 1000$) and isotropic material assumption is used instead, based on the *JMAG Designer 19.1*. A non-slotted concentric stator geometry is used (Fig. 2.24). So, the occurrence of the eccentricity-originated additional air gap field waves $B_{\mathrm{ecc},\mu,k,\mathrm{r}}$ is explained only qualitatively, which lead to the magnetic eccentricity force F_ecc.

The radial rotor flux density wave $B_{\mathrm{R},\mu',\mu',\mathrm{r}}(r_\mathrm{cal}, \gamma_\mathrm{m}, t)$ in the air gap of a PM machine at the radius $r = r_\mathrm{cal}$ from (2.5) is approximately given by (2.85), if a 1D radial air gap field

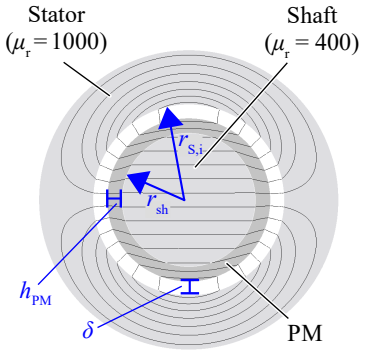

(a) "Healthy" machine: field plot and model geometry

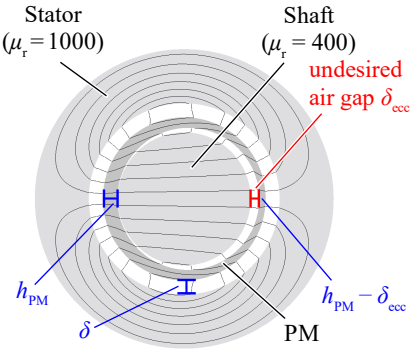

(b) "Unhealthy" machine: field plot and model geometry with undesired air gap δ_{ecc}

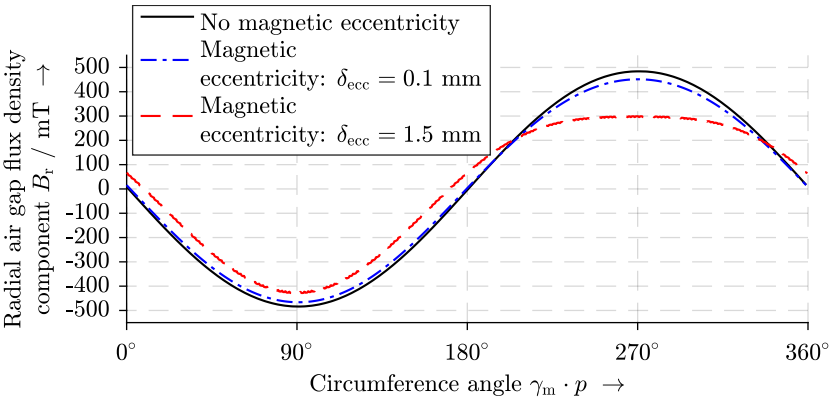

(c) Simulated radial component of the air gap flux density B_r with and without eccentricity

Fig. 2.24.: Visualization of the magnetic eccentricity, exemplary with an exaggerated big eccentricity air gap width $\delta_{ecc} = 1.5$ mm

without the air gap curvature is assumed. Note that the time harmonic order is always $k = \mu'$. In (2.85), $c_{PM,\delta} = h_{PM}/\delta$ is the ratio of the PM height h_{PM} to the air gap width δ.

$$B_{R,\mu',\mu',r}(r_{cal},\gamma_m,t) = -\frac{h_{PM}}{\delta} \cdot B_{PM,\mu',\mu',r}(r_{cal},\gamma_m,t) = c_{PM,\delta} \cdot B_{PM,\mu',\mu',r}(r_{cal},\gamma_m,t) \tag{2.85}$$

The single-sided additional air gap δ_{ecc} (Fig. 2.24) leads – with respect to the stator side – to a variation of the PM height $h_{\mathrm{PM}}(\gamma_{\mathrm{m}},t)$ and of the air gap width $\delta(\gamma_{\mathrm{m}},t)$. Both vary with the circumference angle γ_{m} and time t in stator-fixed coordinates (2.86), (2.87). Thus, the ratio $c_{\mathrm{PM},\delta}(\gamma_{\mathrm{m}},t)$ also varies (2.88), which can be approximated by (2.89).

$$h_{\mathrm{PM}}(\gamma_{\mathrm{m}},t) \approx h_{\mathrm{PM}} - \frac{\delta_{\mathrm{ecc}}}{2} + \frac{\delta_{\mathrm{ecc}}}{2} \cdot \cos(\gamma_{\mathrm{m}} - 2\pi \cdot n \cdot t + \varphi_{\mathrm{ecc}}) \tag{2.86}$$

$$\delta(\gamma_{\mathrm{m}},t) \approx \delta + \frac{\delta_{\mathrm{ecc}}}{2} - \frac{\delta_{\mathrm{ecc}}}{2} \cdot \cos(\gamma_{\mathrm{m}} - 2\pi \cdot n \cdot t + \varphi_{\mathrm{ecc}}) \tag{2.87}$$

$$c_{\mathrm{PM},\delta}(\gamma_{\mathrm{m}},t) = -\frac{h_{\mathrm{PM}}(\gamma_{\mathrm{m}},t)}{\delta(\gamma_{\mathrm{m}},t)} = c_{\mathrm{PM},\delta,0} + \sum_{i=1}^{\infty} \hat{c}_{\mathrm{PM},\delta,i} \cdot \cos(i \cdot \gamma_{\mathrm{m}} - i \cdot 2\pi \cdot nt + \varphi_{\mathrm{ecc}}) \tag{2.88}$$

$$c_{\mathrm{PM},\delta}(\gamma_{\mathrm{m}},t) \approx \underbrace{-\frac{h_{\mathrm{PM}} - \frac{\delta_{\mathrm{ecc}}}{2}}{\delta + \frac{\delta_{\mathrm{ecc}}}{2}}}_{c_{\mathrm{PM},\delta,0}} + \hat{c}_{\mathrm{PM},\delta,1} \cdot \cos(\gamma_{\mathrm{m}} - 2\pi \cdot n \cdot t + \varphi_{\mathrm{ecc}}) \tag{2.89}$$

By inserting (2.89) into (2.85), the PM magnetization wave is modulated by its shape via the ratio $c_{\mathrm{PM},\delta}(\gamma_{\mathrm{m}},t)$. With the used simplification, the modulation leads to the rotor air gap radial field fundamental (2.90) in stator-fixed coordinates. Additionally, the two air gap field waves $B_{\mathrm{ecc},\mu',k,\mathrm{r}}$ occur (2.91). For 2-pole rotors, $p-1=0$ leads to a homopolar flux component, which especially in magnetically levitated rotors is very small.

$$B_{\mathrm{R},p,p,\mathrm{r}}(r_{\mathrm{cal}},\gamma_{\mathrm{m}},t) = \underbrace{c_{\mathrm{PM},\delta,0} \cdot \hat{B}_{\mathrm{PM},p,p,\mathrm{r}}}_{\hat{B}_{\mathrm{R},p,p,\mathrm{r}}(r_{\mathrm{cal}})} \cdot \cos(p \cdot \gamma_{\mathrm{m}} - 2\pi \cdot n \cdot p \cdot t + \varphi_{\mathrm{R}}) \tag{2.90}$$

$$B_{\mathrm{ecc},\mu',k,\mathrm{r}}(r_{\mathrm{cal}},\gamma_{\mathrm{m}},t) = \frac{\hat{B}_{\mathrm{PM},p,p,\mathrm{r}} \cdot \hat{c}_{\mathrm{PM},\delta,1}}{2} \cdot \cos[(p \pm 1) \cdot \gamma_{\mathrm{m}} - (p \pm 1) \cdot 2\pi \cdot nt + \varphi_{\mathrm{R}} \pm \varphi_{\mathrm{ecc}}] \tag{2.91}$$

Thus, in the considered prototype machine with $2p=2$ poles, the eccentricity air gap δ_{ecc} leads to only one additional radial field wave $B_{\mathrm{ecc},2,2,\mathrm{r}}$ of time order $k=2$ and space order $p+1=\mu'=2$. At magnetically linear material conditions, the amplitude $\hat{B}_{\mathrm{ecc},2,2,\mathrm{r}}$ of this field wave rises linear with the width of the eccentricity air gap δ_{ecc} (Fig. 2.25). Note that $\hat{B}_{\mathrm{ecc},2,2,\mathrm{r}}$ does not depend on the location angle φ_{ecc} of the eccentricity air gap, so that the values of the field amplitude in Fig. 2.25a are equal to Fig. 2.25b. Thus, in the following analysis we set $\varphi_{\mathrm{ecc}}=0$, so that the eccentricity air gap is located at the pole axis.
The amplitude of the fundamental rotor field wave $\hat{B}_{\mathrm{R},1,1,\mathrm{r}}$ decreases almost linear in

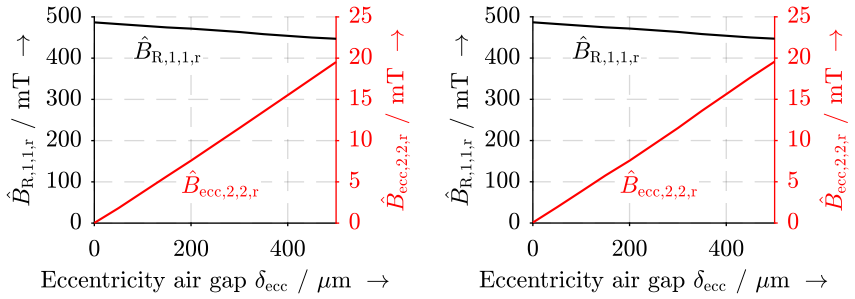

(a) Eccentricity air gap under pole: $\varphi_{\mathrm{ecc}} = 0$ (b) Eccentricity air gap under pole gap: $\varphi_{\mathrm{ecc}} = \frac{\pi}{2}$

Fig. 2.25.: Simulated radial magnetic field waves due to the eccentricity air gap δ_{ecc} for a 2-pole rotor with dimensions according to Table 2.1 and $B_{\mathrm{rem}} = 1$ T

Fig. 2.25 according to $c_{\mathrm{PM},\delta,0} \approx -\left(h_{\mathrm{PM}} - \frac{\delta_{\mathrm{ecc}}}{2}\right)/\delta$, if $\delta_{\mathrm{ecc}} \ll \delta$ (2.89). The rated suspension winding air gap field amplitude is $\hat{B}_{\mathrm{L},2,1,\mathrm{r}} = 8$ mT for the prototype machine. Since the modulated air gap field wave takes values $B_{\mathrm{ecc},2,2,\mathrm{r}} > 5$ mT for $\delta_{\mathrm{ecc}} > 130\ \mu$m (Fig. 2.25), even small eccentricity values can lead to radial force amplitudes in the range of the rotor gravitational force. Compared to the rotor field fundamental, the modulated field waves due to magnetic eccentricity are approximately smaller by factor 50. Thus, they may cause crucial rotor forces but they certainly will not cause considerable additional stator iron losses. So, a loss analysis of the eccentricity effect is omitted.

A more general representation of the air gap field wave harmonics is given in Fig. 2.26, which shows the calculated 2D *Fourier* spectrum of the air gap field radial component B_{r} with respect to the time order k and space order μ'. Fig. 2.26a and 2.26b show the calculated air gap field spectrum without and with an assumed additional air gap $\delta_{\mathrm{ecc}} = 100\ \mu$m. Due to the eccentricity, additional field waves $B_{\mathrm{ecc},\mu,k,\mathrm{r}}$ occur with the time and space harmonic orders $k = \mu'$ according to (2.91). The integration of the *Maxwell* stress tensor (2.1) on a closed surface around the rotor is zero for all combinations of two field waves with space orders μ_1, μ_2 for which $\mu_1 \neq \mu_2 \pm 1$ holds. For $\mu_2 = \mu_1 \pm 1$ a rotating radial force vector occurs. The lateral eccentricity force F_{ecc} on the rotor into an arbitrary direction, e.g. $F_{\mathrm{ecc}} = F_{\mathrm{ecc,x}}$, is given in (2.92) for k_1 and k_2 being the time harmonic orders of the involved field waves. The tangential field components are neglected

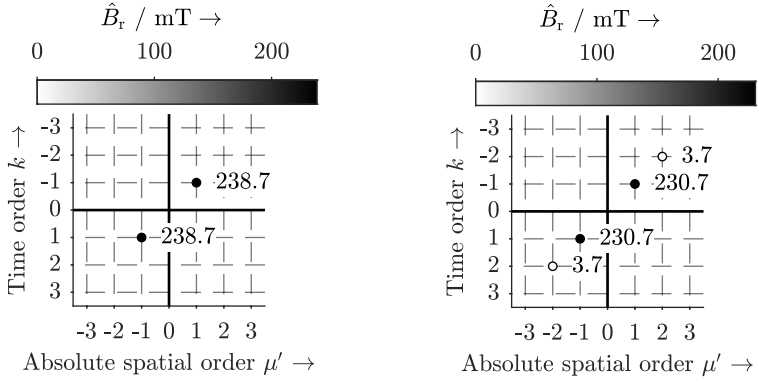

(a) Pole count $2p = 2$, $\delta_{\mathrm{ecc}} = 0$

(b) Pole count $2p = 2$, $\delta_{\mathrm{ecc}} = 100\ \mu\mathrm{m}$

Fig. 2.26.: Calculated 2D *Fourier* spectrum of the air gap flux density radial component $\hat{B}_\mathrm{r}$ in stator reference frame from magnetically linear 2D finite element simulation (k: time harmonic order, μ: space harmonic order, evaluated at radius $r_{\mathrm{S,i}} - \delta/2$), based on [100]

here for simplicity. For 2-pole machines, F_{ecc} is given in (2.93).

$$F_{\mathrm{ecc}}(t) = \frac{\pi \cdot r_{\mathrm{cal}} \cdot l_{\mathrm{Fe}}}{2 \cdot \mu_0} \cdot B_{\mu_1,k_1,\mathrm{r}}(r_{\mathrm{cal}}) \cdot B_{\mu_2,k_2,\mathrm{r}}(r_{\mathrm{cal}}) \cdot \sin((k_2 - k_1)\,2\pi n t + \varphi_1 \pm \varphi_2) \quad (2.92)$$

$$F_{\mathrm{ecc}}(t)\,|_{2p=2} = \frac{\pi \cdot r_{\mathrm{cal}} \cdot l_{\mathrm{Fe}}}{2 \cdot \mu_0} \cdot B_{\mathrm{R},1,1,\mathrm{r}}(r_{\mathrm{cal}}) \cdot B_{\mathrm{ecc},2,2,\mathrm{r}}(r_{\mathrm{cal}}) \cdot \sin(2\pi n t + \varphi_{\mathrm{R}} - \varphi_{\mathrm{ecc}}) \quad (2.93)$$

This shows, that the eccentricity air gap δ_{ecc} always leads to a rotational-frequent rotating radial force vector with rotational frequency $f_\mathrm{m} = n$. It's amplitude $\hat{F}_{\mathrm{ecc}}$ depends on the fundamental rotor field wave amplitude $\hat{B}_{\mathrm{R},p,p,\mathrm{r}}$ and on the bore radius $r_{\mathrm{S,i}} = r_{\mathrm{cal}} + \delta/2$. Note that F_{ecc} is much higher for 4-pole machines, since two field wave combinations $\mu_\mathrm{R} = 2 \,/\, \mu_{\mathrm{ecc},1} = 1$ and $\mu_\mathrm{R} = 2 \,/\, \mu_{\mathrm{ecc},2} = 3$ contribute to the force generation [O12]. The additionally occurring field waves $B_{\mathrm{ecc},\mu,k}$ do no generate eddy current losses in the rotor parts, since these field waves move synchronously with the rotor.

The amplitude of the oscillating eccentricity force $\hat{F}_{\mathrm{ecc}}$ is mainly determined by the machine's pole count $2p$ and by the PM remanence flux density B_{rem} (2.93). Fig. 2.27a indicates the magnetic eccentricity force amplitude $\hat{F}_{\mathrm{ecc}}$ for a 2-pole rotor topology with the dimensions of the *LLM4* in dependence of an assumed eccentricity air gap width $\delta_{\mathrm{ecc}} = 0$, 50 μm, 100 μm, ..., 500 μm and an assumed PM remanence flux density

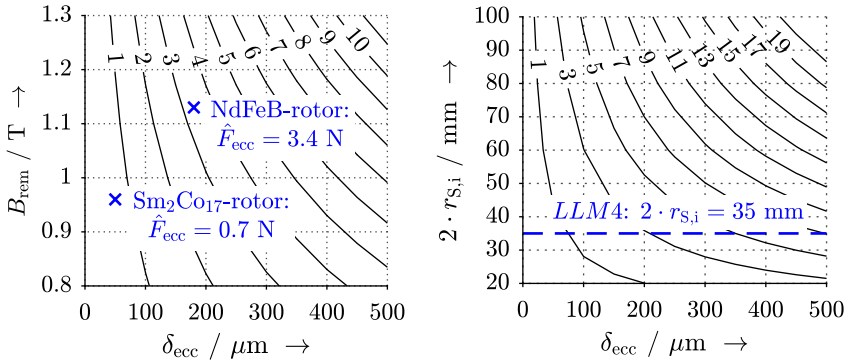

(a) Variation of the remanence flux density B_{rem} (dimensions of the *LLM4* with $2p = 2$)

(b) Variation of the stator bore diameter $2 \cdot r_{\mathrm{S,i}}$ ($2p = 2$)

Fig. 2.27.: Simulated radial magnetic eccentricity force amplitude $\hat{F}_{\mathrm{ecc}}$ in N for a varying magnetic eccentricity air gap width δ_{ecc}

$B_{\mathrm{rem}} = 0.8$ T, 0.9 T, ..., 1.3 T. The variation of the remanence flux density B_{rem} has small influence on $\hat{F}_{\mathrm{ecc}}$ for small values of δ_{ecc} and for large values of $B_{\mathrm{rem}} > 1$ T. The values of the two 2-pole rotors, used in the *LLM4*, are marked in Fig. 2.27a. The NdFeB-rotor with the higher value of $B_{\mathrm{rem}} = 1.13$ T is more prone to eccentricity forces than the Sm_2Co_{17}-rotor ($B_{\mathrm{rem}} = 0.96$ T). The eccentricity air gap is recalculated from measurements as $\delta_{\mathrm{ecc}} = 50\ \mu$m for the Sm_2Co_{17}-rotor and $\delta_{\mathrm{ecc}} = 180\ \mu$m for the NdFeB-rotor. This re-calculation is explained below. Thus, the simulated eccentricity force is $\hat{F}_{\mathrm{ecc}} = 0.7$ N for the Sm_2Co_{17}-rotor and $\hat{F}_{\mathrm{ecc}} = 3.4$ N for the NdFeB-rotor. The bore diameter $2 \cdot r_{\mathrm{S,i}}$ and the eccentricity air gap width δ_{ecc} both increase the $\hat{F}_{\mathrm{ecc}}$-values (Fig. 2.27b). Therefore, especially machines with large bore diameters are prone to magnetic eccentricity-originated forces.

At the *LLM4*, the suspension currents for horizontal rotor forces $i_{\mathrm{d,L}}$ and for vertical rotor forces $i_{\mathrm{q,L}}$ were measured at rotor standstill for 10 different equidistant rotor angle positions (Fig. 4.1 in Section 4.1.2). The actual purpose of these measurements was to determine the force current coefficient $k_{\mathrm{F,DE}}$. The current values are averaged over 1 s. Since the rotor position is constant, the dynamic controller properties are excluded from the measurements. The rotor is – according to the calibrated radial eddy current position sensors – in the centric position. The rotor axis is vertical axis to avoid the influence of the gravitational force.

The measurement was conducted with the Sm_2Co_{17}-rotor (Fig. 4.1a) and with the NdFeB-rotor (Fig. 4.1b). Both rotors exhibit a sine- and cosine-shaped radial disturbing force, which is compensated by the suspension currents $i_{d,L}$ and $i_{q,L}$. Consequently, this radial force wave of amplitude $\hat{F}_{ecc}$ rotates synchronously with the rotor ($f_m = n$).

The measured suspension force-current coefficients from Section 4.1.2 are $k_{F,Nd} = 1.09\ N \cdot A^{-1}$ for the NdFeB-rotor and $k_{F,Sm} = 1.01\ N \cdot A^{-1}$ for the Sm_2Co_{17}-rotor. The measured AC component of the suspension current is $\hat{i}_{ecc} = 3.42$ A for the NdFeB-rotor and $\hat{i}_{ecc} = 0.83$ A for the Sm_2Co_{17}-rotor. Thus, the eccentricity forces are determined to be $\hat{F}_{ecc} = 3.7$ N for the NdFeB-rotor and $\hat{F}_{ecc} = 0.83$ N for the Sm_2Co_{17}-rotor. These results agree with the simulation results at $\delta_{ecc} = 180\ \mu$m for the NdFeB-rotor (simulated: $\hat{F}_{ecc} = 3.4$ N) and at $\delta_{ecc} = 50\ \mu$m for the Sm_2Co_{17}-rotor (simulated: $\hat{F}_{ecc} = 0.7$ N).

The eccentricity force $F_{ecc}(t)$ acts on the rotor according to Fig. 2.28, in which the rotor control circuit is shown without the rotor tilting motions and the rotor gyroscopic effect, for simplicity. The damping and oscillation behavior of the system is determined by the controller settings, which must overcome the negative magnetic stiffness $k_{s,DE}$ (Fig. 2.28). In contrast to rotor unbalance forces, the amplitude $\hat{F}_{ecc}$ of the magnetic eccentricity force is speed-independent. Neglecting the controller influence on the rotor movement and considering only the movement originated by $F_{ecc}(t)$, the actual amplitude $\hat{x}_{ecc}$ of the

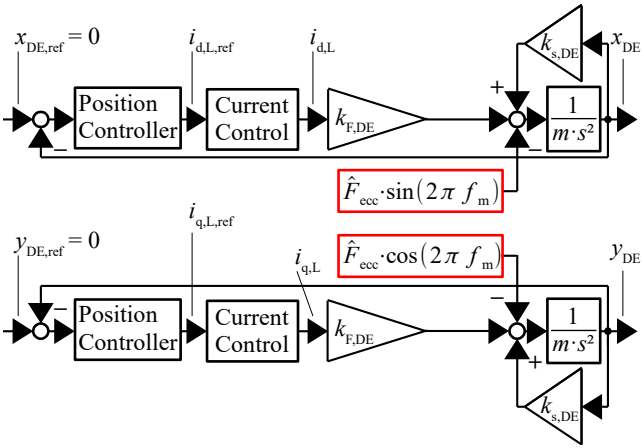

Fig. 2.28.: Simplified x- and y-position controller circuit with magnetic eccentricity force F_{ecc}, acting on the rotor (neglect of rotor tilting motions and gyroscopic effect)

movement due to the eccentricity force decreases with rising speed $n = f_\mathrm{m}$ according to *Newton*'s law with $\hat{x}_\mathrm{ecc} \propto 1/f_\mathrm{m}^2$ (2.94). This also holds for other magnetic disturbing forces, such as saturation originated disturbing forces (Section 2.6). However, this simplified mechanical model is only valid, if no resonances are excited, such as stator housing bending modes or rotor bending modes.

$$F_\mathrm{ecc}(t) = \hat{F}_\mathrm{ecc} \cdot \sin(2\pi \cdot f_\mathrm{m} \cdot t) = m \cdot \ddot{x}_\mathrm{ecc} \quad \Rightarrow \quad \hat{x}_\mathrm{ecc} = \frac{\hat{F}_\mathrm{ecc}}{m \cdot (2\pi \cdot f_\mathrm{m})^2} \tag{2.94}$$

Fig. 2.29a shows the measured actual x_DE-position (DE: drive end) of the motor *LLM4* with the NdFeB-rotor during a speed-up from $n = f_\mathrm{m} = 0$ to $n = f_\mathrm{m} = 240$ Hz. Also the red line indicates the theoretical magnetic eccentricity originated rotor movement amplitude $\hat{x}_\mathrm{ecc}$ according to (2.94). The rotor's rigid body eigenfrequencies for the chosen controller stiffness are at $f_\mathrm{eig,1} = 48$ Hz and $f_\mathrm{eig,2} = 66$ Hz. These eigenfrequencies do not appear in the position signal with increased oscillation amplitudes due to the good damping behavior of the position controller. The rotor orbit decreases from $\hat{x} = 52$ μm at $f_\mathrm{m} = 5$ Hz to $\hat{x} = 26$ μm at $f_\mathrm{m} = 150$ Hz. This decrease is due to $\hat{x}_\mathrm{ecc} \propto 1/f_\mathrm{m}^2$ (2.94). For $f_\mathrm{m} > 155$ Hz a "force-free" rotation [4, 5] is activated by notching f_m in the position controller feedback signal. By this, the rotor orbit is even decreased due to the poor position controller's disturbance reaction in case of high-frequent disturbances.

Fig. 2.29b shows the suspension current $i_\mathrm{d,L}$ for the NdFeB-rotor during a speed-up from $n = f_\mathrm{m} = 0$ to $n = f_\mathrm{m} = 240$ Hz. The current takes high values up to $\hat{i}_\mathrm{d,L} = 3$ A at standstill due to magnetic eccentricity forces (Fig. 4.1b). The current amplitude even increases up to $\hat{i}_\mathrm{d,L} = 4$ A at $f_\mathrm{m} = 150$ Hz, since the position controller's disturbance reaction to the rotational-frequent forces worsens for higher frequencies. Thus, the rotation frequency f_m is canceled from the actual position sensor values for $f_\mathrm{m} > 155$ Hz via an adaptive notch-filter. Consequently, the AC component in the suspension current $i_\mathrm{d,L}$ diminishes.

The effectiveness of the notch filter can also be seen by comparing Fig. 2.29c (operation at $f_\mathrm{m} = 20$ Hz) with Fig. 2.29d (operation at $f_\mathrm{m} = 200$ Hz). At low speed – and, thus, a big eccentricity-originated rotor movement $\hat{x}_\mathrm{ecc}$ – the position controller counteracts the rotor movement with a suspension current nearly in phase opposition to the position signal. At high speed, the rotor orbit is inherently small, since the magnetic eccentricity-originated rotor movement diminishes (2.94). Additionally, the position controller shows no reaction to the rotational-frequent rotor oscillation, which occurs due to the residual rotor unbalance.

The investigation shows that the magnetic eccentricity force F_{ecc} does not influence the bearingless machine's operation at higher speed $n > 50$ Hz. Even though it is not crucial for high-speed operation, the suspension current amplitudes at low speed can be crucial. This criticality is based on the inverter's current limit. In Fig. 2.29a, 2.29b the torque-producing current was only $i_{q,D} = 0.3$ A and, thus, by a factor 10 smaller than the suspension current.

For high machine dynamics, the speed-up process may be carried out with high torque-producing current values $i_{q,D}$. Also, the torque-producing current leads to radial disturbing force orthogonal to the controller's reference force vector (Section 2.5), which worsens the controller's reaction to the magnetic eccentricity forces. Therefore, the inverter's current limit may be reached very fast, if the magnetic eccentricity force is big and the machine

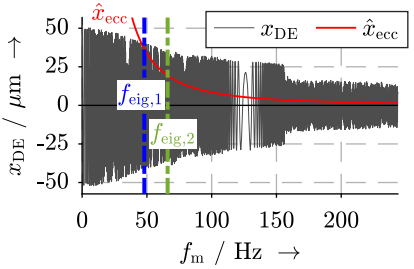

(a) Position sensor signal x_{DE} during speed-up (aliasing effect visible due to sampling frequency: $f_{samp} = 129$ Hz), controller sampling frequency $f_{sw}/2 = 16.5$ kHz

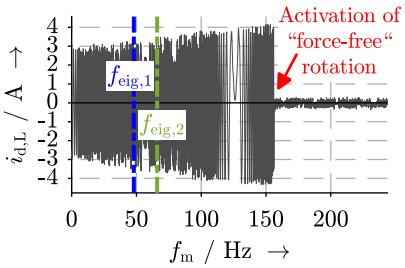

(b) Suspension current $i_{d,L}$ during speed-up (aliasing effect visible due to sampling frequency: $f_{samp} = 129$ Hz), controller sampling frequency $f_{sw}/2 = 16.5$ kHz

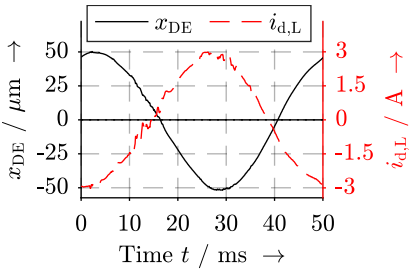

(c) Suspension current $i_{d,L}$ and position x_{DE} at rotation with $f = 20$ Hz

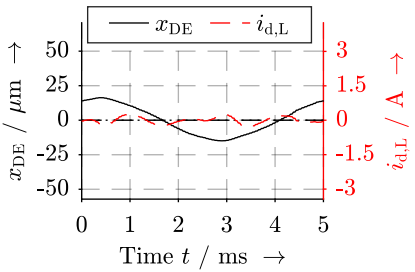

(d) Suspension current $i_{d,L}$ and position x_{DE} at rotation with $f = 200$ Hz

Fig. 2.29.: Measured suspension current and position signal with the NdFeB-rotor at operation with rotational frequency $f_m < 240$ Hz

is accelerated fast. For the prototype machine the inverter's current limit is at $i_{\mathrm{max}} = 16$ A as a momentary value, which is reached if the torque-producing reference current at zero-speed is $i_{\mathrm{q,D,ref}} > 10$ A. Even though the reference currents are below the inverter's current limit, the over-current protection can trip due to the ripple in the actual current, caused by the pulse width modulation. For the *LLM4* with the NdFeB-rotor, values of $i_{\mathrm{q,D,ref}} > 10$ A are only possible at speed $n = f_{\mathrm{m}} > 150$ Hz, when the "force-free" rotation is active.

3. Design and Scaling Effects of Bearingless PM Synchronous Machines

This chapter addresses selected aspects of bearingless motor (BM) design. In particular these aspects refer to a built 1 kW-prototype machine (*LLM4*) (Fig. 3.1, 3.2) of axial active iron length $l_{\mathrm{Fe}} = 40$ mm and an outer stator iron stack diameter $2 \cdot r_{\mathrm{S,o}} = 75$ mm. In order to derive scaling laws also design aspects for a bigger bearingless PM synchronous machine of $l_{\mathrm{Fe}} = 125$ mm and $2 \cdot r_{\mathrm{S,o}} = 135$ mm are discussed.

3.1. Prototype machine *LLM4*

The bearingless PM synchronous machine is located on the drive end (DE), whereas the axial thrust bearing is combined with a radial AMB as "combined" AMB (Appendix A.5) [24] at the non-drive end (NDE) of the shaft, to allow for a short axial length (Fig. 3.1, 3.2). The bearingless PM synchronous machine prototype (Table A.2) is fed by a 2-level 1.2 kVA-inverter at 150 V-DC-link voltage with seven current sensors and twelve MOSFET-half-bridges, operated at a switching frequency of $f_{\mathrm{sw}} = 33$ kHz (Table A.3 in the Appendix). Eddy current sensors are used for measuring the rotor radial and axial position. The rotor angle γ_{R} is determined by an analogue *Hall*-sensor for speed values $n < 10000\ \mathrm{min}^{-1}$ and by two 90°-shifted simple digital *Hall*-switches for speed values $n > 10000\ \mathrm{min}^{-1}$ to reduce the sensor delay [23] (Fig. 2.11).
The pole count $2p_{\mathrm{L}}$ of the suspension winding and $2p$ of the rotor PM fulfill the condition $2p_{\mathrm{L}} = 2p \pm 2$ (Table 1.1) for generating a radial bearing force. With the combination $p/p_{\mathrm{L}} = 1/2$ the PM rotor is composed of a solid magnetic stainless steel shaft, on which a solid rare-earth PM ring is mounted, magnetized with $2p = 2$ poles. It is protected against centrifugal forces by a shrink-fit carbon-fiber sleeve. The twelve-slot stator is equipped with a distributed integer slot winding with $q = 2$ slots per pole and phase. This so-called "double 3-phase" winding, consisting of the systems A and B, serves as a combined drive

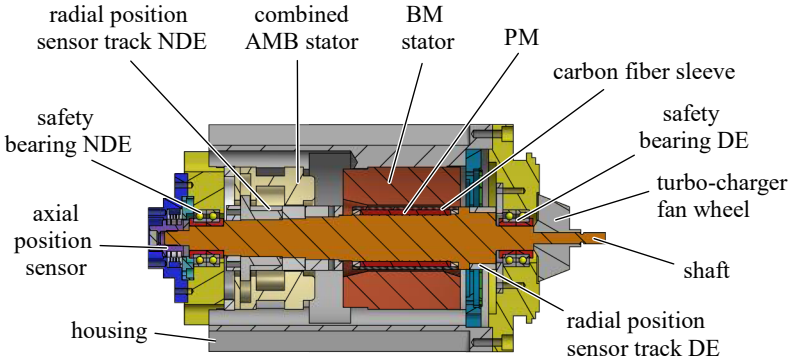

Fig. 3.1.: Axial-radial cross section of the bearingless PM synchronous machine *LLM4* (colors are chosen for better legibility)

and suspension winding. It generates two different field waves with $2p = 2$ for the torque and $2p_{\mathrm{L}} = 4$ for the radial bearing force. The required stator air gap field for the torque and the suspension force generation is excited by the superposition of the phase currents in the two 3-phase systems A and B, as explained in Section 3.2.

The combined radial-axial AMB at the NDE with PM-biased magnetization is commercially available at *KEBA Industrial Automation Germany GmbH*. It is composed of a 4-pole radial magnetic bearing and an axial magnetic bearing. The radial magnetic bearing may be omitted if a second BM is used instead [9].

A standard field-oriented, decentralized position control (Chapter 5) according to [4] is used in the BM for the radial force and the torque, applying controller tuning according the principle of natural stiffness and damping (Chapter 5). With this control, the magnetically levitated BM was operated with a turbo-charger fan wheel as load up to its rated speed $n_{\mathrm{N}} = 60000\ \mathrm{min}^{-1}$.

For the *LLM4*, the rated electric data and the machine geometry data are summarized in Appendix A.2.

3.2. Winding Types

In this work, those bearingless machines are considered, which require a rotating magnetic field wave in order to generate a radial bearing force (see Section 1.3). Together with the

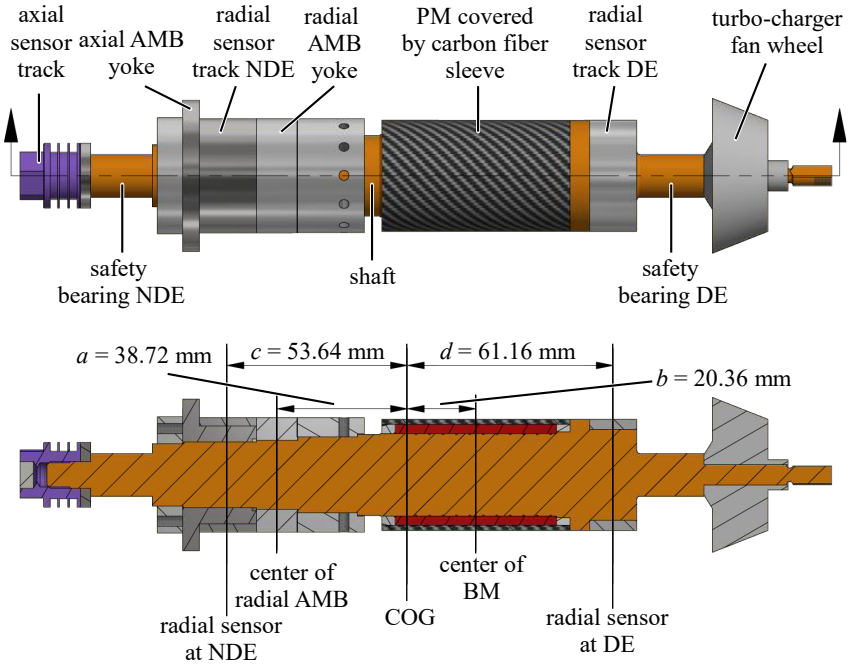

Fig. 3.2.: Rotor of the motor *LLM4*: Actor and sensor planes related to the center of gravity (COG), relevant for the rotor position control

rotor field, the stator winding of these machines generates both, the torque and the lateral rotor force which enables magnetic levitation. The main conditions, that the winding must comply with, are listed in Table 1.1.

For this group of bearingless machines, one can choose between two separated stator windings for torque and suspension force generation each or one combined winding [O04]. The two separated stator 3-phase windings are fed by a symmetrical drive and a symmetrical suspension current system via two 3-phase inverters (Fig. 3.3a). The combined winding can be fed either by two asymmetric current systems (usually by a six-phase inverter) (Fig. 3.3b) or by two symmetrical current systems, if both winding ends are available and connected as in [60] as so called *Dual-Purpose No-Voltage Winding* (Fig. 3.3c). Usually the generation of a $2p$- and $2p \pm 2$-pole field wave is done by using two separated symmetrical single- or two-layer 3-phase windings (called winding systems A and B), differing in pole count by ± 2. They are fed by two 3-phase current systems with the same

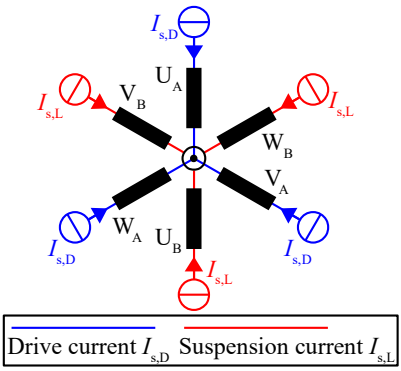

(a) Separated windings fed by two symmetrical current systems [24]

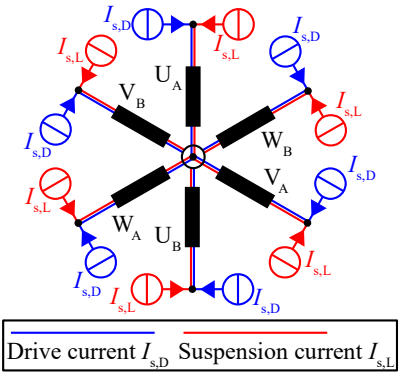

(b) Combined winding fed by two asymmetrical current systems (*LLM4*)

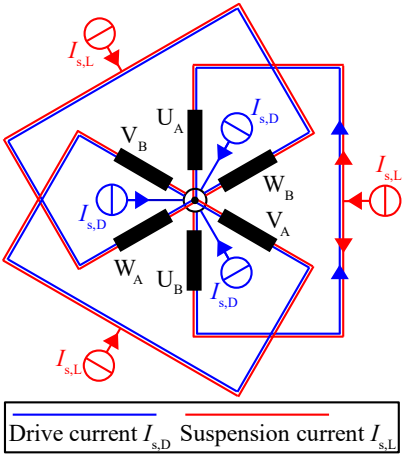

(c) Combined winding fed by two symmetrical current systems [60]

Fig. 3.3.: Winding classifications of bearingless motors for simultaneous torque and lateral rotor force generation (The voltage-source inverters are simplified by equivalent current sources.)

stator frequency f_{syn} to generate a standstill, constant lateral bearing force vector [104]. The symmetrical 3-phase current system with the current space vector $\underline{i}_{\alpha\beta,\mathrm{D,sep}}$, exciting a field wave of $2p$ poles with the so called “drive winding” A, generates torque with the

$2p$-pole rotor field, while the symmetrical 3-phase current system with the current space vector $\underline{i}_{\alpha\beta,\mathrm{L,sep}}$ excites a field wave of $2p \pm 2$ poles with the so called "suspension winding" B. The two winding systems are electrically separated from each other and share the same stator slot area (Fig. 3.4), green winding scheme.
Alternatively, one can use one combined winding (Fig. 3.3b, Fig. 3.3c, Fig. 3.4, black winding scheme). The separated drive winding as well as the suspension winding are 6-zone windings. For torque generation, the same zones are realized artificially in the combined winding by differential-mode feeding of the two windings systems A and B ($\underline{i}_\mathrm{A} = -\underline{i}_\mathrm{B}$) (Fig. 3.5a). This way, a $2p$-pole field wave is generated. The bearing force is either generated by a 6-zone single-layer winding with $q = 1$ slots per pole and phase or by the combined 3-zone double-layer winding. The latter is artificially realized by the common-mode feeding of the two systems A and B ($\underline{i}_\mathrm{A} = \underline{i}_\mathrm{B}$), generating a $2p \pm 2$-pole field wave. This is visualized in Fig. 3.5a. The superposition of the air gap field B_r of the

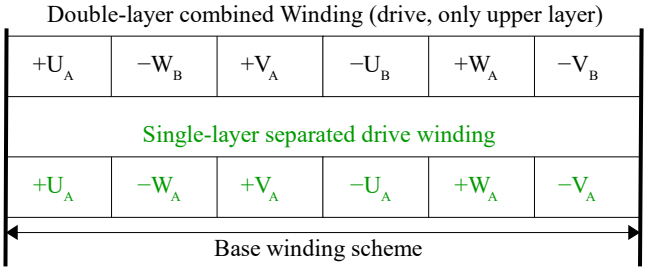

(a) Drive winding

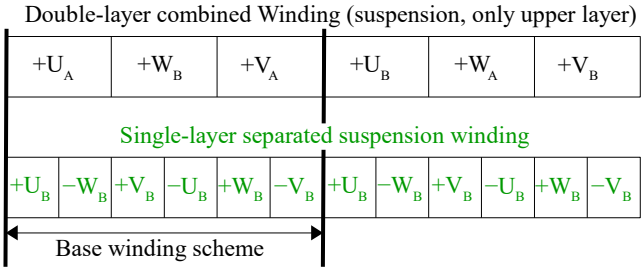

(b) Suspension winding

Fig. 3.4.: Phase belt for the combined winding and the separated windings for the pole pair combination $p/p_\mathrm{L} = 1/2$

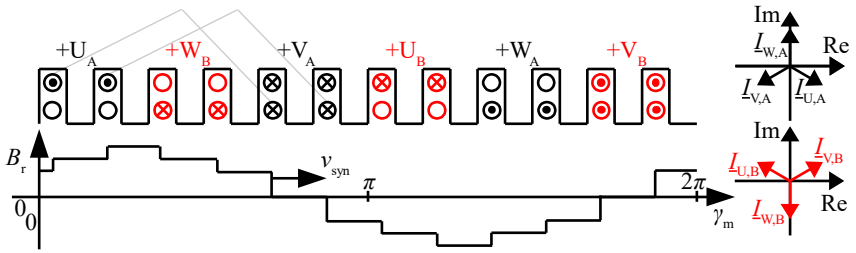

(a) **Torque generation** by 180°-phase shift feeding of the current systems A and B with phase sequence U→V→W (clockwise rotating current space vector $\underline{i}_D$)

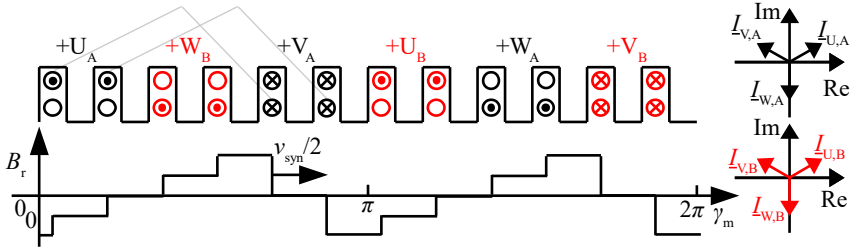

(b) **Lateral bearing force generation** by in-phase feeding of the current systems A and B with phase sequence U→W→V (counter-clockwise rotating current space vector $\underline{i}_L$)

Fig. 3.5.: Radial air gap field distribution (neglect of slot openings, $\mu_{Fe} \to \infty$) and complex current phasors for a combined winding in a 12-slot stator with $q = 2$, $p/p_L = 1/2$, $W/\tau_p = 2/3$

drive and the suspension current systems in the combined winding is illustrated in Fig. 3.5. The rotation direction of the current space vectors that belong to the $2p$-pole field wave ($\underline{i}_D$) and to the $2p \pm 2$-pole field ($\underline{i}_L$) wave must be reversed to ensure that the resulting field wave moves in the same direction as the rotor field wave (D: U-V-W, L: U-W-V). Superimposing these current space vectors results in two asymmetrical current systems A and B with elliptic current space vector orbits in the α-β stator-fixed coordinate system [23], [O02]. For machine control, these current space vectors $\underline{i}_A(t)$ and $\underline{i}_B(t)$ can be decomposed into two symmetrical current space vectors ($\underline{i}_D(t)$ and $\underline{i}_L(t)$), i.e. into two symmetrical current subsystems, from current measurement.

These two symmetrical current systems can be generated by a 3-phase drive inverter and a separated 3-phase suspension inverter as in Fig. 3.3c, where the drive inverter represents a "fictive" star point [60]. The combined winding of the *LLM4*, however, is fed by a single

6-phase inverter with two physical star points (Fig. 3.3b). Here, the decomposition into the two symmetrical subsystems is carried out by the controller of the inverter.
For the combined winding, it must be distinguished between thermal and electromagnetic issues, because physically, and here thermally, the combined winding comprises six phases. However, electromagnetically it acts like a 3-phase winding, having two parallel winding branches each, one in winding system A and one in winding system B (see Table 3.1).

3.3. Winding Selection

This section evaluates different suitable stator windings for BMs and helps selecting a winding topology in dependence of certain design specifications.

3.3.1. Comparison between Combined and Separated Windings

Thermal and Electromagnetic Utilization

In order to compare the combined winding with the separated windings, one has to consider Table 3.1, which distinguishes the thermal and electromagnetic properties of a combined winding. Note that in the following the subscript "sep" is used for separated winding quantities, whereas the combined winding quantities have no extra subscript. For comparison with the *LLM4* which has a combined winding, the built prototype motor *LLM1* [24] with two separated windings (Table 3.2) is considered in the following. In the combined winding, each of the 180° spatially displaced 3-phase terminals, e.g. phase terminals U_A and U_B, according to Fig. 3.3b and Fig. 3.4b may be regarded as the beginning of one winding branch. Hence, the winding branch in system A and in system B together may be considered a 3-phase winding with $a = a_D = a_L = 2$ parallel winding branches. Each of these $a = 2$ winding branches carries the thermally effective coil currents $I_{D,th}$ and $I_{L,th}$. The thermally effective superposition of these currents as I_{th} is calculated according to (3.1) [23].

$$I_{th} = \sqrt{I_{D,th}^2 + I_{L,th}^2} \tag{3.1}$$

The electromagnetically effective current for the imaginary 3-phase stator winding system is $I_{s,D} = 2 \cdot I_{D,th}$ and $I_{s,L} = 2 \cdot I_{L,th}$. These currents are linked to the torque and force gen-

Table 3.1.: Thermal and electromagnetic properties for the combined winding of the *LLM4* with $k_{w,D} = 0.835$ and $k_{w,L} = 0.75$ at *Load A* (Section 4.3.3)

For thermal considerations		For electromagnetic considerations	
m_{th}	6	m	3
$N_{s,D,th} = N_s = \frac{N_c \cdot q_{D,th} \cdot 2p}{a_{D,th}}$	18	$N_{s,D} = N_s = \frac{N_c \cdot q_D \cdot 2p}{a_D}$	18
$N_{s,L,th} = N_s = \frac{N_c \cdot q_{L,th} \cdot 2p_L}{a_{L,th}}$	18	$N_{s,L} = N_s = \frac{N_c \cdot q_L \cdot 2p_L}{a_L}$	18
$q_{D,th}$	1	$q_D = q$	2
$q_{L,th}$	1/2	$q_L = q$	2
$a_{D,th}$	1	$a_D = a$	2
$a_{L,th}$	1	$a_L = a$	2
$I_{D,th} = I_{D,m=6}$	3.71 A	$I_{s,D} = a_D \cdot I_{D,m=6}$	7.42 A
$I_{L,th} = I_{L,m=6}$	2.04 A	$I_{s,L} = a_L \cdot I_{L,m=6}$	4.08 A

eration in the same way as the currents of the two 3-phase systems $I_{s,D,sep}$ and $I_{s,L,sep}$ for the separated windings.

The thermally admissible currents $I_{s,D,sep}$, $I_{s,L,sep}$ of the separated windings for torque and lateral force generation are calculated according to (3.2), (3.3), where $k_{share,L,sep}$ is the slot share, covered by the suspension winding. This calculation is based on an equal thermal utilization $K \cdot J$ for the combined winding and for the separated windings. Other loss groups like iron losses are assumed to be identical for both kinds of windings.

$$I_{s,D,sep} = I_{th} \cdot \frac{N_s}{N_{s,D,sep}} \cdot a \cdot \left(1 - k_{share,L,sep}\right) \tag{3.2}$$

$$I_{s,L,sep} = I_{th} \cdot \frac{N_s}{N_{s,L,sep}} \cdot a \cdot k_{share,L,sep} \tag{3.3}$$

Due to the relationship $M_\delta \propto k_{w,D} \cdot N_s \cdot I_{s,D}$, the torque ratio of a machine with a combined winding and with two separated windings, having an equal thermal utilization $K \cdot J$, is derived in (3.4) as $k_{comp,M} = M_{\delta,sep}/M_\delta$. If $k_{comp,M} > 1$, the torque capability of the machine with separated windings is bigger than of the machine with a combined winding.

Table 3.2.: Winding properties of the built prototype motor *LLM1* with two separated windings [24] with $k_{\mathrm{w,D}} = 0.966$, $k_{\mathrm{w,L}} = 1$ and $k_{\mathrm{share,L,sep}} = 0.42$

m	3
$N_{\mathrm{s,D,sep}} = \frac{N_{\mathrm{c}} \cdot q_{\mathrm{D,sep}} \cdot 2p}{a_{\mathrm{D,sep}}}$	16
$N_{\mathrm{s,L,sep}} = \frac{N_{\mathrm{c}} \cdot q_{\mathrm{L,sep}} \cdot 2p_{\mathrm{L}}}{a_{\mathrm{L,sep}}}$	18
$q_{\mathrm{D,sep}}$	2
$q_{\mathrm{L,sep}}$	1
$a_{\mathrm{D,sep}}$	1
$a_{\mathrm{L,sep}}$	1

$$
\begin{aligned}
k_{\mathrm{comp,M}} &= \frac{k_{\mathrm{w,D,sep}}}{k_{\mathrm{w,D}}} \cdot \frac{N_{\mathrm{s,D,sep}}}{N_{\mathrm{s}}} \cdot \frac{I_{\mathrm{s,D,sep}}}{I_{\mathrm{s,D}}} \\
&= \frac{a \cdot I_{\mathrm{th}}}{I_{\mathrm{s,D}}} \cdot \frac{k_{\mathrm{w,D,sep}}}{k_{\mathrm{w,D}}} \cdot \frac{N_{\mathrm{s,D,sep}}}{N_{\mathrm{s}}} \cdot \frac{N_{\mathrm{s}}}{N_{\mathrm{s,D,sep}}} \cdot \left(1 - k_{\mathrm{share,L,sep}}\right) \\
&= \frac{\sqrt{\left(I_{\mathrm{s,D}}/I_{\mathrm{s,L}}\right)^2 + 1}}{I_{\mathrm{s,D}}/I_{\mathrm{s,L}}} \cdot \frac{k_{\mathrm{w,D,sep}}}{k_{\mathrm{w,D}}} \cdot \left(1 - k_{\mathrm{share,L,sep}}\right)
\end{aligned}
\tag{3.4}
$$

Due to relationship $F_{\mathrm{L}} \propto k_{\mathrm{w,L}} \cdot N_{\mathrm{s}} \cdot I_{\mathrm{s,L}}$, the suspension force ratio of a machine with combined winding and two separated windings is derived in (3.5) as $k_{\mathrm{comp,F}} = F_{\mathrm{L,sep}}/F_{\mathrm{L}}$. If $k_{\mathrm{comp,F}} > 1$, the suspension force capability of the machine with separated windings is bigger than of the machine with a combined winding.

$$
\begin{aligned}
k_{\mathrm{comp,F}} &= \frac{k_{\mathrm{w,L,sep}}}{k_{\mathrm{w,L}}} \cdot \frac{N_{\mathrm{s,L,sep}}}{N_{\mathrm{s}}} \cdot \frac{I_{\mathrm{s,L,sep}}}{I_{\mathrm{s,L}}} \\
&= \frac{a \cdot I_{\mathrm{th}}}{I_{\mathrm{s,L}}} \cdot \frac{k_{\mathrm{w,L,sep}}}{k_{\mathrm{w,L}}} \cdot \frac{N_{\mathrm{s,L,sep}}}{N_{\mathrm{s}}} \cdot \frac{N_{\mathrm{s}}}{N_{\mathrm{s,L,sep}}} \cdot k_{\mathrm{share,L,sep}} \\
&= \frac{\sqrt{\left(I_{\mathrm{s,D}}/I_{\mathrm{s,L}}\right)^2 + 1}}{1} \cdot \frac{k_{\mathrm{w,L,sep}}}{k_{\mathrm{w,L}}} \cdot k_{\mathrm{share,L,sep}}
\end{aligned}
\tag{3.5}
$$

The second line of the equations (3.4) and (3.5) show that the ratios $k_{\mathrm{comp,M}}$, $k_{\mathrm{comp,F}}$ depend on the ratio between the thermally effective current I_{th} and the drive current $I_{\mathrm{s,D}}$ in the machine with combined windings, respectively the suspension current $I_{\mathrm{s,L}}$. By substituting the thermally effective currents $I_{\mathrm{th,D}}$, $I_{\mathrm{th,L}}$ by the electromagnetically

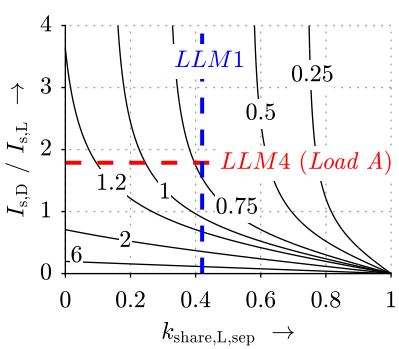

(a) Torque capability $k_{comp,M}$ from (3.4)

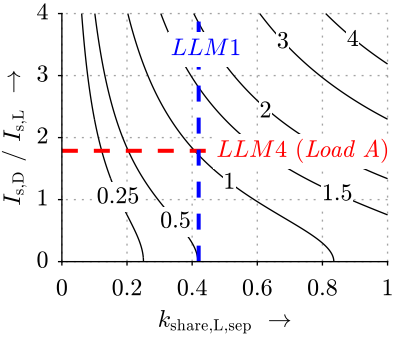

(b) Suspension force capability $k_{comp,F}$ from (3.5)

Fig. 3.6.: Calculated comparison between separated and combined winding approach with the properties of the *LLM1* (Table 3.2: $k_{share,L,sep} = 0.42$) [24] and of the *LLM4* at *Load A*(Section 4.3.3, Table 3.1: $I_{s,D}/I_{s,L} = 1.82$) in terms of torque and suspension force capability

effective currents $I_{s,D}$, $I_{s,L}$ according to Table 3.1 and the third line in (3.4) and (3.5), $k_{comp,M}$, $k_{comp,F}$ can be expressed with regards to the ratio $I_{s,D}/I_{s,L}$. Also $k_{comp,M}$, $k_{comp,F}$ depend on the slot share $k_{share,L,sep}$ of the suspension winding in the stator slots and on the winding factors, which are given by the example of the *LLM1* (Table 3.2) [24] with two separated windings and of the *LLM4* with a combined winding (Table 3.1). Fig. 3.6 shows how $k_{comp,M}$, $k_{comp,F}$ depend on the ratio $I_{s,D}/I_{s,L}$ and the suspension winding slot share $k_{share,L,sep}$. The approach with separated windings has only a higher torque capability ($k_{comp,M} > 1$), if the slot share of the suspension winding is very small, and if the drive current is smaller than the suspension current ($I_{s,D}/I_{s,L} < 1$). Fig. 3.6b shows that the separated windings approach has only a higher force capability ($k_{comp,F} > 1$), if the slot share of the suspension winding is $k_{share,L,sep} \gtrsim 0.4$, and if the drive current is big with regards to the suspension current ($I_{s,D}/I_{s,L} \gtrsim 1$). Altogether, the suspension force capability with two separated windings is similar to the combined winding topology, if the slot share $k_{share,L,sep}$ is sufficiently high. For high values of $k_{share,L,sep}$, only little space remains for the drive winding in the slots. For identical suspension force capability ($k_{comp,F} = 1$), the torque capability of the combined winding is higher than for the separated windings ($k_{comp,M} < 1$). The torque capability is commonly the more important parameter, determining the electromagnetic utilization. Thus, the combined winding approach is favored.

Equivalent circuit parameters

The winding properties for the combined and the separated windings approach are given in Table 3.1 and 3.2. The main inductances L_{h}, $L_{\mathrm{h,sep}}$ for equal machine geometries depend on the product $k_{\mathrm{w}} \cdot N_{\mathrm{s}}$ of the winding factors and the number of turns per phase. In comparison, both winding types are equal with respect to the drive winding, since they are operated at the same inverter voltage limit. Therefore, the machine main inductances $L_{\mathrm{D,h}}$ and $L_{\mathrm{D,h,sep}}$ are similar (Table 3.3).

In machines with two separated windings, the length of the winding overhang is given by the pitching W/τ_{p} and the pole pitch τ_{p} of each winding. In case of a 2-/4-pole machine this results in large winding overhangs for the 2-pole winding. In combined winding machines, the higher number of pole pairs p or p_{L} determines the length of the winding overhang, yielding a shorter winding and a lower winding overhang inductance $L_{\sigma,\mathrm{b}}$ for the same value of N_{s}. Further, the winding resistance R_{s} per phase is decreased by lower winding overhangs. For machines with two separated windings, the drive winding is usually placed at the bottom of the slots, thus, suffering from an increased slot stray inductance $L_{\sigma,\mathrm{Q}}$.

Table 3.3.: Comparison between separated and combined windings regarding the equivalent circuit parameters for the same magnetic iron circuit (analytically calculated according to Section 4.2.2 for $\mu_{\mathrm{r,Fe}} = 1000$), D: drive winding, L: suspension winding

	LLM4: combined winding (2-layer)		*LLM1*: $k_{\mathrm{share,L,sep}} = 0.42$ separated windings (1-layer)	
	D	L	D	L
N_{s}	18	18	16	22
q	2	2	2	1
a	2	2	1	1
$R_{\mathrm{s,75°C}}$ / mΩ	44	44	66 (+65%)	73 (+70%)
L_{h} / μH	61	28	64	37
$L_{\sigma,\mathrm{o}}$ / μH	4	2	4	1
$L_{\sigma,\mathrm{Q}}$ / μH	8	16	21	29
$L_{\sigma,\mathrm{b}}$ / μH	6	8	8	8
L_{d} / μH	79	54	97 (+23%)	74 (+37%)

Manufacturing Effort

In contrast to the insertion of two different windings, a combined winding can be wound in one part, which facilitates the production process. However, this benefit is canceled by the more expensive controller equipment, since six semiconductor half-bridges in a single inverter are required according to Fig. 3.3b.

3.3.2. Conditions for a Combined Winding

Regardless their attractiveness, one should consider that combined windings restrict the design freedom of the stator slot count Q and the pole count $2p$. A combined winding in a bearingless motor must comply with three main conditions which are summarized in Table 3.4, Table 3.5 and Table 3.6. Here, z_q (n_q) is the numerator (denominator) of the number of slots per rotor pole and phase q, m is the phase count, t is the number of base winding schemes. q and t are defined with regards to the drive winding. The conditions are explained in the next subsections in detail. Some of these conditions are also mentioned in [60] for the so-called "dual-purpose no-voltage windings" (see Fig. 3.3c).
The identified windings that are confined to $Q \leq 36$, $p_\mathrm{L} \leq 10$, $p_\mathrm{L} = p + 1$ and that comply with the conditions from Table 3.4, Table 3.5 and Table 3.6, are summarized in Table 3.7.

Winding Symmetry Requirement

Regardless the bearingless motor function, the winding must be symmetric in order to be

Table 3.4.: Phase shift requirement between current systems A and B, given for $p_\mathrm{L} = p \pm 1$

	drive current	suspension current
p even, p_L odd	0	π
p odd, p_L even	π	0

Table 3.5.: Winding symmetry requirement

$\frac{n_\mathrm{q}}{m} \notin \mathbb{N}$	$\frac{p}{m} \notin \mathbb{N}$	$\frac{p_\mathrm{L}}{m} \notin \mathbb{N}$

fed by a symmetric current system for constant power conversion. Combined windings, however, exhibit asymmetrical winding systems (A and B) in order to allow for adjacent space harmonic orders ($p_\mathrm{L} = p \pm 1$). If these asymmetrical winding systems are fed with two current systems with elliptical current space vector orbits, two inherent 3-phase systems (D and L) occur. Therefore, in this section the requirements for standard windings can partially be applied with small adaptions. The following conditions are deduced from [105, 60]. Here, only odd phase counts ($m = 3,5,7,...$) and only 2-layer windings are considered.

- **Condition regarding slot count Q and phase count m**
  The number of slots per phase must be an integer (3.6). In addition to that, combined windings require an even number of coil groups, so that (3.6) can be rewritten as (3.7)

$$\frac{Q}{m} = 2p \cdot q = 2p \cdot \frac{z_\mathrm{q}}{n_\mathrm{q}} \in \mathbb{N} \rightarrow \frac{2p}{n_\mathrm{q}} \in \mathbb{N} \tag{3.6}$$

$$\frac{Q}{m} \in \mathbb{N}_\mathrm{even} \rightarrow \frac{p}{n_\mathrm{q}} \in \mathbb{N} \tag{3.7}$$

- **Condition regarding slot angle α_Q and phase angle α_ph**
  The angle $\alpha_\mathrm{ph} = 2\pi/m$ between two electrically adjacent phases must be an integer multiple of the slot angle $\alpha_{\mathrm{Q},\nu} = \nu \cdot t \cdot 2\pi/Q$ (3.8), where t is the number of base windings. In the following the fundamental field wave ($\alpha_{\mathrm{Q},1} = \alpha_\mathrm{Q}$) is considered. According to [105] this means that n_q and m must be co-prime.

$$\frac{\alpha_\mathrm{ph}}{\alpha_\mathrm{Q}} = \frac{\frac{2\pi}{m}}{\frac{2\pi \cdot t}{Q}} = \frac{Q}{m \cdot t} \in \mathbb{N} \rightarrow \frac{n_\mathrm{q}}{m} \notin \mathbb{N} \tag{3.8}$$

- **Condition regarding drive winding angle $\alpha_\mathrm{Q,D}$ and suspension winding angle $\alpha_\mathrm{Q,L}$**
  Since both spatial harmonics p and p_L must be excited by the same m-phase current system, the two angles $\alpha_\mathrm{Q,D} = 2\pi/Q \cdot p \cdot t$ and $\alpha_\mathrm{Q,L} = 2\pi/Q \cdot p_\mathrm{L} \cdot t$ must be an integer multiple of an integer phase angle (α_ph) multiple (3.9). This leads to the following condition for the ratio of number of pole pairs and phase count, which is

derived in Appendix A.10.

$$\frac{u \cdot \alpha_{\mathrm{ph}}}{\alpha_{\mathrm{Q,D}}} \in \mathbb{N} \wedge \frac{v \cdot \alpha_{\mathrm{ph}}}{\alpha_{\mathrm{Q,L}}} \in \mathbb{N};\ u,v \in \mathbb{N} \rightarrow \frac{p}{m} \notin \mathbb{N}; \frac{p_{\mathrm{L}}}{m} \notin \mathbb{N} \tag{3.9}$$

Note that by this condition the condition regarding the slot and phase count (3.6) is automatically met. Unfortunately (3.9) strongly constrains the available winding topologies, e.g. the very promising combination $p/p_{\mathrm{L}} = 2/3$ is not feasible for $m = 3$. Thus, current research is done on combined windings, violating $\frac{p_{\mathrm{L}}}{m} \notin \mathbb{N}$ [31]. It shows, that the broken symmetry leads to elliptical instead of circular radial rotor force vector orbits, which still may ensure stable operation. Alternatively, a 6- or 12-phase combined winding can be used for the realization of $p/p_{\mathrm{L}} = 2/3$ [106, 107].

Mutual Magnetic De-Coupling Requirement of Drive and Suspension Winding

For the principle of the bearingless motor the fields of the drive and the suspension winding must not mutually induce voltages, i.e. their fundamentals must be magnetically de-coupled. This is realized by either differential or common-mode feeding of the two asymmetrical winding systems A and B according to Table 3.4. By this measure the drive current and the suspension current system excite either only odd or only even harmonics [61]. The resulting conditions are derived in Appendix A.11 and are summarized in Table 3.6.

For combined windings the assignment of the stator slots Q to the phases m differs from the common winding design procedure. Fig. 3.7 shows how the phases $\mathrm{U_A}$, $\mathrm{V_A}$, $\mathrm{W_A}$, $\mathrm{U_B}$, $\mathrm{V_B}$ and $\mathrm{W_B}$ are allocated to the stator slots for $p/p_{\mathrm{L}} = 1/2$, whereas Fig. 3.8 shows it for $p/p_{\mathrm{L}} = 2/1$. In both cases the procedure comprises the following steps:

- Draw the star of slots of the imaginary drive winding (D) for the Q slot phasors

Table 3.6.: Mutual magnetic de-coupling requirement of drive and suspension winding

	integer slot winding	fractional slot winding
p even, p_{L} odd	–	$t \in \mathbb{N}_{\mathrm{even}}$, if n_{q} even
p odd, p_{L} even	$p > 1$, if non-pitched	$n_{\mathrm{q}} \in \mathbb{N}_{\mathrm{odd}}$

Table 3.7.: Overview of feasible combined winding topologies
($Q \leq 36$, $p_\mathrm{L} \leq 10$, $p_\mathrm{L} = p+1$, $m = 3$)

p	1	2	3	4	5	6	7	8	9
p_L	2	3	4	5	6	7	8	9	10
$Q = 6$	$q = 1^{*)}$	–	–	–	–	–	–	–	–
$Q = 12$	$q = 2^{*)}$	–	–	$q = \frac{1}{2}$	–	–	–	–	–
$Q = 18$	$q = 3^{*)}$	–	–	$q = \frac{3}{4}$	–	–	$q = \frac{3}{7}$	–	–
$Q = 24$	$q = 4^{*)}$	–	–	$q = 1$	–	–	$q = \frac{4}{7}$	–	–
$Q = 30$	$q = 5^{*)}$	–	–	$q = \frac{5}{4}$	–	–	$q = \frac{5}{7}$	–	–
$Q = 36$	$q = 6^{*)}$	–	–	$q = \frac{3}{2}$	–	–	$q = \frac{6}{7}$	–	–

$^{*)}$ Only feasible, if pitched

according to [105] with the slot angle $\alpha_\mathrm{Q,D} = t \cdot 2\pi/Q$.

- Assign the slot phasors to the $m = 3$ phases $\mathrm{U_D}$, $\mathrm{V_D}$, $\mathrm{W_D}$ with a deviation of $\alpha_\mathrm{ph} = 2\pi/m$ by maximizing the geometrical sum of the phasors within one phase, i.e. maximizing the distribution factor $k_\mathrm{w,d,D}$. Note that all slots assigned to a drive winding phase, e.g. to $\mathrm{U_D}$, are automatically part of the suspension winding phase, e.g. of $\mathrm{U_L}$. That means, selecting the slots for a maximum drive winding distribution factor $k_\mathrm{w,d,D}$ does not lead to the maximum suspension winding distribution factor $k_\mathrm{w,d,L}$.

- Assign the system A to the first half of the slots of the drive winding phases (e.g. for $\mathrm{U_D}$: 1, 2 $\rightarrow$ $+\mathrm{U_A}$) and the system B to the second half of the slots of the drive winding phases (e.g. for $\mathrm{U_D}$: 7, 8 $\rightarrow$ $+\mathrm{U_B}$), independent of the winding sense $(+/-)$.

- Draw the star of slots of the imaginary suspension winding (L) for the Q slot phasors according to [105] with the slot angle $\alpha_\mathrm{Q,L} = t_\mathrm{L} \cdot 2\pi/Q$.

- Assign the same slots the suspension winding phases as assigned to the drive winding phases (e.g. the slots assigned to $\mathrm{U_D}$ are the same as assigned to $\mathrm{U_L}$).

- Assign the system A to the first half of the slots of the suspension winding phases (e.g for $\mathrm{U_L}$: 1, 2 $\rightarrow$ $+\mathrm{U_A}$) and the system B to the second half of the slots of the suspension winding phases (e.g. for $\mathrm{U_L}$: 7, 8 $\rightarrow$ $+\mathrm{U_B}$), independent of the winding sense $(+/-)$.

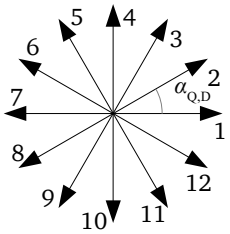

slot phasors asigned to A/B-phases

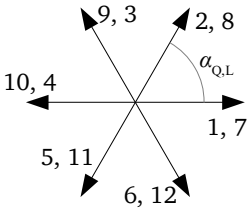

slot phasors asigned to A/B-phases

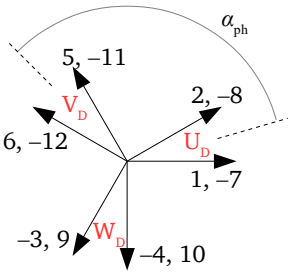

slot phasors assigned to D-phases

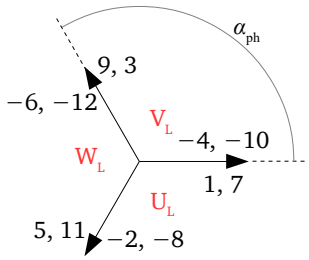

slot phasors assigned to L-phases

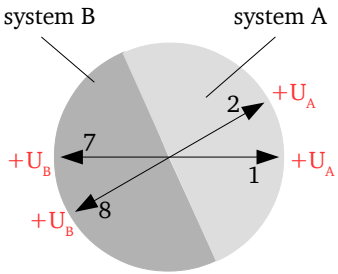

phase U_D assigned
to winding system A and B

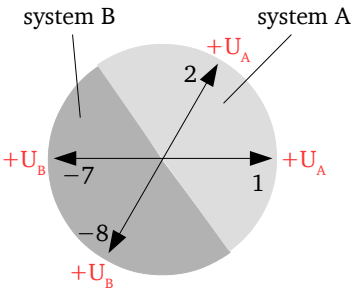

phase U_L assigned
to winding system A and B

(a) Drive Winding

(b) Suspension Winding

Fig. 3.7.: Assignment of the stator slots to the phases for $Q = 12$, $p = 1$, $p_L = 2$ (winding identical to *LLM4*)

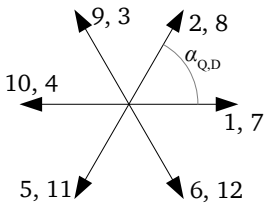

slot phasors asigned to A/B-phases

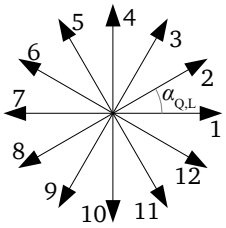

slot phasors asigned to A/B-phases

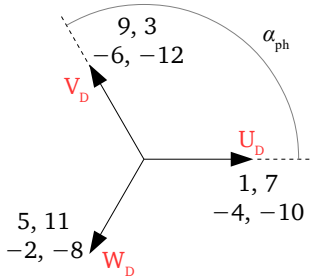

slot phasors assigned to D-phases

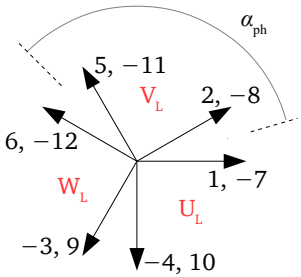

slot phasors assigned to L-phases

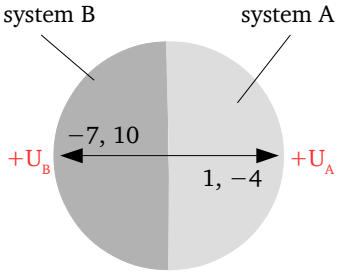

phase U_D assigned
to winding system A and B

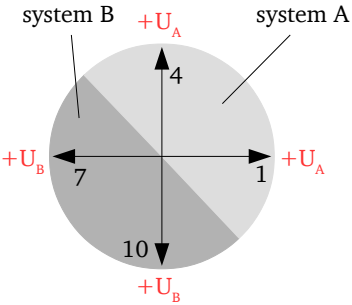

phase U_L assigned
to winding system A and B

(a) Drive Winding

(b) Suspension Winding

Fig. 3.8.: Assignment of the stator slots to the phases for $Q = 12$, $p = 2$, $p_L = 1$

Since the system B can be fed either with a current, which is in phase with the current in system A, or with a current, which is in phase opposition to the current in system A, the slot phasors assigned to the system B can be flipped. For $p \in \mathbb{N}_{\text{odd}}$ it is possible to generate a $2p$-pole field wave by differential-mode feeding of system A and B and to generate a $2p_{\text{L}}$-pole field wave by common-mode feeding (Fig. 3.7). For $p \in \mathbb{N}_{\text{even}}$ it is possible to generate a $2p$-pole field wave by common-mode feeding of system A and B and to generate a $2p_{\text{L}}$-pole field wave by differential-mode feeding (Fig. 3.8).
In Appendix A.12 the slot plans and MMF distributions associated with Fig. 3.7 and 3.8 are shown. In order to realize this mutual de-coupling, an even number of slots per drive and suspension phase must exist, i.e. $Q/(2 \cdot m) \in \mathbb{N}$. This is always true for integer slot windings and fractional slot windings with odd denominator $n_{\text{q}} \in \mathbb{N}_{\text{odd}}$ [105]. For fractional slot windings with $n_{\text{q}} \in \mathbb{N}_{\text{even}}$ the periodicity t of the winding scheme must be an even number (3.10). Other than that, for $p \in \mathbb{N}_{\text{odd}}$ (3.11) holds, what is explained in Appendix A.11.

$$t \in \mathbb{N}_{\text{even}};\ \text{given}\ n_{\text{q}} \in \mathbb{N}_{\text{even}} \tag{3.10}$$

$$n_{\text{q}} \in \mathbb{N}_{\text{odd}};\ \text{given}\ p \in \mathbb{N}_{\text{odd}} \tag{3.11}$$

Pitching Requirement for 2-Pole Machines with Integer-Slot Windings
Integer-slot windings with $p = 1$, i.e. $t = 1$, and $p_{\text{L}} = 2$ meet all symmetry and mutual magnetic de-coupling requirements. However, the winding factor $k_{\text{w,L}}$ of the suspension winding fundamental is zero, if the winding is non-pitched. Non-pitched windings can only be realized for $p > 1$ and $t > 1$. Otherwise the air gap MMF of the winding systems A and B cancel, as shown in Fig. 3.9.

3.3.3. Evaluation Criteria for a Combined Winding

This section analyzes the feasible windings from Table 3.7, i.e. with the constraints $m = 3$, $Q \leq 36$ and $p/p_{\text{L}} = 1/2; 4/5; 7/8$, by discussing the spectrum of winding factors, the harmonic stray coefficient, parasitic harmonic torque and bearing force and the influence of a zero-sequence current feeding (Chapter 6, 7) in order to evaluate these windings.

Winding Factors
The winding factors are calculated according to [108] and are given in Table 3.8 and

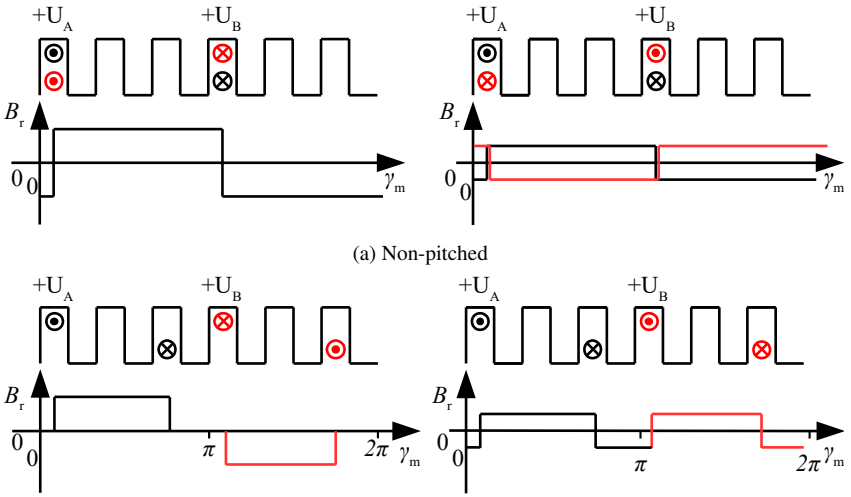

(a) Non-pitched

(b) Pitches with $W/\tau_p = 2/3$

Fig. 3.9.: Comparison between non-pitched and pitched integer-slot combined windings: Slot plan and radial air gap flux density component B_r for phase U for a winding with $Q = 6$, $p = 1$, $p_L = 2$

Table 3.8. The required suspension and drive stator MMF amplitudes always depend on design issues such as rotor weight and rated power. Thus, no general statement can be given whether or not a high drive winding factor is more important than a high suspension winding factor. Further, high-speed machines are usually operated at the inverter voltage limit where the induced voltage represents the major part of the phase voltage so that the (high) drive winding factor must be considered in combination with the number of turns per phase.

Harmonic Stray Coefficient

The harmonic stray coefficient σ_o quantifies the harmonic field content in the air gap field with respect to the fundamental (slot openings are neglected, $\mu_{Fe} \to \infty$) and can be calculated according to [94]. For distributed integer slot windings it is usually $\sigma_o < 0.05$. However, for bearingless machines with combined windings the calculation is adapted as in (3.12), (3.13), where $\nu' = \nu \cdot p$ is the absolute space harmonic order. For selected windings, it is given in Table 3.8 and Table 3.9 for $\nu_{max} \cdot p = 50000$, so that the relative

Table 3.8.: Different Combined Windings: Drive winding factor spectrum (absolute values) and harmonic stray coefficients $\sigma_{o,D}$ ($Q \leq 36$, $p_L \leq 10$, $p_L = p+1$, $m = 3$, bold: fundamental drive winding factors, *LLM4*: built prototype machine, *LLM3*: built as in [23], here only simulated)

	LLM3	*LLM4*				
p/p_L	1/2	1/2	1/2	4/5	4/5	7/8
Q	12	12	24	18	30	30
q	2	2	4	3/4	5/4	5/7
y_c	3	4	9	2	3	2
$\lvert\nu\rvert \cdot p = 1$	**0.683**	**0.837**	**0.885**	-	-	0.021
$\lvert\nu\rvert \cdot p = 2$	-	-	-	0.140	0.088	-
$\lvert\nu\rvert \cdot p = 3$	0.500	0	0.250	-	-	0.145
$\lvert\nu\rvert \cdot p = 4$	-	-	-	**0.945**	**0.910**	-
$\lvert\nu\rvert \cdot p = 5$	0.183	0.224	0.079	-	-	0.173
$\lvert\nu\rvert \cdot p = 6$	-	-	-	0.577	0.235	-
$\lvert\nu\rvert \cdot p = 7$	0.183	0.224	0.146	-	-	**0.951**
$\lvert\nu\rvert \cdot p = 8$	-	-	-	0.061	0.060	-
$\lvert\nu\rvert \cdot p = 9$	0.500	0	0.250	-	-	0.616
$\lvert\nu\rvert \cdot p = 10$	-	-	-	0.061	0	-
$\lvert\nu\rvert \cdot p = 11$	0.683	0.837	0.048	-	-	0.111
$\lvert\nu\rvert \cdot p = 12$	-	-	-	0.577	0.380	-
$\lvert\nu\rvert \cdot p = 13$	0.683	0.837	0.048	-	-	0.045
$\sigma_{o,D}$ [1)]	0.028	0.028	0.007	0.017	0.006	0.006

[1)] Harmonic orders up $\nu' = 50000$ included in calculation

deviation for σ_o between the $\nu_{max} \cdot p$ and $\nu_{max} \cdot p + 1$ gets smaller than 0.1%.

$$\sigma_{o,D} = \frac{1}{k_{w,D}^2} \cdot \sum_{|\nu'| \neq \{p;3;9;15;\ldots\}}^{\infty} \left(\frac{k_{w,\nu'}}{\nu'}\right)^2 \approx \frac{1}{k_{w,D}^2} \cdot \sum_{\nu' \neq \{p;3;9;15;\ldots\}}^{50000} \left(\frac{k_{w,\nu'}}{\nu'}\right)^2 \tag{3.12}$$

$$\sigma_{o,L} = \frac{1}{k_{w,L}^2} \cdot \sum_{|\nu'| \neq \{p_L;6;12;18;\ldots\}}^{\infty} \left(\frac{k_{w,\nu'}}{\nu'}\right)^2 \approx \frac{1}{k_{w,L}^2} \cdot \sum_{\nu' \neq \{p_L;6;12;18;\ldots\}}^{50000} \left(\frac{k_{w,\nu'}}{\nu'}\right)^2 \tag{3.13}$$

Table 3.9.: Different Combined Windings: Suspension winding factor spectrum (absolute values) and harmonic stray coefficients $\sigma_{o,L}$ ($Q \leq 36$, $p_L \leq 10$, $p_L = p+1$, $m = 3$, bold: fundamental suspension winding factors, *LLM4*: built prototype machine, *LLM3*: built as in [23], here only simulated)

	LLM3	*LLM4*				
p/p_L	1/2	1/2	1/2	4/5	4/5	7/8
Q	12	12	24	18	30	30
q	2	2	4	3/4	5/4	5/7
y_c	3	4	9	2	3	2
$\lvert\nu\rvert \cdot p_L = 1$	-	-	-	0.061	0.069	-
$\lvert\nu\rvert \cdot p_L = 2$	**0.866**	**0.750**	**0.592**	-	-	0.045
$\lvert\nu\rvert \cdot p_L = 3$	-	-	-	0.577	0.524	-
$\lvert\nu\rvert \cdot p_L = 4$	0	0.433	0.433	-	-	0.111
$\lvert\nu\rvert \cdot p_L = 5$	-	-	-	**0.945**	**0.721**	-
$\lvert\nu\rvert \cdot p_L = 6$	0	0	0	-	-	0.616
$\lvert\nu\rvert \cdot p_L = 7$	-	-	-	0.140	0.195	-
$\lvert\nu\rvert \cdot p_L = 8$	0	0.433	0	-	-	**0.951**
$\lvert\nu\rvert \cdot p_L = 9$	-	-	-	0	0.076	-
$\lvert\nu\rvert \cdot p_L = 10$	0.866	0.750	0.159	-	-	0.173
$\lvert\nu\rvert \cdot p_L = 11$	-	-	-	0.140	0.098	-
$\lvert\nu\rvert \cdot p_L = 12$	0	0	0	-	-	0.145
$\lvert\nu\rvert \cdot p_L = 13$	-	-	-	0.945	0.421	-
$\sigma_{o,L}$ [1)]	0.024	0.056	0.044	0.017	0.019	0.006

[1)] Harmonic orders up $\nu' = 50000$ included in calculation

Torque and Force Ripple by Interaction of Harmonic Fields

In bearingless PM synchronous machines the occurrence of torque and force ripple depends strongly on the rotor field wave spectrum. So the selection of the winding must be done in accordance with the available permanent magnet rotor field distribution. In case of a perfectly sinusoidal rotor PM magnetization, no force or torque ripple can occur by interaction of stator and rotor field. In case of non-sinusoidal rotor PM magnetization, possible torque ripple frequencies $f_{P,M}$ are given by (7.8), (7.9), whereas the force ripple frequencies $f_{P,F}$ are given by (2.84), (7.13). This results in the ripple frequencies $f_{P,F}$ in Table 3.10

Table 3.10.: Different combined windings: Possible frequencies of torque, force and cogging torque ripple ($f_{\mathrm{P,M}}; f_{\mathrm{P,F}} < 10 \cdot f_{\mathrm{syn}}$, $Q \leq 36$, $p_{\mathrm{L}} \leq 10$, $p_{\mathrm{L}} = p+1$, $m = 3$, *LLM4*: built prototype machine, *LLM3*: built as in [23], here only simulated)

	LLM3	*LLM4*				
p/p_{L}	1/2	1/2	1/2	4/5	4/5	7/8
Q	12	12	24	18	30	30
q	2	2	4	3/4	5/4	5/7
y_{c}	3	4	9	2	3	2
$f_{\mathrm{P,M}}$	$6 \cdot f_{\mathrm{syn}}$	$6 \cdot f_{\mathrm{syn}}$	$6 \cdot f_{\mathrm{syn}}$	$6 \cdot f_{\mathrm{syn}}$	$12 \cdot f_{\mathrm{syn}}$	$6 \cdot f_{\mathrm{syn}}$
$f_{\mathrm{P,F}}$	$2 \cdot f_{\mathrm{syn}}$ $8 \cdot f_{\mathrm{syn}}$	$2 \cdot f_{\mathrm{syn}}$ $4 \cdot f_{\mathrm{syn}}$ $6 \cdot f_{\mathrm{syn}}$ $8 \cdot f_{\mathrm{syn}}$	$2 \cdot f_{\mathrm{syn}}$ $4 \cdot f_{\mathrm{syn}}$ $6 \cdot f_{\mathrm{syn}}$	$2 \cdot f_{\mathrm{syn}}$ $4 \cdot f_{\mathrm{syn}}$ $8 \cdot f_{\mathrm{syn}}$	$2 \cdot f_{\mathrm{syn}}$ $4 \cdot f_{\mathrm{syn}}$ $6 \cdot f_{\mathrm{syn}}$	$2 \cdot f_{\mathrm{syn}}$ $4 \cdot f_{\mathrm{syn}}$ $6 \cdot f_{\mathrm{syn}}$
$f_{\mathrm{cog,min}}$	$12 \cdot f_{\mathrm{syn}}$	$12 \cdot f_{\mathrm{syn}}$	$24 \cdot f_{\mathrm{syn}}$	$18 \cdot f_{\mathrm{syn}}$	$30 \cdot f_{\mathrm{syn}}$	$30 \cdot f_{\mathrm{syn}}$

up to $< 10 \cdot f_{\mathrm{syn}}$. Of importance is that the PM field wave spectrum does not exhibit a considerable third harmonic, since the interaction of $\mu \cdot p = 3 \cdot p$ with $\nu \cdot p_{\mathrm{L}} = 3 \cdot p - 1$ yields $f_{\mathrm{P,F}} = |f_{\mathrm{syn}} \cdot (1-\mu)| = 2 \cdot f_{\mathrm{syn}}$. Note that magnetic saturation also leads to a torque and force ripple, as the fundamental field waves are modulated by the saturation-dependent iron permeance wave 2.83. Saturation introduces a rotor field wave of space and time order $3p$ which leads to the aforementioned $2f_{\mathrm{syn}}$-frequent force ripple. This is further discussed in Section 2.6, 7.2.2 and 7.2.3.

Cogging Torque Ripple

The lowest frequency $f_{\mathrm{cog,min}}$ of cogging torque ripple can be calculated according to [94]. It is an integer multiple of the least common multiple of slot count Q and number of pole pairs p, multiplied by the synchronous frequency f_{syn}, and is increased by raising of the number of base winding schemes t. The values of the possible torque pulsation frequencies $f_{\mathrm{P,M}}$ and force pulsation frequencies $f_{\mathrm{P,F}}$ for selected windings are given in Table 3.10. If a small cogging torque is a relevant criterion for bearingless drives, windings with a higher slot count Q/p should be preferred.

Influence of Zero-Sequence Current Feeding

If the two windings A and B of a bearingless motor are fed by a star point current i_{ax} as described in Chapter 6 in order to operate an axial AMB, a zero-sequence current $i_0 = i_{ax}/3$ flows in each phase U_A, V_A, W_A, U_B, B_B and W_B (Fig. 6.3). Thus, aside from the drive and the suspension current system also the zero-sequence current component $i_0(t)$ introduces field harmonics of order $\nu = 3,\ 9,\ 15,\ \ldots$ into the air gap magnetic flux density distribution. The resulting parasitic effects are discussed in Section 7.2. However, a zero-sequence current i_0 does not excite an air gap MMF distribution, if the winding factors $k_{w,\nu=3,9,15,\ldots}$ are zero (Table 3.8). Thus, for the *LLM4* the winding with $p/p_L = 1/2$, $Q = 12$, $q = 2$ and $y_c = 4$ was selected with $k_{w,\nu=3,9,15,\ldots} = 0$.

3.3.4. Summary of Promising Combined Winding Topologies

By considering Table 3.7 and 3.8 it can be concluded that the choice of stator slot count Q and pole count $2p$ is strongly restricted for combined windings. If a small pole count is aimed at, e.g. for the use as high-speed applications, only the combination $p/p_L = 1/2$, but not $p/p_L = 2/3$ as in [9] is possible. The combination $p/p_L = 1/2$ requires strongly pitched ($W/\tau_p < 0.7$) integer-slot windings, which leads to small fundamental winding factors, but reduces higher spatial harmonic orders.

The fractional slot windings, resulting from $p/p_L = 4/5$, allow high fundamental winding factors. Unfortunately, these windings exhibit sub-harmonics and many higher order space harmonics, leading to a bigger harmonic stray coefficient σ_o. Crucial for these "high" pole counts is that the PM magnetization may exhibit many space harmonics, such as a third harmonic $\mu = 3$, since no sinusoidal magnetization is technically feasible. This can lead to a considerable torque and force ripple for these machines.

For the *LLM4* the winding with $p/p_L = 1/2$, $Q = 12$, $q = 2$ and $y_c = 4$ was selected, due to the low influence of the zero-sequence current-excited air gap field.

3.4. Design of the Rotor Bandage

A fail-safe rotor construction constitutes the primary design requirement for a high-speed machine. Therefore, the consideration of rotor structural mechanics leads to design limitations which are mandatory for the electromagnetic calculation of the next sections. In order to include these limitations into the process, an analytical calculation of the required

bandage height is performed according to [9, 109, 110].
A high-speed PM rotor is usually composed of a massive magnetic steel shaft, surrounded by a PM ring or ring segments, protected by a shrink-fitted or axially pressed carbon-fiber sleeve in order to withstand centrifugal forces. Only in [111] a rotor is presented, where a 2-pole block PM is inserted into a hollow-shaft and a amorphous rotor core. This way an additional bandage is omitted. Here, sleeve-protected PMs are considered. The mechanically relevant material properties of the shaft, the PM and the sleeve are summarized in the Appendix (Table A.5, A.6, A.7). The selection of the PM and shaft material from the electromagnetic point of view is addressed in the Sections 3.7.1 and 3.7.3.
The sleeve consists of an unidirectional multi-layer fiber composite with high tensile strength R_m in fiber, hence, in tangential direction, which is embedded in a matrix of epoxy resin. Therefore, its mechanical properties are orthotropic. The orthotropic calculation is applied for the bandage design, however, it leads to an extensive calculation which is given in [109]. Here, only the isotropic calculation is explained in short which leads to similar results. As in [9] the plain strain condition for solid cylinders is used which does not account for a change in axial length. That means for the strain ε and the stress in axial direction σ_z holds: $\varepsilon_\mathrm{z} = \varepsilon_\mathrm{xz} = \varepsilon_\mathrm{yz} = 0$, $\sigma_\mathrm{z} = \mathrm{const.}$. Generally, it can be distinguished between two failure cases:

- The elasticity limit (yield strength R_m) is reached in any rotor part which leads to a plastic (irreversible) deformation. Usually this happens at high temperatures above the plasticity limit of the used resin, so here a limit of $\vartheta = 150°\mathrm{C}$ ($\Delta\vartheta = 130$ K) is considered.

- Two neighboring rotor parts lose contact. Usually this happens at high speed (high circumferential force on magnets and bandage) and low rotor core temperatures (shrink fit of the rotor shaft), so here $\vartheta = 20°\mathrm{C}$ ($\Delta\vartheta = 0$ K) is considered.

If one of both limits is reached, either the bandage height or the undersize between bandage and PM must be increased. The yield strength is determined in a 1-dimensional tensile test. Therefore, the occurring stress components in radial and tangential direction are expressed as equivalent *Von Mises* stress σ_vM (3.14) [110], which is commonly used for ductile and brittle materials.

$$\sigma_\mathrm{vM} = \sqrt{\sigma_\mathrm{r}^2 + \sigma_\gamma^2 + \sigma_\mathrm{z}^2 + \sigma_\mathrm{r}\sigma_\gamma + \sigma_\mathrm{r}\sigma_\mathrm{z} + \sigma_\gamma\sigma_\mathrm{z} + 3 \cdot \left(\tau_{\mathrm{r}\gamma}^2 + \tau_{\mathrm{rz}}^2 + \tau_{\gamma\mathrm{z}}^2\right)} \tag{3.14}$$

The internal stress and contact pressure to neighboring parts is calculated by combining three elements: *Hooke*'s law including the temperature-dependent stress (3.15), the force equilibrium if centrifugal forces are active (3.16) and the geometrical relationships (3.17), using the displacement method. Only radial displacements are considered. $\varepsilon_{\mathrm{def}}$ is the portion of elastic deformation, E the *Young*'s modulus, ν_{Po} the *Poisson*'s ratio, σ the uniaxial force per unit surface, $\alpha_{\mathrm{th,exp}}$ the thermal expansion coefficient, ρ the mass density and u the displacement of an infinitesimal small mass element.

$$\begin{pmatrix} \varepsilon_{\mathrm{def,r}} \\ \varepsilon_{\mathrm{def},\gamma} \end{pmatrix} = \begin{bmatrix} \frac{1}{\tilde{E}} & \frac{-\tilde{\nu}_{\mathrm{Po}}}{\tilde{E}} \\ \frac{-\tilde{\nu}_{\mathrm{Po}}}{\tilde{E}} & \frac{1}{\tilde{E}} \end{bmatrix} \cdot \begin{pmatrix} \sigma_{\mathrm{r}} \\ \sigma_{\gamma} \end{pmatrix} + \begin{pmatrix} \tilde{\alpha}_{\mathrm{th,exp}} \\ \tilde{\alpha}_{\mathrm{th,exp}} \end{pmatrix} \cdot \Delta\vartheta \tag{3.15}$$

$$\tilde{E} = \frac{E}{1-\nu_{\mathrm{Po}}^2};\ \tilde{\nu}_{\mathrm{Po}} = \frac{\nu_{\mathrm{Po}}}{1-\nu_{\mathrm{Po}}};\ \tilde{\alpha}_{\mathrm{th,exp}} = (1+\nu_{\mathrm{Po}}) \cdot \alpha_{\mathrm{th,exp}}$$

$$0 = r \cdot \frac{\mathrm{d}\sigma_{\mathrm{r}}}{\mathrm{d}r} - \sigma_{\gamma} + \sigma_{\mathrm{r}} + \rho \cdot r^2 \cdot \Omega^2 \tag{3.16}$$

$$\begin{pmatrix} \varepsilon_{\mathrm{def,r}} \\ \varepsilon_{\mathrm{def},\gamma} \end{pmatrix} = \begin{pmatrix} \frac{\mathrm{d}u}{\mathrm{d}r} \\ \frac{u}{r} \end{pmatrix} \tag{3.17}$$

Inserting (3.17) into (3.15), solving for $\vec{\sigma}$ and inserting into (3.16) yields the differential equation (3.18). Its solution for an isotropic ring with inner radius r_{i} and outer radius r_{o} is given by (3.19) [110].

$$r^2 \cdot \frac{\mathrm{d}^2 u}{\mathrm{d}r^2} + r \cdot \frac{\mathrm{d}u}{\mathrm{d}r} - u = -\left(1-\tilde{\nu}_{\mathrm{Po}}^2\right) \cdot \frac{\rho \cdot r^3 \cdot \Omega^2}{\tilde{E}} + (1+\tilde{\nu}_{\mathrm{Po}}) \cdot \tilde{\alpha}_{\mathrm{th,exp}} \cdot r^2 \frac{\mathrm{d}\Delta\vartheta}{\mathrm{d}r} \tag{3.18}$$

$$u = K_1 \cdot r + \frac{K_2}{r} - \frac{\left(1-\tilde{\nu}_{\mathrm{Po}}^2\right) \cdot \rho \cdot r^3 \cdot \Omega^2}{8 \cdot \tilde{E}} + \frac{(1+\tilde{\nu}_{\mathrm{Po}}) \cdot \tilde{\alpha}_{\mathrm{th,exp}}}{r} \cdot \int_{r_{\mathrm{i}}}^{r_{\mathrm{o}}} \Delta\vartheta \cdot r \cdot \mathrm{d}r \tag{3.19}$$

Since (3.18) is a linear, ordinary differential equation, the solution for a (hollow-) cylinder (inner boundary: i, outer boundary: o) can be subdivided into three parts: a centrifugal force-dependent part (u_{Ω}, σ_{Ω}), a temperature stress-dependent part ($u_{\Delta\vartheta}$, $\sigma_{\Delta\vartheta}$) and a part, resulting from the applied undersize of the shrink-fitting (u_{ext}, σ_{ext}). The coefficients K_1 and K_2 can be calculated by applying the boundary conditions for the static pressure at the ring's outer and inner surface (3.20): $p_{\mathrm{ext,o}} = -\sigma_{\mathrm{ext,r}}(r_{\mathrm{o}})$ and $p_{\mathrm{ext,i}} = -\sigma_{\mathrm{ext,r}}(r_{\mathrm{i}})$.

$$p_{\mathrm{ext,i}} = \frac{u_{\mathrm{us,i}}}{c_{\mathrm{i}} \cdot A_{\mathrm{i}}};\ p_{\mathrm{ext,o}} = \frac{u_{\mathrm{us,o}}}{c_{\mathrm{o}} \cdot A_{\mathrm{o}}} \tag{3.20}$$

Here, u_{us} is the undersize of the shrink-fitting at the transition from two concentric (hollow-) cylinders, and c_{i}, c_{o} is the compliance of the inner and outer material according

to [110]. Inserting (3.19) into (3.17) and (3.15) yields the stress distribution in radial and tangential direction.
Fig. 3.10 compares the analytically calculated (similar to (3.19), but orthotropic) and FEM-simulated (*ANSYS Workbench 18.1*) radial and tangential stress components in the prototype rotor, subdivided by its source. Fig. 3.10a reveals that radial stress component caused by centrifugal forces is bigger than zero at the contact surfaces of the concentric cylinders, which requires a shrink-fitted sleeve. The operation at higher temperatures, e.g. 100 °C, leads to a negative radial stress, since the thermal expansion of the steel shaft is bigger than of the surrounding shells. The tangential stress components (Fig. 3.10b) are maximum at the inner cylinder surfaces and are much bigger than σ_r. However, the increase of stress towards the center is lowest for a full cylinder such as the shaft, so that such machines should be equipped with a massive steel shaft [109]. Fig. 3.10c compares the *Von Mises* stress with the material limits and proves that the operation at 100 °C and $n = 60000\ \mathrm{min}^{-1}$ does not violate them. For steel the material limit is given by the tensile yield strength $R_{\mathrm{p0,2}}$, for the PM it is given by the compressive ultimate strength $R_{\mathrm{m,comp}}$ and for the bandage by the tensile ultimate strength R_m in fiber direction. The values are given by Table A.5, A.6 and A.7.
In order to design a high-speed PM machine it is very useful to know the required bandage thickness h_sl for a varying rotor diameter $2 \cdot r_\mathrm{sh}$, which depends on the maximum speed n_N (Fig. 3.11). The underlying calculations are as follows:

- The undersize $u_\mathrm{us,sl,PM}$ between sleeve and PM is given by (3.21). It depends linearly on the maximum rotor surface speed $v_\mathrm{R} = 2\pi \cdot n_\mathrm{N} \cdot r_\mathrm{sl}$ which complies with [24, 9]. The undersize $u_\mathrm{us,PM,sh}$ between PM and shaft is zero, but glue is used in addition as a safety reserve. The *LLM4* rotor diameter is $2 \cdot r_\mathrm{sl} = 33$ mm.

$$u_\mathrm{us,sl,PM} = \frac{v_\mathrm{R}\left[\mathrm{m \cdot s^{-1}}\right]}{10^6 \cdot \mathrm{s^{-1}}}; \quad \mathit{LLM4}: u_\mathrm{us,sl,PM} = \frac{33 \cdot 10^{-3} \cdot \pi \cdot 1000 \cdot \mathrm{m}}{10^6} = 104\ \mu\mathrm{m} \quad (3.21)$$

- In terms of contact loss between two rotor parts, the worst case of $\Delta\vartheta = 0$ is considered. Here, a safety margin of 2 MPa is regarded as a minimum contact pressure.

- If either the yield strength at $\vartheta = 150$ °C is reached in any rotor part or two neighboring rotor parts lose radial contact at $\vartheta = 20$ °C (contract pressure < 2 MPa), the bandage height h_sl is increased by 0.1 mm, until it complies with the safety conditions.

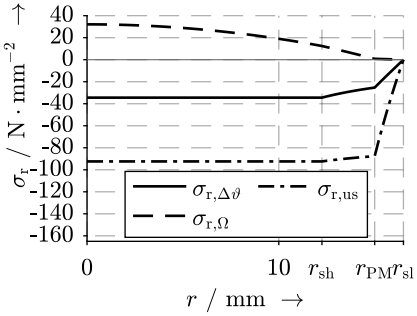

(a) Calculated radial stress component σ_r

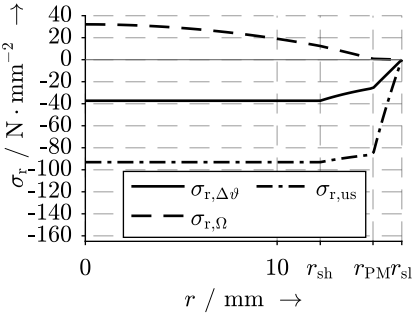

(b) Simulated radial stress component σ_r

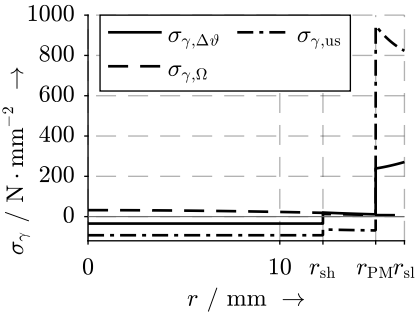

(c) Calculated tangential stress component σ_γ

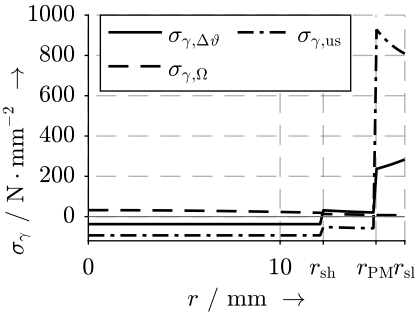

(d) Simulated tangential stress component σ_γ

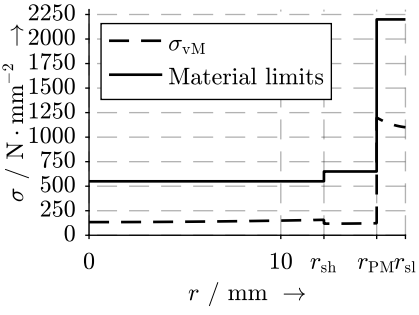

(e) Calculated *Von-Mises*-stress
$\sigma_{vM} = \sigma_{vM,\Delta\vartheta} + \sigma_{vM,\Omega} + \sigma_{vM,us}$

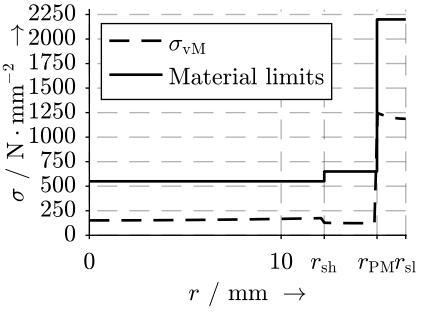

(f) Simulated *Von-Mises*-stress
$\sigma_{vM} = \sigma_{vM,\Delta\vartheta} + \sigma_{vM,\Omega} + \sigma_{vM,us}$

Fig. 3.10.: Comparison of 2D FEM-simulated and analytically calculated rotor mechanical stress components σ_r, σ_γ, σ_{vM} for the Sm_2Co_{17}-rotor (similar results for the NdFeB-rotor): $n = 60000\ \mathrm{min}^{-1}$, $u_{us,sl,PM} = 104\ \mu\mathrm{m}$, $\Delta\vartheta = 130\ \mathrm{K}$

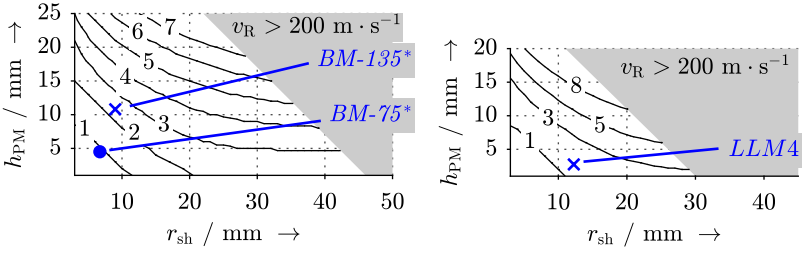

(a) $n_N = 40000\text{min}^{-1}$ (b) $n_N = 60000\text{min}^{-1}$

Fig. 3.11.: Analytically calculated sleeve height h_{sl} for varying shaft diameter r_{sh} and PM height h_{PM} up to a maximum circumferential speed $v_R = 200\ \text{m} \cdot \text{s}^{-1}$; isolines for constant h_{sl} in mm (*BM-75** and *BM-135** from Fig. 3.12)

- Tip speed values $v_R > 200\ \text{m} \cdot \text{s}^{-1}$ are generally disregarded, since the yield strength of common carbon-fiber materials is reached [110].

Also the rigid and bending rotor eigenmodes have to be analyzed to ensure an operation above the rigid body eigenfrequencies (Section 5.1.2) and below the bending mode eigenfrequencies (Appendix A.16). For the *LLM4* the calculated eigenfrequencies at $n = n_N$ are given in Table 3.11. The investigation shows that the target rotational frequency of $n_N = 1000$ Hz is far above the rigid body eigenfrequencies $f_{par,+}$, $f_{par,-}$, $f_{con,+}$, $f_{con,-}$ (overcritical operation) and well below the bending eigenfrequencies $f_{bend,1,+}$, $f_{bend,1,-}$, $f_{bend,2,+}$, $f_{bend,2,-}$.

Table 3.11.: Simulated eigenfrequencies for the bearingless prototype machine *LLM4* at $n = 60000\ \text{min}^{-1}$ with *ANSYS Workbench 18.1*, Appendix A.16 (stiffness values from Table 5.1, +: forward whirl, −: backward whirl)

Parallel rigid body eigenfrequency $f_{par,+}$ / Hz	54.4
Parallel rigid body eigenfrequency $f_{par,-}$ / Hz	32.5
Conical rigid body eigenfrequency $f_{con,+}$ / Hz	84.4
Conical rigid body eigenfrequency $f_{con,-}$ / Hz	60.3
1st order bending eigenfrequency $f_{bend,1,+}$ / Hz	2872.3
1st order bending eigenfrequency $f_{bend,1,-}$ / Hz	2844.4
2nd order bending eigenfrequency $f_{bend,2,+}$ / Hz	4126.1
2nd order bending eigenfrequency $f_{bend,2,-}$ / Hz	4109.3

3.5. Design of the Machine Main Dimensions

The mechanical constraints from Section 3.4 are valid for all kinds of high-speed PM machines. The design of bearingless high-speed PM machines is limited by two more constraints. Firstly, the superposition between the stator drive winding air gap field and the suspension winding field leads to a disturbing lateral force orthogonal to the reference levitation force (superposition effect: Section 2.5). This effect increases with the electromagnetic utilization and the suspension field amplitude. It is load-dependent. The second constraint is based on the asynchronously rotating suspension winding field wave for $2p$-pole bearingless machines, having a suspension pole count $2p_\mathrm{L} = 2p \pm 2$. For a standstill suspension force vector, e.g. for the compensation of the gravitational force F_G, the suspension winding is fed with the same frequency f_syn as the drive winding, resulting in different velocities for the suspension field wave and the rotor. Therefore, eddy currents are induced in the solid, electrically conductive rotor parts by the suspension winding field wave. The occurring reaction field of the eddy currents deflects the air gap field even in case of a standstill suspension force vector $\vec{F}_\mathrm{L}$ and leads to an orthogonal disturbance force (eddy current effect: Section 2.4.1). Due to these two limitations, the choice of the machine's main dimensions is constrained, which may be one of the reasons for the hesitant use of bearingless machines in industrial applications [10].

For a given maximum amount of machine losses $P_\mathrm{d,lim}$, for a given stator outer radius $r_\mathrm{S,o}$ and for given rotor material properties, the eddy current and the superposition effect are mainly influenced by the pole count $2p$, by the bore diameter $2 \cdot r_\mathrm{S,i}$, respectively by the split ratio $r_\mathrm{S,i}/r_\mathrm{S,o}$, and by the PM height h_PM, respectively by the PM height ratio $h_\mathrm{PM}/r_\mathrm{S,o}$. In order to analyze the dependency of the two disturbing effects on the machine dimensions, it is necessary to determine reasonable stator iron circuit dimensions. Thus, before analyzing the eddy current effect and the superposition effect, the bearingless machine must be designed electromagnetically. Here, for each combination of $r_\mathrm{S,i}/r_\mathrm{S,o}$ and $h_\mathrm{PM}/r_\mathrm{S,o}$ this is done by selecting the machine design, which yields the analytically calculated maximum output power P_m at a given amount of losses $P_\mathrm{d,lim}$ (Section 3.6).

The sizing effects are derived at the example of two different machine sizes, operated at the same speed $n_\mathrm{N} = 40000\ \mathrm{min}^{-1}$: (i) $2 \cdot r_\mathrm{S,o} = 135$ mm, $l_\mathrm{Fe} = 125$ mm, subsequently called *BM-135*, and (ii) $2 \cdot r_\mathrm{S,o} = 75$ mm, $l_\mathrm{Fe} = 40$ mm, subsequently called *BM-75* (Data see Table 3.12, overview of investigated topologies given in Table A.4). The speed $n_\mathrm{N} = 40000\ \mathrm{min}^{-1}$ was selected, because at higher speed values, e.g. $n_\mathrm{N} = 60000\ \mathrm{min}^{-1}$,

Table 3.12.: Specifications for the design process of bearingless machines with the pole pair ratio $p/p_L = 1/2$, given by the example of the two prototype machines [23] (similar to the *BM-75*) and [9] (similar to the *BM-135*)

	BM-75	*BM-135*
$2 \cdot r_{S,o}$; l_{Fe} / mm	75; 40	135; 125
δ / mm	1	1.5
Winding type	combined	
$P_{d,lim}$ / W	135	3400
ϑ / °C; $\Delta\vartheta$ / K	100[1)]; 80[1)]	125[1)]; 105[1)]
J_{lim} / A · mm^{-2}	3.5	6.5
Cooling type	Natural convection	Water jacket
$U_{s,lim}$ / V	42	230
m / m_{th}	3 / 6	
k_Q	0.3	
Q	12	
W/τ_p	2/3	
$k_{w,D}$; $k_{w,L}$	0.835; 0.75	
B_{rem} / T	1	
$\mu_{r,sh}$; $\mu_{r,PM}$; $\mu_{r,S}$	400 [112]; 1; 1000	
κ_{sh}; κ_{PM} / MS · m^{-1}	1.25; 1[113]	
Stator core material	M270-35A [93]	
Rotor bandage material	Carbon-fiber [114]	

[1)] Stationary machine temperatures

due to the constraints by maximum mechanical stress in the rotor parts (Section 3.4), only very small bore diameters $2 \cdot r_{S,i}$ are possible (Fig. 3.11b). This would result in very small split ratio values $r_{S,i}/r_{S,o} < 0.4$ for the *BM-135* and, thus, a comparison between *BM-75* and *BM-135* regarding the eddy current and superposition effect would be limited to very small bore diameters. The admissible amount of losses $P_{d,lim}$ and the steady state machine temperature ϑ in Table 3.12 are taken from measured values of the built prototypes in [23] for the *BM-75* and in [9] for the *BM-135*. The water-jacket cooling and the larger dimensions enable a higher utilization of the *BM-135*, compared to the *BM-75*.

The prototype machine *LLM4* has the same outer dimensions as the *BM-75*, but its

rated speed is $n = 60000\ \mathrm{min}^{-1}$. It was not designed on the basis of the here presented procedure. In contrast to the *BM-75* and the *BM-135*, the *LLM4* exhibits a very low stator tooth flux density $B_{\mathrm{max}} = 0.8$ T, so that it does not show any magnetic saturation effect.
Given the machine's outer dimensions and specifications according to Table. 3.12, such as the maximum heat loss $P_{\mathrm{d,lim}}$, the classical machine design theory can be applied, determining the stator magnetic circuit. There is literature available for high speed machines, applying analytical calculation, to discuss the influence of the split ratio on the machine utilization [115, 116, 117], however, not including the variation of the PM height h_{PM} and the influence of the air friction losses P_{Fr}. The following procedure was also presented in [O09].
The investigation of scaling effects and design optimization was already carried out for bearingless slice motors [118] and disk drives [119]. In [120], they investigate bearingless drives up to 280 kW by means of FEM simulations. In [121] an optimization framework is developed for bearingless PM machines, determining the iron circuit dimensions, but keeping the split ratio constant.
The 2-dimensional analytical field calculation from Section 2.2.3 for the stator field and from Section 2.2.4 for the rotor field are used. Lateral rotor forces and the air gap torque are calculated according to Section 2.1. Its accuracy is limited due to the following simplifications: linear magnetic material properties ($\mu_{\mathrm{r,Fe}} = 1000$), neglect of axial end effects, neglect of PM segmentation, neglect of slot opening effects, neglect of field wave time and space harmonics, considering only the fundamental waves. All these simplifications are made, since the eddy current and the superposition effect according to Section 2.4.1 and 2.5 can be well analyzed by these analytical calculations.
The neglect of time and space harmonics other than the fundamental is motivated by the fact that distributed windings and a large effective air gap are considered. The axial end effects for the eddy currents are neglected here, since high-speed machines are usually equipped with slim cylindrical rotors. The eddy current amplitudes are overestimated (Section 3.7.2), which is sufficient for a worst-case estimation of the suspension force error angle. Magnetic saturation is also not included in the analytical calculation, since high-speed machines usually do not exhibit tooth flux densities $B_{\mathrm{max}} > 1.6$ T to limit iron losses. However, even at $B_{\mathrm{max}} > 1.3$ T magnetic saturation can cause significant suspension force ripple and force error angle oscillations (Section 2.6).
In order to show the limitations of all these simplifications, a magnetically non-linear 2D FEM simulation in *JMAG Designer 19.1* was performed with sinusoidal current feeding.

According to the analytical calculation procedure of the following sections one topology for the *BM-75*, called *BM-75**, and one for the *BM-135*, called *BM-135**, are chosen for the simulations. These two topologies were manually chosen, based on a feasible combination of a high efficiency η_{mot} (Fig. 3.28), a low eddy current and superposition effect (Fig. 3.28) and a low PM mass. No optimization algorithm was used, because the work tightly focuses on how the two disturbing effects generally restrict the choice of the machine's main dimensions. In Fig. 3.12 the field lines at rated operation are shown for the *BM-75** and the *BM-135**. In Fig. 3.13 the calculated and simulated suspension force F_{L} is shown with linear and non-linear material assumption. It shows that the magnetically linear analytical calculation does not include the reduction in force by iron saturation and by the slot opening effect and does not include the force ripple due to iron saturation (Section 2.6).

Selection of the Split Ratio and the PM Height – Design Process

The split ratio $r_{\mathrm{S,i}}/r_{\mathrm{S,o}}$ and the magnet height ratio $h_{\mathrm{PM}}/r_{\mathrm{S,o}}$ influence a lot of interdependent machine properties. In order to account for these interdependencies the calculation procedure according to Fig. 3.14 based on the *Matlab* software environment is used to realize the aforementioned analytical field calculation at constant iron permeability. The machine design aims at maximizing the output power P_{m}. Instead of using an optimization algorithm, the parameter set with maximum output power P_{m} for each combination of

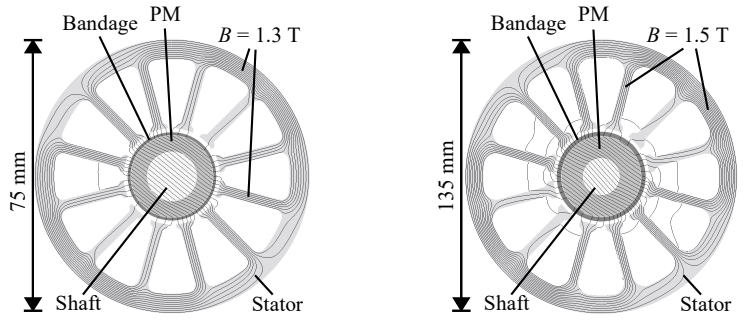

(a) *BM-75**, $p/p_{\mathrm{L}} = 1/2$ (b) *BM-135**, $p/p_{\mathrm{L}} = 1/2$

Fig. 3.12.: FEM-simulated field line plot of analytically selected topologies *BM-75** ($P_{\mathrm{N}} = 1610$ W) and *BM-135** ($P_{\mathrm{N}} = 63.7$ kW) according to Section 3.6 at rated load conditions

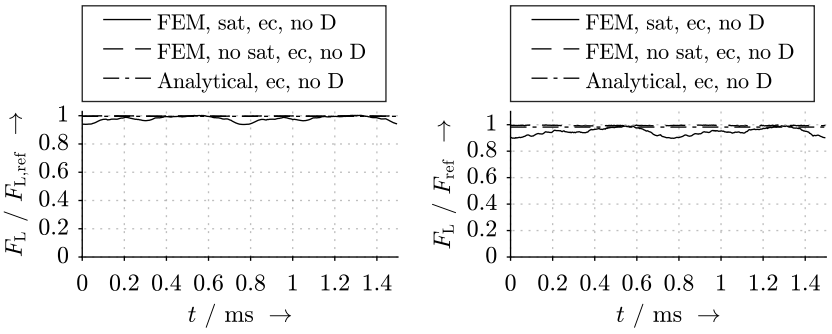

(a) *BM-75**, $p/p_L = 1/2$ (b) *BM-135**, $p/p_L = 1/2$

Fig. 3.13.: Comparison of analytically calculated and FEM-simulated aligned suspension force F_L with magnetically linear and non-linear stator iron material (sat/no sat: with/without magnetic saturation, D/no D: with/without drive current, ec/no ec: with/without eddy currents)

$r_{S,i}/r_{S,o}$, $h_{PM}/r_{S,o}$ is manually selected. A q-current operation is assumed, neglecting saturation effects, so that the term "maximum output power" is only true for these limiting assumptions. For the selected machine designs, the eddy current and superposition effect is evaluated.

Design Process: 1) Specifications

The specifications for two selected machine outer dimensions are listed in Table 3.12. For the relative iron permeability and the electric conductivity, representative values according to [113, 112, 114] are selected. The thermal limitations of the bearingless machines are given by the maximum allowed winding current density J_{lim} in order to avoid local overheating and by the maximum allowed amount of motor losses $P_{d,lim}$, which are related to the motor surface A_{mot} and to the cooling concept (3.22) [122].

$$P_{d,lim} = \alpha_{th} \cdot \Delta\vartheta \cdot A_{mot} \tag{3.22}$$

For instance, for the *BM-75* (outer dimensions of active part identical to the *LLM4*), applying natural air cooling with a slight forced air convection by a free-blowing turbocharger wheel at rated operation, the mean values of the heat transfer coefficient $\alpha_{th} = 20\ \mathrm{W} \cdot (\mathrm{m}^2 \cdot \mathrm{K})^{-1}$ and of the motor housing surface $A_{mot} = 0.09\ \mathrm{m}^2$ are estimated

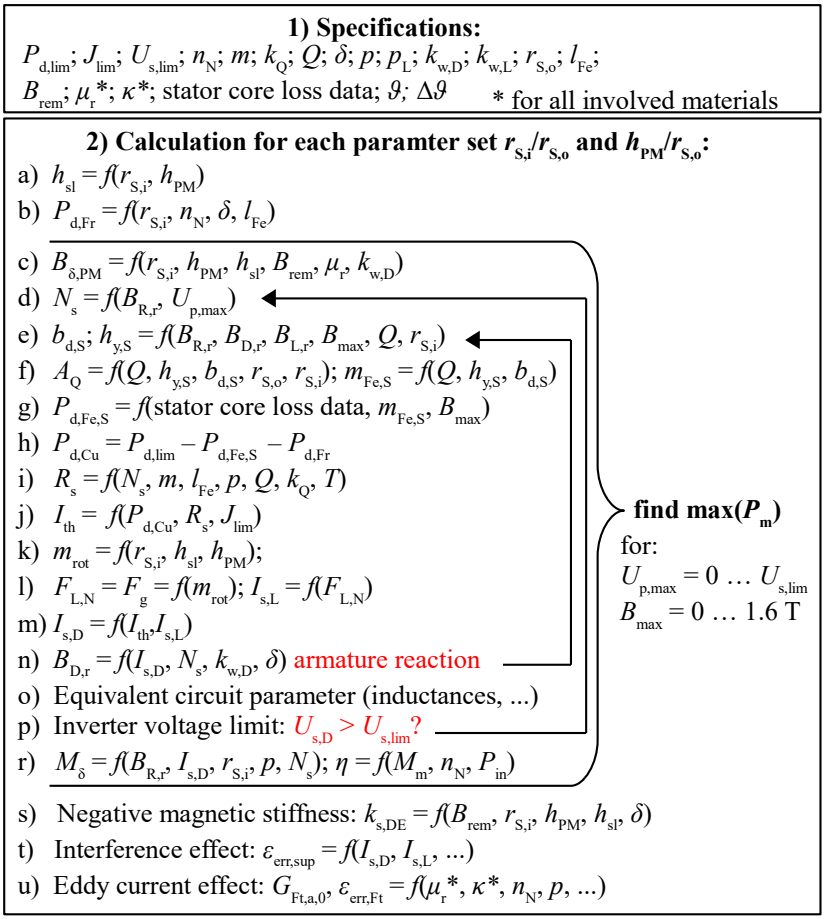

Fig. 3.14.: Design process for bearingless motors based on analytical calculations at constant iron permeability

and verified by measurement in Section 4.3, leading to $P_{d,lim} = 150$ W. Depending on the feeding inverter, the maximum phase voltage $U_{s,lim}$ and the phase count $m = 3$ of the stator winding are defined. The slot fill factor as the ratio of the conductor and the slot cross section area is given by the rather low value $k_Q = 0.3$, since no tooth tips are included in the applied simplified analytical model according to Fig. 3.14. Feasible

winding topologies, determining the stator slot count Q, the coil pitching W/τ_p, and the fundamental winding factors $k_{w,D}$ and $k_{w,L}$ are chosen according to Section 3.2 for a combined drive and suspension winding and according to [104] for separated drive and suspension windings. In case of separated windings the choice of Q is ruled by the condition $p_L/p = q/q_L$ [9]. Note that the *BM-75* and the *BM-135* with $p/p_L = 1/2$ are designed here with a combined winding. However, topologies with $p/p_L = 2/3$, which will serve as comparison in Section 3.6, require two separated windings. The mechanical air gap width δ must comply with feasible mechanical tolerances and the clearance of the safety bearings. The main dimensions, stator outer radius $r_{S,o}$ and axial active length l_{Fe}, are determined by external requirements. For a representative parameter set, typical values for the PM remanence flux density B_{rem}, the relative permeability μ_r (sh: shaft, PM: permanent magnets, S: stator yoke) and the electric conductivity of the magnets (κ_{PM}) and the solid shaft (κ_{sh}) are selected (Table 3.12). The stator iron core material is chosen here as M330-35A [123]. The steady state winding temperature ϑ and the allowed temperature rise $\Delta\vartheta$ for the given machines is chosen in accordance with Thermal Class B (*IEC 60034-1* standard [124]) for the *BM-75* with natural cooling and according to the Thermal Class F for the *BM-135* with water jacket cooling at an ambient coolant temperature 20 °C.

The rotor carbon-fiber bandage height h_{sl} and its shrink-fit value must be calculated for keeping the magnets in position, having the glue only as an additional reserve. The value h_{sl} increases the effective magnetic air gap δ_{eff}. The used 2D analytical calculation technique for the required bandage thickness h_{sl} for varying rotor diameter $2 \cdot r_{sh}$ is given in Section 3.4, based on [109, 9]. Fig. 3.11 shows the design results.

Design Process: 2) Calculation of Machine Properties for Varying $r_{S,i}/r_{S,o}$ and Relative PM Height $h_{PM}/r_{S,o}$

The considered loss groups are the *ohm*ic DC losses in the stator winding P_{Cu}, the iron losses in the stator lamination $P_{Fe,S}$ and the air friction losses P_{Fr} along the entire rotor length. In order to obtain the residual losses $P_{d,lim} - P_{Fr} = P_{Fe,S} + P_{Cu}$ from the totally allowed losses, the air friction losses are calculated first according to [125], which is in good accordance with measurements from Section 4.3.2. The underlying r-z-cross section of the simplified machine geometry for the calculation is given in Appendix A.15. It gives a rough, scalable estimation of the axial machine dimensions. For simplicity, it does not account for the winding topology which certainly influences the axial machine length by

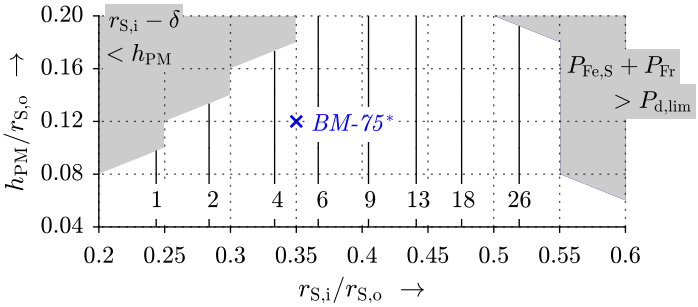

(a) *BM-75*, $p/p_L = 1/2$

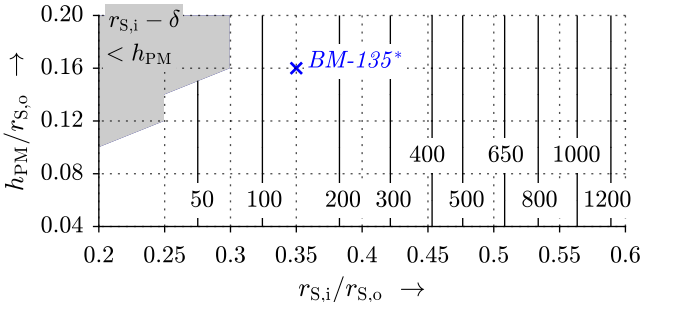

(b) *BM-135*, $p/p_L = 1/2$

Fig. 3.15.: Analytically calculated air friction losses P_{Fr} at $n_N = 40000\,\mathrm{min}^{-1}$ (isolines for constant P_{Fr} in W) according to [125]

its winding overhang. The dimensions in Appendix A.15 are chosen to agree with the built prototypes *LLM4* and from [23, 9]. The results in Fig. 3.15 show that the losses P_{Fr} increase strongly with the rotor diameter at a given speed.

The stator tooth width $b_{d,S}$ and yoke height $h_{y,S}$ as well as the number of turns per phase N_s are calculated, if the maximum induced voltage $U_{p,max}$ and the maximum magnetic flux density B_{max} in the stator are already defined. The output results vary strongly with these specifications, since the iron losses depend on B_{max}^2. Therefore, the following calculations are carried out with different values of $U_{p,max} = 0 \ldots U_{s,lim}$ and different values of $B_{max} = 0 \ldots 1.6$ T. Afterwards, the parameter set with maximum output power P_m is selected.

Note that this procedure is only valid for combined windings. For separated windings

($N_{s,D} \neq N_L$), the procedure can be used for the drive winding turn count. For the suspension winding turn count, (3.30) must be considered, complying with the inverter current rating.

The calculation of the radial component of the rotor field flux density at the stator bore surface $\hat{B}_{R,p,p,r}\left(r_{S,i}\right)$ according to (2.53), (2.57) and of the winding turn count per phase $N_s = f\left(U_{p,max}/\hat{B}_{R,p,p,r}\left(r_{S,i}\right)\right)$ precedes the calculation of the stator main dimensions (3.23), (3.24), (3.25), where τ_Q is the stator slot pitch and A_Q the stator slot cross section, neglecting tooth tips and assuming parallel-sided teeth for the round-wire winding. Note that the maximum air gap flux density B_{tot} is approximately given by the geometric sum of the two perpendicular flux density space vectors of the rotor and the drive winding fundamental (q-current operation). The suspension winding fundamental may be neglected, since it is usually by the factor 10 smaller than the rotor and the drive winding field. The influence of the armature reaction by $\hat{B}_{D,p,p,r}\left(r_{S,i}\right)$ and $\hat{B}_{L,p_L,p,r}\left(r_{S,i}\right)$ according to (2.32) is omitted in a first calculation step. After the calculation of the possible drive and suspension currents, the stator iron circuit dimensions are re-calculated in a second step, now including the two stator field components. The re-calculation is repeated until $b_{d,s}$ does not change more than 5% from the former calculation. Typically 5 ... 7 iterations are required.

$$b_{d,S} = \tau_Q \cdot \frac{B_{tot}}{B_{max}}, \text{ where } B_{tot} \approx \sqrt{\hat{B}^2_{R,p,p,r}(r_{S,i}) + \hat{B}^2_{D,p,p,r}\left(r_{S,i}\right)} \tag{3.23}$$

$$h_{y,S} = \frac{\tau_p}{2} \cdot \frac{\frac{2}{\pi} \cdot B_{tot}}{B_{max}} \tag{3.24}$$

$$A_Q = \pi \cdot \frac{\left(r_{S,o} - h_{y,S}\right)^2 - r^2_{S,i}}{Q} - b_{d,S} \cdot \left(r_{S,o} - r_{S,i} - h_{y,S}\right) \tag{3.25}$$

From that, the stator iron volume and mass m_{Fe} are calculated. For the given synchronous frequency $f_{syn} = n \cdot p$ and with the given loss data of the iron core material (M330-35A, [123]) the specific loss coefficient $k_{hys,Ft} = f\left(f_{syn}, B_{max}\right)$ is interpolated so that the iron loss $P_{Fe,S}$ with supplement factors for cutting and manufacturing influences (here: 1.6 for the yoke and 1.9 for the teeth) are determined as in [94]. Fig. 3.16 shows the stator iron losses $P_{Fe,S}$ for the *BM-75* and the *BM-135* in comparison. Note that the analytical iron loss calculation often differs considerably from the FEM results due to local flux concentrations. Thus, also in Table 3.13 deviations in $P_{Fe,S,N}$ up to $\approx 10\%$ between analytical calculation and simulation occur.

The remaining admissible copper losses in the stator winding P_{Cu} are then given by $P_{Cu} = P_{d,lim} - P_{Fr} - P_{Fe,S}$ (Fig. 3.17). From now on the design process is different for combined and separate winding machines. Here, only the procedure for the combined winding is shown, since it is feasible for pole pair combinations $p/p_L = 1/2$, e.g. for the *BM-75* and the *BM-135*. For combinations $p/p_L = 2/3$ a separate winding approach must be taken. The design process for this is given in Appendix A.17.

The copper round wire cross section A_{Cu} of one turn is calculated with (3.26), where $k_Q = 0.3$ is the slot fill factor. The thermally allowed RMS current I_{th} in each of the m_{th} phases is calculated with (3.27), (3.28), which must comply with $I_{th}/A_{Cu} < J_{lim}$. The number of parallel winding branches in combined windings (Section 3.3.1) is $a_{th} = 2$ and the average winding overhang length [94] is l_b. The possible drive current $I_{s,D}$ is given by

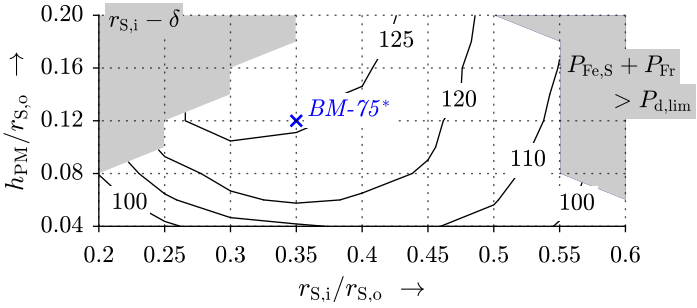

(a) *BM-75*, $p/p_L = 1/2$

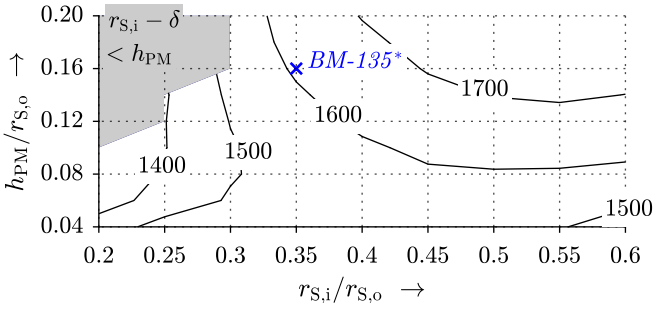

(b) *BM-135*, $p/p_L = 1/2$

Fig. 3.16.: Analytically calculated stator iron losses $P_{Fe,S}$ at $n_N = 40000$ min^{-1} (isolines for constant $P_{Fe,S}$ in W)

(3.29), where the suspension current $I_{s,L}$ must be calculated first.

$$A_{Cu} = \frac{\frac{A_Q}{2} \cdot k_Q \cdot Q}{m \cdot N_s \cdot a_{th}} \tag{3.26}$$

$$R_{s,100°C} = \frac{2 \cdot N_s \cdot (l_{Fe} + l_b)}{A_{Cu} \cdot a_{th} \cdot \kappa_{Cu,100°C}} \tag{3.27}$$

$$I_{th} = \sqrt{\frac{P_{Cu}}{m_{th} \cdot R_{s,100°C}}} \tag{3.28}$$

$$\hat{I}_{s,D,N} = \sqrt{2} \cdot \frac{m_{th}}{m} \cdot \sqrt{I_{th}^2 - \left(\frac{\frac{\hat{I}_{s,L,N}}{\sqrt{2}} \cdot m}{m_{th}} \right)^2} = i_{q,D,N} \tag{3.29}$$

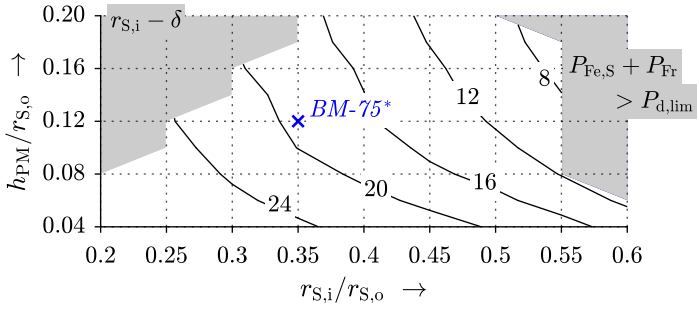

(a) *BM-75*, $p/p_L = 1/2$

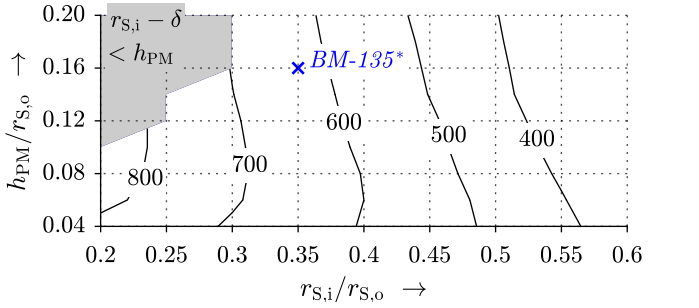

(b) *BM-135*, $p/p_L = 1/2$

Fig. 3.17.: Analytically calculated copper losses P_{Cu} at $n_N = 40000\ \text{min}^{-1}$ (isolines for constant P_{Cu} in W)

The gravitational rotor force $F_G = m_R \cdot g$ is considered the rated bearing force $F_{L,N}$. It determines the needed suspension current RMS value $I_{s,L}$ per one of the m phases. Here, we consider a combination of a bearingless motor and an axial-radial AMB (Appendix A.15). So the partial rotor weight, which is suspended by the bearingless machine, is assumed to be the weight of the active rotor $m_{R,act}$. As supplement for the rotor mass in the winding overhang area and in the end shield area, $m_{R,act}$ is multiplied with $3 \cdot 2 \cdot r_{S,i}/l_{Fe}$. The factor $3 \cdot 2 \cdot r_{S,i}/l_{Fe}$ is derived from the mean values of the suspension currents and rotor gravitational forces of the built prototype machines *LLM4*, *LLM3* [23], *LLM2* [9] and *LLM1* [24] (overview of investigated topologies given in Table A.4). The suspension current $I_{s,L}$ is then calculated by (3.30) where $k_{F,DE}$ denotes the magnetostatically calculated force current factor according to Section 4.1.2.

$$\hat{I}_{s,L,N} = \frac{m_{R,act} \cdot g \cdot 3 \cdot 2 \cdot \frac{r_{S,i}}{l_{Fe}}}{k_{F,DE}} = i_{q,L,N} \tag{3.30}$$

The machine's main and stray inductances are calculated as shown in Section 4.2.2. Together with the stator current values $\hat{I}_{s,D}$ and $\hat{I}_{s,L}$ the voltage phasor diagram is used to check the compliance with the given inverter voltage limit $U_{s,lim}$ and to reduce the phase turn count N_s if necessary. Also $\hat{I}_{s,D}$ and $\hat{I}_{s,L}$ enable the magnetostatic calculation of the stator field radial components of the air gap flux density $\hat{B}_{D,p,p,r}(r_{S,i})$ and $\hat{B}_{L,p_L,p,r}(r_{S,i})$ at $r = r_{S,i}$ according to (2.32). It is needed for the re-calculation of the stator iron circuit dimensions (3.23), (3.24), (3.25).

The air gap torque $M_\delta = k_M \cdot i_{q,D}$ is calculated with the torque-current coefficient k_M (Section 4.1.1). The mechanical output power P_m and the motor efficiency η_{mot} are finally given as in (3.31).

$$P_m = 2\pi \cdot n_N \cdot M_\delta - P_{Fr}\,; \qquad \eta_{mot} = \frac{P_m}{P_m + P_{Fe,S} + P_{Fr} + P_{Cu}} \tag{3.31}$$

For each set of $r_{S,i}/r_{S,o}$ and $h_{PM}/r_{S,o}$, the values for B_{max} and $U_{p,max}$ are selected in accordance with the maximum P_m-value among all combinations of B_{max} and $U_{p,max}$. Fig. 3.18 shows the resulting machine output power P_m for each set of $r_{S,i}/r_{S,o}$ and $h_{PM}/r_{S,o}$ for the *BM-75* and the *BM-135*. It leads to the conclusion that the highest output power for the predefined machine losses $P_{d,lim}$ results from a compromise between high stator iron losses for large $h_{PM}/r_{S,o}$, high air friction losses for large $r_{S,i}/r_{S,o}$ and high copper losses for small $h_{PM}/r_{S,o}$ and small $r_{S,i}/r_{S,o}$. The parameter sets, for which the design limits

are exceeded, are marked by shaded areas. The topologies *BM-75** and *BM-135** were manually chosen as a compromise of high efficiency, low eddy current and superposition effect and small PM mass. The results of the analytical calculation are compared to those of the FEM simulation in Table 3.13. For the *BM-75** the analytical, magnetically linear calculation results in an output power of $P_\mathrm{m} = 1613.7$ W, overestimating the FEM simulation with saturation by 0.2%. The analytically calculated output power of the *BM-135** is $P_\mathrm{m} = 67.2$ kW with an overestimation of 5.2%. Still the analytical calculations and the FEM simulations lead to very similar results, so that in the following the much faster analytical calculation is used to analyze, how the eddy current and superposition effect restricts the choice of the PM height and the split ratio with respect to high output power values.

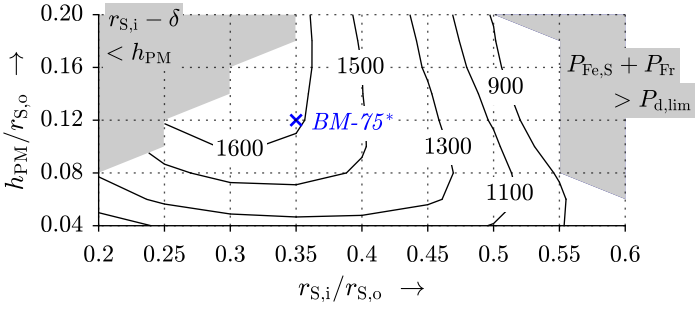

(a) *BM-75*, $p/p_\mathrm{L} = 1/2$: Isolines for constant P_m in W

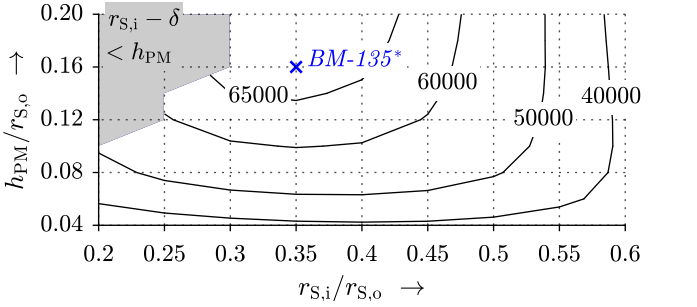

(b) *BM-135*, $p/p_\mathrm{L} = 1/2$: Isolines for constant P_m in kW

Fig. 3.18.: Analytically calculated bearingless motor output power P_m at $n_\mathrm{N} = 40000$ min^{-1} including air friction, stator iron and DC copper losses

Table 3.13.: Comparison between analytical calculation and FEM-simulated results: Losses and output power of the analytically selected topologies *BM-75** and *BM-135** out of the motor variants for the *BM-75* and the *BM-135*

	*BM-75**		*BM-135**	
	$2D_{an}$	$2D_{FEM}$	$2D_{an}$	$2D_{FEM}$
Fundamental input power $P_{e,1,in,N}$ / W	1763.7	1750.2	69586.4	66203.1
Copper losses $P_{Cu,N}$ / W	19.2	19.2	630.2	630.2
Iron losses $P_{Fe,s,N}$ / W	125.8	115.2	1611.8	1702.2
Air friction losses[1)] $P_{Fr,N}$ / W	4.8	4.8	133.2	133.2
Rotor eddy current losses $P_{Ft,R,N}$ / W	-	0.6	-	65.3
Total losses $P_{d,N}$ / W	150	139.8	2375.2	2530.9
Air gap torque $M_{\delta,N}$ / mNm	0.3864	0.3856	16.077	15.248
Mechanical output power P_m / W	1613.7	1610.4	67211.2	63672.2
Motor efficiency (fundamental) η_{mot}	0.915	0.913	0.966	0.963

[1)] From analytical calculation [125], geometry according to Appendix A.15

3.6. Design Guidelines with Respect to Scaling Effects

This section discusses, how $r_{S,i}/r_{S,o}$ and $h_{PM}/r_{S,o}$ influence the bearing force error angle $\varepsilon_{err,sup}$ due to the superposition effect and the bearing force error angle $\varepsilon_{err,Ft}$ due to the eddy current effect.

For the investigation of the eddy current effect (Section 2.4.1), for each resulting geometry an analytical eddy current calculation (Section 2.2.3) is conducted for a standstill bearing force vector, compensating the gravitational force (3.30), to determine the force amplitude attenuation $G_{Ft,a,0}$ and the force error angle $\varepsilon_{err,Ft}$. The calculation of the force error angle $\varepsilon_{err,sup}$ by the superposition effect (Section 2.5) is done via (2.77).

There is no generally valid upper limit for the force error angles $\varepsilon_{err,sup}$ and $\varepsilon_{err,Ft}$, above which the rotor position control becomes unstable. The stability limit depends on the sensor and actuator distances from the rotor center of gravity and on the speed-dependent gyroscopic rotor properties (Section 5.3.5). For evaluating the system stability, both error angles must be summed up as $\varepsilon_{err,Ft} + \varepsilon_{err,sup}$. Experience from the prototype machine *LLM4* has shown that a total error angle of $\approx 20°$ potentially causes instability. To provide

a reasonable stability margin, accounting for additional disturbance forces by magnetic saturation (Section 2.6) and for sensor and controller deficiencies, it is recommended that the machine designs keep the error angles below $\varepsilon_{\mathrm{err,Ft}} + \varepsilon_{\mathrm{err,sup}} < 7^\circ + 7^\circ = 14^\circ$. In the following this is considered a rough upper limit for the error angles. However, individual machines can certainly have higher error angles without instability issues.

3.6.1. Scaling of the Superposition Effect

The superposition effect is explained in Section 2.5. Fig. 3.19 visualizes the calculated spatial force error angle $\varepsilon_{\mathrm{err,sup}}$ due to the superposition of the drive and suspension field for varying split ratio and magnet height ratio. The error angle $\varepsilon_{\mathrm{err,sup}}$ decreases with thicker magnets, which reduces the armature field requirement. $\varepsilon_{\mathrm{err,sup}}$ also decreases with a bigger bore diameter, since the air friction losses are bigger for larger diameters. Thus, it reduces the available iron and copper losses and lower available copper losses come along with a lower drive winding current loading, reducing $\varepsilon_{\mathrm{err,sup}}$.

Derivation of Scaling Factor $k_{\mathrm{scal,sup}}$

Obviously the force error angle $\varepsilon_{\mathrm{err,sup}}$ depends on the ratio between the armature reaction field and the rotor field. Therefore, the armature reaction field for bearingless drives should be kept small in relation to the rotor field. A dimensionless factor $k_{\mathrm{scal,sup}}$ is defined in (3.32) to account for this ratio. It is related linearly to the error angle $\varepsilon_{\mathrm{err,sup}}$ (compare Fig. 3.19 and 3.20). $k_{\mathrm{scal,sup}}$ is based on a suspension force calculation via a 1-dimensional (1D) magnetostatic field calculation ($\rightarrow F_{\mathrm{err,sup}}$, equation (2.75)) according to [61]. The resulting disturbing force $F_{\mathrm{err,sup,1D}}$ by the superposition effect is normalized to the suspension force $F_{\mathrm{L,1D}}$ without superposition effect (3.32). It only considers the superposition effect. Its characteristic agrees well with the 2D calculation of $\varepsilon_{\mathrm{err,sup}}$ for both machine sizes *BM-75* and *BM-135*. Only for small bore diameters and thick PM rings (3.32) gives less reliable values due to the neglected air gap curvature in the 1D calculation.

$$k_{\mathrm{scal,sup}} = \frac{F_{\mathrm{err,sup,1D}}}{F_{\mathrm{L,1D}}} = \frac{m \cdot k_{\mathrm{w,D}} \cdot N_{\mathrm{s}} \cdot \hat{I}_{\mathrm{s,D}} \cdot \mu_0 \cdot \left(r_{\mathrm{S,i}}^2 + r_{\mathrm{S,i}} \cdot \delta_{\mathrm{eff}} - p \cdot p_{\mathrm{L}} \cdot \delta_{\mathrm{eff}}^2 \right)}{r_{\mathrm{S,i}} \cdot h_{\mathrm{PM}} \cdot p \cdot B_{\mathrm{rem}} \cdot \pi \left(r_{\mathrm{S,i}} + \delta_{\mathrm{eff}} \cdot p_{\mathrm{L}} \right)} \tag{3.32}$$

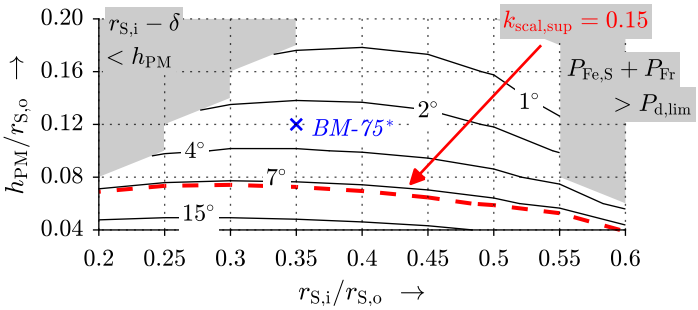

(a) *BM-75*, $p/p_L = 1/2$

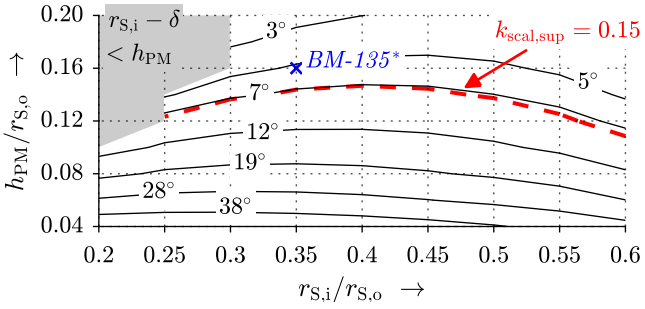

(b) *BM-135*, $p/p_L = 1/2$

Fig. 3.19.: Analytically calculated disturbing force error angle $\varepsilon_{err,sup}$ (isolines for constant $\varepsilon_{err,sup}$)

Due to the approximately linear relationship between $\varepsilon_{err,sup}$ and $k_{scal,sup}$ design recommendations can be based on an upper limit for the factor $k_{scal,sup}$. The advantage of this factor is its applicability without any field calculation. If a maximum admissible force error angle is defined to be $\varepsilon_{err,sup} < 7°$, as stated in the beginning of this section, a design guideline is given in (3.33). It is derived from the comparison between Fig. 3.19 and 3.20.

$$k_{scal,sup} \overset{!}{<} 0.15 \tag{3.33}$$

$k_{scal,sup}$ can be used to estimate the superposition error angle $\varepsilon_{err,sup}$ by means of (3.34) (in degrees). The accuracy of this estimation is limited by the neglect of the air gap curvature and of the iron saturation. This inaccuracy is also visible in Fig. 3.22 in case of magnetic saturation.

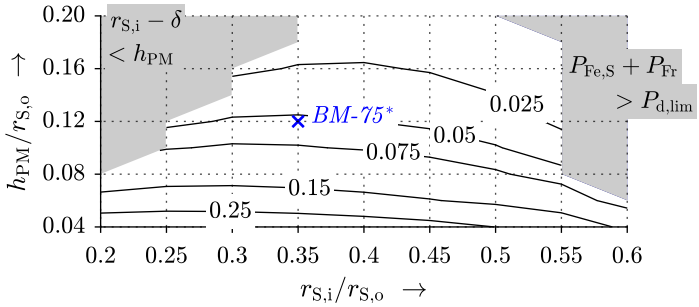

(a) *BM-75*, $p/p_L = 1/2$

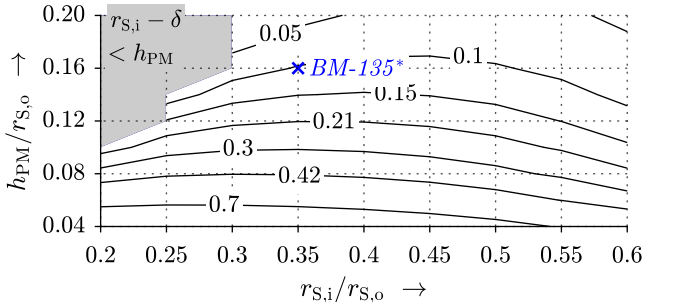

(b) *BM-135*, $p/p_L = 1/2$

Fig. 3.20.: Analytically calculated coefficient $k_{scal,sup}$, quantifying the superposition effect (isolines for constant $k_{scal,sup}$)

$$\varepsilon_{err,sup} \approx \frac{k_{scal,sup}}{\pi} \cdot 180^\circ \tag{3.34}$$

Measures for Mitigation of the Superposition Effect

If a machine design is close to the limit (3.33) and the output power P_m must be increased further, there are mainly two options, derived from (3.32): (i) Increasing the PM height h_{PM} or (ii) increasing the pole count $2p$. On the opposite, thicker magnets increase the machine's costs. Therefore, there is a tradeoff between higher costs and a smooth rotor position control. Increasing the pole count for a given stator impairs the space harmonic content of the winding. This can result in higher rotor losses and additional force and torque ripple. However, we still consider relatively low pole counts ($p = 1$, $p = 2$) and

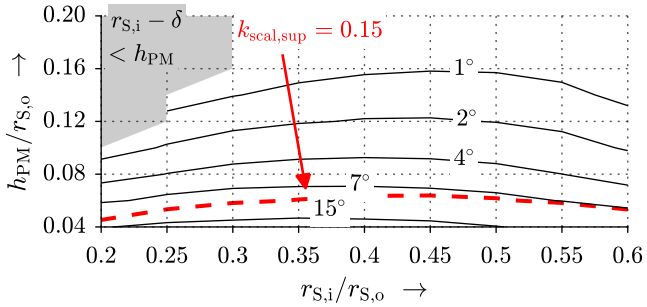

Fig. 3.21.: Analytically calculated disturbing force error angle $\varepsilon_{err,sup}$ for the *BM-135* with $p/p_L = 2/3$ instead of $p/p_L = 1/2$ (isolines for constant $\varepsilon_{err,sup}$)

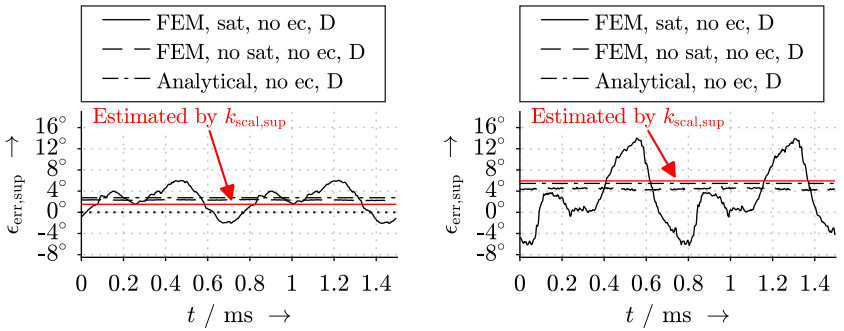

(a) *BM-75**, $p/p_L = 1/2$ (b) *BM-135**, $p/p_L = 1/2$

Fig. 3.22.: Comparison of analytically calculated and FEM-simulated force error angle $\varepsilon_{err,sup}$ due to the superposition effect with magnetically linear and non-linear stator iron material (sat/no sat: with/without magnetic saturation, D/no D: with/without drive current, ec/no ec: with/without eddy currents)

distributed windings, so that these effects are small (Fig. 3.22). Also a higher pole count results in more elaborate requirements for sensor and inverter equipment. Thus, this measure is only worthy for motors of higher power classes, as shown in Section 3.6.3. Apart from that, one should rather increase the independent active length l_{Fe} than the bore radius $r_{S,i}$ in order to comply with the limits given by the eddy current effect (Section 3.6.2).

Exemplary, Fig. 3.21 gives the calculated values for $\varepsilon_{err,sup}$ for the *BM-135* for the

combination $p/p_{\mathrm{L}} = 2/3$ instead of $p/p_{\mathrm{L}} = 1/2$, proving that the error angle $\varepsilon_{\mathrm{err,sup}}$ can significantly be reduced by a pole count increase.

Comparison to the 2D FEM Simulation

The accuracy of the superposition effect calculation is verified by 2D FEM simulations in Fig. 3.22 and by measurement on the *LLM4* in Section 2.5.

Fig. 3.22 shows that the 2D analytical calculation fits the 2D FEM simulations under the assumption of linear material. The geometries from Fig. 3.12 are considered. The linear analytical calculation cannot reproduce the saturation-based oscillation of $\varepsilon_{\mathrm{err,sup}}$ (Section 2.6). Especially for the *BM-135* with $B_{\mathrm{max}} = 1.5$ T it only represents the mean value of the error angle. If such high flux densities are chosen, a FEM simulation for the final machine design is necessary.

3.6.2. Scaling of the Eddy Current Effect

The eddy current effect is explained in Section 2.4.1. A standstill suspension force vector is considered, compensating the gravitational force F_{G}. The attenuation of the suspension force amplitude is considered via the factor $G_{\mathrm{Ft,a,0}} = F_{\mathrm{y}}/F_{\mathrm{y,ref}}$ (Fig. 3.23). The orthogonal disturbance force is expressed by means of the error angle $\varepsilon_{\mathrm{err,Ft}} = \mathrm{atan}\left(F_{\mathrm{x}}/F_{\mathrm{y}}\right)$ (Fig. 3.24).

Since all machine geometries are considered at the same speed $n_{\mathrm{N}} = 40000$ min^{-1}, the rotor frequency $f_{\mathrm{R}} = n$ stays constant (2.14). Thus, in this section the influence of geometrical relationships such as the suspension winding pole pitch $\tau_{\mathrm{p,L}}$ or the bore diameter $2 \cdot r_{\mathrm{S,i}}$ are investigated. Fig. 3.23 and 3.24 show that a bigger bore diameter $2 \cdot r_{\mathrm{S,i}}$ and a thin PM ring, associated with a small rotor bandage height h_{sl}, increase the bearing force deviation from the set-point value (increased force error angle $\varepsilon_{\mathrm{err,Ft}}$, smaller value $G_{\mathrm{Ft,a,0}}$). Comparing Fig. 3.23a, 3.24a with 3.23b, 3.24b, hence, comparing the *BM-75* with the *BM-135*, the eddy current effect is bigger for larger machines, such as the *BM-135*, having a larger bore diameter. For small dimensions (e.g. for the *BM-75*) the eddy current effect is so small, that it is hardly noticeable.

Derivation of Scaling Factor $k_{\mathrm{scal,Ft}}$

In order to explain the findings of Fig. 3.23 and 3.24, mainly four parameter ratios can explain this phenomenon, which are introduced in Section 2.2.3:

- ratio $\frac{\tilde{\tau}_{\mathrm{p,L}}}{h_{\mathrm{sl}}+\delta}$: The bigger the pole pitch $\tilde{\tau}_{\mathrm{p,L}}$ of the exciting field wave relative to the air gap between the PM and stator bore, the stronger is the field on the PM surface and the field reaction in the PM.

- ratio $\frac{\tilde{\tau}_{\mathrm{p,L}}}{h_{\mathrm{PM}}}$: The bigger the pole pitch of the exciting field wave relative to the PM height, the bigger is the portion of the radial suspension field component within the PM and the smaller is the tangential suspension field component in the PM. Since the eddy current reaction to the intruding radial air gap field determines the damping and deflection of the air gap field, big values of $\frac{\tilde{\tau}_{\mathrm{p,L}}}{h_{\mathrm{PM}}}$ lead to bigger force error angle values, where $\tilde{\tau}_{\mathrm{p,L}}$ is given by (3.35).

- ratio $\frac{h_{\mathrm{PM}}}{d_{\mathrm{E,PM}}}$: The bigger the PM height relative to the penetration depth $d_{\mathrm{E,PM}}$, the

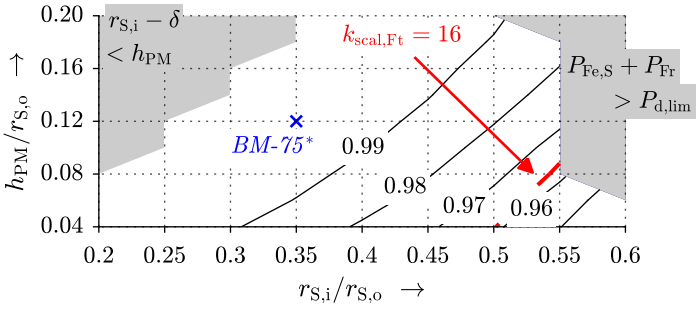

(a) *BM-75*, $p/p_{\mathrm{L}} = 1/2$

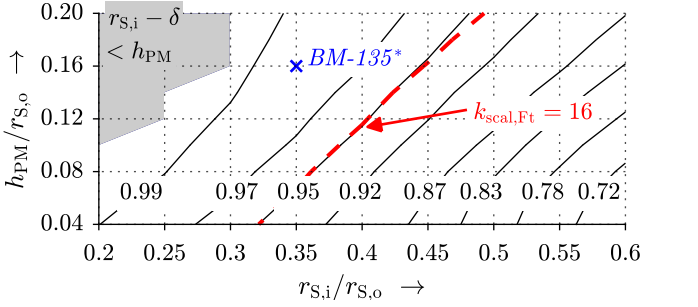

(b) *BM-135*, $p/p_{\mathrm{L}} = 1/2$

Fig. 3.23.: Analytically calculated amplitude frequency response $G_{\mathrm{Ft,a,0}}$ for a standstill bearing force vector at $n_{\mathrm{N}} = 40000\ \mathrm{min}^{-1}$ (isolines for constant $G_{\mathrm{Ft,a,0}}$)

larger is the eddy current reaction field. Hence, the more the eddy currents are inductance-limited.

- ratio $\frac{\tilde{\tau}_{\mathrm{p,L}}}{d_{\mathrm{E,PM}}}$: The bigger the pole pitch of the inducing field relative to the penetration depth, the bigger is the eddy current reaction field. Hence, the more the eddy currents are resistance-limited if the pole pitch of the field is small.

In order to derive a dimensionless factor $k_{\mathrm{scal,Ft}}$ that is linearly related to the error angle $\varepsilon_{\mathrm{err,Ft}}$, these four ratios 1)...4) are linked multiplicatively (3.35), where the suspension field pole pitch $\tilde{\tau}_{\mathrm{p,L}}$ is here defined at half of the PM height h_{PM} (radial center of the PM).

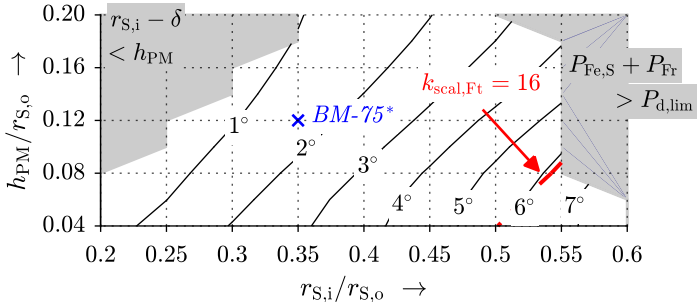

(a) *BM-75*, $p/p_{\mathrm{L}} = 1/2$

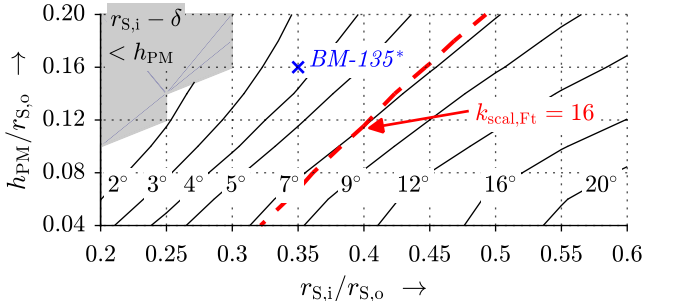

(b) *BM-135*, $p/p_{\mathrm{L}} = 1/2$

Fig. 3.24.: Analytically calculated bearing force error angle $\varepsilon_{\mathrm{err,Ft}}$ for a standstill bearing force vector at $n_{\mathrm{N}} = 40000\ \mathrm{min}^{-1}$ (isolines for constant $\varepsilon_{\mathrm{err,Ft}}$)

It only considers the eddy current effect. The superposition effect is treated in (3.32).

$$k_{\mathrm{scal,Ft,simp}} = \frac{\tilde{\tau}_{\mathrm{p,L}}}{h_{\mathrm{sl}}+\delta} \cdot \frac{\tilde{\tau}_{\mathrm{p,L}}}{h_{\mathrm{PM}}} \cdot \frac{\tilde{\tau}_{\mathrm{p,L}}}{d_{\mathrm{E,PM}}} \cdot \frac{h_{\mathrm{PM}}}{d_{\mathrm{E,PM}}}\,; \quad \text{where } \tilde{\tau}_{\mathrm{p,L}} = \frac{\pi \cdot \left(r_{\mathrm{PM}} - \frac{h_{\mathrm{PM}}}{2}\right)}{p_{\mathrm{L}}} \tag{3.35}$$

$$= \frac{\pi^4 \cdot \left(r_{\mathrm{S,i}} - \delta - h_{\mathrm{sl}} - \frac{h_{\mathrm{PM}}}{2}\right)^3 \cdot \kappa_{\mathrm{PM}} \cdot \mu_{\mathrm{PM}} \cdot |f_{\mathrm{R}}|}{p_{\mathrm{L}}^3 \cdot (h_{\mathrm{sl}}+\delta)}$$

Since air gap curvature plays a major role for large effective air gaps and small bore diameters, the corrected effective air gap width $\delta_{\mathrm{eff,cur}}$ (3.36), the corrected PM height $h_{\mathrm{PM,cur}}$ (3.37) and the corrected penetration depth $d_{\mathrm{E,PM,cur}}$ (3.38) are introduced according to [96]. This results in the scaling factor $k_{\mathrm{scal,Ft}}$ (3.39), which represents the eddy current effect more precise than $k_{\mathrm{scal,Ft,simp}}$ (3.35).

$$\delta_{\mathrm{eff,cur}} = \left(r_{\mathrm{S,i}} - \frac{r_{\mathrm{S,i}} - r_{\mathrm{sh}}}{2}\right) \cdot \ln\left(\frac{r_{\mathrm{S,i}}}{r_{\mathrm{sh}}}\right) \tag{3.36}$$

$$h_{\mathrm{PM,cur}} = \left(r_{\mathrm{PM}} - \frac{r_{\mathrm{PM}} - r_{\mathrm{sh}}}{2}\right) \cdot \ln\left(\frac{r_{\mathrm{PM}}}{r_{\mathrm{sh}}}\right) \tag{3.37}$$

$$d_{\mathrm{E,PM,cur}} = \left(r_{\mathrm{PM}} - \frac{d_{\mathrm{E,PM}}}{2}\right) \cdot \ln\left(\frac{r_{\mathrm{PM}}}{r_{\mathrm{PM}} - \delta_{\mathrm{E,PM}}}\right) \tag{3.38}$$

$$k_{\mathrm{scal,Ft}} = \frac{\tilde{\tau}_{\mathrm{p,L}}}{\delta_{\mathrm{eff,cur}} - h_{\mathrm{PM,cur}}} \cdot \frac{\tilde{\tau}_{\mathrm{p,L}}}{h_{\mathrm{PM,cur}}} \cdot \frac{\tilde{\tau}_{\mathrm{p,L}}}{d_{\mathrm{E,PM,cur}}} \cdot \frac{h_{\mathrm{PM,cur}}}{d_{\mathrm{E,PM,cur}}} \tag{3.39}$$

$k_{\mathrm{scal,Ft}}$ is displayed in Fig. 3.23, Fig. 3.24 and Fig. 3.25, but for the interpretation, $k_{\mathrm{scal,Ft,simp}}$ is used: Keeping the pole count $2p_{\mathrm{L}}$ constant, $k_{\mathrm{scal,Ft,simp}}$ shows that $\varepsilon_{\mathrm{err,Ft}}$ increases with the bore diameter, with the electric conductivity of the PM and with the rotor speed n. If $G_{\mathrm{Ft,a,0}} > 0.95$ and $\varepsilon_{\mathrm{err,Ft}} < 7^\circ$ is defined to be the upper limit for the eddy current effect, as stated in the beginning of this section, (3.40) can be introduced as another design guideline. It is derived from the comparison between Fig. 3.23, 3.24 and 3.25 and holds independent of the machine size.

$$k_{\mathrm{scal,Ft}} \overset{!}{<} 16 \tag{3.40}$$

If a linear relationship between $k_{\mathrm{scal,Ft}}$ and $\varepsilon_{\mathrm{err,Ft}}$ is assumed the force error angle can be estimated in degrees by (3.41). The estimated values are given in Fig. 3.27 compared to the simulations. Since for a higher speed n the eddy currents change from resistance-limitation to inductance-limitation (Section 2.4.2), the relationship between $k_{\mathrm{scal,Ft}}$ and

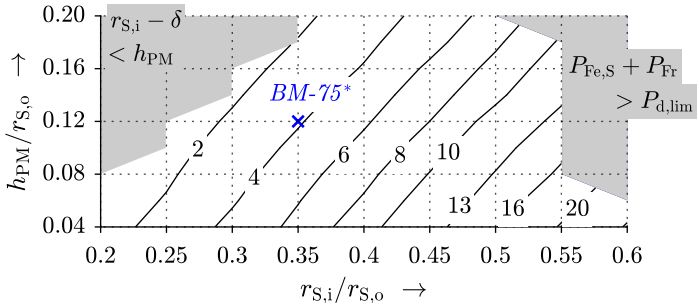

(a) *BM-75*, $p/p_L = 1/2$

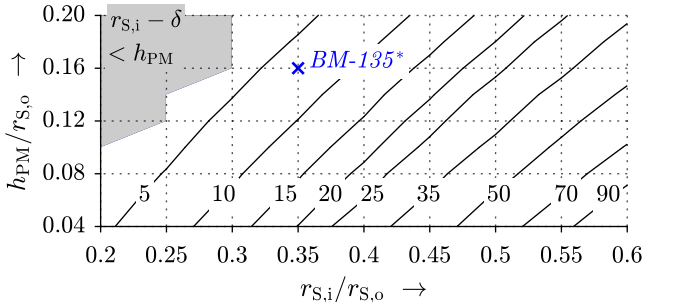

(b) *BM-135*, $p/p_L = 1/2$

Fig. 3.25.: Analytically calculated coefficient $k_{scal,Ft}$ at $n_N = 40000\ \mathrm{min}^{-1}$, quantifying the eddy current effect (isolines for constant $k_{scal,Ft}$)

$\varepsilon_{err,Ft}$ is not linear anymore. The disturbing force is overestimated by the assumption of a linear relationship.

$$\varepsilon_{err,Ft} \approx \frac{7^\circ}{16} \cdot k_{scal,Ft}; \quad G_{Ft,a,0} \approx 1 - \frac{0.05}{16} \cdot k_{scal,Ft} \tag{3.41}$$

Measures for Mitigation of the Eddy Current Effect

The factor $k_{scal,Ft,simp}$ shows which measures mitigate the eddy current effect, provided that the speed n is fixed. One option is to decrease the effective PM conductivity κ_{PM} for the eddy circuits, e.g. by PM segmentation (Section 3.7.2). However, the most effective measure is the increase of pole count p_L in relation to the bore diameter $2 \cdot r_{S,i}$. The shaft

geometry and the shaft material properties κ_{sh}, μ_{sh} do not influence the phenomenon significantly.
Fig. 3.26 gives the values for $\varepsilon_{err,Ft}$ for the *BM-135* with $p/p_L = 2/3$, proving that the error angle can significantly be reduced by the pole count increase (compare Fig. 3.24b)).

Comparison to the 2D FEM Simulation

Fig. 3.27 shows how the simplified analytical calculation fits the 2D FEM simulations under the assumption of magnetically linear material. The geometries *BM-75** and *BM-135** from Fig. 3.12 are considered. The magnetically linear analytical calculation cannot reproduce the saturation-caused lateral rotor force oscillations (Section 2.6), but the mean value of $\varepsilon_{err,Ft}$ is well represented. Thus, for machines with tooth or yoke flux densities $B_{max} > 1.3$ T a magnetically non-linear FEM simulation is required for the final machine design.

3.6.3. Motor Efficiency for varying Split Ratio and PM Height

The choice of the PM height h_{PM} and the bore radius $r_{S,i}$ for maximum efficiency η_{mot} (3.31) is constrained by the superposition effect and eddy current effect. The losses caused by the armature current $I_{s,D}$ and by its field amplitude $\hat{B}_{D,p,p,r}$ are included in this efficiency calculation, so that the influence of the superposition effect on the efficiency η_{mot} is included. Apart from the force error angle $\varepsilon_{err,Ft}$ the rotor eddy currents cause

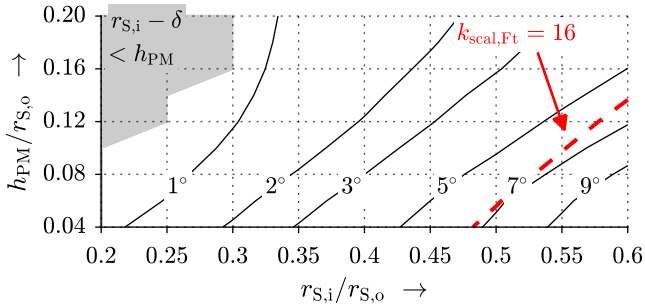

Fig. 3.26.: Analytically calculated bearing force error angle $\varepsilon_{err,Ft}$ for a standstill bearing force vector for the *BM-135* with $p/p_L = 2/3$ instead of $p/p_L = 1/2$ (isolines for constant $\varepsilon_{err,Ft}$)

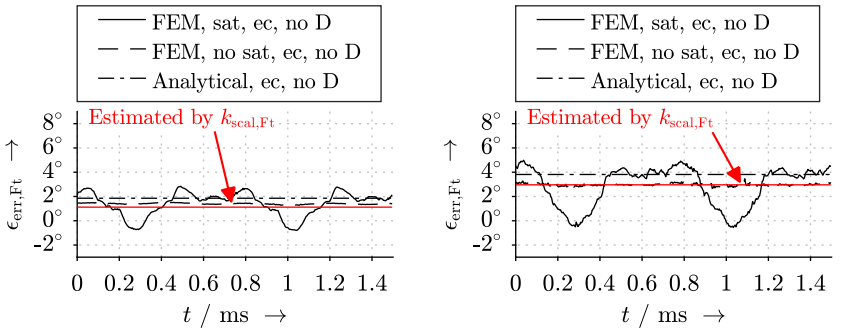

(a) *BM-75**, $p/p_{\mathrm{L}} = 1/2$ (b) *BM-135**, $p/p_{\mathrm{L}} = 1/2$

Fig. 3.27.: Comparison of analytically calculated and FEM-simulated force error angle $\varepsilon_{\mathrm{err,Ft}}$ at $n_{\mathrm{N}} = 40000\ \mathrm{min}^{-1}$ due to the eddy current effect with magnetically linear and non-linear stator iron material (sat/no sat: with/without magnetic saturation, D/no D: with/without drive current, ec/no ec: with/without eddy currents)

losses. Thus, a higher value for $\varepsilon_{\mathrm{err,Ft}}$ also means higher rotor eddy current losses by the suspension field. Rotor eddy current losses are generally not included in the efficiency calculation of (3.31). They certainly play an important thermal role, since rotor temperature is crucial for the PM and the bandage. However, their absolute value, which is usually dominated by the slot modulation of the air gap field (Section 3.7.1), is small, when compared to the other loss groups P_{Cu}, $P_{\mathrm{Fe,S}}$ and P_{Fr} (Table 3.13). Therefore, rotor eddy current losses do not substantially contribute to the efficiency value.

The values $\varepsilon_{\mathrm{err,Ft}} = \varepsilon_{\mathrm{err,sup}} = 7°$ are considered a rough upper limit for the admissible error angles. Possibly, highly efficient designs with $\varepsilon_{\mathrm{err,Ft}}, \varepsilon_{\mathrm{err,sup}} > 7°$ enable stable operation, however, require a more sophisticated position controller. Also Fig. 3.22 and 3.27 show that magnetic iron saturation can considerably increase the error angle additionally to the eddy current and superposition effects (Section 2.6). Thus, highly saturated machines should be developed for values $\varepsilon_{\mathrm{err,Ft}}, \varepsilon_{\mathrm{err,sup}} > 7°$.

Small Low-Utilized Machines

In case of small machines like the *BM-75*, typically designed for natural cooling, the main constraints are given by the limited heat dissipation capacity and by the inherently given geometrical constraints regarding the PM height. The superposition effect only

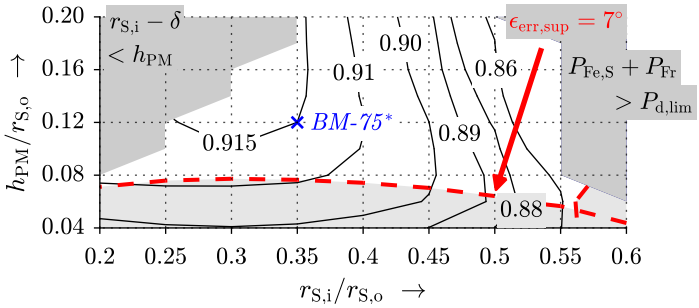

(a) *BM-75*, $p/p_L = 1/2$

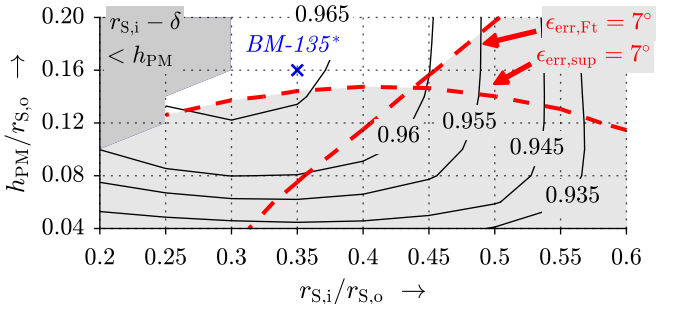

(b) *BM-135*, $p/p_L = 1/2$

Fig. 3.28.: Analytically calculated bearingless motor efficiency η_{mot} at $n_N = 40000\ \mathrm{min}^{-1}$ including air friction, stator iron and DC copper losses (isolines for constant η_{mot}; shaded areas highlight designs with $\epsilon_{err} > 7°$)

leads to a small error angle $\epsilon_{err,sup}$, as shown in Fig. 3.28a for $h_{PM}/r_{S,o} < 0.08$. This is due to the low electromagnetic utilization, leading to a low stator field and due to the low rotor weight, leading to a low bearing force requirement. The eddy current effect is not of importance, since the pole pitch of the suspension winding field is small compared to the effective air gap length (Section 3.6.2). Therefore, for such low-utilized small bearingless PM machines the design limits are similar to conventional high speed machines. Also such machines often exhibit tooth and yoke flux densities $B_{max} < 1.3$ T, so that the saturation-caused disturbance forces are small.

Large Highly-Utilized Machines

Highly-utilized, large machines like the *BM-135* need intensified cooling techniques to

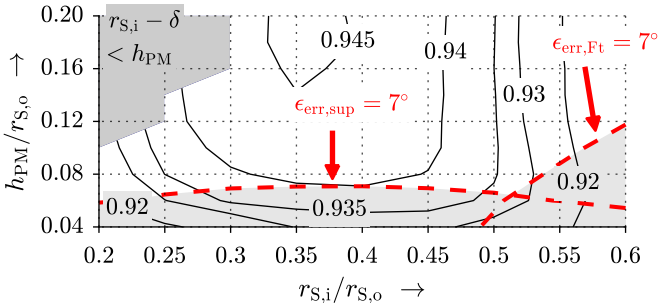

Fig. 3.29.: Analytically calculated bearingless motor efficiency η_{mot} at $n_N = 40000\ \text{min}^{-1}$ including air friction, stator iron and DC copper losses for the *BM-135* with $p/p_L = 2/3$ instead of $p/p_L = 1/2$ (isolines for constant η_{mot}; shaded areas highlight designs with $\varepsilon_{err} > 7°$)

get a high heat transfer capacity. Besides the inherently given geometrical constraints, such as $r_{S,i} - \delta > h_{PM}$, Fig. 3.28b shows that a severe design limitation is given by the superposition effect, requiring a high amount of PM material $h_{PM}/r_{S,o} > 0.15$. The second design limitation is the eddy current effect which requires the bore diameter to be as small as possible. According to Fig. 3.12b these machines can exhibit iron flux densities of $B_{max} = 1.5$ T, causing local saturation. As shown in Fig. 3.22 and 3.27 the iron saturation causes error angle oscillations of amplitudes which are twice the value from the eddy current and superposition effect. Thus, especially for these machines a small value for $\varepsilon_{err,sup}$ and $\varepsilon_{err,Ft}$ is important, so that the choice of h_{PM} and $r_{S,i}$ is strongly constrained (Fig. 3.28b).

Increase of Pole Count

As stated in Section 3.6.1 and 3.6.2, the most promising measure in order to reduce the influence of the design constraints, due to the eddy current effect and the superposition effect, is the increase in suspension field pole count $2p_L$. Fig. 3.29 shows the efficiency of the *BM-135* for the pole pair combination $p/p_L = 2/3$ instead of $p/p_L = 1/2$. Compared to the topology $p/p_L = 1/2$ (Fig. 3.28b), it enables more design freedom, since it is less constrained by these two disturbing effects. However, this advantage is only noticeable for large, highly utilized machines like the *BM-135*. Due to the higher synchronous frequency, Fig. 3.29 also shows that the motor efficiency is smaller than for the topologies with $p/p_L = 1/2$. Since the demand for sensor and inverter equipment increases with

Table 3.14.: Electromagnetic PM material properties

		$SmCo_5$	Sm_2Co_{17}	NdFeB
Remanence flux density B_{rem} / T	20 °C	0.85 ... 1.01[4,5)]	0.97 ... 1.12[4,5)]	1.09 ... 1.41[4,5)]
	100 °C	0.82 ... 0.98[4,5)]	0.95 ... 1.09[4,5)]	0.99 ... 1.28[4,5)]
	used[2)]	0.947	0.947	1.096
Temperature coefficient[3)] $\alpha_{th,rem}$ / % · K^{-1}	used	−0.04[4)]	−0.03[4)]	−0.114[4)]
Relative permeability $\mu_{r,PM}$		1.03 ... 1.07[4,5)]	1 ... 1.22[4,5)]	0.98 ... 1.15[4,5)]
	used[2)]	1.056	1.056	1.068
Electric conductivity κ_{PM} / MS · m^{-1}	20 °C	1.67 ... 2[1)]	1.18 ... 1.33[1)]	0.63 ... 0.71[1)]
	used[2)]	1.8	1.25	0.8

[1)] According to *IEC 60404-8-1* standard [126]; [2)] Used value for the analysis; [3)] Regarding the remanence flux density at $B_{rem} = 20$ C°; [4)] According to [113]; [5)] According to [127]

synchronous frequency and, hence, with an increased pole count at a given speed n, the topology $p/p_L = 1/2$ is usually the favored topology for low power applications. Higher power classes often require a bigger rotor diameter, mechanically limiting the maximum speed $n \propto f_{syn}$. Thus, machines of higher power classes can afford a higher pole count, but still keep the synchronous frequency at a moderate level (usually < 1000 Hz [9, 8]).

3.7. Rotor Material Influence on the Suspension Force

3.7.1. PM Material

For high-speed machines, the PM material is not restricted to NdFeB material such as for highly utilized drives, since for the iron loss reduction low air gap flux density values (typically $B_r < 0.6$ T) are employed. Thus, $SmCo_5$ and Sm_2Co_{17} are feasible alternatives. The electromagnetic PM properties, such as the remanence flux density B_{rem} and the electric PM conductivity κ_{PM}, vary much, depending on the manufacturer and on the chemical composition. Table 3.14 shows this variety. The electric conductivity κ_{PM} of the PM material has great influence on the penetration depth (Fig. 2.4a), considering frequencies < 1000 Hz, because the PM height h_{PM} is in this range. Thus, the conductivity of the

used PM and shaft materials was measured at the *Institute for Functional Materials*, *TU Darmstadt*, for varying temperature (Fig. 3.30). The measurement method is described in [128, 129]. Demagnetized samples were used. The conductivity was measured perpendicular to the former magnetization direction. According to [127] the magnetization has negligible impact on the conductivity. The values in Table 2.1 are taken from Fig. 3.30 for $\vartheta = 70\,^{\circ}\mathrm{C}$.

In [127] a detailed analysis of a PM conductivity measurement is presented, showing the temperature dependence and anisotropy of the conductivity in and perpendicular to the magnetization direction (Table 3.14). It reveals that the anisotropy has bigger impact on the conductivity ($\pm 20\%$) than the temperature variation ($\pm 5\%$) up to 150 °C. Unfortunately, it is not possible to model the anisotropy by analytical (section 2.2.2) or standard FEM methods, since the decoupling of the vector potential components is not possible. The anisotropic conductivity may also be one reason for the deviation of the eddy current error angles between measurement and simulation in Section 2.4.1.

As explained in Section 2.4 and in [O06], the electric conductivity of the PM material κ_{PM} influences the damping and the phase-shifting of the suspension air gap field. Fig. 3.31a shows that the suspension force amplitude decrease $G_{\mathrm{Ft,a,0}}$ (2.62) decreases for rising electric PM conductivity κ_{PM}. Also the force error angle $\varepsilon_{\mathrm{err,Ft}}$ (2.61) in Fig. 3.31b increases almost linear with rising electric PM conductivity κ_{PM} due to the resistance limitation of the eddy currents (at $f = 1000$ Hz: $d_{\mathrm{E,PM}} \approx 14$ mm $\gg h_{\mathrm{PM}} = 2.75$ mm). Thus, for non-segmented PM, NdFeB leads to the smallest suspension force reduction. Consequently, also the rotor eddy current losses $P_{\mathrm{Ft,R}}$ are the smallest for the NdFeB material (Fig. 3.32).

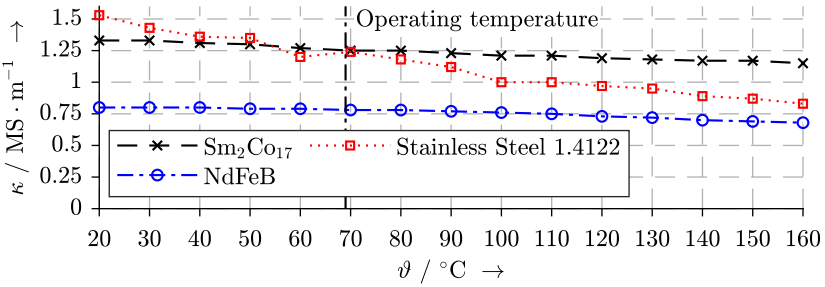

Fig. 3.30.: Measured specific conductivity of different PM materials and the shaft stainless steel material for varying temperature ϑ

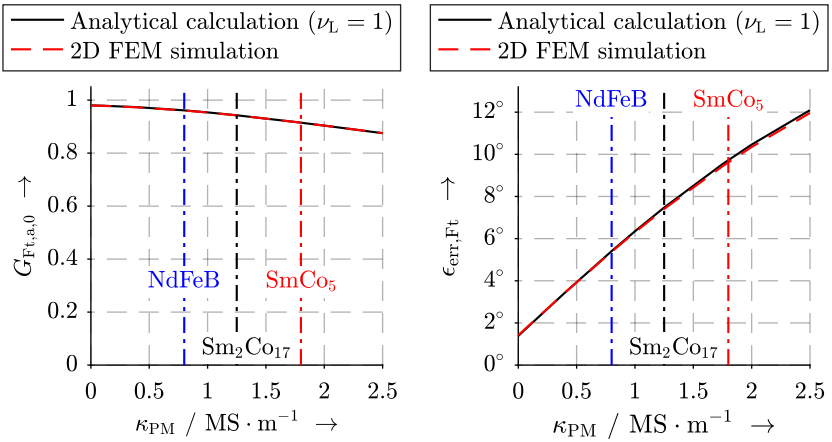

(a) Influence on bearing force reduction

(b) Influence on spatial error angle

Fig. 3.31.: Calculated and simulated suspension force amplitude attenuation $G_{Ft,a,0}$ and error angle $\varepsilon_{err,Ft}$ of the *LLM4* for a standstill suspension force vector $\vec{F} = F_G \cdot \vec{e}_y$, depending on the electric PM conductivity κ_{PM} (remanence flux density: $B_{rem} = 1$ T, model from Table 2.1)

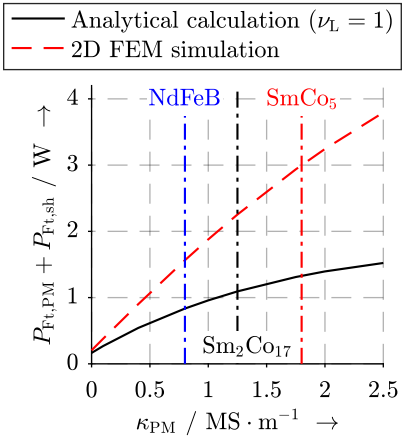

Fig. 3.32.: Calculated and simulated rotor eddy current losses $P_{Ft,R} = P_{Ft,PM} + P_{Ft,sh}$ for the *LLM4* depending on the electric PM conductivity κ_{PM} (remanence flux density: $B_{rem} = 1$ T, model from Table 2.1)

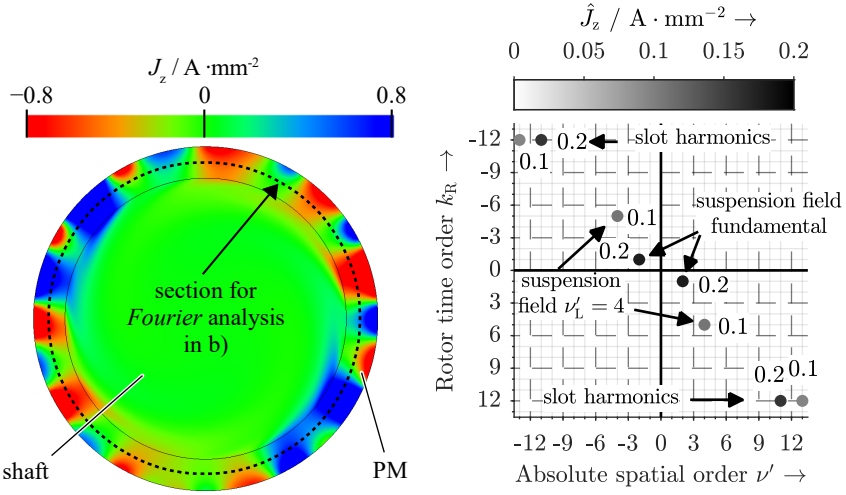

(a) Contour plot of J_z in the rotor parts

(b) 2D *Fourier* spectrum of J_z in the PM (rotor-fixed coordinates, section marked in (a)), based on [100]

Fig. 3.33.: 2D simulated axial current density J_z in the rotor of the *LLM4* for a standstill suspension force vector $\vec{F} = F_G \cdot \vec{e}_y$ (PM material: Sm_2Co_{17}, $i_{q,L} = 5.78$ A, motor no-load at $n = 60000$ min^{-1})

The big deviation between analytical calculation and FEM simulation is due to the neglect of the slot opening effect in the analytical model. It shows that the asynchronously rotating field waves due to the modulation of the rotor field by the slot openings account for approximately half of the total eddy current losses. This is visualized by Fig. 3.33, which shows the 2D simulated rotor current density J_z as contour plot (Fig. 3.33a) and as 2D *Fourier* spectrum (Fig. 3.33b). Besides the resistance-limited eddy current distribution of the suspension fundamental ($\nu_L = 1$), which is also present at the shaft surface, the slot harmonics ($\nu = 11$, $\nu = 13$) and the field harmonic $\nu_L = 4$ (second column in Table 3.8) are present with high time harmonic orders. Note that the high amplitudes of $J_z \approx 0.4$ A · mm^{-1} for $\nu = 11$ and $\nu = 13$ are mainly due to the slot opening modulation of the rotor field (Fig. 2.8a) and are already present at generator no-load.

3.7.2. PM Segmentation

Circumferential and particularly axial segmentation of the rotor PMs is a well-known procedure in order to reduce rotor eddy current losses. This is based on the idea of reducing the size of the eddy current loops. That means, the radial flux variation is linked with a smaller conductive cross section and, thus, induces smaller voltages, which drive the eddy currents. The eddy current loop can be shortened by both circumferential and axial segmentation. Bearingless PM machines require a sinusoidal PM air gap field to avoid suspension force ripple (Section 3.3.3). High-speed PM machines require a preferably low rotor unbalance, so that concentric rotor parts are desired. Also for high-speed drives usually holds $l_{\mathrm{Fe}}/\tau_{\mathrm{p,L}} > 1$, so that axial segmentation is more effective. Therefore, only axial segmentation is considered in the following.

The prototype *LLM4* is composed of one solid PM ring of length $1.2 \cdot l_{\mathrm{Fe}}$. For more general conclusions about the segmentation effect, only for this analysis the total PM length is defined to be equal to the axial iron length l_{Fe}. Fig. 3.34 visualizes the effect of the axial segmentation on the axial current density J_z for the *LLM4* (with PM length l_{Fe}) at motor no-load with $i_{\mathrm{q,L}} = 5.78$ A. It clearly shows that the field harmonics caused by the modulation of the rotor field and the stator slot openings dominate the eddy current losses in the PM. On the shaft surface mainly the 4-pole suspension field is visible by eddy current reactions, since the field waves by the slot opening modulation have a much smaller pole pitch and are shielded by the eddy current reaction field in the PM (3.34b). To evaluate the segmentation effect, a 3D FEM simulation is employed (Fig. 3.34). Due to the fine meshing in the conductive machine parts (mesh element size $\approx d_{\mathrm{E}}/3$) such simulations are time consuming. Alternatively a 2D FEM simulation or analytical calculation can be used, by introducing the segmentation effect into the electric PM conductivity κ_{PM}. κ_{PM} is multiplied with a geometry factor k_{seg} to get the effective conductivity $k_{\mathrm{PM,eff}} = k_{\mathrm{PM}} \cdot k_{\mathrm{seg}}$ ($k_{\mathrm{seg}} \to 0$ for infinite number of axial segments, $k_{\mathrm{seg}} \to 1$ for solid PM ring of length $l_{\mathrm{Fe}} \gg \tau_{\mathrm{p,L}}$).

k_{seg} contains the circumferential width of the eddy current loop, here the suspension pole pitch in the radial middle of the PM ($\tilde{\tau}_{\mathrm{p,L}}$), and the axial length of the loop, here the active length l_{Fe} divided by the number of axial segments n_{seg}. The underlying 2D eddy current calculations assume no field variation in radial direction, which is equivalent to resistance-limited eddy currents in the PM ($d_{\mathrm{E,PM}} \gg h_{\mathrm{PM}}$). Problematic for the use of k_{seg} is that the scaled conductivity $\kappa_{\mathrm{PM,eff}}$ is only accurate for one field wave of order ν' with a certain pole pitch $\tilde{\tau}_{\mathrm{p},\nu'}$. Here, the suspension field wave of order $\nu'_{\mathrm{L}} = p_{\mathrm{L}}$ is of in-

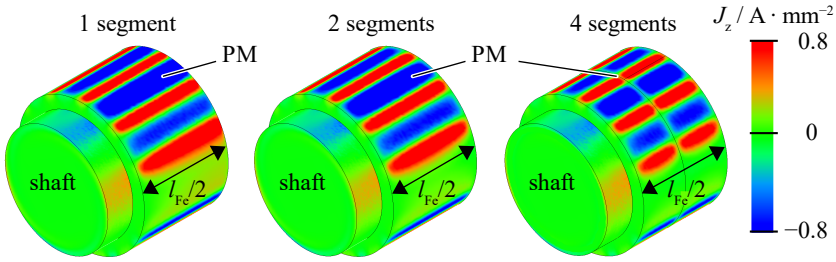

(a) PM and shaft

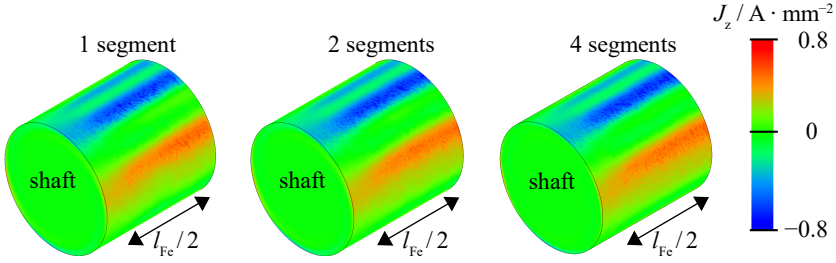

(b) Shaft

Fig. 3.34.: Numerically calculated axial current density J_z in the rotor of the prototype for 1, 2 and 4 axial PM segments (only one axial half rotor shown, $\kappa_{PM} = 1.25\,\mathrm{MS/m}$, $\kappa_{sh} = 1.25\,\mathrm{MS/m}$, $n = 60000\,\mathrm{min}^{-1}$, $\vec{F}_L = F_G \cdot \vec{e}_y$, $i_{q,L} = 5.86\,\mathrm{A}$)

terest and, therefore, $\tilde{\tau}_{p,L}$ is used. However, for other asynchronous field harmonics, such as the field waves by slot opening modulation, the 2D eddy current calculation via k_{seg} is not accurate.

Three different factors are compared in the following. The *O'Kelly*-coefficient $k_{seg,Bin}$ (3.42) is presented in [1]. It decreases the conductivity in relation to the circumferential eddy current loop extension. The *Russell-Norsworthy*-coefficient $k_{seg,Rus}$ (3.43) is presented in [3], where the eddy current losses are calculated for conducting shells of induction machine rotors in *Cartesian* coordinates. The losses with and without end effect are related to each other. The *Ruoho*-coefficient $k_{seg,Ruo}$ (3.44) is presented in [2], where the eddy current loop is simplified by a rectangle. The turn of the loop from axial into circumferential direction is assumed to be located at the diagonals of the rectangle.

$$k_{seg,Bin} = \frac{1}{1 + \frac{\tilde{\tau}_{p,L}}{l_{Fe}/n_{seg}}} \tag{3.42}$$

$$k_{\mathrm{seg,Rus}} = 1 - \frac{2 \cdot \tilde{\tau}_{\mathrm{p,L}}}{\pi \cdot l_{\mathrm{Fe}}/n_{\mathrm{seg}}} \cdot \tanh\left(\frac{\pi \cdot l_{\mathrm{Fe}}/n_{\mathrm{seg}}}{2 \cdot \tilde{\tau}_{\mathrm{p,L}}} \right) \tag{3.43}$$

$$k_{\mathrm{seg,Ruo}} = \frac{3}{4} \cdot \frac{\left(l_{\mathrm{Fe}}/n_{\mathrm{seg}}\right)^2}{\tilde{\tau}_{\mathrm{p,L}}^2 + \left(l_{\mathrm{Fe}}/n_{\mathrm{seg}}\right)^2} \tag{3.44}$$

Fig. 3.35 shows a comparison of the three different calculation techniques for the eddy current related bearing force disturbance, including the end effect and the segmentation effect. The axial segmentation mitigates the bearing force amplitude attenuation $G_{\mathrm{Ft,a,0}}$ and the spatial error angle $\varepsilon_{\mathrm{err,Ft}}$. Considering $G_{\mathrm{Ft,a,0}}$ (Fig. 3.35a), the 2D calculations with $k_{\mathrm{seg,Bin}}$ match the 3D simulation results, whereas $k_{\mathrm{seg,Ruo}}$ and $k_{\mathrm{seg,Rus}}$ lead to an underestimation of the eddy currents by a too low conductivity value $k_{\mathrm{PM,eff}}$. $\varepsilon_{\mathrm{err}}$ is dominated by phase lagging eddy currents (with a phase lag towards $\rightarrow 90°$), which means they are resistance-limited. This meets the assumption for the derivation of k_{seg} in [1, 2, 3]. Therefore, the employment of $k_{\mathrm{seg,Rus}}$ and especially $k_{\mathrm{seg,Ruo}}$ leads to results, which match the 3D simulated results. k_{Bin} overestimates the eddy currents by a too high effective PM conductivity $\kappa_{\mathrm{PM,eff}}$.

Also the axial segmentation of the PM reduces the eddy current losses, which are mainly related to resistance-limited eddy currents (Fig. 3.36). The curve gradient of the 2D calculations including k_{seg} is similar to the 3D simulation. The too low values for the analytically calculated eddy currents are due to the involving of only the suspension field fundamental and neglecting the influence of the stator slotting.

Table 3.15.: Calculated axial segmentation factors k_{seg} for a geometry similar to the *LLM4* (PM length: $l_{\mathrm{Fe}} = 40$ mm, suspension field pole pitch in the radial middle of the PM $\tilde{\tau}_{\mathrm{p,L}} = 21.4$ mm)

n_{seg}	1	2	3	4
$k_{\mathrm{seg,Bin}}$	0.65	0.48	0.37	0.32
$k_{\mathrm{seg,Rus}}$	0.66	0.39	0.22	0.15
$k_{\mathrm{seg,Ruo}}$	0.58	0.35	0.20	0.13

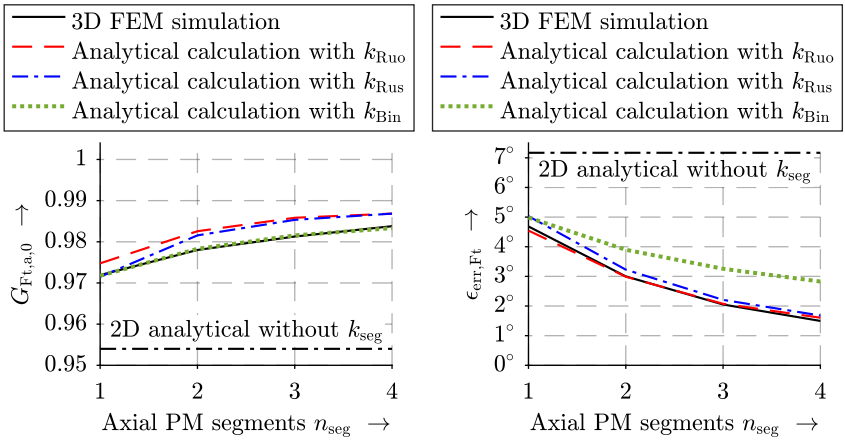

(a) Suspension force amplitude attenuation $G_{\mathrm{Ft,a,0}}$

(b) Suspension force error angle $\epsilon_{\mathrm{err,Ft}}$

Fig. 3.35.: Calculated influence of axial PM segmentation on the bearing force amplitude reduction and the spatial error angle of the *LLM4* ($\kappa_{\mathrm{PM}} = 1.25$ MS/m, $\kappa_{\mathrm{sh}} = 1.25$ MS/m, $n = 60000$ min^{-1}, $i_{\mathrm{q,L}} = 5.78$ A)

3.7.3. Shaft Material Selection

The shaft material of high-speed machines is required to have a high (0.2% offset-) yield strength $R_{\mathrm{p0,2}}$ (Table A.5) to withstand the high mechanical stress due to the high centrifugal forces (Section 3.4). Usually stainless steel is used, to avoid steel contamination by surface oxidation. Also the shaft material for machines of small diameters – like the *LLM4* – must be magnetic, since it guides the main field, avoiding the use of a rotor iron stack of sheets. Austenitic steel exhibits excellent mechanical properties, but it is non-magnetic. Ferritic stainless steels exhibit a high relative permeability $\mu_{\mathrm{r,sh}} = 500 \ldots 3000$, but has a low yield strength $R_{\mathrm{p0,2}} < 500\ \mathrm{N \cdot mm^{-2}}$ (Fig. 3.37). Austenitic-ferritic steels are called duplex steels. They exhibit a higher yield strength $R_{\mathrm{p0,2}} = 500 \ldots 700\ \mathrm{N \cdot mm^{-2}}$ but only a very low relative permeability $\mu_{\mathrm{r,sh}} = 50 \ldots 150$. The most prominent steel for magnetic applications with high mechanical stress is the martensitic steel with $R_{\mathrm{p0,2}} = 500 \ldots 1150\ \mathrm{N \cdot mm^{-2}}$ and $\mu_{\mathrm{r,sh}} = 100 \ldots 550$, which is also used for the *LLM4* as the stainless steel 1.4122, X39CrMo17-1. Unfortunately no magnetic $B(H)$-data sheet for this steel was available. For the simulations and calcu-

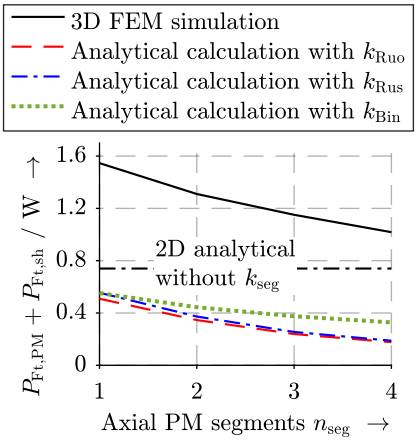

Fig. 3.36.: Calculated influence of axial PM segmentation on the rotor eddy current losses $P_{\mathrm{Ft,R}} = P_{\mathrm{Ft,PM}} + P_{\mathrm{Ft,sh}}$ for the *LLM4* ($\kappa_{\mathrm{PM}} = 1.25$ MS/m, $\kappa_{\mathrm{sh}} = 1.25$ MS/m, $n = 60000$ min^{-1}, $i_{\mathrm{q,L}} = 5.78$ A)

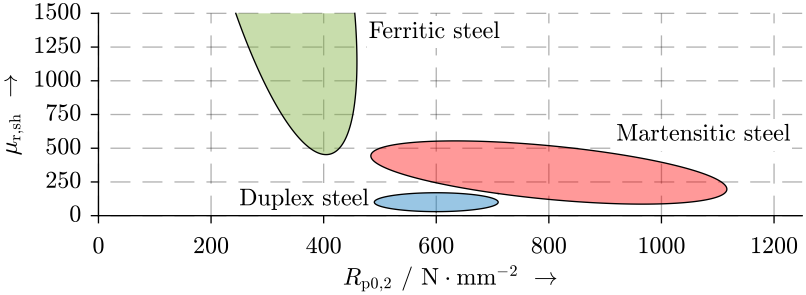

Fig. 3.37.: Magnetic permeability $\mu_{\mathrm{r,sh}}$ in correlation to the yield strength $R_{\mathrm{p0,2}}$ for magnetic steels [130]

lations the value $\mu_{\mathrm{r,sh}} = 400$ was used, as a suitable value according to [130]. The electric conductivity of the already mentioned stainless steel is typically in the range $\kappa_{\mathrm{sh}} = 1.1 \ldots 1.4$ MS · m^{-1}. This was also proven by measurements (Fig. 3.30). For the simulations, $\kappa_{\mathrm{sh}} = 1.25$ MS · m^{-1} was used. The magnetic field in the rotor of a high-speed PM synchronous machine is a pure DC field (Fig. 2.2). Despite the asynchronously rotating suspension field, also in bearingless machines it can be considered a pure mag-

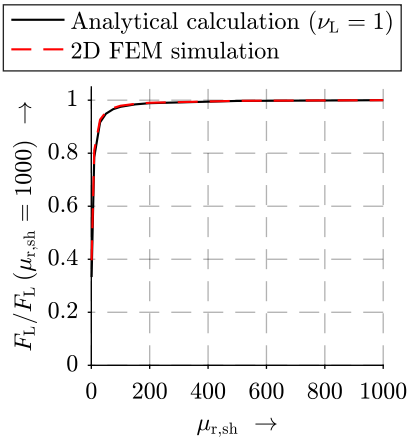

Fig. 3.38.: Motor *LLM4*: Calculated and FEM-simulated suspension force amplitude F_L with respect to F_L at a relative shaft permeability $\mu_{r,sh} = 1000$ (remanence flux density: $B_{rem} = 1$ T, without rotor eddy currents, model from Table 2.1)

netic DC field, since the rotor field amplitude is much higher than the suspension field. The flux density in solid high-speed rotors is rather low, since the flux path has a big cross-section area. It does not take values much higher than the anyway low air gap flux density amplitude ($B_{sh} \approx B_r < 0.6$ T). Thus, the shaft material can be modeled magnetically linear. For the *LLM4*, Fig. 3.38 shows the dependency of the suspension force amplitude – without eddy currents – on the relative shaft permeability $\mu_{r,sh}$. For $\mu_{r,sh} < 100$ the suspension force decreases considerably together with the air gap flux density amplitude due to the higher shaft reluctance. Because of the large effective air gap $\delta_{eff} = 5.25$ mm, for $\mu_{r,sh} > 100$ the suspension force is approximately independent of $\mu_{r,sh}$, as the air gap reluctance dominates. However, between $\mu_{r,sh} = 100$ and $\mu_{r,sh} = 500$, which are possible values for martensitic steel, the suspension force amplitude still changes by 2%. Thus, for high accuracy in simulation and calculation, a correct value of the relative shaft permeability is required.

As explained in Section 2.4, not only the eddy currents in the PM, but also in the shaft contribute to the suspension winding field distortion in the air gap. Since the penetration depth is much smaller than the shaft radius (at $f = 1000$ Hz: $d_{E,sh} \approx 0.6\text{mm} \ll r_{sh} = 12.25$ mm, Fig. 2.4b), they are inductance-limited and, thus, result mainly in a damping of the air gap field. Fig. 3.39a shows that the suspension force amplitude attenuation $G_{Ft,a,0}$ (2.62) does

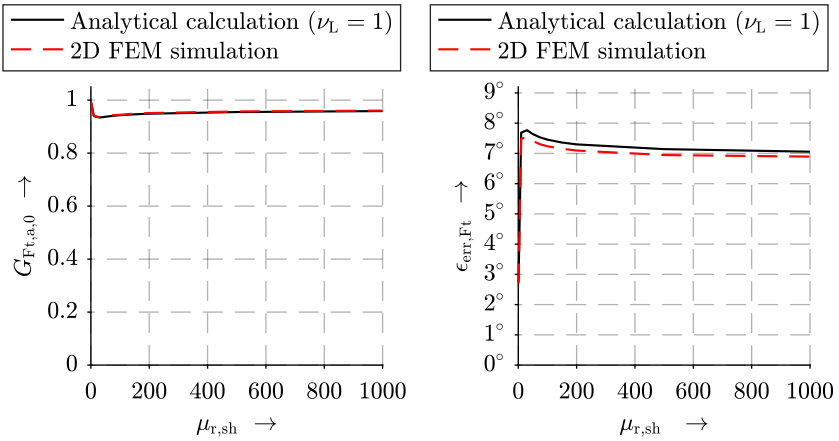

(a) Influence on bearing force reduction

(b) Influence on spatial error angle

Fig. 3.39.: Motor *LLM4*: Calculated and FEM-simulated suspension force amplitude attenuation $G_{Ft,a,0}$ and error angle $\varepsilon_{err,Ft}$ of the *LLM4* for a standstill suspension force vector $\vec{F} = F_G \cdot \vec{e}_y$, depending on the relative shaft permeability $\mu_{r,sh}$ (remanence flux density: $B_{rem} = 1$ T, without rotor eddy currents, model from Table 2.1)

not vary much with rising $\mu_{r,sh}$. Only for $\mu_{r,sh} < 20$ it decreases, since the eddy current reaction is low due to resistance-limitation of the eddy currents. For $\mu_{r,sh} = 20 \ldots 80$, $G_{Ft,a,0}$ has a minimum, since here the eddy current reaction is the biggest. It is on the transition from resistance- to inductance-limitation. The force error angle $\varepsilon_{err,Ft}$ is mainly independent of $\mu_{r,sh}$ due to the inductance limitation of the shaft eddy currents. Only for $\mu_{r,sh} < 100$ a slight increase of $\varepsilon_{err,Ft}$ occurs, since for such low $\mu_{r,sh}$-values the eddy current lagging in the shaft also contributes to the phase-shifting of the suspension winding field.

4. Machine Parameter Identification

This chapter discusses different methods for the determination of bearingless machine properties. At the example of the bearingless prototype machine *LLM4*, the results from measurements, finite element simulations and analytical calculations are compared.
Table 4.1 evaluates and characterizes the different applied simulation and calculation

Table 4.1.: Evaluation of the different applied determination techniques for machine output quantities (magnetostatic calculation, no eddy currents considered)

	$1D_{an}$	$2D_{an,simp}$	$2D_{an}$	$2D_{FEM}$	$3D_{FEM}$
Calculation at radius	$r_{S,i}$	$r_{S,i} - \frac{\delta}{2}$	$r_{S,i} - \frac{\delta}{2}$	$r_{S,i} - \frac{\delta}{2}$	$r_{S,i} - \frac{\delta}{2}$
Closed term available	✓	✓			
Air gap curvature included[1)]		✓	✓	✓	✓
Non-use of: $\mu_{r,PM} = 1$		✓	✓	✓	✓
Circumferential rotor air gap field component included			✓	✓	✓
Non-use of: $\mu_{r,Fe} \to \infty$, $r_{S,o} \to \infty$			✓	✓	✓
Iron saturation included				✓	✓
Slot opening effect included				✓	✓
Axial end effects included					✓
Calculation time for one electrical period[2)]	< 1 s	< 1 s	< 2 min	< 3 min	< 2 d
Accuracy[3)] (deviation of $k_{F,DE}$)	$+2\%$	-10%	-10%	-10%	$+1\%$

[1)] Including flux concentration effects from field sources towards the bore center.
[2)] Model diameter: $2 \cdot r_{S,o} = 75$ mm, machine length: $l_{Fe} = 40$ mm; analytical calculation including up to $\nu = \mu = 50$ space harmonics, space and time period discretized in 360 sections; PC with 16 GB RAM, *Intel* Core^{TM} *i5-6600K* CPU @ 3.5 GHz, 64 bit processor, 4 cores.
[3)] Reference: Measured value with Sm_2Co_{17}-rotor for the force-current coefficient $k_{F,DE} = 1.00\,N \cdot A^{-1} = 100\%$.

methods, which will be discussed subsequently. "$1D_{an}$" refers to 1-dimensional field calculations, only including radial air gap field components without air gap curvature, "$2D_{an}$" refers to two dimensional field calculations in cylindrical coordinates, "$2D_{an,simp}$" means the same with the simplifications from Table 4.1. Variables, indexed by $2D_{FEM}$/$3D_{FEM}$, are related to a 2-dimensional/3-dimensional finite element method simulation by means of the software *JMAG Designer 19.1*. The 2D FEM model for the *LLM4* is introduced in Section 2.2.3 and 2.2.4, whereas a 3D FEM model is presented in Section 3.7.2 for the segmentation of the rotor PM. Therefore, in this chapter only the results of these simulations are shown. The prototype machine *LLM4* exhibits a low degree of saturation with a maximum iron flux density of $B_{Fe,max} < 0.9$ T. So the 2D analytical calculations with constant permeabilities agree well with the 2D FEM results. The rotor PM is axially 4 mm longer on both sides than the stator iron sheet package, so that the PM flux linkage is increased by the factor 1.09. Thus, for accurate calculations a 3D FEM simulation is required.

4.1. Determination of Air Gap Torque and Suspension Force

Table 4.2 gives an overview of the derived machine output quantities, using the calculation methods from Table 4.1. M_δ is the air gap torque, F_L is the rotor suspension force at the

Table 4.2.: Comparison of different determination techniques for the torque and the suspension force of the *LLM4* at *Load A* (Section 4.3.3), values for both rotors: Sm_2Co_{17}/NdFeB, coefficients referenced to current peak values, Sm_2Co_{17}: $i_{q,D} = 10.50$ A, $i_{q,L} = 5.77$ A, NdFeB: $i_{q,D} = 9.28$ A, $i_{q,L} = 5.22$ A

	k_M / mNm · A^{-1}	M_δ / mNm	$k_{F,DE}$ / N · A^{-1}	F_L / N
$1D_{an}$	15.1 / 16.8	158 / 156	1.02 / 1.15	5.9 / 6.0
$2D_{an,simp}$	12.8[2] / 14.2[2]	134[2] / 132[2]	0.90 / 1.01	5.2 / 5.3
$2D_{an}$	13.2 / 14.9	138 / 138	0.90 / 1.01	5.2 / 5.3
$2D_{FEM}$	13.2 / 14.9	137 / 137	0.90 / 1.01	5.2 / 5.3
$3D_{FEM}$	14.5 / 16.2	151 / 151	1.01 / 1.12	5.8 / 5.8
Measurement[1]	14.4 / 16.1	151 / 151	1.00 / 1.07	5.8 / 5.8

[1] Presented in Section 4.3.3, measured at 20°C and scaled by $B_{rem}(\vartheta_{PM,N})/B_{rem}(20°C)$ according to Section 4.3.1.
[2] Values smaller than for $2D_{an}$ due to neglect of tangential rotor field component.

drive end of the bearingless machine (subscript: DE). k_{M} is the air gap torque-current coefficient and $k_{\mathrm{F,DE}}$ the suspension force-current coefficient at the DE. The considered torque current $i_{\mathrm{q,D}}$ and the suspension current $i_{\mathrm{q,L}}$ are taken from the measurement with *Load A* (Section 4.3.3).

Mainly, three sources of inaccuracies are identified: The 1- and 2-dimensional methods underestimate the torque and force capability by $\approx 9\%$ (Table 4.2), since the PM in the machine is axially on both sides 4 mm longer than the stator, resulting in a higher PM flux, which is only considered in the measurements and in the simulation $3\mathrm{D}_{\mathrm{FEM}}$. $2\mathrm{D}_{\mathrm{an}}$ and $2\mathrm{D}_{\mathrm{an,simp}}$ yield similar results. The results of $2\mathrm{D}_{\mathrm{an}}$ fit very well with the simulation results of $2\mathrm{D}_{\mathrm{FEM}}$ due to the small slot opening effect (Section 2.3). The method $1\mathrm{D}_{\mathrm{an}}$ overestimates the torque and force capability by $\approx 2...4\%$ (Table 4.2), since a radially constant flux density over the air gap width δ is considered. Altogether, the analytical methods $2\mathrm{D}_{\mathrm{an}}$/$2\mathrm{D}_{\mathrm{an,simp}}$ yield quite accurate result, providing closed terms for the torque and suspension force calculation. In the following, the different determination methods are presented in detail.

4.1.1. Air Gap Torque and Torque-Current Coefficient

The air gap torque of a bearingless PM machine can be calculated like in common PM machines with surface-mounted magnets. Since these high-speed machines are usually equipped with distributed windings and since the PM is required to be sinusoidally magnetized (Section 3.3.2), the torque ripple is very small. The analytical torque calculation can be done by only including the fundamental field waves of the stator winding and rotor PM. Due to synchronism, instead of the dynamic calculation of Section 2.2.2 a magnetostatic calculation is sufficient and leads to an analytical expression for k_{M}. The magnetostatic torque calculation is extensively treated in literature, e.g.the 1D calculation in [61] and the 2D calculation in [23]. The calculation of the air gap torque $M_{\delta}(t)$ is addressed in Section 2.1. An analytical expression for k_{M} is only available, if the tangential rotor field component $B_{\mathrm{R},\gamma}$ is neglected, as for "$1\mathrm{D}_{\mathrm{an}}$" and "$2\mathrm{D}_{\mathrm{an,simp}}$". With the assumption $B_{\mathrm{R},\gamma} = 0$, the mean value of the air gap torque M_{δ} is calculated according (4.1), which only includes the fundamental field waves. It only depends on the angle $\varphi_{\mathrm{D}} - \varphi_{\mathrm{R}}$ between the stator drive and rotor field waves. Using field-oriented control, q-current feeding allows maximum torque per ampere turns, hence, $M_{\delta} = \hat{M}_{\delta}$. This leads to the torque-current

coefficient k_M in (4.3) ($1\mathrm{D}_\mathrm{an}$) and (4.4) ($2\mathrm{D}_\mathrm{an}$) via $k_\mathrm{M} = \hat{M}_\delta / i_\mathrm{q,D}$.

$$\begin{aligned} M_\delta &= \frac{\pi \cdot l_\mathrm{Fe} \cdot r_\mathrm{cal}^2}{\mu_0} \cdot \hat{B}_{\mathrm{R},p,p,\mathrm{r}}(r_\mathrm{cal}) \cdot \hat{B}_{\mathrm{D},p,p,\gamma}(r_\mathrm{cal}) \cdot \sin(\varphi_\mathrm{D} - \varphi_\mathrm{R}) \\ &= \hat{M}_\delta \cdot \sin(\varphi_\mathrm{D} - \varphi_\mathrm{R}) \end{aligned} \tag{4.1}$$

$1\mathrm{D}_\mathrm{an}$: 1D analytical calculation

$$\begin{aligned} \hat{M}_{\delta,1\mathrm{D}} &= B_\mathrm{rem} \cdot l_\mathrm{Fe} \cdot r_\mathrm{S,i} \cdot m \cdot k_\mathrm{w,D} \cdot N_\mathrm{s} \cdot \hat{I}_\mathrm{s,D} \cdot \frac{r_\mathrm{sh} - r_\mathrm{PM}}{r_\mathrm{S,i} - r_\mathrm{sh}} \\ &= B_\mathrm{rem} \cdot l_\mathrm{Fe} \cdot r_\mathrm{S,i} \cdot m \cdot k_\mathrm{w,D} \cdot N_\mathrm{s} \cdot \hat{I}_\mathrm{s,D} \cdot \frac{h_\mathrm{PM}}{\delta_\mathrm{eff}} \end{aligned} \tag{4.2}$$

$$k_\mathrm{M} = B_\mathrm{rem} \cdot l_\mathrm{Fe} \cdot r_\mathrm{S,i} \cdot m \cdot k_\mathrm{w,D} \cdot N_\mathrm{s} \cdot \frac{h_\mathrm{PM}}{\delta_\mathrm{eff}} \tag{4.3}$$

$2\mathrm{D}_\mathrm{an}$/$2\mathrm{D}_\mathrm{an,simp}$: 2D analytical calculation

For the 2D calculation it is distinguished between 2-pole machines and machines of higher pole count, since the term for the rotor field flux density components varies (Section 2.2.4). Here, the solution for $p > 1$ is presented, whereas it can be found in Appendix A.18 for $p = 1$. This method is called $2\mathrm{D}_\mathrm{an}$ and its calculation is given in (2.20). To derive a still simple analytical expression for k_M, the tangential rotor field component $B_{\mathrm{R},\gamma}$ is neglected, resulting in an error $< 0.5\%$. The coefficient $c_{\mu'=p}$ and the tangential magnetization amplitude $\hat{M}_{\gamma,\mu'=p}$ result from (2.44) and (2.46).

$$\begin{aligned} k_\mathrm{M} = {} & l_\mathrm{Fe} \cdot m \cdot k_\mathrm{w,D} \cdot N_\mathrm{s} \cdot r_\mathrm{PM}^p \cdot r_\mathrm{S,i}^p \cdot \left[1 + \left(\frac{r_\mathrm{S,i}}{r_\mathrm{cal}}\right)^{2p}\right] \cdot \\ & \frac{\left(r_\mathrm{PM}^{4p} - r_\mathrm{sh}^{2p} \cdot r_\mathrm{cal}^{2p}\right) \cdot \left(\mu_{r,\mathrm{PM}} - 1\right) + r_\mathrm{PM}^{2p} \cdot \left(r_\mathrm{sh}^{2p} - r_\mathrm{cal}^{2p}\right) \cdot \left(\mu_{r,\mathrm{PM}} + 1\right)}{\left[\left(r_\mathrm{PM}^{4p} - r_\mathrm{sh}^{2p} \cdot r_\mathrm{S,i}^{2p}\right) \cdot \left(\mu_{r,\mathrm{PM}} - 1\right) + r_\mathrm{PM}^{2p} \cdot \left(r_\mathrm{sh}^{2p} - r_\mathrm{S,i}^{2p}\right) \cdot \left(\mu_{r,\mathrm{PM}} + 1\right)\right]^2} \cdot \\ & \left\{c_{\mu'=p} \cdot \left[r_\mathrm{PM}^{2p+1} \cdot (p-1) + 2 \cdot r_\mathrm{PM}^p \cdot r_\mathrm{sh}^{p+1} - r_\mathrm{PM} \cdot r_\mathrm{sh}^{2p} \cdot (p+1)\right] - \right. \\ & \left. \hat{M}_{\gamma,\mu'=p} \cdot \mu_0 \cdot \left(r_\mathrm{PM}^{2p+1} - r_\mathrm{PM}^p \cdot r_\mathrm{sh}^{p+1} + r_\mathrm{PM} \cdot r_\mathrm{sh}^{2p}\right)\right\} \end{aligned} \tag{4.4}$$

Measurement

The test bench does not allow the direct measurement of the shaft torque via a torque

sensor. Therefore, the air gap torque M_δ is determined indirectly from electric power measurements (Section 4.3). The rotor losses, i.e. air friction losses P_{Fr} and rotor eddy current losses $P_{\mathrm{Ft,R}}$, are added to the mechanical output power P_{m} (4.30) to derive the air gap power P_δ. The air gap torque M_δ is given by (4.5). The accuracy of this method is restricted by the fact that the rotor eddy current losses $P_{\mathrm{Ft,R}}$ are determined in 3D FEM simulations only with fundamental current feeding. Additional eddy currents due to stator current harmonics, caused by the PWM of the feeding inverter, are neglected.

$$M_\delta = \frac{P_{\mathrm{m}} + P_{\mathrm{Fr}} + P_{\mathrm{Ft,R}}}{2\pi \cdot n} \tag{4.5}$$

4.1.2. Bearing Force and Force-Current Coefficient

In order to derive the bearing force-current coefficient $k_{\mathrm{F,DE}}$ as an analytical expression in a bearingless machine, instead of the dynamic calculation of Section 2.2.2 a magnetostatic calculation is sufficient, if a constant and stand-still force vector is considered (e.g. $F_{\mathrm{L}} = F_{\mathrm{G}}$). In practice, this calculation overestimates the coefficient $k_{\mathrm{F,DE}}$ by about 3% due the neglected damping influence of the rotor eddy currents (Section 2.4). For 2-pole machines, a calculation with 1D field characteristics is presented in [61], whereas a 2D field calculation is given in [23]. It is also given in Appendix A.18. The solution for machines of pole count $2p > 2$ is given hereafter. The calculation of the rotor suspension force is addressed in Section 2.1. An analytical expression for $k_{\mathrm{F,DE}}$ is derived with neglected tangential rotor field component $B_{\mathrm{R},\gamma}$, as for "$1\mathrm{D}_{\mathrm{an}}$" and "$2\mathrm{D}_{\mathrm{an,simp}}$". At $r_{\mathrm{cal}} = r_{\mathrm{S,i}}$, the tangential rotor field component yields $B_{\mathrm{R},\gamma}$ is zero, and the expression for a standstill bearing force F_{L} is given by (4.6). This equation only includes the fundamental field waves, assumes $p_{\mathrm{L}} = p+1$ and only depends on the angle between the stator and rotor field waves. Field-oriented control leads to $F_{\mathrm{L}} = \hat{F}_{\mathrm{L}}$ which is given in (4.7) for the 1D calculation ($1\mathrm{D}_{\mathrm{an}}$). This leads to the force-current coefficient $k_{\mathrm{F,DE}}$ in (4.8) ($1\mathrm{D}_{\mathrm{an}}$) and (4.9) ($2\mathrm{D}_{\mathrm{an,simp}}$) via $k_{\mathrm{F,DE}} = \hat{F}_{\mathrm{L}}/i_{\mathrm{q,L}}$.

$$F_{\mathrm{L}} = \frac{\pi \cdot r_{\mathrm{cal}} \cdot l_{\mathrm{Fe}}}{2 \cdot \mu_0} \cdot \hat{B}_{\mathrm{R},p,p,\mathrm{r}}(r_{\mathrm{cal}}) \cdot \left(\hat{B}_{\mathrm{L},p_{\mathrm{L}},p,\mathrm{r}}(r_{\mathrm{cal}}) + \hat{B}_{\mathrm{L},p_{\mathrm{L}},p,\gamma}(r_{\mathrm{cal}})\right) \cdot \cos(\varphi_{\mathrm{R}} - \varphi_{\mathrm{L}}) \tag{4.6}$$

$1\mathrm{D}_{\mathrm{an}}$: 1D analytical calculation

$$\hat{F}_{\mathrm{L,1D}} = B_{\mathrm{rem}} \cdot l_{\mathrm{Fe}} \cdot r_{\mathrm{S,i}} \cdot m \cdot k_{\mathrm{w,L}} \cdot N_{\mathrm{s}} \cdot \hat{I}_{\mathrm{s,L}} \cdot \frac{h_{\mathrm{PM}}}{\delta_{\mathrm{eff}}} \cdot \left(\frac{1}{2 \cdot \delta_{\mathrm{eff}} \cdot p_{\mathrm{L}}} + \frac{1}{2 \cdot r_{\mathrm{S,i}}}\right) \tag{4.7}$$

$$k_{\mathrm{F}} = B_{\mathrm{rem}} \cdot l_{\mathrm{Fe}} \cdot r_{\mathrm{S,i}} \cdot m \cdot k_{\mathrm{w,L}} \cdot N_{\mathrm{s}} \cdot \frac{h_{\mathrm{PM}}}{\delta_{\mathrm{eff}}} \cdot \left(\frac{1}{2 \cdot \delta_{\mathrm{eff}} \cdot p_{\mathrm{L}}} + \frac{1}{2 \cdot r_{\mathrm{S,i}}} \right) \tag{4.8}$$

2D$_{\mathrm{an}}$/2D$_{\mathrm{an,simp}}$: 2D analytical calculation

The analytical 2D suspension force expression is given in (2.11). An analytical expression for the force-current coefficient $k_{\mathrm{F,DE}}$ is found in (4.9) with the simplifications from Table 4.2. The coefficient $c_{\mu'=p}$ and the tangential magnetization amplitude $\hat{M}_{\gamma,\mu'=p}$ result from (2.44) and (2.46).

$$\begin{aligned} k_{\mathrm{F,DE}} = {} & l_{\mathrm{Fe}} \cdot m \cdot k_{\mathrm{w,L}} \cdot N_{\mathrm{s}} \cdot r_{\mathrm{PM}}^{p} \cdot r_{\mathrm{S,i}}^{p+1} \cdot \left(r_{\mathrm{cal}}^{2p} + r_{\mathrm{S,i}}^{2p} \right) \cdot \\ & \left\{ c_{\mu'=p} \cdot \left[r_{\mathrm{PM}}^{2p+1} \cdot (p-1) + 2 \cdot r_{\mathrm{PM}}^{p} \cdot r_{\mathrm{sh}}^{p+1} - r_{\mathrm{PM}} \cdot r_{\mathrm{sh}}^{2p} \cdot (p+1) \right] - \right. \\ & \left. \hat{M}_{\gamma,\mu'=p} \cdot \mu_0 \cdot \left(r_{\mathrm{PM}}^{2p+1} - 2 \cdot r_{\mathrm{PM}}^{p} \cdot r_{\mathrm{sh}}^{p+1} + r_{\mathrm{PM}} \cdot r_{\mathrm{sh}}^{2p} \right) \right\} \cdot \\ & \frac{r_{\mathrm{PM}}^{2p+2} \cdot (\mu_{r,\mathrm{PM}} + 1) + r_{\mathrm{sh}}^{2p+2} \cdot (\mu_{r,\mathrm{PM}} - 1)}{\left[\left(r_{\mathrm{PM}}^{2p+2} \cdot r_{\mathrm{sh}}^{2p+2} - r_{\mathrm{PM}}^{2p+2} \cdot r_{\mathrm{S,i}}^{2p+2} \right) \cdot (\mu_{r,\mathrm{PM}} + 1) + \right.} \\ & \left. \left(r_{\mathrm{PM}}^{4p+4} - r_{\mathrm{sh}}^{2p+2} \cdot r_{\mathrm{S,i}}^{2p+2} \right) \cdot (\mu_{r,\mathrm{PM}} - 1) \right] \cdot \left[\left(r_{\mathrm{PM}}^{4p} - r_{\mathrm{sh}}^{2p} \cdot r_{\mathrm{S,i}}^{2p} \right) \cdot \right. \\ & \left. (\mu_{r,\mathrm{PM}} - 1) + \left(r_{\mathrm{PM}}^{2p} \cdot r_{\mathrm{sh}}^{2p} - r_{\mathrm{PM}}^{2p} \cdot r_{\mathrm{S,i}}^{2p} \right) \cdot (\mu_{r,\mathrm{PM}} + 1) \right] \end{aligned} \tag{4.9}$$

Measurement

In order to derive $k_{\mathrm{F,DE}}$, a measurement in vertical rotor position to avoid a radial gravitational force (Fig. 4.1a, 4.1b) is compared to a measurement in horizontal rotor position (Fig. 4.1c, 4.1d). At rotor standstill, at 10 circumferentially equidistant rotor angle positions, the position currents $i_{\mathrm{d,L}}$, $i_{\mathrm{q,L}}$ are measured and averaged over 1 s. The position controller is active, and the rotor is, according to the calibrated sensors, in the radial zero position. From Fig. 4.1 one can identify constant currents $i_{\mathrm{x,NDE}}$ and $i_{\mathrm{y,NDE}}$ for the radial bearing and a sinusoidal current shape of $i_{\mathrm{d,L}}$ and $i_{\mathrm{q,L}}$ for the bearingless machine. This sinusoidal shape as an AC component in the levitation currents $i_{\mathrm{d,L}}$ and $i_{\mathrm{q,L}}$ is caused by a magnetic rotor asymmetry [131, 132]. The rotor rotates around its center point with ω_{syn}/p, but this center point rotates around the stator center on a circular orbit with the same frequency ω_{syn}/p. The origin of this eccentricity is explained in Section 2.7. It is due to an undesired half moon-shaped air gap between the PM and the

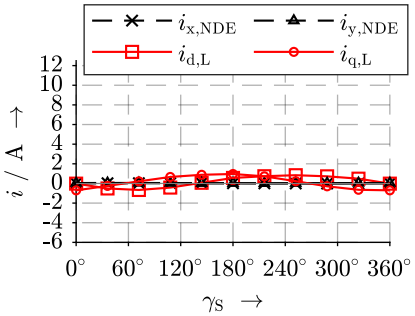

(a) Vertical rotor operation: Sm_2Co_{17}-rotor

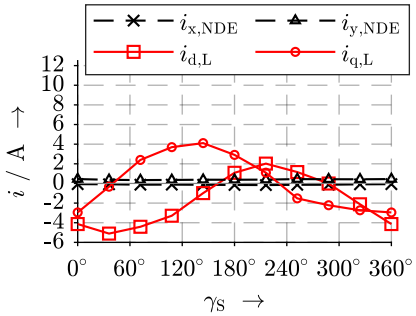

(b) Vertical rotor operation: NdFeB-rotor

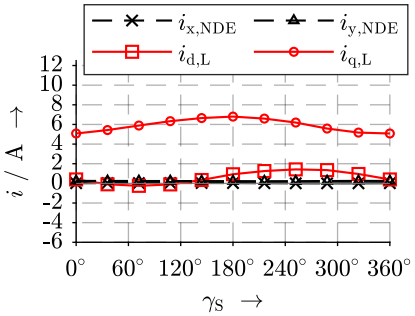

(c) Horizontal rotor operation: Sm_2Co_{17}-rotor

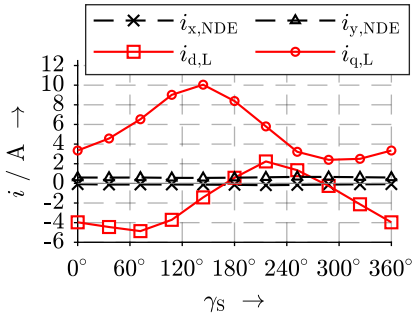

(d) Horizontal rotor operation: NdFeB-rotor

Fig. 4.1.: Measured suspension currents $i_{d,L}$, $i_{q,L}$ of the bearingless motor unit and of the radial magnetic bearing $i_{x,NDE}$, $i_{y,NDE}$ for the *LLM4* at standstill and different rotor angle values γ_S

shaft. This air gap occurs because no shrink-fitting between PM and shaft can be applied due to the low yield strength R_m of the PM material (Table A.6). Since this eccentricity air gap for the NdFeB PM was accidentally much bigger ($\delta_{ecc} = 180\ \mu$m) than for the Sm_2Co_{17} PM ($\delta_{ecc} = 50\ \mu$m), its AC force and current component is much bigger in Fig. 4.1. The shape of $i_{d,L}(\gamma_s)$ and $i_{q,L}(\gamma_s)$ is separated into an average value I_{DC} and into an AC amplitude I_{AC} in Table 4.3.

For the derivation of the force-current coefficients $k_{F,DE}$, $k_{F,NDE}$, the partial gravitational force $F_{G,DE}$ at the DE and $F_{G,NDE}$ at the NDE is divided through the difference of the suspension current mean values over all rotor positions in horizontal ($\bar{i}_{y,hori}$) and vertical ($\bar{i}_{y,vert}$) rotor position (4.10).

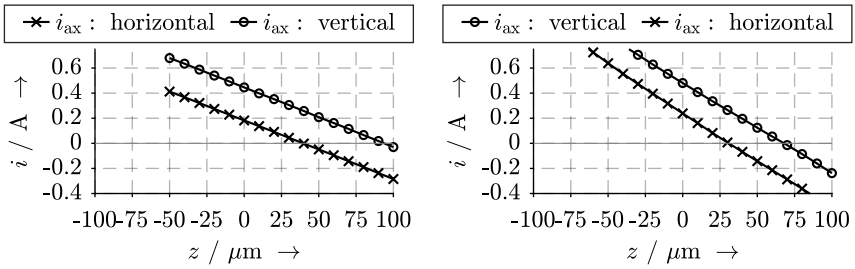

(a) Sm_2Co_{17}-rotor (b) NdFeB-rotor

Fig. 4.2.: Measured suspension current i_{ax} at the *LLM4* for different axial rotor positions z for horizontal and vertical rotor alignment

$$k_{F,DE} = \frac{F_{G,DE}}{\bar{i}_{y,DE,hori} - \bar{i}_{y,DE,vert}}; \quad k_{F,NDE} = \frac{F_{G,NDE}}{\bar{i}_{y,NDE,hori} - \bar{i}_{y,NDE,vert}} \tag{4.10}$$

In the same way, the axial force-current coefficient $k_{F,ax}$ is derived from Fig. 4.2. The results are summarized in Table 4.3 for the Sm_2Co_{17}-rotor and in Appendix A.19 for the NdFeB-rotor.

Table 4.3.: Determination of the force-current coefficient $k_{F,DE}$ from measured currents for the *LLM4* with the Sm_2Co_{17}-rotor at concentric rotor position: The rotor center of gravity is at $x = y = z = 0$. (results for the NdFeB-rotor are given in Appendix A.19)

	$i_{d,L}$	$i_{q,L}$	$i_{x,NDE}$	$i_{y,NDE}$	i_{ax}
Vertical rotor position (y-axis is direction of gravity)					
I_{DC} / A	0.16	0.1	0.01	0.03	0.33
I_{AC} / A	0.72	0.86	0.02	0.01	–
Horizontal rotor position (y-axis is direction of gravity)					
I_{DC} / A	0.60	5.89	0.02	0.24	0.07
I_{AC} / A	0.82	0.88	0.02	0.01	–
	$F_{G,DE} = 5.85$ N		$F_{G,NDE} = 3.08$ N		$F_{G,ax} = 8.93$ N
	$k_{F,DE} = 1.01\ \mathrm{N \cdot A^{-1}}$		$k_{F,NDE} = 15.2\ \mathrm{N \cdot A^{-1}}$		$k_{F,ax} = 34.22\ \mathrm{N \cdot A^{-1}}$

4.2. Determination of Back-EMF, Inductances and Negative Stiffness Coefficient

In this section, the determination techniques from Table 4.1 are compared for the back-EMF U_p, for the drive and suspension winding inductances $L_\mathrm{d,D} = L_\mathrm{q,D}$, $L_\mathrm{d,L} = L_\mathrm{q,L}$ and for the static negative magnetic stiffness $k_\mathrm{s,DE}$ in the bearingless prototype machine *LLM4*. Table 4.4 gives an overview of these machine parameters. Their calculation follows subsequently.

4.2.1. Back-EMF

The back-EMF in a bearingless machine is calculated in the same way as for common PM synchronous machines according to (4.11). From that, the 1- and 2-dimensional calculations result in (4.12) and (4.13) by means of equation (2.53) for the 2-pole machine *LLM4*.

$$\hat{U}_\mathrm{p} = \frac{2}{\pi} \cdot \omega_\mathrm{syn} \cdot l_\mathrm{Fe} \cdot \tau_\mathrm{p} \cdot k_\mathrm{w,D} \cdot N_\mathrm{s} \cdot \hat{B}_{\mathrm{R},\mu'=p,k=p,\mathrm{r}} \left(r_\mathrm{cal} = r_\mathrm{S,i}\right) \tag{4.11}$$

Table 4.4.: Comparison of different determination techniques for the machine parameters of the *LLM4* with the Sm_2Co_{17}/NdFeB-rotor

	$\hat{U}_\mathrm{p,N}$ [2] / V	$L_\mathrm{d,D}$ / µH	$L_\mathrm{d,L}$ / µH	$k_\mathrm{s,DE}$ / $\mathrm{N \cdot mm^{-1}}$
$1D_\mathrm{an}$	63.1 / 70.9	87 / 87	52 / 52	– / –
$2D_\mathrm{an,simp}$	60.1 / 64.6	79 / 79	51 / 51	−26 / −32
$2D_\mathrm{an}$	55.0 / 62.0	78 / 78	50 / 50	– / –
$2D_\mathrm{FEM}$	57.1 / 63.8	80 / 80	41 / 41	−26 / −32
$3D_\mathrm{FEM}$	62.5 / 70.4	80 / 80	41 / 41	−28 / −35
Measurement	61.4[1] / 69.4[1]	160 / 160	93 / 93	−28[3] / −37[3]

[1] Measurement at $\vartheta_\mathrm{PM,N}$ according to Section 4.3.1.
[2] At $n_\mathrm{N} = 60000\ \mathrm{min^{-1}}$.
[3] Measured at 20°C and scaled by $B^2_\mathrm{rem}(\vartheta_\mathrm{PM,N}) / B^2_\mathrm{rem}(20°\mathrm{C})$ according to Section 4.3.1

1D$_{\mathrm{an}}$: 1D analytical calculation

$$\hat{U}_{\mathrm{p}} = \frac{2}{\pi} \cdot \omega_{\mathrm{syn}} \cdot l_{\mathrm{Fe}} \cdot \tau_{\mathrm{p}} \cdot k_{\mathrm{w,D}} \cdot N_{\mathrm{s}} \cdot B_{\mathrm{rem}} \cdot \frac{h_{\mathrm{pm}}}{\delta_{\mathrm{eff}}} \tag{4.12}$$

2D$_{\mathrm{an,simp}}$: 2D analytical calculation

$$\hat{U}_{\mathrm{p}} = \frac{\frac{8}{\pi} \cdot \omega_{\mathrm{syn}} \cdot l_{\mathrm{Fe}} \cdot \tau_{\mathrm{p}} \cdot k_{\mathrm{w,D}} \cdot N_{\mathrm{s}} \cdot B_{\mathrm{rem}} \cdot \left[1 - \left(\frac{r_{\mathrm{sh}}}{r_{\mathrm{PM}}}\right)^2\right]}{\left(\mu_{\mathrm{r,PM}} - 1\right) \cdot \left(\frac{r_{\mathrm{sh}}^2 \cdot r_{\mathrm{S,i}}^2}{r_{\mathrm{PM}}^4} - 1\right) + \left(\mu_{\mathrm{r,PM}} + 1\right) \cdot \frac{r_{\mathrm{S,i}}^2 - r_{\mathrm{sh}}^2}{r_{\mathrm{PM}}^2}} \tag{4.13}$$

Measurement

Since the bearingless prototype machine *LLM4* was not operated as generator at no-load at the given test bench, the back-EMF U_{p} was determined from the motor no-load measurements in Section 4.3.2. The voltage drops $X_{\mathrm{q,D}} \cdot I_{\mathrm{q,D,0}} < 3$ V and $X_{\mathrm{q,L}} \cdot I_{\mathrm{q,L,0}} < 3$ V are very small for the *LLM4* in comparison to U_{P} at $n = 60000\ \mathrm{min}^{-1}$. Thus, U_{p} is approximated from the fundamental phase voltages $U_{\mathrm{U,A,1}}$, $U_{\mathrm{V,A,1}}$, ... as shown in (4.14).

$$\hat{U}_{\mathrm{p}} = \sqrt{2} \cdot \frac{U_{\mathrm{U,A,1}} + U_{\mathrm{V,A,1}} + U_{\mathrm{W,A,1}} + U_{\mathrm{U,B,1}} + U_{\mathrm{V,B,1}} + U_{\mathrm{W,B,1}}}{6} \tag{4.14}$$

4.2.2. Synchronous Inductance

Bearingless machines with surface-mounted magnets do not exhibit saliency, thus, $L_{\mathrm{d}} = L_{\mathrm{q}}$ holds. The analytical calculation of the stator winding synchronous inductance $L_{\mathrm{d,h}} = L_{\mathrm{q,h}}$ per phase comprises the calculation of the stray inductances, such as the winding overhang inductance $L_{\sigma,\mathrm{b}}$, the slot leakage inductance $L_{\sigma,\mathrm{Q}}$ and the harmonic stray inductance $L_{\sigma,\mathrm{o}}$, in addition to the calculation of the main inductance $L_{\mathrm{d,h}}$. Since a distributed winding with semi-closed slots is considered, the equations for the leakage inductances can be used from [94], as in the case of induction machines. With these formulas the slot stray inductance is determined to be $L_{\sigma,\mathrm{Q,D}} = 7.8\ \mu$H, $L_{\sigma,\mathrm{Q,L}} = 16\ \mu$H and the winding overhang inductance is $L_{\sigma,\mathrm{b,D}} = 5.5\ \mu$H, $L_{\sigma,\mathrm{b,L}} = 8.0\ \mu$H. The winding main inductance per phase of a $2\nu'$-pole stator winding, is calculated according to (4.15) which results in (4.16) for the 1D and in (4.17) for the simplified 2D calculation. A split into the

different stray and main inductances is given in Table 3.3.

$$L_{\mathrm{d,h},\nu'} = \frac{2 \cdot l_{\mathrm{Fe}} \cdot \tau_{\mathrm{p},\nu'}}{\pi} \cdot \frac{k_{\mathrm{w},\nu'} \cdot N_{\mathrm{s}}}{I_{\mathrm{s}}} \cdot \hat{B}_{\delta,\mathrm{r,S},\nu'} \left(r_{\mathrm{cal}} = r_{\mathrm{S,i}}\right) \tag{4.15}$$

1D$_{\mathrm{an}}$: 1D analytical calculation

$$L_{\mathrm{d,h},\nu'} = \frac{2 \cdot \mu_0 \cdot l_{\mathrm{Fe}} \cdot \tau_{\mathrm{p},\nu'} \cdot m \cdot k_{\mathrm{w},\nu'}^2 \cdot N_{\mathrm{s}}^2}{\nu' \cdot \pi^2 \cdot \delta_{\mathrm{eff}}} \tag{4.16}$$

2D$_{\mathrm{an,simp}}$: Simplified 2D analytical calculation

$$L_{\mathrm{d,h},\nu'} = \frac{2 \cdot \mu_0 \cdot m \cdot N_{\mathrm{s}}^2 \cdot k_{\mathrm{w},\nu'}^2 \cdot l_{\mathrm{Fe}}}{\pi \cdot \nu'} \cdot \frac{r_{\mathrm{s,i}}^{2\nu'} + r_{\mathrm{sh}}^{2\nu'}}{r_{\mathrm{S,i}}^{2\nu'} - r_{\mathrm{sh}}^{2\nu'}} \tag{4.17}$$

Measurement

Since the short-circuit current of the *LLM4* is very high and levitation is not possible during short-circuit, the synchronous inductance cannot be determined from no-load and short-circuit tests. Instead the motor is driven at its rated speed n_{N} ($f_{\mathrm{syn}} = 1000$ Hz), where the voltage drop at the winding resistance R_{s} is negligible, compared to the voltage drop at the inductances. From the measured current values $I_{\mathrm{d,D}}$, $I_{\mathrm{q,D}}$, $I_{\mathrm{d,L}}$, $I_{\mathrm{q,L}}$ and voltage values $U_{\mathrm{d,D}}$, $U_{\mathrm{q,D}}$, $U_{\mathrm{d,L}}$, $U_{\mathrm{q,L}}$ of the machine controller, the inductance of the drive winding $L_{\mathrm{d,D}}$ and of the suspension winding $L_{\mathrm{d,L}}$ are determined according to (4.18). Note that for $I_{\mathrm{q,D}} > 0$ the voltage drop in the d-axis is $U_{\mathrm{d,D}} < 0$. The procedure is adopted from [23].

$$L_{\mathrm{d,D}} = -\frac{U_{\mathrm{d,D}}}{\omega_{\mathrm{syn}} \cdot I_{\mathrm{q,D}}} \; ; \quad L_{\mathrm{d,L}} = \frac{\sqrt{U_{\mathrm{d,L}}^2 + U_{\mathrm{q,L}}^2}}{\omega_{\mathrm{syn}} \cdot \sqrt{I_{\mathrm{d,L}}^2 + I_{\mathrm{q,L}}}} \tag{4.18}$$

4.2.3. Axial AMB Inductance

For the analysis of the zero-sequence current feeding in Chapter 6 and 7 the inductance L_{ax} and the resistance R_{ax} of the winding of the axial active magnetic bearing is needed, since the its impedance $\underline{Z}_{\mathrm{ax}}$ between the two star-points $\mathrm{N_A}$ and $\mathrm{N_B}$ consists of $\underline{Z}_{\mathrm{ax}} = R_{\mathrm{ax}} + j\omega L_{\mathrm{ax}}$ for sinusoidal currents with angular frequencies ω. For the measurement of this impedance, the axial AMB is operated with the 4-quadrant chopper to exclude

the stator winding impedance. The DC winding resistance of the axial AMB is measured to be $R_{ax} = 0.875\ \Omega$ at 20 °C. For the measurement of the inductance L_{ax}, a voltage $u_{ax} = \hat{U}_{ax} \cdot \sin(2\pi \cdot f \cdot t)$ with variable frequency f and fixed amplitude $\hat{U}_{ax}$ is applied to the axial AMB by the inverter (Table A.3 in the Appendix). The voltage u_{ax} and the current i_{ax} are measured with a differential voltage probe, a current probe and an oscilloscope (Appendix A.24). After performing a *Fourier* analysis to get the f-frequent voltage and current components $\hat{U}_{ax}$ and $\hat{I}_{ax}$, L_{ax} is calculated from (4.19) with the amplitudes $\hat{U}_{ax}$, $\hat{I}_{ax}$ of the f-frequent oscillations. It is given for various frequencies f in Fig. 4.3 which shows that the inductance is constant, as long as the eddy currents are resistance-limited ($f < 3$ Hz). The inductance with rising frequency $f > 3$ Hz decreases in the solid conductive iron parts of the axial AMB.

$$L_{ax} = \frac{1}{2\pi \cdot f} \cdot \sqrt{\frac{\hat{U}_{ax}^2}{\hat{I}_{ax}^2} - R_{ax}^2} \tag{4.19}$$

Since the harmonics with frequencies close to f_{sw} and $2f_{sw}$ dominate the voltage and current characteristics for $f > 2000$ Hz, the values for L_{ax} are fitted for higher frequencies (red curve in Fig. 4.3). According to [91], inductance-limited eddy currents lead to the relationship $L_{ax} \propto d_E \propto 1/\sqrt{f}$, where $d_E \propto 1/\sqrt{f}$ is the penetration depth of the eddy currents in the solid conductive parts of the axial AMB. Thus, (4.20) is used as a fitting function with $\omega = 2\pi \cdot f$, including the measurement values for $f = 100 \ldots 2000$ Hz (Fig. 4.3).

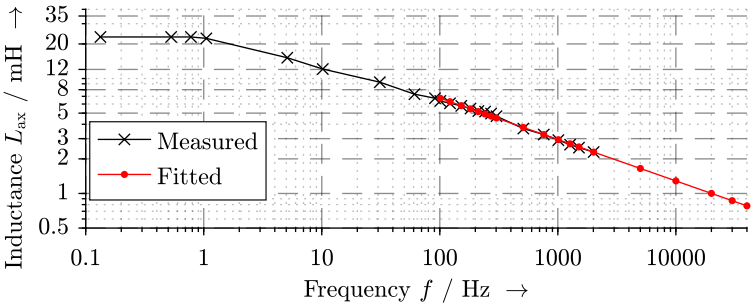

Fig. 4.3.: Measured inductance L_{ax} for varying frequency f for the *LLM4* with the Sm_2Co_{17}-rotor

$$\lg\left(\frac{L_{\mathrm{ax}}(\omega)}{L_{\mathrm{ax}}(\omega_0)}\right) = a\cdot\lg\left(\frac{\omega}{\omega_0}\right) \;\rightarrow\; \lg\left(L_{\mathrm{ax}}(\omega)\right) = \lg\left(L_{\mathrm{ax}}(\omega_0)\right) + a\cdot\lg\left(\frac{\omega}{\omega_0}\right), \quad (4.20)$$

$$\text{where } a = -0.36,\ \omega_0 = 2\pi\cdot 100\ \text{Hz},\ L_{\mathrm{ax}}(\omega_0) = 6.7\ \text{mH}$$

A significant decrease of L_{ax} is identified in Fig. 4.3 for frequencies $f > 10$ Hz which leads to an increased current ripple in the winding of the axial AMB, caused by the inverter switching ($f_{\mathrm{sw}} = 33$ kHz). The frequency dependency of L_{ax} is not included in the simulations of Chapter 6 and 7, so that the increased current ripple by a decrease of L_{ax} is neglected in the simulations.

4.2.4. Static Magnetic Stiffness

If the rotor is not centered in the stator iron bore due to eccentricity, a single-sided magnetic pull occurs. Mainly two types of eccentricities can be distinguished: Static and dynamic eccentricity [131], [132]. Static eccentricity means that the rotor rotates around its center point but this rotational axis is displaced from the concentric stator bore position. In the context of magnetically suspended drives this can happen if actuator and sensor planes are not concentric due to manufacturing inaccuracies. Dynamic eccentricity occurs if the rotor center point whirls around the geometric center of the stator bore. At super-critical speed n (speed above the rigid body eigenfrequencies, but below the bending eigenfrequencies), the principal axis of inertia coincides with the stator bore center axis, but the geometric center axis of the rotor whirls around the principal axis of inertia with the same speed n. Independent of the kind of eccentricity, a radial magnetic force acts on the rotor which pulls the rotor towards stator in the axis which is aligned with the narrowest part of the air gap as single-sided magnetic pull. For the position control the ratio $k_{\mathrm{s,DE}}$ between this force and the magnitude of radial eccentricity is important. Even though it is a static consideration, it gives a first guess for the required controller proportional gain. Note that for reliable system investigation always the dynamic stiffness $k_{\mathrm{s}}(\omega)$ as the inverse of the disturbance transfer function (= dynamic compliance) must be considered.

The influence of the single-sided magnetic pull has been extensively discussed in literature not only for high-speed PM motors, but also for induction machines which are sensitive to single-sided pull, caused by eccentricity, due to their small air gap. For the latter,

often 1-dimensional permeance functions are used to consider the air gap variation and to calculate the single-sided pull [131]. However, this leads to a strong over-estimation of the forces for PM machines with a big magnetically effective air gap, since the radial field component is not radially constant along the air gap width. Moreover, the tangential field component must be considered as well.

Commonly a bi-linear conformal mapping method is used in order to solve this problem analytically [102]. Alternatively, the perturbation method according to [103, 23] can be used which results in (4.21) for a 2-pole machine. Due to its negative value, a decrease of the air gap width yields an increase of the magnetic pull. A detailed derivation is given in [23]. Note that all 2D calculations and simulations can only consider translational eccentricity in the *x*-*y*-plane, but no tilting influence of the rotor in the *x*-*z*- and *y*-*z*-plane.

2D$_{\mathrm{an}}$: 2D analytical calculation

$$k_{\mathrm{s,DE}} = -\frac{\pi \cdot \mathrm{l_{Fe}} \left[\left(1+\mu_{\mathrm{r,PM}}\right) - \left(1-\mu_{\mathrm{r,PM}}\right) \cdot \frac{r_{\mathrm{sh}}^4}{r_{\mathrm{PM}}^4} \right]}{\mu_0 \cdot \left[\left(\mu_{\mathrm{r,PM}}+1\right) \cdot \left(1-\frac{r_{\mathrm{sh}}^4}{r_{\mathrm{s,i}}^4}\right) + \left(1-\mu_{\mathrm{r,PM}}\right) \cdot \left(\frac{r_{\mathrm{PM}}^4}{r_{\mathrm{s,i}}^4} - \frac{r_{\mathrm{sh}}^4}{r_{\mathrm{PM}}^4}\right) \right]} \cdot \tag{4.21}$$

$$B_{\mathrm{rem}} \cdot \frac{\left[\left(1+\frac{r_{\mathrm{S,i}}}{r}\right)^2\right] \cdot \left[1-\left(\frac{r_{\mathrm{sh}}}{r_{\mathrm{PM}}}\right)^2\right]}{\left(\mu_{\mathrm{r,PM}}-1\right) \cdot \left(\frac{r_{\mathrm{sh}}^2 \cdot r_{\mathrm{S,i}}^2}{r_{\mathrm{PM}}^4} - 1\right) + \left(\mu_{\mathrm{r,PM}}+1\right) \cdot \frac{r_{\mathrm{S,i}}^2 - r_{\mathrm{sh}}^2}{r_{\mathrm{PM}}^2}}$$

Measurement

For the measurement of $k_{\mathrm{s,DE}}$ (and also $k_{\mathrm{s,NDE}}$) the following procedure is taken: a): Determination of $k_{\mathrm{F,DE}}$ according to Section 4.1.2; b): Measurement of the suspension currents $i_{\mathrm{d,L}}$, $i_{\mathrm{q,L}}$ and $i_{\mathrm{x,NDE}}$, $i_{\mathrm{y,NDE}}$ at a shift of the rotor in *x*-direction at the DE and NDE as $x_{+,\mathrm{DE}} = x_{+,\mathrm{NDE}} = +10\,\mu\mathrm{m}$ ($i_{\mathrm{x},+,\mathrm{DE}} = i_{\mathrm{d},+,\mathrm{L}}$, $i_{\mathrm{x},+,\mathrm{NDE}}$) and as $x_{-,\mathrm{DE}} = x_{-,\mathrm{NDE}} = -10\,\mu\mathrm{m}$ ($i_{\mathrm{x},-,\mathrm{DE}} = i_{\mathrm{d},-,\mathrm{L}}$, $i_{\mathrm{x},-,\mathrm{NDE}}$) at rotor standstill for 10 different rotor angle positions γ_{S}; c): Calculation of $k_{\mathrm{s},\parallel}(\gamma_{\mathrm{S}})$, $k_{\mathrm{s},\perp}(\gamma_{\mathrm{S}})$ according to (4.22) at the DE and at the NDE.

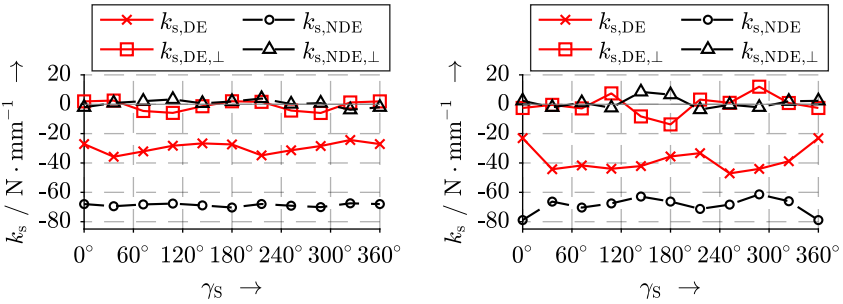

(a) Sm_2Co_{17}-rotor (b) NdFeB-rotor

Fig. 4.4.: Measured static magnetic stiffness coefficients k_s of the *LLM4* for varying rotor angles γ_S ($k_{s,\parallel,DE} = k_{s,DE}$, $k_{s,\parallel,NDE} = k_{s,NDE}$)

$$\begin{cases} k_{s,\parallel,DE}(\gamma_S) = -\frac{|i_{x,+,DE}(\gamma_S) - i_{x,-,DE}(\gamma_S)| \cdot k_{F,DE}}{x_{+,DE} - x_{-,DE}} = k_{s,DE}(\gamma_S) \\ k_{s,\perp,DE}(\gamma_S) = -\frac{|i_{y,+,DE}(\gamma_S) - i_{y,-,DE}(\gamma_S)| \cdot k_{F,DE}}{x_{+,DE} - x_{-,DE}} \\ k_{s,\parallel,NDE}(\gamma_S) = -\frac{|i_{x,+,NDE}(\gamma_S) - i_{x,-,NDE}(\gamma_S)| \cdot k_{F,NDE}}{x_{+,NDE} - x_{-,NDE}} = k_{s,NDE}(\gamma_S) \\ k_{s,\perp,NDE}(\gamma_S) = -\frac{|i_{y,+,NDE}(\gamma_S) - i_{y,-,NDE}(\gamma_S)| \cdot k_{F,NDE}}{x_{+,NDE} - x_{-,NDE}} \end{cases} \tag{4.22}$$

Due to manufacturing tolerances and sensor deficiencies the rotor does not move parallelly at the DE and the NDE, resulting in a small rotor tilting. This tilting also causes a perpendicular rotor force, leading to a cross-coupling negative stiffness $k_{s,\perp}$ in y-direction. Since $k_{s,\perp}$ is small ($k_{s,\perp} < k_{s,\parallel}/5$), only the aligned components $k_{s,\parallel,DE}$ and $k_{s,\parallel,NDE}$ are of major interest for the position control in Chapter 5. Therefore, in this work the nomenclature $k_{s,\parallel,DE} = k_{s,DE}$ and $k_{s,\parallel,NDE} = k_{s,NDE}$ is used.

Fig. 4.4 shows the measured negative magnetic stiffness coefficient for varying circumferential rotor position. One can identify that the negative stiffness coefficient in the bearingless machine $k_{s,DE}$ varies nearly sinusoidally with γ_S with the period 180°. This sinusoidal variation is, as explained in Section 2.7, due to the single-sided magnetic asymmetry of the PM on the shaft. The calculation of the axial static magnetic stiffness coefficient $k_{s,ax}$ is done in the same way, using the results for $k_{F,ax}$ from Section 4.1.2. However, $k_{s,ax}$ does of course not vary with the rotor angle γ_S. Table 4.5 summarizes the results.

Table 4.5.: Measured static magnetic stiffness coefficients k_s for the *LLM4* ($k_{s,\parallel,DE} = k_{s,DE}$, $k_{s,\parallel,NDE} = k_{s,NDE}$)

	Sm_2Co_{17}-rotor			NdFeB-rotor		
	Max.	Mean	Min.	Max.	Mean	Min.
$k_{s,DE}$ / N · mm^{-1}	−29.4	−29.3	−35.8	−23.1	−37.9	−47.1
$k_{s,\perp,DE}$ / N · mm^{-1}	2.5	−1.0	−5.9	11.9	−0.5	−13.7
$k_{s,NDE}$ / N · mm^{-1}	−67.5	−68.7	−70.3	−61.4	−68.9	−78.9
$k_{s,\perp,NDE}$ / N · mm^{-1}	3.9	0.5	−3.8	11.3	1.5	−4.9
$k_{s,z}$ / N · mm^{-1}	–	−159.0	–	–	−233.7	–

4.3. Indirect Efficiency Measurement

At the test bench (Fig. A.24 in the Appendix), the *LLM4* was operated at motor no-load and load. A coupling with a load machine was not feasible. Thus, no mechanical quantities can be directly measured. The motor was loaded with three free-blowing propeller wheels without a propeller housing (*Load A*, *Load B*, *Load C*) of an automotive turbo-charger application (Fig. 4.5).

For the measurement of the phase voltages and currents of the *LLM4* a *Norma* power analyzer was used (Appendix, Table A.10). The DC-link voltage and and the inverter input current were measured with a *Zimmer* power analyzer (Appendix, Table A.11).

The composition of losses in a bearingless machine is visualized in Fig. 4.6, which also

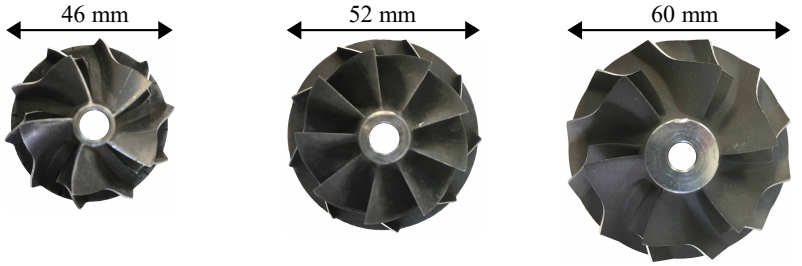

(a) *Load A*: $n = 60000$ min^{-1}, $P_m \approx 840$ W (b) *Load B*: $n = 55062$ min^{-1}, $P_m \approx 980$ W (c) *Load C*: $n = 42600$ min^{-1}, $P_m \approx 1060$ W

Fig. 4.5.: Turbo-charger propeller wheels as load for the *LLM4*

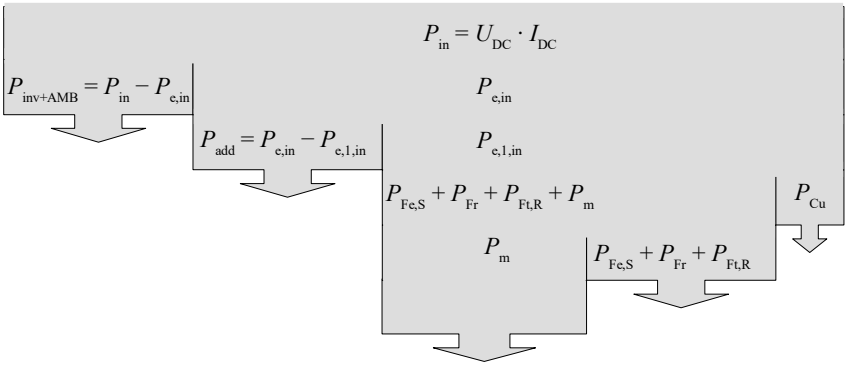

Fig. 4.6.: Power flow for the bearingless machine prototype *LLM4* (proportions not to scale)

shows, how the different loss groups are determined by measurements. The I^2R-losses P_{Cu} in the combined drive and suspension stator winding are calculated in (4.23) with the fundamental phase RMS currents $I_{\mathrm{U,A,1}}$, $I_{\mathrm{V,A,1}}$... and the winding temperature ϑ from Fig. 4.7.

$$P_{\mathrm{Cu}}(\vartheta) = R_{\mathrm{s}}(\vartheta) \cdot \left(I^2_{\mathrm{U,A,1}} + I^2_{\mathrm{V,A,1}} + I^2_{\mathrm{W,A,1}} + I^2_{\mathrm{U,B,1}} + I^2_{\mathrm{V,B,1}} + I^2_{\mathrm{W,B,1}} \right) \tag{4.23}$$

4.3.1. Two Methods of Temperature Measurement

To ensure accurate power measurements, the machine must be operated in thermal steady state conditions. Fig. 4.7 shows the temperature rise at different position at the *LLM4* at no-load and at *Load A* conditions. The temperature ϑ is measured with PT100 sensors in the winding overhang of the bearingless machine winding, at the radial position sensor of the drive end, at the radial position sensor of the non-drive end. The permanent magnet temperature ϑ_{PM} is determined via a back-EMF measurement according to (4.14),(4.24) with the knowledge of the temperature coefficient $\alpha_{\mathrm{th,rem}}$ from Table 3.14.

$$\Delta\vartheta_{\mathrm{PM}} = \frac{1 - \frac{U_{\mathrm{p}} = f(\vartheta_{\mathrm{PM}})}{U_{\mathrm{p,20°C}}}}{\alpha_{\mathrm{th,rem}}} \;\Rightarrow\; \vartheta_{\mathrm{PM}} = \Delta\vartheta_{\mathrm{PM}} + \vartheta_{\mathrm{amb}} \text{ , where } \vartheta_{\mathrm{amb}} = 29°\mathrm{C} \tag{4.24}$$

The ambient air temperature during the measurements was $\vartheta_{amb} = 29\,^{\circ}\mathrm{C}$. The *LLM4* is not actively cooled, but its housing contains cooling fins (Fig. 1.1a) to increase the motor

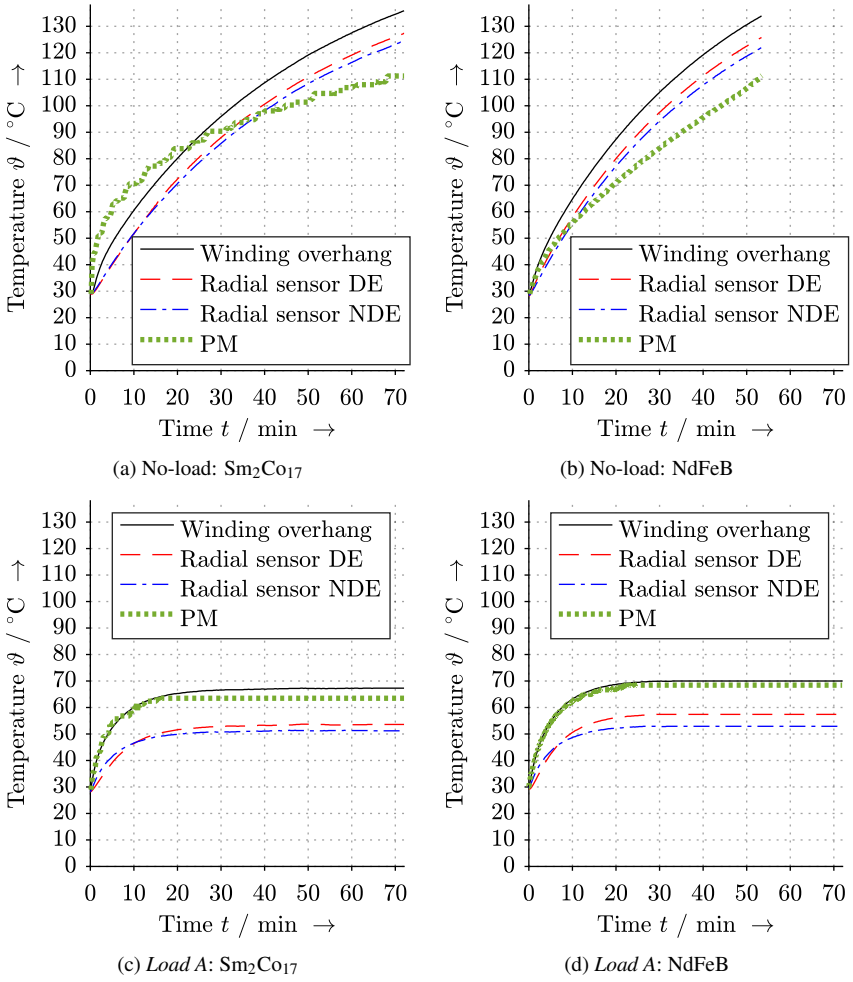

(a) No-load: Sm_2Co_{17}

(b) No-load: NdFeB

(c) *Load A*: Sm_2Co_{17}

(d) *Load A*: NdFeB

Fig. 4.7.: Measured temperature ϑ of the *LLM4* at motor no-load and *Load A* ($P_m = P_N = 1000$ W) both at rated speed ($n_N = 60000\ \mathrm{min}^{-1}$, ambient air temperature: $\vartheta_{amb} = 29\,^{\circ}\mathrm{C}$)

surface. Thus, the thermal resistance from the housing to the environment is decreased. The used machine winding is designed according to Thermal Class F, allowing for a temperature limit of $\vartheta = 155\ ^\circ\text{C}$ and a temperature rise of $\Delta\vartheta = 105$ K at $\vartheta_{\text{amb}} = 50\ ^\circ\text{C}$ (*IEC 60034-1* standard [124]). Fig. 4.7 shows that at load conditions the temperature rise is much lower than at no-load conditions due to the forced air convection by the free-blowing turbo-charger propeller wheels. However, at motor no-load, without the additional air flow of the propeller, the thermal limit $\Delta\vartheta = 105$ K is reached after 72 minutes for the Sm_2Co_{17} PM and after 53 minutes for the NdFeB PM due to the 15 W higher no-load losses (Table 4.6).

4.3.2. Measurements at Motor No-Load Operation

At motor no-load operation (subscript: "0") the following losses occur:

- Copper losses in the stator winding $P_{\text{Cu,0}}$ due to fundamental phase current flow, dominated by the suspension force producing current $i_{\text{q,L}}$
- Sum of the stator iron losses, the air friction losses and the rotor eddy current losses $P_{\text{Fe,S,0}} + P_{\text{Fr}} + P_{\text{Ft,R,0}}$ as "drag" losses $P_{\text{dr,0}}$

Table 4.6.: Measured and simulated no-load losses at $n_{\text{N}} = 60000/\text{min}^{-1}$ for the *LLM4* with the Sm_2Co_{17}/NdFeB-rotor

	$2D_{\text{FEM}}$	Measurement
Input power $P_{\text{in,0}}$ / W	–	248.6 / 274.4
Inverter, magnetic bearing losses $P_{\text{inv,AMB}}$ / W	–	71.9 / 78.0
Motor input power $P_{\text{e,in,0}}$ / W	–	176.7 / 196.4
Additional losses[3)] $P_{\text{add,0}}$ / W	–	37.0 / 41.9
Motor fundamental input power $P_{\text{e,1,in,0}}$ / W	133.9 / 147.4	139.7 / 154.5
Copper losses $P_{\text{Cu,0}}$ / W	1.5 / 1.2	1.7 / 1.5
Drag losses $P_{\text{dr,0}} = P_{\text{Fe,S,0}} + P_{\text{Fr}} + P_{\text{Ft,R,0}}$ / W	132.4 / 146.1	138.0 / 153.0
Iron losses $P_{\text{Fe,S,0}}$ / W	58.0 / 72.3	63.7 / 79.3
Air friction losses P_{Fr} / W	72.2[1)] / 72.2[1)]	72.2 / 72.2
Rotor eddy current losses[2)] $P_{\text{Ft,R,0}}$ / W	2.2 / 1.6	2.2 / 1.6

[1)] From measurement; [2)] From $3D_{\text{FEM}}$; [3)] Due to inverter feeding

- Additional losses due to inverter feeding $P_{\mathrm{add,0}}$ such as I^2R-losses, caused by current harmonics, and additional rotor eddy current losses

- Sum of the internal inverter losses and the radial magnetic bearing losses $P_{\mathrm{inv,AMB}}$

According to Fig. 4.6 the sum of the internal inverter losses and the radial magnetic bearing losses $P_{\mathrm{inv,AMB}}$ is determined as $P_{\mathrm{inv,AMB}} = P_{\mathrm{in,0}} - P_{\mathrm{e,in,0}}$. The additional losses due to inverter feeding $P_{\mathrm{add,0}}$ are given by the subtraction of the fundamental input power $P_{\mathrm{e,1,in,0}}$ from the motor electric input power $P_{\mathrm{e,in,0}}$ ($P_{\mathrm{add,0}} = P_{\mathrm{e,in,0}} - P_{\mathrm{e,1,in,0}}$). The I^2R-losses $P_{\mathrm{Cu,0}}$ are calculated with the RMS values of the fundamental phase currents at no-load via (4.23). The "drag" losses P_{dr} are the sum of the stator iron losses $P_{\mathrm{Fe,S,0}}$, the air friction losses P_{Fr} and the rotor eddy current losses $P_{\mathrm{Ft,R,0}}$. They are determined by the subtraction of the I^2R-losses $P_{\mathrm{Cu,0}}$ from fundamental input power $P_{\mathrm{e,1,in,0}}$ ($P_{\mathrm{dr,0}} = P_{\mathrm{e,1,in,0}} - P_{\mathrm{Cu,0}}$). Since the no-load measurement is conducted with two different PM materials, the iron losses $P_{\mathrm{Fe,S,0}}$ and the air friction losses P_{Fr} can be determined by (4.25), (4.26). For example, the stator iron losses for the Sm_2Co_{17}-rotor are calculated in (4.27).

$$P_{\mathrm{Fe,S,0,Sm}} + P_{\mathrm{Fr}} = P_{\mathrm{dr,0,Sm}} - P_{\mathrm{Ft,R,0,Sm}}{}^{*} \qquad {}^{*}) \text{ from } 3\mathrm{D}_{\mathrm{FEM}} \tag{4.25}$$

$$P_{\mathrm{Fe,S,0,Sm}} \cdot \left(\frac{B_{\mathrm{rem,Nd}}}{B_{\mathrm{rem,Sm}}}\right)^2 + P_{\mathrm{Fr}} = P_{\mathrm{dr,0,Nd}} - P_{\mathrm{Ft,R,0,Nd}}{}^{*} \qquad {}^{*}) \text{ from } 3\mathrm{D}_{\mathrm{FEM}} \tag{4.26}$$

$$P_{\mathrm{Fe,S,0,Sm}} = B_{\mathrm{rem,Sm}}^2 \cdot \frac{\left(P_{\mathrm{dr,0,Nd}} - P_{\mathrm{Ft,R,0,Nd}}\right) - \left(P_{\mathrm{dr,0,Sm}} - P_{\mathrm{Ft,R,0,Sm}}\right)}{B_{\mathrm{rem,Nd}}^2 - B_{\mathrm{rem,Sm}}^2} \tag{4.27}$$

As expected, the no-load losses are higher for the NdFeB-rotor than for the Sm_2Co_{17}-rotor due to the remanence flux density B_{rem}, which is higher by the factor $B_{\mathrm{rem,Nd}}/B_{\mathrm{rem,Sm}} = 1.07/0.95 = 1.12$ at $\vartheta_{\mathrm{PM}} = 70\ ^{\circ}\mathrm{C}$.
Table 4.6 compares the measured no-load losses with the simulated no-load losses. In the 2D FEM simulation, the measured drive and suspension currents $i_{\mathrm{q,D}}$, $i_{\mathrm{q,L}}$ are impressed as current fundamentals. The simulated tooth, respectively yoke iron losses are multiplied with the factor 1.9, respectively 1.4, to account for the loss increase due to the punching of the iron sheets [105]. The used material for the iron sheets is M270-35A (Appendix A.14) [93]. The stator iron losses $P_{\mathrm{Fe,S,0}}$ are roughly 10% lower in the 2D FEM simulation than in the measurement due to the neglect of the axially 4 mm longer rotor PM ring on both machine ends, which increases the main flux.
Three major loss groups are identified which determine the thermal limit of bearingless machines: The iron losses $P_{\mathrm{Fe,S}}$ due to high synchronous frequency of $f_{\mathrm{syn}} = 1000$ Hz

and the air friction losses P_{Fr} due to the high rotor surface speed of $v_{\mathrm{R}} = 104\ \mathrm{m \cdot s^{-1}}$, which is typical for high-speed machines. Also the additional losses due to the inverter feeding P_{add} play an important role. This is due to the small machine inductance values (Section 4.2.2), which lead to a big harmonic ripple of the phase currents (Fig. 4.8). The current harmonics in Fig. 4.8 close to the frequency $f = f_{\mathrm{sw}}/2 = 16$ kHz are due to the position controller, whose sampling frequency is $f_{\mathrm{sw}}/2$. The nature of the other dominating harmonic orders is discussed in Section 6.5. The total harmonic distortion THD_{I} of the phase currents is calculated according to (4.28) [133] as the RMS value of all harmonics apart from the fundamental with respect to the fundamental. Note that usually the THD_{I} does not include DC current components, however, here I_0 must be considered due to the zero-sequence current feeding of the axial AMB (Chapter 6). Fig. 4.8a and Fig. 4.8b show the amplitude *Fourier* spectrum of the phase current $I_{\mathrm{U,A}}$ at no-load and load. For the Sm_2Co_{17}-rotor, the mean values of the THD_{I} over all phases $\mathrm{U_A}$, $\mathrm{V_A}$, $\mathrm{W_A}$, $\mathrm{U_B}$, $\mathrm{V_B}$ and $\mathrm{W_B}$ are $THD_{\mathrm{I}} = 81.0\ \%$ at no-load and $THD_{\mathrm{I}} = 41.3\ \%$ at *Load A* operation. These high THD_{I} values are due to the low synchronous inductance values (Section 4.2.2) for the prototype machine *LLM4*.

$$THD_{\mathrm{I}} = \frac{\sqrt{I_{\mathrm{s},0}^2 + \sum_{k=2}^{\infty} {I_{\mathrm{s},k}}^2}}{I_{\mathrm{s},1}} \tag{4.28}$$

The additional losses $P_{\mathrm{add},0}$ due to inverter feeding are higher by the factor $41.9/37 = 1.13$ for the NdFeB-rotor than for the Sm_2Co_{17}-rotor, since the inverter modulation degree

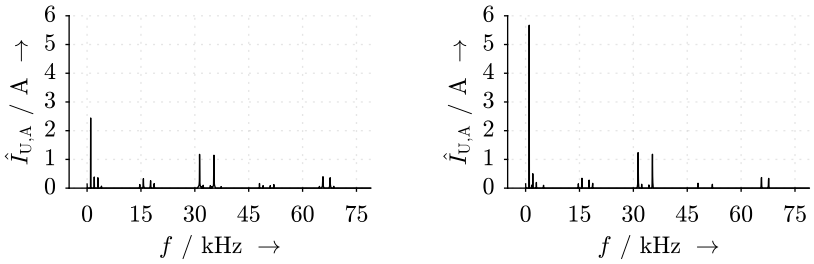

(a) No-load operation

(b) Operation at *Load A*

Fig. 4.8.: Measured *Fourier* amplitude spectrum of the phase current $i_{\mathrm{U,A}}$ at no-load and at *Load A* operation at rated speed n_{N} with $f_{\mathrm{sw}} = 33$ kHz for the *LLM4* with the Sm_2Co_{17}-rotor

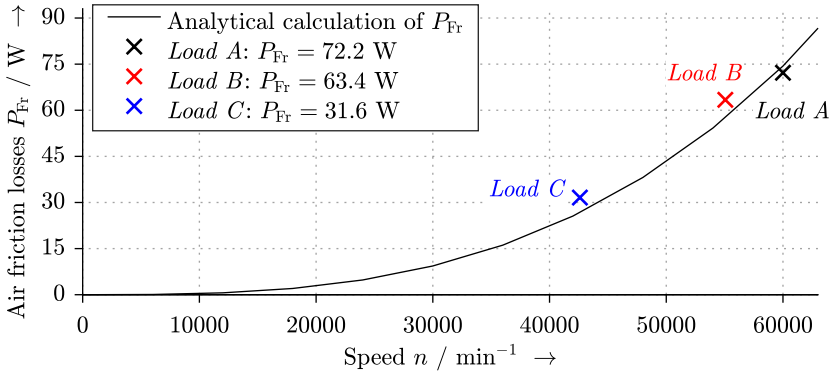

Fig. 4.9.: Analytically calculated air friction losses P_{Fr} at varying speed n with the average air gap air temperature $\vartheta_{amb} = 67$ °C and measured air friction losses at *Load A*, *Load B* and *Load C* for the Sm_2Co_{17}-rotor

m_a (Section 6.5) is higher, leading to increased voltage harmonics. For verification, the air friction losses P_{Fr} can also be determined via analytical formulas according to [125] which are based on empirical findings. Alternative approaches can be found in [134, 135]. Fig. 4.9 shows that the air friction losses significantly increase with speed according to $P_{Fr} \propto n^3$. The analytical calculation validates the measured air friction losses P_{Fr}. For the optimum design of high-speed machines, these dominating air friction losses must be included in the design process, as it is done in Section 3.5.
The no-load measurements were conducted right after each load measurement at approximately the same stator winding, air and PM temperature, since the measured air friction and stator iron losses are needed for the loss determination at load.

4.3.3. Measurements at Motor Operation with Different Loads

Measurements at motor operation at *Load A*, *Load B* and *Load C* (Fig. 4.5) were conducted. The following losses occur at load (subscript: "1"):

- I^2R-losses in the stator winding $P_{Cu,1}$ due to fundamental phase current flow, dominated by the torque producing q-current $i_{q,D}$, measured in the same way as at no-load

- Sum of the stator iron losses, the air friction losses and the rotor eddy current losses $P_{\mathrm{Fe,S,1}} + P_{\mathrm{Fr}} + P_{\mathrm{Ft,R,1}}$ as "drag" losses $P_{\mathrm{dr,1}}$
- Additional losses due to inverter feeding $P_{\mathrm{add,1}}$ such as harmonic I^2R-losses and additional rotor eddy current losses, which can be measured in the same way as at no-load
- Sum of the internal inverter losses and the radial magnetic bearing losses $P_{\mathrm{inv,AMB}}$, which can be measured in the same way as at no-load

The air friction losses are of course identical to the no-load operation. The eddy current losses $P_{\mathrm{Ft,R,1}}$ in the rotor due to the modulation of the air gap field by the slot frequent air gap permeance function are determined by the 2D FEM simulation. The stator iron losses $P_{\mathrm{Fe,S,1}}$ depend on the square of the main voltage drop $U_{\mathrm{h,1}}^2$. For the *LLM4*, $U_{\mathrm{h,1}} \approx U_{\mathrm{s,1}}$ holds due to the very small stray inductances (Table 3.3). Thus, the iron losses at load

Table 4.7.: Measured and simulated losses at *Load A* at $n_{\mathrm{N}} = 60000/\mathrm{min}^{-1}$ for the *LLM4* with the Sm_2Co_{17}/NdFeB-rotor

	$2D_{\mathrm{FEM}}$ *Load A*	Measurement *Load A*
Input power $P_{\mathrm{in,1}}$ / W	–	1129.9 / 1152.2
Inverter, magnetic bearing losses $P_{\mathrm{inv,AMB}}$ / W	–	101.4 / 113.5
Motor input power $P_{\mathrm{e,in,1}}$ / W	–	1028.5 / 1038.7
Motor additional losses $P_{\mathrm{add,1}}$ / W	–	39.0 / 46.2
Motor fundamental input power $P_{\mathrm{e,1,in,1}}$ / W	935.8 / 935.2	989.5 / 992.5
Copper losses $P_{\mathrm{Cu,1}}$ / W	8.5 / 6.7	9.2 / 7.6
Drag losses $P_{\mathrm{dr,1}} = P_{\mathrm{Fe,S,1}} + P_{\mathrm{Fr}} + P_{\mathrm{Ft,R,1}}$ / W	131.3 / 143.3	139.0 / 153.5
Iron losses $P_{\mathrm{Fe,S,1}}$ / W	58.1 / 72.4	63.7[3)] / 79.3[3)]
Air friction losses P_{Fr} / W	72.2[1)] / 72.2[1)]	72.2 / 72.2
Rotor eddy current losses[2)] $P_{\mathrm{Ft,R,1}}$ / W	3.1 / 2.0	3.1 / 2.0
Mechanical output power P_{m} / W	793.9 / 781.9	841.3 / 831.4
Motor efficiency η_{mot}	0.849 / 0.836	0.818 / 0.801
System efficiency η	–/–	0.745 / 0.722

[1)] From measurement; [2)] From $3D_{\mathrm{FEM}}$; [3)] From no-load measurement according to (4.29)

$P_{\mathrm{Fe,S,1}}$ can be calculated from the no-load iron losses $P_{\mathrm{Fe,S,0}}$ as in (4.29).

$$P_{\mathrm{Fe,1}} \approx P_{\mathrm{Fe,0}} \cdot \left(\frac{U_{\mathrm{s,1,1}}}{U_{\mathrm{s,1,0}}} \right)^2 \tag{4.29}$$

The measured loss values are compared to simulations by a 2D FEM model in Table 4.7. The 2D FEM simulation underestimates the stator iron losses $P_{\mathrm{Fe,S,1}}$ by roughly 10%, as explained in Section 4.3.2. They are nearly independent from load (compare $P_{\mathrm{Fe,S,0}}$ and $P_{\mathrm{Fe,S,1}}$ in the Tables 4.6, 4.7) due to the very small stator field ($\hat{B}_{\mathrm{D,r}}/\hat{B}_{\mathrm{R,r}} \approx 0.067$). Finally, the mechanical output power P_{m}, the motor efficiency η_{mot} and the system efficiency η are calculated in (4.30).

$$P_{\mathrm{m}} = P_{\mathrm{e,1,in,1}} - P_{\mathrm{Cu,1}} - P_{\mathrm{dr,1}} \; ; \quad \eta_{\mathrm{mot}} = \frac{P_{\mathrm{m}}}{P_{\mathrm{e,in,1}}}; \quad \eta = \frac{P_{\mathrm{m}}}{P_{\mathrm{in}}} \tag{4.30}$$

Table 4.8 shows the measured results for *Load B* and *Load C*. The iron losses $P_{\mathrm{Fe,S,1}}$, air

Table 4.8.: Measured losses at *Load B* at $n = 55062/\mathrm{min}^{-1}$ and *Load C* at $n = 42600/\mathrm{min}^{-1}$ for the *LLM4* with the Sm_2Co_{17}/NdFeB-rotor

	Measurement *Load B*	Measurement *Load C*
Input power $P_{\mathrm{in,1}}$ / W	1259.1 / 1284.2	1323.3 / 1332.0
Inverter, magnetic bearing losses $P_{\mathrm{inv,AMB}}$ / W	111.5 / 125.0	133.0 / 140.3
Motor input power $P_{\mathrm{e,in,1}}$ / W	1147.6 / 1159.2	1190.3 / 1191.7
Motor additional losses[3)] $P_{\mathrm{add,1}}$ / W	40.1 / 42.7	34.1 / 38.0
Motor fundamental input power $P_{\mathrm{e,1,in,1}}$ / W	1107.4 / 1116.5	1156.2 / 1153.7
Copper losses $P_{\mathrm{Cu,1}}$ / W	12.3 / 10.3	19.2 / 15.2
Drag losses $P_{\mathrm{dr,1}} = P_{\mathrm{Fe,S,1}} + P_{\mathrm{Fr}} + P_{\mathrm{Ft,R,1}}$ / W	118.0 / 129.9	75.5 / 84.8
Iron losses[2)] $P_{\mathrm{Fe,S,1}}$ / W	52.0 / 63.7	42.3 / 52.1
Air friction losses P_{Fr} / W	63.4 / 63.4	31.6 / 31.6
Rotor eddy current losses[1)] $P_{\mathrm{Ft,R,1}}$ / W	2.6 / 1.7	1.6 / 1.0
Mechanical output power P_{m} / W	977.1 / 976.6	1061.4 / 1053.8
Motor efficiency η_{mot}	0.852 / 0.843	0.892 / 0.884
System efficiency η	0.776 /0.760	0.802 / 0.791

[1)] From $3D_{\mathrm{FEM}}$; [2)] From no-load measurement according to (4.29); [3)] Due to inverter feeding

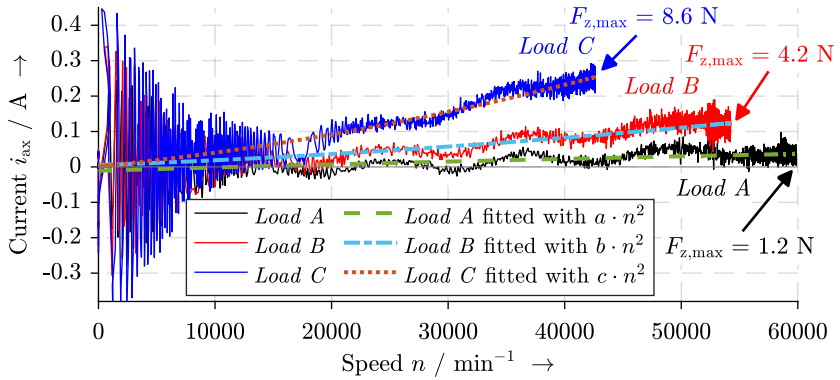

Fig. 4.10.: Measured axial AMB current i_{ax}, proportional to the turbo-charger axial thrust force, during run-up with *Load A*, *Load B* and *Load C* in horizontal rotor alignment (Motor *LLM4* with Sm_2Co_{17}-rotor, aliasing effect visible due to sampling frequency: $f_{samp} = 34.5$ Hz), controller sampling frequency $f_{sw}/2 = 16.5$ kHz

Table 4.9.: Measured zero-sequence current related losses at *Load C* at $n = 42600\text{min}^{-1}$ for the *LLM4* with the Sm_2Co_{17}-rotor for the 4-quadrant chopper feeding (4Q-CB-PWM) and the zero-sequence current feeding (CB-PWM)

	CB-PWM	4Q-CB-PWM
Inverter, magnetic bearing losses $P_{inv,AMB}$ / W	133.4	133.0
Motor additional losses[1)] $P_{add,1}$ / W	33.7	34.1

[1)]) Due to inverter feeding

friction losses P_{Fr} and additional inverter feeding losses $P_{add,1}$ in the *LLM4* dominate the total losses for both PM rotors, nearly independent of the load.

All the loss measurements were conducted while the zero-sequence current feeding of the axial active magnetic bearing was applied (Chapter 6, 7). Thus, the zero-sequence current in the winding phases of the *LLM4* also generates losses, which are generally assigned to the additional losses P_{add}. These *ohm*ic losses are very small ($P_{ax} < 1$ W) due to the resistance $R_{ax} = 0.875\ \Omega$ and the small axial AMB current $i_{ax} < 0.2$ A, which is shown in Fig. 4.10 for varying speed n. The relationship $F_z \propto n^2 \Rightarrow i_{ax} \propto n^2$ is confirmed due to the thrust force of the rotating propeller wheels which is $\propto n^2$. A test measurement with the 4-quadrant chopper feeding and zero-sequence feeding at *Load C* was conducted. The results are shown in Table 4.9, proving that the zero-sequence current feeding of an axial AMB does not significantly influence the machine's losses.

5. Four Degrees of Freedom Control of the Rigid Rotor

This chapter focuses on two aspects regarding the position control of "rigid" rotors, which is a valid simplification as long as the first bending mode eigenfrequency is about 1.2-times higher than the maximum rotor speed. Then only the rigid eigenmodes of rotor vibration occur and the elastic bending eigenmodes are neglected. The rotor vibration parallel to the z-axis is called parallel rigid body eigenmode, occurring at the angular frequencies $\omega_{\mathrm{par},+}$ and $\omega_{\mathrm{par},-}$. The conical movement of the rigid rotor around the z-axis is called the conical rigid rotor eigenmode, occurring at the angular frequencies $\omega_{\mathrm{con},+}$ and $\omega_{\mathrm{con},-}$. The subscript "+" denotes a whirl motion with $\omega_{\mathrm{par},+}$, $\omega_{\mathrm{con},+}$ in the same direction as the rotor rotation (forward whirl). The subscript "$-$" denotes a whirl motion with $\omega_{\mathrm{par},-}$, $\omega_{\mathrm{con},-}$ in the opposite direction (backward whirl).
First, the so called "centralized position control" approach is compared to the classical "decentralized position control" in terms of the system eigenvalues. The necessity of the centralized control approach is discussed a) at the example of the *LLM4* and b) on a flywheel energy storage system [136]. These two different drive units, both developed at the *Institute for Electrical Energy Conversion*, are chosen because the flywheel system exhibits a rather high ratio of polar to axial moment of inertia, whereas this ratio is low for the motor *LLLM4*. The consequence of these different properties is discussed.
Second, the impact of the eddy current effect, introduced in Section 2.4, and of the superposition effect, introduced in Section 2.5, on the rotor position control in bearingless machines is analyzed.
Active magnetic bearing control has been extensively discussed, e.g. in [4] and [5]. Therefore, this chapter solely addresses aspects which are necessary for the analysis of the aforementioned aspects.

5.1. Control Mechanism for Magnetically Suspended Drives

A rotor is discussed, whose six degrees of freedom are actively controlled. The tilting angles φ_y around the y-axis and φ_x around the x-axis are considered small, so that the movement in axial direction is decoupled and $\sin(\varphi) \approx \varphi$ holds. The one-dimensional axial movement in z-direction and the torque/speed control are not treated here. Further, the rotor is considered to be in the concentric position within the stator bore, having only small deviations from the operating point, so that a linearized approach is possible.

The nomenclature of the used terms is visualized in Fig. 5.1. The meaning of the variables are given in Table 5.1 along with the used values. The two rotor systems a) and b) with significantly different plant properties are considered: a) the bearingless prototype machine *LLM4* and b) a flywheel energy storage system [136]. The dimensions and the composition of the rotor of the *LLM4* is visualized in Fig. 3.2. The flywheel system was built as part of a different project at the *Institute for Electrical Energy Conversion*. However, the magnetic bearing control is part of this work [O08]. The composition, dimensions and pictures of the flywheel energy storage system are given in the Appendix A.20.

The mechanical differential equation, describing the rotor movement in the center of gravity (COG), is given in (5.1), where $\boldsymbol{M}$ is the mass matrix and $\boldsymbol{G}$ the matrix which accounts for the coupling between the tilting motions during rotation ($\Omega \neq 0$). Forces F_x, F_y and torques M_x, M_y, usually magnetically originated, are considered by the vector $\vec{F}$. The rotor position in the stationary inertial system x-y-z, originated in the COG, is described by $\vec{q}$.

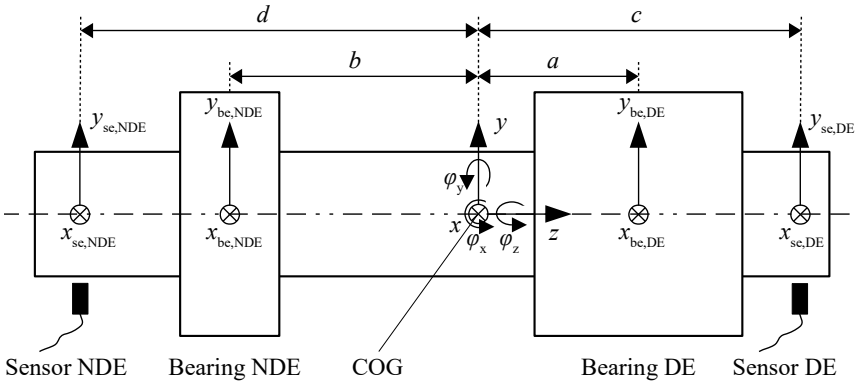

Fig. 5.1.: Nomenclature of the coordinate systems relevant for the rotor position control

Table 5.1.: Control system parameters a) of the bearingless machine *LLM4* and b) of the flywheel energy storage system (Appendix A.20), determined from measurements

	Bearingless machine *LLM4*[1)]	Flywheel energy storage system[2)]
Rated speed n_N / min^{-1}	60000	24000
Rated power P_N / kW	1	28
Mass m / kg	0.915	88.97
Axial moment of inertia Θ_{ax} / $\mathrm{kg \cdot mm^2}$	2551	1270653
Polar moment of inertia Θ_{pol} / $\mathrm{kg \cdot mm^2}$	117	589948
Distance between bearing NDE and COG a / mm	38.7	212.2
Distance between bearing DE and COG b / mm	20.4	310.8
Distance between sensor NDE and COG c / mm	53.6	182.4
Distance between sensor DE and COG d / mm	61.2	310.8
Distance between safety bearing NDE and COG a_{FL} / mm	85	268
Distance between safety bearing DE and COG b_{FL} / mm	78	363
Force-displacement coefficient NDE $k_{s,NDE}$ / $\mathrm{N \cdot mm^{-1}}$	−69	−350
Force-displacement coefficient DE $k_{s,DE}$ / $\mathrm{N \cdot mm^{-1}}$	−29	−540
Force-current coefficient NDE $k_{F,NDE}$ / $\mathrm{N \cdot A^{-1}}$	15	140
Force-current coefficient DE $k_{F,DE}$ / $\mathrm{N \cdot A^{-1}}$	1.0	34
Axial force-displacement coefficient $k_{s,z}$ / $\mathrm{N \cdot mm^{-1}}$	−159	−2300
Axial force-current coefficient $k_{F,ax}$ / $\mathrm{N \cdot A^{-1}}$	34	288

[1)] NDE: Combined radial axial AMB, DE: Bearingless machine; [2)] NDE: Combined radial axial AMB, DE: Radial AMB

$$\underbrace{\begin{pmatrix} m & 0 & 0 & 0 \\ 0 & \Theta_{ax} & 0 & 0 \\ 0 & 0 & m & 0 \\ 0 & 0 & 0 & \Theta_{ax} \end{pmatrix}}_{\boldsymbol{M}} \underbrace{\begin{pmatrix} \ddot{x} \\ \ddot{\varphi}_y \\ \ddot{y} \\ \ddot{\varphi}_x \end{pmatrix}}_{\ddot{\vec{q}}} + \underbrace{\begin{pmatrix} 0 & 0 & 0 & 0 \\ 0 & 0 & 0 & -\Theta_{pol} \cdot \Omega \\ 0 & 0 & 0 & 0 \\ 0 & \Theta_{pol} \cdot \Omega & 0 & 0 \end{pmatrix}}_{\boldsymbol{G}} \underbrace{\begin{pmatrix} \dot{x} \\ \dot{\varphi}_y \\ \dot{y} \\ \dot{\varphi}_x \end{pmatrix}}_{\dot{\vec{q}}} = \underbrace{\begin{pmatrix} F_x \\ M_y \\ F_y \\ M_x \end{pmatrix}}_{\vec{F}} \tag{5.1}$$

The forces $F_{\mathrm{x,be}}$, $F_{\mathrm{y,be}}$ act on the rotor in the bearing planes at the non-drive end (NDE) and at the drive end (DE), which are distanced by a and b from the COG. The position signals for the closed-loop feedback are monitored in the sensor planes at the NDE and at the DE, which are distanced by c and d from the COG (Fig. 5.1). The rotor position deviation in the bearing planes is described by $\vec{q}_{\mathrm{be}}$ (5.2) in the bearing planes and by $\vec{q}_{\mathrm{se}}$ (5.3) in the sensor planes. Bearing planes and sensor planes are at different axial positions a, respectively c, and b, respectively d, so they are non-collocated. The bearing forces at the DE $F_{\mathrm{x,DE}}$, $F_{\mathrm{y,DE}}$ and at the NDE $F_{\mathrm{x,NDE}}$, $F_{\mathrm{y,NDE}}$ are summarized in $\vec{F}_{\mathrm{be}}$ (5.4). In order to integrate the motions $\vec{q}_{\mathrm{be}}$, $\vec{q}_{\mathrm{se}}$ and forces $\vec{F}_{\mathrm{be}}$ in these three planes (COG, sensor, bearing) into (5.1), the transformations (5.2)–(5.4) are used, assuming that the tilting angles φ_{x}, φ_{y} are small.

$$\underbrace{\begin{pmatrix} x_{\mathrm{be,NDE}} \\ x_{\mathrm{be,DE}} \\ y_{\mathrm{be,NDE}} \\ y_{\mathrm{be,DE}} \end{pmatrix}}_{\vec{q}_{\mathrm{be}}} = \underbrace{\begin{pmatrix} 1 & -a & 0 & 0 \\ 1 & b & 0 & 0 \\ 0 & 0 & 1 & a \\ 0 & 0 & 1 & -b \end{pmatrix}}_{\boldsymbol{T}_{\mathrm{q,COG,be}}} \underbrace{\begin{pmatrix} x \\ \varphi_{\mathrm{y}} \\ y \\ \varphi_{\mathrm{x}} \end{pmatrix}}_{\vec{q}} \tag{5.2}$$

$$\underbrace{\begin{pmatrix} x_{\mathrm{se,NDE}} \\ x_{\mathrm{se,DE}} \\ y_{\mathrm{se,NDE}} \\ y_{\mathrm{se,DE}} \end{pmatrix}}_{\vec{q}_{\mathrm{se}}} = \underbrace{\begin{pmatrix} 1 & -c & 0 & 0 \\ 1 & d & 0 & 0 \\ 0 & 0 & 1 & c \\ 0 & 0 & 1 & -d \end{pmatrix}}_{\boldsymbol{T}_{\mathrm{q,COG,se}}} \underbrace{\begin{pmatrix} x \\ \varphi_{\mathrm{y}} \\ y \\ \varphi_{\mathrm{x}} \end{pmatrix}}_{\vec{q}} \tag{5.3}$$

$$\underbrace{\begin{pmatrix} F_{\mathrm{x}} \\ M_{\mathrm{y}} \\ F_{\mathrm{y}} \\ M_{\mathrm{x}} \end{pmatrix}}_{\vec{F}} = \underbrace{\begin{pmatrix} 1 & 1 & 0 & 0 \\ -a & b & 0 & 0 \\ 0 & 0 & 1 & 1 \\ 0 & 0 & a & -b \end{pmatrix}}_{\vec{T}_{\mathrm{F,be,COG}}} \underbrace{\begin{pmatrix} F_{\mathrm{x,NDE}} \\ F_{\mathrm{x,DE}} \\ F_{\mathrm{y,NDE}} \\ F_{\mathrm{y,DE}} \end{pmatrix}}_{\vec{F}_{\mathrm{be}}} \tag{5.4}$$

By means of (5.2)–(5.4) the motion equation (5.1) is extended to the bearing and sensor planes. In the first step, the inherently given magnetic forces $\vec{F}_{\mathrm{be}}$ due to the biasing magnetic field are included. The negative magnetic stiffness coefficients are given by $k_{\mathrm{s,NDE}}$ and $k_{\mathrm{s,DE}}$ as the derivative of the radial force with respect to the deviation from the rotor concentric position (see Section 4.2). Along with that, in (5.5) the controlled forces $\vec{F}_{\mathrm{be}}$ by the magnetic bearing currents $\vec{i}$ and the linearized force-current coefficients $k_{\mathrm{F,NDE}}$ and

$k_{\mathrm{F,DE}}$ (see Section 4.1.2) are considered.

$$\underbrace{\begin{pmatrix} F_{\mathrm{x,NDE}} \\ F_{\mathrm{x,DE}} \\ F_{\mathrm{y,NDE}} \\ F_{\mathrm{y,DE}} \end{pmatrix}}_{\vec{F}_{\mathrm{be}}} = -\underbrace{\begin{pmatrix} k_{\mathrm{s,NDE}} & 0 & 0 & 0 \\ 0 & k_{\mathrm{s,DE}} & 0 & 0 \\ 0 & 0 & k_{\mathrm{s,NDE}} & 0 \\ 0 & 0 & 0 & k_{\mathrm{s,DE}} \end{pmatrix}}_{\boldsymbol{K}_{\mathrm{s}}} \underbrace{\begin{pmatrix} x_{\mathrm{NDE}} \\ x_{\mathrm{DE}} \\ y_{\mathrm{NDE}} \\ y_{\mathrm{DE}} \end{pmatrix}}_{\vec{q}_{\mathrm{be}}} + \underbrace{\begin{pmatrix} k_{\mathrm{F,NDE}} & 0 & 0 & 0 \\ 0 & k_{\mathrm{F,DE}} & 0 & 0 \\ 0 & 0 & k_{\mathrm{F,NDE}} & 0 \\ 0 & 0 & 0 & k_{\mathrm{F,DE}} \end{pmatrix}}_{\boldsymbol{K}_{\mathrm{F}}} \underbrace{\begin{pmatrix} i_{\mathrm{x,NDE}} \\ i_{\mathrm{d,L}} \\ i_{\mathrm{y,NDE}} \\ i_{\mathrm{q,L}} \end{pmatrix}}_{\vec{i}} \tag{5.5}$$

With the aid of (5.4) the bearing forces $\vec{F}_{\mathrm{be}}$ are related to the forces $\vec{F}$ acting in the COG (5.6).

$$\begin{aligned} \vec{F} &= \boldsymbol{T}_{\mathrm{F,be,COG}} \cdot \vec{F}_{\mathrm{be}} = -\boldsymbol{T}_{\mathrm{F,be,COG}} \cdot \boldsymbol{K}_{\mathrm{s}} \cdot \vec{q}_{\mathrm{be}} + \boldsymbol{T}_{\mathrm{F,be,COG}} \cdot \boldsymbol{K}_{\mathrm{F}} \cdot \vec{i} \\ &= -\underbrace{\boldsymbol{T}_{\mathrm{F,be,COG}} \boldsymbol{K}_{\mathrm{s}} \boldsymbol{T}_{\mathrm{q,be,COG}}}_{\boldsymbol{K}_{\mathrm{s,COG}}} \cdot \vec{q} + \boldsymbol{T}_{\mathrm{F,be,COG}} \cdot \vec{i} \end{aligned} \tag{5.6}$$

The matrix $\boldsymbol{K}_{\mathrm{s,COG}}$ is given in (5.7) in order to point out that the terms k_{12} and k_{21} lead to a coupling between translational and rotatory motions. Only in case of a symmetrical system ($a = b$, $k_{\mathrm{s,NDE}} = k_{\mathrm{s,DE}}$) the coupling vanishes, which is for example the case for the conical bearingless machine in [23]. Inserting (5.6) into (5.1) yields (5.8).

$$\boldsymbol{K}_{\mathrm{s,COG}} = \begin{pmatrix} k_{11} & k_{12} & 0 & 0 \\ k_{21} & k_{22} & 0 & 0 \\ 0 & 0 & k_{11} & -k_{12} \\ 0 & 0 & -k_{21} & k_{22} \end{pmatrix} \quad \text{, where} \quad \begin{aligned} k_{11} &= k_{\mathrm{s,NDE}} + k_{\mathrm{s,DE}} \\ k_{12} &= k_{21} = -a \cdot k_{\mathrm{s,NDE}} + b \cdot k_{\mathrm{s,DE}} \\ k_{22} &= a^2 \cdot k_{\mathrm{s,NDE}} + b^2 \cdot k_{\mathrm{s,DE}} \end{aligned} \tag{5.7}$$

$$\boldsymbol{M} \cdot \ddot{\vec{q}} + \boldsymbol{G} \cdot \dot{\vec{q}} + \boldsymbol{K}_{\mathrm{s,COG}} \cdot \vec{q} = \boldsymbol{T}_{\mathrm{F,be,COG}} \cdot \underbrace{\boldsymbol{K}_{\mathrm{F}} \cdot \vec{i}}_{\vec{F}_{\mathrm{ref}}} \tag{5.8}$$

5.1.1. Decentralized Position Control

In the classical decentralized position control, the force-generating currents $\vec{i}$ are demanded by a PID position controller (5.9) with a cascaded current control loop, whose closed loop behavior is considered here ideal ($\vec{i} = \vec{i}_{\mathrm{ref}}$). The proportional, derivative and integrating gains of the PID position controller are given by $\boldsymbol{K}_{\mathrm{P}}$, $\boldsymbol{K}_{\mathrm{D}}$ and $\boldsymbol{K}_{\mathrm{I}}$ in (5.10).

$$\vec{i} = \vec{i}_{\mathrm{ref}} = -\left(\boldsymbol{K}_{\mathrm{P}} \vec{q}_{\mathrm{se}} + \boldsymbol{K}_{\mathrm{D}} \dot{\vec{q}}_{\mathrm{se}} + \boldsymbol{K}_{\mathrm{I}} \int \vec{q}_{\mathrm{se}} \, \mathrm{d}t \right) \tag{5.9}$$

$$\begin{aligned} \boldsymbol{K}_{\mathrm{P}} &= \mathrm{diag}\left(k_{\mathrm{P,A}}, k_{\mathrm{P,B}}, k_{\mathrm{P,A}}, k_{\mathrm{P,B}}\right); \; \boldsymbol{K}_{\mathrm{D}} = \mathrm{diag}\left(k_{\mathrm{D,A}}, k_{\mathrm{D,B}}, k_{\mathrm{D,A}}, k_{\mathrm{D,B}}\right); \\ \boldsymbol{K}_{\mathrm{I}} &= \mathrm{diag}\left(k_{\mathrm{I,A}}, k_{\mathrm{I,B}}, k_{\mathrm{I,A}}, k_{\mathrm{I,B}}\right) \end{aligned} \tag{5.10}$$

Since the integral part is only necessary for stationary accuracy, but not for stability, it is omitted in the following for clearness. Bringing all terms to the left side and applying the transformation (5.3) yields (5.11), which fully describes the closed loop system.

$$\begin{aligned} \boldsymbol{M} \ddot{\vec{q}} + \left(\boldsymbol{G} + \boldsymbol{T}_{\mathrm{F,be,COG}} \cdot \underbrace{\boldsymbol{K}_{\mathrm{F}} \boldsymbol{K}_{\mathrm{D}} \boldsymbol{T}_{\mathrm{q,COG,se}}}_{\boldsymbol{K}_{\mathrm{D,be}}} \right) \dot{\vec{q}} + \\ \left(\boldsymbol{K}_{\mathrm{s,COG}} + \boldsymbol{T}_{\mathrm{F,be,COG}} \cdot \underbrace{\boldsymbol{K}_{\mathrm{F}} \boldsymbol{K}_{\mathrm{P}} \boldsymbol{T}_{\mathrm{q,COG,se}}}_{\boldsymbol{K}_{\mathrm{P,be}}} \right) \vec{q} = \boldsymbol{0} \end{aligned} \tag{5.11}$$

In order to investigate system stability, the system (5.11) is modeled in the state space according to Fig. 5.2. The subsystems $\boldsymbol{K}_{\mathrm{sup}}$ and $\boldsymbol{K}_{\mathrm{Ft}}$ describe the superposition and eddy current effect, which are discussed in Section 5.3.2 and 5.3.1. Here, both effects are represented by unity matrices $\boldsymbol{I}$ ($\boldsymbol{K}_{\mathrm{sup}} = \boldsymbol{I}$, $\boldsymbol{K}_{\mathrm{Ft}} = \boldsymbol{I}$) as in the case, when none of the two effects are present.

The open-loop state vector $\vec{x}_{\mathrm{o}}$, the input vector $\vec{u}_{\mathrm{o}}$ and the output vector $\vec{y}_{\mathrm{o}}$ are given in

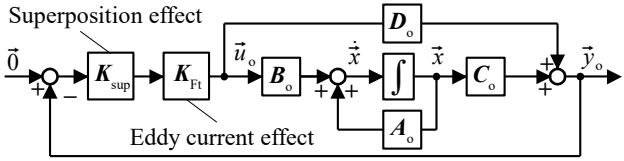

Fig. 5.2.: Rotor position control in state space representation

(5.12), whereas the vectors for the closed loop are given in (5.15) with subscript "w". The system matrix $\boldsymbol{A}_\mathrm{o}$, the input matrix $\boldsymbol{B}_\mathrm{o}$, the output matrix $\boldsymbol{C}_\mathrm{o}$ and the feed-through matrix $\boldsymbol{D}_\mathrm{o}$ are given by (5.13) and (5.14) for the open loop and by (5.16) and (5.17) for the closed loop. All sub-matrices, including the zero matrix $\boldsymbol{O}$ and the unity matrix $\boldsymbol{I}$, are 4×4-matrices. The stability analysis considers the eigenvalues of the closed-loop system matrix $\boldsymbol{A}_\mathrm{w}$ (5.16).

$$\vec{x}_\mathrm{o}=\left(\vec{q},\dot{\vec{q}}\right)^\mathrm{T};\quad \vec{y}_\mathrm{o}=\vec{F}_\mathrm{ref}=\boldsymbol{K}_\mathrm{F}\cdot\vec{i};\quad \vec{u}_\mathrm{o}=\boldsymbol{K}_\mathrm{sup}\cdot\boldsymbol{K}_\mathrm{Ft}\cdot\vec{F}_\mathrm{ref} \tag{5.12}$$

$$\boldsymbol{A}_\mathrm{o}=\underset{[8\times8]}{\begin{pmatrix}\boldsymbol{O} & \boldsymbol{I}\\ -\boldsymbol{M}^{-1}\cdot\boldsymbol{K}_\mathrm{s,COG} & -\boldsymbol{M}^{-1}\cdot\boldsymbol{G}\end{pmatrix}} \tag{5.13}$$

$$\boldsymbol{B}_\mathrm{o}=\underset{[8\times4]}{\begin{pmatrix}\boldsymbol{O}\\ \boldsymbol{M}^{-1}\cdot\boldsymbol{T}_\mathrm{F,be,COG}\end{pmatrix}};\quad \boldsymbol{C}_\mathrm{o}=\underset{[4\times8]}{\begin{pmatrix}\boldsymbol{K}_\mathrm{P,be} & \boldsymbol{K}_\mathrm{D,be}\end{pmatrix}};\quad \boldsymbol{D}_\mathrm{o}=\underset{[4\times4]}{\begin{pmatrix}\boldsymbol{O}\end{pmatrix}} \tag{5.14}$$

$$\vec{x}_\mathrm{w}=\vec{x}_\mathrm{o};\quad \vec{y}_\mathrm{w}=\vec{y}_\mathrm{o};\quad \vec{u}_\mathrm{w}=\boldsymbol{0} \tag{5.15}$$

$$\boldsymbol{A}_\mathrm{w}=\underset{[8\times8]}{\begin{pmatrix}\boldsymbol{O} & \boldsymbol{I}\\ -\boldsymbol{M}^{-1}\cdot\left(\boldsymbol{K}_\mathrm{s,COG}+\boldsymbol{T}_\mathrm{F,be,COG}\boldsymbol{K}_\mathrm{P,be}\right) & -\boldsymbol{M}^{-1}\cdot\left(\boldsymbol{G}+\boldsymbol{T}_\mathrm{F,be,COG}\boldsymbol{K}_\mathrm{D,be}\right)\end{pmatrix}} \tag{5.16}$$

$$\boldsymbol{B}_\mathrm{w}=\underset{[8\times4]}{\begin{pmatrix}\boldsymbol{O}\\ \boldsymbol{M}^{-1}\cdot\boldsymbol{T}_\mathrm{F,be,COG}\end{pmatrix}};\quad \boldsymbol{C}_\mathrm{w}=\boldsymbol{C}_\mathrm{o};\quad \boldsymbol{D}_\mathrm{w}=\boldsymbol{D}_\mathrm{o} \tag{5.17}$$

The bottom line of $\boldsymbol{A}_\mathrm{w}$ reveals that for system stability the controller proportional gain $\boldsymbol{T}_\mathrm{F,be,COG}\boldsymbol{K}_\mathrm{P,be}$ must overcome the stiffness matrix $\boldsymbol{K}_\mathrm{s,COG}$, which has negative stiffness entries. If this condition is fulfilled, the overall stiffness takes a positive value as in a mechanical spring-mass system, which oscillates marginally stable. On the other hand, the proportional gain must not be chosen too high in order to keep the eigenfrequencies of the controlled system and thereby the bandwidth requirements low. A good compromise is the choice of the controller gain in such a way, that the overall positive stiffness has the same absolute value as the negative magnetic stiffness. This approach, resulting in $\boldsymbol{K}_\mathrm{P}=\boldsymbol{K}_\mathrm{P,n}$ (5.18), is called controller tuning according to the "natural stiffness" [4] with the subscript "n" for "natural".

$$\boldsymbol{K}_\mathrm{P,n}=2\cdot\mathrm{diag}\left(\frac{k_\mathrm{s,NDE}}{k_\mathrm{F,NDE}},\frac{k_\mathrm{s,DE}}{k_\mathrm{F,DE}},\frac{k_\mathrm{s,NDE}}{k_\mathrm{F,NDE}},\frac{k_\mathrm{s,DE}}{k_\mathrm{F,DE}}\right) \tag{5.18}$$

Reasonable system damping, i.e. natural damping $\boldsymbol{K}_{\mathrm{D}} = \boldsymbol{K}_{\mathrm{D,n}}$, is applied, if the system differential equation (5.8) is considered, which has a PT2 transfer behavior. For a single-axis magnetic bearing the damping ratio for natural damping $k_{\mathrm{D}} = k_{\mathrm{D,n}}$ is given by (5.19) with $\xi_{\mathrm{D,n}} = 0.5$ with the parameters for the DE and the NDE. In (5.19) m_{NDE} and m_{DE} is the partial mass carried by the bearings NDE and DE.

$$\begin{cases} \xi_{\mathrm{D,n,DE}} = \frac{k_{\mathrm{D,n,DE}} \cdot k_{\mathrm{F,DE}}}{2 \cdot \sqrt{(k_{\mathrm{P,DE}} \cdot k_{\mathrm{F,DE}} + k_{\mathrm{s,DE}}) \cdot m_{\mathrm{DE}}}} = 0.5 \\ \xi_{\mathrm{D,n,NDE}} = \frac{k_{\mathrm{D,n,NDE}} \cdot k_{\mathrm{F,NDE}}}{2 \cdot \sqrt{(k_{\mathrm{P,NDE}} \cdot k_{\mathrm{F,NDE}} + k_{\mathrm{s,NDE}}) \cdot m_{\mathrm{NDE}}}} = 0.5 \\ \boldsymbol{K}_{\mathrm{D,n}} = \boldsymbol{K}_{\mathrm{F}}^{-1} \cdot \mathrm{diag}\left(\sqrt{m_{\mathrm{NDE}} \cdot \left(k_{\mathrm{P,NDE}} \cdot k_{\mathrm{F,NDE}} + k_{\mathrm{s,NDE}}\right)}, \right. \\ \qquad \sqrt{m_{\mathrm{DE}} \cdot \left(k_{\mathrm{P,DE}} \cdot k_{\mathrm{F,DE}} + k_{\mathrm{s,DE}}\right)}, \sqrt{m_{\mathrm{NDE}} \cdot \left(k_{\mathrm{P,NDE}} \cdot k_{\mathrm{F,NDE}} + k_{\mathrm{s,NDE}}\right)}, \\ \qquad\qquad \left. \sqrt{m_{\mathrm{DE}} \cdot \left(k_{\mathrm{P,DE}} \cdot k_{\mathrm{F,DE}} + k_{\mathrm{s,DE}}\right)} \right) \end{cases} \tag{5.19}$$

5.1.2. Limits of the Decentralized Position Control

Obviously the advantage of the decentralized rotor position control is the simple choice of the position controller proportional and derivative gains $k_{\mathrm{P,DE}}$, $k_{\mathrm{P,NDE}}$ and $k_{\mathrm{D,DE}}$, $k_{\mathrm{D,DE}}$ according to the natural stiffness, where each degree of freedom is considered individually. In practice, the system also benefits from the simple position signal treatment. However, this so-called decentralized control has some major drawbacks, listed in the following, which motivate the idea of the centralized control (Section 5.2).

- **Non-Collocation between Sensor and Bearing Plane**
  In bearingless machines the distance between the bearing and the sensor plane is approximately equal to the active length ($d - b \approx l_{\mathrm{Fe}}$), which applies to [23, 9]. For the conical rotor motions, this can lead to a considerable phase lag between the position trajectory in the bearing plane and the sensor plane, which can even cause a positive feed-back and thereby instability (called observability problem) [4]. Even though this is one of the first arguments against the decentralized control, in practice two aspects should be considered. First, if the two planes NDE and DE exhibit a large distance to the COG, the tilting angles φ_{x} and φ_{y} are very small ($\varphi_{\mathrm{x}}, \varphi_{\mathrm{y}} < 0.2^{\circ}$), since the stiffness against the tilting motions is high. This is usually the case for cylindrical rotor machines with a big slimness, such as the built prototype machine *LLM4* (Fig. 5.10b). Thus, the observability problem is small. Second, the sensor coordinates can be transformed from the sensor plane into the bearing

Table 5.2.: Analytically calculated angular eigenfrequencies for a) the bearingless prototype machine *LLM4* and for b) the flywheel system (considered is the undamped system with natural stiffness control and data from Table 5.1)

	a) Bearingless machine		b) Flywheel system	
	$n = 0$	$n_\mathrm{N} = 60000\ \mathrm{min}^{-1}$	$n = 0$	$n_\mathrm{N} = 24000\ \mathrm{min}^{-1}$
$\omega_{\mathrm{par},+}$ / rad $\cdot$ s^{-1}	291.8	341.7	88.1	96.9
$\omega_{\mathrm{par},-}$ / rad $\cdot$ s^{-1}	291.8	204.4	88.1	32.9
$\omega_{\mathrm{con},+}$ / rad $\cdot$ s^{-1}	406.1	530.3	228.5	1208.3
$\omega_{\mathrm{con},-}$ / rad $\cdot$ s^{-1}	406.1	378.9	228.5	105.5

plane by a simple linear transformation, similar to (5.2). This transformation was successfully used for the control of both the *LLM4* and of the flywheel system.

- **Non-Symmetrical Bearing System**
  If the system is non-symmetrical, i.e. $a \neq b$ and $c \neq d$, not only the conical mode eigenvalues, but also the parallel mode eigenvalues of the rigid rotor are speed-dependent. This is due to the coupling of the skew-symmetric matrices $\boldsymbol{K}_{\mathrm{s,COG}}$ and $\boldsymbol{G}$. However, in practice often the COG is inherently approximately in the geometrical center between the two bearings. Thus, the speed-dependency of the conical mode eigenvalues is bigger, so that the parallel modes do no state a bandwidth problem.

- **Large Difference between System Eigenfrequencies**
  In order to simplify the rotor position control, the system eigenfrequencies are

Table 5.3.: Analytically calculated critical speeds for a) the bearingless prototype machine *LLM4* and b) the flywheel system (considered is the undamped system with natural stiffness control and data given in Table 5.1)

	$f_{\mathrm{crit},1}$ / Hz	$n_{\mathrm{crit},1}$ / min^{-1}	$f_{\mathrm{crit},2}$ / Hz	$n_{\mathrm{crit},2}$ / min^{-1}
a) LLM4	47.7	2864.8	66.0	3963.0
b) Flywheel system	14.3	859.4	49.3	2960.3

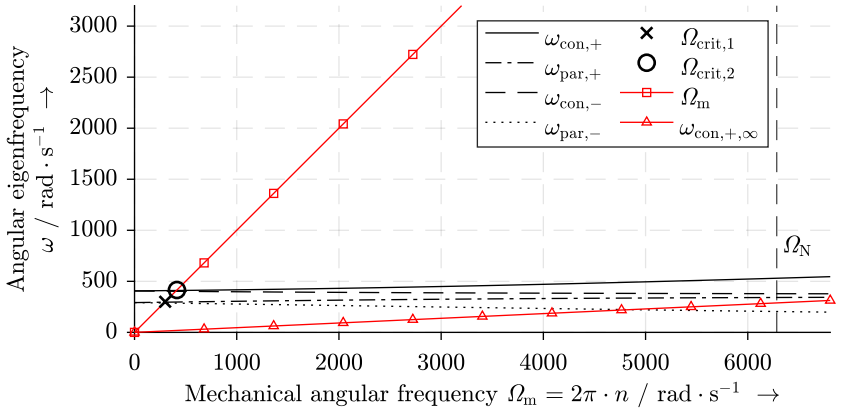

(a) *LLM4*

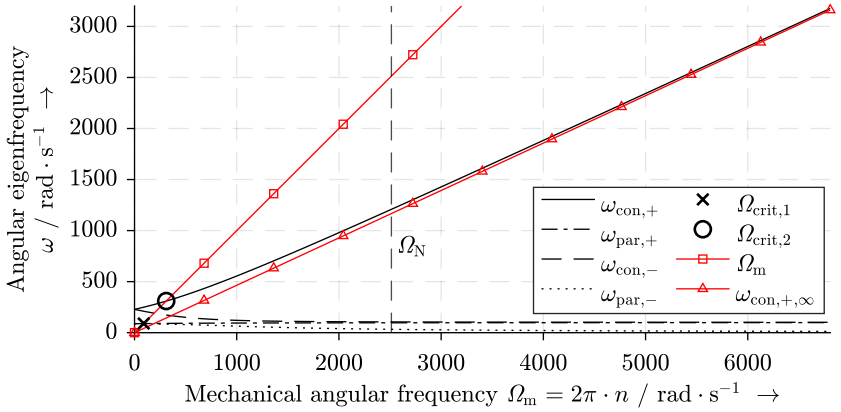

(b) Flywheel system

Fig. 5.3.: Analytically calculated angular eigenfrequencies ω for parallel and conical forward- ("+") and backward- ("−") whirling rigid rotor eigenmodes and critical speeds Ω_{crit} at position control with natural stiffness for the undamped systems and the data given in Table 5.1

desired to be small for a low bandwidth requirement and close to each other, since one controller setting manages both the conical mode and the parallel mode of the rigid rotor. Usually the parallel rigid rotor eigenmode angular eigenfrequencies $\omega_{par,+}$, $\omega_{par,-}$ are hardly speed-dependent. The backward-whirling conical rigid

rotor eigenmode angular eigenfrequency $\omega_{\mathrm{con},-}$ strongly decreases with rising speed. However, most crucial, the forward-whirling mode angular frequency $\omega_{\mathrm{con},+}$ increases with speed. In the *Campbell* diagram (Fig. 5.3) it approaches asymptotically the straight line $\omega_{\mathrm{con},+} \rightarrow \omega_{\mathrm{con},+,\infty}$, which is inclined by the slope $\Theta_{\mathrm{pol}}/\Theta_{\mathrm{ax}}$. This can result in a large difference between the eigenfrequencies at high speed $n = \Omega_{\mathrm{m}}/(2\pi)$. Therefore, the bearingless machine *LLM4* as an example with a small value $\Theta_{\mathrm{pol}}/\Theta_{\mathrm{ax}} = 0.046$ and the flywheel system with a big value $\Theta_{\mathrm{pol}}/\Theta_{\mathrm{ax}} = 0.465$ behave totally different. The calculated eigenfrequencies at standstill ($n = 0$) and at rated speed ($n = n_{\mathrm{N}}$) are given in Table 5.2, proving that the difference between the eigenfrequencies of the bearingless machines is much smaller. The angular frequency of the forward conical whirl of the flywheel system, however, has a 12-times higher value than the other angular eigenfrequencies at $n = 24000\ \mathrm{min}^{-1}$. This makes the choice for appropriate position controller parameters more difficult. To mitigate this problem, the centralized control is discussed in Section 5.2.1 as an alternative.

The critical rotor oscillation frequency of both systems a) and b) is $f_{\mathrm{crit},1} = \Omega_{\mathrm{crit},1}/(2\pi)$ for rotor motions parallel to the z-axis and it is $f_{\mathrm{crit},2} = \Omega_{\mathrm{crit},2}/(2\pi)$ for conical motions around the z-axis. The critical speeds $\Omega_{\mathrm{crit},1}$ and $\Omega_{\mathrm{crit},2}$ are given in Table 5.3. Fig. 5.3 shows that both systems are driven in supercritical operation ($\Omega_{\mathrm{N}} = 2\pi \cdot n_{\mathrm{N}} > \Omega_{\mathrm{crit},2}$). This enables the so called "force-free" rotation around the principal axis of inertia over the entire speed range between $n_{\mathrm{crit},2} = f_{\mathrm{crit},2}$ and n_{N}. The rotational-frequent rotor movements are canceled in the measured position signals by an adaptive notch filter, as explained in [4]. For the flywheel system, the required notch filter for the rotational frequency is active for speeds $n > 8400\ \mathrm{min}^{-1}$ whereas it is active for speeds $n > 5000\ \mathrm{min}^{-1}$ for the bearingless machine *LLM4*.

5.2. Decentralized versus Centralized Control

5.2.1. Introduction into the Centralized Control

In order to overcome the shortcomings of the decentralized control in Section 5.1.2, the centralized control enables the separation of the conical from the parallel rotor eigenmodes. This is realized by means of coordinate transformations, so that the control is set

up in the COG plane of a fictive symmetrical system ($a = b$, $c = d$) instead of the real, non-symmetrical system ($a \neq b$, $c \neq d$) with two bearing planes. In the end, one controller is tuned for the parallel eigenmodes (x, y) and one is tuned for the conical eigenmodes (φ_x, φ_y). The idea is thoroughly discussed in [4]. Here, only the main aspects are presented to show that such a sophisticated controller is only needed for systems with a high ratio of Θ_{pol}/Θ_{ax} as in the case of the flywheel system. Fig. 5.4a visualizes the structure of the decentralized control in comparison to the centralized control (Fig. 5.4b).
The coordinate transformations are carried with the matrices given in (5.2), (5.3) and (5.4) and their inverses. The matrix $\boldsymbol{T}_{F,COG,be}$ (Fig. 5.4b) transforms the calculated reference force vector $\vec{F}_{COG,ref}$ in COG coordinates into the reference bearing currents $\vec{i}_{ref}$ in bearing coordinates. In case of the decentralized control, the controller gains $\boldsymbol{K}_P$ and $\boldsymbol{K}_D$ incorporate the inverse force-current transformation matrix $\boldsymbol{K}_F$ (see (5.18), (5.19)). For the centralized control, the controller gains are given by $\boldsymbol{K}_{PD,COG} = \mathrm{diag}\left(k_{PD,par}, k_{PD,con}, k_{PD,par}, k_{PD,con}\right)^T$. The inverse $\boldsymbol{K}_F^{-1}$ cannot be applied to the conical motion gains, since the controller reference quantities are the tilting angles φ_x and φ_y. Therefore, $\boldsymbol{T}_{F,COG,be}$ (5.20) includes the transformation into bearing coordinates, before $\boldsymbol{K}_F^{-1}$ can be applied. Therewith, the simple choice of the position controller gains according to the natural stiffness control rule is lost, since the controller gains are associated to the COG degrees of freedom.

$$\boldsymbol{T}_{F,COG,be} = \boldsymbol{K}_F^{-1} \cdot \boldsymbol{T}_{F,be,COG}^{-1} \tag{5.20}$$

In order to remove all skew-symmetric matrix entries – apart from the given gyroscopic matrix $\boldsymbol{G}$ – two more things have to be counteracted, which are present for non-symmetric motor systems ($a \neq b$, $c \neq d$): the bearing forces, resulting from the different static stiffness coefficients $k_{s,DE}$, $k_{s,NDE}$ in the bearing planes A and B, and the tilting torque M_x, M_y, resulting from $a \neq b$. This is realized by the feed-forward path $\boldsymbol{K}_{s,COG} \cdot \boldsymbol{T}_{q,se,COG}$ (Fig. 5.4b). Altogether, the closed loop system is described by (5.21) which, in contrast to (5.11), only contains diagonal matrices apart from $\boldsymbol{G}$. The matrix $\boldsymbol{G}$, in turn, only couples the conical modes, so that the parallel modes are decoupled from the conical ones.

$$\begin{aligned}
&\boldsymbol{M} \cdot \ddot{\vec{q}} + \boldsymbol{G} \cdot \dot{\vec{q}} + \boldsymbol{K}_{s,COG} \cdot \vec{q} = -\boldsymbol{T}_{F,be,COG} \cdot \boldsymbol{K}_F \cdot \vec{i}\,; \quad \text{where} \\
&\vec{i} = \boldsymbol{T}_{F,COG,be} \cdot \left(\boldsymbol{K}_{P,COG} - \boldsymbol{K}_{s,COG}\right) \cdot \boldsymbol{T}_{q,se,COG} \cdot \vec{q}_{se} + \boldsymbol{T}_{F,COG,be} \cdot \boldsymbol{K}_{D,COG} \cdot \boldsymbol{T}_{q,se,COG} \cdot \dot{\vec{q}}_{se} \\
&\Rightarrow \boldsymbol{M} \cdot \ddot{\vec{q}} + \left(\boldsymbol{G} + \boldsymbol{K}_{D,COG}\right) \cdot \dot{\vec{q}} + \boldsymbol{K}_{P,COG} \cdot \vec{q} = 0
\end{aligned} \tag{5.21}$$

If the inertia ratio is $\Theta_{\mathrm{pol}}/\Theta_{\mathrm{ax}}$ is big, as in the case of the flywheel system, the still speed-dependent forward-whirling conical mode eigenfrequency can take high values, which can lead to destabilization, if the digital controller sampling frequency is less than 5- ... 10-times of the highest eigenfrequency [137]. In the used inverter for the flywheel system, the sampling frequency is $f_{\mathrm{samp}} = 12.5$ kHz and, thus, 65-times higher than the highest system eigenfrequency of $f_{\mathrm{con+}} = 192$ Hz or $\omega_{\mathrm{con+}} = 1208.3\,\mathrm{rad}\cdot\mathrm{s}^{-1}$ (Table 5.2). Not only to prevent the system from instability but also to increase the robustness, a total motion separation can be applied [137, 138]. To do so the cross-coupling term $\Omega \cdot \Theta_{\mathrm{pol}}$ in

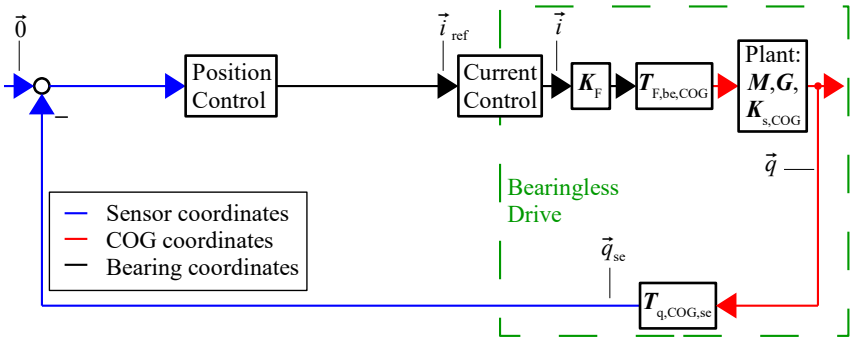

(a) Decentralized Control

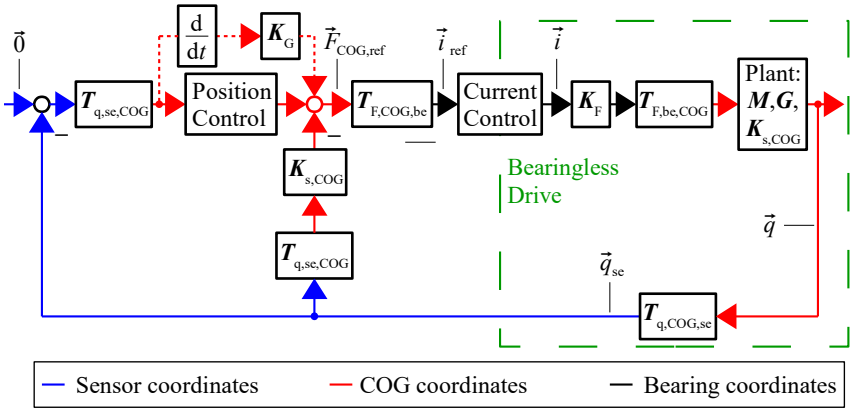

(b) Centralized Control (dashed red line indicates the option of total motion separation)

Fig. 5.4.: Structure of the decentralized and the centralized control

the gyroscopic matrix $\boldsymbol{G}$ is counteracted via a feed-forward, based on the matrix $\boldsymbol{K}_{\mathrm{G}}$, according to (5.22). The coefficient k_{att} represents an attenuation factor 0 ... 1, since a total compensation $k_{\mathrm{att}} = 1$ of the gyroscopic effect can lead to a loss of robustness in digital controllers. Values of $k_{\mathrm{att}} = 0.75$ have proved to be a good compromise [137]. The closed loop system matrix $\boldsymbol{A}_{\mathrm{w}}$ is then given by (5.23). In case of $k_{\mathrm{att}} = 1$, the lower half part of the closed-loop system matrix $\boldsymbol{A}_{\mathrm{w}}$ in equation (5.23) does not contain skew-symmetric matrix entries (5.23) so that a complete separation of parallel and conical eigenmodes for the control design is achieved. Therewith, the system poles of the corresponding transfer transfer functions in *Laplace*-domain can be chosen for zero speed $n = 0$ and remain constant at maximum speed $n = n_{\mathrm{N}}$.

$$\boldsymbol{K}_{\mathrm{G}} = k_{\mathrm{att}} \cdot \begin{pmatrix} 0 & 0 & 0 & 0 \\ 0 & 0 & 0 & \Theta_{\mathrm{pol}} \cdot \Omega \\ 0 & 0 & 0 & 0 \\ 0 & -\Theta_{\mathrm{pol}} \cdot \Omega & 0 & 0 \end{pmatrix} \quad \text{where } k_{\mathrm{att}} = 0 \ldots 1 \tag{5.22}$$

$$\boldsymbol{A}_{\mathrm{w}} = \begin{pmatrix} \boldsymbol{O} & \boldsymbol{I} \\ -\boldsymbol{M}^{-1} \cdot \left(\boldsymbol{K}_{\mathrm{s,COG}} + \boldsymbol{K}_{\mathrm{P,COG}}\right) & -\boldsymbol{M}^{-1} \cdot \left(\boldsymbol{G} + \boldsymbol{K}_{\mathrm{D,COG}} + \boldsymbol{K}_{\mathrm{G}}\right) \end{pmatrix} \tag{5.23}$$

5.2.2. Comparison between Centralized and Decentralized Control

The system poles in the *Laplace*-domain as complex-valued closed-loop system eigenvalues are compared for a) the bearingless machine *LLM4* and b) the flywheel system with their data from Table 5.1. As before, ideal current control and no integrator controller gain are considered.

Fig. 5.5 shows the root locus of the closed loop eigenvalues of the two systems a) and b) for varying controller proportional gains $\boldsymbol{K}_{\mathrm{P}}$, applying decentralized control. As expected from the *Campbell* diagram in Fig. 5.3, the system poles of the bearingless machine *LLM4* (Fig. 5.5a) only exhibit a small dependence on speed n. However, the forward-whirling eigenfrequency of the conical movement can take high values of $\omega_{\mathrm{con},+} = 750\,\mathrm{rad \cdot s^{-1}}$, if the controller stiffness is selected too high (e.g. $2 \cdot \boldsymbol{K}_{\mathrm{P,n}}$). For the flywheel system (Fig. 5.5b), the forward-whirling eigenfrequencies of conical movement are strongly speed-dependent, as shown in Fig. 5.3. A rising controller proportional gain $\boldsymbol{K}_{\mathrm{P}}$ moves the pole of the backward-whirl farther to the left, i.e. the damping increases, however, at the

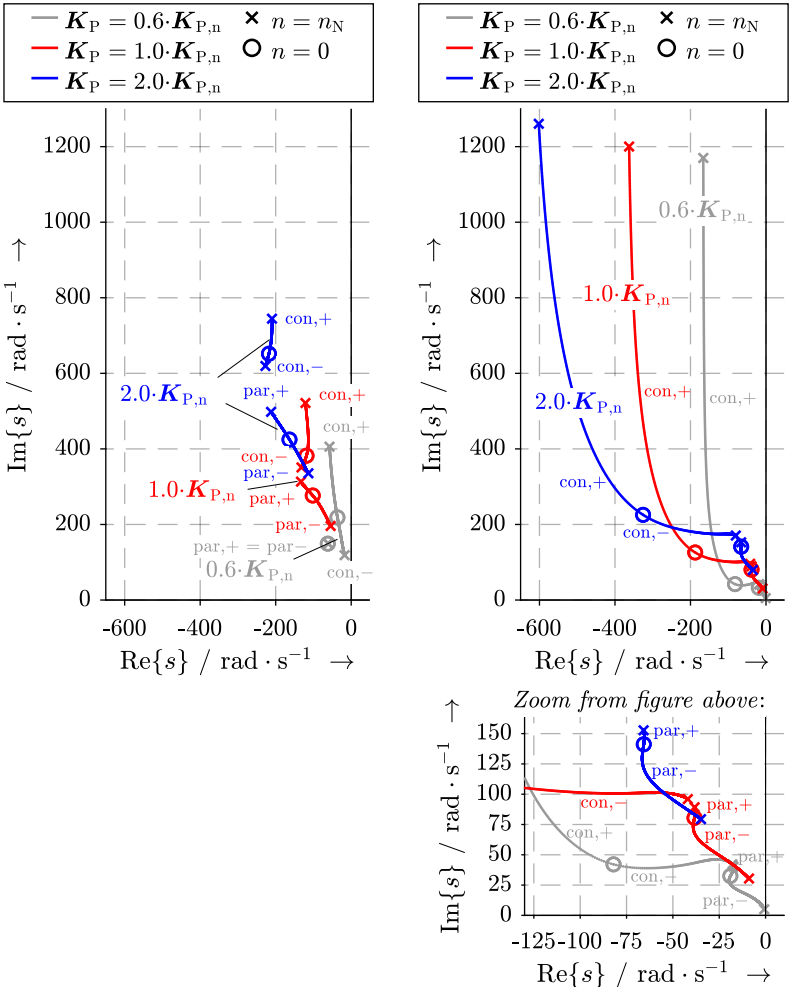

(a) Bearingless machine *LLM4*

(b) Flywheel system

Fig. 5.5.: Analytically calculated root loci of the closed-loop system eigenvalues for varying speed n and different stiffness properties $\boldsymbol{K}_\mathrm{P}$ (decentralized rotor position control), a) bearingless machine *LLM4*: $\boldsymbol{K}_\mathrm{D} = \boldsymbol{K}_\mathrm{D,n}$, b) flywheel system: $\boldsymbol{K}_\mathrm{D} = 0.6 \cdot \boldsymbol{K}_\mathrm{D,n}$

same time with an increasing eigenfrequency of the forward-whirling conical eigenmode. The increase of the controller damping $\boldsymbol{K}_{\mathrm{D}}$ in Fig. 5.6 helps damping all four rigid body eigenmodes for the bearingless machine *LLM4* (Fig. 5.6a). However, it does not improve the damping of the parallel eigenmodes and of the backward-whirling conical modes for the flywheel system.

Thus, it can be concluded that the control of the bearingless machine *LLM4* can be done with the classical decentralized control approach, since the closed loop poles in the complex s-plane, even at high speed n, are similar to each other ($\mathrm{Re}\{\mathrm{s}\} < 350\,\mathrm{rad}\cdot\mathrm{s}^{-1}$, $\mathrm{Im}\{\mathrm{s}\} < 550\,\mathrm{rad}\cdot\mathrm{s}^{-1}$). The flywheel systems suffers from the strongly speed-dependent eigenfrequencies of the conical mode. This leads to a poor damping of the backward-whirling conical and parallel eigenmodes at very low eigenfrequencies $f < 15$ Hz. Also the strong increase of the eigenfrequencies of the forward-whirling conical modes may lead to instability in combination with the delay, caused by the sensor transfer behavior and by the discrete behavior of the digital controller. This motivates the use of the centralized control in the following. Despite the described shortcomings of the decentralized control, the flywheel energy storage system was operated in our laboratory with a decentralized rotor position control. Measurement results are given in Appendix A.21. The measurement results confirm the poor damping of the backward-whirling eigenmodes at high speed n. Also they show, that special care has to be taken of the flexible body modes, whose eigenfrequencies are partially in the range of the rotational speed n.

The calculated closed-loop eigenvalues for the centralized control for the flywheel system are given in Fig. 5.7 and 5.8 with the controller settings according to Table 5.4. Due to the decoupling of the parallel and the conical modes, the parallel forward and backward whirling modes are independent from speed. Therefore, the associated poles can be placed individually. The values of the conical mode poles, however, still show a big variation with speed n. This situation can not be changed by increasing the controller proportional gain $\boldsymbol{K}_{\mathrm{P}}$ (Fig. 5.7a) or derivative gain $\boldsymbol{K}_{\mathrm{D}}$ (Fig. 5.8a) for the conical modes. Remedy is only given, if the cross-coupling between the conical modes by the gyroscopic effect ($\boldsymbol{G}$) is mitigated by the matrix $\boldsymbol{K}_{\mathrm{G}}$ according to (5.22). The root locus of eigenvalues for the then separated conical motion with $k_{\mathrm{att}} = 0.75$ is given in Fig. 5.7b and 5.8b, proving that finally the poles can be placed in a desired region by proportional and derivative controller settings to allow stable operation. Still a small speed dependency of the conical motion poles is present due to $k_{\mathrm{att}} < 1$, since the total separation by $k_{\mathrm{att}} = 1$ is not recommended due to a loss in control robustness [137].

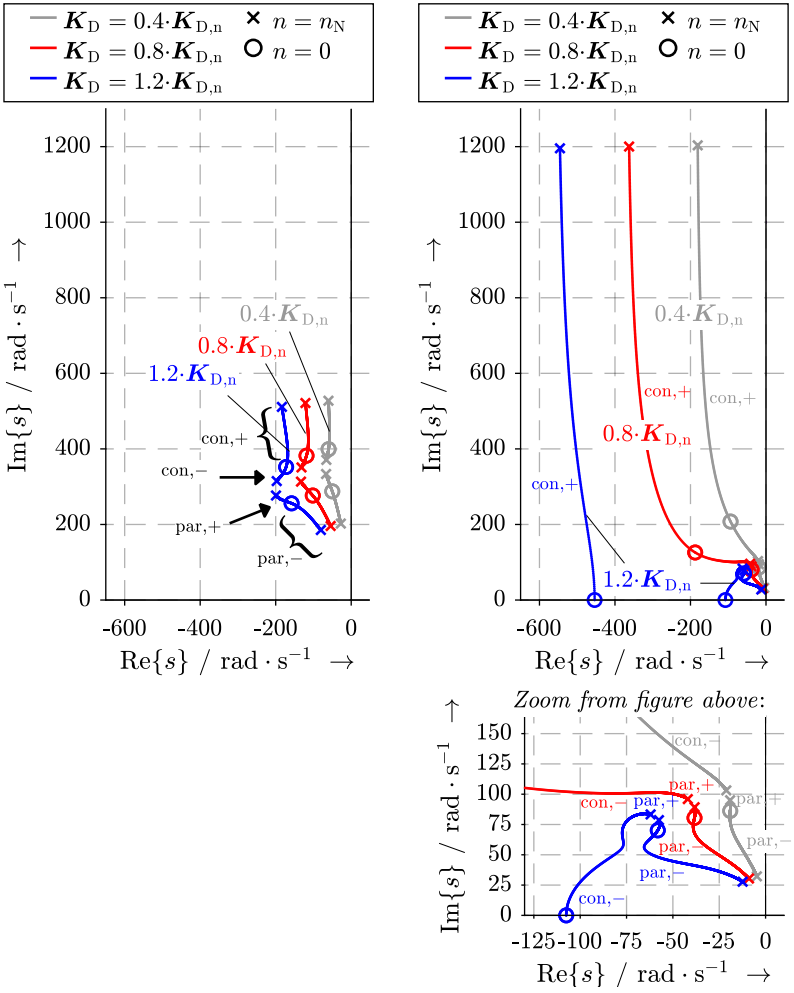

(a) Bearingless machine *LLM4*

(b) Flywheel system

Fig. 5.6.: Analytically calculated root loci of the closed-loop system eigenvalues for varying speed n and different damping properties $\boldsymbol{K}_D$ (decentralized rotor position control), a) bearingless machine *LLM4*: $\boldsymbol{K}_P = \boldsymbol{K}_{P,n}$, b) flywheel system: $\boldsymbol{K}_P = \boldsymbol{K}_{P,n}$

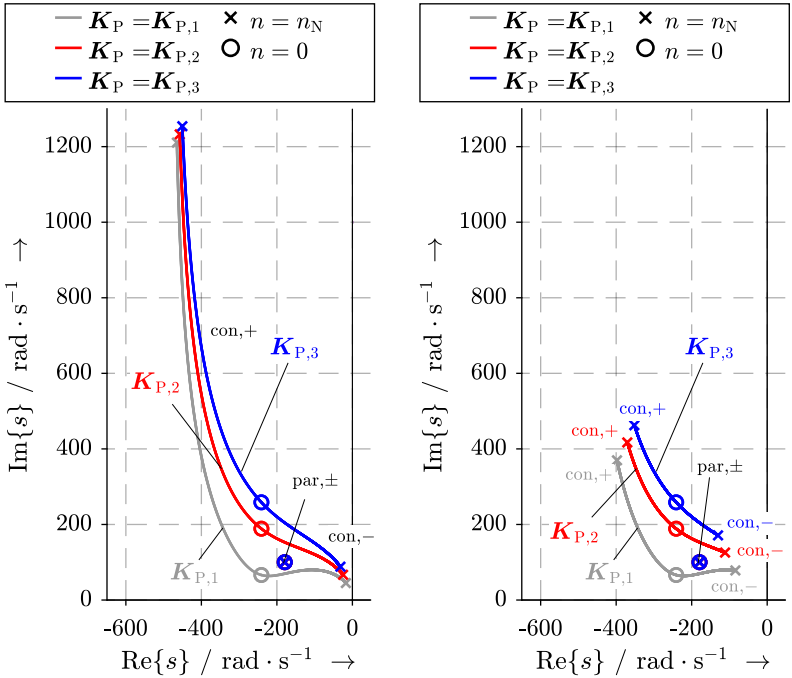

(a) Without total motion separation

(b) With total motion separation ($k_\mathrm{att} = 0.75$)

Fig. 5.7.: Analytically calculated root loci of the closed-loop flywheel system eigenvalues for varying speed n and different stiffness properties $\boldsymbol{K}_\mathrm{P}$ (centralized rotor position control), $\boldsymbol{K}_\mathrm{D} = \boldsymbol{K}_{\mathrm{D},2}$ according to Table 5.4

The investigation shows that the effort, associated with the centralized control, pays off only, if it is combined with a separation of the two conical modes. This, in turn, is only

Table 5.4.: Controller settings for the centralized position control of the flywheel system

	Parallel mode	Conical mode		Parallel mode	Conical mode
$\boldsymbol{K}_{\mathrm{P},1}$	$4 \cdot 10^6\,\mathrm{N \cdot m^{-1}}$	$79\,\mathrm{kNm \cdot rad^{-1}}$	$\boldsymbol{K}_{\mathrm{D},1}$	$32\,\mathrm{kN \cdot s \cdot m^{-1}}$	$245\,\mathrm{Nm \cdot s \cdot rad^{-1}}$
$\boldsymbol{K}_{\mathrm{P},2}$	$4 \cdot 10^6\,\mathrm{N \cdot m^{-1}}$	$119\,\mathrm{kNm \cdot rad^{-1}}$	$\boldsymbol{K}_{\mathrm{D},2}$	$32\,\mathrm{kN \cdot s \cdot m^{-1}}$	$612\,\mathrm{Nm \cdot s \cdot rad^{-1}}$
$\boldsymbol{K}_{\mathrm{P},3}$	$4 \cdot 10^6\,\mathrm{N \cdot m^{-1}}$	$159\,\mathrm{kNm \cdot rad^{-1}}$	$\boldsymbol{K}_{\mathrm{D},3}$	$32\,\mathrm{kN \cdot s \cdot m^{-1}}$	$795\,\mathrm{Nm \cdot s \cdot rad^{-1}}$

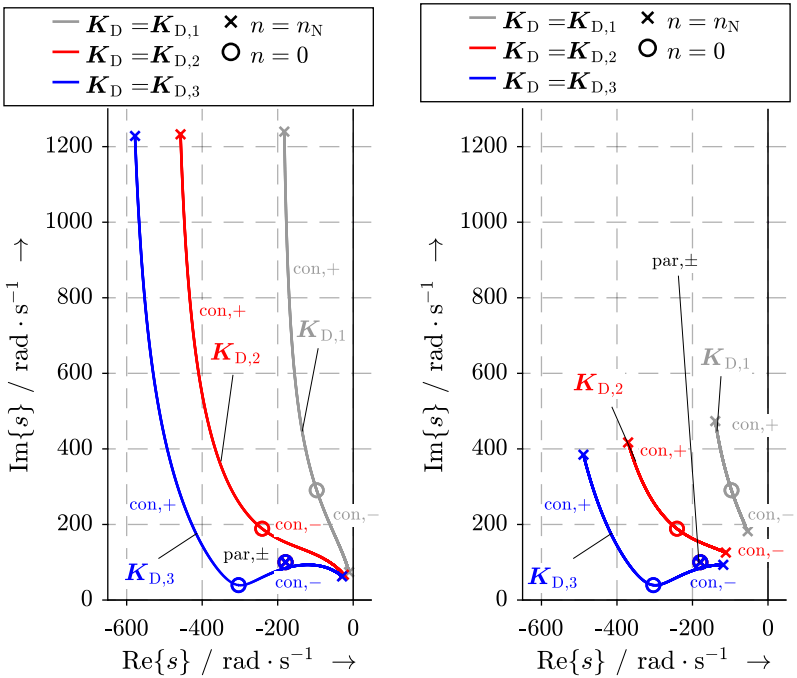

(a) Without total motion separation

(b) With total motion separation ($k_\mathrm{att} = 0.75$)

Fig. 5.8.: Analytically calculated root loci of the closed-loop flywheel system eigenvalues for varying speed n and different damping properties $\boldsymbol{K}_\mathrm{D}$ (centralized rotor position control), $\boldsymbol{K}_\mathrm{P} = \boldsymbol{K}_{\mathrm{P},2}$ according to Table 5.4

necessary, if the rotor shows a strongly speed-dependent forward-whirling eigenfrequency. This is the case for big values of $\Theta_\mathrm{pol}/\Theta_\mathrm{ax}$, as it is the case of the built flywheel system. Only with this rather sophisticated control strategy the flywheel system shows a similar dynamic behavior as the bearingless machine *LLM4* (compare Fig. 5.6a,5.7b).

5.2.3. Limits of the Centralized Control

The centralized control is based on coordinate transformations. Besides the known geometrical dimensions also the stiffness and force-current coefficients are included. In practice this can be crucial, since these values are either not known exactly or can change

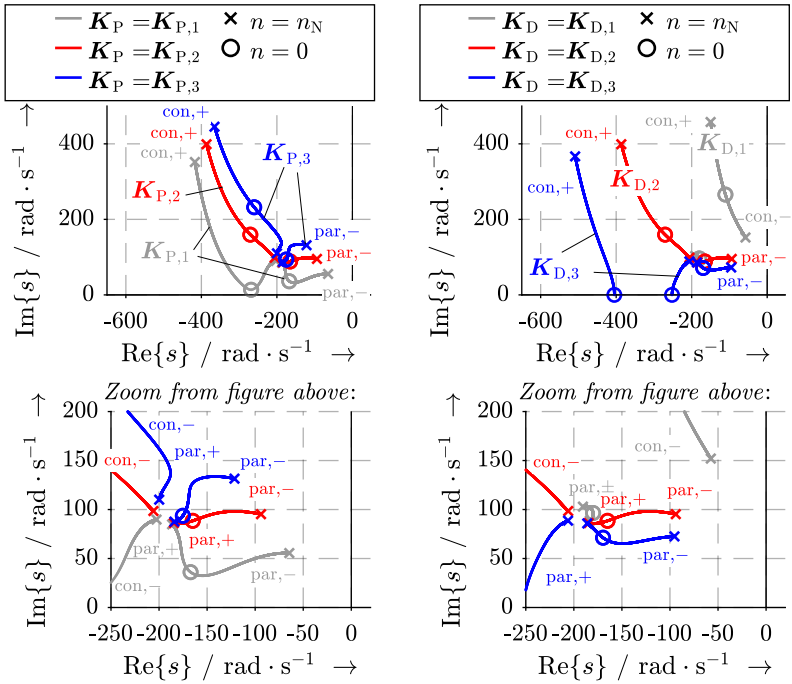

(a) Variable stiffness with total motion separation ($k_{att} = 0.75$, $\boldsymbol{K}_D = \boldsymbol{K}_{D,2}$)

(b) Variable damping with total motion separation ($k_{att} = 0.75$, $\boldsymbol{K}_P = \boldsymbol{K}_{P,2}$)

Fig. 5.9.: Analytically calculated root loci of the closed-loop flywheel system eigenvalues for varying speed n and different stiffness and damping properties $\boldsymbol{K}_P$, $\boldsymbol{K}_D$ according to Table 5.4 (centralized rotor position control), assuming that the magnetic stiffness coefficients $k_{s,DE}$, $k_{s,NDE}$ of the control model are estimated 20% too high and the force-current coefficients $k_{F,DE}$, $k_{F,NDE}$ are estimated 20% too low in comparison to the real values

during operation, e.g. due to temperature rise. Therefore, a situation is discussed, in which the control model values of the negative stiffness are estimated to be 20% too high and the force-current coefficients to be 20% too low in comparison to the real values. This shall represent an example of parameter uncertainty. The root loci of eigenvalues in the complex s-plane of the *Laplace*-domain reveal, that the separation of the two conical rigid rotor eigenmodes is violated, however, without endangering the system stability, as the poles still exhibit negative real values (Fig. 5.9). Also the damping of the rigid body

motions is higher than for the decentralized approach.

5.3. Modification of the Rigid Rotor Control due to Parasitic Effects with Increasing Bearingless Machine Size

Apart from the cross-coupling of the conical rigid rotor motions by the gyroscopic effect, in bearingless machines additional disturbing effects (Section 2.4, 2.5) lead to a coupling of the rotor bearing forces in the bearing plane (x_{DE},y_{DE}). That means, the system transfer function of bearingless machines, following the principle of Section 1.3.1, differs from the system transfer function of active magnetic bearings. This is on the one hand due to the already discussed load-dependent superposition of the drive winding field with the suspension winding field ("superposition effect"). This results in an additional disturbance force component, which is orthogonal to the desired bearing force, causing a spatial error angle $\varepsilon_{\mathrm{err,sup}}$ between both force components. A comparison between calculation, simulation and measurement of this effect is given in Section 2.5. The influence of the machine size on this superposition effect is treated in Section 3.6.1. Secondly, a disturbance of the bearing force vector by the rotor eddy current reaction field occurs as an additional orthogonal force component, causing an additional error angle $\varepsilon_{\mathrm{err,Ft}}$ of the bearing force ("eddy current effect"). This effect is discussed in Section 2.4. The influence of the PM material on this effect is discussed in Section 3.7.1, whereas the scaling of this effect with machine size is treated in Section 3.6.2.

Both, the superposition and the eddy current effect increase with the machine size and with speed n. Even for the rather small prototype *LLM4* with 1 kW/60000 min^{-1} both measured effects are visible in Fig. 5.10. The following results are partially presented in [O07]. Fig. 5.10a shows the drive current $i_{\mathrm{q,D}}$ and the suspension currents $i_{\mathrm{d,L}}$ (proportional to a horizontal bearing force in x-direction), $i_{\mathrm{q,L}}$ (proportional to a vertical bearing force in y-direction) during a run-up/run-down of the *LLM4* with the Sm_2Co_{17}-rotor. The levitation current $i_{\mathrm{q,L}}$ compensates for the gravitational force. An error angle $\varepsilon_{\mathrm{err}}$ of the radial rotor force in a bearingless machine is visible by a force perpendicular (orthogonal) to the desired force. As the desired bearing force points into the positive y-direction, associated with a positive high value of $i_{\mathrm{q,L}}$, the error angle is noticeable by a non-zero force in x-direction, associated with a non-zero current $i_{\mathrm{d,L}}$. Thus, the error angle is calculated by $\varepsilon_{\mathrm{err}} = \arctan\left(i_{\mathrm{d,L}}/i_{\mathrm{q,L}}\right)$. The superposition error angle $\varepsilon_{\mathrm{err,sup}}$ depends on the drive current amplitude $i_{\mathrm{q,D}}$, but not on the speed n. The eddy current error angle $\varepsilon_{\mathrm{err,Ft}}$ only depends

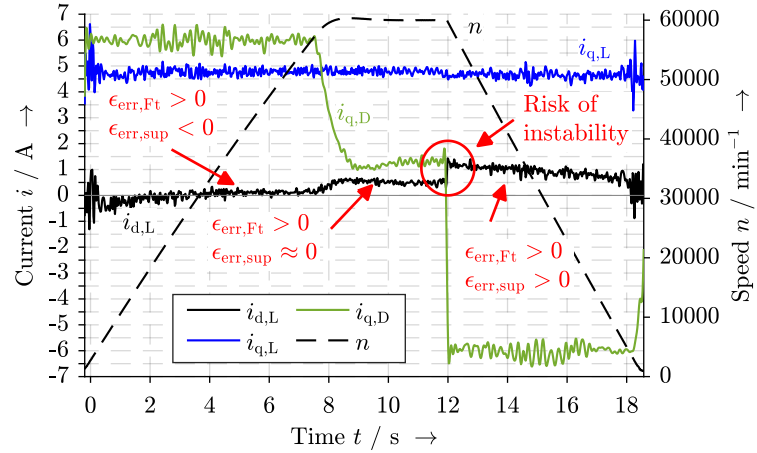

(a) Measured suspension currents $i_{d,L}$, $i_{q,L}$, drive current $i_{q,D}$ and speed n

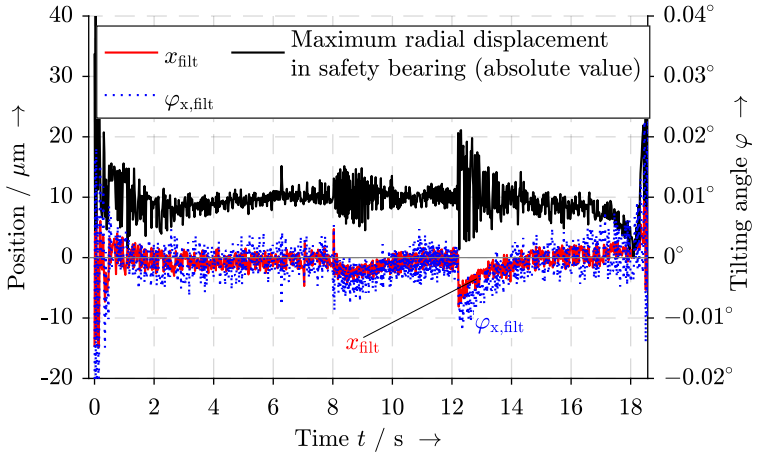

(b) Measured filtered position sensor signals x_{filt}, $\varphi_{x,filt}$, transformed into the COG-coordinates (adaptive notch filter at rotational frequency for $n > 6000$ min^{-1}) and radial displacement in the safety bearing with a clearance of 150μm

Fig. 5.10.: Measured run-up/run-down for the prototype machine *LLM4* with the Sm_2Co_{17}-rotor, acceleration/deceleration with $|i_{q,D}| = 6$ A ($0 \le t \le 8$ s: motor operation; 8 s $\le t \le 12$ s: motor no-load; $t > 12$ s: braking generator operation (aliasing effect visible due to sampling frequency: $f_{samp} = 34.5$ Hz), controller sampling frequency $f_{sw}/2 = 16.5$ kHz

on speed n. In Fig. 5.10 both effects are present at the same time, resulting in an $i_{q,D}$-dependent and in a speed-dependent overall error angle $\varepsilon_{err} = \varepsilon_{err,sup} + \varepsilon_{err,Ft}$. The same measured characteristic is given in Appendix A.22 for the NdFeB-rotor with a smaller eddy current effect due to the smaller PM electric conductivity. A separate determination of $\varepsilon_{err,sup}$ and $\varepsilon_{err,Ft}$ is shown in Section 2.4 and Section 2.5. During acceleration with $i_{q,D} > 0$ (and in the same way at deceleration with $i_{q,D} < 0$) $i_{d,L}$ decreases due to a negative error angle $\varepsilon_{err,sup} < 0$ (respectively at deceleration it increases due to $\varepsilon_{err,sup} > 0$). At rated speed n_N and motor no-load operation, $i_{q,D}$ is small and the superposition effect is negligible. Additionally, $i_{d,L}$ decreases with rising speed n independent of $i_{q,D}$ due to the eddy current effect with $\varepsilon_{err,Ft} > 0$. Thus, at high speed n in motor operation both effects almost cancel each other, whereas in generator braking mode the effects add up, which can potentially lead to system instability.

Fig. 5.10b shows the associated filtered (adaptive notch filter at rotational frequency for $n > 6000\ \text{min}^{-1}$) position signal x_{filt} and the tilting angle around the x-axis $\varphi_{x,filt}$ in the center of gravity (COG). In the position signal the rotating frequency $f = n$ is filtered for $n > 6000\ \text{min}^{-1}$ for a "force-free rotation" [4]. Also the measured radial displacement is shown. If the force error angles by the superposition and the eddy current effect are as low as in Fig. 5.10, no risk of system instability occurs. The safety bearing clearance of $\pm 150\ \mu$m is sufficient.

In general the eddy current and superposition effect are very small at the *LLM4* due to the small ratio of $\tau_{p,L}/\delta$ (compare Section 3.6.2). Therefore, in the following section a second geometry, called $LLM4_{r+}$, is introduced, having a larger bore diameter at the same pole count (overview of investigated topologies given in Table A.4). Thus, the $LLM4_{r+}$ serves to visualize the position control deficiencies, caused by a bigger eddy current and superposition effect. The shaft geometry of the $LLM4_{r+}$ is determined according to Fig. A.11 in Appendix. Its system properties are summarized in Table 5.5. The geometrical properties are given in Table 2.6.

The eddy current and the superposition effect only influence the controller behavior in the bearingless machine plane (DE), not in the combined radial-axial AMB at the NDE. Therefore, here these two effects have only an impact on the coordinates of the motor plane (coordinates $x_{se,DE}, y_{se,DE}$). So they will mainly influence the eigenfrequencies of the conical rigid rotor motions. In the radial AMB plane at the NDE, eddy currents are small and, thus, neglected, since the rotor yoke of the radial AMB is composed of a laminated stack of insulated 0.1 mm-thin iron sheets. If a drive is composed of two bearingless

Table 5.5.: Control system parameters of the bearingless machines *LLM4* and *LLM4*$_{r+}$

Bearingless machine with $p/p_L = 1/2$	*LLM4*[1)]	*LLM4*$_{r+}$[1)]
Rated speed n_N / min^{-1}	60000	40000
Rated power P_N / kW	1	40
Mass m / kg	0.923	6.97
Axial moment of inertia Θ_{ax} / kg · mm^2	2551	88400
Polar moment of inertia Θ_{pol} / kg · mm^2	117	2600
Distance between bearing NDE and COG a / mm	38.7	91.7
Distance between bearing DE and COG b / mm	20.4	49.6
Distance between sensor NDE and COG c / mm	53.6	132.9
Distance between sensor DE and COG d / mm	61.2	153.3
Force-displacement coefficient NDE $k_{s,NDE}$ / N · mm^{-1}	−82	−203
Force-displacement coefficient DE $k_{s,DE}$ / N · mm^{-1}	−40	−134
Force-current coefficient NDE $k_{F,NDE}$ / N · A^{-1}	15.2	40
Force-current coefficient DE $k_{F,DE}$ / N · A^{-1}	1.8	3.9
Position control proportional gain K_P	$K_{P,n}$	$K_{P,n}$
Position control derivative gain K_D	$K_{D,n}$	$K_{D,n}$
Superposition effect coefficient[2)] $k_{err,sup}$ / N · A^{-2}	0.0042	0.0049
Eddy current error angle[2)] $\varepsilon_{err,Ft}$ at n_N	6.7°	11°
Eddy current amplitude degradation[2)] $G_{Ft,a,0}$ at n_N	0.95	0.9
Stator inner radius $r_{S,i}$ / mm	17.5	30
Magnet height h_{PM} / mm	2.75	8
Effective air gap width $\delta_{eff} = h_{PM} + h_{sl} + \delta$ / mm	5.25	12

[1)] NDE: Combined radial-axial AMB, DE: Bearingless machine; [2)] From 2D analytical calculation

half motors, these two effects are present in both bearing planes DE and NDE simultaneously, also influencing the rigid rotor parallel mode eigenfrequencies.

5.3.1. Modeling of the Eddy Current Effect for the Rotor Position Control

In Section 2.4 the frequency response data $\underline{G}_{Ft} = \underline{F}_L/\underline{F}_{L,ref}$ is derived, which describes the amplitude and the phase of the actual radial force vector $\underline{F}_L$ with rotor eddy currents in the bearingless machine with respect to the reference bearing force vector $\underline{F}_{L,ref}$ without eddy currents. A decomposition into the aligned force vector component yields

$\underline{G}_{\mathrm{Ft,a}}$ (Fig. 2.10). The frequency dependency of the perpendicular force vector component is given by $\underline{G}_{\mathrm{Ft,p}}$ (Fig. 2.10). Note that the static transfer behavior at $f_{\mathrm{L}} = 0$ is expressed as $G_{\mathrm{Ft,a,0}}$ and $G_{\mathrm{Ft,p,0}}$ as real values. In order to include the frequency-response data into the system model, the frequency response functions $\underline{G}_{\mathrm{Ft,a}}(j\omega_{\mathrm{L}})$ and $\underline{G}_{\mathrm{Ft,p}}(j\omega_{\mathrm{L}})$ are used as transfer functions $\underline{G}_{\mathrm{Ft,a}}(s)$ and $\underline{G}_{\mathrm{Ft,p}}(s)$ in the *Laplace* domain. These functions are simplified for easier representation by first order functions of the type $(t+u\cdot s)/(v+w\cdot s)$ with the calculated complex-valued constants t, u, v and w as linear time invariant (LTI)-representation of the frequency response by using the *Matlab-tfest*-function as $\underline{\tilde{G}}_{\mathrm{Ft,a}}(s) \approx \underline{G}_{\mathrm{Ft,a}}(s)$, $\underline{\tilde{G}}_{\mathrm{Ft,p}}(s) \approx \underline{G}_{\mathrm{Ft,p}}(s)$. Fig. 5.11 gives the implementation of the transfer functions $\underline{\tilde{G}}_{\mathrm{Ft,a}}(s)$, $\underline{\tilde{G}}_{\mathrm{Ft,p}}(s)$ in the system model. For example, Fig. 5.12 and 5.13 show the analytically calculated frequency response $\underline{G}_{\mathrm{Ft}}(f_{\mathrm{L}})$ as amplitude and phase response according to Fig. 2.14 and the approximated first order LTI transfer functions $\underline{\tilde{G}}_{\mathrm{Ft}}$ of the motor *LLM4*$_{\mathrm{r+}}$. It proves the good accuracy of the *Matlab*-approximation $\underline{\tilde{G}}_{\mathrm{Ft}}(s) \approx \underline{G}_{\mathrm{Ft}}(s)$. Only for $\angle\underline{G}_{\mathrm{Ft,p}}$ at $f_{\mathrm{L}} > 800$ Hz the calculated and approximated characteristics differ considerably. For $f_{\mathrm{L}} < 500$ Hz the transfer function is similar to that at $f_{\mathrm{L}} = 0$: $\left|\underline{\tilde{G}}_{\mathrm{Ft,a}}\right| \approx \left|\underline{G}_{\mathrm{Ft,a,0}}\right|$, $\angle\underline{\tilde{G}}_{\mathrm{Ft,a}} \approx 0$, $\left|\underline{\tilde{G}}_{\mathrm{Ft,p}}\right| \approx \left|\underline{G}_{\mathrm{Ft,p,0}}\right|$ and $\angle\underline{\tilde{G}}_{\mathrm{Ft,p}} \approx 180°$ for pos-

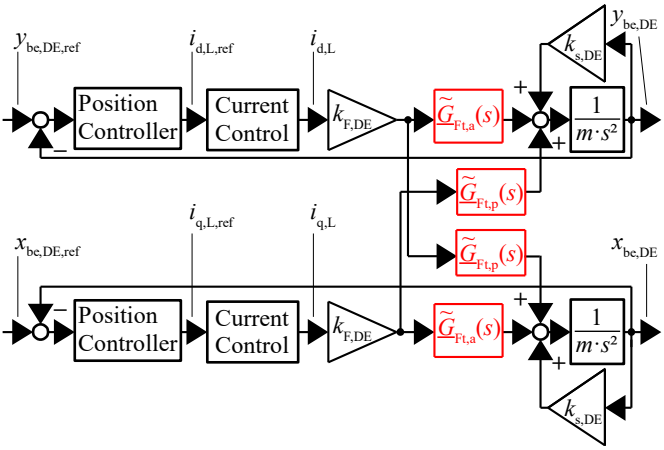

Fig. 5.11.: Simplified block diagram for the position control of a bearingless PM synchronous machine with rotor eddy currents. Only the *x*-*y* bearingless machine plane be,DE is considered (Fig. 5.1), neglecting conical rigid rotor motions.

itive speed ($n > 0$), respectively $\angle\tilde{\underline{G}}_{\mathrm{Ft,p}} \approx 0°$ for negative speed ($n < 0$). The state space description can be significantly simplified by using these "static" approximations, which are assumed to be independent from f_{L}, but speed-dependent: $G_{\mathrm{Ft,a,0}} = \left|\underline{G}_{\mathrm{Ft,a}}(f_{\mathrm{L}} = 0)\right|$, $G_{\mathrm{Ft,p,0}} = -\left|\underline{G}_{\mathrm{Ft,p}}(f_{\mathrm{L}} = 0)\right|$ for $n > 0$ and $G_{\mathrm{Ft,p,0}} = \left|\underline{G}_{\mathrm{Ft,p}}(f_{\mathrm{L}} = 0)\right|$ for $n < 0$.
Fig. 5.14 shows the calculated influence of the eddy current effect on the system eigenvalues of $\boldsymbol{A}_{\mathrm{w}}$ at motor no-load condition, where no superposition effect occurs. The gray lines indicate in addition the situation without eddy currents, hence, $\varepsilon_{\mathrm{err,Ft}} = 0$. The blue lines consider the case, in which the eddy current effect is approximated by its static transfer behavior ($G_{\mathrm{Ft,a,0}}$, $G_{\mathrm{Ft,p,0}}$, $f_{\mathrm{L}} \to 0$). The red line is the result for the eddy current representation by 1st order LTI functions. It can be concluded that the system behavior is described

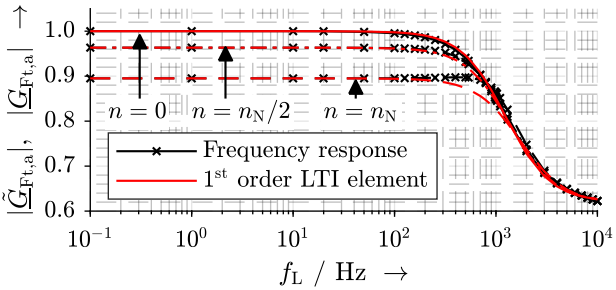

(a) Amplitude response

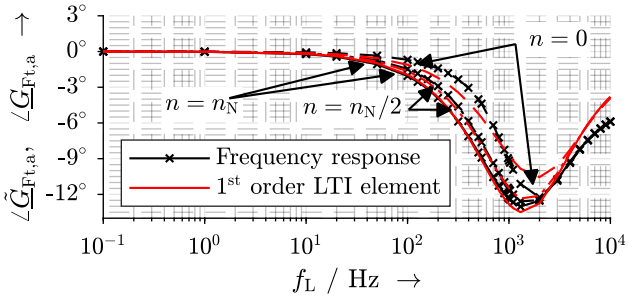

(b) Phase response

Fig. 5.12.: Motor *LLM4*$_{\mathrm{r+}}$: Analytically calculated bearing force frequency response $\underline{G}_{\mathrm{Ft,a}}$ and approximated LTI characteristic $\tilde{\underline{G}}_{\mathrm{Ft,a}}$ at different speed 0, $n_{\mathrm{N}}/2 = 20000\ \mathrm{min}^{-1}$, $n_{\mathrm{N}} = 40000\ \mathrm{min}^{-1}$ (values with respect to the magnetostatic calculation at zero rotor eddy currents)

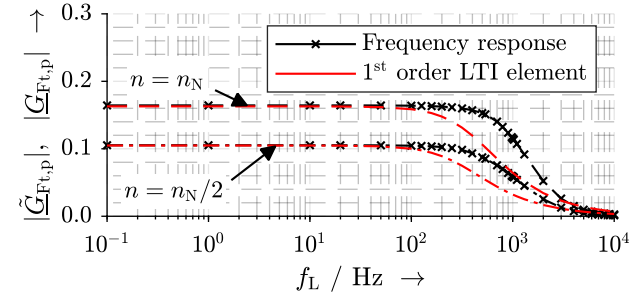

(a) Amplitude response

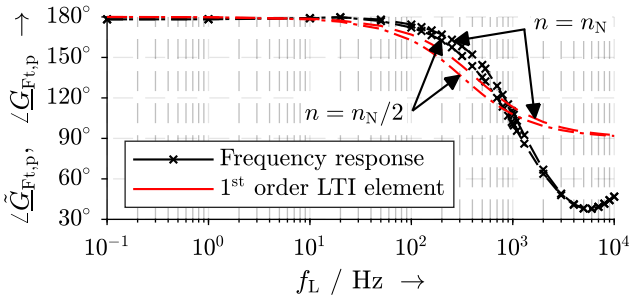

(b) Phase response

Fig. 5.13.: Motor *LLM4*$_{\mathrm{r+}}$: Analytically calculated disturbing bearing force frequency response $\underline{G}_{\mathrm{Ft,p}}$ and approximated LTI characteristic $\tilde{\underline{G}}_{\mathrm{Ft,p}}$ at different speed 0, $n_{\mathrm{N}}/2 = 20000\ \mathrm{min}^{-1}$, $n_{\mathrm{N}} = 40000\ \mathrm{min}^{-1}$ (values with respect to the magnetostatic calculation at zero rotor eddy currents)

well by the static transfer behavior, since the red and the blue lines are close in Fig. 5.14. Therefore, the eddy current effect is represented well by the feed-through matrix $\boldsymbol{D}_{\mathrm{w}} = \boldsymbol{K}_{\mathrm{Ft}}$ in the state space model (5.24). The values $G_{\mathrm{Ft,a,0}}$, $G_{\mathrm{Ft,p,0}}$ are obtained for different values of speed (0 ... n_{N}). The distinction between positive and negative speed in (5.24) results from the fact that the perpendicular levitation force $F_{\mathrm{L,p}}$ is aligned with the positive x-direction for negative speed and it is aligned with the negative x-direction

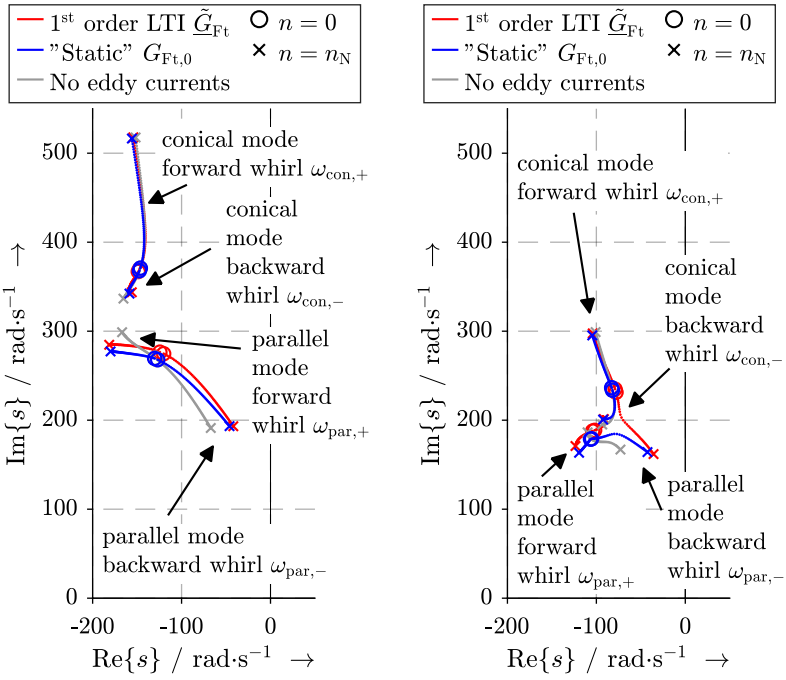

(a) *LLM4* (b) *LLM4*$_{\mathrm{r+}}$

Fig. 5.14.: Analytically calculated root loci of the closed-loop system eigenvalues of $\boldsymbol{A}_{\mathrm{w}}$ for varying speed n for controller parameters tuned according to natural stiffness and damping for no-load motor operation at $0 < n < n_{\mathrm{N}}$ (the four additional eigenvalues of the 1st order LTI functions are not displayed since their real part is $< -800\,\mathrm{rad}\cdot\mathrm{s}^{-1}$.)

for positive speed due to the speed dependence of the rotor frequency $f_{\mathrm{R}}(n)$ (2.14).

$$\boldsymbol{K}_{\mathrm{Ft}}(n) = \begin{pmatrix} 1 & 0 & 0 & 0 \\ 0 & G_{\mathrm{Ft,a,0}}(n) & 0 & \mp G_{\mathrm{Ft,p,0}}(n) \\ 0 & 0 & 1 & 0 \\ 0 & \pm G_{\mathrm{Ft,p,0}}(n) & 0 & G_{\mathrm{Ft,a,0}}(n) \end{pmatrix}; \; n \gtrless 0 \tag{5.24}$$

The system eigenvalues in Fig. 5.14 have negative real parts, corresponding to a stable levitation, even in case with disturbing rotor eddy currents. The backward-whirling eigen-

values in the s-plane are shifted closer to the imaginary axis, which is the stability limit, by the eddy current effect. Thus, the stability margin is reduced by rotor eddy currents. Even though the field distortion by eddy currents is small for the *LLM4*, both machines *LLM4* and $LLM4_{r+}$ exhibit a similar shift of eigenvalues towards the imaginary axis in the s-plane. The reason for that is the larger gyroscopic effect in the *LLM4*, associated with the higher rated speed (*LLM4*: $n_N = 60000\ \mathrm{min}^{-1}$, $LLM4_{r+}$: $n_N = 40000\ \mathrm{min}^{-1}$) and a higher ratio of Θ_{pol}/Θ_{ax} of 0.046 instead of 0.029 (Table 5.5).
The cross-coupling terms $\pm\Theta_{pol} \cdot 2\pi n$ between x- and y-axis in the gyroscopic matrix $\boldsymbol{G}$ (5.1) exhibit the same sign as the cross-coupling terms $\pm G_{Ft,p,0}$ in $\boldsymbol{K}_{Ft}$ ((5.24)), which decreases the stability margin. Nevertheless, the eddy current effect alone does not destabilize the system.

5.3.2. Modeling of the Superposition Effect for the Rotor Position Control

The superposition effect is based on the reaction between stator drive field and the suspension winding field and results – neglecting magnetic iron saturation – solely in a perpendicular disturbance force $F_{err,sup}$, causing the error angle $\varepsilon_{err,sup}$, if the motor is driven in q-current operation with the drive current $i_{q,D}$ (Section 2.5). Neglecting iron saturation, the magnitude of $\varepsilon_{err,sup}$ depends on $i_{q,D}$ as a load dependency and on the required suspension current i_L as a bearing force dependency. The perpendicular force $F_{err,sup}$ is calculated in Section 2.5 by $i_{q,D} \cdot i_L \cdot k_{err,sup}$ and strongly depends on the load torque M due to $M \propto i_{q,D}$. Therefore, the dimensionless force angle $\varepsilon_{err,sup}$ (5.25) is used in (5.26) to describe the superposition effect as transfer function via the matrix $\boldsymbol{K}_{int}$. The superposition effect does not add new poles to the closed-loop system because its state space representation is given by a feed-through matrix $\boldsymbol{D}_w = \boldsymbol{K}_{int}$, having its entries at the same position as $\boldsymbol{G}$ (5.1).

$$\varepsilon_{err,sup} = \arctan\left(-\frac{i_{q,D} \cdot k_{err,sup}}{k_{F,DE}}\right) \tag{5.25}$$

$$\boldsymbol{K}_{int} = \begin{pmatrix} 1 & 0 & 0 & 0 \\ 0 & 1 & 0 & -\tan\left(\varepsilon_{err,sup}\right) \\ 0 & 0 & 1 & 0 \\ 0 & \tan\left(\varepsilon_{err,sup}\right) & 0 & 1 \end{pmatrix} \tag{5.26}$$

For $i_{\mathrm{q,D}} < 0$, the cross-coupling terms $\pm\Theta_{\mathrm{pol}} \cdot 2\pi n$ between x- and y-axis in the gyroscopic matrix $\boldsymbol{G}$ (5.1) exhibit the same sign as the cross-coupling terms $\pm\tan\left(\varepsilon_{\mathrm{err,sup}}\right)$ in $\boldsymbol{K}_{\mathrm{int}}$ ((5.26)), which decreases the stability margin.

5.3.3. Superposition of the Eddy Current and Superposition Effect for the Rotor Position Control

Including the eddy current effect via $\boldsymbol{K}_{\mathrm{Ft}}$ and the superposition effect via $\boldsymbol{K}_{\mathrm{int}}$ into the state space description (5.12)–(5.17) leads to the description according to (5.27)–(5.30). The Sections 5.3.1 and 5.3.2 have shown that in case of positive speed $n > 0$ and generator mode operation $i_{\mathrm{q,D}} < 0$ the cross-coupling terms in $\boldsymbol{K}_{\mathrm{Ft}}$ and $\boldsymbol{K}_{\mathrm{int}}$ exhibit the same sign as the gyroscopic matrix $\boldsymbol{G}$. Thus, for the stability analysis only the worst case is considered, where the cross-coupling terms in $\boldsymbol{G}$, $\boldsymbol{K}_{\mathrm{int}}$ and $\boldsymbol{K}_{\mathrm{Ft}}$ add up.

$$\boldsymbol{x}_{\mathrm{w}} = \boldsymbol{x}_{\mathrm{o}}; \quad \boldsymbol{y}_{\mathrm{w}} = \boldsymbol{y}_{\mathrm{o}}; \quad \boldsymbol{u}_{\mathrm{w}} = \boldsymbol{0} \tag{5.27}$$

$$\boldsymbol{A}_{\mathrm{w}} = \begin{pmatrix} \boldsymbol{O} & \boldsymbol{I} \\ \boldsymbol{A}_{\mathrm{w,1}} & \boldsymbol{A}_{\mathrm{w,2}} \end{pmatrix} \tag{5.28}$$

$$\boldsymbol{A}_{\mathrm{w,1}} = -\boldsymbol{M}^{-1} \cdot \left(\boldsymbol{K}_{\mathrm{s,COG}} + \boldsymbol{T}_{\mathrm{F,be,COG}} \boldsymbol{K}_{\mathrm{sup}} \boldsymbol{K}_{\mathrm{Ft}} \boldsymbol{K}_{\mathrm{P,be}}\right)$$

$$\boldsymbol{A}_{\mathrm{w,2}} = -\boldsymbol{M}^{-1} \cdot \left(\boldsymbol{G} + \boldsymbol{T}_{\mathrm{F,be,COG}} \boldsymbol{K}_{\mathrm{int}} \boldsymbol{K}_{\mathrm{Ft}} \boldsymbol{K}_{\mathrm{D,be}}\right)$$

$$\boldsymbol{B}_{\mathrm{w}} = \begin{pmatrix} \boldsymbol{O} \\ \boldsymbol{M}^{-1} \cdot \boldsymbol{T}_{\mathrm{F,be,COG}} \cdot \boldsymbol{K}_{\mathrm{int}} \cdot \boldsymbol{K}_{\mathrm{Ft}} \end{pmatrix}; \tag{5.29}$$

$$\boldsymbol{C}_{\mathrm{w}} = \boldsymbol{C}_{\mathrm{o}}; \quad \boldsymbol{D}_{\mathrm{w}} = \boldsymbol{D}_{\mathrm{o}} \tag{5.30}$$

Consequently, a big eddy current error angle $\varepsilon_{\mathrm{err,Ft}}$ reduces the admissible drive error angle $\varepsilon_{\mathrm{err,sup}} \propto i_{\mathrm{q,D}}$ (5.26) and, hence, the admissible torque M. In Table 5.6, four differently strong of the eddy current effects (Set 0 $\rightarrow$ small eddy current effect ... Set 3 $\rightarrow$ strong eddy current effect) are given together with the associated maximum superposition error angle $\varepsilon_{\mathrm{err,sup}}$. Set 1 corresponds to the eddy current effect in the motor *LLM4*, set 2 corresponds to the motor $LLM4_{\mathrm{r+}}$. Set 0 and set 3 shall exemplify how the system stability of the two motors would be influenced, if the motors were physically designed with a smaller respectively a bigger eddy current effect. The maximum admissible drive error angle $\varepsilon_{\mathrm{err,sup}}$ in Table 5.6 is derived from Fig. 5.15, which shows the analytically calculated system eigenvalues of $\boldsymbol{A}_{\mathrm{w}}$ (5.28) for Set 0 ... Set 3. Note that the eight eigenvalues

of $\boldsymbol{A}_{\mathrm{w}}$ consist of four pairs of complex conjugated eigenvalues, among which only the eigenvalues with positive imaginary part are shown in Fig. 5.15. A set (Set 0 ... Set 3) is defined to have its maximum drive error angle if the real part of one eigenvalue reaches zero at $n = n_{\mathrm{N}}$. Throughout the analysis, position controller tuning according to natural stiffness (5.18) and damping (5.19) is assumed [4], applying decentralized control. As shown in Section 5.2.2, this is a feasible control setup for bearingless machines. Further, ideal current control and sensor transfer behavior are assumed for conclusions, which are independent of particular current control and sensor deficiencies. Certainly the stability margin is reduced in practice by non-ideal current control and by sensor detection errors in addition.

Table 5.6 shows that the same intensity of the eddy current effect leads to a smaller maximum drive error angle for the smaller machine *LLM4* (Fig. 5.15a), since the gyroscopic coupling term $\Theta_{\mathrm{pol}}/\Theta_{\mathrm{ax}}$ is bigger than for the $LLM4_{\mathrm{r}+}$ (Fig. 5.15b). However, the small machine *LLM4* exhibits inherently a smaller eddy current effect (set 1) than the larger machine $LLM4_{\mathrm{r}+}$ (set 2), so that the admissible drive error angle of the motor *LLM4* is slightly bigger ($20^\circ > 17.5^\circ$). According to Fig. 5.15 and Table 5.6, the admissible drive error angle decreases disproportionately with an increasing eddy current error angle because besides the spatial shift of the bearing force vector also the bearing force amplitude is reduced by $0 < G_{\mathrm{Ft,a,0}} < 1$ (Fig. 2.10).

At the prototype machine *LLM4*, it is difficult to prove the system instability at maximum influence of the eddy current and superposition effect, since damage can occur at necessarily high speed. Therefore, in comparison to the measurement in Fig. 5.10, a four-times bigger acceleration and four-times bigger load torque during acceleration and deceleration

Table 5.6.: Eddy current effect properties $G_{\mathrm{Ft,a,0}}$, $\varepsilon_{\mathrm{err,Ft}}$ at rated speed n_{N} and resulting maximum drive current $i_{\mathrm{q,D}}$ associated with maximum drive error angle $\varepsilon_{\mathrm{err,sup}}$

			LLM4		$LLM4_{\mathrm{r}+}$	
	$G_{\mathrm{Ft,a,0}}$ [1)]	$\varepsilon_{\mathrm{err,Ft}}$ [1)]	$i_{\mathrm{q,D}}$	$\varepsilon_{\mathrm{err,sup}}$	$i_{\mathrm{q,D}}$	$\varepsilon_{\mathrm{err,sup}}$
Set 0	1.00	0°	-165 A	39°	-563 A	45°
Set 1	0.95	6.7°	-90 A	20°	-343 A	25.5°
Set 2	0.90	11°	-54 A	12°	-239 A	17.5°
Set 3	0.83	15°	-21 A	4.5°	-129 A	9.3°

[1)] calculated at $n = n_{\mathrm{N}}$

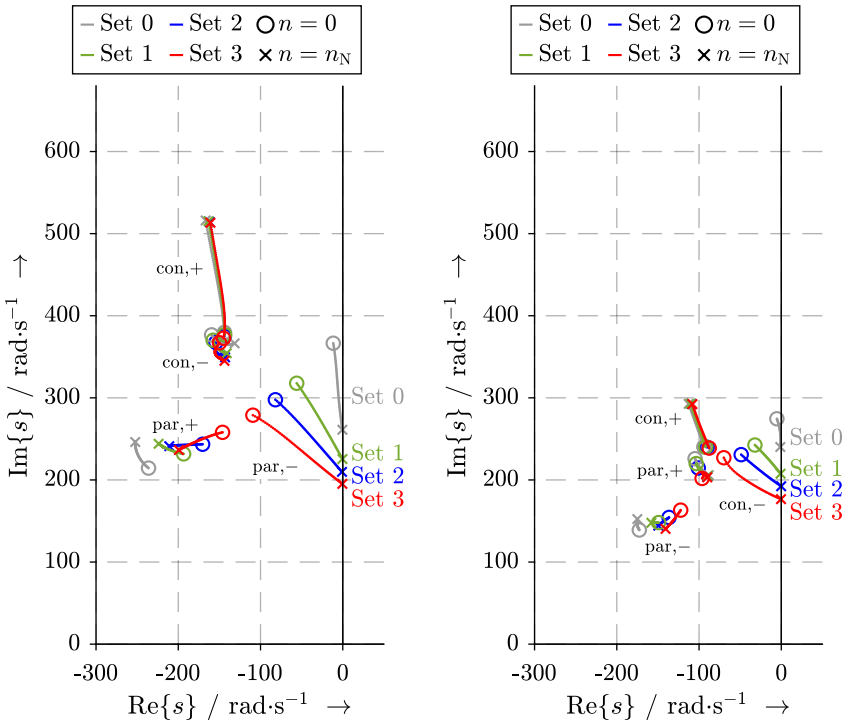

(a) *LLM4* (b) *LLM4*$_{r+}$

Fig. 5.15.: Analytically calculated root loci of the closed-loop system eigenvalues of $\boldsymbol{A}_w$ for varying speed n for controller parameters tuned according to natural stiffness and damping ($0 < n < n_N$) for the following eddy current parameter sets, Set 0: no eddy current effect, Set 1: small eddy current effect typical for the *LLM4*, Set 2: increased eddy current effect typical for the *LLM4*$_{r+}$, Set 3: strong eddy current effect

was simulated for the *LLM4* in *Simulink* (Fig. 5.16). The goal of this increase is to increase the superposition effect up to $\varepsilon_{err,sup} = 18°$ instead of the measured $\varepsilon_{err,sup} = 1.5°$. The same simplifying assumptions as in the calculation before are taken, such as ideal current control and sensor transfer behavior, using natural stiffness and damping controller settings. Rotor unbalance forces are neglected, since they can be filtered by a notch-filter as in Fig. 5.10. In contrast to Fig. 5.15 and Table 5.6, the maximum drive error angle

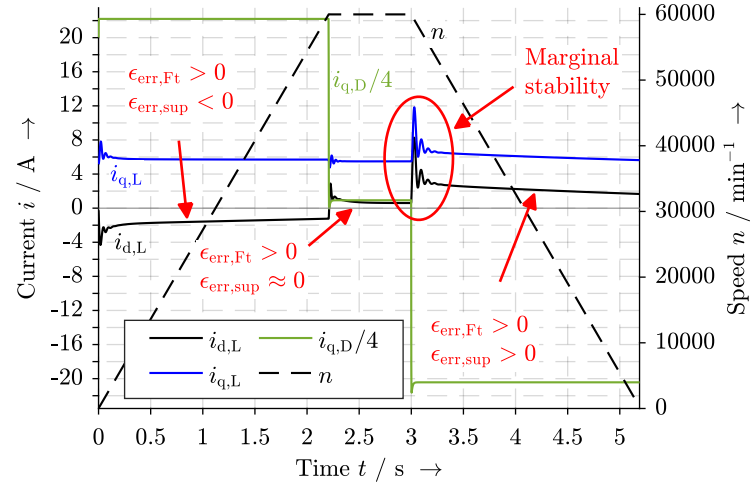

(a) Position current $i_{\mathrm{dq,L}}$, drive current $i_{\mathrm{q,D}}$ and speed n characteristic

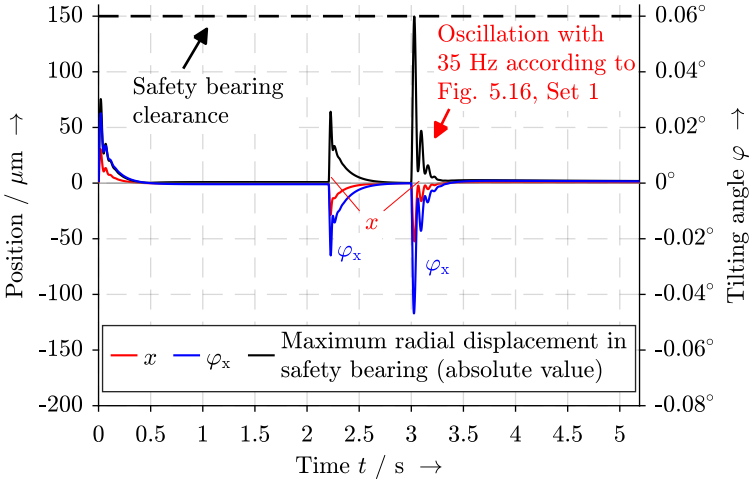

(b) x-position and φ_{x} tilting angle in COG coordinates and radial displacement in the safety bearing with a clearance of 150 μm

Fig. 5.16.: Simulated run-up/run-down for the prototype machine *LLM4*, acceleration/deceleration with $|i_{\mathrm{q,D}}| = 89$ A ($0 \le t \le 2.3$ s: motor operation; 2.3 s $\le t \le 3$ s: motor no-load; $t > 3$ s: generator braking operation; sampling time: 29 ms)

is $\varepsilon_{\mathrm{err,sup}} = 18^\circ < 20^\circ$ to avoid contact in the DE safety bearing, which has clearance of 150 μm. At $t = 3$ s the eddy current and the superposition error angle add up to $18^\circ + 6.7^\circ$ and lead to a weakly damped oscillation of the tilting angle φ_x. The oscillation takes place with the dominant eigenfrequency $f_\mathrm{eig} = 35$ Hz of the dominant pole in Fig. 5.15, Set 1.

5.3.4. Measures for Increasing the Stability Margin

The eddy current and superposition effect can be reduced by a proper machine design, i.e. by increasing the pole count $2p$, by decreasing the bore radius $r_\mathrm{S,i}$ and by PM segmentation (Section 3.6). A further improvement of the system stability can be achieved by reducing the influence of the cross-coupling terms in $\boldsymbol{K}_\mathrm{int}$, $\boldsymbol{K}_\mathrm{Ft}$ and $\boldsymbol{G}$. The gyroscopic coupling can be well counteracted by a centralized control approach with complete separation of the conical rigid rotor modes (Section 5.2.2). The influence of the superposition effect can be counteracted by a feed-forward control [139], since the disturbing force is known by the drive and suspension current amplitude. The eddy current effect could also be mitigated by a feed-forward, if the quantities $G_\mathrm{Ft,a,0}$ and $G_\mathrm{Ft,p,0}$ are known in advance, e.g. from simulations and measurement in Fig. 2.13. Here, the influence of an increase in controller proportional gain $K_\mathrm{P} = 1.5 \cdot K_\mathrm{P,n}$ (Fig. 5.17) and derivative gain $K_\mathrm{D} = 1.5 \cdot K_\mathrm{D,n}$ (Fig. 5.18) is discussed if a standard decentralized controller design is applied.

Comparing Fig. 5.15 with natural stiffness controller settings and Fig. 5.17 with 50% higher proportional gain K_P, one can see that the critical poles associated with the backward-whirling mode (*LLM4*: parallel mode, $LLM4_{\mathrm{r}+}$: conical mode) are moved to the positive real part of the s-plane. The stability limit is especially violated if the superposition effect is strong. Therefore, instability can be present even at standstill. Comparing Fig. 5.15 with natural damping controller settings and Fig. 5.18 with 50% higher derivative gain K_D, one can see that the critical poles associated with the backward-whirling mode (*LLM4*: parallel mode, $LLM4_{\mathrm{r}+}$: conical mode) are moved farther to the negative real part of the s-plane, thus, increasing the stability margin. The increase of the controller derivative gain turns out to be a good measure to counteract the loss of stability margin by the eddy current and superposition effect.

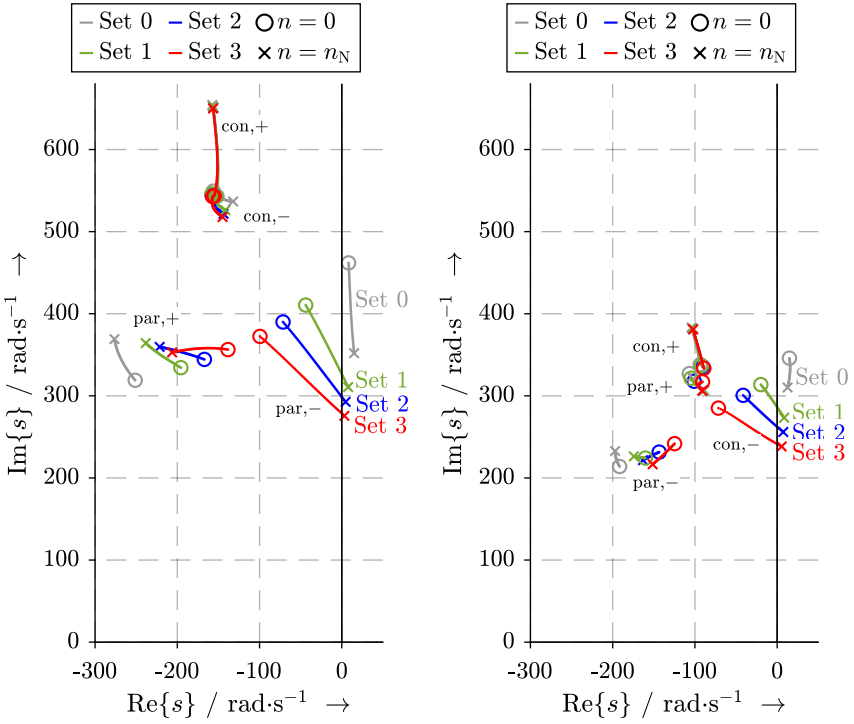

(a) *LLM4* (b) *LLM4*$_{r+}$

Fig. 5.17.: Analytically calculated root loci of the closed-loop system eigenvalues of $\boldsymbol{A}_w$ for varying speed n for the eddy current and superposition parameter (Set 0 ... Set 3) according to Fig. 5.15, applying natural damping, but 1.5-times natural stiffness $K_P = 1.5 \cdot K_{P,n}$

5.3.5. Recommendation for Maximum Force Error Angle

Sections 5.3.1–5.3.4 have shown that the maximum admissible drive error angle $\varepsilon_{err,sup}$ depends on the eddy current error angle $\varepsilon_{err,Ft}$ and on the cross-coupling due to the gyroscopic rotor properties. Due to these interdependencies no general design rule for the maximum error angles can be given. Also it depends on the application, e.g. how much settling time and overshoot are desired. The maximum error angles in Table 5.6 are based on the condition that the real part of the dominant system pole pair of the matrix $\boldsymbol{A}_w$ gets zero, hence, reaching the stability limit. In practice, current control, sensor deficiencies

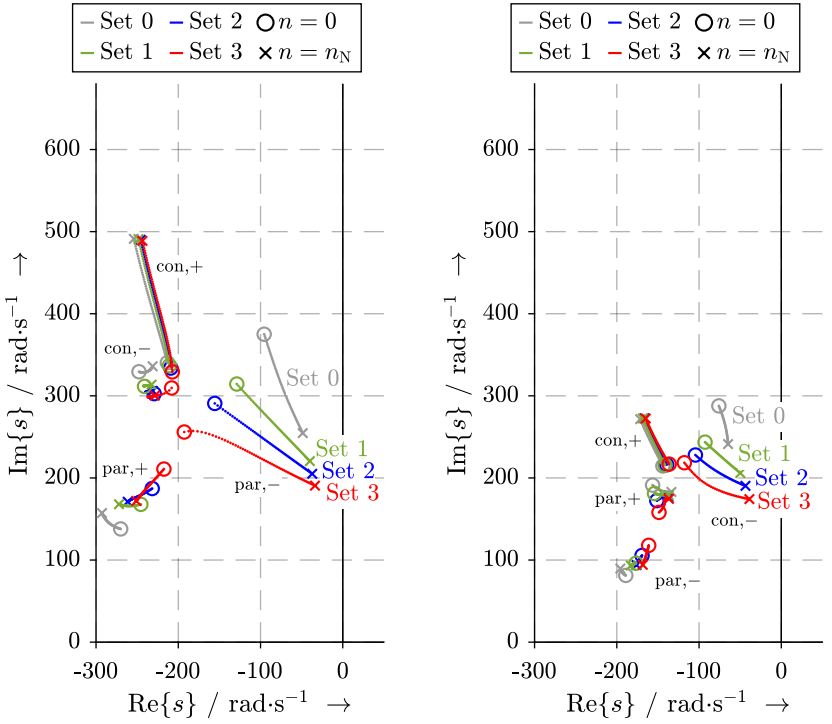

(a) *LLM4* (b) *LLM4*$_{r+}$

Fig. 5.18.: Analytically calculated root loci of the closed-loop system eigenvalues of $\boldsymbol{A}_w$ for varying speed n for the eddy current and superposition parameter (Set 0 ... Set 3) according to Fig. 5.15, applying natural stiffness, but 1.5-times natural damping $K_D = 1.5 \cdot K_{D,n}$

and cross-coupling forces, based on magnetic saturation (see Section 2.6), further reduce the stability margin and restrict the admissible error angles by the eddy current and the superposition effect. Therefore, it is recommended to stay below the maximum values for $\varepsilon_{err,sup}$ from Table 5.6.

Motivated by these deficiencies, for the *LLM4* a damping ratio of 0.12, equal to 70% overshoot, is defined as stability reserve, which corresponds to the gray area in Fig. 5.19. Applying this stability margin instead of no stability margin in Fig. 5.15 and Table 5.6, leads to a maximum admissible drive error angle of only $\varepsilon_{err,sup} = 7°$ for the *LLM4*

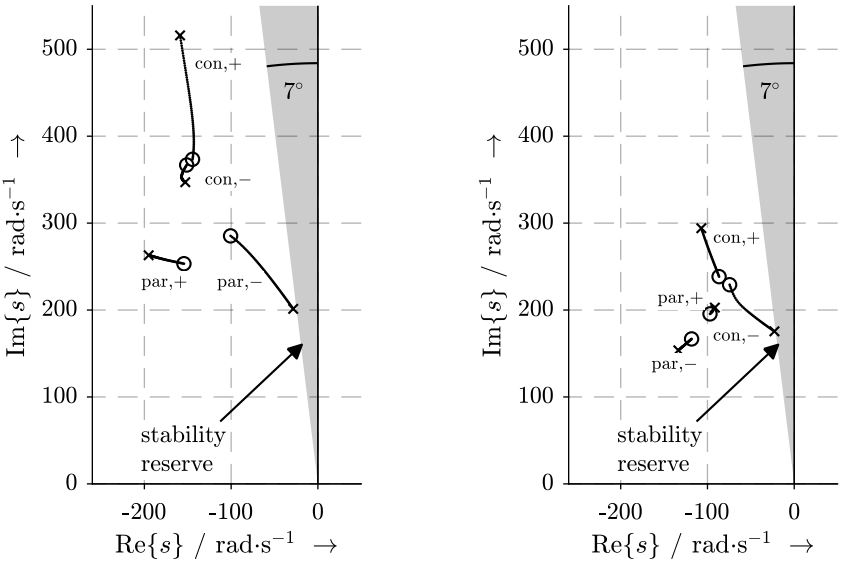

(a) *LLM4* with $\varepsilon_{\mathrm{err,Ft}} = 6.7°$, $G_{\mathrm{Ft,a,0}} = 0.95$, $\varepsilon_{\mathrm{err,sup}} = 7°$

(b) *LLM4*$_{\mathrm{r+}}$ with $\varepsilon_{\mathrm{err,Ft}} = 11°$, $G_{\mathrm{Ft,a,0}} = 0.9$, $\varepsilon_{\mathrm{err,sup}} = 7°$

Fig. 5.19.: Defined stability reserve and calculated root loci of the closed-loop system eigenvalues of $\boldsymbol{A}_{\mathrm{w}}$ for varying speed n for controller parameters tuned according to natural stiffness and damping ($0 < n < n_{\mathrm{N}}$)

with $\varepsilon_{\mathrm{err,Ft}} = 6.7°$, corresponding to $i_{\mathrm{q,D}} = -32$ A in Fig. 5.15a. For the *LLM4*$_{\mathrm{r+}}$ with $\varepsilon_{\mathrm{err,Ft}} = 11°$ Fig. 5.15b shows that the introduced stability margin limits the maximum drive error angle to be also $\varepsilon_{\mathrm{err,sup}} = 7°$, corresponding to $i_{\mathrm{q,D}} = -97$ A.

6. Generation of the Axial Force Current

6.1. Concept Presentation

The position control of the axial rotor degree of freedom (in z-direction) by a zero-sequence current i_0 was identified in Section 1.4 as one promising option to reduce costs and system complexity of bearingless high-speed drives. As such, small rotor diameters are necessary to keep the mechanical stress in the rotor at a suitable level. However, for these rotors, commonly cylindrical, a separate AMB for axial position control, a so-called thrust AMB (Appendix A.5), is required. It is usually fed by a 4-quadrant chopper, which requires four power switches, thus, increasing the system costs.
The novel feeding technique avoids this additional DC supply. BMs are usually equipped with two 3-phase stator windings with two star-points, either as one combined torque and suspension winding, like for the considered prototype machine *LLM4*, or as two separated

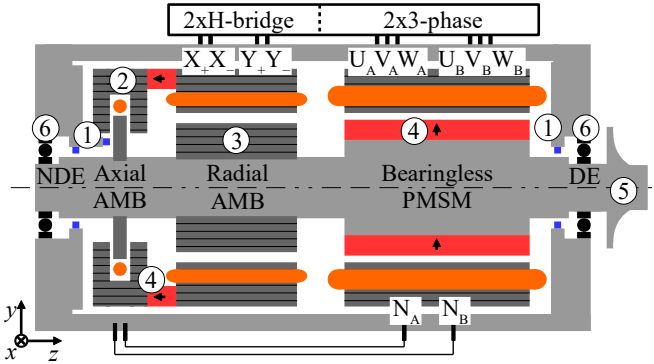

Fig. 6.1.: Drive components of the *LLM4* (schematic): ① position and rotor angle sensors, ② axial part of combined AMB, ③ radial part of combined AMB, ④ PM with 2-pole magnetization direction, ⑤ turbo-compressor wheel, ⑥ safety bearings at drive and non-drive end (DE / NDE)

torque and suspension windings as described in [24]. With the new concept, all the six stator winding terminals are used to generate torque, radial and axial bearing force at the same time. This is realized by feeding the axial bearing with the star-point current i_{ax} as superposition of the three zero-sequence phase currents in both 3-phase systems A and B ($i_{ax} = 3 \cdot i_0$). The implementation is shown schematically in Fig. 6.1.

In contrast to the topology presented in [66, 67, 68] (see Section 1.4), the axial bearing current i_{ax} is not generated between one star point and the neutral inverter terminal (Fig. 6.2a), but between two star-points N_A and N_B (Fig. 6.1, 6.2b). This is realized by using the electric potentials $\varphi_{N,A}$ and $\varphi_{N,B}$ of the two star points [63]. This way, the full DC-link voltage U_{DC} is applied to the axial magnetic bearing. If two bearingless half-motors are used, it is also possible to use the difference of four star-point potentials in order to control the axial current i_{ax} (Fig. 6.2c). This is not considered here, since the axial bearing voltage requirement is low (Section 7.3). Generally, the zero-sequence current feeding can also be used in higher power classes, if insulated-gate bipolar transistors (IGBT) instead of the here applied metal oxide semiconductor field-effect transistors (MOSFET) are used. Merits and constraints of this technique are discussed in Chapter 7.

The star point current i_{ax}, flowing through the axial bearing winding between the two star points of the 3-phase stator windings A and B, also flows as zero-sequence phase current $i_0 = i_{ax}/3$ through the bearingless motor 3-phase windings. Thus, the voltage drop over the impedance of the motor windings in one phase, consisting of the phase winding resistance R_s and the (stray) inductance $L_{s,\sigma,0}$, is considered in Fig. 6.3. The three motor phase impedances are in parallel for the current i_{ax}. This parallel configuration is twice in series, for the in- and out flowing current i_{ax}. The related parasitic effects of the zero-sequence current within the active part of the bearingless motor and the calculation of $L_{s,\sigma,0}$ are treated in Section 7.2.

According to Fig. 6.3 the *ohm*ic-inductive voltage drop u_{ax} over the axial AMB is determined by the difference in the mean value of the electric potential between the phase terminals $\frac{\varphi_{U,A}+\varphi_{V,A}+\varphi_{W,A}}{3}$ and $\frac{\varphi_{U,B}+\varphi_{V,B}+\varphi_{W,B}}{3}$. Thus, the here considered modulation techniques – presented in Section 6.3 and 6.4 – are based on adapting the mean value of the motor terminal electric potentials. On the other hand, a current i_{ax} inherently flows, if any difference in potential ($\varphi_{N,A} - \varphi_{N,B}$) between the star points occurs. Such a difference automatically arises from the generation of the drive and suspension winding voltage space vectors. This can lead to unwanted oscillations of i_{ax} at high inverter modulation indices (see Section 7.1).

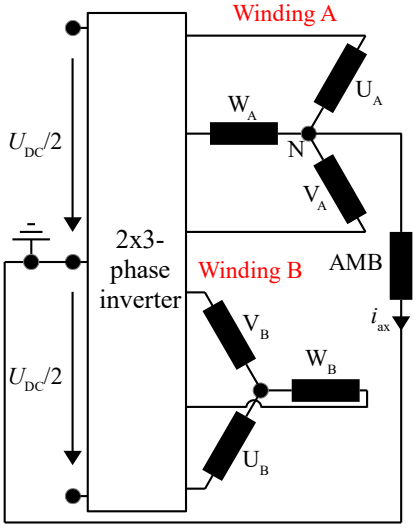

(a) Single star-point current i_{ax}

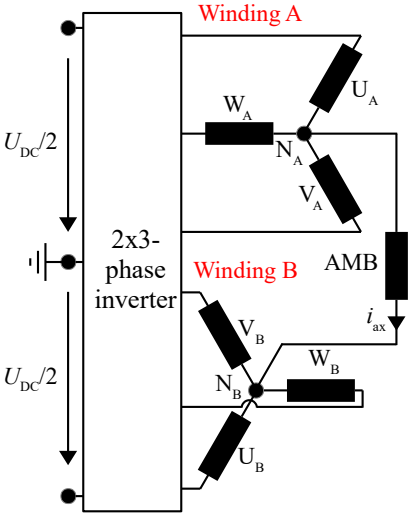

(b) Twofold star-point current i_{ax}

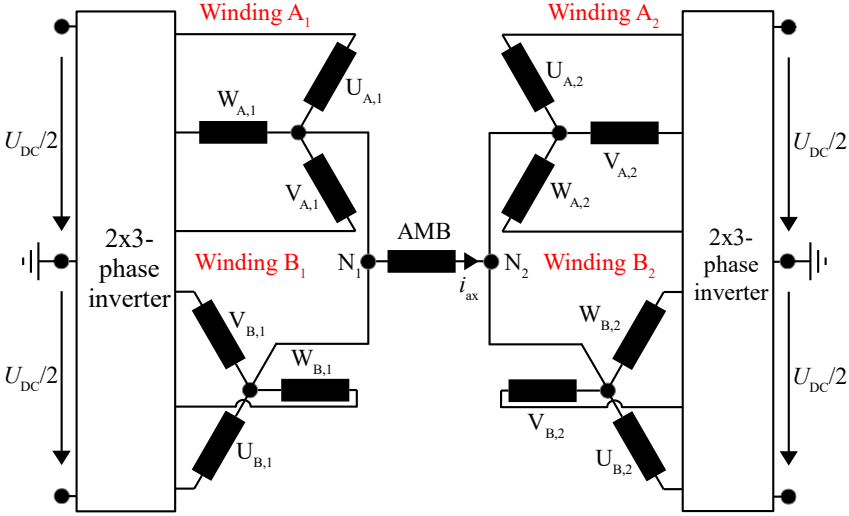

(c) Fourfold star-point current i_{ax}

Fig. 6.2.: Different topologies of feeding an axial AMB with a star-point current i_{ax}

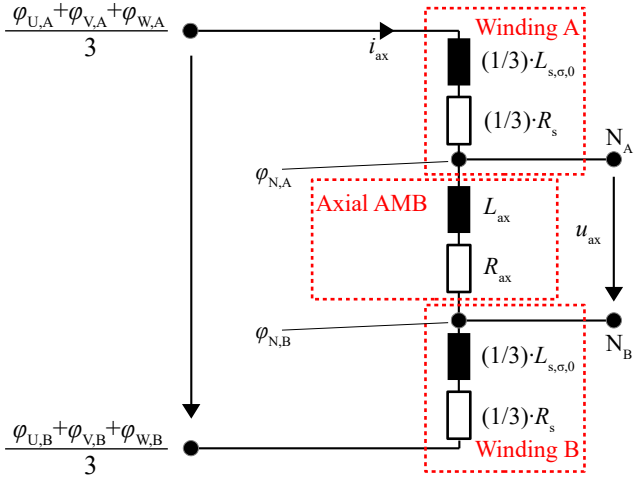

Fig. 6.3.: Equivalent circuit for the axial magnetic bearing current component i_{ax}

Also the relation between the motor phase impedance $(1/3)\cdot\left(R_s + j\omega L_{s,\sigma,0}\right)$ and the axial AMB winding impedance $R_{ax} + j\omega L_{ax}$ as voltage divider k_{eq} (6.1) determines the voltage drop $u_{ax} = \varphi_{N,A} - \varphi_{N,B}$ over the axial AMB.

$$k_{eq} = \frac{\sqrt{(\omega \cdot L_{ax})^2 + R_{ax}^2}}{\sqrt{\left[\omega \cdot \left(L_{ax} + 2 \cdot \frac{L_{s,\sigma,0}}{3}\right)\right]^2 + \left(R_{ax} + 2 \cdot \frac{R_s}{3}\right)^2}} \tag{6.1}$$

$$k_{eq} \approx \frac{L_{ax}}{L_{ax} + 2 \cdot \frac{L_{s,\sigma,0}}{3}}, \text{ where } \omega = 2\pi \cdot f_{sw};\ L_{ax} = f\left(f_{sw}\right) \text{ according to Fig. 4.3} \tag{6.2}$$

Since nowadays switching frequencies $f_{sw} > 18$ kHz are used for high-speed machines, the resistances in Fig. 6.3 can be neglected. Obviously for a high voltage drop over the winding of the axial AMB, its winding impedance should be high in relation to the motor zero-sequence impedance. The calculated ratio k_{eq} for the *LLM4* with $L_{s,\sigma,0} = 6\ \mu$H and for the *LLM3* with $L_{s,\sigma,0} = 60\ \mu$H is shown in Fig. 6.4. Due to the small stray inductance $L_{s,\sigma,0}$ (Section 7.2.5), almost the entire DC-link voltage is available at the axial AMB, i.e. $k_{eq} \approx 1$. Thus, in the following the simplifications $\frac{\varphi_{U,A}+\varphi_{V,A}+\varphi_{W,A}}{3} = \varphi_{N,A}$ and $\frac{\varphi_{U,B}+\varphi_{V,B}+\varphi_{W,B}}{3} = \varphi_{N,B}$ are used. Also, Fig. 6.4 illustrates that k_{eq} decreases at frequencies $f > 100$ Hz due to the eddy currents in the solid axial bearing yoke (Section 4.2.3).

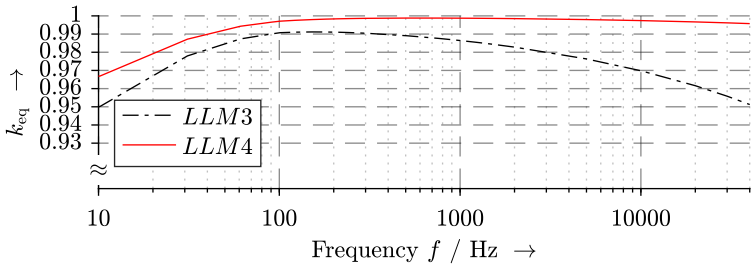

Fig. 6.4.: Calculated voltage divider ratio k_{eq} according to (6.1) with $L_{ax} = f(f_{sw})$ according to Fig. 4.3 for varying frequency $f = f_{sw}$

6.2. Coordinate Transformations

An overview of the torque/speed control and of the rotor position control is given in Fig. 6.5. While the focus was on the rotor position control in Chapter 5, here the focus is on the cascaded current control and the required modulation of the controller output reference voltages. Fig. 6.5 illustrates that the used field oriented control applies several coordinate transformations to the measured bearingless motor phase currents and to the controller output voltages. The current control of the separate radial AMB is not considered here, since its action does not depend on the rotor rotation angle and its implementation is commercially available.

In the following the coordinate transformations that apply to the 2x3 phases of the *LLM4* are shown in order to clarify the implementation of the zero-sequence current feeding. The equations are valid for all bearingless motors with combined windings and an odd number of pole pairs p (see Section 3.2) and they are based on the common *Clarke*- and *Park*-transformations. The six motor phase currents $i_{U,A}$, $i_{V,A}$, $i_{W,A}$, $i_{U,B}$, $i_{V,B}$ and $i_{W,B}$ are transformed from UVW to α-β-γ coordinates for each of the 3-phase winding systems A and B (6.3). Since the star point currents $i_{\gamma,A}$ and $i_{\gamma,B}$ are equal, the last line of (6.3) is omitted in practice to save one current sensor.

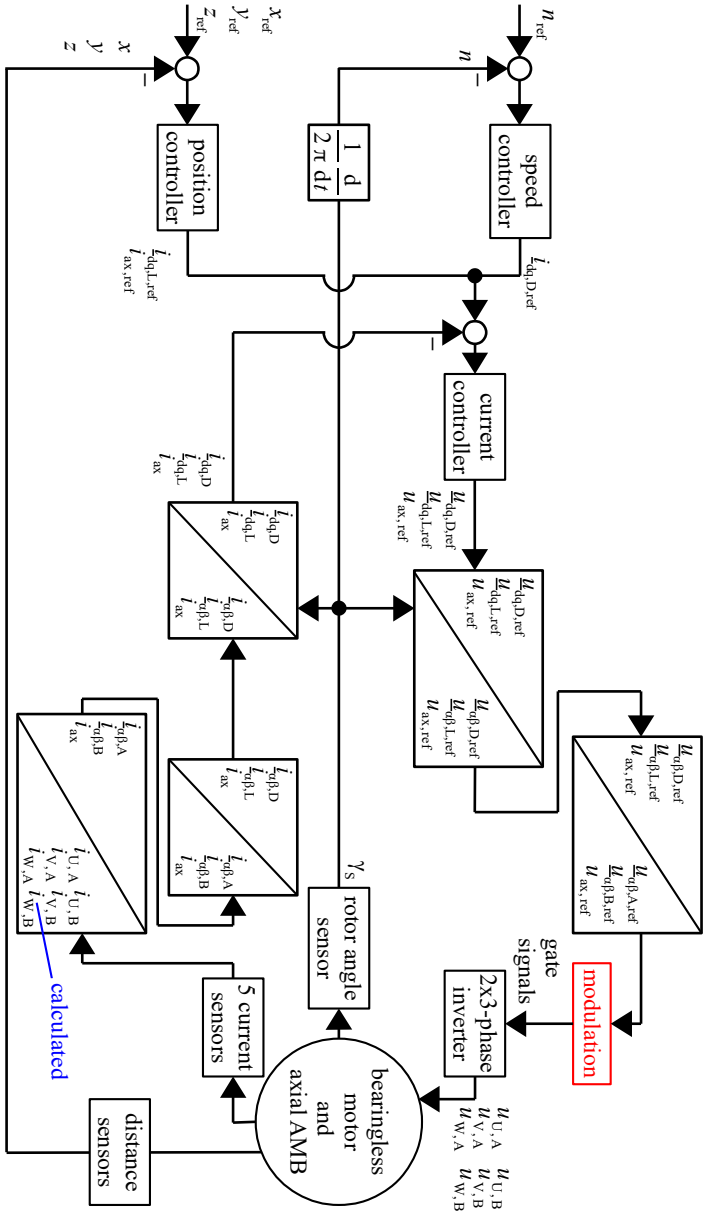

Fig. 6.5.: Cascaded control circuit of the axial position control, the speed control and the radial rotor position control, omitting the radial AMB at the NDE

$$\begin{pmatrix} i_{\alpha,\mathrm{A}} \\ i_{\beta,\mathrm{A}} \\ i_{\gamma,\mathrm{A}} \\ i_{\alpha,\mathrm{B}} \\ i_{\beta,\mathrm{B}} \\ i_{\gamma,\mathrm{B}} \end{pmatrix} = \frac{1}{3} \cdot \begin{bmatrix} 2 & -1 & -1 & 0 & 0 & 0 \\ 0 & \sqrt{3} & \sqrt{3} & 0 & 0 & 0 \\ 1 & 1 & 1 & 0 & 0 & 0 \\ 0 & 0 & 0 & 2 & -1 & -1 \\ 0 & 0 & 0 & 0 & \sqrt{3} & \sqrt{3} \\ 0 & 0 & 0 & 1 & 1 & 1 \end{bmatrix} \cdot \begin{pmatrix} i_{\mathrm{U,A}} \\ i_{\mathrm{V,A}} \\ i_{\mathrm{W,A}} \\ i_{\mathrm{U,B}} \\ i_{\mathrm{V,B}} \\ i_{\mathrm{W,B}} \end{pmatrix} \tag{6.3}$$

The current space vectors $i_{\mathrm{A}} = \left(i_{\alpha,\mathrm{A}}, i_{\beta,\mathrm{A}}\right)$, $i_{\mathrm{B}} = \left(i_{\alpha,\mathrm{B}}, i_{\beta,\mathrm{B}}\right)$ with their components $i_{\alpha,\mathrm{A}}$, $i_{\beta,\mathrm{A}}$ and $i_{\alpha,\mathrm{B}}$, $i_{\beta,\mathrm{B}}$ may be denoted as complex numbers $\underline{i}_{\mathrm{A}} = i_{\alpha,\mathrm{A}} + j \cdot i_{\beta,\mathrm{A}}$ and $\underline{i}_{\mathrm{B}} = i_{\alpha,\mathrm{B}} + j \cdot i_{\beta,\mathrm{B}}$. They exhibit elliptical orbits in the complex α-β-plane, since they are composed of two symmetrical space vectors $\underline{i}_{\alpha\beta,\mathrm{D}} = i_{\alpha,\mathrm{D}} + j \cdot i_{\beta,\mathrm{D}}$ and $\underline{i}_{\alpha\beta,\mathrm{L}} = i_{\alpha,\mathrm{L}} + j \cdot i_{\beta,\mathrm{L}}$, rotating in opposite directions [23]. The currents $i_{\alpha,\mathrm{A}}$, $i_{\beta,\mathrm{A}}$ and $i_{\alpha,\mathrm{B}}$, $i_{\beta,\mathrm{B}}$ have no meaning for the current control, but illustrate that the stator current loading is not distributed equally around the bore circumference, which may lead to local overheating. (6.4) transforms the current space vectors, representing the 3-phase winding systems A and B, into the physically non-existent complex planes α_{D}-β_{D} and α_{L}-β_{L}. In these α_{D}-β_{D}- and α_{L}-β_{L}-planes, the current space vectors with their components $i_{\alpha,\mathrm{D}}$, $i_{\beta,\mathrm{D}}$ and $i_{\alpha,\mathrm{L}}$, $i_{\beta,\mathrm{L}}$ exhibit circular orbits, describing two symmetrical current systems. Note that the zero-sequence component is $i_0 = \left(i_{\gamma,\mathrm{A}} - i_{\gamma,\mathrm{B}}\right)/2$. The current components $i_{\gamma,\mathrm{A}}$, $i_{\gamma,\mathrm{B}}$ result from the *Clarke*-transformation of the measured phase currents as offset of the AC current components. A representation of the α-β-γ-coordinate system is given Fig. 7.7.

$$\begin{pmatrix} i_{\alpha,\mathrm{D}} \\ i_{\beta,\mathrm{D}} \\ i_{\alpha,\mathrm{L}} \\ i_{\beta,\mathrm{L}} \\ i_0 \end{pmatrix} = \begin{bmatrix} 1 & 0 & 0 & -1 & 0 & 0 \\ 0 & 1 & 0 & 0 & -1 & 0 \\ 1 & 0 & 0 & 1 & 0 & 0 \\ 0 & 1 & 0 & 0 & 1 & 0 \\ 0 & 0 & 1/2 & 0 & 0 & -1/2 \end{bmatrix} \cdot \begin{pmatrix} i_{\alpha,\mathrm{A}} \\ i_{\beta,\mathrm{A}} \\ i_{\gamma,\mathrm{A}} \\ i_{\alpha,\mathrm{B}} \\ i_{\beta,\mathrm{B}} \\ i_{\gamma,\mathrm{B}} \end{pmatrix} \tag{6.4}$$

The current space vector $\underline{i}_{\alpha\beta,\mathrm{D}}$ with the components $i_{\alpha,\mathrm{D}}, i_{\beta,\mathrm{D}}$ describes the current, which generates the drive winding field. It is transformed by (6.5) into the complex current space vector with the components $i_{\mathrm{d,D}}, i_{\mathrm{q,D}}$ in the rotor-fixed coordinates, which are fed back to the torque/speed current controller. The angle γ_{S} is the rotational rotor angle, including a

certain offset in a way that the d-axis coincides with the rotor pole axis. The suspension current space vector $\underline{i}_{\alpha\beta,\mathrm{L}}$ with its components $i_{\alpha,\mathrm{L}}$, $i_{\beta,\mathrm{L}}$ is transformed into a coordinate system, which rotates synchronously with the suspension field wave, i.e. here with $v_{\mathrm{syn}}/2$. To ensure the same rotation sense as the rotor field, the negative rotational angle $-\gamma_{\mathrm{S}}$ is used [23]. An offset for $-\gamma_{\mathrm{S}}$ is used in a way that the component $i_{\mathrm{d,L}}$ respectively $i_{\mathrm{q,L}}$ only generates a rotor force in x- respectively in y-direction. A feedback of this current components enables the rotor position control according to Chapter 5. The current i_{ax} through the axial AMB is given by three times the zero-sequence phase current $i_0 = i_{\mathrm{ax}}/3$.

$$\begin{pmatrix} i_{\mathrm{d,D}} \\ i_{\mathrm{q,D}} \\ i_{\mathrm{d,L}} \\ i_{\mathrm{q,L}} \\ i_{\mathrm{ax}} \end{pmatrix} = \begin{bmatrix} \cos\gamma_{\mathrm{S}} & \sin\gamma_{\mathrm{S}} & 0 & 0 & 0 \\ -\sin\gamma_{\mathrm{S}} & \cos\gamma_{\mathrm{S}} & 0 & 0 & 0 \\ 0 & 0 & \cos(-\gamma_{\mathrm{S}}) & \sin(-\gamma_{\mathrm{S}}) & 0 \\ 0 & 0 & -\sin(-\gamma_{\mathrm{S}}) & \cos(-\gamma_{\mathrm{S}}) & 0 \\ 0 & 0 & 0 & 0 & 3 \end{bmatrix} \cdot \begin{pmatrix} i_{\alpha,\mathrm{D}} \\ i_{\beta,\mathrm{D}} \\ i_{\alpha,\mathrm{L}} \\ i_{\beta,\mathrm{L}} \\ i_0 \end{pmatrix} \tag{6.5}$$

The reference voltage space vectors of the current controllers for the drive winding with $u_{\mathrm{d,D,ref}}$, $u_{\mathrm{q,D,ref}}$ and for the suspension winding $u_{\mathrm{d,L,ref}}$, $u_{\mathrm{q,L,ref}}$ are transformed by (6.6) and (6.7) into the stator-fixed complex coordinates α, β, representing the voltage space vectors of the 3-phase winding systems A and B.

$$\begin{pmatrix} u_{\alpha,\mathrm{D,ref}} \\ u_{\beta,\mathrm{D,ref}} \\ u_{\alpha,\mathrm{L,ref}} \\ u_{\beta,\mathrm{L,ref}} \end{pmatrix} = \begin{bmatrix} \cos\gamma_{\mathrm{S}} & -\sin\gamma_{\mathrm{S}} & 0 & 0 \\ \sin\gamma_{\mathrm{S}} & \cos\gamma_{\mathrm{S}} & 0 & 0 \\ 0 & 0 & \cos(-\gamma_{\mathrm{S}}) & -\sin(-\gamma_{\mathrm{S}}) \\ 0 & 0 & \sin(-\gamma_{\mathrm{S}}) & \cos(-\gamma_{\mathrm{S}}) \end{bmatrix} \cdot \begin{pmatrix} u_{\mathrm{d,D,ref}} \\ u_{\mathrm{q,D,ref}} \\ u_{\mathrm{d,L,ref}} \\ u_{\mathrm{q,L,ref}} \end{pmatrix} \tag{6.6}$$

$$\begin{pmatrix} u_{\alpha,\mathrm{A,ref}} \\ u_{\beta,\mathrm{A,ref}} \\ u_{\alpha,\mathrm{B,ref}} \\ u_{\beta,\mathrm{B,ref}} \end{pmatrix} = \begin{bmatrix} 1 & 0 & 1 & 0 \\ 0 & 1 & 0 & 1 \\ -1 & 0 & 1 & 0 \\ 0 & -1 & 0 & 1 \end{bmatrix} \cdot \begin{pmatrix} u_{\alpha,\mathrm{D,ref}} \\ u_{\beta,\mathrm{D,ref}} \\ u_{\alpha,\mathrm{L,ref}} \\ u_{\beta,\mathrm{L,ref}} \end{pmatrix} \tag{6.7}$$

$$\begin{pmatrix} u_{\mathrm{U,A,ref}} \\ u_{\mathrm{V,A,ref}} \\ u_{\mathrm{W,A,ref}} \\ u_{\mathrm{U,B,ref}} \\ u_{\mathrm{V,B,ref}} \\ u_{\mathrm{W,B,ref}} \end{pmatrix} = \begin{bmatrix} 1 & 0 & 0 & 0 & 1/2 \\ -1/2 & \sqrt{3}/2 & 0 & 0 & 1/2 \\ -1/2 & -\sqrt{3}/2 & 0 & 0 & 1/2 \\ 0 & 0 & 1 & 0 & -1/2 \\ 0 & 0 & -1/2 & \sqrt{3}/2 & -1/2 \\ 0 & 0 & -1/2 & -\sqrt{3}/2 & -1/2 \end{bmatrix} \cdot \begin{pmatrix} u_{\alpha,\mathrm{A,ref}} \\ u_{\beta,\mathrm{A,ref}} \\ u_{\alpha,\mathrm{B,ref}} \\ u_{\beta,\mathrm{B,ref}} \\ u_{\mathrm{ax,ref}} \end{pmatrix} \tag{6.8}$$

If a carrier-based pulse-width modulation (CB-PWM) is applied, the space vectors (6.7) are transformed into six phase voltages via an inverse *Clarke*-transformation (6.8). Each phase reference voltage $u_{\mathrm{U,A,ref}}$, $u_{\mathrm{V,A,ref}}$, $u_{\mathrm{W,A,ref}}$ and $u_{\mathrm{U,B,ref}}$, $u_{\mathrm{V,B,ref}}$, $u_{\mathrm{W,B,ref}}$ is modulated, as described in Section 6.3. If a space vector pulse-width modulation (SV-PWM) is used, the voltage space vectors $\underline{u}_{\alpha\beta,\mathrm{A,ref}}$, $\underline{u}_{\alpha\beta,\mathrm{B,ref}}$ (6.7) are modulated directly as described in Appendix A.23.
In this work, a CB-PWM and a SV-PWM are considered. The here presented SV-PWM prioritizes the generation of the voltage space vectors for the drive and the suspension winding over the generation of the voltage $u_{\mathrm{ax,ref}}$ for the axial AMB. The CB-PWM generates $\underline{u}_{\alpha\beta,\mathrm{D}}$, $\underline{u}_{\alpha\beta,\mathrm{L}}$ and u_{ax} without prioritization. For the SV-PWM, the reference voltage $u_{\mathrm{ax,ref}}$ for the feeding of the axial AMB is directly included into the calculation of the "active" and "passive" time sections (Section 6.4). For the CB-PWM $u_{\mathrm{ax,ref}}$ is added as an offset $\pm u_{\mathrm{ax,ref}}/2$ to the reference AC phase voltages of the 3-phase winding systems A and B (6.8).

6.3. Zero-Sequence Current Feeding applying Carrier-based Pulse Width Modulation

The CB-PWM is a widely used modulation technique for voltage source inverters, feeding inductive loads. Also for the *LLM4* a CB-PWM is used for the feeding of the stator winding. The modulation of the reference voltage is part of the cascaded current control

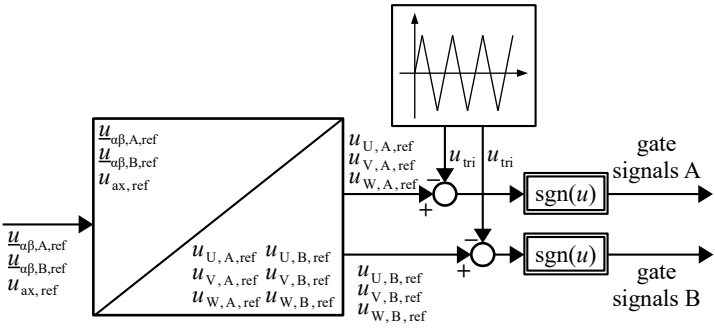

Fig. 6.6.: Schematic representation of the carrier-based PWM for zero-sequence current feeding (CB-PWM)

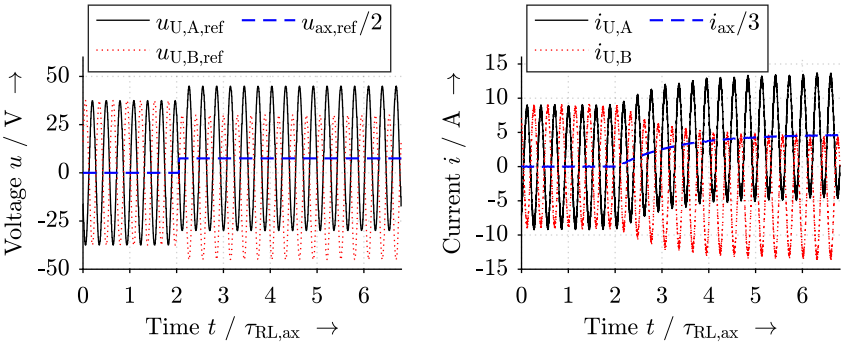

(a) Reference phase voltages

(b) Actual phase currents

Fig. 6.7.: Simulated arbitrary reference phase voltages $u_{U,A,ref}$, $u_{U,B,ref}$ to be modulated and corresponding actual phase currents $i_{U,A}$, $i_{U,B}$ during a step in reference axial voltage $\Delta u_{ax,ref} = 15$ V at $t = 2 \cdot \tau_{RL,ax}$, $R = 1\ \Omega$, $L = 1$ mH, using the CB-PWM

loop (Fig. 6.5). The required coordinate transformations were explained in Section 6.2. The carrier-based PWM adapts the mean value of a single-phase voltage over one switching period T_{sw}. A triangular carrier voltage u_{tri} of amplitude $U_{DC}/2$ is compared to the reference voltage in each phase (e.g. $u_{U,A,ref}$) in order to determine the switching instants (Fig. 6.6) [140].

Often a zero-sequence voltage with $3 \cdot f_{syn}$ is added to the sinusoidal reference signal at synchronous frequency f_{syn} for a higher linear modulation index m_a [140]. This approach is not considered here, because an artificial DC offset $\pm u_{ax,ref}/2$ is added to the above noted reference phase voltages. The DC offset $u_{ax}/2$ is of opposite polarity in the two 3-phase systems A and B, so that a DC voltage drop of u_{ax} occurs between the two star points N_A and N_B. The block diagram of this method is given in Fig. 6.6.

One advantage of the CB-PWM is its simple realization, since it is only based on an offset $\pm u_{ax,ref}/2$ of the reference phase voltages (Fig. 6.7). Its drawback is, that the required axial AMB voltage u_{ax} is allocated equally as $\pm u_{ax}/2$ to the two 3-phase systems without being adapted during operation. As explained in Section 7.1.4, this introduces even harmonics into the phase voltages, if the inverter is driven at its voltage limit, which motivates the alternative use of a SV-PWM.

6.4. Space Vector Modulation for Zero-Sequence Current Feeding

The here presented inclusion of the axial AMB voltage modulation into the space vector pulse-width modulation is abbreviated by SV-PWM. It was partially presented in [O05]. The fundamental principle of the space vector pulse-width modulation is given in Appendix A.23, which shows how the "active" time sections t_1 and t_2 are calculated. For the two 3-phase winding systems, $t_{1,\mathrm{A}}$, $t_{2,\mathrm{A}}$, $t_{1,\mathrm{B}}$ and $t_{2,\mathrm{B}}$ are determined by the reference voltages of the drive current control and the suspension current control. The goal of the axial AMB voltage modulation within the SV-PWM is that the drive voltage space vector $\underline{u}_{\mathrm{dq,D,ref}}$ and the suspension voltage space vector $\underline{u}_{\mathrm{dq,L,ref}}$ are modulated with priority over the axial voltage $u_{\mathrm{ax,ref}}$. Thus, the "active" time sections $t_{1,\mathrm{A}}$, $t_{2,\mathrm{A}}$, $t_{1,\mathrm{B}}$ and $t_{2,\mathrm{B}}$ are calculated in a first step identical to a common space vector modulation (Appendix A.23). These time sections are not influenced by the modulation of u_{ax}.

In the symmetrical space vector PWM (Appendix A.23), without zero-sequence current feeding, the remaining "passive" time sections are divided into two equal parts t_0 and t_7, which are allocated likewise to the beginning and end of each switching period T_{sw}. This way, the number of switching actions is reduced and the DC-link voltage utilization is increased. The mean value of the voltage over one switching period T_{sw} is independent from the allocation of the switching states. For example, t_0 must not be equal to t_7 as long as $t_0 + t_7 = t_{\mathrm{pas}}$ holds. This is used for the here presented technique.

Since the time sections $t_{1,\mathrm{A}}$, $t_{2,\mathrm{A}}$, $t_{1,\mathrm{B}}$, $t_{2,\mathrm{B}}$, $t_{\mathrm{pas,A}} = T_{\mathrm{sw}} - t_{1,\mathrm{A}} - t_{2,\mathrm{A}}$ and $t_{\mathrm{pas,B}} = T_{\mathrm{sw}} - t_{1,\mathrm{B}} - t_{2,\mathrm{B}}$ are known, the unknowns are the time spans $t_{0,\mathrm{A}}$, $t_{7,\mathrm{A}}$, $t_{0,\mathrm{B}}$ and $t_{7,\mathrm{B}}$. Four conditions (6.9)–(6.12) are used for the solution.

The influence of the reference axial voltage mean value $u_{\mathrm{ax,ref}} = \bar{u}_{\mathrm{ax}}$ over one switching period T_{sw} on the switching time spans is given by (6.9). The star point potential $\varphi_{\mathrm{N,A}}$ and $\varphi_{\mathrm{N,B}}$ for the eight possible switching states are given in Appendix in Fig. A.21.

$$
\begin{aligned}
u_{\mathrm{ax,ref}} = \bar{u}_{\mathrm{ax}} &= \frac{1}{T_{\mathrm{sw}}} \cdot \int_0^{T_{\mathrm{sw}}} \left(\varphi_{\mathrm{N,A}}(t) - \varphi_{\mathrm{N,B}}(t) \right) \mathrm{d}t \qquad (6.9) \\
&= \frac{U_{\mathrm{DC}}}{T_{\mathrm{sw}}} \cdot \left(0 \cdot t_{0,\mathrm{A}} + \frac{1}{3} \cdot t_{1,\mathrm{A}} + \frac{2}{3} \cdot t_{2,\mathrm{A}} + 1 \cdot t_{7,\mathrm{A}} - \right. \\
&\qquad \left. 0 \cdot t_{0,\mathrm{B}} - \frac{1}{3} \cdot t_{1,\mathrm{B}} - \frac{2}{3} \cdot t_{2,\mathrm{B}} - 1 \cdot t_{7,\mathrm{B}} \right)
\end{aligned}
$$

$$
\begin{aligned}
&= \frac{U_{\mathrm{DC}}}{2 \cdot T_{\mathrm{sw}}} \cdot \left(\frac{2 \cdot t_{1,\mathrm{A}}}{3} + \frac{4 \cdot t_{2,\mathrm{A}}}{3} + 2 \cdot t_{7,\mathrm{A}} - \frac{2 \cdot t_{1,\mathrm{B}}}{3} - \frac{4 \cdot t_{2,\mathrm{B}}}{3} - 2 \cdot t_{7,\mathrm{B}} \right) \\
&= \frac{U_{\mathrm{DC}}}{2 \cdot T_{\mathrm{sw}}} \cdot \Bigg(-\frac{1}{3} \cdot t_{1,\mathrm{A}} + \frac{1}{3} \cdot t_{2,\mathrm{A}} + t_{7,\mathrm{A}} + \frac{1}{3} \cdot t_{1,\mathrm{B}} - \frac{1}{3} \cdot t_{2,\mathrm{B}} - t_{7,\mathrm{B}} + \\
&\qquad\qquad t_{1,\mathrm{A}} + t_{2,\mathrm{A}} + t_{7,\mathrm{A}} - t_{1,\mathrm{B}} - t_{2,\mathrm{B}} - t_{7,\mathrm{B}} \Bigg) \\
&= \frac{U_{\mathrm{DC}}}{2 \cdot T_{\mathrm{sw}}} \cdot \left(\underbrace{\frac{t_{2,\mathrm{A}} - t_{1,\mathrm{A}}}{3} + \frac{t_{1,\mathrm{B}} - t_{2,\mathrm{B}}}{3}}_{\text{given time spans}} + \underbrace{t_{7,\mathrm{A}} - t_{0,\mathrm{A}} + t_{0,\mathrm{B}} - t_{7,\mathrm{B}}}_{\text{controllable time spans}} \right) \\
\Rightarrow \quad t_{\mathrm{ax}} &= t_{7,\mathrm{A}} - t_{0,\mathrm{A}} + t_{0,\mathrm{B}} - t_{7,\mathrm{B}} = \underbrace{\frac{\bar{u}_{\mathrm{ax}} \cdot 2 \cdot T_{\mathrm{sw}}}{U_{\mathrm{DC}}} - \left(\frac{t_{2,\mathrm{A}} - t_{1,\mathrm{A}}}{3} + \frac{t_{1,\mathrm{B}} - t_{2,\mathrm{B}}}{3} \right)}_{t_{\mathrm{ax}}}
\end{aligned}
$$

The conditions (6.10) and (6.11) follow from the definitions of the symmetrical space vector modulation. An increase of u_{ax} is caused by the difference of the time sections $t_{7,\mathrm{A}} - t_{0,\mathrm{A}}$ as well as by $t_{0,\mathrm{B}} - t_{7,\mathrm{B}}$. Therefore, the fourth condition (6.12) allocates the time spans $t_{7,\mathrm{A}} - t_{0,\mathrm{A}}$ and $t_{0,\mathrm{B}} - t_{7,\mathrm{B}}$ to the systems A and B in the same ratio as the available "passive" time spans $t_{\mathrm{pas,A}}$ and $t_{\mathrm{pas,B}}$. Thus, more "passive" time span is available to contribute to the desired change of the mean voltage $\bar{u}_{\mathrm{ax}}$ over one period T_{sw}. From that, the linear equation system (6.13) results, which can be solved e.g. by applying *Cramer*'s rule [90], yielding (6.14).

$$
t_{\mathrm{pas,A}} = t_{0,\mathrm{A}} + t_{7,\mathrm{A}} = T_{\mathrm{sw}} - t_{1,\mathrm{A}} - t_{2,\mathrm{A}} \tag{6.10}
$$

$$
t_{\mathrm{pas,B}} = t_{0,\mathrm{B}} + t_{7,\mathrm{B}} = T_{\mathrm{sw}} - t_{1,\mathrm{B}} - t_{2,\mathrm{B}} \tag{6.11}
$$

$$
\frac{t_{\mathrm{pas,A}}}{t_{\mathrm{pas,B}}} = \frac{t_{7,\mathrm{A}} - t_{0,\mathrm{A}}}{t_{0,\mathrm{B}} - t_{7,\mathrm{B}}} \tag{6.12}
$$

$$
\begin{pmatrix} t_{\mathrm{pas,A}} \\ t_{\mathrm{pas,B}} \\ t_{\mathrm{ax}} \\ 0 \end{pmatrix} = \begin{bmatrix} 1 & 1 & 0 & 0 \\ 0 & 0 & 1 & 1 \\ -1 & 1 & 1 & -1 \\ t_{\mathrm{pas,B}} & -t_{\mathrm{pas,B}} & t_{\mathrm{pas,A}} & -t_{\mathrm{pas,A}} \end{bmatrix} \cdot \begin{pmatrix} t_{0,\mathrm{A,lin}} \\ t_{7,\mathrm{A,lin}} \\ t_{0,\mathrm{B,lin}} \\ t_{7,\mathrm{B,lin}} \end{pmatrix} \tag{6.13}
$$

$$\begin{cases} t_{0,\mathrm{A,lin}} = \frac{1}{2} \cdot \left(t_{\mathrm{pas,A}} - \frac{t_{\mathrm{pas,B}}}{t_{\mathrm{pas,A}} + t_{\mathrm{pas,B}}} \cdot t_{\mathrm{ax}} \right) \\ t_{7,\mathrm{A,lin}} = \frac{1}{2} \cdot \left(t_{\mathrm{pas,A}} + \frac{t_{\mathrm{pas,B}}}{t_{\mathrm{pas,A}} + t_{\mathrm{pas,B}}} \cdot t_{\mathrm{ax}} \right) \\ t_{0,\mathrm{B,lin}} = \frac{1}{2} \cdot \left(t_{\mathrm{pas,A}} + \frac{t_{\mathrm{pas,A}}}{t_{\mathrm{pas,A}} + t_{\mathrm{pas,B}}} \cdot t_{\mathrm{ax}} \right) \\ t_{7,\mathrm{B,lin}} = \frac{1}{2} \cdot \left(t_{\mathrm{pas,A}} - \frac{t_{\mathrm{pas,A}}}{t_{\mathrm{pas,A}} + t_{\mathrm{pas,B}}} \cdot t_{\mathrm{ax}} \right) \end{cases} \tag{6.14}$$

$$\begin{cases} t_{0,\mathrm{A}} = t_{0,\mathrm{A,lin}} & \text{if } t_{0,\mathrm{A,lin}} > 0 \\ t_{0,\mathrm{A}} = 0 \wedge t_{7,\mathrm{A}} = t_{\mathrm{pas,A}} & \text{if } t_{0,\mathrm{A,lin}} < 0 \end{cases}$$
$$\begin{cases} t_{7,\mathrm{A}} = t_{7,\mathrm{A,lin}} & \text{if } t_{7,\mathrm{A,lin}} > 0 \\ t_{7,\mathrm{A}} = 0 \wedge t_{0,\mathrm{A}} = t_{\mathrm{pas,A}} & \text{if } t_{7,\mathrm{A,lin}} < 0 \end{cases}$$
$$\begin{cases} t_{0,\mathrm{A}} = t_{0,\mathrm{B,lin}} & \text{if } t_{0,\mathrm{B,lin}} > 0 \\ t_{0,\mathrm{B}} = 0 \wedge t_{7,\mathrm{B}} = t_{\mathrm{pas,B}} & \text{if } t_{0,\mathrm{B,lin}} < 0 \end{cases}$$
$$\begin{cases} t_{7,\mathrm{B}} = t_{7,\mathrm{B,lin}} & \text{if } t_{7,\mathrm{B,lin}} > 0 \\ t_{7,\mathrm{B}} = 0 \wedge t_{0,\mathrm{B}} = t_{\mathrm{pas,B}} & \text{if } t_{7,\mathrm{B,lin}} < 0 \end{cases} \tag{6.15}$$

However, (6.14) yields solutions $t_{0,\mathrm{A,lin}}$, $t_{7,\mathrm{A,lin}}$, $t_{0,\mathrm{B,lin}}$, $t_{7,\mathrm{B,lin}}$ which can be both positive and negative. Therefore, the solution space must be limited to (6.15), ensuring positive time spans, but resulting in a nonlinear switching behavior. Since the calculation of $t_{0,\mathrm{A}}$, $t_{7,\mathrm{A}}$, $t_{0,\mathrm{B}}$ and $t_{7,\mathrm{B}}$ requires the knowledge of the "active" time spans in both current systems A and B, the software for the gate driver control differs from standard 3-phase SV-PWM gate driver control. Therefore, the here presented SV-PWM method could not be implemented with the used commercially available inverter (Table A.3 in Appendix).

Fig. 6.8 shows the simulated axial AMB voltage u_{ax} over two switching periods $2 \cdot T_{\mathrm{sw}}$, when a change in reference signal happens within the first of both periods. Here, the two 3-phase voltage systems A and B are fed in differential-mode ($\underline{u}_{\alpha\beta,\mathrm{A,ref}} = -\underline{u}_{\alpha\beta,\mathrm{B,ref}}$) as in the case of the feeding of the drive winding voltage in the *LLM4*. In the first period T_{sw} (Fig. 6.8), when $u_{\mathrm{ax,ref}} = 0$, the mean value of u_{ax} is zero, but u_{ax} is affected by the "active" time sections $t_{1,\mathrm{A}}$, $t_{2,\mathrm{A}}$, $t_{1,\mathrm{B}}$ and $t_{2,\mathrm{B}}$ and takes the values $-U_{\mathrm{DC}}/3$, 0, $U_{\mathrm{DC}}/3$. This "coupling" between the voltage space vectors $\underline{u}_{\alpha\beta,\mathrm{A,ref}}$, $\underline{u}_{\alpha\beta,\mathrm{B}}$ and the axial voltage generation introduces additional harmonics into the axial AMB voltage, especially at high inverter modulation indices. When comparing the high-side signals of the three half-bridges $\mathrm{U_A}$, $\mathrm{V_A}$, $\mathrm{W_A}$ of winding system A with $\mathrm{U_B}$, $\mathrm{V_B}$, $\mathrm{W_B}$ of winding system B, the following observations can be made: The "active" time section, when not all high-side

gate signals are high or low at the same time, remain constant over both switching periods. Thus, the mean value of the length of the voltage space vector $|\underline{u}_{\alpha\beta,\mathrm{A}}|$ in system A remains constant over both switching periods.

In the first switching period T_{sw} of differential mode operation (Fig. 6.8), the "passive" time spans are equal: $t_{0,\mathrm{A}} = t_{7,\mathrm{A}} = t_{0,\mathrm{B}} = t_{7,\mathrm{B}}$, as in the case of the symmetrical space vector PWM. In the second period, when $u_{\mathrm{ax,ref}} = U_{\mathrm{DC}}/2$, the "passive" time spans are $t_{7,\mathrm{A}} = t_{0,\mathrm{B}} \gg t_{7,\mathrm{B}} = t_{0,\mathrm{A}}$. Therefore, the time is extended, during which all high-side switches of system A and all low-side switches of system B are conducting, leading to a higher mean value of voltage $\bar{u}_{\mathrm{ax}}$. Still u_{ax} is not constant over one switching period due to the necessary switching actions to generate the "active" voltage space vectors.

Fig. 6.9 illustrates equivalently the simulated axial AMB voltage u_{ax} over two switching periods $2 \cdot T_{\mathrm{sw}}$ with a change in reference signal during the first of both periods, however, considering a common-mode feeding of the two 3-phase voltage systems A and B ($\underline{u}_{\alpha\beta,\mathrm{A,ref}} = \underline{u}_{\alpha\beta,\mathrm{B,ref}}$). This is for example the case for the drive winding voltage generation in combined winding bearingless motors with even pole count, e.g. $2p = 8$ (see Table 3.4). During the first switching period (Fig. 6.9) the high-side gate signals of the systems A and B are equal. No difference in electric potential between the two star points $\mathrm{N_A}$ and $\mathrm{N_B}$ occurs, so that u_{ax} is constantly zero. During the second switching period, when $u_{\mathrm{ax,ref}} = U_{\mathrm{DC}}/2$, the electric potential of $\mathrm{N_A}$ stays longer at $+U_{\mathrm{DC}}/2$ than at $-U_{\mathrm{DC}}/2$. In the same way, the electric potential of $\mathrm{N_B}$ stays longer at $-U_{\mathrm{DC}}/2$ than at $+U_{\mathrm{DC}}/2$. Without influencing the mean value of the voltage space vector $|\underline{u}_{\alpha\beta,\mathrm{A}}|$, the mean value of u_{ax} is equal to the set-point value.

Note that $u_{\mathrm{ax}} = \varphi_{\mathrm{N,A}} - \varphi_{\mathrm{N,B}}$ theoretically takes the values from Fig. A.21, i.e. $u_{\mathrm{ax}} \in \{\pm U_{\mathrm{DC}}, \pm 2U_{\mathrm{DC}}/3, \pm U_{\mathrm{DC}}/3, 0\}$. In Fig. 6.8, 6.9, u_{ax} is slightly smaller than multiples of $U_{\mathrm{DC}}/3$ due to the voltage drop at the stator winding impedance (see Equation 6.1).

6.5. Evaluation of the Modulation Techniques by Simulation and Measurement

Measurements on the 1 kW/60 000 min^{-1}-prototype bearingless PM synchronous machine (*LLM4*) were conducted in order to evaluate the zero-sequence current feeding technique. The properties of the used measurement equipment are listed in Table A.12–A.14 in the Appendix. The used inverter is a 1.2 kVA MOSFET-based 2-level voltage source inverter with $U_{\mathrm{DC}} = 150$ V DC-link voltage and a variable switching frequency

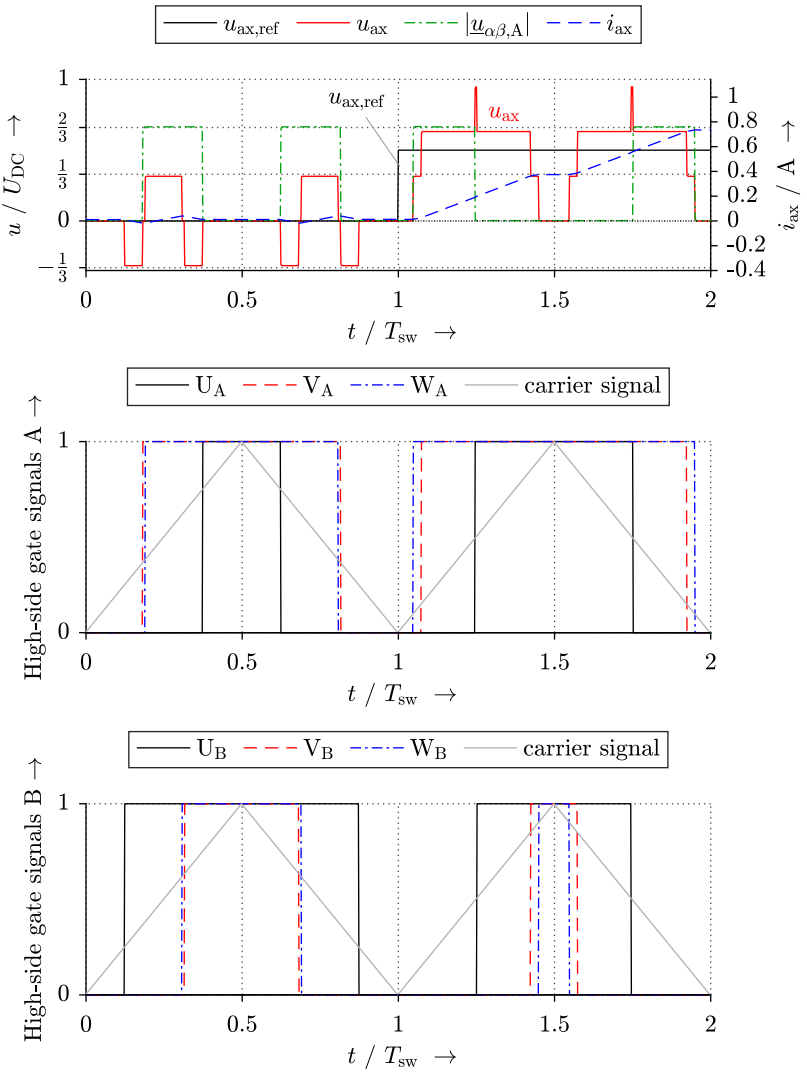

Fig. 6.8.: Differential-mode feeding of $\underline{u}_{\alpha\beta,A}$ and $\underline{u}_{\alpha\beta,B}$: Simulated voltage characteristics of u_{ax}, $|\underline{u}_{\alpha\beta,A}|$ and high-side voltage signals for the SV-PWM

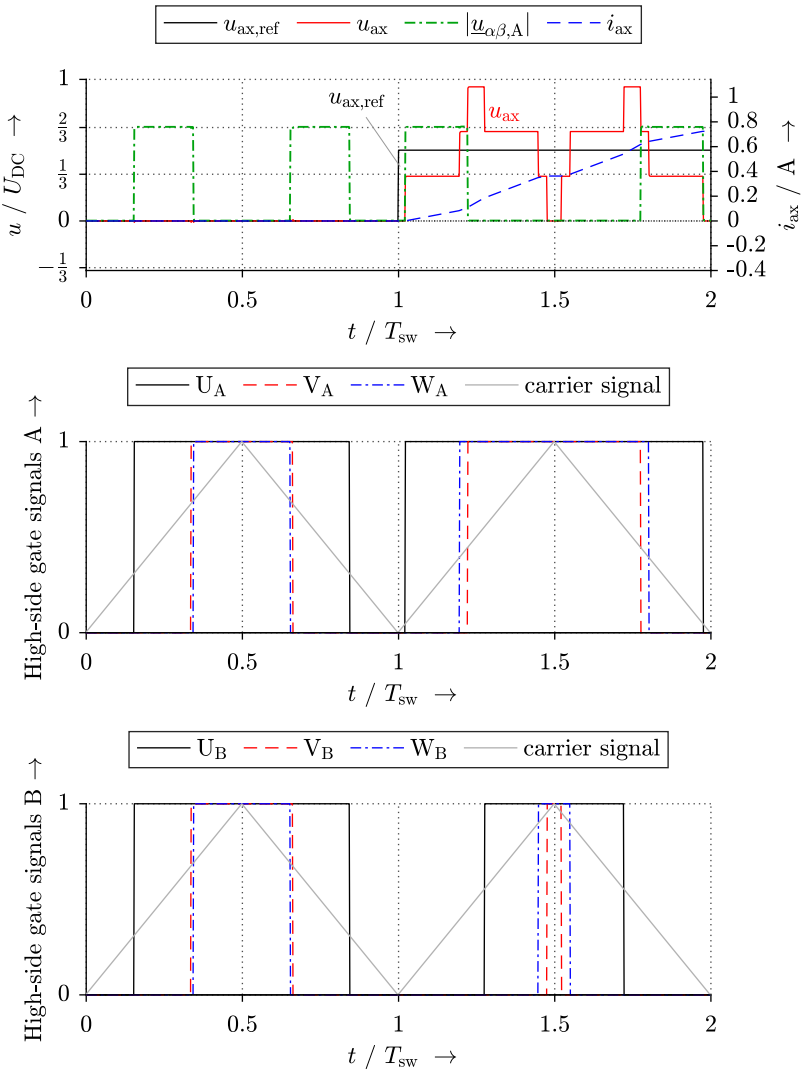

Fig. 6.9.: Common-mode feeding of $\underline{u}_{\alpha\beta,A}$ and $\underline{u}_{\alpha\beta,B}$: Simulated voltage characteristics of u_{ax}, $|\underline{u}_{\alpha\beta,A}|$ and high-side voltage signals for the SV-PWM

Table 6.1.: Settings for the numerical simulation in time-domain, used in Chapter 7 (power electronic properties at 100 C° from [141] with symmetrical regular sampling)

Solver type (*Simulink*/*Simscape*)	2^{nd} order *Heun* / 1^{st} order *Backward Euler*
DC-link voltage U_{DC}	150 V
Inverter switching frequency f_{sw} (MOSFET)	33 kHz
Voltage attenuation by dead time $k_{\text{att,U}}$ (at $u_{\text{ref}} = U_{\text{DC}}$)	0.88
Step time T_{st}	303 ns $= T_{\text{sw}}/100$
Threshold voltage U_{th}	4 V
Drain-source resistance (on) $R_{\text{DS,on}}$	11 mΩ
Drain-source resistance (off) $R_{\text{DS,off}}$	600 kΩ

up to $f_{\text{sw}} = 60$ kHz. The *LLM4* was operated at $f_{\text{sw}} = 33$ kHz, applying asynchronous switching. It is commercially available at *KEBA Industrial Automation Germany GmbH*

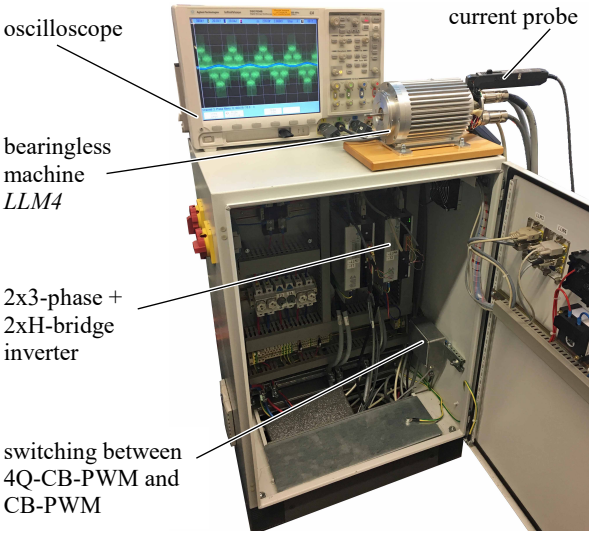

Fig. 6.10.: Test bench for the *LLM4*, which enables to switch between the axial AMB operation by the 4-quadrant chopper with carrier-based PWM (4Q-CB-PWM) and the zero-sequence current feeding with a carrier-based PWM (CB-PWM)

(Table A.3 in Appendix). The test bench (Fig. 6.10) enables to switch between the zero-sequence current feeding (CB-PWM) of the axial AMB and the classical operation with a 4-quadrant chopper (4Q-CB-PWM), which is considered the benchmark. Note that the SV-PWM method could not be realized with the used inverter, as it was not possible to realize the artificial adaption of the "passive" time spans according to Section 6.4.
In order to derive operational limits of the zero-sequence current feeding, it is necessary to vary the actuator load between the two star points of the bearingless machine. Therefore, time domain simulations in the *Matlab/Simulink*-environment are used, which compare the CB-PWM, the SV-PWM and the 4Q-CB-PWM with the model settings from Table 6.1. The simulation is based on symmetrical regular sampling without phase delay compensation [140]. This *Matlab/Simulink*-model is used throughout Chapter 7 to evaluate the zero-sequence current feeding.
Two dimensionless quantities are used in the analysis of inverter switching patterns [142, 140]: The first quantity is the amplitude modulation index m_a (6.16), which quantifies the DC-link voltage utilization by the reference phase voltage amplitude $|\underline{u}_{\alpha\beta,\mathrm{ref}}|$.

$$m_\mathrm{a} = \frac{|\underline{u}_{\alpha\beta,\mathrm{ref}}|}{U_\mathrm{DC}/2} \tag{6.16}$$

The second quantity is the frequency modulation index $m_\mathrm{f} = f_\mathrm{sw}/f_\mathrm{syn}$ to describe the harmonic content of the applied voltage, where f_syn is the synchronous and f_sw the inverter switching frequency. The harmonic spectrum of a single-phase PWM voltage is given by the voltage harmonics of order k (6.17) for synchronous switching, for odd m_f or for high values of m_f, e.g. $m_\mathrm{f} > 21$, according to [142].

$$k = \begin{cases} l \cdot m_\mathrm{f} \pm 2g, & l = \mathbb{N}_\mathrm{odd};\ g = \mathbb{N} \\ l \cdot m_\mathrm{f} \pm (2g-1), & l = \mathbb{N}_\mathrm{even};\ g = \mathbb{N} \end{cases} \tag{6.17}$$

In Fig. 6.11 and 6.12, the AC-phase voltage and the axial AMB voltage harmonic spectrum from simulation and measurements at stationary conditions validate the simulation model with a good agreement between measurements and simulations. The voltage harmonic spectrum of the AC phase voltage $\hat{u}_\mathrm{U,A}$ clearly exhibits the harmonic orders k according to (6.17) at low modulation indices, such as $m_\mathrm{a} = 0.84$ (Fig. 6.11a, 6.11b). At high modulation indices, such as $m_\mathrm{a} = 1.55$, (Fig. 6.11c, 6.11d) additional side bands close to

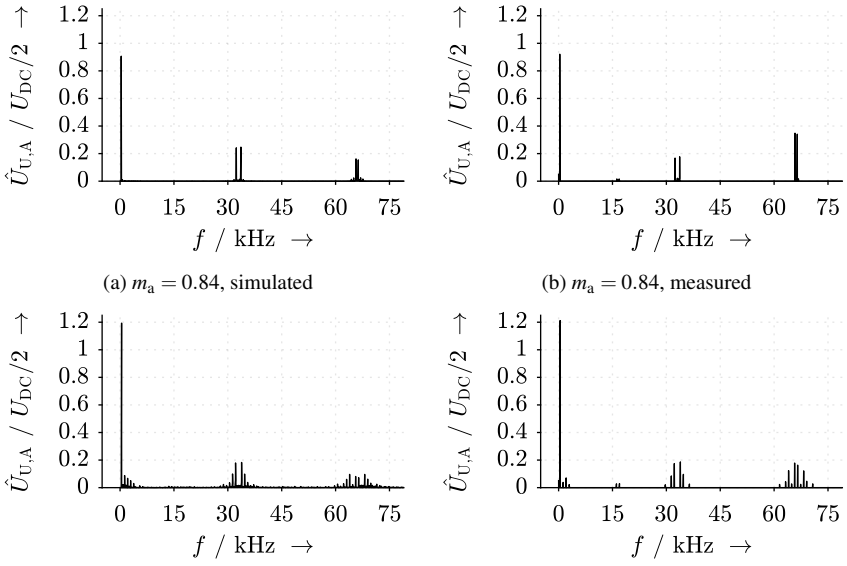

(a) $m_\mathrm{a} = 0.84$, simulated

(b) $m_\mathrm{a} = 0.84$, measured

(c) $m_\mathrm{a} = 1.55$, simulated

(d) $m_\mathrm{a} = 1.55$, measured

Fig. 6.11.: Simulated and measured phase voltage harmonic spectrum of $u_{\mathrm{U,A}}$ at $m_\mathrm{a} = 0.84$ and $m_\mathrm{a} = 1.55$ for the CB-PWM in steady state with $f_\mathrm{sw} = 33$ kHz

multiples of the switching frequency occur. Especially, harmonics of order $k = -5, 7, ...$ are visible, being in accordance to [140, 142].

Fig. 6.12 shows the axial AMB voltage harmonic spectrum of $\hat{u}_\mathrm{ax}$ for the 4Q-CB-PWM and the CB-PWM operation both from measurement and simulation. At the modulation index $m_\mathrm{a} = 0.84$, Fig. 6.12a, 6.12b give the voltage harmonic spectrum of $\hat{u}_\mathrm{ax}$ for the zero-sequence feeding, whereas Fig. 6.12c, 6.12d show the results for the classical 4Q-CB-PWM for feeding the winding of the axial AMB. Due to the low winding impedance of the axial AMB, the voltage demand $u_\mathrm{ax,ref} = \hat{u}_\mathrm{ax,0}$ is very low. For such small reference values, the zero-sequence current feeding results in higher harmonics close to $f = 2 \cdot f_\mathrm{sw}$ (Fig. 6.12a, 6.12b), whereas the 4Q-CB-PWM has a higher harmonic at $f = f_\mathrm{sw}$ (Fig. 6.12a, 6.12b).

Differences between the real inverter operation and the simulation exist, such as listed in the following, and are responsible for minor deviations:

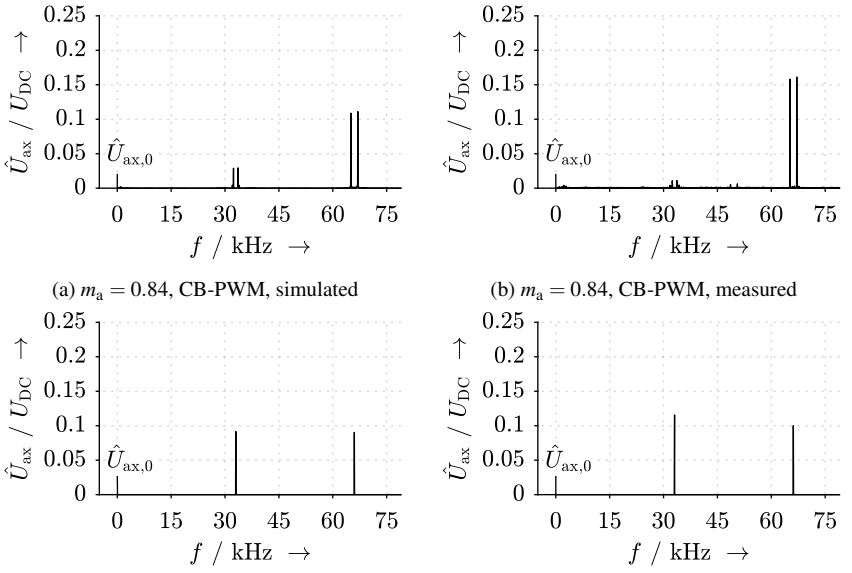

(a) $m_{\mathrm{a}} = 0.84$, CB-PWM, simulated

(b) $m_{\mathrm{a}} = 0.84$, CB-PWM, measured

(c) $m_{\mathrm{a}} = 0.84$, 4Q-CB-PWM, simulated

(d) $m_{\mathrm{a}} = 0.84$, 4Q-CB-PWM, measured

Fig. 6.12.: Comparison between 4Q-CB-PWM and CB-PWM: Simulated and measured harmonic spectrum of the axial AMB voltage u_{ax} at $m_{\mathrm{a}} = 1.55$ and $m_{\mathrm{a}} = 0.84$ in steady state with $f_{\mathrm{sw}} = 33$ kHz

- The inverter is equipped with N-channel MOSFETs and a bootstrap driver. The required dead time for recharging the bootstrap capapcitor is considered in the simulation by a reduced DC-link voltage in form of the factor $k_{\mathrm{att,U}}$ according to Table 6.1.
- The required dead time for switching the MOSFETs on or off is not considered.
- The required dead time between switching on and off to avoid DC-link short-circuiting is not considered.
- The capacitive behavior of the conductor between the two star points and the conductors between the inverter and the motor terminals is not modeled.

7. Evaluation of the Zero-Sequence Current Feeding

The zero-sequence current feeding is evaluated in three parts. Section 7.1 focuses on the constraints of the zero-sequence feeding, which result from the inverter voltage limit and discusses the voltage harmonic content. Section 7.2 shows the impact of the zero-sequence current on the bearingless machine performance. Section 7.3 relates the zero-sequence current feeding to the application of an axial active magnetic bearing. A comparison between the classical 4-quadrant chopper operation (4Q-CB-PWM), the zero-sequence current operation with carrier-based pulse width modulation (CB-PWM) and the zero-sequence current operation with space vector modulation (SV-PWM) is drawn. The contents of this chapter were partially published in [O10, O11, O15].

7.1. Constraints by the Inverter

7.1.1. Zero-Sequence Voltage Capability

For more general conclusions, the zero-sequence current feeding technique shall be assessed independently of current controller settings. Therefore, only the transfer behavior between the current controller output voltage $u_{\mathrm{ax,ref}}$ and the actual current i_{ax} respectively the actual voltage u_{ax} is of interest. Fig. 7.1 shows the simulated axial AMB step response current i_{ax} to a step of the reference voltage of $u_{\mathrm{ax,ref}} = U_{\mathrm{DC}}/10$. Different values for the load, consisting of the resistive load R_{ax} and the inductive load L_{ax}, are considered in Fig. 7.1. The feeding current is i_{ax}, which takes the maximum value in steady state $i_{\mathrm{max}} = \frac{U_{\mathrm{DC}}/10}{R_{\mathrm{ax}}}$. The classical DC-chopper operation (4Q-CB-PWM) is compared with the zero-sequence current feeding (CB-PWM, according to Section 6.3) at different modulation indices m_{a}. For low modulation indices, such as $m_{\mathrm{a}} = 0.84$, the final current value is slightly lower ($\approx 5\%$) than the final current value for the 4Q-CB-PWM. This is due to the

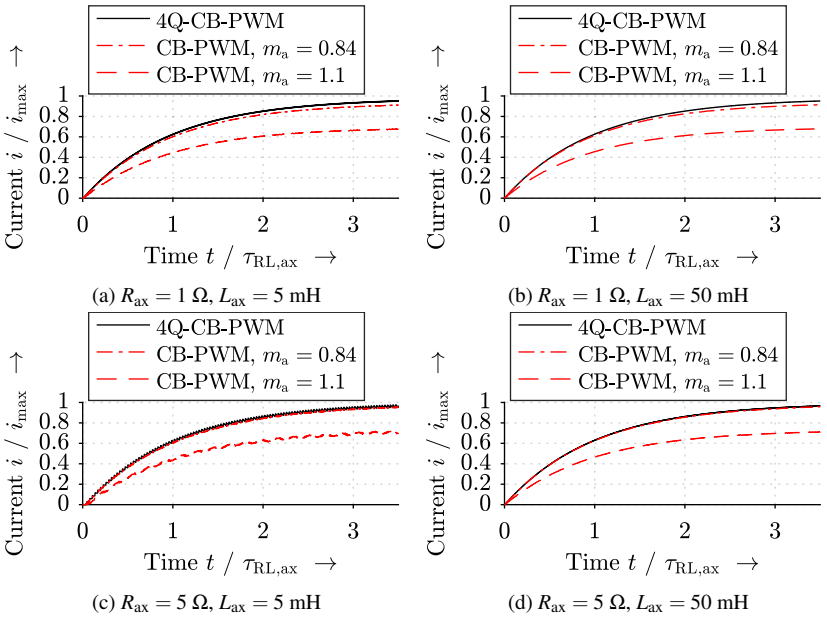

(a) $R_{ax} = 1\ \Omega$, $L_{ax} = 5$ mH

(b) $R_{ax} = 1\ \Omega$, $L_{ax} = 50$ mH

(c) $R_{ax} = 5\ \Omega$, $L_{ax} = 5$ mH

(d) $R_{ax} = 5\ \Omega$, $L_{ax} = 50$ mH

Fig. 7.1.: Simulated step response current i_{ax} for a step in axial reference voltage of $u_{ax,ref} = U_{DC}/10$ for different values of R_{ax} and L_{ax} of the axial AMB, considering the 4Q-CB-PWM and zero-sequence current operation with the CB-PWM and $m_a = 0.84$, $m_a = 1.1$ (*Simscape/Simulink/Matlab* simulation model according to Section 6.5)

voltage drop over the 3-phase stator windings A and B of the bearingless machine. For very high modulation indices, such as $m_a = 1.1$, the capability to generate axial voltage is strongly reduced to $\approx 72\%$ compared to the classical DC-chopper operation for the axial AMB. These conclusions are independent of the load impedance $R_{ax} + j\omega L_{ax}$. A considerable ripple in the axial current i_{ax} occurs, if the electrical time constant τ_{RL} of the axial AMB load between the two star points is small, such as in Fig. 7.1c (see explanation in Section 7.1.3).

The simulated attenuation of the axial voltage u_{ax}, depending on the inverter modulation index m_a with respect to the DC-link voltage U_{DC}, is given in Fig. 7.2 for varying modulation indices m_a and axial reference voltages $u_{ax,ref}$, comparing the 4Q-CB-PWM, the CB-PWM and the SV-PWM. As expected, for the 4Q-CB-PWM, the axial voltage u_{ax} linearly

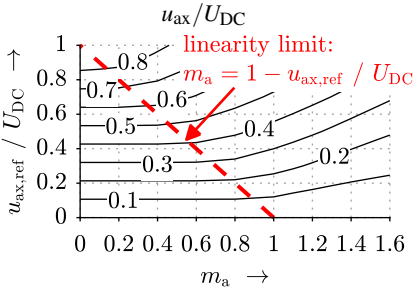

(a) CB-PWM

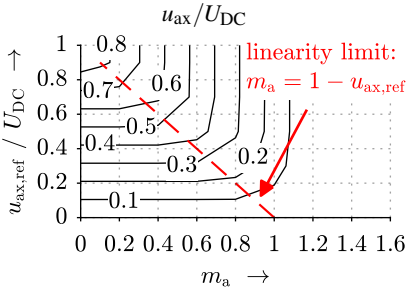

(b) SV-PWM

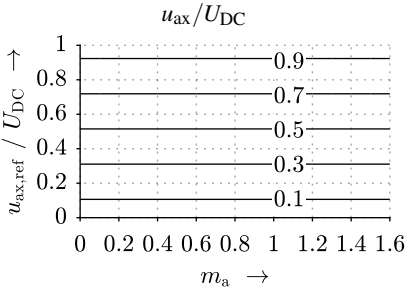

(c) 4Q-CB-PWM

Fig. 7.2.: Comparison between CB-PWM, SV-PWM and 4Q-CB-PWM: Simulated axial voltage u_{ax}/U_{DC} for varying modulation index m_a and varying axial reference voltage $u_{ax,ref}/U_{DC}$ (*Simscape/Simulink/Matlab* simulation model according to Section 6.5)

follows the reference $u_{ax,ref}$ and does not depend on the modulation index (Fig. 7.2c). The zero-sequence current feeding exhibits a modulation index limit $m_a < 1 - \left(u_{ax,ref}/U_{DC}\right)$, above which the dependency between $u_{ax,ref}$ and u_{ax} is not any longer linear (Fig. 7.2a, 7.2b). According to Fig. 7.2b, the axial voltage u_{ax} is strongly limited above the linearity limit for the SV-PWM due to the prioritization of the AC-phase voltage modulation (Section 6.4). Above $m_a > 2/\sqrt{3}$ no axial voltage can be generated anymore. In contrast, the CB-PWM is capable of considerable axial voltage values even at high modulation indices $m_a > 2/\sqrt{3}$.

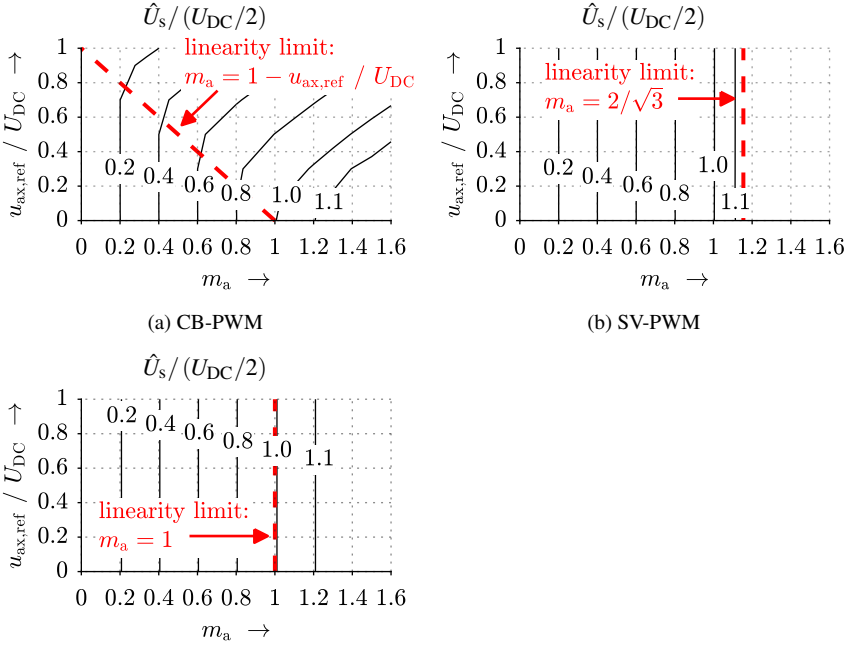

(a) CB-PWM

(b) SV-PWM

(c) 4Q-CB-PWM

Fig. 7.3.: Comparison between CB-PWM, SV-PWM and 4Q-CB-PWM: Simulated AC-phase voltage fundamental $\hat{U}_s/(U_{DC}/2)$ for varying modulation index m_a and varying axial reference voltage $u_{ax,ref}/U_{DC}$ (*Simscape/Simulink/Matlab* simulation model according to Section 6.5)

7.1.2. AC-Phase Voltage Capability

For the 4Q-CB-PWM (Fig. 7.3c) the linearity limit is at $m_a = 1$ for generating the required AC-phase voltages for the *d-q* current control and radial position control as given in [142]. In contrast, for the CB-PWM with zero-sequence current feeding (Fig. 7.3a) the relationship between $\hat{U}_{s,ref}$ and $\hat{U}_s$ depends on the voltage u_{ax}. A nonlinearity occurs for $m_a > 1 - (u_{ax,ref}/U_{DC})$ due to the missing prioritization of the AC-phase voltage generation. The SV-PWM exhibits the highest linearity limit at $m_a = 2/\sqrt{3}$ as shown in [142] (Fig. 7.3b). This limit is also independent of the voltage $u_{ax,ref}$ due to the prioritization of the AC-phase voltage modulation, which is discussed in Section 6.4.

7.1.3. Zero-Sequence Voltage Harmonic Content

Another criterion to evaluate modulation techniques is the voltage harmonic content derived by the weighted total harmonic distortion ($WTHD0$) with respect to half of the DC-link voltage $U_{\mathrm{DC}}/2$ (7.1) [140]. In (7.1) k is the harmonic order of the voltage amplitude spectrum. Hence, for the 3-phase voltage system of a 2-pole machine (*LLM4*) $k = p = 1$ represents the fundamental frequency f_{syn}. The voltage u_{ax} is considered to be a DC voltage ($k = 0$).

$$WTHD0 = \frac{\sqrt{\sum_{k=2}^{\infty}\left(\frac{\hat{U}_k}{k}\right)^2}}{U_{\mathrm{DC}}/2} \cdot 100 \tag{7.1}$$

For the different modulation techniques the Fig. 7.4a–7.4d show the simulated $WTHD0$ of u_{ax}, applying the zero-sequence current feeding. Two cases are distinguished: The voltage space vectors of the winding systems A and B, i.e. $\underline{u}_{\alpha\beta,\mathrm{A}}$ and $\underline{u}_{\alpha\beta,\mathrm{B}}$, are either in phase opposition ("differential-mode") or in phase ("common-mode"). The differential-mode feeding is required for bearingless machines with combined windings and an odd number of pole pairs $p = 1, 7, \ldots$ as in the case of the prototype machine *LLM4*. Common-mode feeding is required for combined windings with an even number of pole pairs $p = 4, 10, \ldots$ (see Section 3.2).

The $WTHD0$ for the 4Q-CB-PWM does not depend on the modulation index m_{a}. It exhibits high values up to $WTHD0 \approx 4\%$, if half of the DC-link voltage is demanded: $u_{\mathrm{ax,ref}} = U_{\mathrm{DC}}/2$. For very low and high voltage demands the $WTHD0$ of u_{ax} tends to $WTHD0 = 0$. For AMB systems the demanded bearing voltage is rather low in steady state due to the pure *ohm*ic voltage drop at R_{ax} for the stationary DC current i_{ax}.

If the zero-sequence current feeding is applied in combination with a common-mode feeding of the phase voltages in the winding systems A and B, the $WTHD0$ exhibits small values $WTHD0 < 2\%$ (Fig. 7.4b, 7.4d). This is because the "active" time sections of the PWM occur at the same time in the systems A and B and lead to $u_{\mathrm{ax}} = \pm(U_{\mathrm{DC}}/6) \mp (U_{\mathrm{DC}}/6) = 0$. This is also visible in Fig. 6.9, where the common-mode feeding leads to no oscillation of the axial voltage u_{ax}.

If the AC voltages in the winding systems A and B are fed in differential-mode, an increased $WTHD0$ occurs either for very small modulation indices $m_{\mathrm{a}} < 0.1$ and medium axial voltage demands ($u_{\mathrm{ax,ref}} = U_{\mathrm{DC}}/2$) or for high modulation indices $m_{\mathrm{a}} > 1$ and high axial voltage demands (Fig. 7.4a, 7.4c).

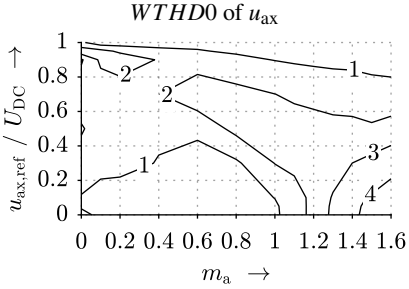

(a) CB-PWM: differential-mode

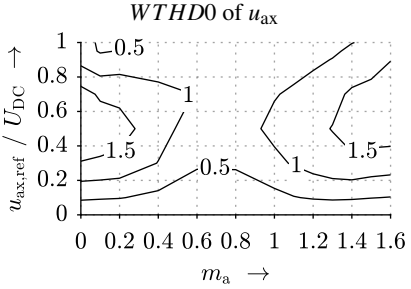

(b) CB-PWM: common-mode

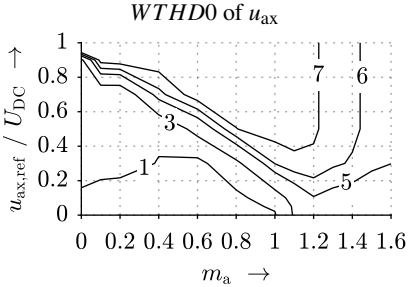

(c) SV-PWM: differential-mode

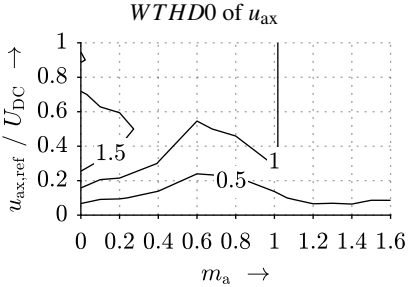

(d) SV-PWM: common-mode

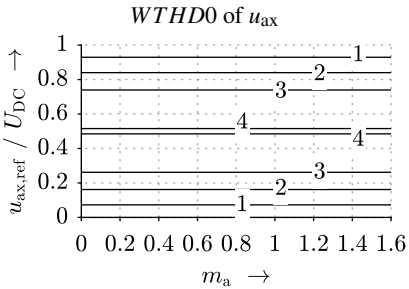

(e) 4Q-CB-PWM

Fig. 7.4.: Comparison between CB-PWM, SV-PWM and 4Q-CB-PWM: Simulated $WTHD0$ of the axial voltage u_{ax} in % for varying modulation index m_a and varying axial reference voltage $u_{ax,ref}/U_{DC}$ (*Simscape/Simulink/Matlab* simulation model according to Section 6.5)

The increase in $WTHD0$ at low modulation indices can be explained by Fig. 7.5, where the axial voltage u_{ax} is given in time domain for different reference values $u_{\mathrm{ax,ref}}$ and modulation indices. It shows, that u_{ax} can only take certain values 0, $\pm U_{\mathrm{DC}}/3$, $\pm 2U_{\mathrm{DC}}/3$ and $\pm U_{\mathrm{DC}}$ according to Fig. A.21. For $u_{\mathrm{ax,ref}} = 0$ in Fig. 7.6a, the "passive" PWM time sections occur simultaneously in the systems A and B. The very short "active" time sections due to $m_{\mathrm{a}} = 0.1$ lead to voltage peaks of amplitude $U_{\mathrm{DC}}/3$, yielding $WTHD0 \approx 0.3\%$. For $u_{\mathrm{ax,ref}} = U_{\mathrm{DC}}$ in Fig. 7.5c, the $WTHD0$ is also small, since the axial voltage only takes values between U_{DC} and $U_{\mathrm{DC}}/3$. The highest $WTHD0$ is reached for $u_{\mathrm{ax,ref}} = U_{\mathrm{DC}}/2$ in Fig. 7.4b, since the axial voltage oscillates between $u_{\mathrm{ax}} = U_{\mathrm{DC}}$ and $u_{\mathrm{ax}} = 0$ with equal pulse widths. If for the same axial voltage demand $u_{\mathrm{ax,ref}} = U_{\mathrm{DC}}/2$ the modulation index is increased from $m_{\mathrm{a}} = 0.1$ to $m_{\mathrm{a}} = 0.3$, the "active" time sections have a longer duration, leading to longer periods, in which the axial voltage takes the value $u_{\mathrm{ax,ref}} = U_{\mathrm{DC}}/3$. Therefore, the pulse widths at $u_{\mathrm{ax}} = U_{\mathrm{DC}}$ and $u_{\mathrm{ax}} = 0$ are not equal anymore, leading to

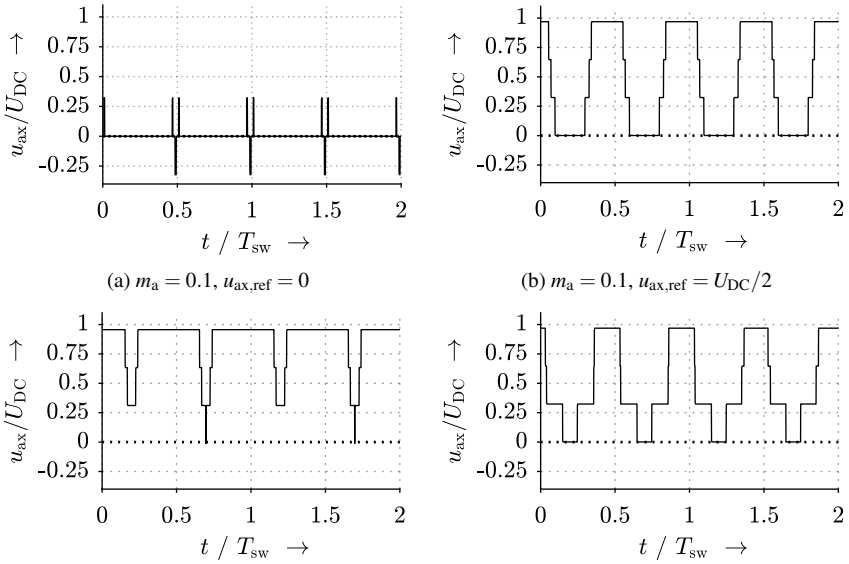

(a) $m_{\mathrm{a}} = 0.1$, $u_{\mathrm{ax,ref}} = 0$

(b) $m_{\mathrm{a}} = 0.1$, $u_{\mathrm{ax,ref}} = U_{\mathrm{DC}}/2$

(c) $m_{\mathrm{a}} = 0.1$, $u_{\mathrm{ax,ref}} = U_{\mathrm{DC}}$

(d) $m_{\mathrm{a}} = 0.3$, $u_{\mathrm{ax,ref}} = U_{\mathrm{DC}}/2$

Fig. 7.5.: Simulated axial voltage u_{ax} over two switching periods T_{sw} for different values of $u_{\mathrm{ax,ref}} = 0; U_{\mathrm{DC}}/2; U_{\mathrm{DC}}$ and $m_{\mathrm{a}} = 0.1; 0.3$, applying the SV-PWM (*Simscape/Simulink/Matlab* simulation model according to Section 6.5)

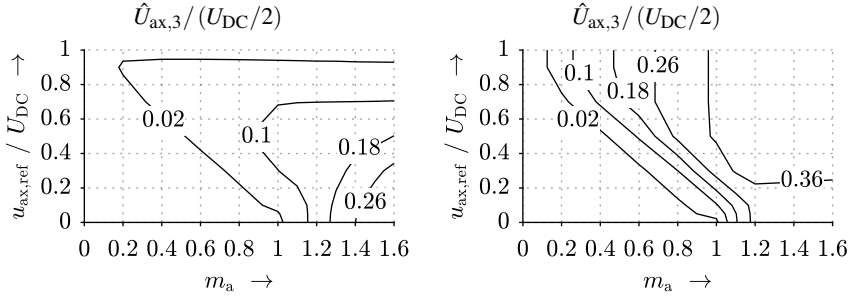

(a) CB-PWM (b) SV-PWM

Fig. 7.6.: Comparison between CB-PWM and SV-PWM: Simulated 3rd harmonic amplitude $\hat{U}_{\mathrm{ax},3}/(U_{\mathrm{DC}}/2)$ for varying modulation index m_{a} and varying axial reference voltage $u_{\mathrm{ax,ref}}/U_{\mathrm{DC}}$ (*Simscape/Simulink/Matlab* simulation model according to Section 6.5)

smaller values of the voltage amplitude side bands close to $2 \cdot f_{\mathrm{sw}}$.

The increase in $WTHD0$ for values of $m_{\mathrm{a}} > 1 - u_{\mathrm{ax,ref}}/U_{\mathrm{DC}}$ in differential-mode operation is caused by the inverter voltage limit. The axial voltage exhibits a $3 \cdot f_{\mathrm{syn}}$-frequent voltage harmonic component. This valuated 3rd harmonic component is given in Fig. 7.6. For $u_{\mathrm{ax,ref}} = 0$ it occurs for $m_{\mathrm{a}} > 1$. Due to the rather low harmonic order $k = 3$, compared to the switching frequency, it substantially increases the $WTHD0$ and leads to a strong ripple in i_{ax}. However, this ripple is not crucial for the position control, which is shown in Section 7.3. The SV-PWM exhibits higher values for $\hat{U}_{\mathrm{ax},3}$ due to the prioritization of the "active" time sections, which results from a comparison between Fig. 7.6a and 7.6b.

The $3 \cdot f_{\mathrm{syn}}$-frequent component in u_{ax} is caused by the inherent variation of the star point potential $\varphi_{\mathrm{N,A}}$ and $\varphi_{\mathrm{N,B}}$ due to the active inverter switching states. In Fig. 7.7 these star point potentials are visualized according to Fig. A.21 as γ-component u_γ related to the switching states ⓪, ①, ... ⑦. During one electric period $1/f_{\mathrm{syn}}$, the voltage space vectors $\underline{u}_{\alpha\beta,\mathrm{A}}$, $\underline{u}_{\alpha\beta,\mathrm{A}}$ rotate in the stator-fixed α-β-plane by 360°. At the edges of the hexagon in Fig. A.21, the star point potential alternates between $U_{\mathrm{DC}}/6$ and $-U_{\mathrm{DC}}/6$. Therefore, $\varphi_{\mathrm{N,A}}$, $\varphi_{\mathrm{N,B}}$ oscillate with the frequency $3 \cdot f_{\mathrm{syn}}$ between $\pm U_{\mathrm{DC}}/6$. For common-mode feeding ($\underline{u}_{\alpha\beta,\mathrm{A}} = \underline{u}_{\alpha\beta,\mathrm{B}}$), this occurs simultaneously in system A and B, so that no oscillation in u_{ax} occurs. For differential-mode feeding ($\underline{u}_{\alpha\beta,\mathrm{A}} = -\underline{u}_{\alpha\beta,\mathrm{B}}$), the oscillations of $\varphi_{\mathrm{N,A}}$, $\varphi_{\mathrm{N,B}}$ exhibit a difference in phase of 180°. Thus, $u_{\mathrm{ax}} = \varphi_{\mathrm{N,A}} - \varphi_{\mathrm{N,B}}$ oscillates between $\pm U_{\mathrm{DC}}/3$ with the frequency $3 \cdot f_{\mathrm{syn}}$.

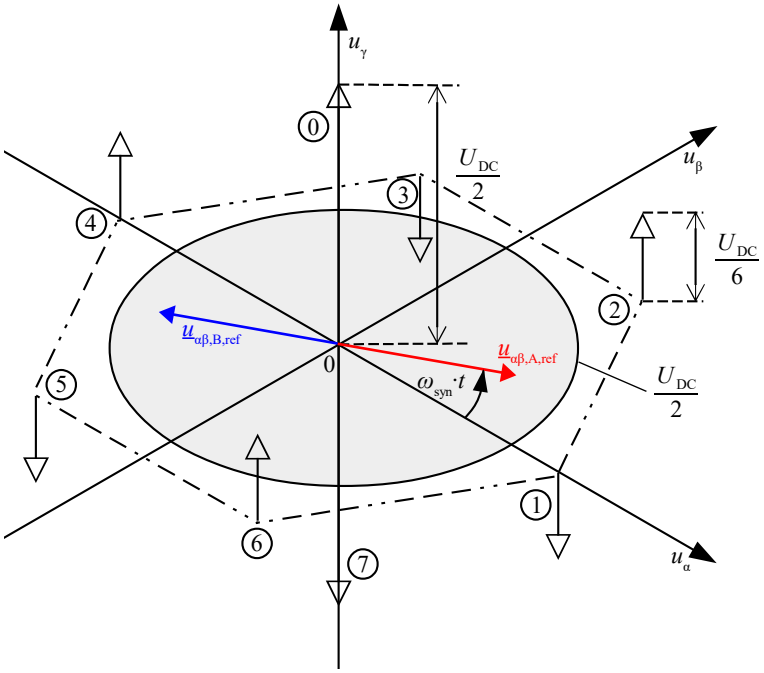

Fig. 7.7.: Discrete voltage space vectors of the eight switching states ⓪, ①, ..., ⑦ for the SV-PWM in the complex stator-fixed α-β-γ-reference frame with related electric star point potential φ_N according to Fig. A.21 (differential-mode feeding assumed: $\underline{u}_{\alpha\beta,A} = -\underline{u}_{\alpha\beta,B}$)

If the "passive" inverter time section t_{pas} is not too short, i.e. the modulation index m_a is not too big, the occurring voltage during t_{act} can be balanced over one switching period T_{sw} according to (7.2).

$$\bar{u}_\gamma\big|_{T_{sw}} = \pm\frac{U_{DC}}{6}\cdot t_{act} \mp \frac{U_{DC}}{2}\cdot t_{pas} \stackrel{!}{=} 0 \tag{7.2}$$

This condition and the condition $t_{act} + t_{pas} = T_{sw}$ result in (7.3) and explains why a $3 \cdot f_{syn}$-frequent component occurs in i_{ax} for modulation indices $m_a > 1$.

$$t_{act} \le \frac{3}{4}\cdot T_{sw} \quad \Rightarrow \quad t_{pas} \ge T_{sw}/4 \quad \Rightarrow \quad \hat{U}_{s,ref} \le \frac{U_{DC}}{2} \Leftrightarrow m_a \le 1 \tag{7.3}$$

7.1.4. AC-Phase Voltage Harmonic Content

The harmonic voltage content of the AC-phase voltages, applying zero-sequence current feeding, is not only influenced by the modulation index m_a – as for common AC motor applications – but also by the demanded axial set point voltage $u_{ax,ref}$. Thus, in Fig. 7.8 the $WTHD0$ for the α-component of the differential-mode voltage $u_{\alpha,D} = u_{\alpha,A} - u_{\alpha,B}$ and of the common-mode voltage $u_{\alpha,L} = u_{\alpha,A} + u_{\alpha,B}$ are given. This distinction is made, since the axial voltage u_{ax}, resulting from the difference of the star point potentials $\varphi_{N,A} - \varphi_{N,B}$, only influences the differential-mode voltage components of the AC-phase voltages. In

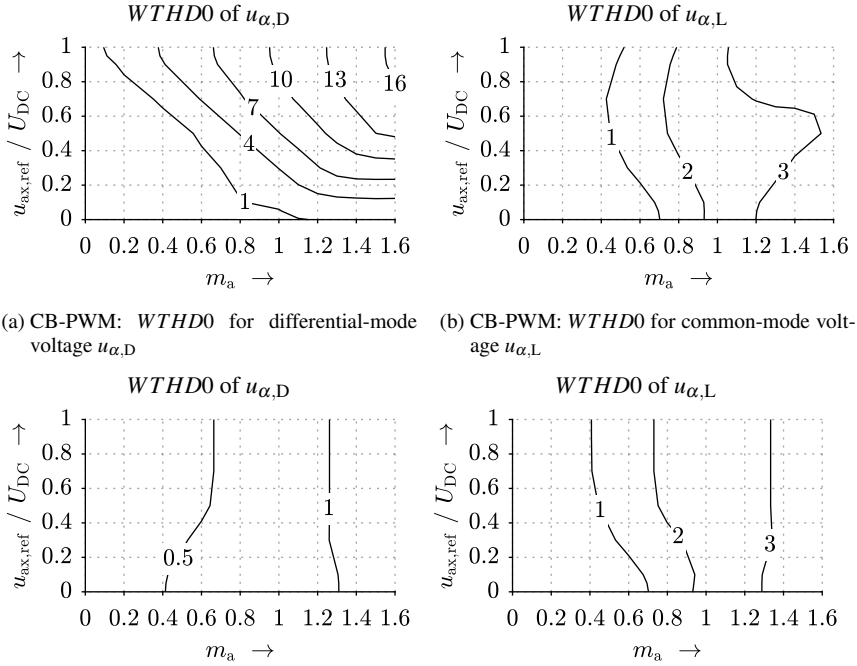

(a) CB-PWM: $WTHD0$ for differential-mode voltage $u_{\alpha,D}$

(b) CB-PWM: $WTHD0$ for common-mode voltage $u_{\alpha,L}$

(c) SV-PWM: $WTHD0$ for differential-mode voltage $u_{\alpha,D}$

(d) SV-PWM: $WTHD0$ for common-mode voltage $u_{\alpha,L}$

Fig. 7.8.: Comparison between CB-PWM, SV-PWM and 4Q-CB-PWM: Simulated $WTHD0$ of the differential-mode voltage $u_{\alpha,D}$ and common-mode voltage $u_{\alpha,L}$ in % for varying modulation index m_a and varying axial reference voltage $u_{ax,ref}/U_{DC}$ ($\hat{U}_{\alpha,D,ref} = m_a \cdot U_{DC}/2$, $\hat{U}_{\alpha,L,ref} = 0$, *Simscape/Simulink/Matlab* simulation model according to Section 6.5)

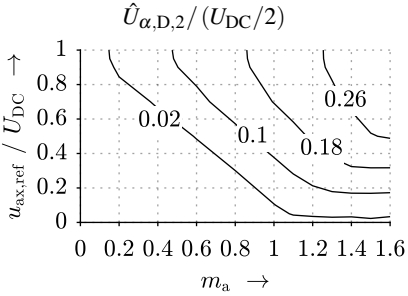

Fig. 7.9.: Simulated differential-mode voltage harmonic $\hat{U}_{\alpha,\mathrm{D},2}/(U_{\mathrm{DC}}/2)$ for varying modulation index m_{a} and varying axial reference voltage $u_{\mathrm{ax,ref}}/U_{\mathrm{DC}}$, using the CB-PWM ($\hat{U}_{\alpha,\mathrm{D,ref}} = m_{\mathrm{a}} \cdot U_{\mathrm{DC}}/2$, $\hat{U}_{\alpha,\mathrm{L,ref}} = 0$, *Simscape/Simulink/Matlab* simulation model according to Section 6.5)

case of an AC-phase voltage demand in differential-mode, the modulated reference voltage is the differential-mode voltage $\hat{U}_{\alpha,\mathrm{D,ref}}$, determined by the modulation index according to $\hat{U}_{\alpha,\mathrm{D,ref}} = m_{\mathrm{a}} \cdot U_{\mathrm{DC}}/2$. The AC-phase voltage common-mode component is assumed to be zero $\hat{U}_{\alpha,\mathrm{L,ref}} = 0$.

For the CB-PWM (Fig. 7.8a), the simulated $WTHD0$ of the differential-mode voltage $u_{\alpha,\mathrm{D}}$ increases together with m_{a} and also together with $u_{\mathrm{ax,ref}}$. In the nonlinear region above $m_{\mathrm{a}} > 1 - \left(u_{\mathrm{ax,ref}}/U_{\mathrm{DC}}\right)$ (Fig. 7.3), the differential-mode AC-phase voltages suffer from a big voltage harmonic distortion up to $WTHD0 \approx 15\%$. This increase is mainly due to a big amplitude of the $2 \cdot f_{\mathrm{syn}}$-frequent harmonic component $\hat{U}_{\alpha,\mathrm{D},2}$ of the differential-mode voltage which is given in Fig. 7.9. It results from the instant that one half-wave of the reference voltage signal per phase is far above $U_{\mathrm{DC}}/2$ (compare Fig. 6.7a), violating the voltage pattern symmetry and introducing even harmonic orders into the voltage spectrum. Additionally, these voltage harmonics $\hat{U}_{\alpha,\mathrm{D},2}$ occur if high dynamics such as a step response in the star point-connected AMB are required, which is shown in Section 7.3.

In contrast, the SV-PWM exhibits a very low $WTHD0$-level for the differential-mode voltage, agreeing with [142] (Fig. 7.8c). It is almost independent of the axial voltage requirement, due to the prioritization of $\underline{u}_{\mathrm{A,ref}}$, $\underline{u}_{\mathrm{B,ref}}$ over $u_{\mathrm{ax,ref}}$.

In general, the common-mode voltage component $u_{\alpha,\mathrm{L,ref}}$ is hardly affected by the zero-sequence current feeding. Its $WTHD0$ only increases with rising m_{a}. In the prototype machine *LLM4* with $p = 1$, this leads to a bigger suspension current ripple at high speed, since the suspension current i_{L} results from a common-mode feeding of the windings

systems A and B. For the common-mode feeding, the SV-PWM yields a similar voltage harmonic distortion compared to the CB-PWM.
The $WTHD0$ for the 4Q-CB-PWM operation shows obviously no dependency between axial bearing voltage and the AC-phase voltages, as there is no electrical connection between the 3-phase motor windings and the axial AMB. It is given by the values for the CB-PWM in the case of $u_{\mathrm{ax,ref}} = 0$ (Fig. 7.8a, 7.8b). Altogether, the SV-PWM exhibits a lower AC-phase voltage harmonic content than the CB-PWM and the 4Q-CB-PWM technique despite the applied zero-sequence current feeding.

7.2. Constraints by the Bearingless Motor

The current i_{ax} is designated to flow in the coil of the axial bearing with N_{ax} turns to generate the axial force F_{ax}. Applying the zero-sequence current feeding, this current also flows in the bearingless machine's active part as $i_{\mathrm{ax}}/3$ in each phase of the double 3-phase winding system with N_{s} turns per phase. N_{s} is chosen in accordance with the inverter voltage limit and the machine current limit. If the zero-sequence current feeding is used, the choice of N_{s} must also take into account, that the magneto-motive force $N_{\mathrm{s}} \cdot i_{\mathrm{ax}}/3$ may have a harmful influence on the machine performance. Thus, the zero-sequence current feeding is especially applicable for bearingless drives with a high ratio of $N_{\mathrm{ax}}/N_{\mathrm{s}}$. Fortunately, N_{ax} is usually chosen big in order to keep the axial force current low ($i_{\mathrm{ax}} \propto 1/N_{\mathrm{ax}}$). Mainly five parasitic effects occur in a bearingless motor with zero-sequence current feeding:

- Additional impedance for the axial force current i_{ax}
- Additional suspension force ripple $\hat{w}_{\mathrm{F}} = \frac{F_{\max} - F_{\min}}{F_{\max} + F_{\min}}$
- Additional torque ripple $\hat{w}_{\mathrm{M}} = \frac{M_{\max} - M_{\min}}{M_{\max} + M_{\min}}$
- Additional rotor eddy current losses $P_{\mathrm{Ft,R}}$
- Additional *ohm*ic losses P_{Cu} in the stator winding
- Magnetic coupling between the drive winding field, the suspension winding field and the zero-sequence current excited field due to magnetic saturation

The winding in the built prototype machine *LLM4* has a pitching of $W/\tau_{\mathrm{p}} = 2/3$. There-

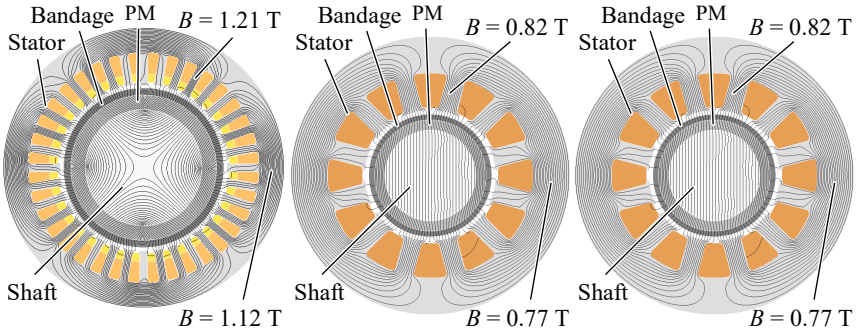

(a) ***LLM2***: 40 kW/40000 min^{-1}, $p/p_{\mathrm{L}} = 2/3$, $r_{\mathrm{S,i}} = 40$ mm, $l_{\mathrm{Fe}} = 125$ mm [9]

(b) ***LLM3***: 1 kW/60000 min^{-1}, $p/p_{\mathrm{L}} = 1/2$, $r_{\mathrm{S,i}} = 17.5$ mm, $l_{\mathrm{Fe}} = 40$ mm [23]

(c) ***LLM4***: 1 kW/60000 min^{-1}, $p/p_{\mathrm{L}} = 1/2$, $r_{\mathrm{S,i}} = 17.5$ mm, $l_{\mathrm{Fe}} = 40$ mm

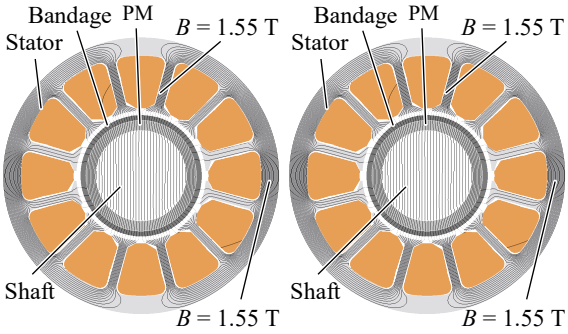

(d) ***LLM3***$_{\mathrm{I+}}$: 2.3 kW/60000 min^{-1}, $p/p_{\mathrm{L}} = 1/2$, $r_{\mathrm{S,i}} = 17.5$ mm, $l_{\mathrm{Fe}} = 40$ mm

(e) ***LLM3***$_{\mathrm{N+}}$: 2.3 kW/60000 min^{-1}, $p/p_{\mathrm{L}} = 1/2$, $r_{\mathrm{S,i}} = 17.5$ mm, $l_{\mathrm{Fe}} = 40$ mm

Fig. 7.10.: Overview of the considered bearingless machine topologies *LLM2* (built), *LLM3* (built), *LLM4* (built), *LLM3*$_{\mathrm{I+}}$ and *LLM3*$_{\mathrm{N+}}$ intended for a zero-sequence current feeding (general overview of investigated topologies given in Table A.4)

fore, the winding factors of the air gap field harmonic order divisible by $m = 3$ are $k_{\mathrm{w},3,9,15,\ldots} = 0$ (Table 3.8). Thus, the zero-sequence current has no effect on air gap forces or rotor eddy current losses. In order to investigate how the zero-sequence current feeding affects the performance of a bearingless motor, four other prototype machines are considered additionally. One is a 1 kW/60000 min^{-1} [23] machine similar to the *LLM4*, but

exhibiting $W/\tau_p = 1/2$ and $k_{w,3,9,15,...} = 0.5$, which is subsequently referred to as *LLM3*. Another one is the 40 kW/40000 min^{-1} machine [9] with two separated drive and suspension windings, which is subsequently referred to as *LLM2*. For the *LLM2* with two separated windings, the zero-sequence current feeding can be either applied by a current between the suspension winding star point and the neutral DC-link inverter clamp or by a current between the two suspension winding star points of two half-motors. The 6-pole single-layer suspension winding with $Q = 36$ slots ($q = 2$) has winding factors $k_{w,3,9,15,...} = 0.707$ [9]. It is equipped with a 4-pole PM rotor with parallel magnetization. All these topologies exhibit very low stator iron flux densities of $B_{Fe} < 1.1$ T. To investigate the parasitic effects of the zero-sequence current feeding under magnetic saturation the topologies *LLM3*$_{I+}$ and *LLM3*$_{N+}$ are also considered. These topologies exhibit half the stator tooth and yoke width of the *LLM3*. Instead their stator current loadings are increased: For the *LLM3*$_{I+}$ by a drive current, which is 2.3-times bigger than in the *LLM3*, and for the *LLM3*$_{N+}$ by the number of turns per coil, which are $N_c = 25$ instead of $N_c = 11$.

Fig. 7.11 shows the radial component B_r of the stator air gap field, if only the drive current $I_{s,D} = I_{s,D,N}$ per phase, only suspension current $I_{s,L} = I_{s,L,N}$ per phase and only the axial force current $i_{ax} = 15$ A are fed. As expected, the motor *LLM4* does not show any air gap field by the axial force current i_{ax}. *LLM3* and *LLM2* exhibit a small third harmonic field component $\nu = 3$, whose amplitude is in the range of the suspension air gap field. However, the here considered axial force current is very high ($i_{ax} = 15$ A) and much higher than usually required for steady state operation ($i_{ax,N} < 1$ A). For comparison, the radial component of the rotor PM air gap field wave amplitude is $B_{R,1,1,r} = 0.45$ T for the *LLM3* and *LLM4*. It is $B_{R,2,2,r} = 0.6$ T for the *LLM2*, resulting in a very small armature reaction for these high-speed machines.

7.2.1. Coupling due to Magnetic Saturation

If no magnetic saturation in the iron circuit of the bearingless machine occurs, the magnetic field of the axial current cannot induce a residual voltage in the stator drive winding and in the suspension winding, since the induced voltage exhibits the same phase in each winding phase U, V, W and cancels for star-connection as line-to-line voltage. A possible coupling between the fields can occur in case of magnetic saturation. The motors *LLM2*, *LLM3* and *LLM4* with synchronous frequencies $f_{syn} > 500$ Hz are inherently designed

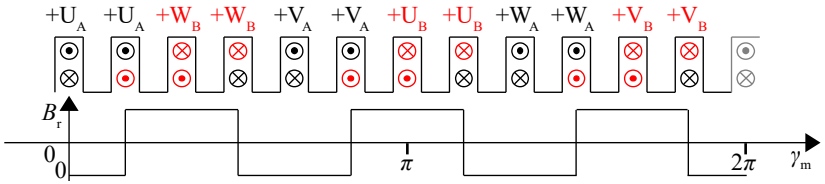

(a) Ampere-turns distributions for a zero-sequence current feeding of the *LLM3* and corresponding schematic radial field characteristic with neglected slot openings

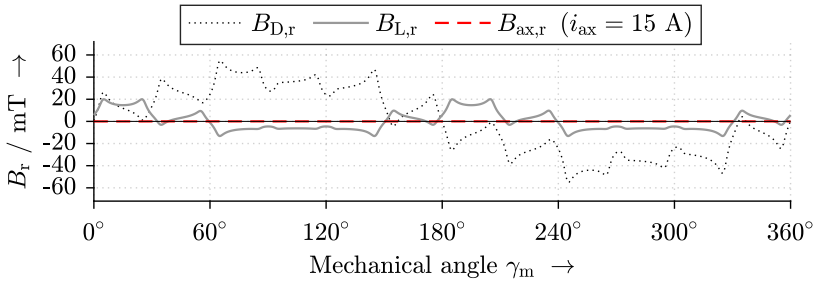

(b) *LLM4*

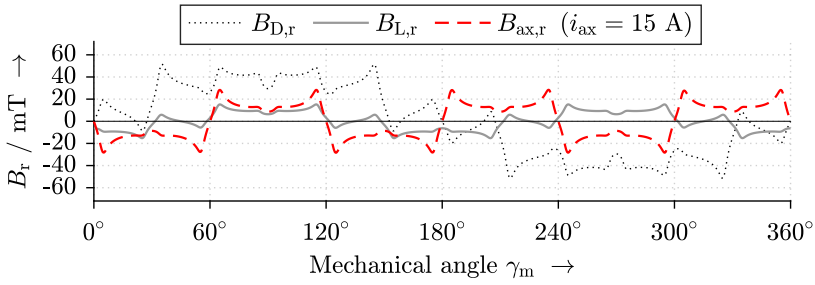

(c) *LLM3*

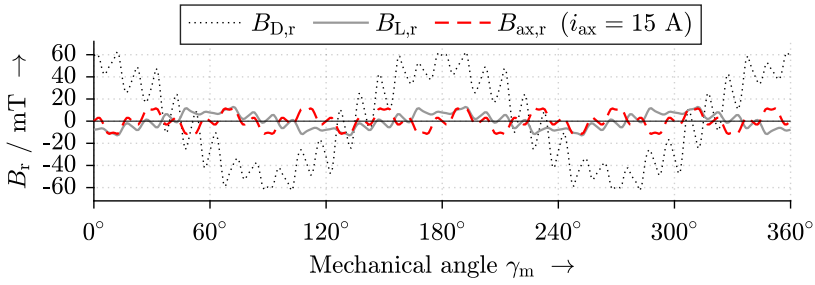

(d) *LLM2*

Fig. 7.11.: Motor *LLM4*, *LLM3*, *LLM2*: Simulated radial air gap field component B_r at a current feeding of $\hat{I}_D = 12$ A, $\hat{I}_L = 5.8$ A and $i_{ax} = 15$ A

with a rather small value of the maximum air gap flux density $B_{\mathrm{r,max}} \approx 0.6$ T to keep the iron losses low. Thus, these machines are not prone to magnetic coupling in case of the zero-sequence current feeding. Additionally, bearingless machines are designed to have a rather low armature reaction field to keep the undesired superposition effect (Section 2.5) small.

Magnetic saturation is mainly driven by the stator tooth flux density $B_{\mathrm{d,S}} \approx 1.8 \cdot B_{\mathrm{r,max}}$. The maximum air gap flux density in bearingless motors is given by through the superposition of the rotor field wave, drive air gap field wave, the suspension field wave and the field wave due to the zero-sequence current. 2D FEM simulations for the motors *LLM2*, *LLM3* and *LLM4* have shown, that the maximum tooth flux density $B_{\mathrm{d,S}}$ can be approximated by (7.4), which incorporates the radial air gap field wave components of the rotor field $B_{\mathrm{R},\mu'=p,k=p,\mathrm{r}}$, of the drive winding field $B_{\mathrm{D},\nu'=p,k=p,\mathrm{r}}$, of the suspension winding field $B_{\mathrm{L},\nu'_{\mathrm{L}}=p_{\mathrm{L}},k=p,\mathrm{r}}$ and of the zero-sequence current field of the drive winding field $B_{\mathrm{ax},\nu'=3p,k=0,\mathrm{r}}$.

$$B_{\mathrm{d,S}} \approx 1.8 \cdot \left(\sqrt{B^2_{\mathrm{R},p,p,\mathrm{r}} + B^2_{\mathrm{D},p,p,\mathrm{r}}} + B_{\mathrm{L},p_{\mathrm{L}},p,\mathrm{r}} + B_{\mathrm{ax},3p,0,\mathrm{r}} \right), \quad \text{where} \tag{7.4}$$

$$B_{\mathrm{D},p,p,\mathrm{r}} \propto \frac{\sqrt{2} \cdot \mu_0 \cdot m \cdot N_{\mathrm{s}} \cdot k_{\mathrm{w,D}} \cdot I_{\mathrm{s,D}}}{p \cdot \pi \cdot \delta_{\mathrm{eff}}}; \quad B_{\mathrm{L},p_{\mathrm{L}},p,\mathrm{r}} \propto \frac{\sqrt{2} \cdot \mu_0 \cdot m \cdot N_{\mathrm{s}} \cdot k_{\mathrm{w,L}} \cdot I_{\mathrm{s,L}}}{p_{\mathrm{L}} \cdot \pi \cdot \delta_{\mathrm{eff}}}$$

$$B_{\mathrm{ax},3p,0,\mathrm{r}} \propto \frac{\sqrt{2} \cdot \mu_0 \cdot m \cdot N_{\mathrm{s}} \cdot k_{\mathrm{w},3}}{3 \cdot p \cdot \pi \cdot \delta_{\mathrm{eff}}} \cdot \frac{I_{\mathrm{ax}}}{3}$$

The contribution of the zero-sequence current field to the total air gap field is only noticeable, if its amplitude $B_{\mathrm{ax},3p,0,\mathrm{r}}$ is in the range of total magnetic field without the zero-sequence current feeding. The maximum air gap flux density value without the zero-sequence current feeding can be approximately calculated by sum of the suspension winding field $B_{\mathrm{L},\nu'_{\mathrm{L}}=p_{\mathrm{L}},k=p,\mathrm{r}}$ and the *Euklid*ean norm of the rotor field $B_{\mathrm{R},\mu'=p,k=p,\mathrm{r}}$ and of the drive winding field $B_{\mathrm{D},\nu'=p,k=p,\mathrm{r}}$ (q-current operation). Thus, to influence the saturation state of the machine, the axial AMB current i_{ax} must roughly exceed the term in (7.5).

$$\frac{I_{\mathrm{ax}}}{3} \gtrapprox \frac{3 \cdot p \cdot \pi \cdot \delta_{\mathrm{eff}}}{\sqrt{2} \cdot \mu_0 \cdot m \cdot N_{\mathrm{s}} \cdot k_{\mathrm{w},3}} \cdot \left(\sqrt{B^2_{\mathrm{R},p,p,\mathrm{r}} + B^2_{\mathrm{D},p,p,\mathrm{r}}} + B_{\mathrm{L},p_{\mathrm{L}},p,\mathrm{r}} \right) \tag{7.5}$$

The radial component $B_{\mathrm{ax},3p,0,\mathrm{r}}$ is proportional to the factor $1/(3 \cdot p)$, whereas the flux density amplitudes of the drive and suspension field are only proportional to the factors $1/p$ and $1/p_{\mathrm{L}}$ respectively. Since the rotor field amplitude $B_{\mathrm{R},p,p,\mathrm{r}}$ is much bigger than the stator field amplitude, the axial current I_{ax} must take very high values to influence

Table 7.1.: Stator iron losses $P_{\mathrm{Fe,S}}$ and maximum of air gap field amplitudes from 2D FEM simulations for the topologies $LLM3_{\mathrm{I}+}$ and $LLM3_{\mathrm{N}+}$ for varying axial AMB current I_{ax}

I_{ax} / A	0	1	3	6	15	30
$LLM3_{\mathrm{I}+}$: $B_{\mathrm{max,r}}$ / mT	473	473	473	474	475	476
$LLM3_{\mathrm{N}+}$: $B_{\mathrm{max,r}}$ / mT	473	473	475	467	477	487
$LLM3_{\mathrm{I}+}$: $P_{\mathrm{Fe,S}}$ / W	151	151	151	152	154	155
$LLM3_{\mathrm{N}+}$: $P_{\mathrm{Fe,S}}$ / W	150	150	151	151	153	160

the saturation state of the machine, e.g. $\frac{I_{\mathrm{ax}}}{3} \gtrapprox 500$ A for the *LLM3*. Thus, no magnetic saturation results from the zero-sequence current feeding of an axial AMB in bearingless drives. Table 7.1 shows, how the current I_{ax} influences the air gap flux density and the stator iron losses $P_{\mathrm{Fe,S}}$ for the topologies with the strongest influence of the zero-sequence current feeding, i.e. $LLM3_{\mathrm{I}+}$ and $LLM3_{\mathrm{N}+}$. Even these topologies show only a very small dependency on the zero-sequence current amplitude.

However, magnetic saturation can occur from the $2p$-pole rotor PM and respectively the drive winding field for highly-utilized designs like the $LLM3_{\mathrm{I}+}$ or the $LLM3_{\mathrm{N}+}$. The saturation results in a permeance wave of space order $\tilde{\nu}' = 2p$ and time order $\tilde{k} = 2p$, which modulates the field waves. It is discussed in Section 2.6. Fig. 7.12 shows the *Fourier* spectrum of the non-saturated *LLM3* and the saturated $LLM3_{\mathrm{N}+}$. From the comparison of Fig. 7.12a and 7.12b one can identify, which additional field harmonics occur from the modulation by the saturation-based permeance wave. Only the two field harmonics with the highest amplitudes $B_{\mathrm{R},1,1,\mathrm{r}}$ and $B_{\mathrm{ax},3,0,\mathrm{r}}$ result in modulated field waves of noticeable amplitudes which are given in (7.6), (7.7). Note that the third harmonic rotor field amplitude for the *LLM3* ($B_{\mathrm{R},3,3,\mathrm{r}} = 2.2$ mT) is less than half the third harmonic rotor field amplitude of the $LLM3_{\mathrm{N}+}$ ($B_{\mathrm{R},3,3,\mathrm{r}} = 5.8$ mT).

$$B_{\mathrm{R},3,3,\mathrm{r}}(\gamma_{\mathrm{m}},t) = \hat{B}_{\mathrm{R},3,3,\mathrm{r}} \cdot \cos((p+2p)\cdot\gamma_{\mathrm{m}} - (p+2p)\cdot nt) \tag{7.6}$$

$$B_{\mathrm{R},-1,-1,\mathrm{r}}(\gamma_{\mathrm{m}},t) = \hat{B}_{\mathrm{R},-1,-1,\mathrm{r}} \cdot \cos((p-2p)\cdot\gamma_{\mathrm{m}} - (p-2p)\,nt)$$

$$B_{\mathrm{ax},5,2,\mathrm{r}}(\gamma_{\mathrm{m}},t) = \hat{B}_{\mathrm{ax},5,2,\mathrm{r}} \cdot \cos((3p+2p)\cdot\gamma_{\mathrm{m}} - 2p\cdot nt) \tag{7.7}$$

$$B_{\mathrm{ax},1,-2,\mathrm{r}}(\gamma_{\mathrm{m}},t) = \hat{B}_{\mathrm{ax},1,-2,\mathrm{r}} \cdot \cos((3p-2p)\cdot\gamma_{\mathrm{m}} + 2p\cdot nt)$$

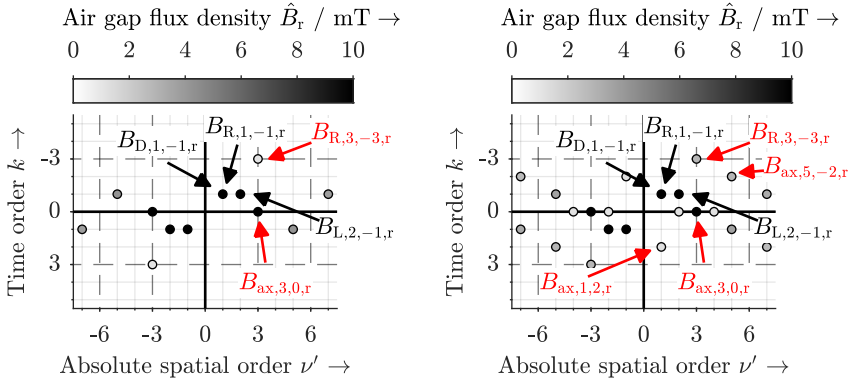

(a) *LLM3* (b) *LLM3*$_{\mathrm{N+}}$

Fig. 7.12.: Motors *LLM3*, *LLM3*$_{\mathrm{N+}}$: 2D *Fourier* spectrum of the air gap flux density radial component B_r in the middle of the mechanical air gap (retrieved from a 2D FEM simulation), based on [100] ($i_{\mathrm{q,D}} = 10.5$ A, $i_{\mathrm{q,L}} = 5.8$ A, $i_{\mathrm{ax}} = 3 \cdot 10 = 30$ A)

The reduction of the stator iron permeance mean value λ_0 (Section 2.6) and the modulation by the permeance wave $\lambda_{\mathrm{sat},\tilde{\nu}',\tilde{k}}$ leads to a reduction of the fundamental field waves $B_{\mathrm{R},p,p,\mathrm{r}}$, $B_{\mathrm{D},p,p,\mathrm{r}}$ and $B_{\mathrm{L},p_\mathrm{L},p,\mathrm{r}}$. This results in a reduction of the air gap torque,

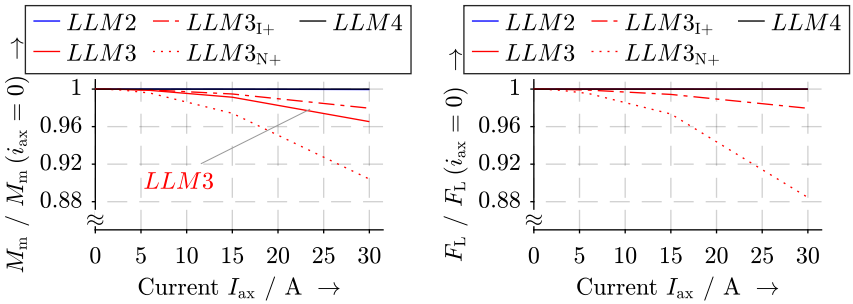

(a) Reduction of shaft torque M_m due to magnetic saturation and additional losses $P_{\mathrm{Ft,PM}}$

(b) Reduction of suspension force F_L due to magnetic saturation

Fig. 7.13.: Motors *LLM2*, *LLM3*, *LLM3*$_{\mathrm{I+}}$, *LLM3*$_{\mathrm{N+}}$, *LLM4*: Shaft torque and suspension force mean values for varying axial AMB current I_ax (retrieved from a 2D FEM simulation)

respectively of the shaft torque M_m (Fig. 7.13a), and to a reduction of the suspension force F_L (Fig. 7.13b). Note that this reduction leads to a cross-coupling of the zero-sequence current i_ax, the torque-generating current $i_\mathrm{q,D}$ and the levitation current $i_\mathrm{q,L}$, which can be harmful for the rotor position control. However, Fig. 7.13 shows that this reduction is only present for unrealistically high axial AMB currents i_ax. The cross-coupling is stronger for machines with a large armature reaction field such as the $LLM3_\mathrm{N+}$. The reduction of the shaft torque is also caused by the additional rotor eddy current losses $P_\mathrm{Ft,PM}$, which increase with rising zero-sequence current (Section 7.2.4). Thus, also the unsaturated *LLM3* suffers from a reduction in the shaft torque for $i_\mathrm{ax} > 10$ A.

7.2.2. Torque Ripple due to Zero-Sequence Current Feeding

The calculation of torque oscillation frequencies $f_\mathrm{P,M}$ is shown in [94]. One source of these torque ripples is the interaction of stator drive field harmonics of space order $\nu'_\mathrm{D} = \nu_\mathrm{D} \cdot p$ and fixed time order $k = p$ with rotor field harmonics of space order $\mu' = \mu \cdot p$ and time order $k = \mu'$, resulting in AC torque components of frequency $f_\mathrm{P,M}$ (7.8). The torque ripple occurs independently of the zero-sequence current feeding and independent of field modulation due to slot openings or saturation.

$$f_\mathrm{P,M} = |n \cdot (\mu \cdot p \mp p)| = \left|f_\mathrm{syn} \cdot (\mu \mp 1)\right| \text{ for } |\nu_\mathrm{D}| \cdot p = \pm\mu \cdot p \tag{7.8}$$

If a zero-sequence current (DC-current) is fed into the winding, an additional torque ripple of frequency $f_\mathrm{P,M,ax}$ can occur, if the condition in (7.9) is valid.

$$f_\mathrm{P,M,ax} = \left|f_\mathrm{syn} \cdot \mu\right| \text{ for } |\nu_\mathrm{ax}| \cdot p = \pm\mu \cdot p \text{ , where } \nu_\mathrm{ax} = 3, 9, 15, \ldots \tag{7.9}$$

Despite the low harmonic content of the rotor PM field due to the parallelly magnetized PM, the small third harmonic of the rotor PM field $B_\mathrm{R,3,3,r}$ yields a $3 \cdot f_\mathrm{syn}$-frequent torque pulsation in interaction with the third harmonic $\nu_\mathrm{D} = 3$ of the stator field due to zero-sequence feeding (Fig. 7.14b). As shown in Section 7.2.1, $B_\mathrm{R,3,3,r}$ increases with magnetic saturation, so that the $3f_\mathrm{syn}$-frequent torque ripple is bigger. Design guidelines to keep this $f_\mathrm{P,M,ax}$-frequent torque ripple $\hat{w}_\mathrm{M}$ low can be derived from (7.10)–(7.12). The torque amplitude $\hat{M}_{\delta,3}$ is low for big values of the drive current $I_\mathrm{s,D}$ with respect to the axial current I_ax. Thus, a high number of turns N_ax in the axial AMB is of advantage to keep the

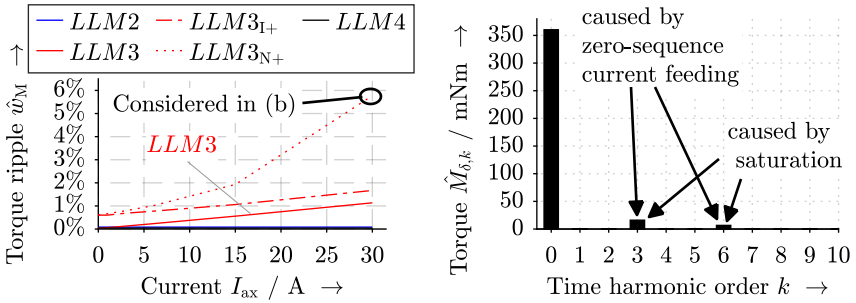

(a) Air gap torque ripple $\hat{w}_\mathrm{M}$ for varying axial AMB current I_ax

(b) *Fourier* spectrum of the air gap torque M_δ for the $LLM3_{\mathrm{N}+}$ at $i_\mathrm{ax} = 30$ A

Fig. 7.14.: Motors *LLM2*, *LLM3*, $LLM3_{\mathrm{I}+}$, $LLM3_{\mathrm{N}+}$, *LLM4*: Air gap torque ripple $\hat{w}_\mathrm{M}$ and $\hat{M}_{\delta,\mathrm{k}}$ for varying axial AMB current I_ax (retrieved from a 2D FEM simulation)

needed current I_ax low. Consequently, the $LLM3_{\mathrm{I}+}$ exhibits 44% less torque ripple than the $LLM3_{\mathrm{N}+}$ in unsaturated conditions (Fig. 7.14a).

$$M_\delta \propto N_\mathrm{s} \cdot k_\mathrm{w,D} \cdot I_\mathrm{s,D} \cdot B_{\mathrm{R},p,p,\mathrm{r}} \tag{7.10}$$

$$\hat{M}_{\delta,3} \propto N_\mathrm{s} \cdot k_\mathrm{w,3} \cdot \frac{I_\mathrm{ax}}{3} \cdot B_{\mathrm{R},3,3,\mathrm{r}} \tag{7.11}$$

$$\rightarrow \frac{\hat{M}_{\delta,3}}{M_\delta} \propto \frac{I_\mathrm{ax}/3 \cdot k_\mathrm{w,3} \cdot B_{\mathrm{R},3,3,\mathrm{r}}}{I_\mathrm{s,D} \cdot B_{\mathrm{R},1,1,\mathrm{r}} \cdot k_\mathrm{w,D}} \tag{7.12}$$

For highly-utilized machines, such as the $LLM3_{\mathrm{I}+}$ and the $LLM3_{\mathrm{N}+}$, the magnetic saturation in the stator iron due to the rotor and the drive winding field leads to additional air gap field waves by the modulation of the saturation-originated permeance function (Fig. 7.12b). This results in an increase of the torque ripple $\hat{w}_\mathrm{M}$, explaining the non-linear increase of the torque ripple $\hat{w}_\mathrm{M}$ for the $LLM3_{\mathrm{N}+}$ in Fig. 7.14a. Fig. 7.14b considers the saturated topology $LLM3_{\mathrm{N}+}$ for $I_\mathrm{ax} = 30$ A. Besides the torque component $M_{\delta,3}$, a torque component $\hat{M}_{\delta,6}$ occurs. It is caused by the saturation due to the standstill $3p$-pole zero-sequence current field. The resulting standstill $6p$-pole permeance function modulates the $2p$-pole rotor field fundamental and leads to two field waves of time order ∓ 1 and space order $\nu = 5$ and $\nu = 7$, which generate torque with the rotor field harmonics of space and time order $\mu = k = 5$ and $\mu = k = 7$.

7.2.3. Force Ripple due to Zero-Sequence Current Feeding

In Section 2.6, the occurrence of saturation-originated force ripple was explained. Here, the focus is on the additional force ripple by the zero-sequence current feeding. If a zero-sequence current is fed into the winding, additional force ripple of frequency $f_{\mathrm{P,F,ax}}$ can occur, if one of the three conditions in (7.13) is valid. Note that the drive winding air gap field includes harmonic orders $\nu_{\mathrm{D}} = 3, 9, 15, ...$, if the zero-sequence current is fed into a combined winding drive and suspension winding. For separated windings, the suspension winding air gap field exhibits harmonic orders $\nu_{\mathrm{L}} = 3, 9, 15, ...$, if only the suspension winding is fed with a zero-sequence current.

$$f_{\mathrm{P,F,ax}} = \begin{cases} |\pm f_{\mathrm{syn}}| & \text{for } |\nu_{\mathrm{L}}| \cdot p_{\mathrm{L}} = |\nu_{\mathrm{D}}| \cdot p \pm 1 \\ |\pm \mu \cdot f_{\mathrm{syn}}| & \text{for } |\nu_{\mathrm{L}}| \cdot p_{\mathrm{L}} = \mu \cdot p \pm 1 \quad \text{(separated)} \\ |\pm \mu \cdot f_{\mathrm{syn}}| & \text{for } |\nu_{\mathrm{D}}| \cdot p = \mu \cdot p \pm 1 \quad \text{(combined)} \end{cases} \tag{7.13}$$

Bearingless machines with parallel PM rotor magnetization and $2p = 2$ poles exhibit small rotor field harmonics. Thus, mainly the third harmonic of the stator field due to zero-sequence feeding $\nu_{\mathrm{D}} = 3$ yields a f_{syn}-frequent force pulsation in interaction with the suspension field fundamental ($\nu_{\mathrm{L}} \cdot p_{\mathrm{L}} = 2$), which is visible Fig. 7.15b. Design guidelines to keep the $f_{\mathrm{P,F,ax}}$-frequent force oscillation of normalized amplitude $\hat{w}_{\mathrm{F}}$ low can be derived

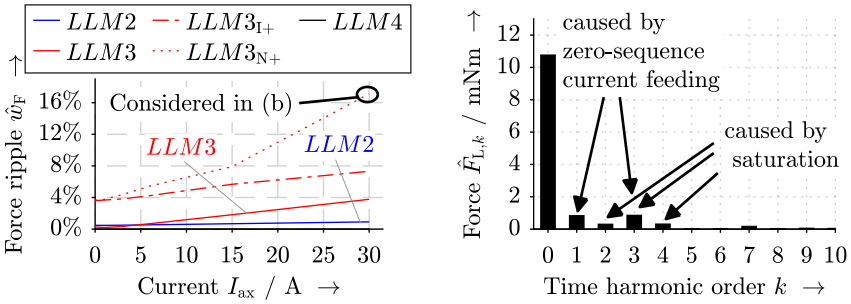

(a) Force ripple $\hat{w}_{\mathrm{F}}$ for varying axial AMB current I_{ax}

(b) *Fourier* spectrum of the suspension force F_{L} for the $LLM3_{\mathrm{N+}}$ at $i_{\mathrm{ax}} = 30$ A

Fig. 7.15.: Motors *LLM2*, *LLM3*, $LLM3_{\mathrm{I+}}$, $LLM3_{\mathrm{N+}}$, *LLM4*: Suspension force ripple $\hat{w}_{\mathrm{F}}$ and $\hat{F}_{\mathrm{L},k}$ for varying axial AMB current I_{ax} (retrieved from a 2D FEM simulation)

from (7.14)–(7.16). Here, F_L is the average suspension force and $\hat{F}_\mathrm{L,k}$ is the amplitude of the $f_\mathrm{P,F,ax}$-frequent force ripple. The force ripple $\hat{w}_\mathrm{F}$ is low for small values of $N_\mathrm{s} \cdot I_\mathrm{ax}$ and for a big value of the rotor field fundamental $B_\mathrm{R,}p,p,\mathrm{r}$. Thus, a high ratio $N_\mathrm{ax}/N_\mathrm{s}$ strongly reduces the force ripple $\hat{w}_\mathrm{F}$, so that the force ripple of the topology $LLM3_\mathrm{N+}$ is 44% higher than for the $LLM3_\mathrm{I+}$ in unsaturated conditions (Fig. 7.15a).

$$F_\mathrm{L} \propto N_\mathrm{s} \cdot k_\mathrm{w,L} \cdot I_\mathrm{s,L} \cdot B_\mathrm{R,}p,p,\mathrm{R} \tag{7.14}$$

$$\hat{F}_\mathrm{L,1} \propto N_\mathrm{s}^2 \cdot k_\mathrm{w,L} \cdot k_\mathrm{w,3} \cdot I_\mathrm{s,L} \cdot \frac{I_\mathrm{ax}}{3} \tag{7.15}$$

$$\rightarrow \frac{\hat{F}_\mathrm{L,1}}{F_\mathrm{L}} \propto \frac{N_\mathrm{s} \cdot I_\mathrm{ax}/3 \cdot k_\mathrm{w,3}}{B_\mathrm{R,}p,p,\mathrm{r} \cdot k_\mathrm{w,L}} \tag{7.16}$$

For highly-utilized machines, such as the $LLM3_\mathrm{I+}$ and the $LLM3_\mathrm{N+}$, the magnetic saturation in the stator iron due to the PM rotor field and the stator drive field leads to a modulation of the air gap field waves (Section 7.2.1), which increases $\hat{F}_\mathrm{L,3}$. The occurrence of a $2f_\mathrm{syn}$- and a $4f_\mathrm{syn}$-frequent force ripple was discussed in Section 2.6. Due to the zero-sequence current feeding, additionally a $3f_\mathrm{syn}$-frequent force ripple may occur in case of magnetic saturation. It is caused by the interaction of the modulated zero-sequence current field harmonic $B_\mathrm{ax,1,-2,r}$ (Fig. 7.12) and the suspension winding field fundamental $B_\mathrm{L,2,1,r}$. The *Fourier* spectrum of the suspension force for the extreme case of $i_\mathrm{ax} = 30$ A in the $LLM3_\mathrm{N+}$ is shown in Fig. 7.15b. Fig. 7.15a shows that the zero-sequence current feeding increases the force ripple $\hat{w}_\mathrm{F}$ and leads to a non-linear increase of the force ripple in magnetically saturated bearingless machines.

7.2.4. Influence of the Zero-Sequence Current on the Losses

The axial current I_ax causes *ohm*ic losses in the stator winding. The thermally effective phase current is given by (7.17) according to Section 3.3.1, showing that the influence of I_ax on the total losses is rather small as long as $I_\mathrm{ax} < 3 \cdot \sqrt{\frac{1}{4} \cdot \left(I_\mathrm{s,D}^2 + I_\mathrm{s,L}^2\right)}$ holds.

$$I_\mathrm{th} = \sqrt{\frac{1}{4} \cdot \left(I_\mathrm{s,D}^2 + I_\mathrm{s,L}^2\right) + \frac{I_\mathrm{ax}^2}{9}} \tag{7.17}$$

In addition, the standstill air gap field $B_\mathrm{r,ax}$ (Fig. 7.11) causes rotor eddy currents. The occurring losses $P_\mathrm{Ft,R}$ according to (7.18) are related to the square of the resulting flux

Table 7.2.: Motor $LLM3_{I+}$: Loss composition from 2D FEM simulations with sinusoidal current feeding for varying axial AMB current i_{ax}

i_{ax} / A	0	1	3	6	15	30
$P_{e,in}$ / W	2561	2561	2561	2559	2547	2504
P_{Cu} / W	41.9	41.9	42.2	43.0	49.0	70.5
$P_{Fe,S}$ / W	151	151	151	152	154	155
$P_{Ft,R}$ / W	8.9	8.9	8.9	10.1	16.6	39.6
P_{Fr} / W	65	65	65	65	65	65
$P_{d,tot}$ / W	267	267	267	270	285	330
$P_{m,out}$ / W	2295	2295	2294	2289	2262	2174
η_{mot}	0.896	0.896	0.896	0.895	0.888	0.868

density amplitude $B_{r,ax}$ and the slip frequency $f_{R,ax}$ which is $3 \cdot n \cdot p$.

$$\begin{aligned} P_{Ft,R} &\propto B_{r,ax}^2 \cdot f_{R,ax}^2 \\ &\propto N_s^2 \cdot k_{w,3}^2 \cdot \frac{I_{ax}^2}{9} \cdot (3 \cdot n \cdot p)^2 \end{aligned} \tag{7.18}$$

Equation (7.18) shows that a reduction N_s/N_{ax} also helps reducing the rotor eddy current losses. For example, Table 7.3 contains the loss components of the $LLM3_{N+}$ and Table 7.2 the loss components of the $LLM3_{I+}$ for varying axial AMB current I_{ax}. The comparison

Table 7.3.: Motor $LLM3_{N+}$: Loss composition from 2D FEM simulations with sinusoidal current feeding for varying axial AMB current i_{ax}

i_{ax} / A	0	1	3	6	15	30
$P_{e,in}$ / W	2568	2569	2563	2568	2579	2635
P_{Cu} / W	40.7	40.8	42.1	46.4	76.6	184.2
$P_{Fe,S}$ / W	149	150	151	152	153	160
$P_{Ft,R}$ / W	8.9	9.0	10.5	15.3	48.3	155
P_{Fr} / W	65	65	65	65	65	65
$P_{d,tot}$ / W	264	264	269	278	343	564
$P_{m,out}$ / W	2304	2304	2295	2290	2236	2070
η_{mot}	0.897	0.897	0.895	0.892	0.867	0.786

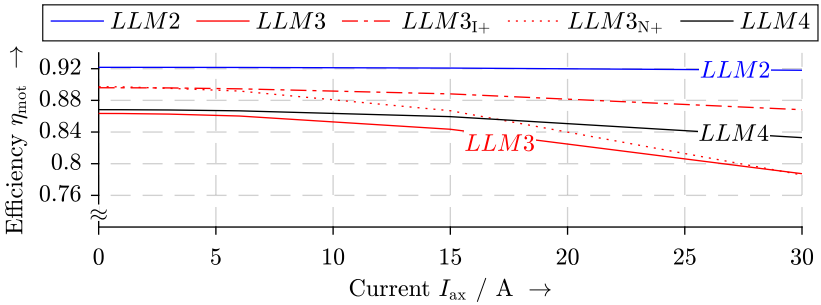

Fig. 7.16.: Motors *LLM2*, *LLM3*, *LLM3*$_{\mathrm{I+}}$, *LLM3*$_{\mathrm{N+}}$, *LLM4*: Comparison of the motor efficiency η_{mot} from 2D FEM simulations for varying axial AMB current I_{ax}

shows that even for these saturated machines the only loss groups, which are affected by the zero-sequence current feeding, are $P_{\mathrm{Ft,R}}$ and P_{Cu}. The motor efficiency η_{mot}, derived from 2D FEM simulations, is shown in Fig. 7.16 for the different topologies in comparison. It can be concluded that a zero-sequence current feeding does not influence the motor efficiency, as long as the phase turn count N_{s} is not too high, and if the axial AMB current is $I_{\mathrm{ax}} < 10$ A.

7.2.5. Zero-Sequence Motor Impedance

Since the axial current i_{ax} flows through the stator winding of the bearingless machine, the voltage drop over the phase resistance $R_{\mathrm{s,ax}} = 2 \cdot R_{\mathrm{s}}/3$ and the additional inductance $L_{\mathrm{s},\sigma,\mathrm{ax}}$ is in series with the axial AMB coil voltage drop (Section 6.1). The stator stray reactance per phase $L_{\mathrm{s},\sigma,\mathrm{ax}}$ (7.19) consists of the air gap inductance $L_{\sigma,\delta,\mathrm{ax}}$, calculated according to Section 4.2, as well as of the slot leakage inductance $L_{\sigma,\mathrm{Q,ax}}$ and the winding overhang inductance $L_{\sigma,\mathrm{b,ax}}$, which can be analytically calculated according to [94]. The axial current inductances for the three machines *LLM2*, *LLM3* and *LLM4* are derived from 2D finite-element simulations and are given in Table 7.4 together with drive winding and suspension winding inductances $L_{\mathrm{d,D}}$, $L_{\mathrm{d,L}}$.

$$L_{\mathrm{s},\sigma,\mathrm{ax}} = \frac{2}{3} \cdot \left(L_{\sigma,\delta,\mathrm{ax}} + L_{\sigma,\mathrm{Q,ax}} + L_{\sigma,\mathrm{b,ax}} \right) \tag{7.19}$$

Due to the inherently big effective air gap in high-speed PM machines these inductances (Table 7.4) are generally rather low (μH-range), especially when compared with the in-

Table 7.4.: Non-saturated inductances in the bearingless machines *LLM2*, *LLM3*, $LLM3_{I+}$, $LLM3_{N+}$ and *LLM4* from 2D FEM simulations, including analytically calculated winding overhang inductances

	$L_{d,D}$/ μH	$L_{d,L}$ / μH	$L_{s,\sigma,ax}$ / μH
LLM2 [9]	47[1)]	416	288
LLM3 [23]	85	59	40
$LLM3_{I+}$	85	59	40
$LLM3_{N+}$	439	305	207
LLM4	80	41	6

[1)] Separated drive winding

ductance of the axial AMB (mH-range) (Section 4.2.3).
This high ratio $\frac{L_{ax}}{R_{ax}}/\frac{L_{s,\sigma,ax}}{R_{s,ax}}$ is one of the key aspects, which allows the zero-sequence current feeding. For a given current density, the ratio $\frac{L_{s,\sigma,ax}}{R_{s,ax}}$ can be significantly reduced with a reduction in turns per phase due to $\frac{R_{s,ax}}{L_{s,\sigma,ax}} \propto N_s^4$.

7.3. Applicability to AMB Systems

7.3.1. Rotor Position Command Response

The benchmark for the here presented novel axial position control performance is the classical and commercially available 4-quadrant chopper operation of AMBs. In Fig. 7.17 a position step responses to a change in reference position of $\Delta z = 20\ \mu$m at different speed, i.e. at three different modulation indices $m_a = 0,\ 0.84, 1.55$ are shown for the 4-quadrant chopper (4Q-CB-PWM) and the zero-sequence current operation CB-PWM in comparison. The current and position controller settings are equal for both feeding techniques. No significant difference between 4Q-CB-PWM and CB-PWM in the settling behavior of the position signal can be recognized. The zero-sequence current based position control dynamics do not depend on the inverter modulation index m_a. Only a slight oscillation in z is visible in Fig. 7.17f for $m_a = 1.55$ due to the reduced damping capability.
In Fig. 7.18a, 7.18b the measured axial current response i_{ax} and the torque-generating q-current $i_{q,D}$ at the moment of the step in the reference signal z_{ref} are shown. A high modulation index is of $m_a = 1.55$ is considered. In contrast to the 4Q-CB-PWM, the CB-

PWM (Fig. 7.18b) shows a coupling between the drive current $i_{q,D}$ and the axial current i_{ax} as an oscillation of $i_{q,D}$ at the moment of the step in i_{ax}. This is not a magnetic coupling. It only occurs at inverter over-modulation $m_a > 1$. The reason for this ripple has al-

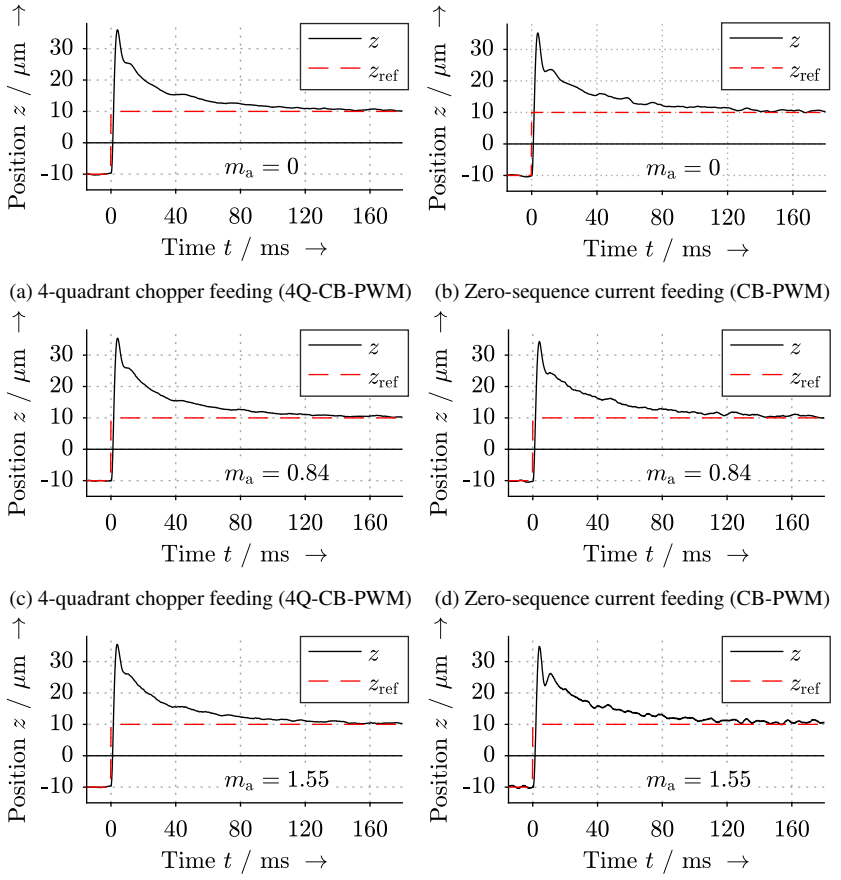

(a) 4-quadrant chopper feeding (4Q-CB-PWM)

(b) Zero-sequence current feeding (CB-PWM)

(c) 4-quadrant chopper feeding (4Q-CB-PWM)

(d) Zero-sequence current feeding (CB-PWM)

(e) 4-quadrant chopper feeding (4Q-CB-PWM)

(f) Zero-sequence current feeding (CB-PWM)

Fig. 7.17.: Comparison of DC-chopper (4Q-CB-PWM) and zero-sequence current operation (CB-PWM) of the axial AMB of the *LLM4*: Measured axial displacement z for a step response of $\Delta z = 20\ \mu$m at $t = 0$ for different modulation indices $m_a = 0;\ 0.84;\ 1.55$

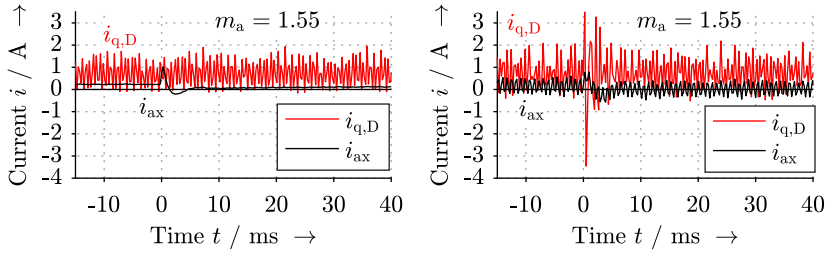

(a) 4-quadrant chopper feeding (4Q-CB-PWM) (b) Zero-sequence current feeding (CB-PWM)

Fig. 7.18.: Comparison of DC-chopper (4Q-CB-PWM) and zero-sequence current operation (CB-PWM) of the axial AMB of the *LLM4*: Measured axial AMB current i_{ax} and drive current $i_{q,D}$ for a step response of $\Delta z = 20\ \mu$m at $t = 0$ at $m_a = 1.55$

ready been addressed in Section 7.1.4: $u_{q,D}$ respectively $i_{q,D}$ exhibit a ripple of frequency $3 \cdot f_{syn}$, which results from the even order voltage harmonic $\hat{U}_{\alpha,D,2}$. The even harmonic order is due to asymmetry of the phase voltage pattern, when only one half-wave of the reference phase voltage reaches values $u_{s,ref} > U_{DC}/2$. Since the axial voltage u_{ax} results from $\varphi_{N,A} - \varphi_{N,B}$, only the differential-mode feeding of the winding systems A and B is affected. Therefore, in the *LLM4* this ripple in the AC-phase voltage only leads to ripples in the drive current $i_{q,D}$, but not in the suspension current. It is the major drawback of the CB-PWM. The SV-PWM does not exhibit this ripple (Section 7.1.4). However, the ripple of the torque-producing current $i_{q,D}$ is not crucial for applications, in which the torque ripple does not play an important role.

Generally, the required axial current i_{ax} takes very low values due to the big force-current coefficient $k_{F,z}$ (Section 4.1.2) together with the low axial thrust due to the turbo-charger rotor (Fig. 4.10). Even in transient situations, there is only a low axial AMB voltage needed ($u_{ax,ref} < U_{DC}/4$), which is depicted in Fig. 7.19. It also shows that the reference voltage ripple in $u_{ax,ref}$ as well as in $u_{q,D,ref}$ increases at over-modulation $m_a > 1$ in order to compensate for the vanishing voltage reserve. Also u_{ax} exhibits a $3 \cdot f_{syn}$-frequent component, which is discussed in the following in Section 7.3.2.

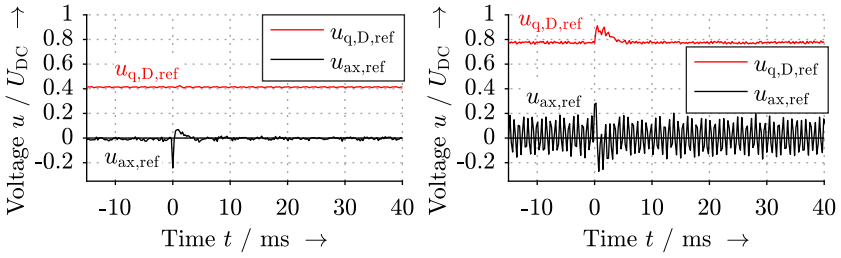

(a) Zero-sequence current feeding (CB-PWM), $m_a = 0.84$

(b) Zero-sequence current feeding (CB-PWM), $m_a = 1.55$

Fig. 7.19.: Motor *LLM4*: Measured reference voltages $u_{q,D,ref}$ and $u_{ax,ref}$ at zero-sequence current operation (CB-PWM) for a step response of $\Delta z = 20\ \mu$m at $t = 0$ for two different modulation indices $m_a = 0.84;\ 1.55$

7.3.2. Operation at Over-modulation

A safe motor operation with the zero-sequence current operation is ensured if the inverter is not driven at its voltage limit, i.e. for modulation indices $m_a < 1$, since then the current control transfer function does not differ between the 4Q-CB-PWM and the

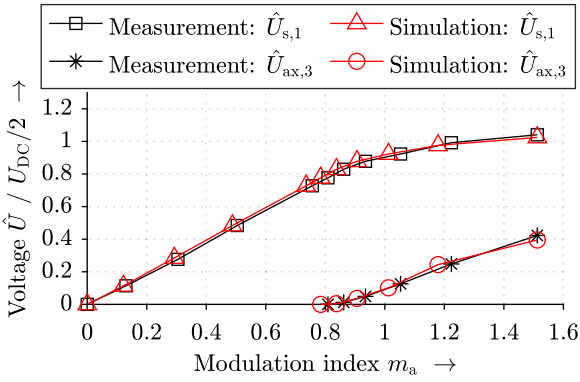

Fig. 7.20.: Motor *LLM4*: Measured and simulated fundamental voltage $\hat{U}_{s,1}$ and third harmonic component of the axial voltage $\hat{U}_{ax,3}$ for varying modulation index m_a at $U_{DC} = 48$ V (*Simscape/Simulink/Matlab* simulation model according to Section 6.5)

CB-PWM and the same position control dynamics are present (Fig. 7.17 (a)-(d)). Operation at over-modulation $m_a > 1$ is crucial, since not enough voltage reserve for axial current dynamics may be available. If the two 3-phase systems A and B are fed in differential-mode as in case of the *LLM4*, the axial AMB voltage u_{ax} additionally exhibits a $3 \cdot f_{syn}$-frequent harmonic component at over-modulation $m_a > 1$ (Section 7.1.3). Measurements and simulations have shown that this component $\hat{U}_{ax,3}$ already occurs at modulation indices $m_a > 0.88$ (Fig. 7.20) simultaneously with the beginning of the nonlinear relationship between m_a and $\hat{U}_{s,1}$. This over-modulation behavior even for $m_a < 1$ is caused by the reloading of the capacitor in the bootstrap driver circuit of the N-MOSFET-based inverter, which results in an additional dead time per switching period. Thus, the

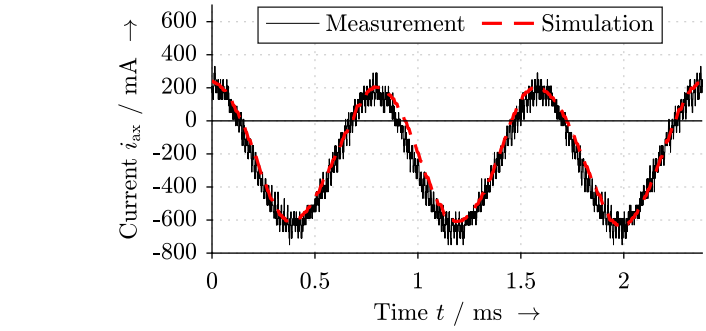

(a) Measurement versus simulation with $L_{ax} = 3$ mH, $R_{ax} = 0.875\ \Omega$

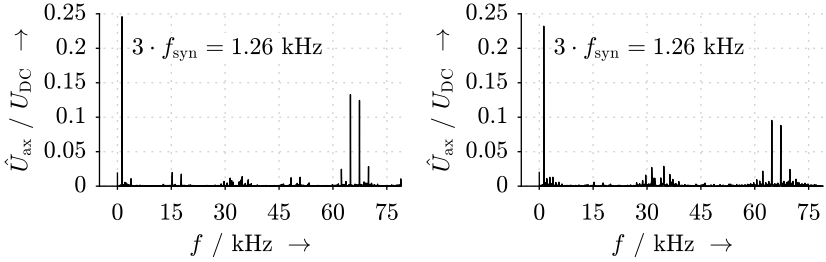

(b) Measurement

(c) Simulation

Fig. 7.21.: Motor *LLM4*: Measured and simulated axial AMB current i_{ax} and harmonic amplitude spectrum of the axial AMB voltage u_{ax} at $m_a = 1.55$ and $n = 25200\ \text{min}^{-1}$ (*Simscape/Simulink/Matlab* simulation model according to Section 6.5)

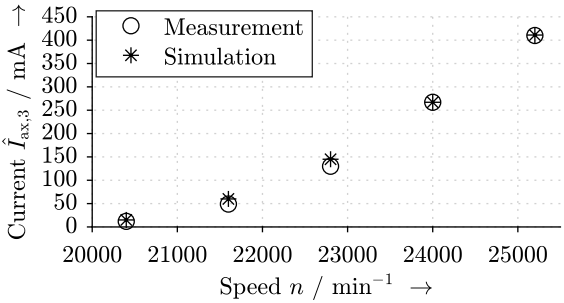

Fig. 7.22.: Measured and simulated $3 \cdot f_{syn}$-frequent axial current component $\hat{I}_{ax,3}$ for varying speed at $U_{DC} = 48$ V (*Simscape/Simulink/Matlab* simulation model according to Section 6.5)

maximum voltage is smaller by the voltage attenuation factor of $k_{att,U} = 0.88$ (Table 6.1), i.e. $U_{DC,eff} = k_{att} \cdot U_{DC}$.

The rated speed $n_N = 60000$ min^{-1} at $U_{DC} = 150$ V is also the maximum mechanically allowed speed with a safety factor of 1.2 for the over-speed test. It is reached with a modulation index of $m_a \approx 0.8$ (load-dependent). In order to investigate, if a safe operation of the axial bearing even at over-modulation is possible, a reduced DC-link voltage of $U_{DC} = 48$ V is applied to enforce over-modulation at reduced speed n.

The resulting third harmonic of the axial current $\hat{I}_{ax,3}$ is given in Fig. 7.21a, where the measured and simulated current i_{ax} are shown for one electrical period $1/f_{syn}$. The oscillation with $3 \cdot f_{syn} = 1.26$ kHz at $m_a = 1.55$ is clearly visible. The measured current exhibits an additional current ripple around the frequencies $f_{sw} = 33$ kHz and $2 \cdot f_{sw} = 66$ kHz. The eddy currents in the axial AMB solid steel rotor disk decrease the inductance L_{ax} for such high switching frequencies, so that an increased switching current ripple occurs. The decrease of L_{ax} with rising frequency f_{ax} is discussed in Section 4.2.3, but it is not considered here in the simulation. The according *Fourier* amplitude voltage harmonic spectrum (Fig. 7.21b, 7.21c) shows the amplitude of the $3 \cdot f_{syn}$-frequent component, which is approximately $\hat{U}_{ax,3} \approx U_{DC}/4$ at $f = 1.26$ kHz. Compared to this, the side-bands close to $2 \cdot f_{sw} = 66$ kHz exhibit rather small values $< U_{DC}/8$.

The increase of the $3 \cdot f_{syn}$-frequent current component $\hat{I}_{ax,3}$ with increasing modulation index and , hence, with increasing fundamental voltage $\hat{U}_{s,1} \propto n$ and speed n, is shown in Fig. 7.22, proving a good fit between measurement and simulation.

This $3 \cdot f_{\mathrm{syn}}$-current component is not crucial for the axial position control, since the time constant of the mechanical system is much bigger than the current oscillation period $1/\left(3 \cdot f_{\mathrm{syn}}\right)$. This is shown by (7.20): For the given configuration the axial position ripple as variation of z is $< 1\mu$m even for $\hat{I}_{\mathrm{ax},3} = 1$ A and $f_{\mathrm{syn}} = 300$ Hz. Besides that, also the eddy currents in the solid rotor steel disk of the axial AMB help to damp such unwanted $z(t)$-oscillations.

$$\begin{aligned} \ddot{z}(t) &= \frac{F_{\mathrm{z}}(t)}{m_{\mathrm{R}}} = \frac{k_{\mathrm{F,z}} \cdot \hat{I}_{\mathrm{ax},3}}{m_{\mathrm{R}}} \cdot \cos(3 \cdot \omega_{\mathrm{s}} \cdot t) \\ z(t) &= -\frac{k_{\mathrm{F,z}} \cdot \hat{I}_{\mathrm{ax},3}}{m_{\mathrm{R}}} \cdot \frac{1}{(3 \cdot \omega_{\mathrm{s}})^2} \cdot \cos(3 \cdot \omega_{\mathrm{s}} \cdot t) \end{aligned} \tag{7.20}$$

7.3.3. DC-Link Voltage Requirement and Comparison between the SV-PWM and the CB-PWM

As visible in Fig. 7.19, only a very low rated value for the star-point voltage $u_{\mathrm{ax,N}}$ is required in steady state due to the pure *ohm*ic voltage drop at the small winding resistance R_{ax} of the axial AMB. The required current $i_{\mathrm{ax,N}}$ depends on the rated load, which may be the gravitational rotor force $F_{\mathrm{z,N}} = m_{\mathrm{R}} \cdot g$ in vertical rotor operation, and on the axial force-current coefficient $k_{\mathrm{F,z}}$. Section 7.1 and Section 7.3.2 have shown that for $m_{\mathrm{a}} < 0.8$ and $u_{\mathrm{ax}} < U_{\mathrm{DC}}/10$ hardly any constraints are noticeable in the current controller plant by the zero-sequence current feeding, if the two 3-phase winding systems of the bearingless machine are operated in differential-mode. If a voltage reserve of $u_{\mathrm{ax,max}} = 10 \cdot u_{\mathrm{ax,N}}$ for transient responses is considered, the rule of thumb (7.21) for the DC-link voltage is derived. For the prototype machine *LLM4*, the condition (7.21) is given by $U_{\mathrm{DC}} \overset{!}{>} 23$ V $\wedge\, U_{\mathrm{DC}} \overset{!}{>} 150$ V.

$$U_{\mathrm{DC}} \overset{!}{>} R_{\mathrm{ax}} \cdot \frac{F_{\mathrm{z,N}}}{k_{\mathrm{F,z}}} \cdot 100 = 23 \text{ V} \quad \wedge \quad U_{\mathrm{DC}} \overset{!}{>} \hat{U}_{\mathrm{s,max}} \cdot 2.5 = 150 \text{ V} \tag{7.21}$$

The modulation index m_{a} as the most important influencing factor on the operational limit of the zero-sequence current feeding is not only determined by the speed-dependent back-EMF $\hat{U}_{\mathrm{p}} \propto f_{\mathrm{syn}}$. Also the inductive armature voltage drop of the drive current $i_{\mathrm{q,D}} \cdot X_{\mathrm{q,D}}$ and the voltage drop at the suspension winding must be considered. For the *LLM4*, the latter is given by $\hat{U}_{\mathrm{q,L}} = 4.5$ V in steady state. The drop $i_{\mathrm{q,D}} \cdot X_{\mathrm{q,D}}$ depends on the demanded torque $M \propto i_{\mathrm{q,D}}$. The resulting voltage limit for a circular voltage space vector orbit of

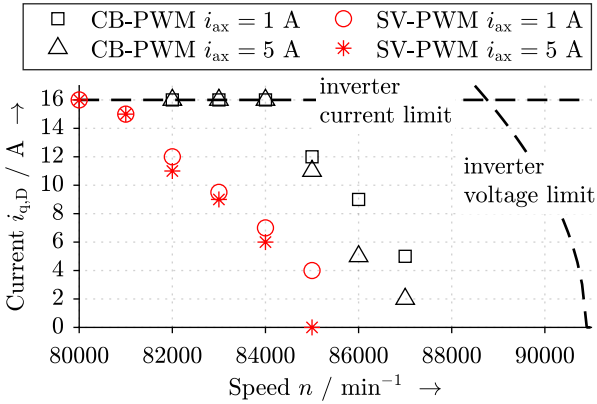

Fig. 7.23.: Motor *LLM4*: Simulated voltage and current limit at high speed with respect to the rated speed $n_N = 60\,000$ min^{-1} (*Simscape/Simulink/Matlab* simulation model according to Section 6.5)

radius $\hat{U}_{s,max} = U_{DC}/\sqrt{3}$ with $R_s \ll X_{q,D}$ is given in (7.22) and is depicted in Fig. 7.23 as dashed line.

$$\hat{I}_{q,D,max} = \frac{\sqrt{\hat{U}_{s,max}^2 - \hat{U}_p^2}}{X_{q,D}} \tag{7.22}$$

In Fig. 7.23 this theoretical limit is compared to the actual voltage limit of the *LLM4* by simulation, applying the SV-PWM and the CB-PWM in comparison. The maximum speed for stable operation is a little lower than the theoretical limit, when only a drive voltage space vector $\underline{u}_{dq,D}$ is demanded due to the additional voltage drop $\underline{u}_{dq,L}$ at the suspension winding. The decrease of the voltage limit due to the voltage drop of $R_s \cdot i_{ax}/3$ is negligibly small. This is also visible in Fig. 7.23, when the voltage limits for $i_{ax} = 1$ A and $i_{ax} = 5$ A are compared. The voltage limit of the SV-PWM is generally a little lower than the one of the CB-PWM, because at such high modulation indices $m_a \approx 2/\sqrt{3}$ hardly any axial voltage is available to control the axial bearing current to be $i_{ax} = 1$ A, $i_{ax} = 5$ A (compare Fig. 7.2). As shown in Fig. 7.2, the CB-PWM (Fig. 7.24b) exhibits a higher voltage reserve for the generation of u_{ax} than the SV-PWM (Fig. 7.24a), since the latter prioritizes the generation of the 3-phase voltage systems with the space vectors $\underline{u}_{\alpha\beta,A}$, $\underline{u}_{\alpha\beta,B}$. Thus, the CB-PWM is the better choice for stable operation at the inverter voltage

limit.

However, Section 7.1.4 has revealed that the CB-PWM exhibits a high voltage harmonic distortion of the AC-phase voltages, if a high axial AMB voltage $u_{\mathrm{ax,ref}}$ is demanded in over-modulation operation. It was shown that in such cases a $2 \cdot f_{\mathrm{syn}}$-frequent voltage component $\hat{U}_{\mathrm{s},2}$ is introduced into the AC-phase voltages of the 3-phase systems. This voltage component has a phase shift of 180° between the winding systems A and B, i.e. $\varphi_{\mathrm{U,A}} = \varphi_{\mathrm{U,B}} + \pi$. Thus, in the *LLM4* only the drive winding voltage is affected, when a high axial AMB voltage $u_{\mathrm{ax,ref}}$ is demanded. Thus, a sudden step response in i_{ax} due to an axial force disturbance causes a distortion of the voltage in the drive current system. Fig. 7.24 shows the simulated axial current i_{ax} and the drive winding torque current $i_{\mathrm{q,D}}$ during an axial force disturbance step of $\Delta F_{\mathrm{z}} = 68$ N for the SV-PWM and the CB-PWM at $n = 80000\ \mathrm{min}^{-1}$. The CB-PWM exhibits a considerable ripple in the drive current $i_{\mathrm{q,D}}$, when a high axial current i_{ax}, i.e. a high axial voltage u_{ax}, is demanded (Fig. 7.9). The SV-PWM shows no such ripple in $i_{\mathrm{q,D}}$ due to the prioritization (Fig. 7.24a), but the current i_{ax} tends to oscillate, since a too small voltage u_{ax} is available for high dynamics (Fig. 7.2). Thus, the CB-PWM enables more damping for the axial position control.

That means, the SV-PWM is the better choice, if a distortion of the AC-phase voltages by the axial AMB voltage may not be tolerated. The CB-PWM is the better choice, if additional oscillations in the AC-phase voltages are not relevant for safe operation, and if high axial position control dynamics must be provided in over-modulation operation. In [143], a novel axial position control, based on a fractional-order flux estimator, is presented. De-

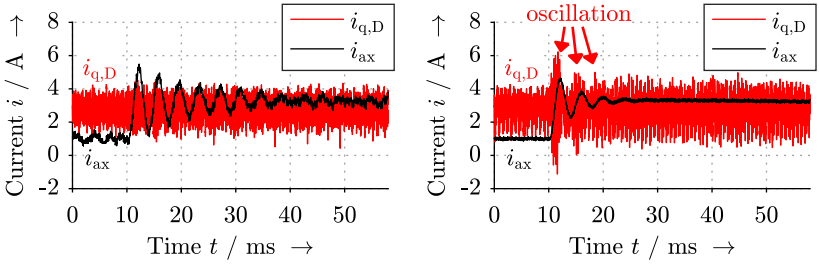

(a) SV-PWM (b) CB-PWM

Fig. 7.24.: Motor *LLM4*: Simulated actual drive current $i_{\mathrm{q,D}}$ and axial AMB current i_{ax} during a step of axial disturbance force of $\Delta F_{\mathrm{z}} = 68$ N at $n = 80000\ \mathrm{min}^{-1}$ at $t = 0$ (*Simscape/Simulink/Matlab* simulation model according to Section 6.5)

spite the eddy currents in the solid core of axial magnetic bearings, it enables a highly dynamic axial position control. However, this is on the cost of high axial voltage values u_{ax}, which may be up to $\approx$ 5-times higher than for standard controllers with a cascaded current control-loop. Thus, for this application the CB-PWM is also the better choice, allowing for high values of u_{ax} even at inverter over-modulation.

7.3.4. Influence of the PWM Switching Frequency

If the zero-sequence current feeding concept is applied to bigger machines in the kW-range, usually two separated 3-phase windings D (drive) and L (levitation) for torque and suspension force generation are used, since the voltage and current rating of the two windings are very different. In this case, the 3-phase suspension winding L, which usually requires currents less than 10 A, is fed by a MOSFET-based inverter. This inverter can also be used for the zero-sequence current feeding. If a combined winding is used for higher power classes [50], insulated gate bipolar transistors (IGBT) for higher current ratings are suited. Due to their inherently given bigger dead time [140] they require lower switching frequencies.

To decide, if a lower switching frequency might be crucial for the concept of zero-sequence current feeding in the AMB, measurements with the *LLM4* at a reduced switching frequency of $f_{\mathrm{sw}} = 18$ kHz are conducted, but still with the MOSFET-based inverter (Section 6.5). A decrease of the switching frequency mainly influences the delay behavior

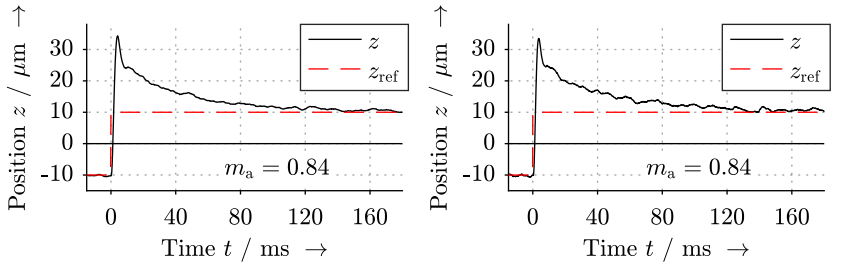

(a) $f_{\mathrm{sw}} = 33$ kHz (b) $f_{\mathrm{sw}} = 18$ kHz

Fig. 7.25.: Motor *LLM4*: Measured axial displacement for a step response of $\Delta z = 20$ μm at $t = 0$, applying the CB-PWM for $f_{\mathrm{sw}} = 18$ kHz and $f_{\mathrm{sw}} = 33$ kHz switching frequency

of the controller, losing dynamics for lower switching frequencies. Thus, the current controller settings must be adapted as shown in [144]. The decrease in dynamics is especially crucial for the radial rotor position control in bearingless PM machines with a large air gap width δ_{eff}, resulting in a low force-current coefficient and a high magnetic stiffness coefficient.

Fig. 7.25 shows that the position control, based on the zero-sequence current feeding, is not much affected by a decrease of the switching frequency f_{sw}, since the electrical time constant of the axial AMB winding is still big enough compared to the switching period. A modulation index of $m_{\text{a}} = 0.84$ is considered. The axial rotor movement is slightly less damped for $f_{\text{sw}} = 18$ kHz than for $f_{\text{sw}} = 33$ kHz. Since for larger machines the axial AMB inductance L_{ax} increases, compared to this 1 kW-prototype, the switching frequency is not expected to have much influence on the control performance. Thus, the zero-sequence current feeding can also be used in IGBT inverters with high current ratings.

8. Conclusion and Outlook

Bearingless motors have gained rising attractiveness in the past 20 years as an alternative for classical active magnetic bearings. Among the bearingless motors, the PM synchronous machine is the most prominent candidate, when it comes to high-speed operation in the kW-range. Therefore, this work focuses on the bearingless PM synchronous machine. It has all the advantages, which classical magnetically levitated machines usually are featuring, such as the avoiding of bearing friction and wear. Additionally, bearingless drives enable the use of axially shorter rotors, thus, increasing the first rotor bending mode eigenfrequency and decreasing the machine overall length. On the other hand, bearingless PM machines come along with several crucial aspects, among which the first two are discussed in this work:

- The design of bearingless machines is restricted in comparison to conventional electric machines. Bearingless machines need an additional suspension winding in the stator, increasing the outer machine diameter. Also the asynchronously rotating suspension winding field wave leads to eddy current losses in the rotor and to a deflection of the bearing force vector (eddy current effect), impeding a robust rotor position control. Further, the superposition of the torque-generating drive winding field with the suspension winding field leads to a disturbing lateral rotor force (superposition effect), which has to be counteracted by the position control.

- Bearingless machines allow the use of standard 3-phase inverters for the lateral rotor levitation. However, for the axial levitation, an additional axial magnetic bearing, fed by a full-bridge DC-chopper, is required, if e.g. no conical rotor shape is employed [9]. To reduce system costs, alternatives to the costly full-bridge inverter are aimed at.

- Bearingless machines with a $2p$-pole rotor and a $2p_{\mathrm{L}}$-pole suspension winding ($p_{\mathrm{L}} = p \pm 1$) require the rotor rotation angle, so that the radial position control –

via the field-oriented control of the suspension winding currents – equals the classical active magnetic bearing control. This gives rise to alternative bearingless motor concepts, such as homo-polar machines or consequent pole machines.

Design of Bearingless PM Machines Accounting for the Eddy Current and the Superposition Effect

The eddy current and the superposition effect can be described well by linear analytical calculations, which enable the derivation of scaling rules. Thus, the *Maxwell* equations are solved analytically with the vector potential approach. The lateral and tangential rotor force calculation is done via the integration of the *Mawell* stress tensor on a closed surface around the rotor. The suspension force and torque calculations are verified by finite element simulations and by measurements at a 1 kW / 60000 min^{-1}-prototype machine (*LLM4*).

Based on these analytical calculations, the machine design incorporates the following aspects: Selection of the stator winding with the focus on the combined drive and suspension winding, rotor bandage calculation, magnetic circuit calculation aiming at maximum output power, disturbing rotor force calculation, originated by the eddy current and superposition effect. Finally, scaling laws for the last two effects are derived: Low suspension winding pole counts $2p_{\text{L}}$ and big stator bore diameters give rise to the disturbing magnetic lateral rotor forces. The disturbing rotor forces reduce the stability margin of the rotor position control, which may lead to weakly damped oscillations at high speed and in generator-mode operation. Besides the use of higher pole counts or smaller bore diameters, the axial PM segmentation is a good measure to decrease the eddy current effect. However, even with these deficiencies, bearingless motors with slim rotors can employ the standard decentralized position control. This may be critical for rotors with a strong gyroscopic effect, such as the investigated flywheel energy storage system.

Replacement of the Classical Full-Bridge Inverter for the Axial Active Magnetic Bearing by a Zero-Sequence Current Feeding

As an alternative to the feeding of the winding of the axial active magnetic bearing by a full-bridge inverter, it is connected to the two star-points of the double 3-phase stator winding for the torque and radial suspension force generation. It is shown at the prototype machine *LLM4* that a controlled star-point current can be used for a stable axial position control. As long as the inverter is not close to its voltage limit, the zero-sequence current control is decoupled from the 3-phase current systems for torque and radial force

generation. Only for high modulation degrees $m_a > 1$, e.g. due to the big back-EMF at high speed, the zero-sequence current exhibits a $3 \cdot f_s$-frequent oscillation. If a high voltage between the two star-points is needed, e.g. at a step of the axial rotor force, the phase currents of the 3-phase system may exhibit a superimposed $2 \cdot f_s$-frequent oscillation. Both effects are not critical for a stable operation, but they increase losses. This interdependence between zero-sequence current and 3-phase current can be avoided by giving priority to one of both current systems such as in the presented space vector modulation. For magnetic bearing applications the zero-sequence current feeding has turned out to be an excellent alternative which is not restricted to low power classes.

Outlook

The investigations have shown that the bearingless motor concept has grown beyond the phase of feasibility studies. It has turned out to be a good alternative to active magnetic bearings and even brings some advantages. For the next years, the focus must be laid on the systematic optimization of bearingless motors for the high-power range (e.g. > 50 kW). Bearingless motors only will be accepted for industrial applications, if their efficiency is similar to conventional machines. Thus, efficiency optimization must include magnetic saturation effects and the employment of novel materials.

Following the here presented suggestions, such a bearingless "high-power" drive could be realized with two bearingless half-motors, applying the pole pair combination $p/p_L = 2/3$ with separated drive and suspension windings. In this case, the zero-sequence current feeding of the axial active magnetic bearing may be realized with the star points of the two suspension windings of the two half-motors. By this, a five degrees of freedom position control may be realized with six power electronic half-bridges, which seems to be a promising topology for low system costs. The two 3-phase drive windings could be fed in parallel by one standard 3-phase inverter. For testing purposes, the two drive windings may be operated by two independent 3-phase inverters, so that one half-motor is the test machine and the other one the load machine.

List of Tables

List of Figures

Bibliography

[1] A. Binder, "Analytical Calculation of Eddy Current Losses in massive rotor parts of High-speed permanent magnet machines," in *International Symposium on Power Electronics Power Electronics, Electrical Drives, Automation and Motion (SPEEDAM)*, Ischia, Italy, Jun. 2000, pp. C2/1–C2/6.

[2] S. Ruoho, T. Santa-Nokki, J. Kolehmainen, and A. Arkkio, "Modeling Magnet Length In 2-D Finite-Element Analysis of Electric Machines," *IEEE Transactions on Magnetics*, vol. 45, no. 8, pp. 3114–3120, Aug. 2009.

[3] R. Russell and K. Norsworthy, "Eddy currents and wall losses in screened-rotor induction motors," *Proceedings of the IEE Part A: Power Engineering*, vol. 105, no. 20, pp. 163–175, Apr. 1958.

[4] G. Schweitzer and E. H. Maslen, Eds., *Magnetic Bearings: Theory, Design, and Application to Rotating Machinery*. Berlin, Dordrecht, Heidelberg, London, New York: Springer, 2009.

[5] A. Chiba, T. Fukao, O. Ichikawa, M. Oshima, M. Takemoto, and D. Dorrell, *Magnetic bearings and bearingless drives*. Amsterdam, London: Elsevier/Newnes, 2005.

[6] H.-D. Stölting, E. Kallenbach, and W. Amrhein, Eds., *Handbook of fractional-horsepower drives*. Berlin, Heidelberg, New York: Springer, 2008.

[7] Y. Fu, M. Takemoto, S. Ogasawara, and K. Orikawa, "Investigation of Operational Characteristics and Efficiency Enhancement of an Ultra-High-Speed Bearingless Motor at 100,000 r/min," *IEEE Transactions on Industry Applications*, vol. 56, no. 4, pp. 3571–3583, Apr. 2020.

[8] Z. Liu, A. Chiba, Y. Irino, and Y. Nakazawa, "Optimum Pole Number Combination

of a Buried Permanent Magnet Bearingless Motor and Test Results at an Output of 60 kW With a Speed of 37000 r/min," *IEEE Open Journal of Industry Applications*, vol. 1, pp. 33–41, Feb. 2020.

[9] G. Bergmann, "Five-Axis Rotor Magnetic Suspension with Bearingless PM Motor Levitation Systems," Ph.D. Thesis, Technical University of Darmstadt, Institute for Electrical Energy Conversion, Darmstadt, Germany, 2013.

[10] J. Chen, J. Zhu, and E. L. Severson, "Review of Bearingless Motor Technology for Significant Power Applications," *IEEE Transactions on Industry Applications*, vol. 56, no. 2, pp. 1377–1388, Mar. 2020.

[11] W. Amrhein, S. Silber, K. Nenninger, G. Trauner, and M. Reisinger, "Developments On Bearingless Drive Technology," in *International Symposium on Magnetic Bearings (ISMB)*, Mito, Japan, Aug. 2002, pp. 229–234.

[12] R. Gasch, R. Nordmann, and H. Pfützner, *Rotordynamik*, 2nd ed. Berlin, Heidelberg, New York: Springer, 2006.

[13] H. Bleuler, "A survey of magnetic levitation and magnetic bearing types," *JSME International Journal*, vol. 35, no. 3, pp. 335–342, Sep. 1992.

[14] S. Earnshaw, "On the Nature of the Molecular Forces which Regulate the Constituion of the Luminiferous Ether," *Transactions of the Cambridge Philosophical Society*, vol. 7, pp. 97–112, 1842.

[15] W. Braunbeck, "Freischwebende Körper im elektrischen und magnetischen Feld," *Zeitschrift der Physik*, vol. 112, no. 11/12, pp. 753–763, Nov. 1939.

[16] H. Sugimoto, I. Shimura, and A. Chiba, "A Novel Stator Structure for Active Axial Force Improvement in a One-Axis Actively Positioned Single-Drive Bearingless Motor," *IEEE Transactions on Industry Applications*, vol. 53, no. 5, pp. 4414–4421, Sep. 2017.

[17] J. Asama, T. Asami, T. Imakawa, A. Chiba, A. Nakajima, and M. A. Rahman, "Effects of Permanent-Magnet Passive Magnetic Bearing on a Two-Axis Actively Regulated Low-Speed Bearingless Motor," *IEEE Transactions on Energy Conversion*, vol. 26, no. 1, pp. 46–54, Mar. 2011.

[18] W. Bauer, “The Bearingless Axial Force-Torque Motor (Der lagerlose Axialkraft-Momentenmotor),” Ph.D. Thesis, Johannes Kepler University Linz, Institute for Electric Drives and Power Electronics, Linz, Austria, Sep. 2018.

[19] S. O. Siems, H. May, E. Portabella, and W.-R. Canders, “Application of HTSC-Bearings for High Speed Machines,” in *International Symposium on Magnetic Bearings (ISMB)*, Zurich, Switzerland, Aug. 2000, pp. 607–612.

[20] G. Ries and F. Werfel, “In der Schwebe: Supraleitende Magnetlager,” *Physik in unserer Zeit*, vol. 35, no. 3, pp. 134–140, May 2004.

[21] V. Kluyskens, J. V. Verdeghem, C. Dumont, and B. Dehez, “Experimental Investigations on a Heteropolar Electrodynamic Bearing-self-bearing Motor,” in *International Symposium on Magnetic Bearings (ISMB)*, Beijing, China, Aug. 2018, 8 pages.

[22] H. Sugimoto, T. Srichiangsa, and A. Chiba, “Design of a high-speed single-drive bearingless motor,” in *International Electric Machines and Drives Conference (IEMDC)*, Miami, USA, May 2017, 6 pages.

[23] G. Messager, “Self-bearing permanent magnet synchronous machine configurations and control for high-speed applications,” Ph.D. Thesis, Technical University of Darmstadt, Institute for Electrical Energy Conversion, Darmstadt, Germany, Sep. 2019.

[24] T. Schneider and A. Binder, “Design and Evaluation of a 60 000 rpm Permanent Magnet Bearingless High Speed Motor,” in *International Conference on Power Electronics and Drive Systems (PEDS)*, Bangkok, Thailand, Nov. 2007, pp. 1–8.

[25] P. Kascak, R. Jansen, T. Dever, A. Nagorny, and K. Loparo, “Bearingless Five-Axis Rotor Levitation with Two Pole Pair Separated Conical Motors,” in *IEEE Industry Applications Society Annual Meeting*, Houston, USA, Oct. 2009, 9 pages.

[26] J. Asama, Y. Hamasaki, T. Oiwa, and A. Chiba, “Proposal and Analysis of a Novel Single-Drive Bearingless Motor,” *IEEE Transactions on Industrial Electronics*, vol. 60, no. 1, pp. 129–138, Jan. 2013.

[27] J. Van Verdeghem, E. L. Severson, and B. Dehez, “Hybrid Active-Passive Actua-

tion Approach of Passively Levitated Thrust Self-Bearing Machines," *IEEE Transactions on Industry Applications*, vol. 57, no. 6, pp. 7035–7045, 2021.

[28] R. T. Schöb, "Contributions to Bearingless Induction Machines (Beiträge zur lagerlosen Asynchronmaschine)," Ph.D. Thesis, ETH Zürich, Power Electronic Systems Laboratory, Zurich, Switzerland, 1993.

[29] U. Bikle, "The Design of Bearingless Induction Machines (Die Auslegung lagerloser Induktionsmaschinen)," Ph.D. Thesis, ETH Zürich, Power Electronic Systems Laboratory, Zurich, Switzerland, 1999.

[30] J. Chen, Y. Fujii, M. W. Johnson, A. Farhan, and E. L. Severson, "Optimal Design of the Bearingless Induction Motor," *IEEE Transactions on Industry Applications*, vol. 57, no. 2, pp. 1375–1388, Mar. 2021.

[31] J. Chen and E. L. Severson, "Bearingless Induction Motor Design with the DPNV Winding and Reduced Axial Length Pole-Specific Rotor," in *International Symposium on Magnetic Bearings (ISMB)*, Aug. 2021, pp. 408–421.

[32] L. Hertel and W. Hofmann, "Basic Approach for the Design of Bearingless Motors," in *International Symposium on Magnetic Bearings (ISMB)*, Zurich, Switzerland, Aug. 2000, pp. 341–347.

[33] L. Chen and W. Hofmann, "Performance Characteristics of one Novel Switched Reluctance Bearingless Motor Drive," in *Power Conversion Conference*, Nagoya, Japan, Apr. 2007, pp. 608–613.

[34] Y. Hao, X. Wang, and D. Cheng, "An Improved Radial Force Model of Sharing Suspension Windings Bearingless Switched Reluctance Motor," in *International Electric Machines and Drives Conference (IEMDC)*, San Diego, USA, May 2019, pp. 1996–2001.

[35] Z. Islam, A. Arafat, and S. Choi, "Design of Five-phase Bearingless Permanent Magnet Assisted Synchronous Reluctance Motor for High Speed Applications," in *Energy Conversion Congress and Exposition (ECCE)*, Portland, USA, Sep. 2018, pp. 4419–4424.

[36] V. Mukherjee, M. Sokolov, J. Pippuri, M. Hinkkanen, and A. Belahcen, "Comparative Study of Inner and Outer Rotor Bearingless Synchronous Reluctance

Motors," in *International Converence on Electrical Machines (ICEM)*, Alexandroupoli, Greece, Sep. 2018, pp. 1388–1394.

[37] Q. Ding, T. Ni, X. Wang, and Z. Deng, "Optimal Winding Configuration of Bearingless Flux-Switching Permanent Magnet Motor With Stacked Structure," *IEEE Transactions on Energy Conversion*, vol. 33, no. 1, pp. 78–86, Mar. 2018.

[38] W. Gruber, K. Radman, and E. Göbl, "Novel Bearingless Flux-Switching Motor with Exterior Rotor," in *Energy Conversion Congress and Exposition (ECCE)*, Portland, USA, Sep. 2018, pp. 2314–2318.

[39] M. I. Nejad, "Self-Bearing Motor Design & Control," Ph.D. Thesis, Massachusetts Institute of Technology, Department of Mechanical Engineering, Cambridge, USA, 2013.

[40] L. Zhou, M. Imani Nejad, and D. L. Trumper, "One-axis hysteresis motor driven magnetically suspended reaction sphere," *Elsevier Mechatronics*, vol. 42, pp. 69–80, Apr. 2017.

[41] P. N. Bösch, "Bearingless Slice Motors of Higher Power Rating (Lagerlose Scheibenläufermotoren höherer Leistung)," Ph.D. Thesis, ETH Zürich, Power Electronic Systems Laboratory, Zurich, Switzerland, 2004.

[42] B. Klammer, H. Mitterhofer, A. Zöchbauer, and W. Gruber, "Topology Comparison and Design of a Slotted Bearingless High-Speed Permanent Magnetic Synchronous Machine," in *International Electric Machines and Drives Conference (IEMDC)*, San Diego, USA, May 2019, 8 pages.

[43] H. Mitterhofer, "Towards high-speed bearingless disk drives," Ph.D. Thesis, Johannes Kepler University Linz, Institute for Electric Drives and Power Electronics, Linz, Austria, Apr. 2017.

[44] P. Puentener, M. Schuck, D. Steinert, and J. W. Kolar, "Comparison of Bearingless Slice Motor Topologies for Pump Applications," in *International Electric Machines and Drives Conference (IEMDC)*, San Diego, USA, May 2019, pp. 9–16.

[45] Q. D. Nguyen and S. Ueno, "Modeling and Control of Salient-Pole Permanent Magnet Axial-Gap Self-Bearing Motor," *IEEE/ASME Transactions on Mechatronics*, vol. 16, no. 3, pp. 518–526, Jun. 2011.

[46] W. Gruber, W. Bauer, D. Wetsch, B. Klammer, and N. Kurita, "Implementation of a Bearingless Axial-Force/Torque Motor Fan with Flex-PCB Windings," in *International Electric Machines and Drives Conference (IEMDC)*, San Diego, USA, May 2019, pp. 179–184.

[47] J. Amemiya, A. Chiba, D. Dorrell, and T. Fukao, "Basic characteristics of a consequent-pole-type bearingless motor," *IEEE Transactions on Magnetics*, vol. 41, no. 1, pp. 82–89, Jan. 2005.

[48] T. Noguchi, H. Sugimoto, and A. Chiba, "Combined Winding Structure of a Consequent-Pole Bearingless Motor with Parallel Motor Winding Topology," in *International Electric Machines and Drives Conference (IEMDC)*, San Diego, USA, May 2019, pp. 17–24.

[49] H. Kleinrath, *Stromrichtergespeiste Drehfeldmaschinen*. Vienna, New York: Springer, 1980.

[50] E. Severson and N. Mohan, "Bearingless motor system design for industrial applications," in *International Electric Machines and Drives Conference (IEMDC)*, Miami, USA, May 2017, 8 pages.

[51] W. Gruber, M. Rothbock, and R. T. Schob, "Design of a Novel Homopolar Bearingless Slice Motor With Reluctance Rotor," *IEEE Transactions on Industry Applications*, vol. 51, no. 2, pp. 1456–1464, Mar. 2015.

[52] P. Kascak, R. Jansen, T. Dever, A. Nagorny, and K. Loparo, "Levitation performance of two opposed permanent magnet pole-pair separated conical bearingless motors," in *Energy Conversion Congress and Exposition (ECCE)*, Phoenix, USA, Sep. 2011, pp. 1649–1656.

[53] A. Schleicher and R. Werner, "Theoretical and Experimental Analysis of Controllability of a Novel Bearingless Rotary-Linear Reluctance Motor with Optimal Chessboard Toothing," in *International Conference on Industrial Technology (ICIT)*, Lyon, France, Feb. 2018, pp. 540–545.

[54] W. Bauer and W. Amrhein, "Electrical Design Considerations for a Bearingless Axial-Force/Torque Motor," *IEEE Transactions on Industry Applications*, vol. 50, no. 4, pp. 2512–2522, Jul. 2014.

[55] V. Kluyskens, C. Dumont, and B. Dehez, "Description of an Electrodynamic Self-Bearing Permanent Magnet Machine," *IEEE Transactions on Magnetics*, vol. 53, no. 1, Jan. 2017, 9 pages.

[56] W. Amrhein and S. Silber, "Bearingless Single-Phase Motor with Concentrated Full Pitch Windings in Interior Rotor Design," in *International Symposium on Magnetic Bearings (ISMB)*, Cambridge, USA, Aug. 1998, pp. 497–506.

[57] K. Raggl, T. Nussbaumer, and J. W. Kolar, "A Comparison of Separated and Combined Winding Concepts for Bearingless Centrifugal Pumps," *Journal of Power Electronics*, vol. 9, no. 2, pp. 243–258, Mar. 2009.

[58] H. Mitterhofer, B. Mrak, and W. Gruber, "Comparison of High-Speed Bearingless Drive Topologies With Combined Windings," *IEEE Transactions on Industry Applications*, vol. 51, no. 3, pp. 2116–2122, May 2015.

[59] D. Steinert, T. Nussbaumer, and J. W. Kolar, "Concept of a 150 krpm bearingless slotless disc drive with combined windings," in *International Electric Machines and Drives Conference (IEMDC)*, Chicago, USA, May 2013, pp. 311–318.

[60] E. L. Severson, R. Nilssen, T. Undeland, and N. Mohan, "Design of Dual Purpose No-Voltage Combined Windings for Bearingless Motors," *IEEE Transactions on Industry Applications*, vol. 53, no. 5, pp. 4368–4379, May 2017.

[61] G. Messager and A. Binder, "Analytical comparison of conventional and modified winding for high speed bearingless permanent magnet synchronous motor applications," in *International Conference on Optimization of Electrical and Electronic Equipment (OPTIM)*, Bran, Romania, May 2014, pp. 330–337.

[62] M. Reisinger, H. Grabner, S. Silber, W. Amrhein, C. Redemann, and P. Jenckel, "A Novel Design of a Five Axes Active Magnetic Bearing System," in *International Symposium on Magnetic Bearings (ISMB)*, Wuhan, China, Aug. 2010, pp. 561–566.

[63] G. Messager and A. Binder, "Six-Axis Rotor Magnetic Suspension Principle for Permanent Magnet Synchronous Motor with Control of the Positive, Negative and Zero-Sequence Current Components," *Applied Computational Electromagnetics Society (ACES) Journal*, vol. 32, no. 8, pp. 657–662, 2017.

[64] D. Jiang, T. Li, Z. Hu, and H. Sun, "Novel Topologies of Power Electronics Converter as Active Magnetic Bearing Drive," *IEEE Transactions on Industrial Electronics*, vol. 67, no. 2, pp. 950–959, Feb. 2020.

[65] W. Amrhein, W. Gruber, W. Bauer, and M. Reisinger, "Magnetic Levitation Systems for Cost-Sensitive Applications - Some Design Aspects," *IEEE Transactions on Industry Applications*, vol. 52, no. 5, pp. 3739–3752, Sep. 2016.

[66] J. Asama, Y. Fujii, T. Oiwa, and A. Chiba, "Novel control method for magnetic suspension and motor drive with one three-phase voltage source inverter using zero-phase current," *Mechanical Engineering Journal*, vol. 2, no. 4, pp. 15–25, 2015.

[67] J. Asama, T. Oi, T. Oiwa, and A. Chiba, "Investigation of integrated winding configuration for a two-DOF controlled bearingless PM motor using one three-phase inverter," in *International Electric Machines and Drives Conference (IEMDC)*, Miami, USA, May 2017, 6 pages.

[68] J. Asama, T. Oi, T. Oiwa, and A. Chiba, "Simple Driving Method for a 2-DOF Controlled Bearingless Motor Using One Three-Phase Inverter," *IEEE Transactions on Industry Applications*, vol. 54, no. 5, pp. 4365–4376, Sep. 2018.

[69] P. Hermann, "Radiales aktives magnetisches Lager mit Drehantrieb," Germany Patent DE2 406 790, Aug., 1975.

[70] P. Hermann, "Radiales aktives magnetisches Lager," Germany Patent DE2 358 527, May, 1975.

[71] P. Hermann, "Radiales aktives magnetisches Lager," Germany Patent DE2 457 084, Jun., 1976.

[72] H. Sequenz, *Die Wicklungen elektrischer Maschinen*. Vienna: Springer, 1950, vol. 1.

[73] W. Amrhein and S. Silber, "Lagerlose Permanentmagnetmotoren," in *Elektrische Antriebe - Grundlagen*, 5th ed. Berlin, Heidelberg: Springer Vieweg, 2013, book author: D. Schröder.

[74] P. Meinke and G. Flachenecker, "Electromagnetic drive assembly for rotary bodies using a magnetically mounted rotor," USA Patent US3 988 658, Oct., 1976.

[75] J. Bichsel, “Contributions to the Bearingless Electric Machine (Beiträge zum lagerlosen Elektromotor),” Ph.D. Thesis, ETH Zürich, Power Electronic Systems Laboratory, Zurich, Switzerland, 1990.

[76] N. Barletta, “The Bearingless Disk Drive (Der lagerlose Scheibenmotor),” Ph.D. Thesis, ETH Zürich, Power Electronic Systems Laboratory, Zurich, Switzerland, 1998.

[77] G. Sala, G. Valente, A. Formentini, L. Papini, D. Gerada, P. Zanchetta, A. Tani, and C. Gerada, “Space Vectors and Pseudoinverse Matrix Methods for the Radial Force Control in Bearingless Multisector Permanent Magnet Machines,” *IEEE Transactions on Industrial Electronics*, vol. 65, no. 9, pp. 6912–6922, Sep. 2018.

[78] C. Zwyssig, J. Kolar, and S. Round, “Megaspeed Drive Systems: Pushing Beyond 1 Million r/min,” *IEEE/ASME Transactions on Mechatronics*, vol. 14, no. 5, pp. 564–574, Apr. 2009.

[79] T. Baumgartner, R. M. Burkart, and J. W. Kolar, “Analysis and Design of a 300-W 500 000-r/min Slotless Self-Bearing Permanent-Magnet Motor,” *IEEE Transactions on Industrial Electronics*, vol. 61, no. 8, pp. 4326–4336, Aug. 2014.

[80] D. Gerada, A. Mebarki, N. L. Brown, C. Gerada, A. Cavagnino, and A. Boglietti, “High-Speed Electrical Machines: Technologies, Trends, and Developments,” *IEEE Transactions on Industrial Electronics*, vol. 61, no. 6, pp. 2946–2959, Jun. 2014.

[81] R. Millingen and J. Millingen, “Phase Shift Torquemeters for Gas Turbine Development and Monitoring,” in *International Gas Turbine Aeroengine Congress Exposition*, Orlando, USA, Jun. 1991, pp. 1–10.

[82] C. Redemann, P. Meuter, A. Ramella, and T. Gempp, “30 kW Bearingless Canned Motor Pump on the Test Bed,” in *International Symposium on Magnetic Bearings (ISMB)*, Zurich, Switzerland, Aug. 2000, pp. 189–194.

[83] E. Bolte, *Elektrische Maschinen (Electric Machines)*, 2nd ed. Berlin: Springer Vieweg, 2018.

[84] J. R. Anglada, S. M. Suleiman, and M. A. Yuratich, “Calculation of rotor losses in

PM machines with retaining sleeves using transfer matrices," *IET Electric Power Applications*, vol. 12, no. 8, pp. 1150–1157, Sep. 2018.

[85] M. Markovic and Y. Perriard, "Analytical Solution for Rotor Eddy-Current Losses in a Slotless Permanent-Magnet Motor: The Case of Current Sheet Excitation," *IEEE Transactions on Magnetics*, vol. 44, no. 3, pp. 386–393, Mar. 2008.

[86] A. Rahideh and T. Korakianitis, "Analytical Magnetic Field Distribution of Slotless Brushless Permanent Magnet Motors, Part I: Armature Reaction Feld, Inductance and Rotor Eddy Current Loss Calculations," *IET Electric Power Applications*, vol. 6, no. 9, pp. 628–638, 2012.

[87] A. Rahideh and T. Korakianitis, "Analytical Magnetic Field Distribution of Slotless Brushless PM Motors, Part II: Open-Circuit Field and Torque Calculations," *IET Electric Power Applications*, vol. 6, no. 9, pp. 639–651, Nov. 2012.

[88] Z. Q. Zhu and D. Howe, "Instantaneous Magnetic Field Distribution in Brushless Permanent Magnet DC Motors, Part II: Armature-reaction field," *IEEE Transactions on Magnetics*, vol. 29, no. 1, pp. 136–142, Jan. 1993.

[89] I. Sneddon, *Special Functions Of Mathematical Physics And Chemistry*, 2nd ed. Edinburgh, London: Oliver and Boyd, 1961.

[90] H. J. Dirschmid, *Mathematische Grundlagen der Elektrotechnik*, 4th ed. Wiesbaden: Springer Vieweg, 1990.

[91] R. Stoll, *The Analysis of Eddy Currents*. Oxford: Clarendon Press Oxford, 1974.

[92] R. Stoll and P. Hammond, "Calculation of the magnetic field of rotating machines. Part IV: Approximate determination of the field and the losses associated with eddy currents in conducting surfaces," *Proceedings of the Institution of Electrical Engineers*, vol. 112, no. 11, pp. 2083–2094, Nov. 1965.

[93] C. D. Waelzholz GmbH & Co. KG, "M270-35A Elektroband nach EN 10106," accessed: 20.06.2021. [Online]. Available: https://www.waelzholz.com/stahlwerkstoffe/elektroband/en-10106.html

[94] A. Binder, *Elektrische Maschinen und Antriebe: Grundlagen, Betriebsverhalten*, 2nd ed. Berlin: Springer Vieweg, 2017.

[95] F. Carter, "The Magnetic Field of the Dynamo-Electric Machine," *Journal of the Institution of Electrical Engineers*, vol. 64, no. 359, pp. 1115–1138, Nov. 1926.

[96] J. R. Anglada, S. M. Suleiman, and A. Qazalbash, "Influence of curvature on air-gap magnetic field distribution and rotor losses in PM electric machines," *International journal for computation and mathematics in electrical and electronic engineering (COMPEL)*, vol. 36, no. 4, pp. 871–891, Mar. 2017.

[97] W. J. Gibbs, *Conformal Transformations in Electrical Engineering*. London: Chapman & Hall, 1958.

[98] E. Freeman, "The calculation of harmonics, due to slotting, in the flux-density waveform of a dynamo-electric machine," *Proceedings of the IEE Part C: Monographs*, vol. 109, no. 16, pp. 581–588, Jun. 1962.

[99] D. Zarko, D. Ban, and T. Lipo, "Analytical calculation of magnetic field distribution in the slotted air gap of a surface permanent-magnet motor using complex relative air-gap permeance," *IEEE Transactions on Magnetics*, vol. 42, no. 7, pp. 1828–1837, Jul. 2006. [Online]. Available: http://ieeexplore.ieee.org/document/1644900/

[100] N. Erd, R. Köster, and A. Binder, "Computational Analysis of Air Gap Field in Electrical Machines by Fourier Coefficient Matrices," in *International Conference on Electrical Machines (ICEM)*, Gothenburg, Sweden, Aug. 2020, pp. 2479–2485.

[101] H. O. Seinsch, *Grundlagen elektrischer Maschinen und Antriebe*, 3rd ed. Stuttgart, Germany: B.G. Teubner Verlag / Springer Fachmedien Wiesbaden, 1993.

[102] F. Rezaee-Alam, B. Rezaee-Alam, and J. Faiz, "Unbalanced Magnetic Force Analysis in Eccentric Surface Permanent-Magnet Motors Using an Improved Conformal Mapping Method," *IEEE Transactions on Energy Conversion*, vol. 32, no. 1, pp. 146–154, Mar. 2017.

[103] U. Kim and D. Lieu, "Magnetic field calculation in permanent magnet motors with rotor eccentricity: without slotting effect," *IEEE Transactions on Magnetics*, vol. 34, no. 4, pp. 2243–2252, Jul. 1998.

[104] T. Schneider, J. Petersen, and A. Binder, "Influence of Pole Pair Combinations on High-Speed Bearingless Permanent Magnet Motor Performance," in *Conference*

on Power Electronics, Machines and Drives (PEMD), York, UK, Apr. 2008, pp. 707–711.

[105] J. Pyrhönen, T. Jokinen, and V. Hrabovcová, *Design of Rotating Electrical Machines*. Chichester, UK: John Wiley & Sons Ltd., 2008.

[106] D. Guhl, R. Liebfried, and W. Hofmann, "Design and Comparison of Dual-Purpose Stator Windings for Active Chatter Suppression in Milling Spindles," in *International Symposium on Magnetic Bearings (ISMB)*, Aug. 2021, pp. 186–200.

[107] A. Khamitov, W. Gruber, G. Bramerdorfer, and E. L. Severson, "Comparison of Combined Winding Strategies for Radial Non-Salient Bearingless Machines," *IEEE Transactions on Industry Applications*, vol. 57, no. 6, pp. 6856–6869, 2021.

[108] J. Štěpina, "Matrix Analysis of Space Harmonics of Asymmetrical Stator Windings," *IEE Proceedings B: Electric Power Applications*, vol. 134, no. 4, pp. 207–210, Jul. 1987.

[109] A. Borisavljevic, *Limits, Modeling and Design of High-Speed Permanent Magnet Machines*, ser. Springer Theses (Delft University of Technology, Netherlands). Berlin, Heidelberg: Springer-Verlag, 2013.

[110] M. Schwarz, "Specific Increase of Stiffness and Stability of Machine Elements by Prestressed Ring Bandages of Carbon Fiber Bonds (Gezielte Steifigkeits- und Festigkeitssteigerung von Maschinenbauteilen durch vorgespannte Ringarmierungen aus Faser-Kunststoff-Verbunden)," Ph.D. Thesis, Institute for Light Weight and Building Construction, Technical University of Darmstadt, Darmstadt, Germany, 2007.

[111] Y. Liu, J. Ou, M. Schiefer, P. Breining, F. Grilli, and M. Doppelbauer, "Application of an Amorphous Core to an Ultra-High-Speed Sleeve-Free Interior Permanent-Magnet Rotor," *IEEE Transactions on Industrial Electronics*, vol. 65, no. 11, pp. 8498–8509, Nov. 2018.

[112] P. Oxley, J. Goodell, and R. Molt, "Magnetic properties of stainless steels at room and cryogenic temperatures," *Journal of Magnetism and Magnetic Materials*, vol. 321, no. 14, pp. 2107–2114, Jul. 2009.

[113] Vacuumschmelze GmbH & Co. KG, "Rare Earth Permanent Magnets

Vacodym Vacomax," 2014, accessed: 30.07.2020. [Online]. Available: https://vacuumschmelze.de/shared/quickNav/Downloads

[114] Schunk-Carbon-Technology, *Fiber Reinforced Armor Sleeves for High Performance Motors*, 2018, accessed: 12.11.2020, https://www.schunk-group.com/en/media-downloads.

[115] Y. Wang, J. H. Feng, S. Y. Guo, Y. F. Li, Z. C. Chen, Y. Wang, and Z. Q. Zhu, "Investigation of Optimal Split Ratio for High-Speed Permanent-Magnet Brushless Machines," *IEEE Transactions on Magnetics*, vol. 54, no. 11, Nov. 2018, 5 pages.

[116] Q. Li, M. Dou, and C. Fang, "Analytical determination of optimal split ratio for high-speed permanent magnet brushless motors," in *International Conference on Electrical Machines and Systems (ICEMS)*, Pattaya City, Thailand, Oct. 2015, pp. 636–640.

[117] Z. Zhu, "Design and analysis of high-speed brushless permanent magnet motors," in *International Conference on Electrical Machines and Drives*, vol. 8, Cambridge, UK, Sep. 1997, pp. 381–385.

[118] M. Schuck, P. Puentener, T. Holenstein, and J. W. Kolar, "Scaling and Design of Miniature High-Speed Bearingless Slice Motors," *e&i Elektrotechnik und Informationstechnik*, vol. 136, no. 3, pp. 102–120, 2019.

[119] H. Mitterhofer and S. Silber, "Crucial Parameters and Optimization of High-Speed Bearingless Drives," *Applied Computational Electromagnetics Society (ACES) Journal*, vol. 32, no. 8, pp. 697–703, 2017.

[120] D. Kepsu, R. P. Jastrzebski, O. Pyrhönen, and E. Kurvinen, "Scalability of SPM Bearingless High-Speed Motor for 180–280 kW Applications," in *International Electric Machines and Drives Conference (IEMDC)*, San Diego, USA, May 2019, pp. 329–335.

[121] Y. Kang and E. Severson, "Optimization Framework for a Large, High Speed Bearingless Permanent Magnet Motor," in *International Symposium on Magnetic Bearings (ISMB)*, Beijing, China, Aug. 2018, 10 pages.

[122] T. Reichert, T. Nussbaumer, and J. W. Kolar, "Split Ratio Optimization for High-

Torque PM Motors Considering Global and Local Thermal Limitations," *IEEE Transactions on Energy Conversion*, vol. 28, no. 3, pp. 493–501, May 2013.

[123] Tata Steel Europe Ltd., "Typical data for SURA M330-35A," accessed: 20.06.2021. [Online]. Available: https://www.tatasteeleurope.com/ts/node/8041

[124] "Rotating electrical machines – Part 1: Rating and performance (IEC 60034-1: 2010, modified, Geneva, Switzerland) (German version)," Oct. 2010.

[125] M. Mack, "Air Friction Losses in Electrical Machines of Small Size (Luftreibungsverluste bei elektrischen Maschinen kleiner Baugröße)," Ph.D. Thesis, Institute for Electric Machines, University of Stuttgart, Stuttgart, Germany, 1967.

[126] "Specifications of Individual Materials – Magnetically Hard Materials (IEC 60404-8-1: 2004, Geneva, Switzerland)," Apr. 2004.

[127] S. Ruoho, M. Haavisto, E. Takala, T. Santa-Nokki, and M. Paju, "Temperature Dependence of Resistivity of Sintered Rare-Earth Permanent-Magnet Materials," *IEEE Transactions on Magnetics*, vol. 46, no. 1, pp. 15–20, Jan. 2010.

[128] F. M. Smits, "Measurement of Sheet Resistivities with the Four-Point Probe," *The Bell System Technical Journal*, vol. 57, no. 3, pp. 711–718, 1958.

[129] O. Gutfleisch, M. Verdier, I. Harris, and A. Ray, "Characterisation of rare earth-transition metal alloys with resistivity measurements," *IEEE Transactions on Magnetics*, vol. 29, no. 6, pp. 2872–2874, Nov. 1993.

[130] Informationsstelle-Edelstahl-Rostfrei, *Magnetic properties of stainless steels (Magnetische Eigenschaften nichtrostender Stähle)*, accessed: 06.03.2021, https://www.edelstahl-rostfrei.de/publikationen/iser-publikationen/merkblatt-827-magnetische-eigenschaften-nichtrostender-staehle.

[131] H. Jordan, R. Schroeder, and H. Seinsch, "About the Calculation of Single-Sided Magnetic Pulling Forces in AC Rotating Machines (Zur Berechnung einseitig magnetischer Zugkräfte in Drehfeldmaschinen)," *Archiv für Elektrotechnik*, vol. 63, pp. 117–124, 1981.

[132] D. Dorrell, W. Thomson, and S. Roach, "Combined effects of static and dynamic eccentricity on airgap flux waves and the application of current monitoring to detect

dynamic eccentricity in 3-phase induction motors," in *International Conference on Electrical Machines and Drives (ICEM)*, vol. 1995, Durham, UK, Aug. 1995, pp. 151–155.

[133] "Electromagnetic compatibility (EMC) - Part 2-4: Environment - Compatibility levels in industrial plants for low-frequency conducted disturbances (IEC 61000-2-4: 2002, modified 2014, Geneva, Switzerland) (English version)," 2014.

[134] J. Saari, "Thermal analysis of high speed induction machines," Ph.D. Thesis, Laboratory of Electromechanics, Helsinki University of Technology, Espoo, Finland, Jan. 1998.

[135] P. M. Wild, N. Djilali, and G. W. Vickers, "Experimental and Computational Assessment of Windage Losses in Rotating Machinery," *ASME Journal of Fluids Engineering*, vol. 118, no. 1, pp. 116–122, Mar. 1996.

[136] X. Li, "Evaluation and Design of a Flywheel Energy Storage System," Ph.D. Thesis, Technical University of Darmstadt, Institute for Electrical Energy Conversion, Darmstadt, Germany, May 2019.

[137] M. Ahrens and L. Kučera, "Cross Feedback Control of a Magnetic Bearing System," in *International Symposium on Magnetic Suspension Technology (ISMST)*, Tallahassee, USA, Dec. 1995, pp. 177–191.

[138] L. Chen, C. Zhu, Z. Zhong, M. Sun, and W. Zhao, "Internal model control for the AMB high-speed flywheel rotor system based on modal separation and inverse system method," *IET Electric Power Applications*, vol. 13, no. 3, pp. 349–358, Mar. 2019.

[139] G. Messager and A. Binder, "Derivation of forces and force interferences in a double conical high-speed bearingless permanent magnet synchronous motor," in *International Electric Machines and Drives Conference (IEMDC)*, Miami, USA, May 2017, 8 pages.

[140] D. G. Holmes and T. A. Lipo, *Pulse Width Modulation for Power Converters: Principles and Practice*. Hoboken: John Wiley & Sons, Inc., 2003.

[141] IXYS-Corporation, *Datasheet: Littelfuse N-Channel-MOSFET IXTK180N15P*, 2020, accessed: 06.11.2020, https://www.littelfuse.de/sdorigin-

savvis/products/power-semiconductors/discrete-mosfets/n-channel-standard/polar/ixtk180n15p.aspx.

[142] N. Mohan, T. M. Undeland, and W. P. Robbins, *Power electronics: Converters, Applications, and Design*, 2nd ed. New York, Chichester, Brisbane, Toronto, Singapore: John Wiley & Sons, Inc., 1995.

[143] R. Seifert and W. Hofmann, "Highly Dynamic Thrust Bearing Control Based on a Fractional-Order Flux Estimator," *IEEE Transactions on Industry Applications*, vol. 57, no. 6, pp. 6988–6999, 2021.

[144] G. Messager, F. Mink, T. Becker, J. Wang, and A. Binder, "Control interference of electrical machines with double-star winding systems driven by independent current controllers," in *European Conference on Power Electronics and Applications (EPE ECCE-Europe)*, Geneva, Switzerland, Sep. 2015, 10 pages.

[145] T. Matsuzaki, M. Takemoto, S. Ogasawara, S. Ota, K. Oi, and D. Matsuhashi, "Operational Characteristics of an IPM-Type Bearingless Motor With 2-Pole Motor Windings and 4-Pole Suspension Windings," *IEEE Transactions on Industry Applications*, vol. 53, no. 6, pp. 5383–5392, Nov. 2017.

[146] D. Steinert, T. Nussbaumer, and J. W. Kolar, "Slotless Bearingless Disk Drive for High-Speed and High-Purity Applications," *IEEE Transactions on Industrial Electronics*, vol. 61, no. 11, pp. 5974–5986, Nov. 2014.

[147] V. Kluyskens and B. Dehez, "Dynamical Electromechanical Model for Magnetic Bearings Subject to Eddy Currents," *IEEE Transactions on Magnetics*, vol. 49, no. 4, pp. 1444–1452, Apr. 2013.

[148] P. Puentener, F. Hoffmann, D. Menzi, D. Steinert, and J. W. Kolar, "Homopolar bearingless slice motor in temple design," in *International Electric Machines and Drives Conference (IEMDC)*, Miami, USA, May 2017, 8 pages.

[149] T. Holenstein, M. Schuck, and J. W. Kolar, "Performance Benchmarking of a Novel Magnet-Free Bearingless Synchronous Reluctance Slice Motor," *IEEE Open Journal of the Industrial Electronics Society*, vol. 1, pp. 184–193, 2020.

[150] N. Turk, N. Bulic, and W. Gruber, "Nonlinear Control of a Bearingless Flux-

Switching Slice Motor With Combined Winding System," *IEEE/ASME Transactions on Mechatronics*, vol. 25, no. 1, pp. 152–163, Feb. 2020.

[151] T. Holenstein, M. Schuck, and J. W. Kolar, "A Wide Air Gap Flux Switching Bearingless Motor With Odd and Even Pole Pair Numbers," *IEEE Open Journal of Industry Applications*, vol. 1, pp. 52–62, 2020.

[152] M. Noh, W. Gruber, and D. L. Trumper, "Hysteresis Bearingless Slice Motors With Homopolar Flux-Biasing," *IEEE/ASME Transactions on Mechatronics*, vol. 22, no. 5, pp. 2308–2318, Oct. 2017.

[153] F. Zürcher, T. Nussbaumer, and J. W. Kolar, "Motor Torque and Magnetic Levitation Force Generation in Bearingless Brushless Multipole Motors," *IEEE/ASME Transactions on Mechatronics*, vol. 17, no. 6, pp. 1088–1097, Dec. 2012.

[154] E. Severson, S. Gandikota, and N. Mohan, "Practical Implementation of Dual Purpose No Voltage Drives for Bearingless Motors," *IEEE Transactions on Industry Applications*, vol. 52, no. 2, pp. 1509–1518, 2015.

[155] T. Stallinger, W. Gruber, and W. Amrhein, "Bearingless segment motor with a consequent pole rotor," in *International Electric Machines and Drives Conference (IEMDC)*, Miami, USA, May 2009, pp. 1374–1380.

[156] Outokumpu Oyj, "Dura 4122 Datasheet," 2020, accessed: 15.02.2020. [Online]. Available: https://www.outokumpu.com/de-de/products/product-ranges/dura

[157] Valbruna Edel Inox GmbH, "Valbruna V225MN / 1.4462 Duplex," 2020, accessed: 15.02.2020. [Online]. Available: https://www.valbruna.de/de/werkstoff/1.4462.html

[158] Arnold Magnetic Technologies Corp., "RECOMA – The complete range of SmCo5 and Sm2Co17 alloys," 2020, accessed: 07.03.2020. [Online]. Available: https://www.arnoldmagnetics.com/products/recoma-samarium-cobalt-magnets/

[159] D. Schröder, *Electric Drives - Control of Drive Systems (Elektrische Antriebe - Regelung von Antriebssystemen)*, 4th ed. Berlin, Heidelberg: Springer Vieweg, 2015.

Own Publications

[O01] D. Dietz and A. Binder, "Critical review on the benefits of C- and E-Core flux-switching-PM-machines," in *International Conference on Electrical Drives and Power Electronics (EDPE)*, Dubrovnik, Oct. 2017, pp. 226–234.

[O02] D. Dietz, G. Messager, and A. Binder, "1 kW/ 60 000 rpm Bearingless PM Motor with Combined Winding for Torque and Rotor Suspension," *IET Electric Power Applications*, vol. 12, no. 8, pp. 1090–1097, Sep. 2018.

[O03] M. Lehr, D. Dietz, and A. Binder, "Electromagnetic Design of a Permanent Magnet Flux-Switching-Machine as a Direct-Driven 3 MW Wnd Power Generator," in *International Conference on Industrial Technology (ICIT)*, Lyon, France, Feb. 2018, pp. 383–388.

[O04] D. Dietz and A. Binder, "Comparison between a bearingless PM motor with separated and combined winding for torque and lateral force generation," in *European Conference on Power Electronics and Applications (EPE-ECCE Europe)*, Genova, Italy, Sep. 2019, 10 pages.

[O05] D. Dietz and A. Binder, "Bearingless PM Synchronous Machine with Zero-Sequence Current Driven Star Point-Connected Active Magnetic Thrust Bearing," *Transportation Systems and Technology*, vol. 4, no. 3, pp. 5–25, Sep. 2018.

[O06] D. Dietz and A. Binder, "Influence of PM-Material on the Parameter Uncertainty of Bearingless Synchronous Machines," in *ETG/GMM-Symposium Innovative Small Drives and Micro-Motor Systems (IKMT)*, vol. 159, Würzburg, Germany, Sep. 2019, pp. 80–85.

[O07] D. Dietz and A. Binder, "Eddy Current Influence on the Control Behavior of Bearingless PM Synchronous Machines," *IEEE Transactions on Industry Applications*, vol. 57, no. 6, pp. 6944–6955, Nov. 2021.

[O08] X. Li, J. An, N. Erd, D. Dietz, Y. Gemeinder, and A. Binder, "Design and Manufacture of a High-speed Rotor in a Flywheel Demonstrator," in *International Conference on Electrical Machines and Systems (ICEMS)*, Hamamatsu, Japan, Nov. 2020, pp. 384–389.

[O09] D. Dietz and A. Binder, "Design Guidelines and Scaling Effects for Bearingless PM Synchronous Machines accounting for Eddy Current Reaction Field," *IEEE Transactions on Industry Applications*, vol. 57, no. 6, pp. 6844–6855, Nov. 2021.

[O10] D. Dietz and A. Binder, "Bearingless PM Synchronous Machine with Axial Active Magnetic Bearing fed by Zero-Sequence Current," *e&i Elektrotechnik und Informationstechnik*, vol. 138, no. 2, pp. 62–69, Feb. 2021.

[O11] D. Dietz and A. Binder, "Operational Constraints of Zero-Sequence Current Feeding in Bearingless PM Synchronous Machines," *e&i Elektrotechnik und Informationstechnik*, vol. 142, no. 6, pp. 383–393, Jul. 2021.

[O12] D. Dietz and A. Binder, "Influence of Magnetic Eccentricity in Bearingless PM Synchronous Machines," in *International Symposium on Magnetic Bearings (ISMB)*, Online / Rio de Janeiro, Brazil, Aug. 2021, pp. 228–239.

[O13] D. Dietz and A. Binder, "Comparison Between NdFeB and SmCo Permanent Magnets Regarding Eddy Currents in Bearingless Synchronous Machines," in *International Symposium on Magnetic Bearings (ISMB)*, Online / Rio de Janeiro, Brazil, Aug. 2021, pp. 538–550.

[O14] X. Li, D. Dietz, J. An, N. Erd, G. Messager, Y. Gemeinder, and A. Binder, "Discussion of Field Weakening Operation of a High-speed PMSM for Flywheel Application," in *Electromechanical Drive Systems (VDE Elektromechanische Antriebssysteme)*, Online / München, Germany, Nov. 2021, pp. 266–271.

[O15] D. Dietz and A. Binder, "Zero-Sequence Current Feeding of an Axial Active Magnetic Bearing in a Bearingless PM Synchronous Machine," in *mOre driVE (OVE)*, Online / Vienna, Austria, Sep. 2021, 21 slides.

Supervised Student Theses

[S01] F. Hilgert, “Ökonomische und ökologische Konsequenzen beim Serieneinsatz von Permanentmagneten für elektrische Maschinen (engl.: Economical and ecological consequences of permanent magnet series applications in electrical machines),” Study Thesis, Technical University of Darmstadt, Institute for Electrical Energy Conversion, Darmstadt, Germany, Nov. 2017.

[S02] M. Bock, “Optimierung der Wicklungstopologie für eine lagerlose PM-Synchronmaschine mit kombinierter Antriebs- und Tragwicklung (engl.: Optimization of the winding topology for a bearingless PM synchronous machine with combined drive and suspension winding),” Master’s thesis, Technical University of Darmstadt, Institute for Electrical Energy Conversion, Darmstadt, Germany, Oct. 2018.

[S03] L. Groß, “Positionsregelung einer lagerlosen doppelt-dreiphasigen PM-Synchronmaschine mit sternpunktverbundenem axialen Magnetlager (engl.: Position control of a bearingless double-three-phase PM synchronous machine with star point-connected axial magnetic bearing),” Bachelor’s Thesis, Technical University of Darmstadt, Institute for Electrical Energy Conversion, Darmstadt, Germany, Sep. 2018.

[S04] A. Bäumle, “Development of an analytical calculation tool to design bearingless PM synchronous machines,” Master’s thesis, Technical University of Darmstadt, Institute for Electrical Energy Conversion, Darmstadt, Germany, Apr. 2019.

[S05] A. Möller, “Elektromagnetische, thermische und mechanische Auslegung einer lagerlosen PM-Synchronmaschine mit kombinierter Antriebs- und Tragwicklung (engl.: Electromagnetic, thermal and mechanical design of a bearingless PM synchronous machine with combined drive and suspension winding),” Master’s the-

sis, Technical University of Darmstadt, Institute for Electrical Energy Conversion, Darmstadt, Germany, May 2019.

[S06] E. Akkus, "Zentrale und dezentrale Positionsregelung magnetgelagerter Hochdrehzahl-Antriebe (engl.: Centralized and decentralized position control of magnetically suspended high-speed drives)," Bachelor's Thesis, Technical University of Darmstadt, Institute for Electrical Energy Conversion, Darmstadt, Germany, Apr. 2020.

[S07] H. Hoffmann, "Wirbelstrom-verursachte Störkräfte in lagerlosen PM-Synchronmaschinen unterschiedlicher Baugröße (engl.: Parasitc forces in bearingless PM synchronous machines of different sizes caused by eddy currents)," Bachelor's Thesis, Technical University of Darmstadt, Institute for Electrical Energy Conversion, Darmstadt, Germany, Apr. 2020.

[S08] S. Tölle, "Modulationsverfahren eines 2x3-phasigen Spannungszwischenkreisumrichters zur Speisung einer lagerlosen PM-Synchronmaschine mit sternpunktverbundenem Axialmagnetlager (engl.: Modulation techniques of 2x3-phase voltage source inverter for feeding of a bearingless PM synchronous machine with star point-connected axial magnetic bearing)," Bachelor's Thesis, Technical University of Darmstadt, Darmstadt, Germany, Sep. 2020.

[S09] S. Pilatus, "Parasitäreffekte eines nullstromgespeisten axialen Magnetlagers (engl.: Parasitic Effects of Zero-Sequence-Current-Fed Axial Magnetic Bearings)," Bachelor's Thesis, Technical University of Darmstadt, Institute for Electrical Energy Conversion, Darmstadt, Germany, Mar. 2021.

[S10] L. Moser, "Regelverfahren zur Kompensation parasitärer Effekte in magnetgelagerten Hochdrehzahl-Antrieben (engl.: Control strategies for compensating parasitic effects in magnetically levitated high-speed drives)," Master's thesis, Technical University of Darmstadt, Institute for Electrical Energy Conversion, Darmstadt, Germany, Jun. 2021.

[S11] N. Rickertsen, "Parametrische Auslegung von lagerlosen PM-Synchronmaschinen zur Identifizierung von Skalierungseffekten (engl.: Parametric Design of bearingless PM synchronous machines for identification of scaling effects)," Bachelor's Thesis, Technical University of Darmstadt, Darmstadt, Germany, Aug. 2021.

A. Appendix

A.1. Literature Overview of Bearingless Prototype Motors

Table A.1.: Data of bearingless drives related to Fig. 1.7

No., source, year	Research group	Surface speed / $m \cdot s^{-1}$	Type	Stator	Zero-sequence current	Actively controlled DOFs
1, [79], 2014	B	183	PMSM	slotless	no	6
2, [43], 2017	A	181	Slice PMSM	slotless	no	3
3, [7], 2020	I	109	PMSM	6 slots	no	5
4, [42], 2019	A	168	Slice PMSM	12 slots	no	3
5, [23], 2019	H	104	PMSM	12 slots	no	6
6, [9], 2013	H	161	PMSM	36 slots	no	6
7, [8], 2020	D	225	PMSM	36 slots	no	6
8, [145], 2017	I	– [1)]	PMSM	36 slots	no	6
9, [33], 2007	G	96	SRM	8 slots	no	6
10, [32], 2000	G	130	SynRM	24 slots	no	6
11, [146], 2014	B	11	Slice PMSM	slotless	no	3
12, [29], 1999	B	87	IM	24 slots	no	5
13, [9], 2013	H	41	Conical PMSM	12 slots	no	6
14, [18], 2018	A	176	Axial force torque motor	slotless	yes	2
15, [29], 1999	B	43	IM	24 slots	no	5
16, [41], 2004	B	39	Slice PMSM	8 slots	no	3
17, [16], 2017	D	10	Single-Drive Motor	12 slots	no	2

18, [41], 2004	B	24	Slice PMSM	12 slots	no	3
19, [18], 2018	A	168	Axial force torque motor	slotless	yes	2
20, [147], 2013	E	16	Axial Flux PMSM	slotless	no	1
21, [21], 2018	E	8	Slice PMSM	slotless	no	1
22, [68], 2018	D	18	PMSM	6 slots	yes	2
23, [148], 2017	A	16	Homopolar slice motor	6 slots	no	3
24, [149], 2020	B	21	SynRM	6 slots	no	3
25, [47], 2005	D	21	Consequent pole	24 slots	no	-
26, [82], 2000	B	– [1)]	IM	48 slots	no	6
27, [77], 2018	F	8	PMSM	18 slots	no	3
28, [150], 2020	A	24	Flux Switching Machine	12 slots	no	3
29, [151], 2020	B	5	Flux Switching Machine	8 slots	no	3
30, [51], 2015	C	6	Homopolar SynRM	6 slots	no	3
31, [152], 2017	A	5	Hysteresis slice motor	12 slots	no	3
32, [153], 2012	A,B	35	Slice PMSM	24 slots	no	3
33, [154], 2015	C	5	AC Homopolar machine	36 slots	no	5
34, [155], 2009	B	2	Consequent pole	12 slots	no	3

[1)] No data available

A.2. Properties of the Prototype Machine *LLM4*

Table A.2.: Data of the 2x3-phase prototype bearingless PM machine *LLM4*

Rated data: P_N / kW; n_N / min^{-1}	1; 60000
Stator outer diameter $2 \cdot r_{S,o}$ / mm	75
Stator inner diameter $2 \cdot r_{S,i}$ / mm	35
Active iron length l_{Fe} / mm	40
Mechanical air gap width δ / mm	1
Effective air gap width δ_{eff} / mm	5.25
PM height h_{PM} / mm	2.75
Axial PM length l_{PM} / mm	48
Bandage height h_{sl} / mm	1.5
Shaft diameter $2 \cdot r_{sh}$ / mm	24.5
Rotor mass m_R / kg	0.9
Rotor polar moment of inertia Θ / kg $\cdot$ mm^2 (calculated)	117
Rotor axial moment of inertia Θ / kg $\cdot$ mm^2 (calculated)	2551
Stator core material	M270-35A [93]
Stator winding resistance per phase (20 °C) R_s / mΩ	69
Combined winding parameters	
Stator slot count Q	12
Drive (D) winding pole count $2p$	2
Suspension winding (L) pole count $2p_L$	4
Winding factors $k_{w,D}$; $k_{w,L}$	0.835; 0.75
Number of slots per pole and phase q	2
Short-pitching W/τ_p	2/3
Number of parallel winding branches a	2
Copper strand diameter / mm	0.45
Parallel winding strands per turn	8
Thermal Class of winding insulation	F (155 °C)

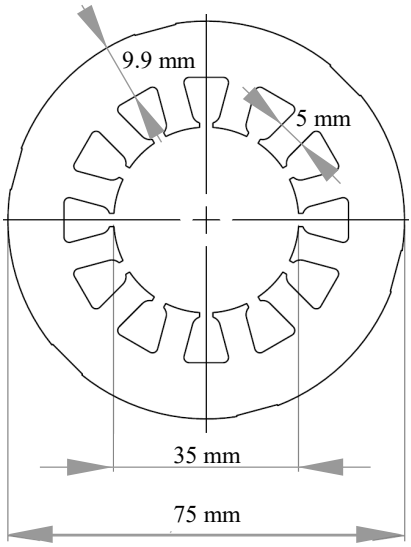

Fig. A.1.: Stator iron cross section of the prototype machine *LLM4* (axial length: $l_{\mathrm{Fe}} = 40$ mm)

A.3. Winding Pattern for the Prototype Machine *LLM4*

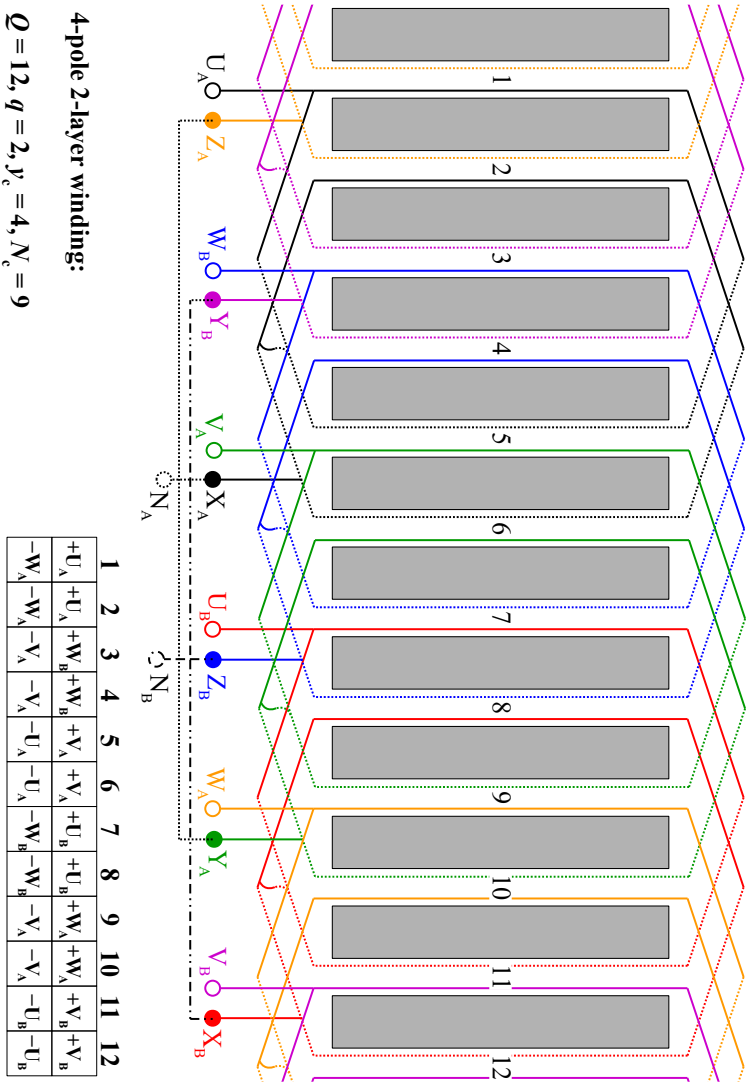

Fig. A.2.: 3-phase winding pattern for the prototype machine *LLM4*

A.4. Properties of the used Inverter for the Operation of the Prototype Machine *LLM4*

Table A.3.: Data of the used 2-level PWM voltage DC-link inverter *LeviOne Junior* from *KEBA Industrial Automation Germany GmbH*

Rated apparent power S_N / VA	1200
Input voltage (DC) U_{DC} / V	48 (−10%) ... 150 [1] (+5%)
Input current (DC) I_{DC} / A	8
Output fundamental frequency f_{syn} / Hz	0 ... 4000
PWM switching frequency f_{sw} / kHz	4 ... 40 [2]
Maximum momentary current per half-bridge $i_{s,max}$ / A	16

[1]) Operated at $U_{DC} = 150$ V; [2]) Operated at $f_{sw} = 33$ kHz

A.5. Composition of the Combined Radial-Axial Active Magnetic Bearing in the *LLM4*

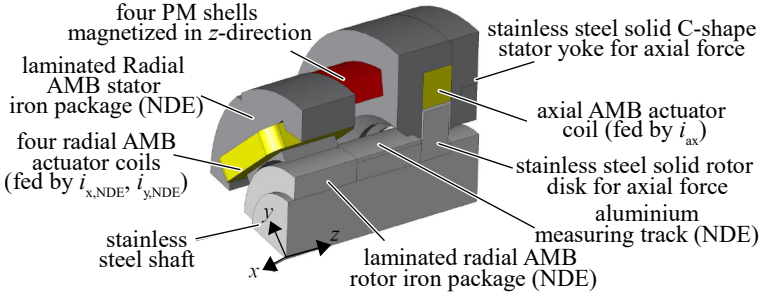

(a) 3D view

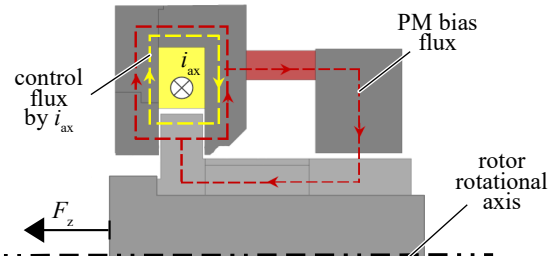

(b) 2D view of the radial-axial plane for the axial force generation

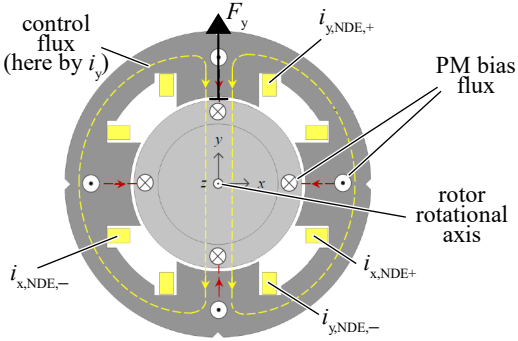

(c) 2D view of the radial-circumferential plane for the radial force generation at the NDE

Fig. A.3.: Schematic representation of the combined radial-axial AMB in the *LLM4* [136], commercially available at *KEBA Industrial Automation Germany GmbH*

A.6. Composition of the Investigated Bearingless Machines

Table A.4.: Investigated bearingless machines

	Prototype	$2 \cdot r_{S,o}$ / mm	$2 \cdot r_{S,i}$ / mm	l_{Fe} / mm	h_{PM} / mm	P_N / kW	n_N / min^{-1}
BM-135	–	135	27 ... 81	125	2.7 ... 13	35 ... 65	40000
*BM-135**	–	135	47	40	11	65	40000
BM-75	–	75	15 ... 45	40	1.5 ... 7.5	0.8 ... 1.6	40000
*BM-75**	–	75	35	36	4.5	1.6	40000
LLM1	✓[24]	60	32	40	3.5	0.5	60000
LLM2	✓[9]	135	80	125	7	40	40000
LLM3	✓[23]	75	35	40	2.75	1	60000
$LLM3_{I+}$	–	75	35	40	2.75	2.3	60000
$LLM3_{N+}$	–	75	35	40	2.75	2.3	60000
LLM4	✓	75	35	40	2.75	1	60000
$LLM4_{I+}$	–	75	35	40	2.75	2.3	60000
$LLM4_{r+}$	–	135	60	125	8	40	60000

A.7. Modified *Bessel* Functions for the Analytical Magnetic Field Calculation allowing for Free Eddy Currents

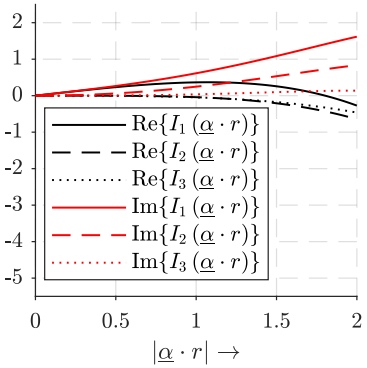

(a) Modified *Bessel* functions of 1st kind

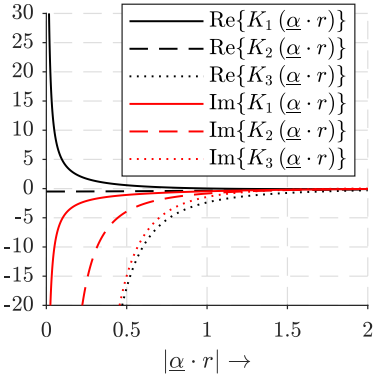

(b) Modified *Bessel* functions of 2nd kind

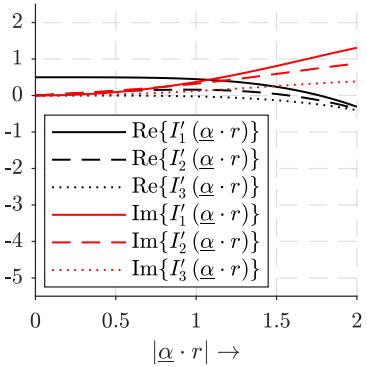

(c) Derivative of modified *Bessel* functions of 1st kind with regards to r

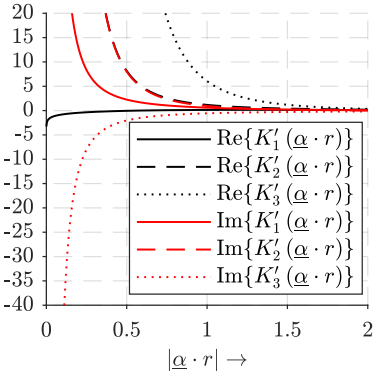

(d) Derivative of modified *Bessel* functions of 2nd kind with regards to r

Fig. A.4.: Modified *Bessel* functions of 1st and 2nd kind and their derivatives with regards to r up to space order 3

A.8. Solution Coefficients for the Analytical Field Calculation

Stator Field Calculation:

The linear equation system (2.31), resulting from the boundary conditions at the transition of two adjacent regions is solved in *Matlab*. In a first step, a symbolic variable is assigned to each region's outer and inner radius and to the region permeability and electric conductivity values by using the *Matlab* command *syms*. In case of eddy currents also symbolic variables are assigned to the modified *Bessel* function values at the transition of two adjacent regions. In a second step, the resulting linear equation system with symbolic variables is solved by using the *Matlab* function *linsolve()*. The solution is given by the solution coefficients $\underline{C}_1 = \underline{C}_{\mathrm{sh}}$, $\underline{C}_2 = \underline{C}_{\mathrm{PM}}$, $\underline{D}_2 = \underline{D}_{\mathrm{PM}}$, $\underline{C}_3 = \underline{C}_\delta$, $\underline{D}_3 = \underline{D}_\delta$, $\underline{C}_4 = \underline{C}_{\mathrm{S}}$, $\underline{D}_4 = \underline{D}_{\mathrm{S}}$ and $\underline{D}_5 = \underline{D}_{\mathrm{ex}}$. As an example, the solution coefficients C_δ and D_δ for the air gap region are given in (A.1), (A.2) with the following simplification for better readability: $\mu_{\mathrm{r,S}} \to \infty$, $r_{\mathrm{S,o}} \to \infty$, $\mu_{\mathrm{r,PM}} = 1$, $\kappa_{\mathrm{sh}} = 0$, $\kappa_{\mathrm{PM}} = 0$.

$$C_\delta = \frac{\mu_0 \cdot m \cdot k_{\mathrm{w},\nu'} \cdot N_{\mathrm{s}} \cdot \hat{I}_{\mathrm{s},k}}{\nu' \cdot \pi \cdot r_{\mathrm{S,i}}} \cdot \frac{{r_{\mathrm{PM}}}^{2\nu'} \cdot r_{\mathrm{S,i}} \cdot {r_{\mathrm{S,i}}}^{\nu'}}{\left({r_{\mathrm{PM}}}^{2\nu'} \cdot {r_{\mathrm{sh}}}^{2\nu'} - {r_{\mathrm{PM}}}^{2\nu'} \cdot {r_{\mathrm{S,i}}}^{2\nu'}\right)} \tag{A.1}$$

$$D_\delta = \frac{\mu_0 \cdot m \cdot k_{\mathrm{w},\nu'} \cdot N_{\mathrm{s}} \cdot \hat{I}_{\mathrm{s},k}}{\nu' \cdot \pi \cdot r_{\mathrm{S,i}}} \cdot \frac{{r_{\mathrm{PM}}}^{2\nu'} \cdot {r_{\mathrm{sh}}}^{2\nu'} \cdot r_{\mathrm{S,i}} \cdot {r_{\mathrm{S,i}}}^{\nu'}}{\left({r_{\mathrm{PM}}}^{2\nu'} \cdot {r_{\mathrm{sh}}}^{2\nu'} - {r_{\mathrm{PM}}}^{2\nu'} \cdot {r_{\mathrm{S,i}}}^{2\nu'}\right)} \tag{A.2}$$

The solution coefficients are inserted into the equations (2.27) and (2.28), resulting in (A.3) and (A.4) for the radius-dependent part of the air gap field wave (radial component: $B_{\mathrm{S},\nu',\mathrm{r},\delta}(r)$, tangential component $B_{\mathrm{S},\nu',\mathrm{r},\delta}(r)$). In this example, no eddy currents are considered, leading to real-valued solution coefficients and to the non-use of the modified *Bessel* functions. Once the symbolic expression of the flux density in the machine is known, a substitution of the symbolic variables by the numerical values regarding the material and geometric properties and regarding the space harmonic order ν' and the time harmonic order k is realized. This way, the time-consuming symbolic calculation is carried out only once, while the fast substitution can be realized many times. Note that the calculation is carried out for each space and time harmonic order separately. Afterwards, the field solutions of the harmonics are superimposed.

$$B_{\mathrm{S},\nu',\mathrm{r},\delta}(r) = \nu' \cdot \left(C_\delta \cdot r^{\nu'-1} + D_\delta \cdot r^{-\nu'-1}\right) \tag{A.3}$$

$$B_{\mathrm{S},\nu',\gamma,\delta}(r) = -\nu' \cdot \left(C_\delta \cdot r^{\nu'-1} + D_\delta \cdot r^{-\nu'-1}\right) \tag{A.4}$$

Rotor Field Calculation:

The linear equation system (2.52), resulting from the boundary conditions at the transition of two adjacent regions is solved in *Matlab*. In a first step, a symbolic variable is assigned to each region's outer and inner radius and to the region permeability values by using the *Matlab* command *syms*. In case of magnetization also symbolic variables are assigned to the magnetization values at the transition of two adjacent regions. In a second step, the resulting linear equation system with symbolic variables is solved by using the *Matlab* function *linsolve()*. The solution is given by the solution coefficients $X_1 = X_{\mathrm{sh}}$, $X_2 = X_{\mathrm{PM}}$, $Y_2 = Y_{\mathrm{PM}}$, $X_3 = X_\delta$, $Y_3 = Y_\delta$, $X_4 = X_{\mathrm{S}}$, $Y_4 = Y_{\mathrm{S}}$ and $X_5 = X_{\mathrm{ex}}$. As an example, the solution coefficients X_δ and Y_δ for the air gap region are given in (A.5), (A.6) for $\mu' = 1$ with the following simplification for better readability: $\mu_{\mathrm{r,S}} \to \infty$, $r_{\mathrm{S,o}} \to \infty$, $\mu_{\mathrm{r,PM}} = 1$.

$$X_\delta = -\frac{B_{\mathrm{rem}}}{2} \cdot \frac{r_{\mathrm{PM}} \cdot \left({r_{\mathrm{PM}}}^3 - r_{\mathrm{PM}} \cdot {r_{\mathrm{sh}}}^2\right)}{{r_{\mathrm{PM}}}^2 \cdot {r_{\mathrm{sh}}}^2 - {r_{\mathrm{PM}}}^2 \cdot {r_{\mathrm{S,i}}}^2} \tag{A.5}$$

$$Y_\delta = -\frac{B_{\mathrm{rem}}}{2} \cdot \frac{r_{\mathrm{PM}} \cdot {r_{\mathrm{S,i}}}^2 \cdot \left({r_{\mathrm{PM}}}^3 - r_{\mathrm{PM}} \cdot {r_{\mathrm{sh}}}^2\right)}{{r_{\mathrm{PM}}}^2 \cdot {r_{\mathrm{sh}}}^2 - {r_{\mathrm{PM}}}^2 \cdot {r_{\mathrm{S,i}}}^2} \tag{A.6}$$

The solution coefficients are inserted into the equations (2.49) and (2.50), resulting in (A.7) and (A.8) for the radius-dependent part of the air gap field wave (radial component $B_{\mathrm{R},\mu',\mathrm{r},\delta}(r)$, tangential component $B_{\mathrm{R},\mu',\gamma,\delta}(r)$). Once the symbolic expression of the flux density in the machine is known, a substitution of the symbolic variables by the numerical values regarding the material and geometric properties and regarding the space harmonic order ν' is realized. This way, the time-consuming symbolic calculation is carried out only once, while the fast substitution can be realized many times. Note that the calculation is carried out for each space and time harmonic order separately. Afterwards, the field solutions of the harmonics are superimposed.

$$B_{\mathrm{R},\mu',\mathrm{r},\delta}(r) = \mu' \cdot \left(X_\delta \cdot r^{\mu'-1} + Y_\delta \cdot r^{-\mu'-1}\right) \tag{A.7}$$

$$B_{\mathrm{R},\mu',\gamma,\delta}(r) = -\mu' \cdot \left(X_\delta \cdot r^{\mu'-1} + Y_\delta \cdot r^{-\mu'-1}\right) \tag{A.8}$$

A.9. Analytical Rotor Field Calculation for Radially Magnetized PM

The magnetization pattern and the characteristic along the rotor circumference are depicted in Fig. A.5 and A.6.

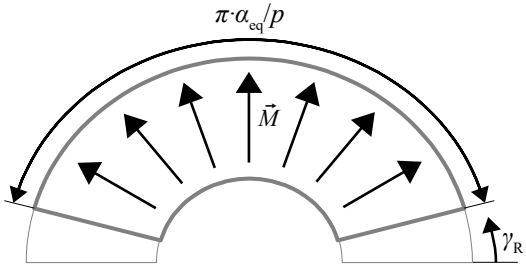

Fig. A.5.: Pole pitch of a radially magnetized PM

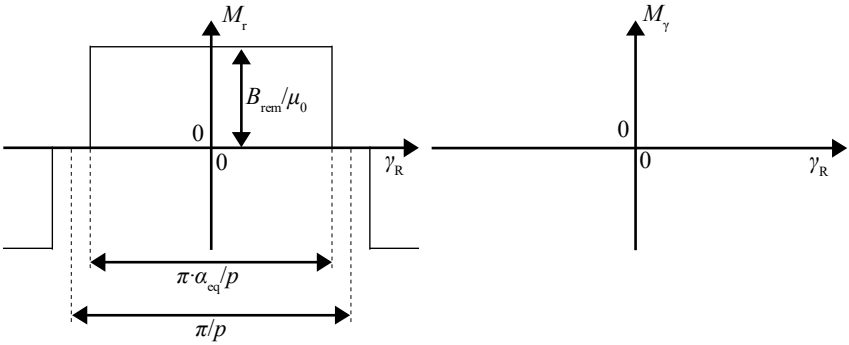

(a) Radial component M_r (b) Tangential component $M_\gamma = 0$

Fig. A.6.: Radial and tangential magnetization component for a radial magnetization pattern, similar to [86]

Accordingly, the *Fourier* coefficients $\hat{M}_{\mu',r}$ and $\hat{M}_{\mu',\gamma}$ from (2.43) are given by (A.9) and (A.10) [86].

$$\hat{M}_{\mu',r} = \frac{4 \cdot B_{rem}}{\mu_0 \cdot \mu \cdot \pi} \cdot \sin\left(\frac{\mu \cdot \pi \cdot \alpha_{eq}}{2}\right) \tag{A.9}$$

$$\hat{M}_{\mu',\gamma} = 0 \tag{A.10}$$

Since only a radial magnetization component $\hat{M}_{\mu',\mathrm{r}}$ is present, the coefficient $c_{\mu'}$ is given by (A.11) (calculation according to Section 2.2.4).

$$c_{\mu'}(r) = \begin{cases} \mu_0 \cdot \frac{\mu' \cdot \hat{M}_{\mu',\mathrm{r}}}{\mu'^2 - 1}; & \text{for } \mu' \neq 1 \\ -\mu_0 \cdot \frac{\hat{M}_{\mu',\mathrm{r}}}{2} \cdot \ln(r); & \text{for } \mu' = 1 \end{cases} \tag{A.11}$$

As an example, the analytically calculated field line plot as $|\underline{A}_\mathrm{z}| = \text{const.}$ for a 2-pole radial magnetization as in the *LLM4* and for a 4-pole radial magnetization are shown in Fig. A.7. In Fig. A.8a and A.8b the radial and circumferential component of the rotor air gap flux density is plotted in the middle of the mechanical air gap.

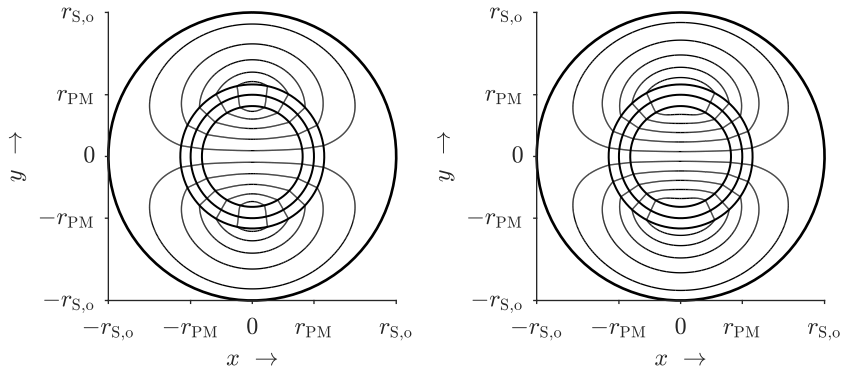

(a) $2p = 2$, $\alpha_{\mathrm{eq}} = 1$ (b) $2p = 2$, , $\alpha_{\mathrm{eq}} = 0.8$

Fig. A.7.: Analytically calculated magnetic field lines as lines $|\underline{A}_\mathrm{z}| = \text{const.}$ of the rotor field with radial magnetization at the time instant $t = 0$ ($B_{\mathrm{rem}} = 1$ T, radial magnetization, space harmonics $\mu < 25$ considered, model data from Table 2.1)

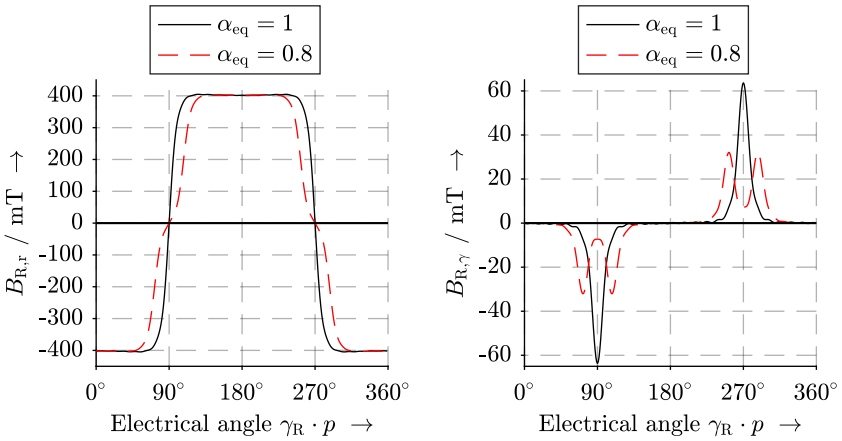

(a) Radial air gap field component

(b) Tangential air gap field component

Fig. A.8.: Analytically calculated rotor air gap field ($2p = 2$, $B_{rem} = 1$ T, radial magnetization, space harmonics $\mu < 25$ considered, model data from Table 2.1)

A.10. Condition Regarding Drive and Suspension Winding Angles

$$\frac{u \cdot \alpha_{ph}}{\alpha_{Q,D}} \in \mathbb{N} \wedge \frac{v \cdot \alpha_{ph}}{\alpha_{Q,L}} \in \mathbb{N};\ u, v \in \mathbb{N} \tag{A.12}$$

$$u \cdot \alpha_{ph} = u' \cdot \alpha_{Q,D} \wedge v \cdot \alpha_{ph} = v' \cdot \alpha_{Q,L};\ u', v' \in \mathbb{N}$$

$$u \cdot \frac{2\pi}{m} = u' \cdot \frac{2\pi}{Q} \cdot p \cdot t \wedge v \cdot \frac{2\pi}{m} = v' \cdot \frac{2\pi}{Q} \cdot p_L \cdot t$$

Suppose $p = w \cdot m; w \in \mathbb{N}, p_L = p \pm 1$:

$$u \cdot \frac{2\pi}{m} = u' \cdot \frac{2\pi}{Q} \cdot w \cdot m \cdot t \wedge v \cdot \frac{2\pi}{m} = v' \cdot \frac{2\pi}{Q} \cdot t \cdot (w \cdot m \pm 1) \tag{A.13}$$

$$\frac{u}{m} = u' \cdot t \cdot \frac{w}{2p \cdot q} \wedge \frac{v}{m} = v' \cdot t \cdot \frac{(w \cdot m \pm 1)}{2p \cdot q \cdot m}$$

$$u = \frac{u' \cdot t}{2 \cdot q} \wedge v = v' \cdot t \cdot \left(\frac{1}{2 \cdot q} \pm \frac{1}{2 \cdot q \cdot w \cdot m} \right) \lightning$$

That means, if the number of pole pairs p is an integer multiple of the phase count m, only

an integer multiple of the slot angle $\alpha_{\mathrm{Q,D}}$ of the drive winding meets an integer multiple of the phase angle α_{ph}. However, there is no integer multiple of the slot angle $\alpha_{\mathrm{Q,L}}$ of the suspension winding which meets an integer multiple of the phase angle α_{ph}. For the same reason, also the number of suspension pole pairs p_{L} must not be an integer multiple of the phase count.

A.11. Mutual Magnetic De-Coupling Requirement of Drive and Suspension Winding

If $p \in \mathbb{N}_{\mathrm{odd}}$, an integer multiple of the drive winding slot angle $\alpha_{\mathrm{Q,D}}$ must meet an odd integer multiple of $t \cdot \pi$, where t is the number of base winding schemes (A.14). In the last line of (A.14) n_{q} is co-prime with m (symmetry requirement) and with z_{q}. Therefore, u must be equal to $m \cdot z_{\mathrm{q}}$, and n_{q} must be odd.

$$\alpha_{\mathrm{Q,D}} \cdot u = \frac{2\pi}{Q} \cdot p \cdot t \cdot u = u' \cdot t \cdot \pi;\ u \in \mathbb{N}; u' \in \mathbb{N}_{\mathrm{odd}} \tag{A.14}$$

$$\frac{2\pi}{2p \cdot m \cdot \frac{z_{\mathrm{q}}}{n_{\mathrm{q}}}} \cdot p \cdot u = u' \cdot \pi$$

$$\frac{p}{p \cdot m \cdot \frac{z_{\mathrm{q}}}{n_{\mathrm{q}}}} \cdot u = u'$$

$$\frac{n_{\mathrm{q}}}{m \cdot z_{\mathrm{q}}} \cdot u = u' \rightarrow n_{\mathrm{q}} \in \mathbb{N}_{\mathrm{odd}}$$

A.12. Slot Plan and MMF Distribution for Odd and Even Pole Count $2p$

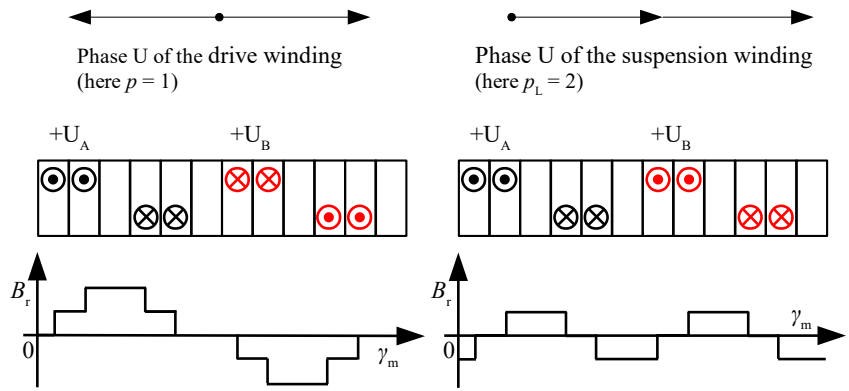

(a) p odd, p_L even

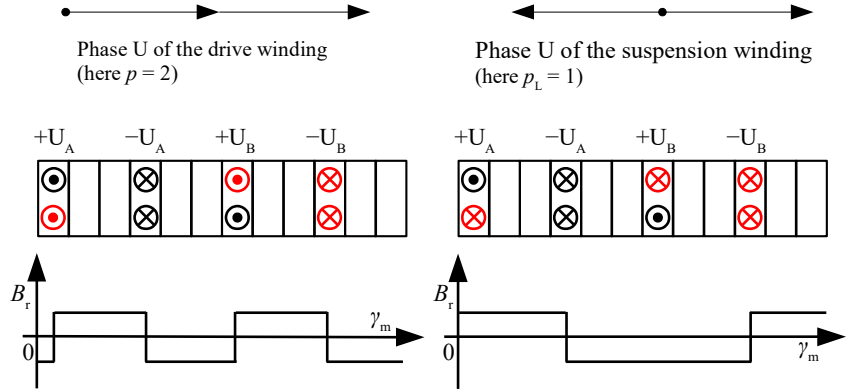

(b) p even, p_L odd

Fig. A.9.: Slot plan and radial air gap flux density $B_r(\gamma_m)$ for phase U for a 2-layer winding with $Q = 12$ stator slots

A.13. Structural Mechanics: Shaft Material Properties

Table A.5.: Structural mechanics: Shaft material properties at 100 °C

Steel:	1.4122 [156] (used)	1.4462 [157]
Type	martensitic	duplex
Young's modulus E / $\mathrm{kN \cdot mm^{-2}}$	215	194
Tensile yield strength $R_{\mathrm{p0.2}}$ / $\mathrm{N \cdot mm^{-2}}$	460	450
Tensile ultimate strength R_{m} / $\mathrm{N \cdot mm^{-2}}$	720 ... 900	650 ... 1000
Thermal expansion coefficient $\alpha_{\mathrm{th,exp}}$ / $10^{-6}/\cdot \mathrm{K^{-1}}$	10.4	13.25
Poisson ratio ν_{Po}	0.31	0.3
Mass density ρ / $\mathrm{kg \cdot m^{-3}}$	7700	7800

Table A.6.: Structural mechanics: PM material properties at 100 °C, (): used values

	$SmCo_5$ [158]	Sm_2Co_{17} [113]	NdFeB [113]
Young's modulus E / $\mathrm{kN \cdot mm^{-2}}$	100 ... 140	140 ... 170 (155)	140 ... 170 (165)
Compressive ultimate strength $R_{\mathrm{m,comp}}$ / $\mathrm{N \cdot mm^{-2}}$	600 ... 1100	400 ... 900 (700)	600 ... 1250 (900)
Tensile ultimate strength R_{m} / $\mathrm{N \cdot mm^{-2}}$	120	70 ... 120 (90)	(90)
Thermal expansion coefficient $\alpha_{\mathrm{th,exp,\parallel}}/\alpha_{\mathrm{th,exp}\perp}$ / $10^{-6}/\cdot \mathrm{K^{-1}}$	4 ... 10 / 10 ... 16	8 ... 12 (10) / 10 ... 14 (12)	4 ...9 (7) / -2 ... 0 (-1)
Poisson ratio ν_{p}	0.27	(0.27)	(0.24)
Mass density ρ / $\mathrm{kg \cdot m^{-3}}$	8400	(8300)	(7650)

Table A.7.: Structural mechanics: Bandage material properties at 100 °C

	glas fiber [114] (*Schunk* GF 411)[2)]	carbon fiber [114] (*Schunk* CF 411)[1)]
Matrix	epoxy resin	epoxy resin
Fiber portion	0.6	0.6
Young's modulus $E_{\parallel}/E_{\perp}$ / $\mathrm{kN \cdot mm^{-2}}$	45 / 10	120
Tensile ultimate strength $R_{\mathrm{m},\parallel}/R_{\mathrm{m},\perp}$ / $\mathrm{N \cdot mm^{-2}}$	1200	2200
Thermal expansion coefficient $\alpha_{\mathrm{th,exp},\parallel}/\alpha_{\mathrm{th,exp}\perp}$ / $10^{-6}/\cdot \mathrm{K^{-1}}$	8 / 35	< 0.2 / 45
Mass ensity ρ / $\mathrm{kg \cdot m^{-3}}$	(1900)	1550

[1)] Poisson ratios were not available, values from [9] were used instead: $\nu_{\mathrm{Po,r,z}}/\nu_{\mathrm{Po,r,\gamma}} = 0.388/0.023$, $\nu_{\mathrm{Po,z,r}}/\nu_{\mathrm{Po,z,\gamma}} = 0.388/0.023$, $\nu_{\mathrm{Po,\gamma,r}}/\nu_{\mathrm{Po,\gamma,z}} = 0.278/0.023$; [2)] Not used, only given for comparison

A.14. Magnetization Curve of Used Stator Iron Sheet Package Material

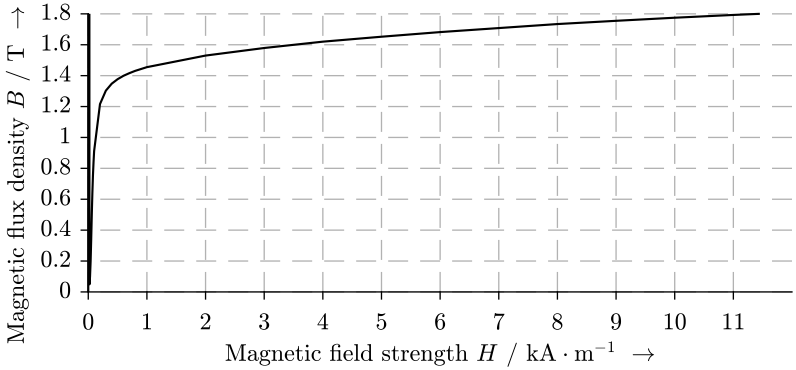

Fig. A.10.: Magnetization curve of used stator iron sheet package material M270-35A from manufacturer *C. D. Waelzholz GmbH & Co. KG* [93]

A.15. Simplified Rotor Geometry for Scaled Air Friction Loss Calculation

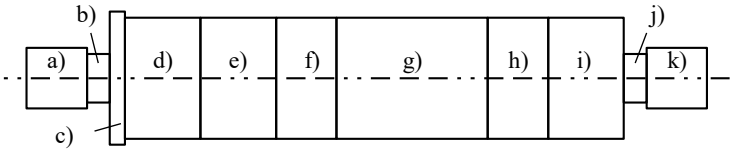

		Cylinder length	Cylinder radius	Distance to stator
a)	End shield:	$0.5 \cdot l_{\mathrm{Fe}}$	$0.6 \cdot (r_{\mathrm{s,i}} - \delta)$	δ
b)	Safety bearing:	$0.15 \cdot l_{\mathrm{Fe}}$	$0.5 \cdot (r_{\mathrm{s,i}} - \delta)$	$0.15 \cdot \delta$
c)	Axial bearing:	$0.1 \cdot l_{\mathrm{Fe}}$	$1.1 \cdot (r_{\mathrm{s,i}} - \delta)$	δ
d)	Measuring track:	20 mm	$r_{\mathrm{s,i}} - \delta$	δ
e)	Radial bearing:	$0.5 \cdot l_{\mathrm{Fe}}$	$r_{\mathrm{s,i}} - \delta$	δ
f)	Winding overhang:	$0.4 \cdot l_{\mathrm{Fe}}$	$r_{\mathrm{s,i}} - \delta$	δ
g)	Bearingless machine:	l_{Fe}	$r_{\mathrm{s,i}} - \delta$	δ
h)	Winding overhang:	$0.4 \cdot l_{\mathrm{Fe}}$	$r_{\mathrm{s,i}} - \delta$	δ
i)	Measuring track:	20 mm	$r_{\mathrm{s,i}} - \delta$	δ
j)	Safety Bearing:	$0.15 \cdot l_{\mathrm{Fe}}$	$0.5 \cdot (r_{\mathrm{s,i}} - \delta)$	$0.15 \cdot \delta$
k)	End shield:	$0.5 \cdot l_{\mathrm{Fe}}$	$0.6 \cdot (r_{\mathrm{s,i}} - \delta)$	δ

Fig. A.11.: Simplified rotor geometry for the calculation of air friction losses P_{Fr} according to [125] for varying machine size under the assumption of shrouded surfaces

A.16. Rotor Bending Eigenmodes

For a rotational symmetric rotor, approximated as one solid cylinder of length l and radius r, the first bending eigenfrequency $f_{\mathrm{bend},1,+} = f_{\mathrm{bend},1,-} = f_{\mathrm{bend},1}$ at standstill can be approximated by (A.15) [12], assuming infinitely stiff rigid bearings. $E = 215$ GPa is the *Young*'s modulus of the stainless steel shaft [156], and k_{bend} is the bending stiffness of the steel shaft as a cylinder. The rotor is approximated by the cylinder model with $m = 0.9$ kg, $r = 16$ mm and $l = 150$ mm. So the rotor overhang on both sides of the bearings is neglected.

$$f_{\text{bend},1} \approx \sqrt{\frac{k_{\text{bend}}}{m}} = 2139 \text{ Hz}, \quad \text{where } k_{\text{bend}} = 48 \cdot \frac{E \cdot \frac{\pi}{4} \cdot r^4}{l^3} \tag{A.15}$$

The result is 33% lower than the simulation result, using *ANSYS Workbench 18.1* (Fig. A.12), although elastic bearings with stiffness values according to Table 5.1 are used for the simulation. The result shows that no critical speed is to be expected from the rotor bending eigenmodes, since the maximum speed is only $n_{\text{max}} = 1000$ Hz. The simulation was carried out for n_{max} and with the material properties from Table A.5, A.6 and A.7.

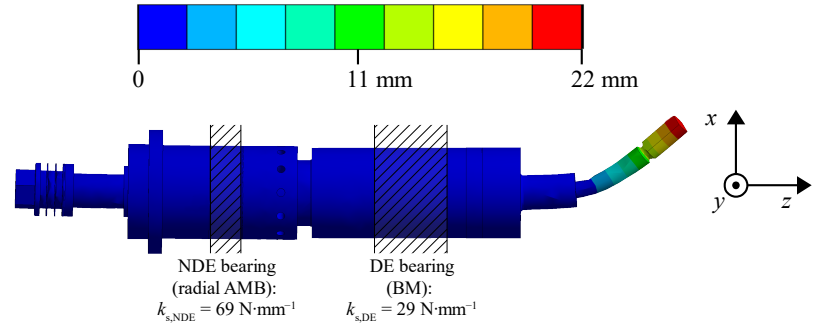

(a) 1st bending eigenmode at $f_{\text{bend},1,-} = 2844.4$ Hz, $f_{\text{bend},1,+} = 2872.3$ Hz

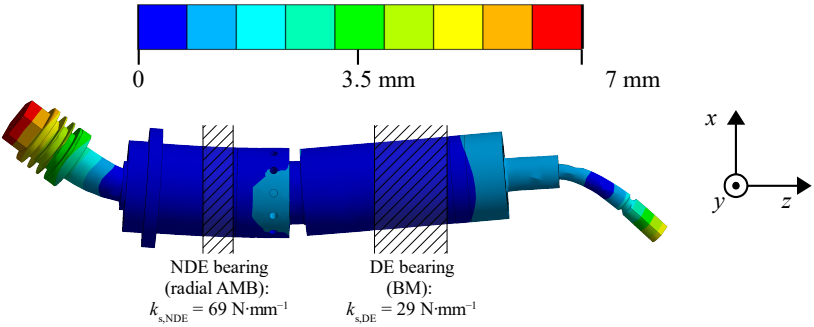

(b) 2nd bending eigenmode at $f_{\text{bend},2,-} = 4109.3$ Hz, $f_{\text{bend},2,+} = 4126.1$ Hz

Fig. A.12.: Simulated total deformation due to the bending body eigenmodes of the rotor of the *LLM4* (*ANSYS Workbench 18.1*), boundary condition: fixed stator (housing), bearing stiffness according to Table 5.1 applied to the shaded areas, speed $n = 60000$ min^{-1}, deformation gain for visibility: 2

A.17. Calculation of the Drive Current for Bearingless Machines with Separated Drive and Suspension Windings

The copper round wire cross section A_{Cu} of one winding turn is calculated with (A.16), (A.17), where $k_{\mathrm{share,L,sep}}$ is the ratio of suspension winding to total stator slot cross section. By means of (A.18) and with the knowledge of the rated suspension winding current $I_{\mathrm{L,N}}$ from (A.22), the suspension winding copper losses are calculated in (A.20). Note that the suspension winding turn count $N_{\mathrm{s,L}}$ should be chosen in order to comply with the suspension winding inverter's current limit. The rest of the available losses is allocated to the drive winding copper losses $P_{\mathrm{Cu,D}}$ in (A.21). With $P_{\mathrm{Cu,D}}$ and $R_{\mathrm{s,D,100°C}}$ from (A.19), the rated drive winding current $I_{\mathrm{D,N}}$ is calculated in (A.23).

$$A_{\mathrm{Cu,L}} = \frac{A_{\mathrm{Q}} \cdot k_{\mathrm{share,L,sep}} \cdot k_{\mathrm{Q}} \cdot Q}{m \cdot N_{\mathrm{s,L}} \cdot a_{\mathrm{L}}} \tag{A.16}$$

$$A_{\mathrm{Cu,D}} = \frac{A_{\mathrm{Q}} \cdot \left(1 - k_{\mathrm{share,L,sep}}\right) \cdot k_{\mathrm{Q}} \cdot Q}{m \cdot N_{\mathrm{s,D}} \cdot a_{\mathrm{D}}} \tag{A.17}$$

$$R_{\mathrm{s,L,100°C}} = \frac{2 \cdot N_{\mathrm{s,L}} \cdot \left(l_{\mathrm{Fe}} + l_{\mathrm{b,L}}\right)}{A_{\mathrm{Cu,L}} \cdot a_{\mathrm{L}} \cdot \kappa_{\mathrm{Cu,100°C}}} \tag{A.18}$$

$$R_{\mathrm{s,D,100°C}} = \frac{2 \cdot N_{\mathrm{s,D}} \cdot \left(l_{\mathrm{Fe}} + l_{\mathrm{b,D}}\right)}{A_{\mathrm{Cu,D}} \cdot a_{\mathrm{D}} \cdot \kappa_{\mathrm{Cu,100°C}}} \tag{A.19}$$

$$P_{\mathrm{Cu,L}} = m \cdot R_{\mathrm{s,100°C}} \cdot \left(\frac{\hat{I}_{\mathrm{s,L,N}}}{\sqrt{2}}\right)^2 \tag{A.20}$$

$$P_{\mathrm{Cu,D}} = P_{\mathrm{d,lim}} - P_{\mathrm{Fr}} - P_{\mathrm{Fe}} - P_{\mathrm{Cu,L}} \tag{A.21}$$

$$\hat{I}_{\mathrm{s,L,N}} \cdot N_{\mathrm{s,L}} = \frac{m_{\mathrm{R,act}} \cdot g \cdot 3 \cdot 2 \cdot r_{\mathrm{S,i}} / l_{\mathrm{Fe}}}{k_{\mathrm{F,DE}} = f\left(N_{\mathrm{s,L}}\right)} \cdot N_{\mathrm{s,L}} = i_{\mathrm{q,L,N}} \cdot N_{\mathrm{s,L}} \tag{A.22}$$

$$\hat{I}_{\mathrm{s,D,N}} = \sqrt{2 \cdot \frac{P_{\mathrm{Cu,D}}}{m \cdot R_{\mathrm{s,D,100°C}}}} = i_{\mathrm{q,D,N}} \tag{A.23}$$

A.18. Torque-Current and Force-Current Coefficients for 2-Pole Rotor Topologies

(A.24) is based on simplifications according to "$2\mathrm{D}_{\mathrm{simp}}$" from Table 4.1. It is valid for a parallelly magnetized rotor PM of full pole coverage ($\alpha_{\mathrm{eq}} = 1$). For simplification, the tangential rotor field component $B_{\gamma,\mathrm{R}}$ is neglected, resulting in an error $< 0.5\%$.

$$k_{\mathrm{M}} = B_{\mathrm{rem}} \cdot l_{\mathrm{Fe}} \cdot m \cdot k_{\mathrm{w,D}} \cdot N_{\mathrm{s}} \cdot r_{\mathrm{PM}}^2 \cdot r_{\mathrm{S,i}}^2 \cdot \left(\frac{r_{\mathrm{S,i}}^2}{r_{\mathrm{calc}}^2} + 1 \right) \cdot \left(r_{\mathrm{PM}}^2 - r_{\mathrm{sh}}^2 \right) \cdot \tag{A.24}$$
$$\frac{\left(\left(r_{\mathrm{PM}}^2 \cdot r_{\mathrm{calc}}^2 - r_{\mathrm{PM}}^2 \cdot r_{\mathrm{sh}}^2 \right) \cdot \left(\mu_{r,\mathrm{PM}} + 1 \right) + \left(r_{\mathrm{sh}}^2 \cdot r_{\mathrm{calc}}^2 - r_{\mathrm{PM}}^4 \right) \cdot \left(\mu_{r,\mathrm{PM}} - 1 \right) \right)}{\left(\left(r_{\mathrm{PM}}^2 \cdot r_{\mathrm{sh}}^2 - r_{\mathrm{PM}}^2 \cdot r_{\mathrm{S,i}}^2 \right) \cdot \left(\mu_{r,\mathrm{PM}} + 1 \right) - \left(r_{\mathrm{sh}}^2 \cdot r_{\mathrm{S,i}}^2 - r_{\mathrm{PM}}^4 \right) \cdot \left(\mu_{r,\mathrm{PM}} - 1 \right) \right)^2}$$

$$k_{\mathrm{F}} = l_{\mathrm{Fe}} \cdot m \cdot k_{\mathrm{w,L}} \cdot N_{\mathrm{s}} \cdot B_{\mathrm{rem}} \cdot r_{\mathrm{PM}}^2 \cdot r_{\mathrm{S,i}}^2 \cdot \left(r_{\mathrm{calc}}^2 + r_{\mathrm{S,i}}^2 \right) \cdot \tag{A.25}$$
$$\frac{\left[\left(\mu_{r,\mathrm{PM}} + 1 \right) \cdot r_{\mathrm{PM}}^4 + \left(\mu_{r,\mathrm{PM}} - 1 \right) \cdot r_{\mathrm{sh}}^4 \right] \cdot \left(r_{\mathrm{PM}}^2 - r_{\mathrm{sh}}^2 \right)}{\left[\left(r_{\mathrm{PM}}^2 \cdot r_{\mathrm{sh}}^2 - r_{\mathrm{PM}}^2 \cdot r_{\mathrm{S,i}}^2 \right) \cdot \left(\mu_{r,\mathrm{PM}} + 1 \right) - \left(r_{\mathrm{sh}}^2 \cdot r_{\mathrm{S,i}}^2 - r_{\mathrm{PM}}^4 \right) \cdot \left(\mu_{r,\mathrm{PM}} - 1 \right) \right] \cdot \left[\left(r_{\mathrm{PM}}^4 \cdot r_{\mathrm{sh}}^4 - r_{\mathrm{PM}}^4 \cdot r_{\mathrm{S,i}}^4 \right) \cdot \left(\mu_{r,\mathrm{PM}} + 1 \right) - \left(r_{\mathrm{sh}}^4 \cdot r_{\mathrm{S,i}}^4 - r_{\mathrm{PM}}^8 \right) \cdot \left(\mu_{r,\mathrm{PM}} - 1 \right) \right]}$$

A.19. Determination of the Suspension Force-Current Coefficient for the NdFeB-Rotor

Table A.8.: Determination of the force-current coefficient $k_{\mathrm{F,DE}}$ from measured currents for the *LLM4* with the NdFeB-rotor at concentric rotor position: The rotor center of gravity is at $x = y = z = 0$.

	$i_{\mathrm{d,L}}$	$i_{\mathrm{q,L}}$	$i_{\mathrm{x,NDE}}$	$i_{\mathrm{y,NDE}}$	i_{ax}
Vertical rotor position (y-axis is direction of gravity)					
I_{DC} / A	1.82	0.14	0.12	0.4	0.50
I_{AC} / A	3.44	3.70	0.04	0.04	–
Horizontal rotor position (y-axis is direction of gravity)					
I_{DC} / A	1.88	5.37	0.12	0.60	0.24
I_{AC} / A	3.32	3.56	0.04	0.04	–
	$F_{\mathrm{G,DE}} = 5.85$ N		$F_{\mathrm{G,NDE}} = 3.08$ N		$F_{\mathrm{G,ax}} = 8.93$ N
	$k_{\mathrm{F,DE}} = 1.09\ \mathrm{N \cdot A^{-1}}$		$k_{\mathrm{F,NDE}} = 15.2\ \mathrm{N \cdot A^{-1}}$		$k_{\mathrm{F,ax}} = 35.34\ \mathrm{N \cdot A^{-1}}$

A.20. Flywheel Energy Storage System: Pictures and Drawings

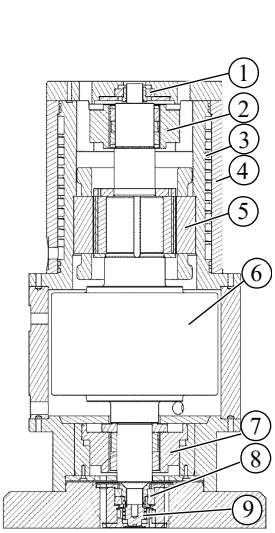

(a) Stator and rotor parts

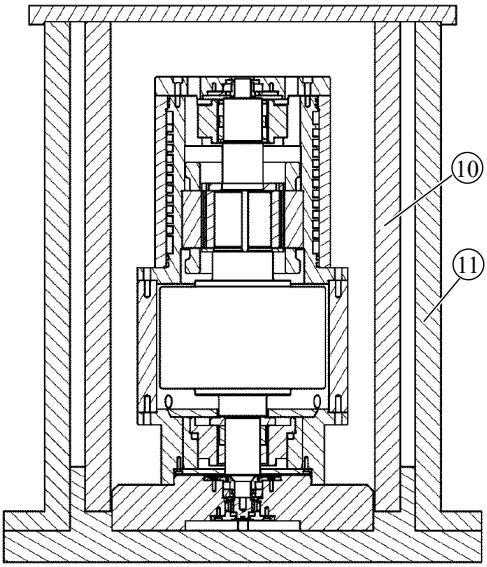

(b) Vacuum- and burst containment

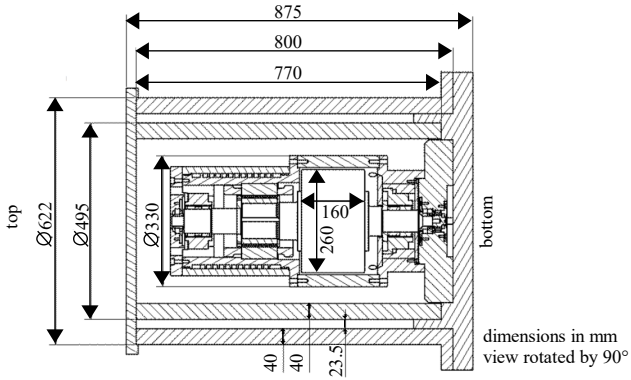

(c) Dimensions

Fig. A.13.: Composition and dimensions of the flywheel energy storage system: ①: DE safety bearing, ②: DE radial magnetic bearing, ③: water cooling channels, ④: stator housing, ⑤: PM synchronous machine stator, ⑥: flywheel body, ⑦: NDE radial-/axial combined magnetic bearing, ⑧: NDE safety bearing, ⑨: axial rotor position sensor, ⑩: inner burst containment, ⑪: outer vacuum- / burst containment

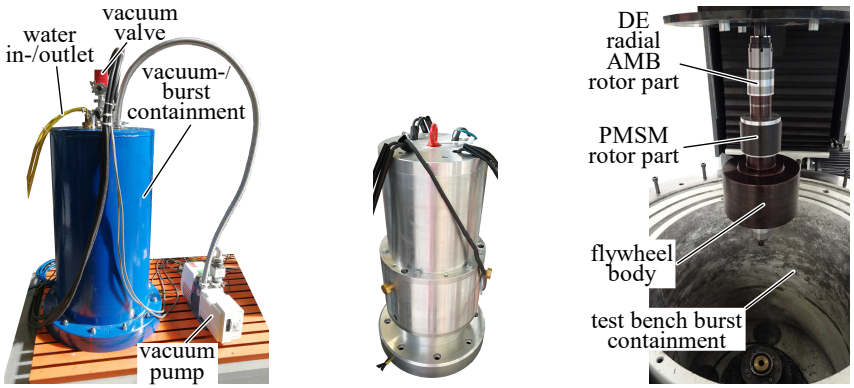

(a) Complete flywheel energy storage system

(b) Stator housing

(c) Rotor at the spin test at *SCHENCK RoTec GmbH, Darmstadt*

Fig. A.14.: Pictures of the flywheel energy storage system

A.21. Validation of the Rotor Position Control of the Flywheel Energy Storage System

The flywheel energy storage system was successfully operated at its maximum speed $n_N = 24000\ \text{min}^{-1}$. Fig. A.15b shows the measured rotor position signals $y_{se,filt,DE}$, $y_{se,filt,NDE}$ during a run-up to maximum speed. In these signals, the rotational frequency $f = n$ is filtered by an adaptive notch filter for $n > 8400\ \text{min}^{-1}$. In Fig. A.15a, the unfiltered signals $y_{se,DE}$, $y_{se,NDE}$. The following conclusions are drawn:

- The parallel and conical rigid body eigenfrequencies (=critical speeds $n_{crit,1}$ (parallel) and $n_{cirt,2}$ (conical)) at low speed are in the range of $f_{crit,1} \approx f_{crit,2} \approx 40$ Hz (compare Table 5.3).
- The controller transfer behavior worsens for higher speed values up to $n = 8400\ \text{min}^{-1}$, so that the orbit of the DE rotor part, which comprises the upper AMB at the opposite side of flywheel body, increases.
- For $n > 8400\ \text{min}^{-1}$, the adaptive notch filter is effective, so that the rotor orbits stay constants until $n = 24000\ \text{min}^{-1}$: $y_{se,DE,max} = 13\ \mu$m, $y_{se,NDE,max} = 29\ \mu$m. The rotor rotates around its principal axis of inertia.
- One stator bending body mode eigenfrequency $f_{flex,1} \approx 200$ Hz is passed at $n = 12000\ \text{min}^{-1}$ by the rotational frequency (compare Fig. A.19).

- At $n = 24000\ \text{min}^{-1}$, the conical forward-whirl and the parallel backward-whirl rigid body eigenmodes are weakly damped, which leads to a slight increase of the rotor orbit (compare Fig. A.18a, A.18b).

In the Fig. A.16 – A.18 the measured frequency sweep amplitude responses (0 ... 1200 Hz) of the AMBs for x- and φ_x-direction at $n = 0$, $n = 9000\ \text{min}^{-1}$ and $n = 24000\ \text{min}^{-1}$ are shown. The sweep of frequency from 0 Hz to 1200 Hz was applied during a time of 0 ... 3 s. For a common-mode sweep amplitude response, in both AMBs a sinusoidal reference position of amplitude $\hat{y}_{\text{se,ref,NDE}} = \hat{y}_{\text{se,ref,DE}} = 10\ \mu\text{m}$ is applied. With that, mainly the parallel rigid body eigenmodes of the rotor are excited. For a differential-mode response, in the NDE AMB a sinusoidal reference position of amplitude $\hat{y}_{\text{se,ref,NDE}} = 10\ \mu\text{m}$ is applied, whereas in phase opposition $\hat{y}_{\text{se,ref,NDE}} = -5.9\ \mu\text{m}$ is demanded in the DE AMB. The values $\hat{y}_{\text{se,ref,NDE}} = 10\ \mu\text{m}$ and $\hat{y}_{\text{se,ref,NDE}} = -5.9\ \mu\text{m}$ result from the location of the COG (Table 5.1). With the differential-mode excitation, mainly the conical rigid body eigenmodes are excited. An exact separation between conical and parallel, forward- and backward-whirling, mode excitation is not possible due to slight inaccuracies in the sensor calibrations. Also the flexible body modes are excited by these frequency sweeps. However, the observability and controllability depends on the location of the bending nodes with respect to the location of the magnetic bearings and the sensors.
The frequency sweep amplitude responses are shown for $n = 0$ (Fig. A.16), for $n = 9000\ \text{min}^{-1}$ (Fig. A.17) and for $n_{\text{N}} = 24000\ \text{min}^{-1}$ (Fig. A.18) to account for the speed dependency of the eigenvalues due to the gyroscopic effect (compare Fig. 5.5, Table 5.2). Regarding the rigid body eigenmodes the following is concluded:

- At standstill ($n = 0$), the eigenfrequency of the parallel (Fig. A.16a) and the conical (Fig. A.16b) mode are in the range of $f \approx 40$ Hz, agreeing with Table 5.2. The parallel eigenmode is less damped than the conical eigenmode.
- At $n = 9000\ \text{min}^{-1}$ both parallel and conical rigid body modes are well damped (Fig. A.17a, A.17b).
- At $n = 24000\ \text{min}^{-1}$ both rigid body modes are weakly damped. The eigenfrequencies of these modes are in the range of $f \approx 8$ Hz. The reduction of the eigenfrequencies associated with a smaller damping agrees with Fig. 5.5. Still the damping is sufficient for a stable operation.

The 3D simulated (*ANSYS* Workbench 18.1) flexible body eigenmodes are shown in Fig. A.19 for a speed of $n_{\text{N}} = 24000\ \text{min}^{-1}$. It is very important that the stator and the

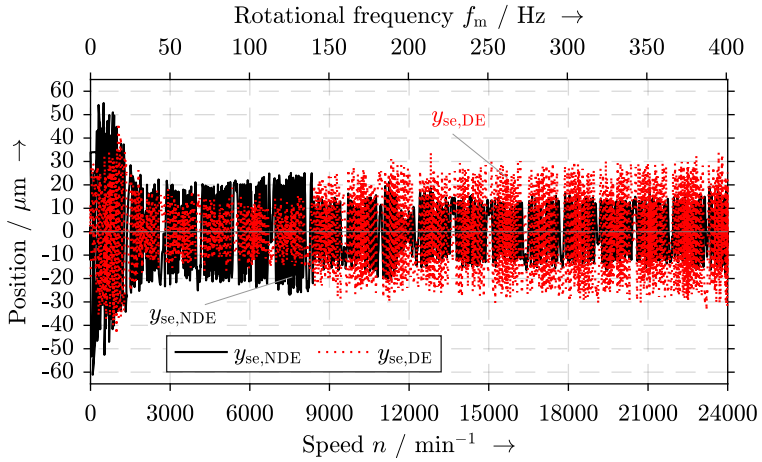

(a) Measured unfiltered position sensor signals y_{se}

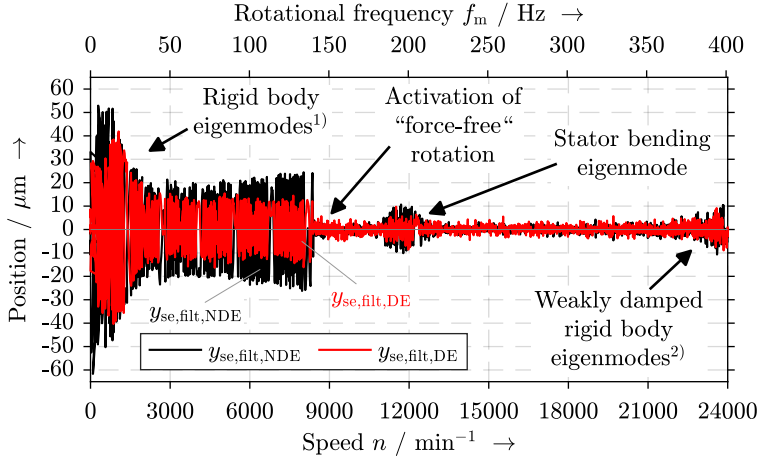

(b) Measured filtered position sensor signals y_{filt} (adaptive notch filter at rotational frequency for $n > 8400$ min^{-1}) [1)]: forward- and backward-whirling, parallel and conical eigenmodes, [2)]: forward-whirling conical eigenmode and backward-whirling parallel eigenmode

Fig. A.15.: Measured position sensor signal during a run-up of the flywheel energy storage system (aliasing effect visible at integer multiples of the sampling frequency $f_{samp} = 23$ Hz), controller sampling frequency $f_{sw}/2 = 11$ kHz

housing of the flywheel system is not considered fixed. A fixation as a boundary condition is only set on the bottom of the housing, where the flywheel system is screwed to

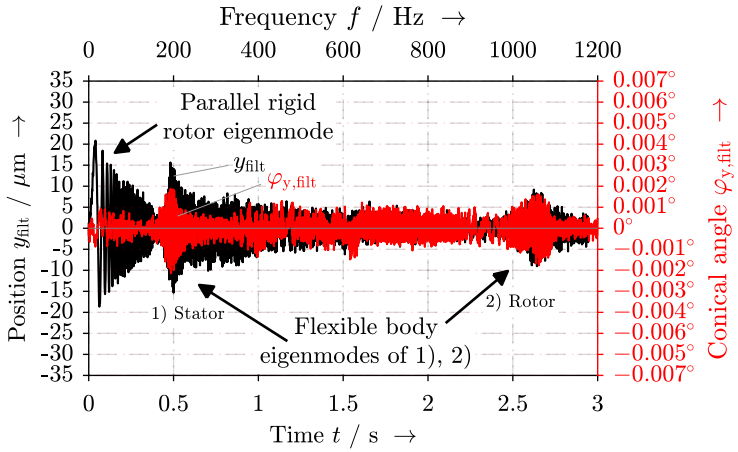

(a) Common-mode sweep amplitude response: $\hat{y}_{\mathrm{se,ref,NDE}} = 10\ \mu\mathrm{m}$, $\hat{y}_{\mathrm{se,ref,DE}} = 10\ \mu\mathrm{m}$, $f = 0...1200$ Hz, $t = 0...3$ s

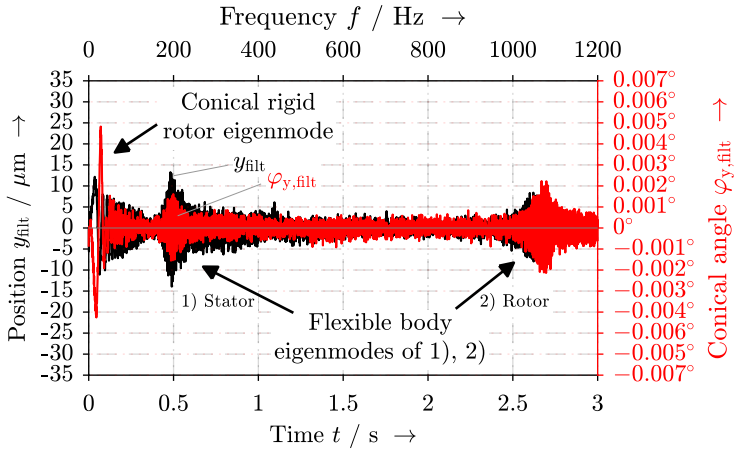

(b) Differential-mode sweep amplitude response: $\hat{y}_{\mathrm{se,ref,NDE}} = -5.9\ \mu\mathrm{m}$, $\hat{y}_{\mathrm{se,ref,DE}} = 10\ \mu\mathrm{m}$, $f = 0...1200$ Hz, $t = 0...3$ s

Fig. A.16.: Flywheel energy storage system at speed $n = 0$: Measured filtered position sensor signals over time, respectively frequency, transformed into the COG-coordinates (y_{filt}, $\varphi_{\mathrm{y,filt}}$) during a frequency sweep (0 ... 1200 Hz) of the reference position signals in the sensor coordinate system ($y_{\mathrm{se,ref,DE}}$, $y_{\mathrm{se,ref,NDE}}$)

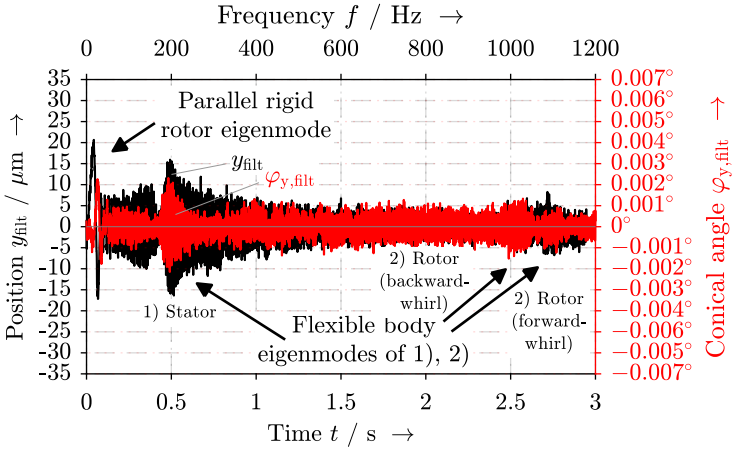

(a) Common-mode sweep amplitude response: $\hat{y}_{\text{se,ref,NDE}} = 10\ \mu\text{m}$, $\hat{y}_{\text{se,ref,DE}} = 10\ \mu\text{m}$, $f = 0...1200$ Hz, $t = 0...3$ s

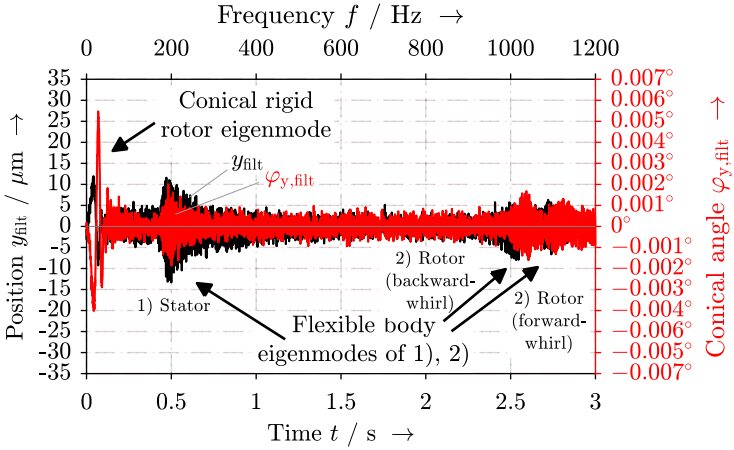

(b) Differential-mode sweep amplitude response: $\hat{y}_{\text{se,ref,NDE}} = -5.9\ \mu\text{m}$, $\hat{y}_{\text{se,ref,DE}} = 10\ \mu\text{m}$, $f = 0...1200$ Hz, $t = 0...3$ s

Fig. A.17.: Flywheel energy storage system at speed $n = 9000\ \text{min}^{-1}$: Measured filtered position sensor signals over time, respectively frequency, transformed into the COG-coordinates (y_{filt}, $\varphi_{\text{y,filt}}$) during a frequency sweep (0 ... 1200 Hz) of the reference position signals in the sensor coordinate system ($y_{\text{se,ref,DE}}$, $y_{\text{se,ref,NDE}}$)

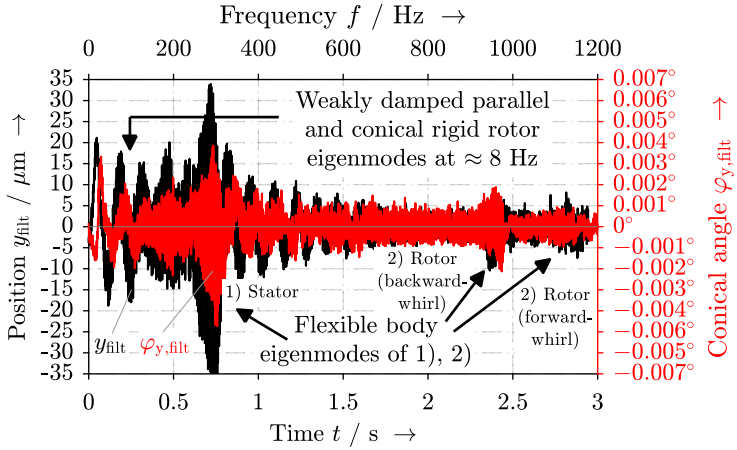

(a) Common-mode sweep amplitude response: $\hat{y}_{\text{se,ref,NDE}} = 10\ \mu\text{m}$, $\hat{y}_{\text{se,ref,DE}} = 10\ \mu\text{m}$, $f = 0...1200$ Hz, $t = 0...3$ s

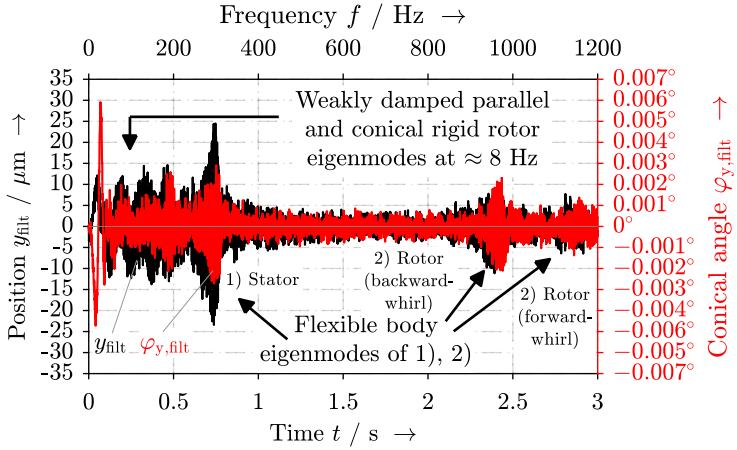

(b) Differential-mode sweep amplitude response: $\hat{y}_{\text{se,ref,NDE}} = -5.9\ \mu\text{m}$, $\hat{y}_{\text{se,ref,DE}} = 10\ \mu\text{m}$, $f = 0...1200$ Hz, $t = 0...3$ s

Fig. A.18.: Flywheel energy storage system at speed $n_{\text{N}} = 24000\ \text{min}^{-1}$: Measured filtered position sensor signals over time, respectively frequency, transformed into the COG-coordinates (y_{filt}, $\varphi_{\text{y,filt}}$) during a frequency sweep (0 ... 1200 Hz) of the reference position signals in the sensor coordinate system ($y_{\text{se,ref,DE}}$, $y_{\text{se,ref,NDE}}$)

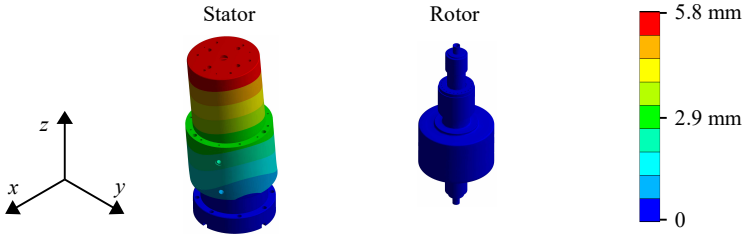

(a) Stator flexible body bending modes at $f_{\text{flex},1,-} = 246.5$ Hz, $f_{\text{flex},1,+} = 246.8$ Hz

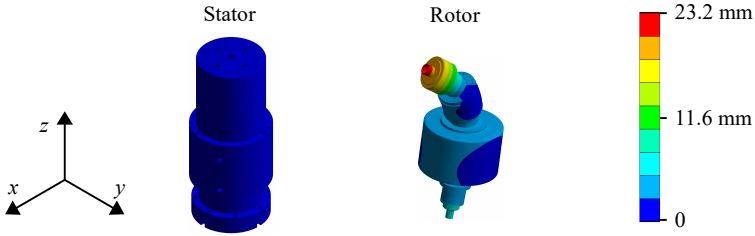

(b) Rotor flexible body bending modes at $f_{\text{flex},2,-} = 1018.9$ Hz, $f_{\text{flex},2,+} = 1183.7$ Hz

Fig. A.19.: Simulated total deformation due to the flexible body eigenmodes of the flywheel energy storage system with flexible housing and rotor (*ANSYS Workbench 18.1*). Boundary conditions: Fixed housing bottom, rotor speed $n_{\text{N}} = 24000\ \text{min}^{-1}$, bearing stiffness according to Table 5.1 applied in the bearing area according to Fig. A.13a, deformation gain for visibility: 50

the bench. If the stator was considered to be fixed and, thus, rigid, and only the rotor bending modes were simulated, the resulting eigenfrequencies would not fit to the sweep amplitude responses (Fig. A.16–A.18). Regarding the flexible body modes the following conclusions are drawn:

- The flexible body modes at $f_{\text{flex},1,-} = 246.5$ Hz, $f_{\text{flex},1,+} = 246.8$ Hz for the stator bending and at $f_{\text{flex},2,-} = 1018.9$ Hz, $f_{\text{flex},2,+} = 1183.7$ Hz for the rotor bending are dominant for varying rotor speed. The flexible body mode at $f_{\text{flex},1}$ is a movement of the top of the housing like a whip (Fig. A.19a). To suppress it, an increase of the housing stiffness would be necessary, which was not possible due to the needed vacuum containment. The flexible mode at $f_{\text{flex},2,+}$, $f_{\text{flex},2,-}$ is the 1^{st} order rotor bending mode (Fig. A.19b) with forward- and backward-whirl.
- The eigenmode of the bending stator housing at $f_{\text{flex},1-} \approx f_{\text{flex},1+}$ is independent of the rotor speed n, since it is a stator eigenmode, which is not affected by the gy-

roscopic effect (compare Fig. A.16 and Fig. A.17). Only at $n_N = 24000\ \text{min}^{-1}$ (Fig. A.18), the maximum rotor position amplitudes are located at $f \approx 300$ Hz, which is due to the superposition of the weakly damped rigid body eigenmodes and the stator flexible body mode.

- The eigenfrequency $f_{\text{flex},2}$ of the 1st rotor bending eigenmode is split into two frequency components $f_{\text{flex},2,-}$, $f_{\text{flex},2,+}$ due to the gyroscopic effect, among which dominant oscillations are observed at $f_{\text{flex},2,-}$. The eigenfrequency $f_{\text{flex},2,-}$ decreases for higher speed, whereas $f_{\text{flex},2,+}$ increases with rising speed (compare Fig. A.16a and Fig. A.18a).
- The deviations between the measured amplitude peaks in the frequency sweep amplitude responses and the simulated eigenfrequencies may be due to deficiencies in the sensor calibration, due to deviations in the assumed magnetic bearing stiffness values and due to the limited observability of the rotor and stator motions, which depends on the location of the bending nodes with respect to the location of the position sensors at the DE and NDE.

Table A.9.: Simulated eigenfrequencies for the flywheel energy storage system at $n_N = 24000\ \text{min}^{-1}$ with *ANSYS Workbench 18.1*, stiffness values from Table 5.1

Rigid rotor modes		Flexible body modes	
$f_{\text{par},+}$ / Hz	15.7	Stator bending: $f_{\text{flex},1,+}$ / Hz	246.5
$f_{\text{par},-}$ / Hz	14.0	Stator bending: $f_{\text{flex},1,-}$ / Hz	246.8
$f_{\text{con},+}$ / Hz	204.2	Rotor bending: $f_{\text{flex},2,+}$ / Hz	1018.9
$f_{\text{con},-}$ / Hz	36.2	Rotor bending: $f_{\text{flex},2,-}$ / Hz	1183.7

A.22. Speed-Up/-Down Test Results with the NdFeB Rotor

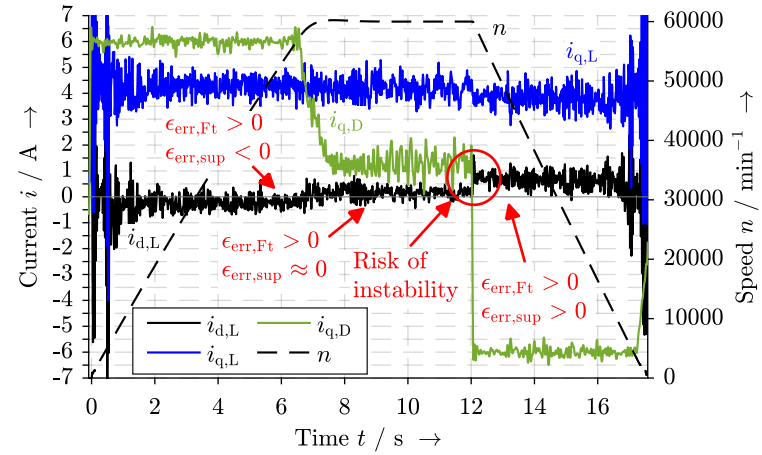

(a) Measured suspension currents $i_{d,L}$, $i_{q,L}$, drive current $i_{q,D}$ and speed n

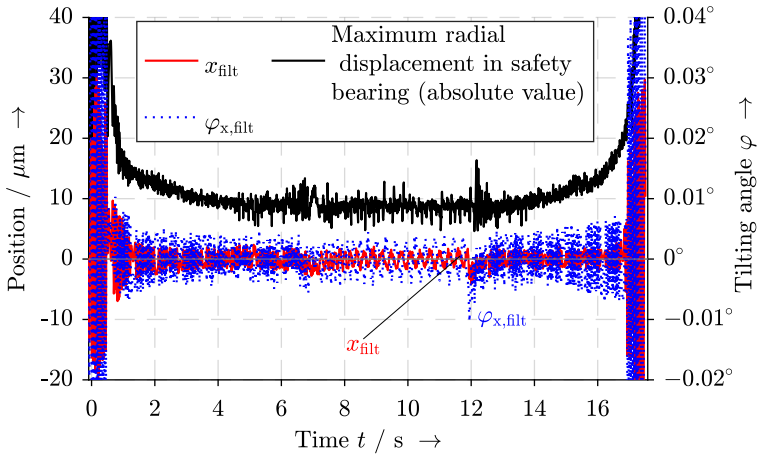

(b) Measured filtered position sensor signals x_{filt}, $\varphi_{x,filt}$, transformed into the COG-coordinates (adaptive notch filter at rotational frequency for $n > 6000$ min^{-1}) and radial displacement in the safety bearing with a clearance of 150μm

Fig. A.20.: Measured run-up/run-down for the prototype machine *LLM4* with the NdFeB-rotor, acceleration/deceleration with $|i_{q,D}| = 6$ A resulting in $|\varepsilon_{err,sup}| = 1.5°$. The eddy current error angle at $n = n_N$ is $\varepsilon_{err,Ft} = 2.7°$. $0 \le t \le 6.5$ s: motor operation; 6.5 s $\le t \le 12$ s: motor no-load; $t > 12$ s: braking generator operation (aliasing effect visible due to sampling frequency: $f_{samp} = 34.5$ Hz), controller sampling frequency $f_{sw}/2 = 16.5$ kHz

A.23. Symmetrical Space Vector Pulse Width Modulation (SV-PWM)

In the symmetrical SV-PWM, the reference voltage space vector in stator-fixed complex α-β-coordinates is approximated over one switching period T_{sw} by the discrete voltage space vectors that result from the discrete switching states ⓪, ..., ⑦ in Fig. A.21. Gen-

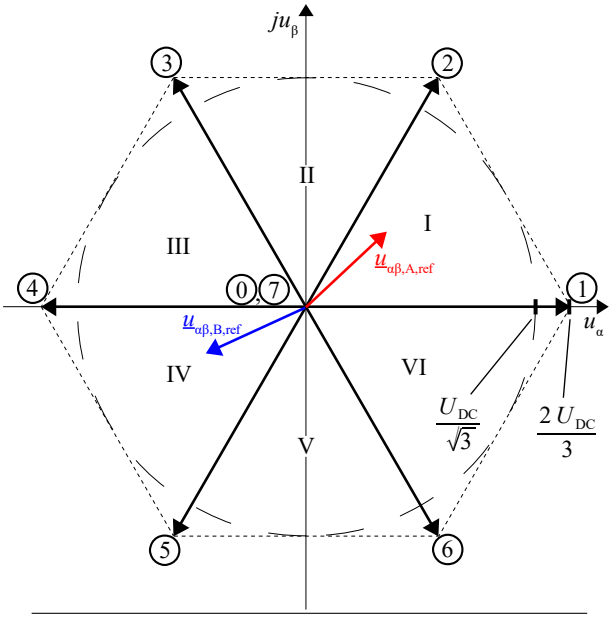

No.	Time span	φ_N	φ_U	φ_V	φ_W
⓪	t_0	$-U_{DC}/2$	$-U_{DC}/2$	$-U_{DC}/2$	$-U_{DC}/2$
①	t_1	$-U_{DC}/6$	$U_{DC}/2$	$-U_{DC}/2$	$-U_{DC}/2$
②	t_2	$U_{DC}/6$	$U_{DC}/2$	$U_{DC}/2$	$-U_{DC}/2$
③	t_3	$-U_{DC}/6$	$-U_{DC}/2$	$U_{DC}/2$	$-U_{DC}/2$
④	t_4	$U_{DC}/6$	$-U_{DC}/2$	$U_{DC}/2$	$U_{DC}/2$
⑤	t_5	$-U_{DC}/6$	$-U_{DC}/2$	$-U_{DC}/2$	$U_{DC}/2$
⑥	t_6	$U_{DC}/6$	$U_{DC}/2$	$-U_{DC}/2$	$U_{DC}/2$
⑦	t_7	$U_{DC}/2$	$U_{DC}/2$	$U_{DC}/2$	$U_{DC}/2$

Fig. A.21.: Discrete voltage space vectors of the eight switching states ⓪, ..., ⑦ for the SV-PWM in the complex stator-fixed α-β-reference frame and related star point potential φ_N and motor terminal potentials φ_U, φ_V, φ_W

erally, a 2-level voltage source inverter is considered. The explanations are based on [159, 6].

Note that for combined windings – and also for the *LLM4* – due to the asymmetric 3-phase current systems A and B also the orbits of the voltage space vectors $\underline{u}_{\alpha,\beta,\mathrm{A}}$ and $\underline{u}_{\alpha,\beta,\mathrm{B}}$ are elliptical. Thus, the main axes of the ellipses determine the inverter voltage rating. These main axes are determined by the algebraic sum of the required drive voltage space vector length $\underline{u}_{\alpha\beta,\mathrm{D}}$ and suspension voltage space vector length $\underline{u}_{\alpha\beta,\mathrm{L}}$. However, since the $2p$-pole rotor field does not induce into the imaginary $2p_{\mathrm{L}}$-pole suspension winding, the voltage drop of the suspension winding is small in stationary conditions. For this reason, the voltage space vector orbits of $\underline{u}_{\alpha,\beta,\mathrm{A}}$ and $\underline{u}_{\alpha,\beta,\mathrm{B}}$ are only slightly elliptical, so that mainly the back-EMF of the $2p$-pole rotor field determines the inverter voltage rating as in common rotating field high-speed machines.

The inverter states ⓪, ..., ⑦ and the related phase terminal electric potentials φ_{U}, φ_{V} and φ_{W} are listed in Fig. A.21 together with the star point potential φ_{N}. As the voltage space vector moves through the sectors I, ..., VI (Fig. A.21), the inverter switching states are realized for a calculated time t_0, ..., t_7. Since the inverter states ⓪ and ⑦ yield a zero phase voltage output, they are called "passive" voltage instants, whereas the remaining states are called "active" voltage vectors. The position of the voltage space vector is sampled within the switching period T_{sw}. Within this period four different states are applied. Every switching period starts and ends with a "passive" voltage vector. The voltage space vector in the α-β-reference frame is transferred into the α_{60}-β_{60}-coordinate system, which is related to the discrete voltage vectors of switching instant 1 and 2 (Fig. A.22). A voltage space vector in the other sectors II, ..., VI is transferred in analogy with the difference, that the α_{60}-β_{60} is rotated to coincide with the sector borders. Here, only the calculation for t_1 and t_2 is shown, where $t_1 \propto u_{\alpha,60,\mathrm{ref}}$ and $t_2 \propto u_{\beta,60,\mathrm{ref}}$ are calculated in every switching period according to (A.26). This way, the length of the inverter switching states is calculated.

$$t_1 = T_{\mathrm{sw}} \cdot \frac{3 \cdot u_{\alpha,60,\mathrm{ref}}}{2 \cdot U_{\mathrm{DC}}} \quad t_2 = T_{\mathrm{sw}} \cdot \frac{3 \cdot u_{\beta,60,\mathrm{ref}}}{2 \cdot U_{\mathrm{DC}}}, \tag{A.26}$$

$$\text{where } u_{\alpha,60,\mathrm{ref}} = u_{\alpha,\mathrm{ref}} - \frac{u_{\beta,\mathrm{ref}}}{\sqrt{3}},\ u_{\beta,60,\mathrm{ref}} = \frac{2 \cdot u_{\beta,\mathrm{ref}}}{\sqrt{3}}$$

For the symmetrical space vector modulation, the remaining time span $t_{\mathrm{pas}} = t_0 + t_7$ which is complementary to $t_{\mathrm{act}} = t_1 + t_2$ is divided into two equal time spans t_0 and t_7 according to (A.27). Often the time spans t_i are referred to as duty states d_i in relation to the switching

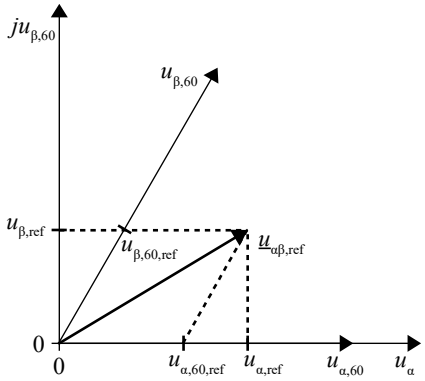

Fig. A.22.: Coordinate transformation for the switching instant calculation

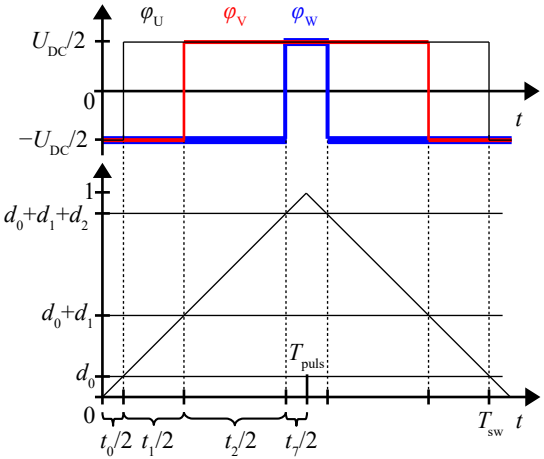

Fig. A.23.: Pulse pattern for a symmetrical space vector modulation (here: $d_0 = d_7 = 0.1$; $d_1 = 0.3; d_2 = 0.5$)

period T_{sw} (A.28). This can be illustrated, e.g. for a symmetrical space vector modulation as in Fig. A.23. When the value d_i is smaller than the triangular reference signal, the upper power switches of the according phases are conducting.

$$t_0 = t_7 = \frac{t_{pas}}{2}, \text{ where } t_{pas} = T_{sw} - t_1 - t_2 = T_{sw} - t_{act} \tag{A.27}$$

$$d_i = \frac{t_i}{T_{\mathrm{sw}}}, \text{ where } i \in \{0,1,...,7\},\ d_i \in [0;1] \tag{A.28}$$

A.24. Measuring Equipment

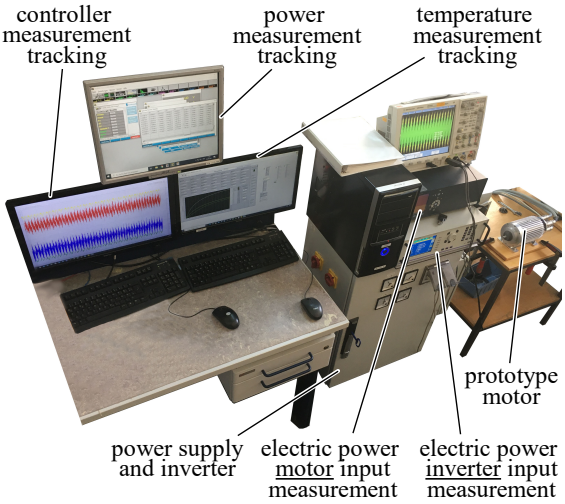

Fig. A.24.: Test bench for the power measurements at the prototype motor *LLM4*

Table A.10.: Technical data of the *Norma* Power Analyzer

Model	*5000, PP50*
Bandwidth	10 MHz
Sampling rate	1024 kHz
Number of measurement channels	6
Maximum voltage range	1000 V RMS
Maximum current range (internal shunts)	10 A RMS
Input impedance	2 MΩ / 20 pF
Accuracy referred to range (10 ... 1000 Hz, internal shunts)	±0.05%
Accuracy referred to range (1 ... 10 kHz, internal shunts)	±0.2%
Accuracy referred to range (10 ... 100 kHz, internal shunts)	±0.4%

Table A.11.: Technical data of the *Zimmer* Power Analyzer

Model	*LMG500*
Bandwidth	3 MHz
Sampling rate	1024 kHz
Number of measurement channels	6
Maximum voltage range	1000 V RMS
Maximum current range (internal shunts)	32 A RMS
Input impedance	4.59 MΩ / 3 pF
Accuracy referred to range (DC, internal shunts)	±0.06%
Accuracy referred to range (< 3 kHz, internal shunts)	±0.03%
Accuracy referred to range (3 ... 15 kHz, internal shunts)	±0.2%
Accuracy referred to range (15 ... 100 kHz, internal shunts)	±0.6%

Table A.12.: Technical data of the *Agilent Technologies* Oscilloscope

Model	*InfiniiVision DSO7034B*
Bandwidth	350 MHz
Sampling rate	2 GHz
Number of measurement channels	4
Memory depth	8 Mpts
Input impedance	50 Ω / 1 MΩ

Table A.13.: Technical data of the *Tektronix* differential voltage probe

Model	*P5200A*
Bandwidth	50 MHz
Maximum differential voltage range	1300 V RMS
Differential input impedance	10 MΩ / 2 pF
Cable length	1.8 m

Table A.14.: Technical data of the *IWATSU* current probe

Model	*SS-250*
Bandwidth	100 MHz
Number of measurement channels	6
Maximum current range	30 A RMS
Output sensitivity	0.1 V/A
Accuracy referred to reading	±1.0%
Cable length	1.5 m

Curriculum Vitae

Persönliche Daten

Daniel Dietz

geboren am 27.12.1990 in Limburg an der Lahn, verheiratet, ein Kind

Beruflicher Werdegang

seit 11/2021	ebm-papst Mulfingen GmbH & Co. KG, Mulfingen Gruppenleiter Basisentwicklung Motortechnik
11/2016 – 10/2021	Institut für Elektrische Energiewandlung, TU Darmstadt Wissenschaftlicher Mitarbeiter
10/2015 – 04/2016	Brose North America, Inc., Detroit Praktikum Entwicklung Fensterhebermotoren
04/2013 – 09/2013	Continental Brasil Indústria Automotiva, Ltda., Sao Paulo / Contintental Mabor – Indústria de Pneus, S.A., Porto Praktikum Controlling
10/2010 – 09/2015	Continental Teves AG & Co. oHG Werksstudent Entwicklung elektromechanische Fahrzeugbremse

Ausbildung

10/2014 – 10/2016	Master of Science: Wirtschaftsingenieurwesen mit Fachrichtung Elektrotechnik, TU Darmstadt
10/2010 – 10/2014	Bachelor of Science: Wirtschaftsingenieurwesen mit Fachrichtung Elektrotechnik, TU Darmstadt
09/2001 – 06/2010	Tilemannschule Limburg (altsprachliches Gymnasium)
09/1997 – 07/2001	Freiherr-vom-Stein-Schule Hünfelden

Darmstadt, den 14.09.2021